PHYS

VOLUME 34

Information for Contributors

Manuscripts

Send manuscripts to the Editor, Brookhaven National Laboratory, Long Island, New York.

Each article submitted will in general consist of (a) textual material, (b) material which is to be set in type, and (c) drawings or photographs from which zinc or copper halftones will be made. The textual material will consist of an abstract, the body of the paper, tabular material, references, and figure captions. All of this material must be double spaced, typewritten (except mathematical symbols) double spaced with wide margins (for instructions to the printer) on a durable white paper, preferably letter size. The original copy, not the carbon, should be submitted.

For general style, spelling, abbreviations, and form, recent issues of the Journal should be consulted.

The prime requisite is that the copy shall be clear to the typesetter, who is neither a physicist nor a mathematician.

Abstracts

An abstract must accompany each article. It should be adequate as an index and as a summary. As an index, it should give all subjects, major and minor, concerning which new information is presented. As a summary it should give the conclusions of the paper and all numerical results of general interest.

Mathematical Expressions

All but the simplest mathematical expressions should be carefully printed in by hand. Be sure to distinguish between capital and small letters. Indicate clearly superscripts and subscripts by inverted carets and caret respectively. Avoid complicated superscripts and subscripts. Avoid repetition of a complicated expression by representing it by some convenient symbol. Identify in the margin Greek letters and unusual symbols. Use fractional exponents instead of root signs. Use the solidus (/) for fractions wherever its use will save vertical space.

References

References should appear as footnotes, numbered consecutively, and arranged thus:

[1] A. B. Smith, Phys. Rev. [vol.] (1933).
[2] H. Lamb, *Hydrodynamics* (Cambridge University Press, Teddington, England, 1945), 6th ed., pp. 573, 603.

Tables

All but the simplest tabular material should be organized in tabular form rather than as a part of the running text. Tables may be typewritten on sheets separate from the text with indications in the margin of the text where the table is to be inserted. Each table should have a caption which will make the data in the table intelligible without reference to the text. Avoid complicated column headings; if necessary, use symbols which are explained in the table caption.

Figures

Wherever possible figures should be planned for the width of a column of the *Physical Review* (3 inches). A convenient reduction ratio is about 2:1 or 3:1. The original drawings or photographs should therefore be in general about 6 to 9 inches wide and the lettering and symbols should be large enough on the original that when reduced they shall not be less than about $\frac{1}{32}$ in. (~1 mm). If the reduction is 3:1, the original lettering should be not less than $\frac{1}{16}$ in. high.

The process of making zinc etchings or copper halftones is a black and white photographic one. Therefore line drawings must be in black ink on white paper or tracing cloth. Coordinate paper is not desirable but if used must be blue lined and the coordinate lines which are to show must be inked over.

Photographs should have maximum black and white contrast.

Plan figures to use space efficiently. Avoid wasting space, particularly at the top or bottom.

Identify on the black or other suitable place on each original drawing or photograph with the author's name and the figure number. Figures should be numbered consecutively and their approximate position indicated in the margin of the running text. Figure captions should be typed and included with the manuscript (not as part of the figure).

Avoid round and oval photographs.

Alterations

Take great care that each manuscript is typographically accurate. A limited number of alterations in proof are unavoidable, but the cost of making extensive alterations after the article has been set in type will be charged to the author.

Proof and all correspondence concerning papers in the process of publication should be addressed to the Publication Manager, American Institute of Physics, 57 East 55 Street, New York 22, New York.

THE PHYSICAL REVIEW

A journal of experimental and theoretical physics established by E. L. Nichols in 1893

VOLUME 84

Second Series

OCTOBER 1–DECEMBER 15, 1951

Published for the

AMERICAN PHYSICAL SOCIETY

by the

AMERICAN INSTITUTE OF PHYSICS

Incorporated

THE PHYSICAL REVIEW

A journal of experimental and theoretical physics established by E. L. Nichols in 1893

Published by the American Institute of Physics for the

AMERICAN PHYSICAL SOCIETY

Officers

President

C. C. LAURITSEN
California Institute of Technology
Pasadena, California

Vice-President

J. H. VAN VLECK
Harvard University
Cambridge, Massachusetts

Secretary

K. K. DARROW
Bell Telephone Laboratories
Office:
Columbia University
New York 27, New York

Treasurer

G. B. PEGRAM
Columbia University
New York 27, New York

Local Secretary for the Pacific Coast

J. KAPLAN
University of California at Los Angeles
Los Angeles, California

Managing Editor

S. A. GOUDSMIT
Brookhaven National Laboratory
Upton, Long Island
New York

BOARD OF EDITORS

Editor

S. A. GOUDSMIT

Assistant Editor

S. PASTERNACK

Associate Editors

J. BARDEEN	HARVEY BROOKS	M. GOLDHABER
T. BONNER	R. F. CHRISTY	R. HOFSTADTER
R. G. HERB	C. L. CRITCHFIELD	A. W. LAWSON
W. E. LAMB, JR.	M. DEUTSCH	A. PAIS
A. J. F. SIEGERT	T. H. JOHNSON	R. SERBER
W. E. STEPHENS	BRUNO ROSSI	C. H. TOWNES

Manuscripts for publication should be submitted to S. A. GOUDSMIT, Brookhaven National Laboratory, Upton, Long Island, New York. The authors' institutions are requested to pay a publication charge of $8 per page which, if honored, entitles them to 100 free reprints. Instructions will be sent with galley proofs.

Proof and all correspondence concerning papers in the process of publication should be addressed to the Publication Manager, American Institute of Physics, 57 East 55 Street, New York 22, New York.

Subscription Price

United States and Canada $25.00
Elsewhere $27.00

Back Numbers [1]

Yearly back number rate when complete year is available:
Prior to 1949: **$20.00**
Thereafter: **$27.00**
Single copies: **$2.00** each, prior to July, 1929;
$1.00 each, July, 1929–December, 1941;
$2.00 each, January, 1942–December, 1946;
$1.00 each, January, 1947–December, 1948;
$1.25 each, thereafter.
General index, 1893–1920: **$4.00**.

Subscriptions, renewals, and orders for back numbers should be addressed to the American Institute of Physics, 57 East 55 Street, New York 22, New York.

Changes of address in the case of members of the American Physical Society should be addressed to the Treasurer; in the case of other subscribers to the American Institute of Physics.

[1] For Series I inquire of Physics Department, Cornell University, Ithaca, New York.

The Physical Review is published semi-monthly at Prince and Lemon Streets, Lancaster, Pennsylvania.

Entered as second-class matter March 6, 1947, at the Post Office at Lancaster, Pennsylvania, under the Act of March 3, 1879.

Acceptance for mailing at special rate of postage provided for in paragraph (d-2), section 34.40, P. L. & R. of 1948, authorized January 27, 1933.

THE
PHYSICAL REVIEW

A journal of experimental and theoretical physics established by E. L. Nichols in 1893

SECOND SERIES, VOL. 84, NO. 1 OCTOBER 1, 1951

Nonlinear Meson Theory of Nuclear Forces. I. Neutral Scalar Mesons with Point-Contact Repulsion

L. I. SCHIFF*
Stanford University, Stanford, California
(Received June 22, 1951)

This paper develops an attempt to account for nuclear saturation and shell structure in terms of many-body forces that are derived from mesons that obey a nonlinear wave equation. Classical field theory is used, and in some cases the practical difficulties of obtaining numerical answers are reduced by employing a variation method. Apart from a cutoff, which appears in this particular form of the theory but could be eliminated, there are two parameters in the theory; they can be chosen so that nuclear matter has a stable density equal to the observed value, and a variational binding energy equal to 42 percent of the observed value, thus approximately accounting for saturation. The two-nucleon interaction has the observed order of magnitude in empty space, and is greatly reduced within nuclei. This suppression of two-body interactions in favor of the interaction of each nucleon with the average nucleon density in heavy nuclei may account for the independent-particle model and hence for shell structure. Although the theory does not account for magnetic moments, it indicates that a more realistic version (for example, a nonlinear pseudoscalar theory) may predict a reduction of the anomalous magnetic moments of nucleons within nuclei. According to a recent suggestion of Bloch, this could account for the deviations of the magnetic moments of even-odd nuclei from the Schmidt lines. The nonlinearity also has the consequence that mesons are scattered from nuclei as though by a strong repulsive potential. The relation of this effect to current observations on interactions between mesons and nuclei is briefly discussed.

I. INTRODUCTION

ONE of the most fundamental and least understood properties of atomic nuclei is saturation: the close proportionality of nuclear volume and binding energy with mass number. Attempts to account for saturation in terms of two-body interactions between nucleons have taken two directions. In his first paper on the neutron-proton structure of nuclei, Heisenberg[1] proposed that sufficient exchange forces be introduced to account for saturation, and this idea has since been followed up extensively. Within the last few years, however, experiments on the scattering of high energy neutrons and protons, mainly at Berkeley,[2] have indicated quite definitely that the actual two-body exchange forces do not supply enough repulsive interaction to prevent the collapse of heavy nuclei. The second attempt to account for saturation assumed that the two-body interaction consists of a central repulsive core surrounded by an attractive region.[3] Quantitative investigation showed that a repulsive core of sufficient diameter to yield the observed density of heavy nuclei would lead to disagreement with the experimental data on two-nucleon scattering.[4] There now appears to be general acceptance of the idea that an explanation of saturation will require the introduction of many-body forces between nucleons, in which case the potential energy of a given configuration of nuclear matter will not be determined unambiguously by the known two-body forces.

A second important property of nuclei that is not

* Assisted in part by the joint program of the ONR and AEC.
[1] W. Heisenberg, Z. Physik **77**, 1 (1932).
[2] See, for example, the nearly symmetric neutron-proton scattering curve obtained by R. Wallace, Phys. Rev. **81**, 493 (1951), and earlier papers cited there, which implies little or no interaction in odd l states (Serber force).
[3] H. A. Bethe and R. F. Bacher, Revs. Modern Phys. **8**, 161 (1936); H. A. Bethe, *Elementary Nuclear Theory* (John Wiley and Sons, Inc., New York, 1947), p. 81.
[4] G. Parzen and L. I. Schiff, Phys. Rev. **74**, 1564 (1948). This question has recently been re-examined by R. Jastrow, Phys. Rev. **81**, 165 (1951). His conclusion that a large enough repulsive core in the singlet neutron-proton interaction could lead to saturation, cannot be accepted, since the most stable configuration of a heavy nucleus would then be a collapsed state with parallel spins (all triplet interactions); the repulsive core in the triplet interaction is much smaller if it exists at all.

now adequately understood is the shell structure.[5] While much attention has been devoted to the details of coupling schemes that lead to particular sets of magic numbers, no quantitative study has been made of the validity of the independent-nucleon model on which these coupling schemes are based. Indeed, it appears at first that the strong, short-range two-body interactions that are known to exist between pairs of isolated nucleons would make the state of any one nucleon in a nucleus dependent mainly on the motions of its neighbors of the moment, and thus prevent the existence of the one-body potential which seems essential to shell structure. However, Wigner[6] has pointed out that for sufficiently short-range two-body interactions, a nucleon may not be able to follow the rapid variations in potential that are produced by the motions of its neighbors, and hence would behave as though it were in a smoothed-out version of the actual potential. Alternatively, it has been suggested that the disturbing effects of the short-range interactions on the motion of a nucleon may be suppressed by the exclusion principle, which makes it difficult for a nucleon to change its state when neighboring states are occupied. This idea, formulated most explicitly by Weisskopf,[7] leads in the direction of the independent-nucleon model for the lowest excited states of nuclei, and perhaps also toward the liquid-drop model for the highly excited states that follow nucleon capture. Neither of these proposed explanations for the independent-nucleon model seems to have been developed quantitatively thus far.

The present series of papers presents an attempt to account for both saturation and the independent-nucleon model in terms of a particular type of many-body force. In this theory the interactions between nucleons arise from mesons which obey a nonlinear wave equation.[8] Some insight into the consequences of such a model can be obtained from a preliminary qualitative discussion based on a classical treatment of the meson field in which the nucleons act as sources. In the usual linear theory, the meson field amplitude is proportional to the nucleon source strength. Meson fields are then superposable, and the interaction energy between a number of nucleons is equal to the sum of the pair interactions. In the present theory, the nonlinearity is chosen in such a way that the meson field amplitude increases less rapidly than linearly with the nucleon source strength. Then the change in meson amplitude produced by the addition of a nucleon is less when many nucleons are already present than when few are present, and the interaction energy between a number of nearby nucleons is less than the sum of the pair interactions. This is just the sort of effect needed to account for saturation; a stable density for very heavy nuclei will be obtained if the (attractive) potential energy per nucleon increases less rapidly than the $\frac{4}{3}$ power of the density for high densities. By the same token, the interaction between a pair of nucleons when they are embedded in a heavy nucleus (as distinguished from the interaction of each with the surrounding nuclear matter) is less than when they are in empty space. This suppression of two-body interactions within a nucleus in favor of the interaction of each nucleon with the average nucleon density, means that the nonlinearity acts as a smoothing mechanism and hence leads in the direction of the one-body potential and shell structure.[9]

These papers develop two ways in which a nonlinearity can be introduced into the usual meson theory of nuclear forces: in those terms that involve only the meson field and in those terms that represent the coupling between mesons and nucleons. A third possibility, placing the nonlinearity in the purely nucleonic terms, leads to meson-independent interactions between nucleons, and will not be pursued further here.[10] In the first case, results that are interesting from the present point of view are obtained if the nonlinearity corresponds to a repulsion between mesons. The appearance of a nonlinear term in the source-free meson equation means that it is very difficult to work with the corresponding quantum field theory. While quantization can be carried through in the usual way, it is not clear that the procedure is self-consistent, and the field energy cannot be diagonalized easily, if at all, even in the absence of nucleons. The nonlinearity can of course be treated as a perturbation, but this is a useful procedure only in special cases (see Secs. III and XI), and throws little light on the more general quantization problem. Therefore, classical field theory will be used throughout; since the field amplitudes in nuclear matter turn out to be large and the mesons obey Einstein-Bose statistics, the use of classical field theory may actually be a fairly good approximation within nuclei. In the second case, the source-free meson equation is the usual one, and can be quantized by standard methods.

The present paper deals with the first case, in which the nonlinearity is in the meson field itself. This nonlinearity can take many forms. Most of this paper is devoted to the neutral scalar meson theory in which the nonlinearity corresponds to a point-contact repulsion between mesons.[8] A positive term proportional to ϕ^4 must be added to the hamiltonian density, or a ϕ^3 term to the wave equation, where ϕ is the meson field amplitude. While this seems a simple and natural form

[5] M. G. Mayer, Phys. Rev. **78**, 16 (1950), and earlier papers cited there.

[6] E. P. Wigner (private communication).

[7] V. Weisskopf, Science **113**, 101 (1951); see also H. Kopferman, Naturwiss. **38**, 29 (1951).

[8] L. I. Schiff, Phys. Rev. **80**, 137 (1950); Phys. Rev. **83**, 239 (1951).

[9] This possible relation between nonlinear meson theory and the saturation and shell structure of nuclei occurred independently to E. Teller (private communication). Similar nonlinearities have been introduced into the theory for different purposes by W. Heisenberg, Z. Naturforsch. **5a**, 251 (1950); and R. Finkelstein and M. Ruderman, Phys. Rev. **81**, 655 (1951).

[10] Terms of this last type also arise if the meson field is eliminated from the usual classical meson-nucleon equations; see S. D. Drell, Phys. Rev. **79**, 220 (1950).

to use, it brings a serious problem into the analysis and the interpretation of the formalism. Because of this difficulty, as many results as possible are established using a general form of nonlinearity, and the specialization to the foregoing form postponed as long as can conveniently be done. The second paper of this series, immediately following,[11] deals with the second case, in which the nonlinearity is put in the meson-nucleon coupling.[12] Since the results obtained there on the basis of classical field theory are unpromising from the point of view of explaining saturation and shell structure, it is not now planned to carry that line of approach further. It is, however, hoped that one or more further papers in this series will deal with other types of mesons and other forms of field nonlinearities, and perhaps also with the problem of quantization. In particular, a form of nonlinearity proposed by Teller[13] (see Eq. (7) and Sec. VI) avoids the difficulty referred to above, although it seems intuitively less natural.

The theory presented here must be regarded as no more than a model for what may eventually turn out to be a reasonably complete meson theory of nuclear forces and structure. The primary objective now is to lay the basis for forming an opinion as to whether or not the general ideas presented here have any relation to reality. For such an exploratory purpose, it seems best to make an inherently difficult analytical development as simple as possible, even at the expense of realism. This relative simplicity is achieved first by using only classical field theory, and second by choosing the mesons to be of the neutral scalar type. It is apparent, then, that results in quantitative agreement with experiment cannot be expected and that such phenomena as exchange forces and anomalous nucleon magnetic moments will not appear at all as consequences of the theory. Nevertheless, a qualitative inference concerning the latter is presented in Sec. X.

II. FORMULATION OF THE THEORY

We choose units such that c, $\hbar$, and the meson mass μ are equal to unity. Then all lengths are measured in units of the meson Compton wavelength $\hbar/\mu c$ ($=1.40\times10^{-13}$ cm for heavy or π-mesons), and all energies are measured in units of the meson rest energy μc^2 ($=140$ Mev). The lagrangian density is assumed to have the form,

$$\mathrm{L}=\tfrac{1}{2}(\partial\phi/\partial t)^2-\tfrac{1}{2}(\nabla\phi)^2-G(\phi)+f(\mathbf{r},t)F(\phi), \quad (1)$$

where $f(\mathbf{r},t)$ is the nucleon source density, $F(\phi)$ the nonlinear coupling function, and $G(\phi)$ the nonlinear field function. In the usual linear theory,

$$F(\phi)=\phi, \quad G(\phi)=\tfrac{1}{2}\phi^2. \quad (2)$$

We shall assume that F and G approach the forms (2) when ϕ is small, so that for weak fields the nonlinear theory becomes the usual one. The momentum canonically conjugate to ϕ is $\pi=\partial\phi/\partial t$, the hamiltonian or energy density is

$$\mathrm{H}=\tfrac{1}{2}\pi^2+\tfrac{1}{2}(\nabla\phi)^2+G(\phi)-f(\mathbf{r},t)F(\phi), \quad (3)$$

and the wave equation is

$$\partial^2\phi/\partial t^2=\nabla^2\phi-G'(\phi)+f(\mathbf{r},t)F'(\phi), \quad (4)$$

where a prime denotes a derivative with respect to ϕ.

Some indication as to useful assumptions concerning the forms of F and G can be obtained by considering the case in which $f(\mathbf{r},t)$ is constant in space and time. This may be thought of as an approximation to the situation in the interior of a heavy nucleus. Then ϕ is also constant, and the wave equation (4) becomes

$$G'(\phi)=fF'(\phi), \quad (5)$$

where f is proportional to the nucleon density. If now ϕ is to increase less rapidly than linearly with f (see Sec. I), the ratio G'/F' must increase more rapidly than linearly with ϕ. In the remainder of this paper we assume the form (2) for F, and therefore assume also that G increases more rapidly than $\frac{1}{2}\phi^2$. Similarly, in II we assume the form (2) for G, and also that F increases less rapidly than ϕ.

With $F(\phi)=\phi$, Eq. (5) becomes $G'(\phi)=f$. It seems plausible to require that there be a unique relation between f and ϕ that has no preference as to sign. We therefore assume that G is a positive even function of ϕ that increases monotonically more rapidly than $\frac{1}{2}\phi^2$. Equation (3) gives for the energy density in this case $G-f\phi$, so that the energy per nucleon is proportional to $(G/f)-\phi$. Suppose now that for high nucleon density, when f and ϕ are large, G is proportional to ϕ^n, where $n>2$. Then the energy per nucleon is negative and proportional to $f^{1/(n-1)}$. Since this energy is the average potential energy of a nucleon, and its kinetic energy increases with nucleon density as $f^{\frac{1}{3}}$, the heavy nuclear system fails to collapse in this approximation if and only if $1/(n-1)<\frac{2}{3}$, or $n>5/2$.

Wherever detailed calculations are made in this paper, it is assumed that

$$G(\phi)=\tfrac{1}{2}\phi^2+\tfrac{1}{4}\alpha^2\phi^4, \quad (6)$$

where α is a constant to be determined later by comparison with experiment; this corresponds to $n=4$. Physically, the first term on the right side of Eq. (6) is the rest mass term in the usual linear theory; the second term is equivalent to a point-contact repulsion between mesons, since its space integral can be written

$$\int\phi^4 d\tau=\int\int\phi^2(\mathbf{r})\delta(\mathbf{r}-\mathbf{r}')\phi^2(\mathbf{r}')d\tau d\tau'.$$

As an alternative to Eq. (6), Teller[13] has suggested the form,

$$G(\phi)=(1/n\alpha^2)[(1+\alpha^2\phi^2)^{n/2}-1], \quad (7)$$

[11] L. I. Schiff, Phys. Rev. **84**, 10 (1951), referred to here as II.
[12] This form of the theory was suggested to the writer by F. Bloch.
[13] E. Teller (private communication).

which has less intuitive appeal but greater flexibility than (6). We shall return briefly to Eq. (7) in Sec. VI.

III. FREE-MESON SOLUTIONS

In the absence of sources ($f=0$), Eq. (4) has solutions in the form of traveling plane waves that approach the usual harmonic plane waves in the weak field limit. To see this, we call the direction of propagation the x axis, and the wave speed v (measured in units of the speed of light). Then

$$\phi(\mathbf{r}, t)=h(x-vt),$$

and h satisfies the equation,

$$(v^2-1)h''=-G'(h), \tag{8}$$

where a prime denotes differentiation with respect to the argument. Since $G'(h)$ has the same sign as h (see Sec. II), Eq. (8) has oscillatory solutions if and only if $v>1$. A first integral of Eq. (8) is easily obtained after both sides are multiplied by h':

$$\tfrac{1}{2}(v^2-1)h'^2=-G(h)+\text{constant}. \tag{9}$$

It is apparent from Eq. (9) that the constant of integration must be sufficiently positive if there is to be a real solution; further examination shows that for given v, the wavelength and period decrease as the wave amplitude increases, and that the form is more sharply peaked than a sinusoidal wave. When G has the form (6), h is an elliptic integral of the first kind.

For infinitesimal amplitudes, these plane wave solutions can be superposed to form wave packets that travel with the group speed $1/v$, as in the usual linear theory. When the amplitude is small but finite, the nonlinear term is relatively small. Then quantization can be carried through in the usual way, and the nonlinearity taken into account as a perturbation if need be. This is actually a physically interesting situation when we think of the free meson beams that are attainable in the laboratory, as we now show.

We tentatively assume that the linear theory provides a useful approximation in this case, so we can put

$$\phi(\mathbf{r}, t)=A\cos(\mathbf{k}\cdot\mathbf{r}-\omega t),$$

for a meson beam of momentum $\mathbf{k}$ and energy $\omega=(\mathbf{k}^2+1)^{\frac{1}{2}}$. Setting $f=0$ and $G=\frac{1}{2}\phi^2$ in Eq. (3) shows that the average energy density is $\frac{1}{2}A^2\omega^2$, so that the number of mesons per unit volume is $\frac{1}{2}A^2\omega$. A very intense meson beam (probably unattainable in the laboratory) would consist of a burst of 10^{10} mesons in a microsecond pulse, confined to a beam of one square millimeter cross section and traveling with a third the speed of light. This corresponds to a density of about 3×10^{-31} meson per Compton wavelength cubed, or an A value of about 8×10^{-16}. If now the nonlinearity is to be significant for nuclear structure, where the linear dimensions and energies involved are of order one when expressed in our units, the nonlinear term should only become important when ϕ is of order one. This expectation is confirmed by the quantitative results of Sec. VII. Thus for attainable free meson densities, the present theory is equivalent to the usual linear theory.

IV. STABILITY OF STATIC SOLUTIONS

Because of the impossibility of separating out the time, static solutions of the wave Eq. (4) that arise from stationary source distributions $f(\mathbf{r})$ are of unusual importance and form the subject matter of the next six sections, where they are used to calculate the energies of various configurations of nucleons. It is of interest, therefore, to see whether or not such solutions are stable in time with respect to small deviations.[14]

Let $\phi_0(\mathbf{r})$ be that solution of the wave equation,

$$\nabla^2\phi_0-G'(\phi_0)+f(\mathbf{r})=0, \tag{10}$$

which obeys suitable boundary conditions.

Then if $\phi_0(\mathbf{r})$ is changed into $\phi_0(\mathbf{r})+\phi_1(\mathbf{r}, t)$, where $\phi_1\ll\phi_0$, we ask whether ϕ_1 is oscillatory in time (stable) or increases (unstable). From Eq. (4) with $F'=1$, we see that ϕ_1 approximately satisfies the linear equation,

$$\partial^2\phi_1/\partial t^2=\nabla^2\phi_1-\phi_1G''(\phi_0), \tag{11}$$

where use has been made of Eq. (10) and higher powers of ϕ_1 have been neglected. Now the assumptions concerning the form of $G(\phi)$ made in Sec. II are consistent with $G''(\phi)$ being everywhere positive, and we suppose that this is always the case, as it is for both of the forms (6) and (7). Moreover, $G''(\phi_0)$ is expected to be of order one in the neighborhood of a source, where ϕ_0 is appreciable (see the end of Sec. III). Thus unless ϕ_1 is very irregular, so that $\nabla^2\phi_1/\phi_1$ is comparable with $G''(\phi_0)$, Eq. (11) shows that $\partial^2\phi_1/\partial t^2$ has the opposite sign from ϕ_1, and the solution ϕ_0 is stable. In any event, further study of the time dependence of $\int\phi_1 d\tau$ over various regions of space shows that any instability due to the largeness of $\nabla^2\phi_1/\phi_1$ is likely to be limited both in space and in time.

V. VARIATION PRINCIPLE FOR STATIC SOLUTIONS

Because of the great difficulty in solving nonlinear differential equations in all but the simplest cases, it is important to have a variation principle available for the estimation of the energies associated with various source distributions. We now show that in the static case, the negative of the lagrangian, computed with the correct source function and an arbitrary trial wave function, gives an upper limit on the energy, and has a stationary value equal to the correct energy when the trial function is in the infinitesimal neighborhood of the correct wave function.

For the source function $f(\mathbf{r})$, the correct wave function $\phi_0(\mathbf{r})$ is a regular solution of the wave Eq. (10); the correct total energy is the integral of Eq. (3) and can

[14] The desirability of investigating this point was suggested to the writer by S. D. Drell.

be written in one of the equivalent forms:

$$H_0=\int[\tfrac{1}{2}(\nabla\phi_0)^2+G(\phi_0)-f(\mathbf{r})\phi_0]d\tau, \tag{12}$$

$$H_0=\int[-\tfrac{1}{2}(\nabla\phi_0)^2+G(\phi_0)-\phi_0G'(\phi_0)]d\tau, \tag{13}$$

$$H_0=\int[G(\phi_0)-\tfrac{1}{2}\phi_0G'(\phi_0)-\tfrac{1}{2}f(\mathbf{r})\phi_0]d\tau. \tag{14}$$

Equations (13) and (14) are obtained from Eq. (12) by use of the wave equation and partial integration, assuming that ϕ_0 obeys boundary conditions that make the resulting surface integral vanish. With the trial function $\phi^{(v)}(\mathbf{r})$, the variation expression is minus the integral of Eq. (1):

$$H^{(v)}=\int[\tfrac{1}{2}(\nabla\phi^{(v)})^2+G(\phi^{(v)})-f(\mathbf{r})\phi^{(v)}]d\tau. \tag{15}$$

We now put $\phi^{(v)}(\mathbf{r})=\phi_0(\mathbf{r})+\phi_1(\mathbf{r})$, where ϕ_1 is not necessarily small. Substitution into Eq. (15) yields, with the help of Eqs. (10) and (12) and partial integration,

$$H^{(v)}=H_0+\int[\tfrac{1}{2}(\nabla\phi_1)^2+G(\phi_0+\phi_1)-G(\phi_0)-\phi_1G'(\phi_0)]d\tau. \tag{16}$$

Now we have assumed that $G(\phi)$ is a positive, even, monotonic increasing function of ϕ that is everywhere concave upward ($G''(\phi)$ everywhere positive). Then $G(\phi_0)+\phi_1G'(\phi_0)$ regarded as a function of ϕ_1 is a straight line that is tangent to the curve $G(\phi_0+\phi_1)$ at the point $\phi_1=0$ and lies below it everywhere else. It follows that the integral on the right side of Eq. (16) is positive or zero, so that $H^{(v)}$ provides an upper limit on H_0. Moreover, $H^{(v)}=H_0$ if and only if ϕ_1 is everywhere zero so that $\phi^{(v)}=\phi_0$; $H^{(v)}$ differs from H_0 by terms of second order in ϕ_1 when ϕ_1 is small, so that $H^{(v)}$ is stationary when $\phi^{(v)}$ is in the infinitesimal neighborhood of ϕ_0. It is interesting to note that the assumed properties of the nonlinear function $G(\phi)$ are decisive in making $H^{(v)}$ an upper limit on H_0, although they do not affect the stationary character of $H^{(v)}$.

VI. SOLUTION FOR AN ISOLATED NUCLEON AT REST

It is interesting to inquire first whether there can be a regular, localized solution of Eq. (10) in the absence of sources ($f=0$). If we assume the solution to be spherically symmetric, it is convenient to put $\phi_0(\mathbf{r})=\chi(r)/r$, when $\chi(r)$ satisfies the equation,

$$d^2\chi/dr^2=rG'(\chi/r). \tag{17}$$

Now $G'(\chi/r)$ has the same sign as χ, so that $d^2\chi/dr^2$ also has the same sign as χ. This means that if χ vanishes at infinite distance and starts to increase as r decreases from infinity, it is always concave upward and continues to increase into the origin. Then $\chi(r)$ cannot be zero at $r=0$, and ϕ_0 is irregular at the origin. We therefore conclude that mesons cannot be permanently localized in the absence of sources. This result is a consequence of the assumed properties of $G(\phi)$, which correspond to a repulsion between mesons (this repulsion was pointed out explicitly in the discussion of Eq. (6), and follows whenever G increases more rapidly than ϕ^2). If G had been chosen to correspond to an attraction between mesons, regular localized solutions could exist, but the theory would not account for saturation.

We now consider the possibility that Eq. (10) has regular, localized solutions when $f(r)$ is a spherically symmetric source of arbitrarily small spatial extension (that is, approaching a point source). We suppose that $f(r)=0$ for $r>a$, so that Eq. (17) is valid in this region. Then $\chi(r)$ increases as r decreases, and reaches the value $\chi(a)$ at $r=a$. For $r<a$, Eq. (17) is replaced by

$$d^2\chi/dr^2=rG'(\chi/r)-rf(r). \tag{18}$$

If now $\chi(a)$ has the opposite sign from f, which is assumed for simplicity to have the same sign throughout the interior of the sphere $r=a$ (so that it approaches a simple or δ function point source), Eq. (18) shows that χ continues to increase into the origin, so that ϕ_0 is irregular there. We therefore consider only the case in which $\chi(a)$, and hence $\chi(r)$ for $r>a$, has the same sign as f. By a repetition of the same argument, ϕ_0 is irregular at the origin if χ changes sign between $r=a$ and $r=0$. Thus the only way in which a regular solution ϕ_0 can exist is for $\chi(r)$ to have the same sign everywhere and vanish at $r=0$.

We suppose without loss of generality that f and χ are everywhere positive. We then multiply Eq. (18) through by $4\pi r$, integrate over r, and obtain an expression for the total source strength:

$$g=4\pi\int_0^\infty r^2f(r)dr=4\pi\int_0^\infty r^2G'(\chi/r)dr-4\pi\int_0^\infty r(d^2\chi/dr^2)dr.$$

The last integral is easily evaluated, and vanishes if ϕ_0 is regular. We are interested in the point-source limit of vanishingly small a. Then since $\chi(r)$ becomes arbitrarily large as r becomes arbitrarily small (but greater than a), we choose a small enough so that there exists a fixed radius b greater than a for which $G'(\phi)$ has attained its asymptotic form $C\phi^{n-1}$ (see Sec. II). We can then obtain a lower limit for g:

$$g=4\pi\int_0^\infty r^2G'(\chi/r)dr\geqq4\pi\int_a^b r^2G'(\chi/r)dr$$

$$=4\pi C\int_a^b(\chi^{n-1}/r^{n-3})dr\geqq4\pi C\chi^{n-1}(b)\int_a^b dr/r^{n-3}.$$

The last integral converges in the limit $a\to 0$ if and only if $n-3<1$, or $n<4$. Thus for a simple or δ-function point source, the source strength g is infinite if $n\geqq 4$. We interpret this to mean that there is no admissible solution for a point source in this case.

It follows that for the $G(\phi)$ given by Eq. (6), a nucleon must be represented by a source of finite extent, so that the size and shape of the nucleon source appear in the theory as independently variable parameters, along with α and g. The number of the independent parameters that appear in the theory can be reduced by adopting the form (7) for $G(\phi)$, with $5/2<n<4$; with this range of n, the theory is expected to lead to saturation (see Sec. II) and nucleons can be represented by point sources. With such point interactions, there is also the hope of eventually developing a relativistically covariant quantum theory.

Since the use of Eq. (6) demands a nucleon of finite size, and there is no *a priori* preference as to shape, we choose an isolated nucleon source function for which the wave equation is easily solved, and which is as small in spatial extent as can conveniently be found. Such a source function can be constructed by choosing a suitable wave function $\phi_1(r)$, and using the wave equation,

$$\nabla^2\phi_1-\phi_1-\alpha^2\phi_1^3+f_1=0, \tag{19}$$

to determine the corresponding source $f_1(r)$. Our choice is

$$\phi_1(r)=\frac{A}{r}(e^{-r}-e^{-\gamma r}), \tag{20a}$$

$$f_1(r)=\frac{A}{r}(\gamma^2-1)e^{-\gamma r}+\frac{\alpha^2A^3}{r^3}(e^{-r}-e^{-\gamma r})^3, \tag{20b}$$

where γ is a parameter that is later allowed to approach infinity; in this limit:

$$\phi_1(r)\to(A/r)e^{-r}, \tag{21a}$$

$$f_1(r)\to 4\pi A\delta(r)+\frac{\alpha^2A^3}{r^3}e^{-3r}, \tag{21b}$$

so that f_1 consists of a point source surrounded by a quite small region in which the source strength is finite.[15]

This choice is convenient so far as the subsequent analysis and the smallness of the source are concerned. However, it is inconvenient as regards the fact that g becomes infinite as $\gamma\to\infty$, so that a cutoff is needed to keep the source strength finite. Since the analysis is simplified by taking the limit $\gamma\to\infty$, we evaluate g by choosing a radius equal to the Compton wavelength of the proton ($=0.150$ in our units), and arbitrarily replacing the second term on the right side of Eq. (21b) for all smaller radii by its value at $r=0.150$. This gives

$$\begin{aligned} g&=4\pi A+4\pi\alpha^2A^3[-\mathrm{Ei}(-0.450)+\tfrac{1}{3}e^{-0.150}]\\ &=4\pi A(1+0.837\alpha^2A^2). \end{aligned} \tag{22}$$

Since the actual divergence in g is only logarithmic, the precise nature of the cutoff is relatively unimportant. This is the only place in the theory at which a cutoff need be introduced, since while all energies diverge like γ for large γ, the divergent parts can be subtracted without ambiguity. The self-energy of the nucleon represented by Eqs. (20) can be found from Eqs. (12), (13), or (14); in the limit of large γ it becomes

$$\begin{aligned} H_1=-4\pi A^2\{&\tfrac{1}{4}\gamma-\tfrac{1}{2}+3\alpha^2A^2[\gamma\ln(32/27)\\ &-\ln(3\gamma/32)-1]\}. \end{aligned} \tag{23}$$

VII. MODEL FOR NUCLEAR MATTER

In order to investigate the predictions of the present theory with regard to the saturation of nuclei, it is desirable to choose as simple a model as possible. We consider a representative sample of the interior of a heavy nucleus, and regard this as typical of a large amount of nuclear matter, thus avoiding boundary effects. The binding energy per nucleon of this material is known experimentally to be about 14 Mev,[16] or 0.10 in our units. This value is the volume term in the mass defect; the neutron excess, coulomb, and surface terms are ignored here because we deal with an equal mixture of neutrons and uncharged protons, with no boundaries present. If we accept the experimental evidence for the independent-nucleon model, the kinetic energy per nucleon can be calculated on the basis of the Fermi gas model,[17] and is equal in our units to

$$\frac{3}{40}(9\pi)^{\frac{1}{3}}\frac{0.150}{r_0^2}=\frac{0.1046}{r_0^2}, \tag{24}$$

where 0.150 is the Compton wavelength of the proton and $4\pi r_0^3/3$ is the volume per nucleon. The problem then is to calculate the potential energy per nucleon, and show that as r_0 is varied, the sum of it and (24) has a minimum value equal to -0.10 when r_0 has its experimental value 1.0. Thus the two experimental parameters of nuclear density and binding energy per nucleon serve to determine the two parameters α and g, or α and A, of the theory, once the cut-off is introduced as in Sec. VI.

Two specific calculations of the potential energy are made in this section. The first is modeled after the discussion of Sec. II, according to which f and ϕ are assumed to have the constant values f_N and ϕ_N, related by the wave equation,

$$\phi_N+\alpha^2\phi_N^3=f_N. \tag{25}$$

[15] A larger and less singular source function has also been investigated by S. D. Drell (private communication), with results similar to those quoted in Sec. VII.

[16] L. Rosenfeld, *Nuclear Forces* (Interscience Publishers, Inc., New York, 1948), p. 24.

[17] L. Rosenfeld, see reference 16, p. 193.

We assume that all nucleons have the same sign of g, and that their sources superpose, so that

$$f_N=\frac{3g}{4\pi r_0^3}=\frac{3A}{r_0^3}(1+0.837\alpha^2A^2). \tag{26}$$

The potential energy per nucleon is then given by Eqs. (12), (13), or (14) when the integral is carried over the volume of one nucleon:

$$H_N=-\frac{4\pi r_0^3}{3}\left(\tfrac{1}{2}\phi_N^2+\frac{3\alpha^2}{4}\phi_N^4\right). \tag{27}$$

Elimination of f_N between Eqs. (25) and (26) gives a relation between ϕ_N and g or A; the sum of Eqs. (24) and (27) gives a relation between binding energy, r_0, and ϕ_N; and minimization of the binding energy with respect to r_0 gives a relation between r_0, ϕ_N, and g. All three of these relations involve α, so that when the experimental values of binding energy and r_0 are inserted into them, they can in principle be solved for the three unknowns α, ϕ_N, and g. Alternatively, if α and g are determined in some other way, the three relations can be solved for binding energy, r_0, and ϕ_N.

The second calculation of the potential energy per nucleon is somewhat more realistic. A nucleon with source distribution f_1 is embedded in nuclear matter represented by the constant source distribution f_N. The combined source distribution is assumed to be f_1+f_N, and the two terms are supposed to have the same sign (so that all nucleons are equivalent sources). The difference in energy between the combined source and the separated sources is then found. This calculation takes the independent-nucleon model quite literally, since it is assumed that there is no correlational change of f_N in the neighborhood of f_1; it is difficult to estimate the sign of this effect, although it does not seem to be large. The wave equation for the combined source cannot be solved analytically, and the variation principle of Sec. V is employed. This overestimates the potential energy, so that the calculated magnitude of the binding energy per nucleon is expected to be less than the experimental value.

The question immediately arises as to whether or not the terms proportional to γ and $\ln\gamma$ in the nucleon self energy expression (23) will cancel with the analogous terms in the energy of the combined source. This question can be answered by considering the exact solution of the wave equation,

$$\nabla^2\phi_{1N}-\phi_{1N}-\alpha^2\phi_{1N}^3+f_1+f_N=0,$$

in the neighborhood of the origin. With the substitution $\phi_{1N}=\chi(r)/r$, the equation becomes

$$\frac{d^2\chi}{dr^2}-\chi-\frac{\alpha^2\chi^3}{r^2}+rf_1+rf_N=0.$$

In the limit $\gamma\to\infty$, the δ-function in Eq. (21b) can be taken into account by requiring that $\chi(0)=A$. We have then to solve the equation,

$$\frac{d^2\chi}{dr^2}-\chi-\frac{\alpha^2\chi^3}{r^2}+\frac{\alpha^2A^3}{r^2}e^{-3r}+rf_N=0, \tag{28}$$

in the neighborhood of the origin; this can be done by using the power series:

$$\chi(r)=A[1+a_1r+a_2r^2+\cdots+r^s(b_0+b_1r+b_2r^2+\cdots)], \qquad s>0.$$

Substitution into Eq. (28) shows that $a_1=-1$, and that s satisfies the equation,

$$s(s-1)=3\alpha^2A^2;$$

this has just one positive root, and it is greater than unity. The quantity b_0 is arbitrary, and is to be chosen in such a way as to satisfy the boundary condition at infinity: $\chi(r)\to r\phi_N$. Thus the $1/r$ and constant terms in the series expansion of ϕ_{1N} are the same as for ϕ_1.

The cancellation of the infinite self-energy terms is now most easily seen by using Eq. (14), according to which

$$H_{1N}=-\int[\tfrac{1}{4}\alpha^2\phi_{1N}^4+\tfrac{1}{2}(f_1+f_N)\phi_{1N}]d\tau. \tag{29}$$

In the limit $\gamma\to\infty$, the infinite terms are of two types, proportional to γ and to $\ln\gamma$. The first type arises from integrals of the forms, $\int dr/r^2$ and $\int\delta(\mathbf{r})dr/r$; the second type arises from integrals of the form, $\int dr/r$. It is easily seen from Eqs. (21b) and (29) that all of these divergent integrals are exactly the same in the expressions for H_{1N} and for H_1, since they depend only on f_1 and on the $1/r$ and constant terms in ϕ_{1N} and ϕ_1. Thus the potential energy per nucleon is finite, and can be calculated by subtracting H_1 and H_N from H_{1N}, when the integrals for the latter two quantities are extended over equal large volumes of nuclear matter.

We now calculate H_{1N} by the variation method. A convenient trial function to use is

$$\phi_{1N}^{(v)}=\frac{A}{r}(e^{-\beta r}-e^{-\gamma r})+\phi_N, \tag{30}$$

where β is the variation parameter. It is apparent that unless $\beta=1+(\phi_N/A)$, the constant term in the series expansion of ϕ_{1N} is not the same as that for ϕ_1 in the limit $\gamma\to\infty$. It might be thought at first that this would make the calculated potential energy diverge like $\ln\gamma$; actually, because of the form of the variation integral (15), this is not the case, as is readily verified. On the other hand, if we were to replace A by A' and γ by γ' in Eq. (30), divergences would appear; indeed, it can be shown that the leading terms in the variational energy for large γ and γ' are minimized by setting $A'=A$ and $\gamma'=\gamma$, and that in this case the divergent terms cancel with those in H_1. We therefore use the

trial function (30), and find that the variation energy given by Eq. (15) yields for the potential energy per nucleon (in the limit $\gamma\to\infty$):

$$H_{1N}^{(v)}-H_1-H_N=4\pi\{\tfrac{1}{4}[A^2(\beta-1)^2/\beta]-A\phi_N+\alpha^2A^4[\beta\ln(4\beta)-(3+\beta)\ln(3+\beta)+6\ln 2]+(3\alpha^2A^3\phi_N^2/4\beta)-3\alpha^2A^3\phi_N\ln\beta\}. \quad (31)$$

As β is varied, the minimum value of Eq. (31) always occurs for $\beta>1$.

The minimum value of Eq. (31) is now used as the potential energy per nucleon to calculate the values of the theoretical parameters as outlined just below Eq. (27). If we assume $r_0=1.00$, we find that we cannot make the total (potential plus kinetic) energy per nucleon as low as -0.10. The lowest value obtained is -0.042, for which the theoretical parameters have the following values: $g=1.49$, $A=0.0854$, $\alpha=7.96$, $\phi_N=0.149$, $f_N=0.356$, $\beta=2.50$. It is of incidental interest to make use of these values for g and α, in connection with Eqs. (24), (25), (26), and (27), to calculate the potential and total energy by the somewhat cruder first method. It turns out that the total energy per nucleon is a minimum when $r_0=1.03$, and then has the value -0.020; the other parameters are: $\phi_N=0.143$, $f_N=0.324$. Note that either of these methods could be used to calculate the compressibility of nuclear matter.

When account is taken of the simplicity of the model (neutral scalar mesons, all nucleons equivalent), and of the use of the variation method, the foregoing results may be regarded as showing sufficient promise to warrant further development of the underlying theoretical ideas, as well as the further application of the present model that are presented in the next four sections.

VIII. TWO-NUCLEON INTERACTION IN EMPTY SPACE

The theoretical parameters obtained in the preceding section should be consistent with the known two-nucleon interactions. For this system, the source function is

$$f_2(\mathbf{r})=f_1(\mathbf{r}-\mathbf{r}_1)+f_1(\mathbf{r}-\mathbf{r}_2),$$

where f_1 is given by Eq. (20b), and $\mathbf{r}_1$ and $\mathbf{r}_2$ are the coordinates of the two nucleons. This again assumes that the sources are superposable and that all nucleons have the same sign of source. The variation method is used, and the trial function taken to be

$$\phi_2^{(v)}(\mathbf{r})=\phi_1(\mathbf{r}-\mathbf{r}_1)+\phi_1(\mathbf{r}-\mathbf{r}_2), \quad (32)$$

where ϕ_1 is given by Eq. (20a). A variational parameter could be introduced into Eq. (32) by replacing $\exp(-r)$ by $\exp(-\epsilon r)$ in Eq. (20a); however, the minimization with respect to ϵ requires more numerical work than seems worth while at this stage. It is expected that Eq. (32) will give best results for the energy when the separation distance R of the nucleons is large and the overlap of the two parts of ϕ_2 is small, and poor results when the nucleons are close together. This turns out to be the case, as is shown below.

The argument presented in Sec. VII for the cancellation of the infinite self-energy is easily extended to include the present situation, since near $\mathbf{r}=\mathbf{r}_1$, the source centered at $\mathbf{r}=\mathbf{r}_2$ has the same kind of effect that the uniform source f_N had in the discussion of the preceding section. The potential energy of interaction between the two nucleons is then the variational energy calculated from Eq. (32), less twice the nucleon self-energy given by Eq. (23). The result is, in the limit $\gamma\to\infty$,

$$-4\pi A^2\frac{e^{-R}}{R}+\frac{6\pi\alpha^2A^4}{R}\int_1^\infty e^{-2Rx}\ln\left(\frac{x+1}{x-1}\right)\frac{dx}{x}. \quad (33)$$

The first term of Eq. (33) is just the usual attractive Yukawa interaction that is obtained from linear neutral scalar mesons, by either classical or quantum theory. The second term is repulsive, and falls off very rapidly for large R, like $[(\ln R)\exp(-2R)]/R^2$.

With the theoretical parameters obtained at the end of Sec. VII, the potential energy (33) is strongly repulsive near $R=0$. This result shows the poorness of the trial function (32) in this region, since a better trial function gives an attraction there.[18] With $R=0$, we have $f_2(\mathbf{r})=2f_1(r)$, and we choose a new trial function to be $C\phi_1(r)$. Variation of the parameter C shows that the interaction potential energy is negatively infinite. A comparison between the form of the divergence in this case and in the linear theory case as $\gamma\to\infty$ shows that the sign and magnitude of the interaction near $R=0$ are similar to those of the first (Yukawa) term of Eq. (33). We thus conclude that the true potential energy is not likely to be greatly different from this Yukawa term for all R. With $A=0.0854$, this has the order of magnitude of the observed two-nucleon interactions.

IX. TWO-NUCLEON INTERACTION IN NUCLEAR MATTER

As discussed in Sec. I, nuclear shell structure can be understood if the interaction between two nucleons embedded in nuclear matter is substantially less than their interaction in empty space. The variational calculation is based on a two-center trial function similar to Eq. (30), and the result is even more complicated than in the preceding section; only the leading term of the interaction potential energy for large R is quoted:

$$\left[-\frac{2\pi A^2(\beta^2-1)}{\beta}+\frac{6\pi\alpha^2A^2\phi_N^2}{\beta}\right]e^{-\beta R}.$$

Since $\beta=2.50$, this falls off much more rapidly than (33) for large R. Numerical comparison shows that the ratio of interaction energy within the nucleus to that in

[18] The writer is indebted to G. Breit and R. P. Feynman for discussion of this point.

empty space is about 0.07 at $R=2$, 0.15 at $R=1.5$, and 0.30 at $R=1$. This indicates a substantial suppression of the two-nucleon interaction within nuclear matter, at least in the domain of R where the two calculations are valid.

X. MAGNETIC MOMENT SUPPRESSION WITHIN NUCLEI

Bloch[19] has recently suggested that the deviations of the magnetic moments of even-odd nuclei from the Schmidt lines be explained in terms of a reduction of the anomalous magnetic moment of the odd neutron or proton as compared with its empty-space value. He finds that the reduction averages about a factor of two for the heavier elements, with fluctuations that correlate to some extent with the known magic numbers.

The type of theory developed here predicts an effect of this kind, since the self mesonic field of a nucleon is expected to be much less when the nucleon is embedded in nuclear matter than when it is in empty space. While the detailed theoretical model of the present paper is too simple to account for magnetic moments, it is nevertheless tempting to speculate that the factor β ($=2.5$) which appears in the exponent of Eq. (30) but not in Eq. (20a) corresponds to an anomalous magnetic moment reduction by a factor of order β. A definitive statement on this point will however have to await the development of, for example, a nonlinear pseudoscalar theory.

XI. INTERACTION OF MESONS WITH NUCLEI

An interesting consequence of a nonlinear meson theory is that a free meson in the neighborhood of a nucleus will be strongly affected by the relatively large static meson amplitude present within the nucleus. To study this effect, we consider the time-dependent wave equation for a static source f_N, to which corresponds a static wave function ϕ_N; f_N and ϕ_N are approximately constant and equal to the values quoted in Sec. VII within the nucleus, and vanish outside. The time-dependent wave equation has a solution of the form $\phi_N(\mathbf{r})+\phi_F(\mathbf{r},l)$; if ϕ_F is a small-amplitude wave, it satisfies to good approximation the linear wave equation,

$$\partial^2\phi_F/\partial l^2=\nabla^2\phi_F-\phi_F-3\alpha^2\phi_N{}^2\phi_F, \qquad (34)$$

which can be derived in precisely the same way as Eq. (11).

Equation (34) can be interpreted as showing that nuclear matter acts as a strongly repulsive potential for small-amplitude meson waves in the vicinity. The strength of this equivalent repulsion is conveniently specified in terms of the distance in which the amplitude of an incident meson wave of unit energy is decreased by a factor e. This distance is $(3\alpha^2\phi_N{}^2)^{-1}=0.487$ in our units, or 0.68×10^{-13} cm.

This result implies that incident mesons will be scattered by a heavy nucleus as though it were a nearly impenetrable sphere. Note, however, that for an isolated nucleon, $\phi_N{}^2$ is replaced by $A^2\exp(-2r)/r^2$ from Eq. (21a), which gives quite a small scattering volume. The related processes of inelastic scattering, absorption, and production (by photons or energetic nucleons) are not so easily discussed, since they must be based on quantum theory. Fortunately, it is in just this case of small-amplitude waves that a quantum field theory can be made (see Sec. III), so that one might hope to go further by quantizing ϕ_F but not the static meson field ϕ_N. So far as meson production in heavy nuclei is concerned, it follows from the foregoing discussion that the outgoing meson wave is much more strongly coupled to the surface than to the interior of the nucleus, so that most mesons will be produced in a surface layer about 10^{-13} cm thick. An effect like this seems to have been observed,[20] although it is doubtful if the layer is actually as thin as predicted here.

XII. CONCLUSIONS

The nonlinear meson theory presented in this paper, which describes neutral scalar mesons with point-contact repulsion, is certainly an oversimplification of the actual situation, and possesses the inherent difficulty of requiring finite nucleon sources. Nevertheless, it gives results that can be related in a sensible way with experimental observation. After the cut-off is fixed at the proton Compton wavelength, there are two free parameters in the theory: the nonlinear parameter α, and the nucleon source strength g. These can be chosen so that nuclear matter has a stable density equal to the observed value, and a binding energy (calculated by the variation method) equal to 42 percent of the observed value. The two-nucleon interaction then comes out to have the observed order of magnitude in empty space. Within nuclei, the two-nucleon interaction is strongly reduced, and provides a qualitative explanation for nuclear shell structure. The self-mesonic field of a nucleon within a nucleus is much smaller in spatial extent than it is in empty space; this may account for the observed deviations of magnetic moments of even-odd nuclei from the Schmidt lines by making the anomalous nucleon magnetic moments smaller when they are within nuclei than when they are in empty space.[19] For attainable free meson beams, the density is so small that the nonlinearity is not significant. When mesons interact with a nucleus, however, the large meson amplitude in and near the nucleus acts through the nonlinearity to produce an effective repulsive potential. This effect may be significant in connection with current observations on the scattering, absorption and production of mesons in the vicinity of nuclei.

[19] F. Bloch, Phys. Rev. **83**, 1062 (1951). *Note added in proof:*— H. Miyazawa, Prog. Theor. Phys. **6**, 263 (1951), has made the same suggestion independently, and proposed also that the magnetic moment suppression may be related to the exclusion principle.

[20] R. F. Mozley, Phys. Rev. **80**, 493 (1950); R. M. Littauer and D. Walker, Phys. Rev. **82**, 746 (1951); Panofsky, Steinberger, and Steller, Phys. Rev., to be published.

Nonlinear Meson Theory of Nuclear Forces. II. Nonlinearity in the Meson-Nucleon Coupling

L. I. SCHIFF
Stanford University, Stanford, California
(Received June 22, 1951)

The possibility of accounting for nuclear saturation by means of classical neutral scalar mesons that are coupled nonlinearly to the nucleons is investigated. It is shown that the interaction energy of an aggregate of nucleons is the same as in the usual linear theory if the nucleons are regarded as point sources. The theory does not, therefore, lead to saturation.

I. INTRODUCTION

THE preceding paper[1] develops a classical nonlinear neutral scalar meson theory of nuclear forces in which the nonlinearity appears in those terms that involve only the meson field. It is pointed out in I that the nonlinearity could also be introduced into the meson-nucleon coupling terms, in which case it corresponds physically to a suppression of meson emission and absorption by nucleons when mesons are already present. Both possibilities were included in the general formulation of the theory; in Eq. (I.1) the first kind of nonlinearity is the $G(\phi)$ term, and the second is the $F(\phi)$ term. The present paper explores the implications of the second kind of nonlinearity so far as saturation is concerned. It is found that the interaction energy of many nucleons is precisely as in the usual linear theory, so that there are no many-body forces and no account is given of saturation.[2] While it is possible that this conclusion would be altered if more complicated theories were studied (for example, a nonlinear pseudoscalar theory), it seems unlikely that this is the case. Also, it does not appear that any advantage is gained by using both the F and G types of nonlinearities at the same time.

In accordance with the discussion of Sec. I.2, we assume that $G(\phi)=\frac{1}{2}\phi^2$, and that $F(\phi)$ is an odd function that approaches ϕ when ϕ is small and increases less rapidly than ϕ for large ϕ. It would then seem at first that an argument like that presented in Sec. I.2 would lead to saturation if $F(\phi)$ has a suitable asymptotic form. According to such an argument, if F is proportional to $\phi^m(0<m<1)$ when ϕ and hence also f is large (high nucleon density), the potential energy per nucleon is negative and proportional to $f^{m/(2-m)}$. Then nuclear matter fails to collapse if, and only if, $m/(2-m)<\frac{3}{2}$, or $m<4/5$. It is also necessary that m be positive in order that the potential energy calculated in this way be negative. The fallacy in this argument lies in the assumption that the smeared-out source function f is approximately equivalent to the original aggregate of localized sources. One way of seeing this is to note that the nonlinear F term reduces the effectiveness of the coupling wherever ϕ is large, and for localized sources this is just at the sources. In the limit of point nucleons, ϕ is always infinite at the source, so that only the asymptotic form of F is significant. Thus any calculation based on the form of F away from $\phi=\infty$ must be incorrect, and this is just the case when the point sources are smeared out. In I, on the other hand, the nonlinearity is in the G term, which involves the entire range of ϕ values, between sources as well as at the sources; in this case the smearing is expected to provide a good approximation.

We need, therefore, to calculate the energy of an aggregate of localized sources. Since the fields are superposable between sources, this will be done by calculating the energy of a single localized source placed in a meson field that is the resultant of the fields produced by all other sources. The total energy of the aggregate can be expressed as the sum of the energies of the individual sources. It turns out that the calculation has a sensible limit when the sources become points, and that the interaction energy is then precisely that obtained from the usual linear theory.

II. SOLUTION FOR AN ISOLATED NUCLEON

We wish to solve the static wave equation [see Eq. (I.4)]

$$\nabla^2\phi-\phi+f(r)F'(\phi)=0 \qquad (1)$$

for a localized spherically symmetric source function $f(r)$ that can later be made to approach a point source. Since the wave equation is easily solved wherever $f=0$, it is convenient to confine f to a spherical shell of radius a and zero thickness: $f(r)=(g/4\pi a^2)\delta(r-a)$, where $g=\int f d\tau$ is the source strength, and the limit $a\to 0$ is to be taken later.[3] The energy can then be calculated

[1] L. I. Schiff, Phys. Rev. **84**, 1 (1951). This paper is referred to here as I, and equations and sections of it are referred to as Eq. (I.1), Sec. I.2, etc. The physical background and notation of I are applicable to the present paper.

[2] According to a manuscript by R. J. Glauber, just received, the corresponding quantum theory with an exponential form for F gives an exceedingly singular two-nucleon interaction. This different result may be due in part to the use there of a series expansion for $F(\phi)$ rather than the asymptotic form used here (see subsequently), and to the assumption there of a finite coupling constant (our source strength g), whereas our Eq. (7) shows that for fixed A, g must vanish as $a\to 0$ if $m>1$ (or if a positive exponential is used for F).

[3] The writer is indebted to R. P. Feynman for suggesting the use of the shell source.

from either of the equations (see Eq. (I.3)),

$$H=\int[\tfrac{1}{2}(\nabla\phi)^2+\tfrac{1}{2}\phi^2-f(r)F(\phi)]d\tau, \quad (2)$$

$$H=\int f(r)[\tfrac{1}{2}\phi F'(\phi)-F(\phi)]d\tau. \quad (3)$$

Equation (3) is obtained from Eq. (2) by use of the wave equation (1) and partial integration. The latter is easier to use, and with the assumed form for $f(r)$ becomes

$$H=g[\tfrac{1}{2}\phi_a F'(\phi_a)-F(\phi_a)], \quad (4)$$

where $\phi_a\equiv\phi(a)$.

The appropriate solution of Eq. (1) is

$$r>a:\ \phi(r)=Ae^{-r}/r,\quad r<a:\ \phi(r)=D\,(\sinh r)/r. \quad (5)$$

One of the boundary conditions at $r=a$ is that ϕ be continuous. The other is obtained by integrating the wave equation across the shell, and is

$$\lim_{\epsilon\to 0}\frac{d}{dr}(r\phi)\Big|_{a-\epsilon}^{a+\epsilon}=\frac{g}{4\pi a}F'(\phi_a).$$

Application of the boundary conditions to Eqs. (5) makes it possible to eliminate D and obtain a relation between g and A:

$$Ae^{-a}(1+\coth a)=\frac{g}{4\pi a}F'\left(\frac{Ae^{-a}}{a}\right). \quad (6)$$

Unless A is zero, which is not an interesting case, ϕ_a becomes infinite as $a\to 0$, and only the asymptotic form of F is significant. We assume for the present that this is $F(\phi)=b\phi^m$, where $m>0$, and substitute in Eq. (6) for small a; it is sufficient to keep the two lowest order terms on each side in order to get all of the terms in the self-energy that fail to vanish when $a\to 0$. The result can be written

$$g=(4\pi/mb)A^{2-m}a^{m-1}[1+(m-1)a]. \quad (7)$$

For $m<1$, the source strength g becomes infinite as $a\to 0$ if A is to remain finite. This must not be regarded as an objection to the theory, as it was in Sec. I.6, since the effective source strength that appears in the wave equation is $gF'(\phi_a)$; this is of course finite as $a\to 0$, as may be seen from the fact that a solution of the form (5) exists. In the limit of small a, the self-energy given by Eq. (4) can be written as

$$-2\pi A^2(2-m)(1-a)/ma, \quad (8)$$

when use is made of Eq. (7).

III. ENERGY OF ONE NUCLEON IN THE PRESENCE OF OTHERS

In order to investigate this case, we assume that ϕ has the form,

$$r>a:\ \phi=B(e^{-r}/r)+C,\quad r<a:\ \phi=D'(\sinh r)/r. \quad (9)$$

Equation (3) then shows that the total energy of an aggregate of such sources is the sum of the energies computed on the basis of Eqs. (9). Actually, if C is a constant in space, the first of Eqs. (9) does not satisfy the wave equation (1). However, only the magnitude of the C term at the origin is significant when the limit $a\to 0$ is taken, as may be verified by a more careful calculation. C represents the resultant of the meson fields produced by all other sources, and B will in general differ from A because the C term changes the effective source strength through the nonlinearity of F. It might also appear at first that the B and D' terms should not be spherically symmetric in general, owing to the nonlinearity; the more careful calculation referred to above shows that the departure from spherical symmetry becomes insignificant in the limit $a\to 0$.

Application of the boundary conditions to Eqs. (9) makes it possible to eliminate D':

$$Be^{-a}(1+\coth a)-C(1-a\coth a)=\frac{g}{4\pi a}F'\left(\frac{Be^{-a}}{a}+C\right). \quad (10)$$

For small a, Eq. (10) can be written, with the help of Eq. (7):

$$B/A=1-[(1-m)Ca/(2-m)A].$$

Substitution into Eq. (4) then gives for the energy:

$$-[2\pi A^2(2-m)(1-a)/ma]-2\pi AC. \quad (11)$$

The interaction energy is the difference between the expressions (11) and (8), or $-2\pi AC$, and thus is independent of the value of m. It can be shown without difficulty that the same interaction energy is obtained if the asymptotic form of F is taken to be $b_0-b_1\phi^{-s}$ with $s>0$, or $b_0-b_1\exp(-c\phi)$ with $c>0$. A general proof of this has been constructed which is independent of the form of F, but it does not seem worth while to include it here.

The usual linear theory is included in the foregoing results as the special case $m=1$. We see then that in the point-source limit, a nonlinear coupling gives the same interaction energy for a number of nucleons as the linear coupling, and so does not lead to saturation.

The Elastic Scattering and Capture of Protons by Oxygen*

R. A. LAUBENSTEIN,† M. J. W. LAUBENSTEIN,† L. J. KOESTER,‡ AND R. C. MOBLEY
University of Wisconsin, Madison, Wisconsin

(Received June 18, 1951)

The yield of elastically scattered protons from oxygen was measured with a magnetic analyzer which detected protons scattered through laboratory angles of 159° to 169°. Using protons accelerated by an electrostatic generator, the proton energy range from 0.6 to 4.5 Mev was covered in 4.4-kev or smaller steps. Two sharp resonances were observed, one at an incident proton energy of 2.66 Mev with a width of 19.9 kev, and the second at 3.47 Mev with an observed width less than 3.5 kev. Near 4.0 Mev a broad maximum in the cross section was obtained, and a broad resonance appears to give another maximum slightly above 4.5 Mev. The resonance at 2.66 Mev appeared as a nearly symmetrical dip in the scattering cross section.

The capture cross section of oxygen for protons was measured for incident proton energies from 1.4 to 4.1 Mev by counting the positrons from the decay of F^{17} built up under the bombardment of oxide targets. Up to a narrow resonance at 3.47 Mev, the capture cross section was observed to increase almost linearly with energy. Above 3.75 Mev, the cross section was found to increase more rapidly to a maximum near 3.99 Mev.

On the basis of the scattering and capture data, energy levels have been assigned to F^{17} at 3.11, 3.88, 4.36, and 4.73 Mev, although the positions of the latter two levels are not clearly defined by the data.

I. INTRODUCTION

A STUDY of the interaction of protons with O^{16} yields information about the energy levels of the compound nucleus, F^{17}. Although this nucleus has been investigated previously, little information is available on the location of the energy levels or their character. Because oxygen is so often a contaminant in target materials, a knowledge of the reactions of protons with oxygen is also important in connection with other experiments. Certain nuclear properties of O^{16} and of the interaction of protons with O^{16} make this reaction not only interesting, but also well suited to a comparison of theory and experiment. A discussion of such a comparison is given in the paper which follows.[1]

In the range of incident proton energies from 0.6 to 4.5 Mev which this experiment covers, previous investigations of the interaction of protons have been comparatively few. Heitler, May, and Powell[2] measured the angular distribution of 4.2-Mev protons elastically scattered from oxygen. Using 4.5-Mev protons, Rhoderick[3] looked for protons inelastically scattered from oxygen but did not observe any. The capture of protons by oxygen has been investigated most extensively by DuBridge, Barnes, Buck, and Strain,[4,5] who used the stacked foil technique to obtain an excitation curve which indicates a resonance near 3.5 Mev and a rapidly increasing yield near 3.9 Mev.

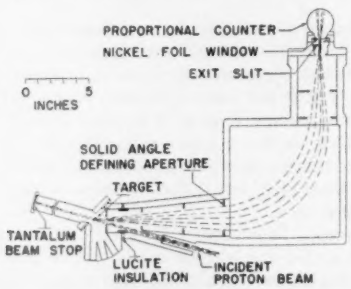

FIG. 1. Horizontal cross section of the magnetic analyzer, showing the proton paths.

II. ELASTIC SCATTERING OF PROTONS BY OXYGEN

Apparatus and Procedure

The yield of elastically scattered protons from oxygen was measured as a function of incident proton energy by using a magnetic analyzer to separate protons scattered by oxygen from protons scattered by other elements in the target. A detailed description of the design and construction of the analyzer and associated equipment is given elsewhere.[6-8] Figure 1 shows a horizontal cross section of the analyzer and the proton paths. Protons scattered by the target through laboratory angles of 159° to 169° enter the analyzer where only those protons with the correct momentum are allowed to pass between the exit slits and enter the proportional counter. Separating the counter from the evacuated region of the analyzer was a nickel foil 0.00005 inch thick. By means of a magnetic balance-type fluxmeter[9,10] the magnetic field was set or its value measured to an accuracy of about 0.15 percent. The Wisconsin electro-

* Supported by the Wisconsin Alumni Research Foundation and the AEC.

† Now at North American Aviation, Inc., Downey, California.

‡ AEC Predoctoral Fellow.

[1] R. A. Laubenstein and M. J. W. Laubenstein, Phys. Rev. **84**, 18 (1951).

[2] Heitler, May, and Powell, Proc. Roy. Soc. (London) **190**, 180 (1947).

[3] E. H. Rhoderick, Proc. Roy. Soc. (London) **201**, 348 (1950).

[4] DuBridge, Barnes, and Buck, Phys. Rev. **51**, 995 (1937).

[5] DuBridge, Barnes, Buck, and Strain, Phys. Rev. **53**, 447 (1938).

[6] J. E. Faulkner, thesis, University of Wisconsin (1950), unpublished.

[7] G. M. B. Bouricius, thesis, University of Wisconsin (1950), unpublished.

[8] Shoemaker, Faulkner, Bouricius, Kaufmann, and Mooring, to be published.

[9] Buechner, Strait, Sperduto, and Malm, Phys. Rev. **76**, 1543 (1949).

[10] G. Goldhaber, unpublished.

static generator provided a collimated proton beam with a well-defined energy spread. For this experiment, a beam current of about 0.4 μa was incident on a target area 2 mm square.

In order to avoid other elements which would give reactions under proton bombardment, only oxides of heavy elements were used as targets. The entire yield curve (shown in Fig. 3) was taken with a target of barium oxide on a backing of 1000A nickel foil. A description of the mounting and preparation of the foils is given by Bashkin and Goldhaber.[11] Barium oxide was deposited on these foils by evaporating a thin film of barium and then admitting dry air to the evaporator in order to allow the oxide to form.

Figure 2, a typical momentum analysis, shows that for an exit slit width of 10 mm, which was used for this experiment, the protons scattered from oxygen and from carbon can be almost completely resolved by the analyzer. Certain characteristics of the analyzer, calculated in terms of $H\rho$, are included in Fig. 2 and indicate why the particular shape of the oxygen "peak" is obtained. There is a range of magnetic field values over which all of the protons scattered by oxygen will pass between the exit slits of the analyzer and be detected.

Momentum analyses of the protons scattered from the target were taken at frequent intervals and served to calibrate the fluxmeter and determine the background correction. All of the momentum analyses showed a background of protons counted at magnetic field settings for which no protons should enter the counter. Some of this background was observed with no target in place and was caused by protons scattered within the analyzer so that they entered the counter. Approximately an equal background resulted from protons scattered first by nickel, barium, or other heavy elements in the target and rescattered in the analyzer slit system so that they entered the counter at relatively low magnetic field settings. Over the energy range for which the oxygen and nickel peaks were well separated, the total background was obtained by extrapolating the yield between these peaks into the oxygen peak. For the target of barium oxide on 1000A nickel with which most of the data were taken, the background was about 5 percent of the yield of protons scattered from oxygen, except at energies below 1 Mev.

As the incident proton energy was decreased, several effects contributed to an increasing uncertainty in the measurement of the relative scattering cross section. At low energies the nickel peak spread out because of increasing target thickness and began to overlap the oxygen peak. In order to overcome the uncertainty in yield caused by this overlap, data taken below 1 Mev with the target used for the entire curve were normalized to data obtained with a target of barium oxide on a 500A nickel foil and a target of barium oxide on diamond. Use of these targets also eliminated the necessity of corrections to the low energy yield because of oxygen which was found to occur on the back surface of the nickel foil. This oxide layer is normally found on nickel, but may have been enhanced here by the chemicals used in the preparation of the foils. At high energies, protons scattered by oxygen on both sides of the nickel pass through the analyzer, but at low energies this is no longer true, and the 5 percent yield obtained from oxygen on the back side will not be present in the main oxygen peak. Increased thickness of the oxygen-containing layer on the target caused an increase in the size of the image formed by protons scattered from oxygen, and this image took up a larger fraction of the exit slit width giving a narrower and more rounded peak at low energies. Thus, below 1 Mev, it was necessary to change the magnetic field every time that the energy of the incident protons was changed. The results were a larger scattering of the data points and more uncertainty in the low energy region of the curve.

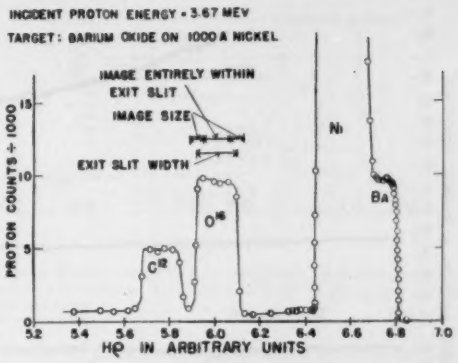

FIG. 2. Momentum analysis of protons scattered from a target of BaO on 1000A nickel foil.

Results

The yield curve obtained for the elastic scattering of protons by oxygen is shown in Fig. 3. Data shown on this curve were all taken with an incident proton energy spread of 0.18 percent at half-maximum intensity, except near the 3.47-Mev resonance, where data are shown for 0.06 percent energy spread. Above 1.35 Mev, data points were obtained no more than 4.4 kev apart, and below this energy no more than 2.9 kev apart. Each point represents about 12 microcoulombs of protons striking the target. Accurate measurement of this proton charge was made with a current integrator designed by Bouricius and Shoemaker.[12]

A differential cross section of $3/4\pi$ barn per steradian on the yield curve corresponds to about 7400 recorded proton counts above background. The statistical uncer-

[11] S. Bashkin and G. Goldhaber, Rev. Sci. Instr. **22**, 112 (1951).

[12] G. M. B. Bouricius and F. C. Shoemaker, Rev. Sci. Instr. **22**, 183 (1951).

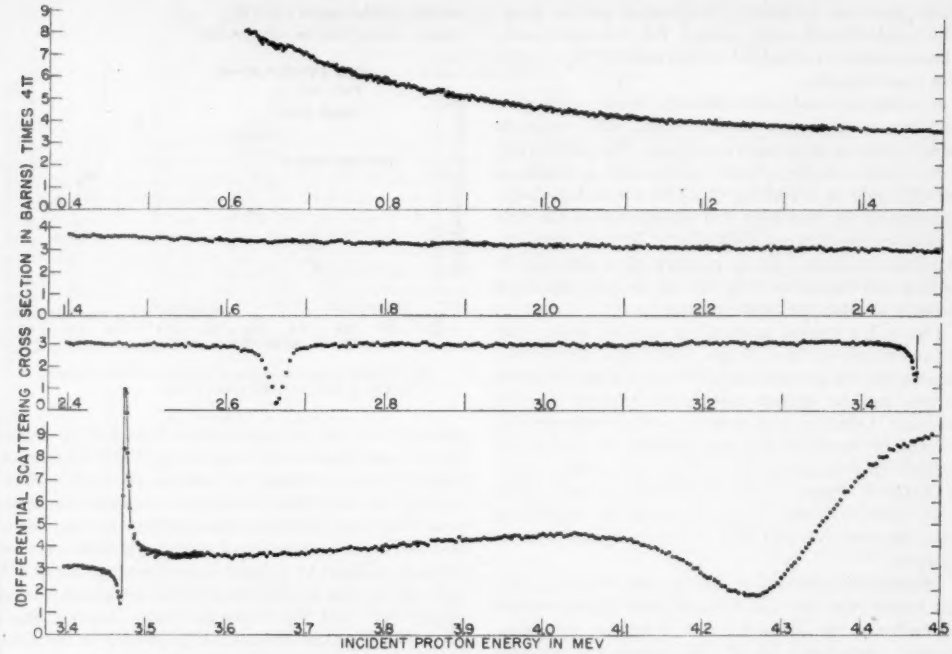

FIG. 3. Yield of protons elastically scattered from oxygen through laboratory angles 159°–169°.

tainties are everywhere smaller than the circles which represent the data points. Above 1.1 Mev, the relative cross sections should be accurate to ±4 percent except near the 2.66-Mev and 3.47-Mev resonances, while below 1.1 Mev, where additional uncertainties were introduced in the background corrections, the relative values may be accurate to only ±15 percent. A large error may be expected in the absolute value of the cross sections indicated by the ordinate scale. Many of the small variations in the yield curve occur at energies where the magnetic field was changed and are caused by the sloping top of the oxygen peak. None of these variations, including the largest at 0.66 Mev, are real. The contributions of the O^{17} and O^{18} isotopes should not be larger than the statistical uncertainty.

In order to plot the shape of the resonance at 2.66 Mev as accurately as possible, thin targets (0.6–0.25 kev) and a proton beam energy resolution of 0.04 percent and 0.02 percent at half-maximum intensity were used. Because the thickness of the nickel was not small compared with the width of the resonance, the oxygen on the back side of the foil or in the foil, a large percentage of the total for thin targets, made large corrections necessary. To avoid these corrections, the target with the diamond backing was employed. A plot of the best results obtained for this 2.66-Mev resonance, which appears as an almost symmetrical dip in the cross section, is shown together with a theoretical fit in the paper which follows.[1] A ratio of maximum to minimum cross section of 11.5 was obtained, and the fit of the resonance gives an observed width, Γ, of 19.9 kev. It must be emphasized that the background at the minimum of the resonance was a large part of the total yield and that the value given for the minimum may be in error by as much as a factor of two.

The resonance at 3.47 Mev was sufficiently narrow so that its shape could not be accurately determined with the smallest beam energy spread and the thinnest targets available. A cross section at the maximum of $16/4\pi$ barns per steradian relative to the scale shown on Fig. 3 was obtained, but the narrowness of the peak of the resonance makes this value uncertain. The width of the resonance is less than 3.5 kev.

Two broad resonances are indicated in the high energy region of the curve, and it appears as if there is interference between these levels, thus making an interpretation of this part of the curve difficult. The gradual increase of the scattering cross section from 3.6 to 4.0 Mev must be caused by a resonance, although the location of the resonance cannot be obtained from a visual inspection of the scattering yield curve. A more detailed analysis of the data indicates that the minimum near 4.27 Mev and the maximum near 4.5 Mev may be caused by another resonance at an incident proton

energy of about 4.39 Mev and with an observed width, Γ_{lab}, of about 0.24 Mev.

In the low energy region the scattering cross section does not decrease with increasing energy as fast as for Rutherford-type scattering, and by comparison the experimental cross section is relatively flat. Some experimental data were obtained on the scattering of protons by oxygen in the energy range from 450 to 600 kev using a scintillation counter. Changes in the efficiency of the counter with energy and a large background made an accurate normalization of these data impossible. The data did indicate that there were no rapid changes in the cross section between 450 and 600 kev, and hence no resonances occur in that energy range.

Attempts to measure the absolute cross section were made. In the various momentum analyses taken at different energies the yield of elastically scattered protons from barium was obtained, and the scattering cross section for barium was found to vary as the reciprocal of the square of the energy. Therefore, the scattering from barium was assumed to be of the Rutherford type for which the cross section can be calculated. Assuming that the compound in the target was BaO, then the cross section for oxygen was the ratio of the yield of protons from oxygen to the yield of protons from barium times the Rutherford cross section of barium. The best experimental value for the cross section is $3.1/4\pi$ barns per steradian in the laboratory system at an incident proton energy of 2.2 Mev. This value was used in drawing the ordinate scale of Fig. 3. In the momentum analyses the dip between the oxygen and carbon peaks was sufficiently low to conclude that nitrogen was not detectable in the target and thus that barium nitride was not formed. Other possible compounds of barium which might have formed instead of the oxide, i.e., barium hydroxide or barium carbonate, give more than one oxygen atom for each barium atom and would result in a lower calculated cross section. During storage of the barium oxide targets in a desiccator, some of the barium oxide may have been converted to these other barium compounds. If all of the oxide were converted to the carbonate, the cross section given above would be too high by a factor of 3. However, the upper limit to the differential scattering cross section given here is an aid in an analysis of the data, and such an analysis indicates that the cross sections given in Fig. 3 are too large by 22 percent.

III. CAPTURE OF PROTONS BY OXYGEN

The capture of protons by O^{16} produces F^{17} with the emission of one or more gamma-rays to carry away the excess energy. Since the Q value of 0.61 Mev is lower than for any other (p,γ) reaction and since the capture cross section is small, the capture gamma-rays are difficult to detect above the background radiation produced by the electrostatic generator and by the annihilation of the positrons emitted by F^{17}. However, the detection of these positrons provides a sensitive method of measuring the capture of protons by O^{16}.

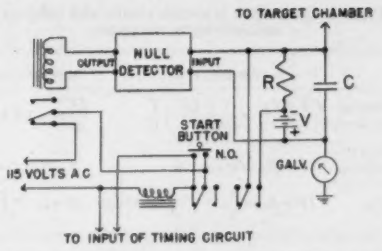

FIG. 4. Electric circuit used to compensate for fluctuating beam current and measure the activity built up in the target during bombardment.

Apparatus and Procedure

An investigation of the capture cross section from 1.1 to 4.1 Mev was made by bombarding oxide targets with protons from the electrostatic generator and taking the resulting F^{17} activity as a measure of the capture cross section. In order to build up a reasonable activity in the target, it was desirable to bombard the targets for a time comparable to the half-life of F^{17}, which was measured and found to be 66.3 ± 1 seconds. If the beam current is not constant, the activity in the target at the end of bombardment will be a function of the variation of the beam current as well as the average current and the bombardment time.

Figure 4 shows an electric circuit similar to one described by Snowdon[13] which was used to measure the activity built up in the target. Except for the resistance R, this circuit is that of the current integrator of Bouricius and Shoemaker,[12] which has a null detector as its essential feature. The operation of the circuit, which will hereafter be called the normalization circuit, may be described as follows: Normally, the condenser C is charged to a voltage V by the battery connected across it through a relay. During bombardment the proton current which strikes the target is allowed to discharge the condenser. When the null detector indicates that the condenser voltage is zero, the beam is shut off. If the beam current should be interrupted during bombardment, the condenser will recharge through the resistance R at the same rate at which the radioactive product decays, because the time constant, RC, is set equal to the mean life of the radioactivity.

Table I compares the differential equation and its solution for the electric circuit with that of the build-up of radioactivity in the target. The notation is: I = proton current as a function of time, E_C = potential of the upper plate of condenser C, V = battery voltage, λ = decay constant of the radioactive product, N = number of radioactive atoms in the target at time t, t = time measured from the start of bombardment, and kI = rate

[13] S. C. Snowdon, Phys. Rev. 78, 299 (1950).

TABLE I. Comparison of electric circuit with build-up of radioactivity in the target.

	Electric circuit	Radioactive product
Differential equation	$\frac{d(V+E_C)}{dT}=\frac{(V+E_C)}{RC}+\frac{I}{C}$	$\frac{dN}{dt}=-\lambda N+kI$
Boundary condition	$(V+E_C)=0$ at $t=0$	$N=0$ at $t=0$
Solution	$(V+E_C)=\frac{1}{C}e^{-t/RC}\int_0^t e^{t/RC}Idt$	$N=ke^{-\lambda t}\int_0^t e^{\lambda t}Idt$

of formation of the radioactive atoms, where k is a constant depending on the cross section for the reaction and the target thickness.

Although the quantity E_C is actually measured by the null detector, the quantity $(V+E_C)$ will be used as a variable to show the similarity in equations.

By putting $RC=1/\lambda$, the two equations in the last row of Table I will give

$$(V+E_C)=N/kC. \tag{1}$$

At the end of bombardment $E_c=0$, and Eq. 1 becomes

$$N=kCV. \tag{2}$$

Substituting for C gives

$$N=kV/\lambda R. \tag{3}$$

Equation 3 can be compared with the case where the beam current is constant and

$$N=(k/\lambda)I(1-e^{-\lambda t}).$$

If the electric circuit is used, the activity in the target at the end of bombardment is equal to the activity obtained after infinite bombardment with a current V/R. Thus, the constants of the circuit must be adjusted so that V/R is less than the beam current available; and for a given beam current, the ratio V/R will determine the length of bombardment. In this experiment the radioactive product has a half-life of about 66 seconds, and the approximate values of the constants used are: $C=16$ μf, $V=6$ volts, $R=6$ megohms, $V/R=1$ μa. Since the proton current available averaged about 2 μa, the length of each bombardment was about 66 seconds.

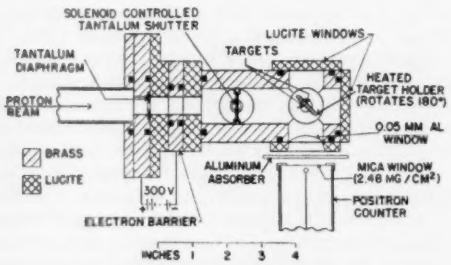

FIG. 5. Horizontal cross section of the positron counting arrangement.

A second circuit was constructed using relays and a clock to provide various timing and switching functions which were needed. This timing circuit operated in response to the normalization circuit as follows:

1. When the start button on the normalization circuit was pressed, the timing circuit released the solenoidally operated shutter in the target chamber and allowed the proton beam to strike the target.

2. When the normalization circuit indicated the proper bombardment, the timing circuit caused the shutter to be raised, started the clock, and turned off the belt spray voltage on the electrostatic generator.

3. After a 15-second delay, during which time the generator voltage decayed to a value at which the x-ray output was negligible, the timing circuit switched on the positron counting circuit.

4. At the end of a pre-set counting time, usually two minutes, the positron counting circuit was turned off, and all relays were returned to their initial positions. Provision was made to time the bombardment, delay, and counting periods, with electric timers to check on the accuracy of the circuit.

Figure 5 shows a horizontal cross section of the target chamber. The use of the tantalum shutter allowed a beam to be established before the bombardment was started. A heated target holder was used which could be rotated through an angle of 180° by remote control so that either one of two targets could be bombarded. Data were taken first on one target and then on the other according to the following sequence of operations: (1) establish beam, (2) bombardment, (3) delay time, (4) count positrons. At the start of counting on one target, the F^{17} produced in that target by the recent bombardment had only 15 sec to decay, while the F^{17} produced by a previous bombardment had about 7 half-lives to decay. Calculation shows that 85 percent of the activity to be measured remained at the start of counting, but only 0.8 percent of any previous activity was left. Thus, by the use of two targets, a waiting period between runs was avoided, and the resulting error due to old activity was less than the statistical fluctuation of the data.

A fraction of the positrons emitted from the target passed through the aluminum window of the target chamber and the aluminum absorber and were detected by a beta-ray counter of the end window type. The aluminum absorber was used between the target and the counter to reduce the counting rate from N^{13} and F^{18} positrons. Although the percentage of O^{18} in ordinary oxygen is small, the $O^{18}(p,n)F^{18}$ reaction has a high cross section[4,5] above the 2.59-Mev threshold,[14] and the F^{18} activity can be greater than the F^{17} activity when an oxide target is bombarded with protons. N^{13} can be formed by the capture of protons by carbon on the target. A total absorber thickness of 224 mg/cm² was used when data were being taken with the thick targets

[14] Richards, Smith, and Browne, Phys. Rev. **80**, 524 (1950).

and 258 mg/cm² when data were being taken with the thin targets. F^{18} has a positron end point of 635±15 kev,[15] which is low enough so that all of the positrons from F^{18} were stopped in the absorber. N^{13} has a positron end point of 1.202±0.005 Mev,[16] which is so high in comparison with the 1.72±0.03-Mev positron end point[17] of F^{17} that it was not practical to use an absorber sufficiently thick to absorb all of the positrons from N^{13}. Some experimental checks showed that no significant background of N^{13} positrons was present, however. Since no resonances have been observed in the scattering of protons from carbon between 1.7 and 4.1 Mev,[18] there are probably no rapid fluctuations in the capture cross section over this energy region, and any background contributed by the presence of carbon should be fairly constant.

In order to determine background counting rates, approximately one out of every four runs was made using an aluminum absorber thickness of 4 mm. This absorber stopped all of the positrons from F^{17}, but had little effect on the annihilation and x-radiation which formed most of the background. From the data thus obtained a background curve was plotted for each target. When thick oxide targets were used, the background amounted to about 10 percent of the total number of counts.

Results

The entire energy range studied was covered twice, once with a pair of thick oxide targets, and once with a thinner pair. For each target of each pair the data were corrected for background and plotted separately. Within the experimental error, the data obtained from the two thin targets gave the same curve. One of the thick oxide targets contained about 50 percent more oxygen than the other, and the data obtained with one of these targets was multiplied by a normalization factor so that the two thick target yield curves would be nearly coincident.

Figure 6 shows the results of the capture cross section measurements. Data from both targets of the pair are included on both the curve representing the thick target data and the thin target data. The statistical uncertainty in the data is given approximately by the diameter of the circles which represent the data points.

The peculiar shapes of the step in the thick target data and the resonance peak in the thin target data near 3.47 Mev are largely due to the characteristics of the targets which were used. All data were taken with targets of tantalum oxidized by electrolysis in distilled water. Under the bombardment of a 2-μa proton beam, the tantalum sometimes came to a dull red heat. Some

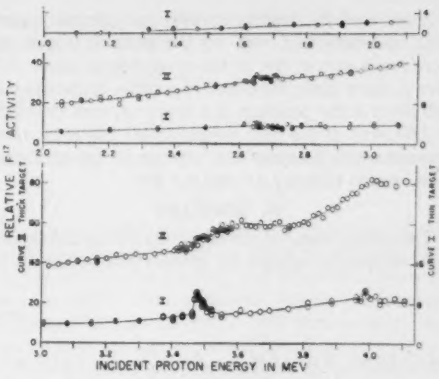

FIG. 6. Relative F^{17} activity produced by the bombardment of oxide targets with protons.

of the oxygen which was originally on the surface of the target in the form of Ta_2O_5 may have diffused into the target during bombardment, giving the distribution of oxygen in the tantalum target shown by the data. A thinner oxide target and better energy resolution of the proton beam were used to take the data of Fig. 7. Here again the observed shape of the resonance was determined by the characteristics of the target and the energy spread of the proton beam. The position of the narrow capture resonance was found to agree within the experimental error with the position of the 3.47-Mev resonance observed in the scattering experiment.

Other features of the variation of the capture cross section with energy which must be examined and correlated with the scattering data are: (1) the fact that within the experimental error the effect of the 2.66-Mev resonance on the capture cross section was not detectable, (2) the almost linear increase in the capture cross section above 3.75 Mev until a maximum is reached near 3.99 Mev. DuBridge, Barnes, Buck, and Strain[5] also found a rapidly increasing capture cross section as a function of energy near 3.9 Mev. The work

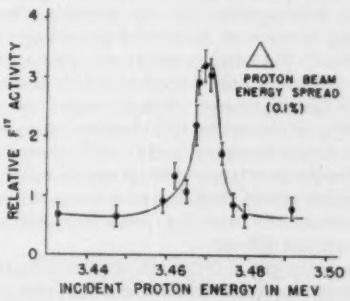

FIG. 7. F^{17} activity produced by the bombardment of a thin oxide target with protons in the energy region near the 3.47-Mev resonance.

[15] Blaser, Boehm, and Marmier, Phys. Rev. **75**, 1953 (1949).
[16] Hornyak, Dougherty, and Lauritsen, Phys. Rev. **74**, 1727 (1948).
[17] V. Perez-Mendez and P. Lindenfeld, Phys. Rev. **80**, 1097 (1950).
[18] G. Goldhaber and R. M. Williamson, Phys. Rev. **82**, 495 (1951).

of these authors, combined with the present experiment, indicates that with the use of thick targets the more rapid rate of rise of the cross section above 3.75 Mev is more easily observed. A possible explanation of this effect is the presence of a broad capture resonance at 3.99 Mev. It has been assumed that this is the same resonance which causes the increase in the scattering cross section between 3.6 and 4.0 Mev.

IV. SUMMARY

The measurement of the elastic scattering and capture cross sections of oxygen for protons gives evidence for resonances at proton energies of 2.66, 3.47, 3.99, and 4.39 Mev. The positions of the 2.66- and 3.47-Mev resonances are well determined, while the positions of the upper resonances are based on less substantial evidence. These four resonances correspond to energy levels in the compound nucleus, F^{17}, at 3.11, 3.88, 4.36, and 4.73 Mev.

The authors wish to thank Professor R. G. Herb, under whose supervision this project was carried out, for his advice and encouragement, and Dr. F. P. Mooring for assistance in taking some of the data.

PHYSICAL REVIEW VOLUME 84, NUMBER 1 OCTOBER 1, 1951

Assignment of Angular Momenta to the Energy Levels of F^{17}

R. A. LAUBENSTEIN* AND M. J. W. LAUBENSTEIN*
University of Wisconsin, Madison, Wisconsin†

(Received June 18, 1951)

An analysis of data on the elastic scattering and capture of protons by oxygen was made for the purpose of assigning angular momenta to certain energy levels in F^{17}. The elastic scattering data were analyzed using a graphic method wherein the phase and amplitude of the refracted partial waves are represented by vectors in the complex plane. As the proton energy is varied over a resonance, a circular locus is obtained for the vector which represents the component of a partial wave which excites the resonance.

Assignments of angular momenta to the energy levels of F^{17} have been made as follows: ground state, $D_{\frac{1}{2}}$; 0.55 Mev, $S_{\frac{1}{2}}$; 3.11 Mev, $S_{\frac{1}{2}}$; 3.88 Mev, $F_{\frac{1}{2}}$; 4.36 Mev, $D_{\frac{1}{2}}$; and 4.73 Mev, $P_{\frac{1}{2}}$. The assignments of the 0.55-Mev, 3.11-Mev, and 3.88-Mev levels are reasonably certain, but the others are based on less substantial evidence. The reduced width of the 3.11-Mev $S_{\frac{1}{2}}$ level was found to be about 0.048×10^{-13} Mev-cm, while the 0.55-Mev $S_{\frac{1}{2}}$ level probably has a reduced width over 100 times as large.

The slowly rising capture cross section observed from 1.4 to 3.4 Mev is probably caused by the broad 0.55-Mev level.

A comparison of the levels in the mirror nuclei, O^{17} and F^{17}, shows a similar structure.

I. INTRODUCTION

THERE are a number of reasons to expect that experimental data obtained on the interaction of protons with O^{16} might be more easily interpreted than in the case of many other nuclei. For proton energies below about 5.6 Mev the only reactions which are energetically possible are elastic scattering and simple capture, with capture much less probable. Thus, complications introduced by several competing reactions are avoided. The binding energy of a proton added to an O^{16} nucleus is only 0.61 Mev, which is the lowest positive binding energy observed with any nucleus. Scattering of protons by O^{16}, therefore, gives information about the low-lying levels of F^{17}. Since the lower levels should have larger reduced widths and should be more widely spaced than the upper levels, the problems of experimentally resolving levels and plotting their shapes are less difficult.

Because the spin of O^{16} is zero, the scattering formulas are greatly simplied over the case of non-zero spin, and the results of an elastic scattering experiment should be relatively easy to fit to these formulas. O^{16} contains 8 neutrons and 8 protons and can be considered as a closed shell in both neutrons and protons.[1,2] If this shell model of the nucleus is correct, the compound nucleus, F^{17}, formed under bombardment of O^{16} by protons, will consist of one proton outside a closed shell. The level structure of F^{17} is of theoretical interest because of the possibility of applying this simple nuclear model. Also, O^{17}, the mirror nucleus of F^{17}, has been rather extensively investigated; and it is of interest to compare the levels of these two nuclei.

The results of the previous paper on the elastic scattering and capture of protons by oxygen[3] are far from being sufficiently extensive, so that a detailed theoretical analysis can be made. However, it is interesting to attempt to fit these data to existing formulas, especially in view of the fact that no reaction yield involving a nucleus more complicated than lithium

* Now at North American Aviation, Inc., Downey, California.

† Supported by the Wisconsin Alumni Research Foundation and the AEC.

[1] M. G. Mayer, Phys. Rev. **78**, 16 (1950).
[2] E. Feenberg and K. C. Hammack, Phys. Rev. **75**, 1877 (1949).
[3] Laubenstein, Laubenstein, Koester, and Mobley, Phys. Rev. 84 12 (1951).

has been fitted theoretically over an extended energy range. Because of the lack of sufficient experimental data, many of the conclusions that are reached in this paper must be regarded as tentative; but it is hoped that the interpretation presented here will point the way to further experimental and theoretical work to confirm or deny the conclusions which are reached.

II. ELASTIC SCATTERING THOERY

The cross section for scattering can be given in terms of the phase shifts, δ_l, between the incident and refracted partial waves. For particles of spin $\frac{1}{2}$ incident on nuclei with spin zero, the partial wave which represents particles with l units of orbital angular momentum (measured in units of $\hbar$) must be separated into two components if $l>0$, because of the two possible orientations of the spin with respect to the orbital angular momentum. The phase shift of the component of the lth partial wave which forms a compound state with total angular momentum $J=l+\frac{1}{2}$ will be designated δ_l^+, and the phase shift of the component which forms a compound state with $J=l-\frac{1}{2}$ will be designated δ_l^-. The differential scattering cross section, σ, as a function of these phase shifts, can be obtained from Eqs. (4) and (5) of the paper by Critchfield and Dodder.[4] It is

$$\sigma=\lambda^2[|A|^2+|B|^2], \tag{1}$$

where

$$A=-\tfrac{1}{2}\eta\csc^2\tfrac{1}{2}\theta\exp(i\eta\ln\csc^2\tfrac{1}{2}\theta)+\sum_{l=0}^{\infty}(l+1)P_l(\cos\theta)\exp(i\alpha_l+i\delta_l^+)\sin\delta_l^+ +\sum_{l=1}^{\infty}lP_l(\cos\theta)\exp(i\alpha_l+i\delta_l^-)\sin\delta_l^-, \tag{2}$$

$$B=\sin\theta\sum_{l=1}^{\infty}P_l'(\cos\theta)e^{i\alpha_l}\times[\sin\delta_l^-\exp(i\delta_l^-)-\sin\delta_l^+\exp(i\delta_l^+)], \tag{3}$$

and

$$\eta=ZZ'/\hbar v,\quad \lambda=\hbar/mv,$$
$$e^{i\alpha_l}=(l+i\eta)/(l-i\eta)\cdots(1+i\eta)/(1-i\eta);\quad l>0$$
$$e^{i\alpha_0}=1,\quad P_l'(\cos\theta)=d[P_l(\cos\theta)]/d(\cos\theta),$$

Z=charge of the proton, Z'=charge of the target nucleus, v=velocity of relative motion, m=reduced mass of the system, and θ=angle of scattering in the center-of-mass system.

The first term in the equation for A (Eq. 2) represents Rutherford or coulomb-type scattering. The other terms in the equations for A and B represent scattering due to nuclear or short-range forces. The phase shifts, δ_l, can be considered, as was done by Adair,[5] to be the sum of a phase shift, $-\phi_l$, due to a hard sphere type of scattering, and of an anomalous phase shift, β_l, due to the energy levels of the compound nucleus. δ_l is then given by

$$\delta_l^+=\beta_l^+-\phi_l,\quad \delta_l^-=\beta_l^--\phi_l,$$

where

$$\phi_l=[\tan^{-1}(F_l/G_l)]_{r=R_l}$$

and $\tan\beta_l^+$ or $\tan\beta_l^-$ is a sum of terms of the form,

$$\tfrac{1}{2}\Gamma_\lambda/(E_\lambda+\Delta_\lambda-E).$$

The sum for $\tan\beta_l^+$ will include only those terms due to resonances caused by energy levels in the compound nucleus which have $J=l+\frac{1}{2}$ and which are formed by protons with l units of orbital angular momentum. Similarly, the sum for $\tan\beta_l^-$ will include only those terms due to resonances caused by energy levels which have $J=l-\frac{1}{2}$ and which are formed by protons with l units of orbital angular momentum. The notation is as follows:[6]

$$\Gamma_\lambda=2k\gamma_\lambda^2/(F_l^2+G_l^2)|_{r=R_l}, \tag{4}$$

$$\Delta_\lambda=-(\gamma_\lambda^2/R_l)[\{d\ln(F_l^2+G_l^2)^{\frac{1}{2}}/d\ln(kr)\}+l]_{r=R_l}, \tag{5}$$

where k=wave number of relative motion, r=distance between the proton and the oxygen nucleus, R_l=effective nuclear radius or reaction radius for the lth partial wave, γ_λ^2=reduced width of the λth level, Δ_λ=level shift of the λth level, E=energy in the center-of-mass system, E_λ=characteristic energy of the λth resonance, and F_l and G_l are the regular and irregular particle wave functions, respectively.[7] If the difference between the incident proton energy and the energy of each resonance excited by l-protons is large compared with the width of that resonance, then it follows that

$$\beta_l^+=\beta_l^-=0,$$

and

$$\delta_l^+=\delta_l^-=-\phi_l.$$

A geometric interpretation of the cross section formula can be obtained by representing the amplitude and phase of each partial wave component by a vector in the complex plane. Adding these vectors to the Rutherford vector gives the resultant A. B can be obtained in a similar manner, but frequently this term is very small compared with A and can be neglected. Because protons scattered near the backward direction were observed in the present experiment,[3] $\sin\theta$ is small and B will be neglected in an analysis of the data. B is, in general, always zero except at energies near a resonance for which $l>0$. Also, at energies which are distant from all resonances except those excited by the lth partial wave, B is zero at those scattering angles for which $P_l'(\cos\theta)$ is zero.

[4] C. L. Critchfield and D. C. Dodder, Phys. Rev. **76**, 602 (1949).
[5] R. K. Adair, Phys. Rev. **81**, 310 (1951).
[6] R. G. Thomas, Phys. Rev. **81**, 148 (1951).
[7] Coulomb wave functions are tabulated in the following papers: Yost, Wheeler, and Breit, Terr. Mag. and Atmos. Elect. **40**, 443 (1935). E. R. Wicher, Terr. Mag. and Atmos. Elect. **41**, 389 (1936). Bloch, Hull, Broyles, Bouricius, Freeman, and Breit, *Coluomb Functions for Reactions of Protons and Alpha Particles with the Lighter Nuclei* (Yale University, New Haven, Connecticut, 1950).

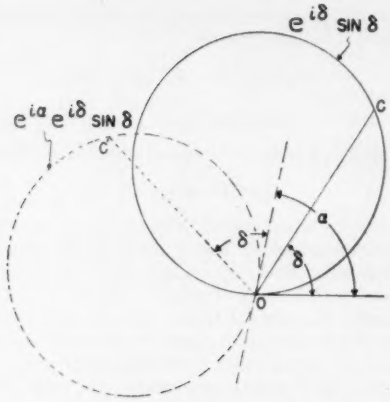

FIG. 1. Representation of terms in the scattering equation by vectors in the complex plane.

If an equation of the form $z=e^{i\delta}\sin\delta$ is plotted in the complex plane, a circle is obtained which passes through the origin and has its center at the point $(0, i/2)$. Such a plot is shown by the solid circle in Fig. 1. The vector OC in this figure is the vector $e^{i\delta}\sin\delta$; and as δ varies from 0° to 180°, the point C will travel counterclockwise once around the circle.[8] Partial waves for which $l>0$ have vectors which are rotated through an additional angle α_l. The dashed circle in Fig. 1 shows that the effect of the $e^{i\alpha l}$ factor in the cross section formula is to rotate the lth locus circles about the origin through an angle α_l. As the $P_{\frac{1}{2}}$ vector is given by $P_1(\cos\theta)\times\exp(i\alpha_1+i\delta_1^-)\sin\delta_1^-$, the vector OC' of Fig. 1 will represent the $P_{\frac{1}{2}}$ vector if $\delta_1^-=\delta$, $\alpha_1=\alpha$, and $\cos\theta>0$. The diameter of the locus circle is given by $(l+1)P_l(\cos\theta)$ for the l^+ partial wave and by $lP_l(\cos\theta)$ for the l^- partial wave.

If the incident proton energy is varied through a resonance, then the term $\beta=\tan^{-1}[\frac{1}{2}\Gamma/(E_\lambda+\Delta_\lambda-E)]$ which is caused by this resonance will vary from near 0° to near 180°. The corresponding vector will travel once around its locus circle. If the angular momentum of the compound state which causes the resonance is J, then the diameter, b, of the locus circle will be $(J+\frac{1}{2})P_l(\cos\theta)$. The ends of the maximum and minimum A vectors will fall at opposite ends of a diameter of the circle; and this diameter, or an extension thereof, will pass through the origin of the A vectors. Thus, it follows that $A_{\max}\pm A_{\min}=(J+\frac{1}{2})P_l(\cos\theta)$, and if B can be neglected, then we have

$$b=\lambda^{-1}[(\sigma_{\max})^{\frac{1}{2}}\pm(\sigma_{\min})^{\frac{1}{2}}]=(J+\tfrac{1}{2})P_l(\cos\theta), \quad (6)$$

where $\sigma_{\max}$ and $\sigma_{\min}$ are the maximum and minimum differential cross sections at the resonance. For Eq. (6) to be valid, the observed width of the resonance must be sufficiently small that the phase shifts of the partial waves which do not excite the resonance will be essentially constant as the energy is varied from the maximum to the minimum of the resonance.

Each scattering vector can be further broken down into two components which represent the "hard sphere" or normal potential scattering and the anomalous potential or resonance scattering. In some cases this breakdown of the scattering vectors will simplify the analysis, but in the discussion which follows, only the resultant of these two vectors will be drawn. Thus, each scattering vector corresponds to one of the terms in Eq. (2). For simplicity in the diagrams, the two scattering vectors for the lth partial wave ($l>0$) are sometimes combined to form one resultant vector. Reference to resonances and to the corresponding energy levels of the compound nucleus will be made in terms of symbols such as $P_{\frac{1}{2}}$. The subscript refers to the total angular momentum of the compound state, and the capital letter refers to the orbital angular momentum of the bombarding protons which form this state.

Sufficient data are not available from the present scattering experiment to carry out an accurate phase shift analysis. However, with the aid of a geometrical representation of the equations for scattering, some of the experimental results can be interpreted in a general manner. In order to apply the scattering equations it was necessary to make certain simplifying assumptions. The reaction radii are assumed to be independent of energy, and the reaction radii for all types of potential and resonance scattering except S scattering are assumed to be the same. These simplifications are probably not correct, but an accurate phase shift analysis would be necessary to determine what the properties of the reaction radii are.

III. THE 2.66-MEV RESONANCE

An analysis of the scattering data is most easily started in the low energy region of the curve because at low energies only the partial waves with low orbital angular momentum will contribute appreciably to the scattering. A convenient starting point for the present data is the 2.66-Mev resonance. Applying Eq. (6) to data on this resonance and using the cross section

TABLE I. Theoretical values for the diameters of the locus circles

Type of energy level	Diameter of locus circle $b=(J+\frac{1}{2})P_l(\cos 165°)$
$S_{1/2}$	1.00
$P_{1/2}$	0.97
$P_{3/2}$	1.93
$D_{3/2}$	1.80
$D_{5/2}$	2.70
$F_{5/2}$	2.41
$F_{7/2}$	3.22
$G_{7/2}$	2.74
$G_{9/2}$	3.42
$H_{9/2}$	2.74
$H_{11/2}$	3.28

[8] S. G. Kaufmann (unpublished) previously used a circular locus for plotting resonances where only interference between resonance and Rutherford-type scattering was considered.

values of the previous paper corrected to the center-of-mass system gives $b=1.12$ if the minus sign of Eq. (6) is used, and $b=2.05$ if the plus sign is used. The nature of the experimental cross section measurement is such that these values of b are not accurate, but they represent a maximum value for b. Table I gives the theoretical values for the diameters of the locus circles for the present experiment if the angular spread of the scattered protons which were detected is neglected. Averaging over the acceptance angle of the analyzer lowers slightly the theoretical diameters of the circles for the higher angular momenta.

A comparison of the experimental values of b with the theoretical values indicates that the only types of resonances which would give reasonable agreement are $S_{\frac{1}{2}}$, $P_{\frac{1}{2}}$, $P_{\frac{3}{2}}$, and $D_{\frac{3}{2}}$. A vector diagram was drawn for each of these four cases, and the shape of the resonance computed from the diagram was compared with the experimental results. The nearly symmetrical dip in the cross section was found to be reproduced theoretically only if the resonance is assumed to be $S_{\frac{1}{2}}$ and if a large phase shift for S-potential scattering is assumed at 2.66 Mev. Later attempts to explain the scattering data obtained from 0.6 to 2.66 Mev indicated that a large S-wave phase shift at 2.66 Mev was also a necessary consequence of a reasonable explanation of these data. The S-wave phase shift obtained from attempts to fit the low energy portion of the curve will be used in further discussion of the 2.66-Mev resonance.

Figure 2 shows the vector diagram for the 2.66-Mev resonance assuming it is an $S_{\frac{1}{2}}$ resonance. A vector drawn between points A and O would be the resultant of the D and P potential scattering and Rutherford scattering vectors, assuming a reaction radius of 5.31×10^{-13} cm and that there are no P or D resonances which influence the scattering at this energy. The vector OC represents the S wave scattering vector at an energy near the resonance but sufficiently far away so that the effect of the resonance is negligible. As the proton energy is varied over the resonance, the point C will move counterclockwise around the circle. Inspection of the vector diagram of Fig. 2 shows that the resonance indicated there will give a dip in the cross section which is nearly symmetric as was observed in the scattering experiment. Estimates were made of the effects of resonances above 2.66 Mev on the phase shifts at 2.66 Mev. These estimates were partially on the basis of the present experiment and partially on the basis of mirror level arguments. Consideration of the broad $P_{\frac{1}{2}}$ and $D_{\frac{3}{2}}$ levels at higher energies as well as a small contribution from F potential scattering at 2.66 Mev gives the vector BC of Fig. 2. The D potential scattering vector is broken down into its $D_{\frac{3}{2}}$ and $D_{\frac{5}{2}}$ components to show the effect of D resonances at higher energies on the scattering; and, similarly, the P vector is broken down into its $P_{\frac{1}{2}}$ and $P_{\frac{3}{2}}$ components. Figure 2 shows that resonances at higher energies will have only a small influence on the scattering at 2.66 Mev.

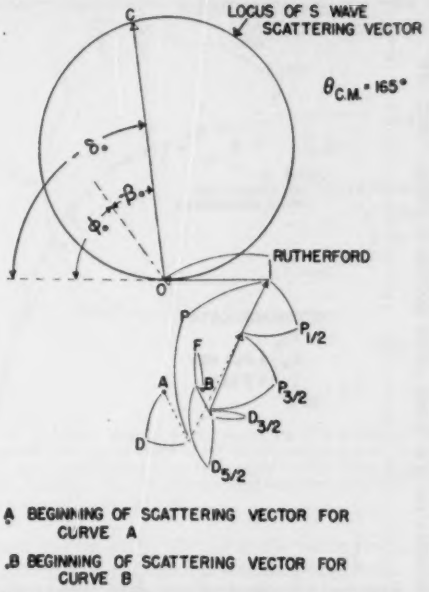

FIG. 2. Vector diagram for the scattering of 2.66-Mev protons from O^{16} through an angle of 165° in the center-of-mass system if an $S_{\frac{1}{2}}$ resonance is assumed at this energy.

The experimental diameter of the locus circle was 1.12, so that if the experimental data on the 2.66 Mev resonance is to be fitted to the theoretical curve for an $S_{\frac{1}{2}}$ resonance, the experimental cross sections must be multiplied by $1/(1.12)^2$. If the conversion from laboratory to center-of-mass system is also included in the factor, the experimental cross section values must be multiplied by 0.72; and in all further comparison of the formulas with experimental results the experimental cross sections will be multiplied by this factor. It should be recalled at this point that the experimental determination of the relative minimum cross section for the 2.66-Mev resonance was subject to a large percentage error. If the minimum were lower than the value used, it would be found that the point B in Fig. 2 would be closer to the locus circle than is shown, and the experimental cross section values would have to be multiplied by a factor smaller than 0.72. Also, moving the point B closer to the locus circle would enable this resonance to be explained with a smaller reaction radius for P and D scattering. Thus, the entire analysis presented here is indirectly dependent on the experimentally determined shape of the 2.66-Mev resonance. However, the general conclusions reached should not be dependent on these uncertainties.

Using the vector diagram of Fig. 2, a curve can be drawn which represents the theoretical shape of the resonance assuming it is $S_{\frac{1}{2}}$. Assuming a width, Γ, of 19.9 kev gave the best fit to the experimental data. A

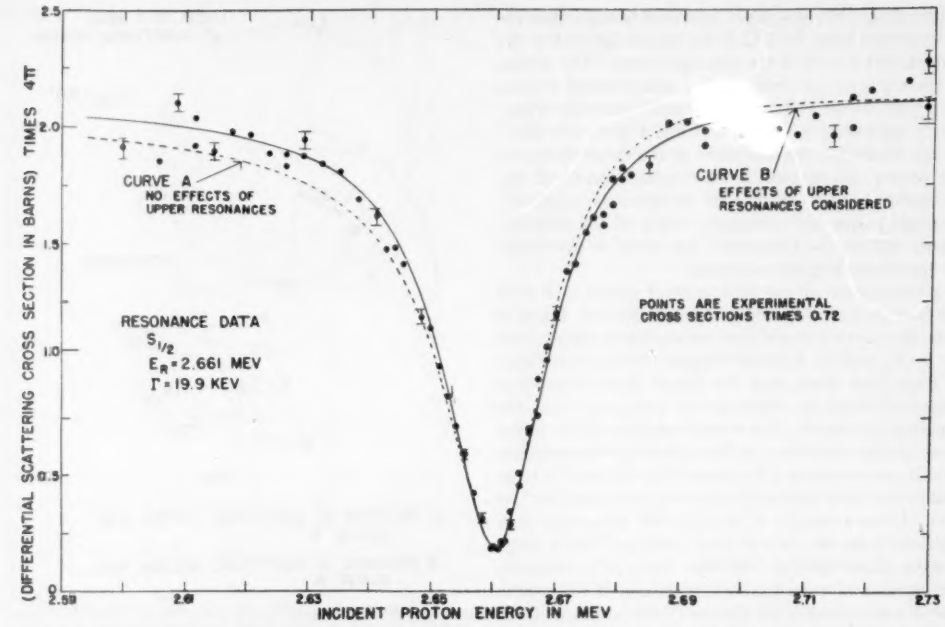

FIG. 3. Comparison of the theoretical shape of the 2.66-Mev resonance with the experimental points. The theoretical shape is based on the vector diagram of Fig. 2. Curve A corresponds to the vectors beginning at point A on Fig. 2 and curve B corresponds to the vectors beginning at point B on Fig. 2.

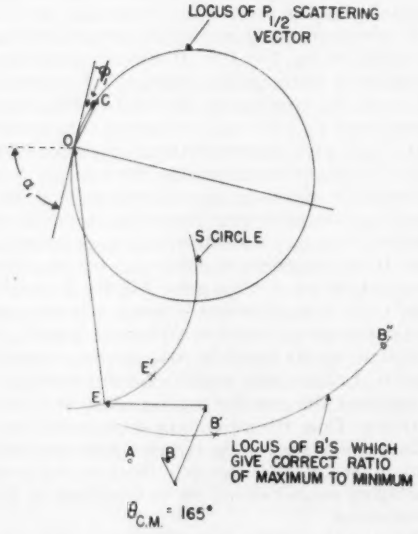

FIG. 4. Vector diagram for the scattering of 2.66-Mev protons from O^{18} through an angle of 165° in the center-of-mass system if a $P_{\frac{1}{2}}$ resonance is assumed at this energy.

comparison of the theoretical curves with the experimental points is shown in Fig. 3. The dashed curve A corresponds to the vectors which start at point A in Fig. 2, and the solid curve B corresponds to the vectors which start at point B in Fig. 2. It is seen that curve B, which takes into account the effect of resonances at higher energies, is a better fit to the experimental data.

If a $P_{\frac{1}{2}}$ resonance is assumed at 2.66 Mev, the vector diagram which is shown in Fig. 4 will be obtained. OC of Fig. 4 represents the $P_{\frac{1}{2}}$ vector off resonance, and EO represents the S wave scattering vector. For convenience, the $P_{\frac{1}{2}}$ vector has been moved to the position of the last vector of the sum. The same assumptions have been made in drawing Fig. 4 as were made for Fig. 2 except for the nature of the resonance. Points A and B of Fig. 4 correspond to the points A and B of Fig. 2. The $P_{\frac{1}{2}}$ locus circle is rotated through an angle of $(180°+\alpha_1°)$, where the extra 180° takes into consideration the fact that all odd legendre polynomials are negative for angles near 180°.

The shape of the 2.66-Mev resonance which results from the vector diagram of Fig. 4 is shown by the curve of Fig. 5 to be too asymmetric. This asymmetry can also be seen from the vector diagram. The locus of the points, B, on Fig. 4 which would give the correct ratio of maximum to minimum cross section is indicated

by the arc $B'B''$. The point B'' is the origin of the vector diagram which would give the experimentally determined shape to the cross section. No simple assumptions about neighboring resonances were found which could move the point B to B''. Moving B to B'' would require the presence of broad resonances near 2.66 Mev, which were not observed because of extremely unlikely interference effects. The arc labeled S circle is the locus of the point E as the S wave phase shift is varied while the point O is held fixed. It can be seen that decreasing the S wave phase shift also will not bring the point B to B''. On the basis of the vector diagram of Fig. 4 it has been concluded that the 2.66-Mev resonance is not $P_{\frac{1}{2}}$.

Vector diagrams for the 2.66-Mev resonance were also drawn assuming it to be $P_{\frac{1}{2}}$ or $D_{\frac{1}{2}}$. Arguments similar to those given above for the $P_{\frac{1}{2}}$ case can be used to rule out these other cases also. When the plus sign is used in Eq. (6), the start of the vector diagram must be inside the locus circle for the resonance. Because this condition is not fulfilled if a $D_{\frac{1}{2}}$ resonance is assumed,

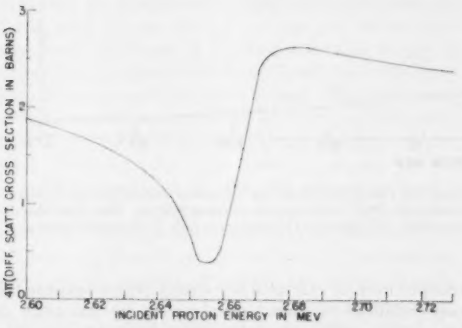

FIG. 5. Calculated shape of the 2.66-Mev resonance if it is assumed to be a $P_{\frac{1}{2}}$ resonance. Calculations are based on the vector diagram of Fig. 4.

this possibility is readily eliminated without additional arguments.

If the analysis of the 2.66-Mev resonance presented above is correct, it should be possible to predict results of other experiments on the scattering of protons in this energy region by oxygen. The simplest experimental method determining the validity of the above analysis would probably be a determination of the shape of the 2.66-Mev resonance when protons scattered through 90° in the center-of-mass system are observed. Figure 6 shows the vector diagram for scattering through 90°, assuming the 2.66-Mev resonance is $S_{\frac{1}{2}}$. OC represents the S wave scattering off resonance, and various S wave vectors for energies in the resonance region are shown by dashed lines. It should be noted that P scattering does not contribute at 90° if there is no P resonance. The predicted shape of the 2.66-Mev resonance if observed at 90° is shown by the upper curve of Fig. 7,

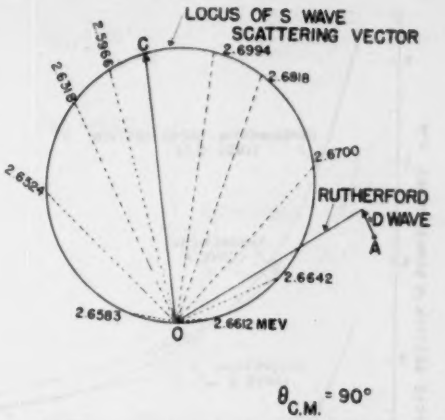

FIG. 6. Vector diagram for the scattering of 2.66-Mev protons from O^{16} through an angle of 90° in the center-of-mass system. The same assumptions have been made for this diagram as for curve A of Fig. 3. The S-wave scattering vectors at various energies are indicated by dashed lines.

which was drawn by the use of the vector diagram of Fig. 6. If a P resonance is assumed, only factor B of Eq. (1) will contain a term due to the resonance, and

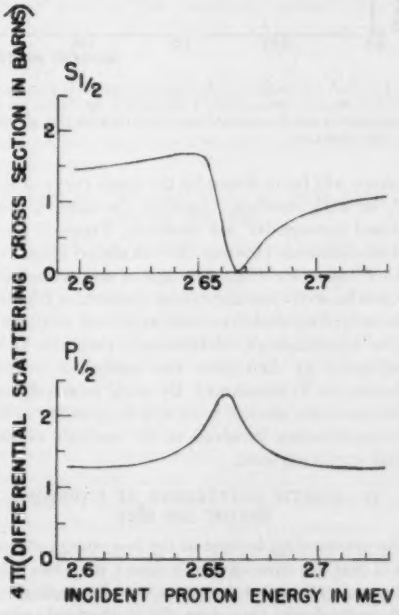

FIG. 7. A comparison of the calculated shape of the 2.66-Mev resonance for scattering through a center-of-mass angle of 90° if either an $S_{\frac{1}{2}}$ or a $P_{\frac{1}{2}}$ resonance is assumed. The $S_{\frac{1}{2}}$ curve is obtained from the vector diagram of Fig. 6. The $P_{\frac{1}{2}}$ curve is obtained using the same parameters except for the type of resonance assumed.

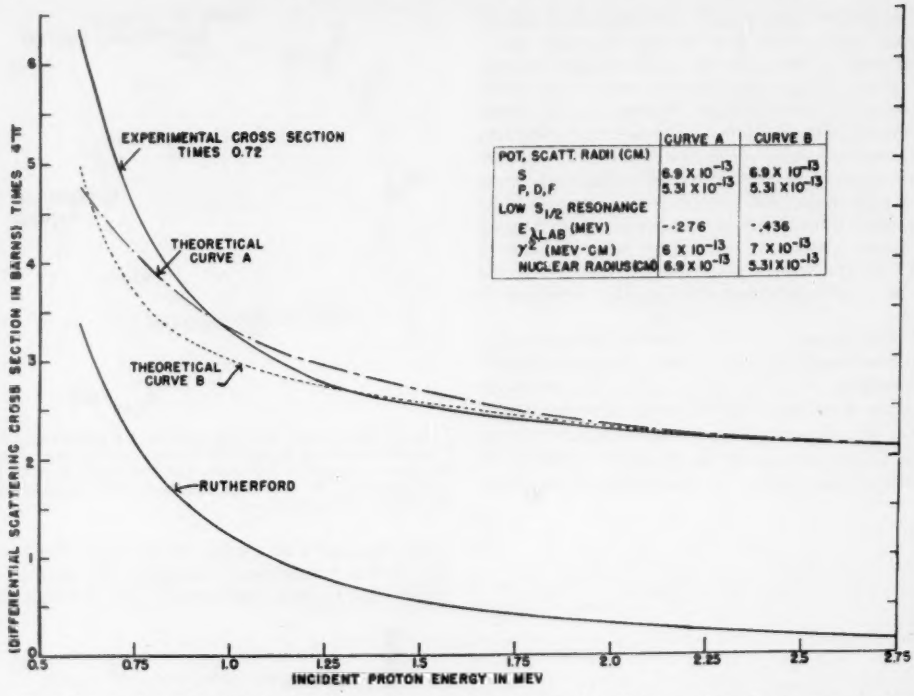

FIG. 8. A comparison of the experimental yield curve for scattering at low energies with curves calculated using assumed values for the nuclear parameters. Calculations are based on scattering through 165° in the center-of-mass system. The 2.66-Mev resonance is not shown on these curves because this resonance is narrow and will influence the scattering only in the neighborhood of the resonance.

the shape will be as shown by the lower curve of Fig. 7. A $P_{\frac{1}{2}}$ or a $P_{\frac{3}{2}}$ resonance appears the same if protons scattered through 90° are observed. Figure 7 shows a marked difference between the calculated shapes of an S or a P resonance when the angle of observation is 90°.

It can be seen from the vector diagram of Fig. 6 that if the ratio of maximum to minimum cross section at 90° can be experimentally determined, then the D wave contribution at 2.66 Mev can easily be calculated (assuming an $S_{\frac{1}{2}}$ resonance). By using relatively simple techniques such as this, it should be possible to lessen the complications involved in an analysis of experimental scattering data.

IV. ELASTIC SCATTERING AT ENERGIES BELOW 2.66 MEV

The outstanding feature of the low energy scattering data is that the cross section is larger than the Rutherford cross section and decreases with increasing energy much more slowly than does the Rutherford cross section. The low energy data can be explained in a general manner by assuming the existence in the compound nucleus of a broad $S_{\frac{1}{2}}$ level at low energies. A P or higher order level will not explain the large cross sections over an extended low energy region because the penetrabilities of these partial waves are too small at low energies. With the information available, the only method of analyzing the low energy data was to assume values of the parameters involved and then compare the calculated curve with experiment. The two best fits to the experimental curve which were obtained after a small number of trials are shown in Fig. 8. The 2.66-Mev resonance is not shown on the curve, because it is narrow and will effect the scattering only in the immediate neighborhood of the resonance.

Some time after the calculations indicated in Fig. 8 were finished, the existence of a low-lying level in F^{17} was established by Ajzenberg,[9] who observed neutrons from the $O^{16}(d,n)O^{17}$ reaction. The position of the level was found to be 551 ± 15 kev above the ground state rather than at 350 kev or 200 kev, which were used in Fig. 8 for curves A and B, respectively. The assumption of a bound level was correct. Recalculation of the curves in Fig. 8 does not seem profitable until more experimental information is available on the scattering of protons by oxygen in the low energy region. Some evi-

[9] F. Ajzenberg, Phys. Rev. 83, 875 (A) (1951).

dence is also presented by Ajzenberg to show that the low-lying level is $S_{\frac{1}{2}}$, in agreement with the assumptions made for analyzing the present experiment.

It has been shown by Thomas[6] that in calculations of scattering cross sections where a broad resonance influences the scattering, the variation of Δ_λ with energy must be considered. If a resonance is narrow, such as the one at 2.66 Mev, then Δ_λ for this level can be assumed to be constant and $(E_\lambda+\Delta_\lambda)$ may be taken as the resonance energy, E_R. For calculations involving the low energy scattering data, the variation of Δ_λ with energy has been considered. Δ_λ is a sum of the values of Δ for the various modes of decay of the compound state λ. In the present experiment gamma-ray emission and proton emission are the only two possible modes of decay of the compound nucleus, and the Δ for gamma-ray emission is small in comparison with that for proton emission. Hence, only the value of Δ for proton emission has been given in Eq. (5) for Δ_λ, and this value was used in the calculations. If the formulas used in this paper are correct, then the 0.55-Mev level in F^{17} has a very peculiar property. This level is a bound level and can decay only by gamma-ray emission so that observation of the level by the $O^{16}(d,n)O^{17}$ reaction should give very nearly the value of E_λ. As the binding energy of oxygen for a proton is 0.61 Mev, E_λ will be -0.06 Mev referred to the center-of-mass system. The value of Δ_λ for low energy S protons will be positive and sufficiently large so that there will exist a proton energy, E_R, for which $(E_\lambda+\Delta_\lambda)=E_R$. For proton energies in the immediate vicinity of E_R, the scattering cross section will behave in an anomalous manner typical of a resonance, although the cause of this behavior is a bound energy level. Experimental data on the scattering of low energy protons by oxygen are needed in order to determine the validity of the above arguments.

Attempts to fit the low energy scattering data of the present experiment have led to the conclusion that the reduced width of the low lying level is near the maximum allowed by Wigner's criterion,[10] which states that the maximum value of the reduced width is given approximately by the relation,

$$\gamma_\lambda^2 \cong \tfrac{3}{2}\hbar^2/mR, \qquad (7)$$

where m is the reduced mass of the system, $\hbar$ is Planck's constant divided by 2π, and R is the reaction radius. All assumptions which were made for the calculations in the low energy region were limited in two respects: (1) to values of γ_λ^2 which obey Wigner's criterion, and (2) to combinations of E_λ, γ_λ^2, and R which give $(E_\lambda+\Delta_\lambda)_{E=E_R}<450$ kev, as was observed experimentally.

Rather large reaction radii have been used in the calculations because they appeared to be necessary in order to fit the experimental data. More accurate and extensive data are needed to obtain accurate values for the reaction radii. Smaller values for the absolute cross sections will lead to somewhat smaller reaction radii. Results of the analysis presented indicate that the reduced width of the F^{17} levels can vary over a wide range. The reduced width of the 3.11-Mev $S_{\frac{1}{2}}$ level is 0.048×10^{-13} Mev-cm, while the 0.55-Mev $S_{\frac{1}{2}}$ level appears to have a reduced width at least 100 times larger. Perhaps this difference in the reduced widths is caused by a fundamentally different mode of excitation for the two states.

[10] E. P. Wigner, Am. J. Phys. **17**, 99 (1949).

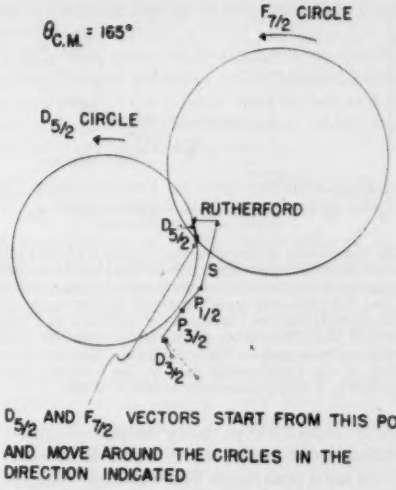

FIG. 9. Vector diagram for the scattering of 3.47-Mev protons from O^{16} through an angle of 165° in the center-of-mass system. The locus circles for both a $D_{5/2}$ and an $F_{7/2}$ resonance at this energy are also shown.

V. THE SCATTERING DATA AT ENERGIES ABOVE 2.66 MEV

If the best experimental values obtained for the 3.47-Mev resonance are substituted in Eq. (6), the result is $b=3.1$ using the minus sign or $b=4.4$ using the plus sign. These values may be low because of the difficulty in obtaining a sufficiently small proton beam spread to determine the true shape of this very narrow resonance. The value of $b=4.4$ can be ruled out immediately because it is larger than any of the possible values of b given in Table I. In order to decide between the several assignments which may be made to the 3.47-Mev resonance on the basis of Eq. (6), the vector diagram shown in Fig. 9 was drawn together with a circular locus for either a $D_{\frac{1}{2}}$ or an $F_{7/2}$ resonance.

It will be assumed in the discussions which follow that the parity of an energy level of F^{17} is equal to the parity of the orbital angular momentum of the proton which interacts with O^{16} to form the energy level. For convenience, a resonance will be said to have even or odd parity depending on whether the orbital angular momentum of the protons which excite the resonance have even or odd parity.

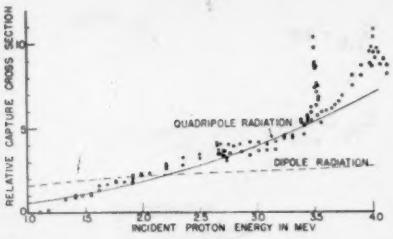

FIG. 10. Comparison of the calculated variation of the capture cross section with the experimental points. Calculations are shown for two possible modes of decay of the compound state, and they assume that the capture is caused by the broad low energy level of F^{17}. No account has been taken of the resonance at a proton energy of 3.99 Mev. The nuclear parameters assumed for curve B of Fig. 8 have been used for the calculations. The curves were normalized to the experimental data at the following points: dipole radiation, 2 Mev; quadrupole radiation, 3 Mev.

All locus circles for even parity resonances caused by D or higher order partial waves would have approximately the same position on Fig. 9 because values of α_l are not sensitive to the value of l for the larger values of l. Similarly, all locus circles for odd parity resonances caused by F or higher order partial waves will have approximately the same position. An inspection of the vector diagram at 3.47 Mev shows that an even parity resonance would give a yield curve exhibiting the maximum cross section at a lower energy than the minimum. However, an odd parity resonance would have the minimum cross section at a lower energy than the maximum. The experimental curve fits the latter case; and, therefore, the 3.47-Mev resonance was taken to be an F or higher order resonance of odd parity. On the assumption that an H resonance would not be expected until higher energies were reached, the resonance at 3.47 Mev was taken to be excited by F protons. The experimental value of b leads to a choice of 7/2 rather than 5/2 as the total angular momentum of the compound state.

The best experimentally determined shape of the 3.47-Mev resonance indicates that if this resonance is $F_{7/2}$, the vector diagram should begin at the point marked by an x in Fig. 9. Resonances at higher energies will have an effect on the 3.47-Mev vector diagram because of the relatively high penetrability of P and D partial waves at this and higher energies. Although the effect of these resonances was estimated for the diagram shown, their influence may be larger than this estimate, and in this case the start of the vector diagram will move toward the point x. The effect of increasing the assumed width of a higher energy $D_{\frac{1}{2}}$ resonance is shown by the dotted $D_{\frac{1}{2}}$ vector in Fig. 9. No reasonable assumptions would enable the vector diagram to indicate an even parity resonance.

If the slowly rising scattering cross section between 3.5 and 4.0 Mev is attributed to the 3.99-Mev resonance, which was indicated by the capture data, then this resonance is of the type which would give a maximum before the minimum. Since the arguments about even and odd parity resonances which were used at 3.47 Mev apply to this case also, the resonance is assumed to be even parity. Mirror level arguments indicate that the total angular momentum should be $\frac{3}{2}$, and hence the assignment $D_{\frac{3}{2}}$ is given to the 3.99-Mev resonance.

If the minimum at 4.26 Mev and the maximum near 4.5 Mev in the scattering yield curve are caused by the same resonance, then b is calculated to be 1.8 or 5.0 using the minus or plus sign, respectively, of Eq. (6). It is assumed that Eq. (6) can be applied in this instance to indicate the value of J, in spite of the interference between resonances, because the variation of the $D_{\frac{1}{2}}$ vector due to the 3.99-Mev resonance is not large between 4.27 and 4.5 Mev. A comparison of the experimental values of b with Table I indicates that the total angular momentum is probably $\frac{3}{2}$. Mirror level arguments indicate that the 4.39-Mev resonance is $P_{\frac{1}{2}}$.

The above discussion explains the general shape of the scattering yield curve at high energies. However, when a detailed theoretical calculation of the shape of the curve was made, it was found that the general level of the experimental cross section above about 3.7 Mev was higher than could be accounted for by the resonances discussed above. This is probably to be expected, since in this energy region penetrabilities of high order partial waves are relatively high, and the observed widths of resonances can be very large. Broad resonances probably occur at energies slightly higher than were reached in the present experiment, and the effects of these resonances may be large above 3.7 Mev.

Effects of the ground state of F^{17} on the scattering have been neglected in the analysis described here. There is evidence that the ground state is $D_{\frac{1}{2}}$, and if the $D_{\frac{1}{2}}$ resonance at 3.99 Mev is caused by a level which forms an inverted doublet with the ground state, then the reduced width of the ground state may be assumed to be large. Below 2.66 Mev the penetrability of D waves is so small that the ground state will have only a small effect on the scattering. At higher energies the influence of the ground state may be large. The start of the 3.47-Mev vector diagram of Fig. 9 would be closer to that expected from the experimental shape of the curve, and the calculated general level of the cross section over the high energy portion of the yield curve would be raised if the effects of a D ground state were included.

VI. ANALYSIS OF THE CAPTURE DATA

The peak observed in the capture cross section near 3.47 Mev can easily be explained by the narrow 3.47-Mev resonance observed in the scattering yield. The large capture cross section which extends over the entire energy range is probably caused by the broad $S_{\frac{1}{2}}$ level in F^{17}. A comparison of the calculated variation of the capture cross section with the experimental points is shown in Fig. 10. The calculated variation is based

on the one-level dispersion formula[11] in the following form:

$$\sigma=\pi\lambda^2\Gamma_\gamma\Gamma_p/[(E_\lambda+\Delta_\lambda-E)^2+\tfrac{1}{4}\Gamma^2],$$

where $\Gamma_p=[2k\gamma_\lambda^2/(F_l^2+G_l^2)]_{r=R_l}$ is the width of the level for proton emission, Γ_γ is the width of the level for gamma-ray emission, and $\Gamma=\Gamma_p+\Gamma_\gamma$. Since Γ_γ is small compared with Γ_p, Γ can be taken as equal to Γ_p. The characteristics of the low-lying F^{17} level which were assumed for curve B of Fig. 8 have been used for the calculated curves of Fig. 10, and the experimental points are those obtained with the thin oxide targets. The variation of Γ_γ with energy will depend on the type of gamma-radiation by which the compound nucleus decays. For dipole radiation, Γ_γ will be proportional to the cube of the gamma-ray energy, while for quadrupole radiation, Γ_γ will be proportional to the fifth power of the gamma-ray energy. The calculated curve of Fig. 10 for dipole radiation was normalized to the experimental data at 2.0 Mev, and the normalization point for the quadrupole radiation curve was at 3.0 Mev.

Figure 10 shows that the capture cross section extending over a large energy region can be explained on the basis of the low-lying level in F^{17}. The large departure of the experimental points from the theoretical curve for quadrupole radiation in the energy range above 3.7 Mev probably results from the broad resonance at 3.99 Mev which was not considered in the calculations. The reasonably good agreement between the curve for quadrupole radiation and the experimental points is an indication that quadrupole radiation is the mode of transition from the low lying $S_{\frac{1}{2}}$ level to the ground state. It is possible, however, that the curve for dipole radiation would fit the experimental points if the possible variation of the nuclear matrix elements with energy could be taken into account.

If it is assumed that quadrupole radiation is responsible for the capture by the broad $S_{\frac{1}{2}}$ level, then some statements about the ground state of F^{17} can be made. It will be assumed that this ground state has even parity and is either an S or a D state. Shell models of the nucleus[1,2] eliminate a P ground state. If the ground state were $S_{\frac{1}{2}}$, then magnetic dipole radiation would be allowed, and the calculated curve for dipole radiation should fit the experimental points. If the ground state were $D_{\frac{1}{2}}$, electric quadrupole or higher order radiation would be required, as is indicated by the present data. A $D_{\frac{1}{2}}$ ground state could be reached from the $S_{\frac{1}{2}}$ level by either magnetic dipole or electric quadrupole radiation. According to a paper by Austern and Sachs,[12] the magnetic dipole radiation should predominate in this case, and the behavior of the cross section would then be expected to follow that for dipole radiation. Thus, the variation of the capture cross section with energy gives some evidence, but is not proof, that the ground state of F^{17} is $D_{\frac{1}{2}}$.

A $D_{\frac{1}{2}}$ ground state can be reached from the $F_{7/2}$ level by electric dipole radiation, which is more likely to give the large peak in the capture cross section at 3.47 Mev than an electric octupole transition, which would be required if the ground state were $S_{\frac{1}{2}}$.

VII. COMPARISON OF THE ENERGY LEVELS IN THE MIRROR NUCLEI, F^{17} AND O^{17}

A summary of the energy levels assigned to F^{17} is shown on Fig. 11 together with the energy levels in O^{17} for comparison. The O^{17} and F^{17} energy level diagrams have been shifted so that their ground states coincide on the vertical energy scale. A detailed list of reactions leading to excited states of O^{17} together with references is given by Hornyak *et al.*[13] In light of more recent experiments, some changes have been made in the energy level diagram for O^{17} which is given in this review. The positions of the 4.56-, 5.08-, and 5.36-Mev energy levels in O^{17} were obtained from the experiments of Bockelman[14] on the scattering of neutrons by oxygen. The positions of the other energy levels of O^{17} have been taken from the work of Rotblat,[15] although it should be mentioned that the position of the 0.87-Mev level has been located by other more accurate experiments.

Experiments by Burrows *et al*[16] on the angular dis-

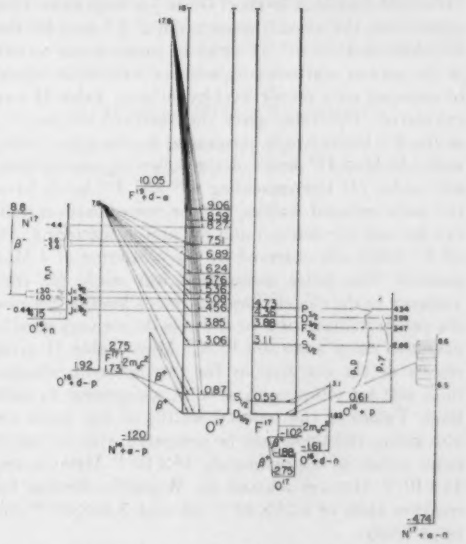

FIG. 11. Comparison of the energy levels in the mirror nuclei, O^{17} and F^{17}.

[11] E. P. Wigner and L. Eisenbud, Phys. Rev. **72**, 29 (1947).
[12] N. Austern and R. G. Sachs, Phys. Rev. **81**, 710 (1951).
[13] Hornyak, Lauritsen, Morrison, and Fowler, Revs. Modern Phys. **22**, 291 (1950).
[14] C. K. Bockelman, Phys. Rev. **80**, 1011 (1950).
[15] J. Rotblat, private communication, courtesy of T. Lauritsen.
[16] Burrows, Gibson, and Rotblat, Phys. Rev. **80**, 1095 (1950).

TABLE II. Calculated widths Γ_p of the F^{17} levels which correspond to levels of O^{17}.

O^{17} energy level Mev	Observed resonance energy for $O^{16}(n,n)$ reaction	Observed width, Γ_n Mev in the lab system	Assumed reaction radius cm	$P_{\frac{1}{2}}$ level assumed		$D_{\frac{1}{2}}$ level assumed	
				γ^2 Mev-cm	Γ_p calculated for 4-Mev protons Mev	γ^2 Mev-cm	Γ_p calculated for 4-Mev protons Mev
4.56	0.44	0.053	3.78×10^{-13}	0.79×10^{-13}	0.26	21.0×10^{-13}	1.9
5.08	1.00	0.100	3.78×10^{-13}	0.57×10^{-13}	0.18	5.9×10^{-13}	0.52
5.36	1.30	0.040	3.78×10^{-13}	0.17×10^{-13}	0.055	1.3×10^{-13}	0.12
4.56	0.44	0.053	5.31×10^{-13}	0.49×10^{-13}	0.24	6.1×10^{-13}	1.4
5.08	1.00	0.100	5.3×10^{-13}	0.39×10^{-13}	0.19	2.0×10^{-13}	0.45
5.36	1.30	0.040	5.3×10^{-13}	0.12×10^{-13}	0.06	0.46×10^{-13}	0.10

tribution of protons from the $O^{16}(d,p)O^{17}$ reaction have been interpreted by Butler[17] to indicate that the ground state of O^{17} is a D state, and the 0.87-Mev level is an $S_{\frac{1}{2}}$ state. A recent measurement of the spin[18] of O^{17} gives the value 5/2, so that the ground state is probably $D_{\frac{1}{2}}$. It therefore appears as if the ground state and first excited state of O^{17} have the same total angular momentum and parity as the corresponding states of F^{17}.

The 3.06- and 3.85-Mev levels in O^{17} correspond in position with the 3.11- and 3.88-Mev levels in F^{17}. No further information is available on the characteristics of these O^{17} levels, so that a more detailed comparison cannot be made.

Experiments on the scattering of neutrons by oxygen[14] indicate that the angular momentum of the 4.56-, 5.08-, and 5.36-Mev levels of O^{17} is $\frac{3}{2}$ in each case. This agrees with the angular momentum of $\frac{3}{2}$ found for the 4.73-Mev level in F^{17}. In order to compare the results of the proton scattering experiment with what would be expected on a mirror level hypothesis, Table II was calculated. This table gives the observed widths, Γ_p, of the F^{17} levels which correspond to the 4.56-, 5.08-, and 5.36-Mev O^{17} levels if the following assumptions are made: (1) Corresponding O^{17} and F^{17} levels have the same reduced widths, (2) the same reaction radii can be used for neutron and for proton scattering, (3) all F^{17} levels are observed by the scattering of 4-Mev protons. The latter assumption was made for convenience in the calculations and was allowable because the penetrabilities for P or D waves do not vary greatly over the range from 4.0 to 4.5 Mev. Table II gives results of the calculations for two different reaction radii and for either a $P_{\frac{1}{2}}$ or a $D_{\frac{1}{2}}$ assignment to each level. Values of the reduced widths of the levels are also given, and these may be compared with the maximum values of approximately 18×10^{-13} Mev-cm and 13×10^{-13} Mev-cm allowed by Wigner's criterion for reaction radii of 3.78×10^{-13} cm and 5.31×10^{-13} cm, respectively.

From the proton scattering data, Γ_p for the 4.73-Mev level in F^{17} is estimated to be about 0.24 Mev, and fitting this value to the data of Table II indicates that reasonable agreement is obtained only if the level is assumed to be $P_{\frac{1}{2}}$. Table II indicates that the 4.73-Mev level of F^{17} may correspond to either the 4.56- or 5.08-Mev level of O^{17}. While agreement appears better with the 4.56-Mev level, the possibility of a larger reaction radius for proton scattering than for neutron scattering could give a good correspondence with the 5.08-Mev level.

The value of Γ_p for the 4.36-Mev level in F^{17} cannot be reliably obtained from the available data, but the best estimate from the capture data gives $\Gamma_p \cong 0.5$ Mev for this level. This estimate takes into consideration the effect of the variation of Δ_λ with energy in making the actual observed width less than Γ_p. A comparison with Table II indicates that this 4.36-Mev level is $D_{\frac{1}{2}}$ and probably corresponds to the 5.08-Mev level of O^{17}. This assignment is in agreement with the D assignment made previously on the basis of the proton scattering data. The two highest levels observed in F^{17} appear, therefore, to have similar characteristics to two mirror levels in O^{17}, although the levels do not appear in the same order in F^{17} as in O^{17}.

In view of the fact that the $D_{\frac{1}{2}}$ level has a large reduced width, the relatively large downward shift of the $F^{17}D_{\frac{1}{2}}$ level with respect to the corresponding $O^{17}D_{\frac{1}{2}}$ level might be expected. The 3.11- and 3.88-Mev levels in F^{17}, which correspond very closely in energy to their mirror levels in O^{17}, have small reduced widths.

The value of Δ_p for the 4.36-Mev F^{17} level cannot be obtained from the present data with sufficient accuracy to rule out the equivalence of this level with the 4.56-Mev level in O^{17}. If the 4.56-Mev O^{17} level is a $D_{\frac{1}{2}}$ level, then Table II indicates that the reduced width of this level is very large. It would be necessary to assign a large reaction radius to the scattering if Wigner's criterion is to be obeyed.

A comparison of the energy levels of O^{17} and F^{17} is very favorable to the mirror nucleus hypothesis.

The authors wish to thank Professor R. G. Herb, under whose supervision this project was carried out, for his assistance and encouragement. Very valuable discussions with Professor H. T. Richards, Dr. R. K. Adair, and Dr. F. P. Mooring are also gratefully acknowledged.

[17] S. T. Butler, Phys. Rev. **80**, 1095 (1950).
[18] F. Alder and F. C. Yu, Phys. Rev. **82**, 105 (1951).

Nuclear Disintegrations Induced by μ-Mesons

G. Cocconi and V. Cocconi Tongiorgi
Cornell University, Ithaca, New York

(Received June 18, 1951)

The absorption curve in water of the cosmic radiation producing nuclear disintegrations was obtained by recording the neutron showers occurring in an absorber surrounded by BF_3 counters. It was found that, while the N-component of the cosmic radiation is responsible for most of the disintegrations observed under the first few meters of water, μ-mesons are the particles causing either directly or indirectly most of the events recorded at depths greater than $\sim$10 m water. The cross section of μ-mesons for nuclear interactions is found to be $\sim 1\times10^{-29}$ cm^2/nucleon at a depth of 20 m water. Estimates of the absolute intensity of the N-component and of the relative contribution to nuclear disintegrations by μ-mesons and N-component at sea level are given.

I. INTRODUCTION

THE problem of the interaction of μ-mesons with nucleons has been faced experimentally by looking either for anomalous scattering of the μ-mesons of the cosmic radiation or for the products of the nuclear disintegrations induced by them.

Using the first method, Amaldi and Fidecaro[1] were able to show that for the μ-mesons at sea level (average energy $\sim 1\times10^9$ ev) the upper limit of the cross section for meson-nucleon interaction is 2.3×10^{-30} cm^2/nucleon. With the second method, several authors have obtained in recent years some indication of the occurrence of nuclear disintegrations underground, at depths large enough for the nucleonic component to be practically eliminated: the events detected were showers of penetrating particles[2] and groups of moderate energy neutrons.[3]

Recently George and Evans[4] reported the observation of stars in photographic plates exposed at 60 m water equiv. Most of these events could be interpreted as direct evidence of nuclear disintegrations induced by μ-mesons, and their frequency indicated a cross section of the order of 10^{-29} cm^2/nucleon (average energy of the mesons $\sim 1.5\times10^{10}$ ev).

Here an experiment is described, in which the absorption curve in water of the radiation producing nuclear disintegrations was obtained. The events were detected by recording the neutron showers produced in an absorber. As has been discussed in several previous papers,[5] whenever a nuclear disintegration occurs, neutrons with energies from $\sim$1 Mev up are released, and if a nucleon cascade develops, each of its steps causes further production of neutrons.

In comparison with the photographic plate technique, this method has the advantage of allowing the detection of the events occurring in thick absorbers, hence of providing data with a comparatively good statistical accuracy.

II. EXPERIMENTAL AND RESULTS

The experiment was performed during the summer of 1950, in Cayuga Lake, Ithaca, New York (altitude of

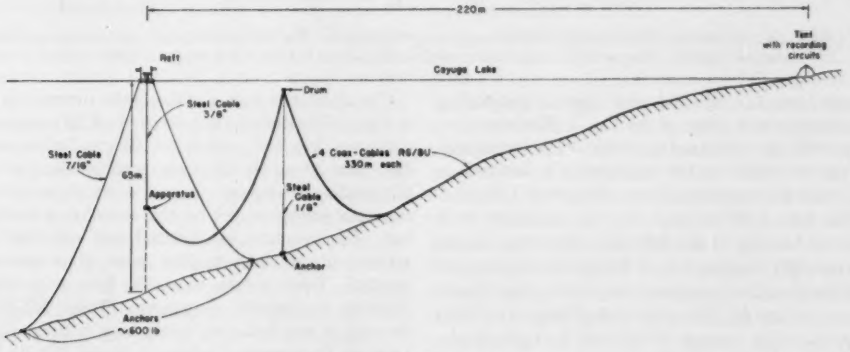

FIG. 1. Layout of the experiment.

[1] E. Amaldi and G. Fidecaro, Phys. Rev. **81**, 339 (1951).
[2] H. J. J. Braddick and G. S. Hensby, Nature **144**, 1012 (1939); E. P. George and P. T. Trent, Nature **164**, 838 (1949).
[3] V. Cocconi Tongiorgi, Phys. Rev. **76**, 517 (1949).
[4] E. P. George and J. Evans, Proc. Phys. Soc. (London) **A, 63**, 1248 (1950).
[5] See, e.g., Cocconi, Cocconi Tongiorgi, and Widgoff, Phys. Rev. **79**, 768 (1950).

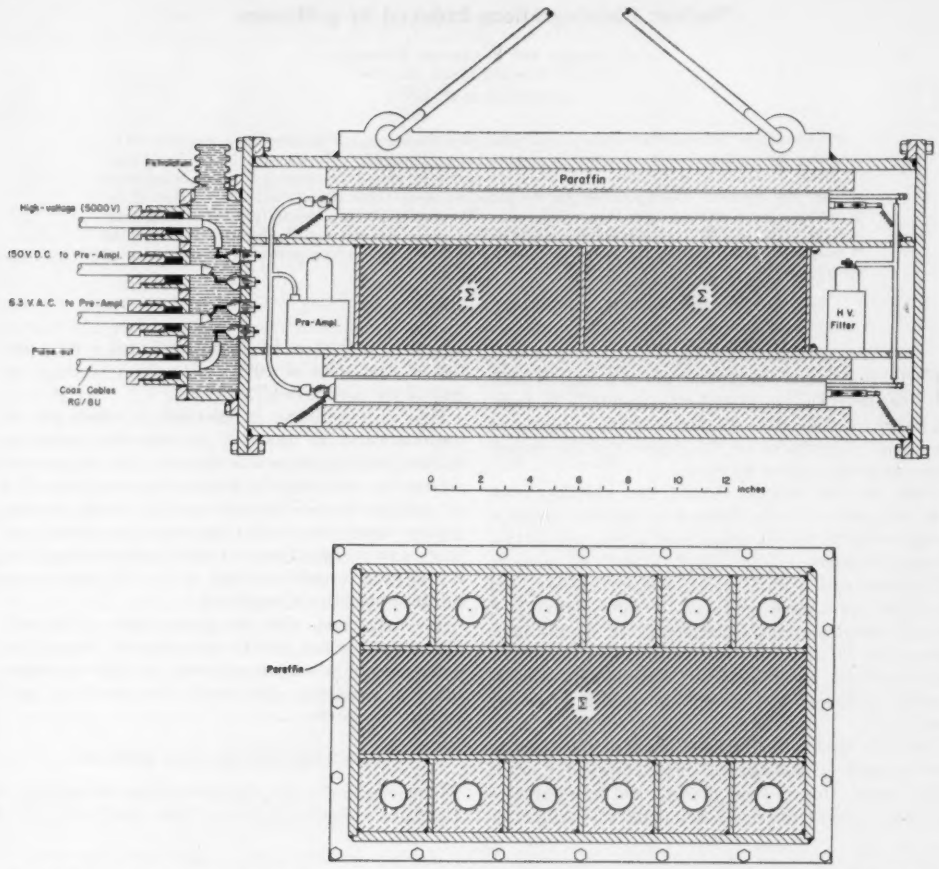

FIG. 2. Side and front views of the water-tight Al box containing the detector. The BF_3 proportional counters had an effective surface of $1'' \times 18''$. They were all connected in parallel and operated at the same voltage ($\sim$4500 volts).

the water level 117 m). Valuable help in performing the experiment was given us by Dr. J. Heidmann, to whom we wish to express our appreciation and gratitude.

The general layout of the experiment is sketched in Fig. 1. A raft was anchored 220 m offshore, in a location where the lake is 65 m deep. A winch mounted on it allowed the hoisting of the detector, which was housed in a water-tight aluminum box. Except for a preamplifier, all the recording apparatus was located on shore.[6] Four coax cables *RG/8U*, each 330 m long, were used to carry the high voltage ($\sim$5000 v) to the neutron counters, to supply the preamplifier, and to bring to shore its pulses. These cables stayed in the water without any protection for four months, and showed no sign of leak or deterioration.

[6] We are very grateful to the Pennsylvania Dixie Cement Corporation for the kind hospitality on its ground.

The aluminum box containing the detector is shown in Fig. 2. The detector consisted of 12 BF_3 proportional counters ($1'' \times 18''$), filled to 101 cm Hg of enriched BF_3, plus 20 cm Hg of Argon, each surrounded by $1\frac{1}{2}''$ of paraffin. Additional slowing down material for the neutrons was provided by the water surrounding the box. The counters, constructed and operated as described in previous papers[3] were all connected in parallel. Their pulses were fed into a preamplifier (Atomic Instrument Company, Model 205-B) then through a matched coax cable, into a linear amplifier (Atomic Instrument Company, Model 204-B) located on shore.

The nuclear disintegrations we intended to study were those occurring inside the absorber Σ placed between the counters; its area was always $18'' \times 18''$; data were taken with absorbers of different thicknesses and materials, as listed in Table I.

TABLE I. Rates recorded in the different channels, at various depths and with various absorbers. A count in channel "$m=3$," e.g., means that an event has occurred, in which at least 3 neutrons gave pulses in our counters and were recorded by our circuit. Whenever the absorber was thinner than 4", it was made of sheets evenly spread in the 4-in. hole. The errors given are standard errors. No errors are given for most of the rates recorded in channel "$m=1$," as the uncertainties due to barometric effect, variations in the amplifier gain, etc., are, in these cases, probably larger than the calculated statistical errors. The figures given in the last column are the over-all efficiencies to record a neutron, as they resulted from measurements taken with a (Ra+Be) source.

Depth	Nature and thickness of absorber (area 18"×18")	Number of neutrons recorded									Efficiency E* (percent)
		$m=1$	$m=2$	$m=3$	$m=4$	$m=5$	$m=6$	$m=7$	$m=8$	$m=9$	
0 m H_2O	$\sum=0$	1370	8.9±0.3	0.34±0.06	0.05±0.02	0					4.8
	$\sum=4$" Pb	8000	937±7	312±4	119±3	49.7±1.7	25.2±1.2	15.2±0.9	8.0±0.7	5.4±0.6	6.3
	$\sum=1$" Pb	3120	188±2	38.8±0.7	8.9±0.4	2.5±0.2	0.87±0.1	0.4±0.07	0.2±0.05	0	5.1
	$\sum=\frac{1}{2}$" Pb	1805	52±0.6	7.6±0.23	1.28±0.1	0.2±0.04	0				4.9
1 m H_2O	$\sum=0$	475	4.15±1	0							
	$\sum=4$" Pb	3500	494±9	158±4.8	62.8±3.0	30.6±2.1	14.6±1.5	8.5±1.1	5.6±0.9	3.3±0.7	
2.5 m H_2O	$\sum=0$	286±6	3.4±0.7	0.25±0.2	0						4.8
	$\sum=4$" Pb	1650	196±3	68±1.7	25±1.2	11.6±0.6	5.1±0.5	2.95±0.4	1.26±0.26	0.61±0.16	6.3
	$\sum=4$" Al	374	4.88±0.3	0.32±0.09	0.07±0.05	0					
5.5 m H_2O	$\sum=0$	169±4	0.3±0.15	0							
	$\sum=4$" Pb	499	39.1±0.4	12.2±0.7	4.7±0.5	2.4±0.3	1.6±0.3	1.03±0.21	0.45±0.14	0.18±0.09	
10.5 m H_2O	$\sum=4$" Pb	321	18.7±0.7	5.0±0.34	2.2±0.23	1.0±0.15	0.6±0.12	0.3±0.08	0.19±0.07	0.07±0.04	
20.5 m H_2O	$\sum=0$	100±2	0.04±0.04	0							
	$\sum=4$" Pb	202±2.1	10.6±0.3	3.58±0.19	1.68±0.13	0.83±0.09	0.39±0.06	0.24±0.05	0.15±0.04	0.05±0.02	
	$\sum=4$" Al	112±1.2	0.37±0.03	0.022±0.008	0						
60.5 m H_2O	$\sum=0$	90±3	0.03±0.03	0							
	$\sum=4$" Pb	109±1.1	3.36±0.15	1.25±0.09	0.64±0.07	0.35±0.05	0.2±0.04	0.13±0.03	0.08±0.02	0.05±0.02	

* The remarkable increase in the efficiency due to presence of the thick Pb-absorber is to be mainly accounted for by the following reasons: (a) the inelastic collisions with absorber-nuclei cause the neutrons to have smaller average energy when they reach the counters; (b) the diffusion in the absorber causes the neutron source to act not as a point source, but rather as an extended source smeared out in the whole volume of the absorber. When, as in our case, the counters are rather close to the surface of the moderating material, both these effects increase the probability of recording the neutrons.

The over-all efficiency E of the system for recording a neutron produced in $\sum$ was experimentally determined by locating a calibrated (Ra+Be) source in different positions inside the absorbers used. It was found to vary from $E=0.048$ to $E=0.063$ depending on the nature and thickness of the absorber. The values determined for E are given in the last column of Table I. It has been proved in a previous work[5] that the spectrum of the neutrons produced in nuclear evaporations is similar enough to the spectrum of the neutrons emitted by a (Ra+Be) source, to make these determinations accurate within less than 20 percent.

As pointed out before, whenever a nuclear disintegration occurs, a shower of neutrons of moderate energies is generated. These neutrons, slowed down in the paraffin and in the water, will produce in the counters a succession of pulses distributed in time according to the neutron lifetime τ in the detector ($\tau\approx 160$ μsec), the event being practically exhausted in a time of the order of 2 or 3τ. If the pulses emerging from the amplifier were observed on a scope, they would appear as single pulses due to incoherent neutrons crossing the counters and to the counter-background, mixed with occasional groups of pulses caused by the neutron showers generated in the nuclear disintegrations, the latter events being the ones we intended to select.

The selection was made as follows. Whenever a pulse occurred in the counters, a gate of duration $T=160$ μsec$\approx\tau$ was opened, and a count registered in channel "$m=1$." If a second pulse was produced while this gate was on, a coincidence would be recorded, a count registered in channel "$m=2$," and a new gate of duration T opened. If a third pulse occured within this gate, a coincidence would be formed, a count registered in channel "$m=3$" and a fourth gate opened; and so forth up to channel "$m=9$." The readings of the nine registers directly give the integral pulse distribution due to the neutrons produced in the nuclear disintegrations, and recorded by our detector.

The rate of chance coincidences was always negligible. In fact, in the least favorable case, namely, in channel "$m=2$" at the depth of 1 m water, the ratio of the chance coincidences to the total coincidences recorded, was of the order of 10^{-3}.

The data taken without absorber, i.e., with $\sum=0$, were used as a background correction, and subtracted from the results obtained with the different absorbers. This correction takes care of the spurious events leading to the production in the counters of a number of ions comparable with that produced by the $B^{10}(n,\alpha)Li^7$ reaction (α-contamination of the counter walls, stars of heavily ionizing particles, electron bursts, etc.), which will affect only the number of counts recorded in channel "$m=1$"; furthermore it takes care of most of the neutrons generated in the nuclear disintegrations occurring in the surroundings of the absorber $\sum$ (paraffin, counters, aluminum box, water, etc.).

As shown in Table I, 99.9 percent of the counts recorded under water with $\sum=0$ occurred in channel "$m=1$," 0.1 percent in channel "$m=2$," none in the following channels.

Data were taken at depths of 1, 2.5, 5.5, 10.5, 20.5, and 60.5 m water. "Ground points," called hereafter points at depth "0," have been obtained by running the

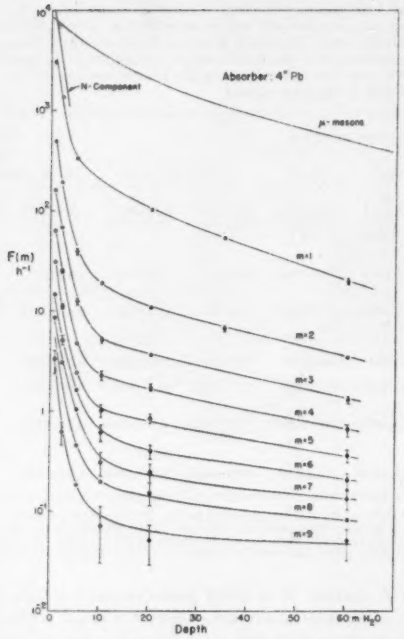

FIG. 3. Rates $F(m)$ recorded in the various channels, *vs* depth in m water, for the absorber $\sum = 4''$ Pb. The absorption curves of the N-component (MFP = 160 g/cm²) and of the μ-mesons are given for comparison.

experiment in the laboratory (260 m above sea level) with the aluminum box used in the lake surrounded on all sides by 6" of paraffin. It was verified, by using the (Ra+Be) source, that the efficiency of the detector in this condition was the same as that measured in the lake.

All the experimental results are collected in Table I with their standard errors.

III. ABSORPTION CURVE OF THE RADIATION PRODUCING NUCLEAR DISINTEGRATIONS

The frequencies $F(m)$ recorded with $\sum = 4''$ Pb, corrected for background, are plotted *versus* depth in Fig. 3.

The depth dependence being approximately the same for the rates recorded in all the channels, we shall discuss all the curves together.

In the first few meters of water, the slope of the curves indicates an absorption length of about 160 g/cm². At greater depths, say from ~10 m water on, the events are produced by a radiation whose absorption length is of the order of 4000 g/cm².

This shows that while the N-component is the radiation producing the great majority of the events observed at the level of the water and under the first few meters of water, at large depths most of the nuclear disintegrations observed are produced by the penetrating component of the cosmic radiation, namely by μ-mesons.

The absorption curves of μ-mesons and N-component are given in the figure for comparison.

By extrapolating to depth "0" the absorption curve obtained at depths greater than 20 m water, one can deduce that at sea level the μ-mesons contribute only ~2 percent of the disintegrations observed, the remaining 98 percent being caused by the N-component.

In reaching the conclusions contained in this section it is implicitly assumed that the probability of recording the nuclear disintegrations is the same at all depths. There is no *a priori* reason for this to be so; however, the procedure is justified by the experimental result that the neutron distribution in the different channels was found to be practically the same everywhere.

IV. QUANTITATIVE INTERPRETATION OF THE RESULTS AT DEPTHS GREATER THAN 10 M WATER

We shall base our discussion on the results obtained at 20 m water, where the frequency of the events still provides good statistics and the intensity of the N-component is already negligible. Curves A and B in Fig. 4 are the results for $\sum = 4''$ Pb and for $\sum = 4''$ Al, corrected for background. We shall call each of these curves the "recorded multiplicity spectrum" of the neutrons produced in the events occurring in the absorber considered.

Let us consider first the data with $\sum = 4''$ Pb. The processes that can give rise to production of neutrons in $\sum$, are:

(a) capture of negative μ-mesons:

using the differential range spectrum given by Rossi[7] and assuming for the slow mesons a $\cos^6\theta$ law of zenith angle dependence, the number of negative μ-mesons expected to stop in Σ (whose mass is 2.37×10^6 g) is 395 hr⁻¹. Assuming that the probability of emitting a neutron is exponential,[8] with average multiplicity 2,[9,10] and using the method described later in this section, one finds that the expected number of counts in the various channels, due to this process, are:

$m=1$	$m=2$	$m=3$
58 hr⁻¹	3 hr⁻¹	0.25 hr⁻¹.

One can see that the contribution of the μ-capture, owing to the low value of the neutron multiplicity, is essentially confined to the first couple of channels.

(b) (γ, n) reactions induced by the photons in equilibrium with the μ-mesons:

this process is discussed in the following paper by Hayakawa, from where one deduces that at 20 m water the equivalent cross

[7] B. Rossi, Revs. Modern Phys. **20**, 537 (1948).

[8] Probably a poisson distribution is nearer to the truth than an exponential one. However, the choice of the exponential spectrum, which was made for sake of simplicity, will not affect the final results.

[9] Groetzinger, Berger, and McClure, Phys. Rev. **81**, 969 (1951); Sard, Crouch, Jones, Conforto, and Stearns, Nuovo cimento **8**, 326 (1951).

[10] M. Widgoff (private communication).

section of the μ-mesons for producing neutrons is $\sigma_{\mu,\gamma,n}=1.0\times10^{-28}$ cm^2/nucleon, and the average number of neutrons per meson is $\bar{\nu}=1$ to 2. The expected number of neutrons is, therefore:

$$g_{\gamma,n}=A_{Pb}\times\sigma_{\mu,\gamma,n}\times\bar{\nu}\ (\text{hr}^{-1})$$

where

$$A_{Pb}=3600\times2\pi MNI_{N_0}\int_0^{\pi/2}\cos^n\theta\sin\theta d\theta.$$

With N=Avogadro's number, M=mass of the absorber, I_{N_0}=vertical intensity of the μ-mesons at 20 m water$=2\times10^{-2}$ cm^{-2} sec^{-1} ster^{-1}, $n=2$ and $\bar{\nu}=1.5$, one has

$$A_{Pb}=2.15\times10^{28}\ \text{cm}^{-2}\ \text{hr}^{-1}$$

and

$$g_{\gamma,n}=320\ \text{hr}^{-1}.$$

These neutrons contribute about $320\times E=320\times0.063=20$ counts per hour in channel "$m=1$," and 0.8 hr^{-1} in channel "$m=2$."

(c) Nuclear disintegrations induced either directly by the μ-mesons or by their secondaries (photons, π-mesons, nucleons). These events will, in general, give rise to many neutrons, both in the primary interaction and in the subsequent nucleon cascade, hence, they will contribute to the counts recorded in all channels.

To discuss these processes, the rates recorded in the various channels have been corrected by subtracting the contributions of the events (a) and (b) (open circles in Fig. 4).

From the recorded neutron multiplicity spectrum thus obtained, one can deduce the true neutron multiplicity spectrum, by taking into account the probability $f(m)$ of recording the counts in the various channels.

Let

$I(\nu)$ = probability that in an event ν neutrons are released in $\sum$, both in the primary interaction and in the subsequent cascade,

$G(\nu,n)=\binom{\nu}{n}E^n(1-E)^{\nu-n}$ = probability that the ν neutrons give n ($n\leqslant\nu$) pulses in the counters,

$P(n,m)=(1-\kappa^{n-1})(1-\kappa^{n-2})\cdots(1-\kappa^{n-m+1})$, with

$$\kappa=\int_T^\infty e^{-t/\tau}dt/\tau,$$

(T is the coincidence gate, and τ is the neutron lifetime) = probability that m out of the n pulses arrive with the right timing to be recorded by channel "m." One has:

$$f(m)=\sum_{\nu=m}^{\infty}\sum_{n=m}^{\nu}I(\nu)G(\nu,n)P(n,m).$$

An appropriate function $I(\nu)$ has to be chosen to make the function $f(m)$ fit the experimental data. With

$$I(\nu)=[\exp(1/\bar{\nu})-1]\exp(-\nu/\bar{\nu})$$

one has:

$$f(1)=B/\exp(-1/\bar{\nu}),\ \text{where}\ B=\frac{E\exp(-1/\bar{\nu})}{1-(1-E)\exp(1-/\bar{\nu})},$$

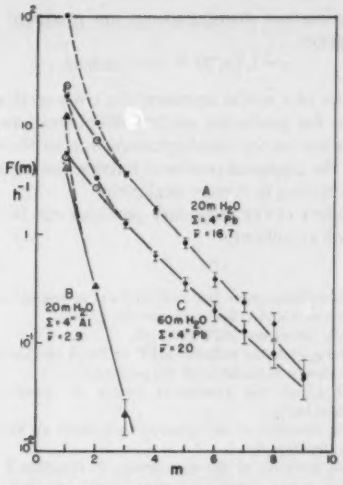

FIG. 4. Rates $F(m)$ recorded in the various channels at a given depth vs the order m of the channel (neutron multiplicity spectra). The solid symbols represent experimental points. The open symbols represent points corrected for effects due to μ-meson capture and (γ,n) reactions. The dotted lines connect the experimental points. The solid lines are the functions calculated in Sec. IV, assuming that the true neutron multiplicity spectra are exponential with average multiplicity $\bar{\nu}$.

$$f(m)_{m\geqslant2}=\frac{1-\exp(-1/\bar{\nu})}{E\exp(-2/\bar{\nu})}B^{m+1}(1-e^{-T/\tau})(1-e^{-2T/\tau})\cdots$$

$$\times(1-e^{-(m-1)T/\tau})\left[1+B\frac{1-e^{-mT/\tau}}{1-e^{-T/\tau}}\right.$$

$$+B^2\frac{(1-e^{-mT/\tau})(1-e^{-(m+1)T/\tau})}{(1-e^{-T/\tau})(1-e^{-2T/\tau})}$$

$$\left.+B^3\frac{(1-e^{-mT/\tau})(1-e^{-(m+1)T/\tau})(1-e^{-(m+2)T/\tau})}{(1-e^{-T/\tau})(1-e^{-2T/\tau})(1-e^{-3T/\tau})}+\cdots\right]$$

where $T/\tau\approx1$.

The curve shown in Fig. 4 is the function $f(m)$ obtined with $\bar{\nu}=16.7$, multiplied by a factor $g=37$. The agreement is satisfactory.

We therefore conclude that the frequency of the disintegrations occurring in the 4" Pb absorber at 20 m water, is $g=37$ hr^{-1}, and that the average multiplicity of the neutrons released in them is ~17. The value of the average multiplicity $\bar{\nu}$ is determined with roughly the same precision as the efficiency E, i.e., $\sim\pm20$ percent. However, the condition that $f(m)$ fit the experimental data makes the value of the frequency g practically independent of the value assumed for E. The uncertainty of our estimate of g, about 10 percent, is mostly due to the statistical errors in the experimental data.

Using the value of A_{Pb} given above, one deduces

that the nuclear disintegrations are produced with a cross section

$$\sigma = 1.7 \times 10^{-29} \text{ cm}^2/\text{nucleon}.$$

This value of σ would represent the cross section of the μ-mesons for producing nuclear disintegrations, if the contribution to the disintegrations due to the secondaries of the μ-mesons produced outside the absorber $\sum$ and interacting in it were negligible.

The effect of the secondary particles can be crudely estimated as follows:

with:

$\lambda_{\mu\,\mathrm{Pb}}$, the collision mean free path in Pb of μ-mesons for production of nuclear disintegrations (in g/cm²),

$\lambda_{\mu w} \approx \lambda_{\mu\,\mathrm{Pb}}$, the meson MFP in water,

$\lambda_{N\,\mathrm{Pb}} = 160$ g/cm², the collision MFP in Pb of the nucleons and π-mesons secondaries of the μ-mesons,

$L_{Nw} = 120$ g/cm², the absorption length in water of these secondaries,

$I_\mu(\theta)$ = the intensity of the μ-meson component at 20 m water, in direction θ,

$I_N(\theta)$ = the intensity of the secondaries, in direction θ.

The frequency ϑ of the disintegrations produced in Σ is:

$$\vartheta = \vartheta_\mu + \vartheta_N = 2\pi \int_0^{\pi/2} I_\mu(\theta) S \cos\theta (h/\cos\theta)(1/\lambda_{\mu\,\mathrm{Pb}}) \sin\theta d\theta + 2\pi \int_0^{\pi/2} I_N(\theta) S \cos\theta [1 - \exp(-h/\lambda_{N\,\mathrm{Pb}} \cos\theta)] \sin\theta d\theta,$$

where S and h are surface and thickness of Σ. Assuming that the secondary particles have the same zenith angle dependence as the μ-mesons, ($I(\theta) = I_v \cos^2\theta$), one has:

$$\vartheta \approx \frac{2\pi}{3} Sh \left[\frac{I_{\mu v}}{\lambda_{\mu\,\mathrm{Pb}}} + \frac{I_{Nv}}{\lambda_{N\,\mathrm{Pb}}} \times 0.72 \right].$$

Owing to their short range, the secondaries are in equilibrium with the μ-mesons, i.e.:

$$I_{\mu v}/\lambda_{\mu w} \times n = I_{Nv}/L_{Nw},$$

where n is the average multiplicity of the secondaries produced by the μ-mesons outside the absorber Σ. This gives:

$$\vartheta = \frac{2\pi}{3} Sh \left[\frac{I_{\mu v}}{\lambda_{\mu\,\mathrm{Pb}}} + 0.72 \frac{I_{\mu v}}{\lambda_{\mu w}} \frac{L_{Nw}}{\lambda_{N\,\mathrm{Pb}}} \right] \approx \frac{2\pi}{3} Sh \frac{I_{\mu v}}{\lambda_{\mu\,\mathrm{Pb}}} [1 + 0.67n].$$

The multiplicity n is unknown, but is likely smaller than 2.

Hence we conclude that $\vartheta_\mu/\vartheta_N \approx 1$, i.e., the contribution by the secondaries of the μ-mesons is not negligible, but of the same order or magnitude as that of the μ-mesons. Using this result, the cross section, σ_μ, of the μ-mesons for producing nuclear disintegrations is about $\frac{1}{2}$ of the σ given above, hence close to 0.8×10^{-29} cm²/nucleon.

The data obtained with the Al-absorber can be analyzed following the same path.

The number of negative μ-mesons stopping in Σ is $\sim$90 hr^{-1}. Assuming that the average number of neutrons produced in each capture is $\sim$1,[10] their contribution to channel "$m = 1$" is $\sim$6 hr^{-1}, to channel "$m = 2$," $\sim$0.1 hr^{-1}.

The number of neutrons caused by (γ, n) reactions is

$$C_{\gamma, n} = A_{\mathrm{Al}} \times \sigma_{\mu, \gamma, n} \times \bar{\nu},$$

where $A_{\mathrm{A}} = 5.2 \times 10^{29}$ cm^{-2} hr^{-1}. Using $\bar{\nu} = 1$ and $\sigma_{\mu, \gamma, n} = 0.8 \times 10^{-29}$ cm²/nucleon,[11] one has $C_{\gamma, n} = 42$ hr^{-1}, which will produce about 2 counts in channel "$m = 1$." The recorded rates, corrected for these two contributions (see the open triangle in Fig. 4), can be interpreted as due to the disintegrations induced in the Al-absorber by μ-mesons and their secondaries.

The function $f(m)$ that fits the data is shown in Fig. 4. The multiplication factor, hence, the true frequency of the events recorded, is $\vartheta = 24$ hr^{-1}, and the average neutron multiplicity is $\bar{\nu} \approx 3$.

The cross section for production of these disintegrations is

$$\sigma = \frac{\vartheta}{A_{\mathrm{Al}}} \approx 4 \times 10^{-29} \text{ cm}^2/\text{nucleon}.$$

The estimate of the contribution of the secondaries (using $\lambda_{N\,\mathrm{Al}} = 80$ g/cm²) gives

$$\vartheta = \frac{2\pi}{3} Sh \frac{I_{\mu v}}{\lambda_{\mu\,\mathrm{Al}}} [1 + 1.6n], \quad \text{hence} \quad \frac{\vartheta_\mu}{\vartheta_N} \approx \frac{1}{3},$$

i.e., the disintegrations produced directly by the μ-mesons in the Al-absorber are about $\frac{1}{3}$ of those produced by their secondaries.

Therefore, the cross section σ_μ for the μ-mesons is found again to be close to 1×10^{-29} cm²/nucleon. Of course, the large statistical errors and the size of the corrections introduced, make this result less reliable than that obtained from the data with lead. Anyway, within the accuracy of the results, the meson cross section per nucleon seems to be independent of the atomic number of the material in which the interaction occurs, as expected. For a definitive answer to this problem more accurate experiments are needed.

Our estimates of the contribution by the secondaries of μ-mesons, both for Pb- and Al-absorber, do not take into account the disintegrations induced by the photons in equilibrium with the μ-mesons. However, as shown by Hayakawa, the equivalent cross section for this process is about 10 times smaller than the cross section obtained above, hence the (γ, star) processes do not affect our results.

We are, therefore, led to conclude that at a depth of 20 m water (average energy of the mesons $\sim$6 Bev) μ-mesons produce nuclear disintegrations, by nuclear interaction, with a cross section $\sigma_\mu = (1 \pm 0.5) \times 10^{-29}$ cm²/nucleon. This result is in agreement with that of George and Evans.

The data obtained at 60 m water for $\sum = 4''$ Pb have also been analyzed. The experimental data are given in curve C, Fig. 4. The corrections in channel "$m = 1$" are:

7 hr^{-1} (for neutrons from μ-capture)

7 hr^{-1} (for neutrons from (γ, n) reactions)

in channel "$m = 2$" are:

0.6 hr^{-1} (for neutrons from μ-capture)

0.3 hr^{-1} (for neutrons from (γ, n) reactions).

A function $f(m)$ with $\bar{\nu} = 20$ and $\vartheta = 10$ fits the corrected data, which gives $\sigma = \sim 1.8 \times 10^{-29}$ cm²/nucleon hence,

$$\sigma_\mu = \sim 0.9 \times 10^{-29} \text{ cm}^2/\text{nucleon}.$$

The ratio of the calculated frequencies of the dis-

[11] We thank Dr. Hayakawa for these estimates.

integrations occurring in $\sum$ at 20 and 60 m water is $37/10=3.7$, close to the ratio between the μ-meson intensities at the two levels, which is 4.

The poor accuracy of our data does not allow us to draw conclusions about the variation of the cross section with the μ-meson energy. In fact, according to the formula given by George and Evans, the cross section at 60 m water is expected to be higher than that at 20 m water only by a factor 1.5. We can only say that the energy dependence of the meson cross section is within the expected range.

According to that formula, the expected value of σ for μ-mesons at sea level ($\sim 10^9$ ev) would be $\sim 2\times 10^{-30}$ cm^2/nucleon, close to the limit set by Amaldi and Fidecaro.[1,12]

V. ANALYSIS OF THE DATA TAKEN AT DEPTH "0"

The data taken at depth "0" (260 m above sea level), corrected for background, are plotted in Fig. 5.

As shown in Sec. III, at this level μ-mesons cause only about 2 percent of the events observed, hence most of the disintegrations recorded are originated by the N-component. The corrections for neutrons arising from μ-capture and (γ, n) reactions are here practically negligible (~ 5 percent in channel "$m=1$").

Figure 5 shows that the thicker the absorber $\sum$, the flatter is the multiplicity spectrum of the neutrons recorded. This is in agreement with the results of a previous experiment,[5] and is caused by the increase, with increasing absorber thickness, of the number of secondary events in the nucleonic cascade which develops inside the absorber. In the quoted experiment, the requirement was made that at least one ionizing particle capable of emerging from the absorber and of penetrating at least 22 g/cm^2 of paraffin be produced along with the neutrons. This set a bias against low energy events, hence the disintegrations recorded in that experiment involved, on the average, higher energies than those selected here. The differences in the relative slope of the three curves are therefore less marked here than there. With the same analysis as given in Sec. IV, one can describe the slopes of the curves in Fig. 5, for $m \geqslant 3$, with exponential spectra whose average multiplicities are 4.5, 7 and 17 respectively. For the same thicknesses of Pb-absorber, in the quoted experiment we obtained average multiplicities 10, 17 and 50.

It is interesting to compare the shape of the neutron spectra for $\sum = 4''$ Pb, obtained at depth "0" and at a depth of 20 m water. The distribution in the various

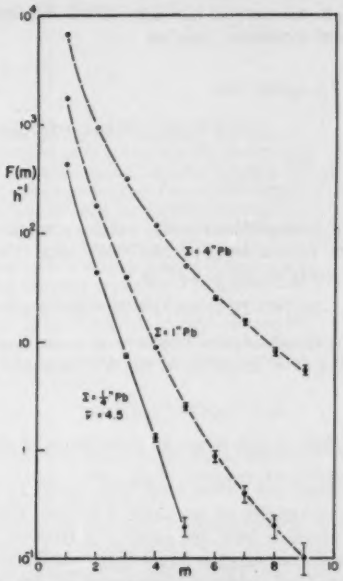

FIG. 5. Rates $F(m)$ recorded in the various channels at depth "0," for $\Sigma = \frac{1}{4}''$ Pb, $\Sigma = 1''$ Pb and $\Sigma = 4''$ Pb. The dotted lines connect the experimental points. The solid line is the function calculated to describe the results with $\Sigma = \frac{1}{4}''$ Pb.

channels of the neutrons recorded is practically the same at the two levels. After the corrections for μ-meson capture and (γ, n) reactions have been introduced, the shapes of the spectra are radically different for low values of m ($m=1$ and 2), but the same within the statistical errors for $m \geqslant 3$. The large number of events, leading to counts in channels $m=1$ and $m=2$ at sea level, are easily accounted for by the disintegrations due to the low energy tail of the N-component present in the atmosphere. The fact that the events in which a large number of neutrons are produced show approximately the same neutron spectrum both for nucleon-initiated and μ-meson-initiated events supports George and Evans's result that the heavy prong distribution of the stars observed at 60 m water does not differ much from that of the stars observed at mountain altitude.

The data obtained with $\sum = \frac{1}{4}''$ Pb, can be utilized to make an estimate of the absolute intensity of the N-component. In fact, in such an absorber, equivalent to only $\sim 1/20$ of an interaction MFP of the N-component, the effect of the nucleonic cascade is negligible, and the neutrons recorded are essentially those produced in the first interaction of the N-component with the Pb-nuclei. The solid line in Fig. 5 is the calculated curve which fits the data, with $\bar{\nu}=4.5$; the multiplication factor, i.e., the frequency of the disintegrations occurring in $\sum$, is $\vartheta = 1800$ hr^{-1}.

[12] Recently, measurements have been taken inside a salt mine at a depth of 1570 m water (average energy of the mesons $\sim 3\times 10^{11}$ ev) with the same apparatus as used at depth "0." With $\Sigma = 4''$ Pb, the rate of counts in channel "$m=3$" was 3/335 hr^{-1}, while with $\Sigma = 0$ the rate recorded in the same channel was 2/320 hr^{-1}. The background was too high to hope for any quantitative result. However, the rate 3/325 hr^{-1} can be used to estimate an upper limit for the meson cross section. Assuming that the neutron spectrum is the same as found at 60 m water, one deduces: $\sigma_{\mu\max} = 12\times 10^{-29}$ cm^2. The expected value, using George and Evans' formula, is close to 3×10^{-29} cm^2.

If $I_{N\nu}$ is the vertical intensity of the N-component at the level considered, one has

$$\beta = \int_0^{\pi/2} I_{N\nu} \cos^n\theta S \cos\theta \times[1-\exp(-h/\lambda_{N\,\mathrm{Pb}}\cos\theta)]2\pi \sin\theta d\theta$$
$$\cong \frac{2\pi}{n+1} Sh \frac{I_{N\nu}}{\lambda_{N\,\mathrm{Pb}}} = 73 I_{N\nu}.$$

We have assumed here $n=7$ and $\lambda_{N\,\mathrm{Pb}}=160$ g/cm^2. Therefore $I_{N\nu}=6.86\times10^{-3}$ cm^{-2} sec^{-1} ster^{-1}, and the total intensity at 260 m a.s.l. is

$$I=2\pi/(n+2)I_{N\nu}=4.75\times10^{-3}\ \mathrm{cm}^{-2}\ \mathrm{sec}^{-1}.$$

Assuming the absorption length in air to be $L_{N\,\mathrm{air}}=150$ g/cm^2, the total intensity of the N-component at sea level is

$$I_0=\sim4\times10^{-3}\ \mathrm{cm}^{-2}\ \mathrm{sec}^{-1}.$$

We attribute to this figure an uncertainty of about 10 percent.

As pointed out before, our figure refers to the N-component capable of producing a nuclear disintegration in which at least one neutron is released, i.e., to particles whose energy is larger than $\sim$10 Mev.

As the total μ-meson component at sea level is $\sim1.3\times10^{-2}$ cm^{-2} sec^{-1}, the N-component is found to constitute about 30 percent of the μ-meson component.

Our result can be compared with estimates of I_0, based on other experimental data. Of course, the comparison is necessarily crude, as each experiment sets a different bias against low energy particles.

The frequency of stars with 3 or more prongs, observed in photographic plates is, at sea level: $n_s\approx5\times10^{-6}$ sec^{-1} g^{-1}.[13] The discrepancies in the results of different authors give to this figure are uncertainty of about 20 percent. If the MFP for interactions in the emulsion is assumed to be $\lambda_{N,\,em}=120$ g/cm^2, one obtains $I_0=n_s\lambda_{N,\,em}(n+1)/(n+2)=5.3\times10^{-4}$ cm^{-2} sec$^{-1}=\sim4$ percent of the μ-mesons. This value of I_0 refers to particles having energies higher than $\sim$100 Mev. To compare with our result, one should include all the stars with 1 or 2 prongs, and also the events in which no ionizing particles but only neutrons are emitted. The extrapolation to stars of 1 or more prongs is very questionable, due to the correction needed for the inefficiency for the detection of small stars. Likely, the figure given above has to be multiplied by a factor larger than 2. Another factor of the same order or larger will probably arise from the addition of stars with no ionizing prongs, which must be very abundant. Therefore, though no agreement can be claimed, our result is not inconsistent with the estimate of the N-component intensity deduced from star frequency.

Our estimate can be more directly compared with the results of the measurements of the neutrons in the free atmosphere. From Yuan's[14] data one deduces that the rate of production in air of neutrons at sea level is $\sim1.0\times10^{-4}$ sec^{-1} g^{-1}. As the diffusion process of the neutrons in the atmosphere leads to practically no loss of particles, the above figure essentially represents the number of particles with energies of some Mev, produced in nuclear disintegrations in 1 g of air. With the assumption that the interaction MFP of the N-component in air is $\lambda_{N,\,\mathrm{air}}=80$ g/cm^2, one has

$$I_0\bar{\nu}=\sim7\times10^{-3}\ \mathrm{cm}^{-2}\ \mathrm{sec}^{-1},$$

where $\bar{\nu}$ is the average number of neutrons released in each interaction in air. Agreement with our estimate of I_0 is obtained for $\bar{\nu}=1.7$, which is not unreasonable.

The authors want to thank Prof. K. Greisen for helpful discussions and to express their appreciation to the foreman of the Laboratory machine shop, Mr. C. F. Van Amber, and to the shop technicians for their work in connection with the construction of the watertight box and with the assembly and anchoring of the raft.

[13] E. P. George and A. C. Jason, Proc. Phys. Soc. (London) **A62**, 243 (1949); Bernardini, Cortini, and Manfredini, Phys. Rev. **76**, 1792 (1949); N. Page, Proc. Phys. Soc. (London) **A63**, 250 (1950).

[14] L. C. L. Yuan, Phys. Rev. **81**, 175 (1951).

Nuclear Interaction of μ-Mesons Underground

SATIO HAYAKAWA*
Cornell University, Ithaca, New York
(Received June 18, 1951)

The nuclear interactions of μ-mesons and the genetic relations among their secondary particles are analyzed on the basis of the data obtained with photographic plates exposed underground by George and Evans. The results are used to analyze the experiment performed by Cocconi and Tongiorgi, in which the neutron showers produced in an absorber at different depths of water were studied. The contributions to the neutron showers from various components are compared. It is shown that the μ-mesons directly producing neutron showers in the absorber and the nucleons produced by the μ-mesons in the water above the apparatus and interacting in the absorber give the main contribution to the large neutron showers observed. The multiplicity spectrum of the neutrons is calculated by making use of a simplified model of the nucleon cascade and is shown to depend upon the selection bias of the detecting apparatus. The experimental results are consistently accounted for by assuming for the μ-mesons a nuclear interaction cross section of ~10 μb per nucleon. The experiments at great depths suggest the predominance of small momentum transfers by nuclear collisions. The large cross section and the small momentum transfer can be described in terms of the virtual photons associated with μ-mesons. These virtual photons produce in nuclear collisions real or virtual π-mesons which can either escape or be absorbed in the nucleus.

I. INTRODUCTION

THE interaction of μ-mesons with matter has generally been considered as an exclusively electromagnetic process, the nuclear interaction being supposed to be extremely small. The behavior of cosmic rays underground has previously been analyzed on this basis.[1] However, recent experimental results obtained from photographic plates exposed underground by George and Evans[2] have presented evidence for the nuclear interactions of μ-mesons, which can be reasonably interpreted in terms of mesonic interaction of their electromagnetic field. The result by Amaldi and Fidecaro[3] about the anomalous scattering of μ-mesons can also be interpreted in this manner.

Additional evidence for nuclear interactions of μ-mesons, described in the preceding paper, has been obtained by Cocconi and Tongiorgi.[4] They recorded neutron showers with a system consisting of BF_3 counters surrounding a lead absorber which was sunk at different depths of water (down to 60 m). It was found that below 10 m of water the frequency of the neutron showers is proportional to the intensity of μ-mesons.

George and Evans' and Cocconi and Tongiorgi's experiments were carried out at nearly the same depths. They seem to give us a satisfactory qualitative information about the nuclear interactions of μ-mesons of around 10 Bev. We shall first elaborate the analysis made by George and Evans and give a qualitative picture of the behavior of μ-mesons at the depths under consideration. The results will then be applied to the experiment of Cocconi and Tongiorgi. The two experiments are found to be quite consistent with one another, which substantially confirms the interpretation of George and Evans.

Interesting information on the problem of μ-meson interactions at high energies (~10^{13} ev) was given by a series of GM-counter experiments at great depth (~1600 m water equivalent).[5,6] A preliminary analysis of the results has indicated the occurrence of penetrating showers and the existence of an anomalous absorption of penetrating rays, which can be accounted for by nuclear interactions induced by μ-mesons.

On the basis of these experimental results, the nature of the nuclear interactions of μ-mesons will be qualitatively discussed.

II. GENETIC RELATION AMONG VARIOUS COMPONENTS UNDERGROUND

A μ-meson interacting with matter produces several kinds of secondaries which, because of their short ranges, can be considered to be in equilibrium with the parent μ-meson. The important secondary components are electrons and photons, π-mesons, and nucleons. Their intensities can be expressed as fractions of the intensity of the μ-mesons:

$$I_e=\alpha_e I_\mu, \quad I_\pi=\alpha_\pi I_\mu, \quad I_N=\alpha_N I_\mu. \tag{1}$$

We assume that most of the secondaries are produced directly by the μ-mesons rather than through roundabout processes involving transformations among the secondary components. Each coefficient is given approximately by the ratio of the absorption mean free path of the component considered to the mean free path for the μ-meson to produce it. These mean free paths, and accordingly the α's, depend upon the energies of both the μ-meson and its secondary ray and upon the material in which the interaction takes place. Since

* Now at Department of Physics, Osaka City University, Osaka, Japan.
[1] S. Hayakawa and S. Tomonaga, Prog. Theor. Phys. **4**, 287, 496 (1949).
[2] E. P. George and J. Evans, Proc. Phys. Soc. (London) **A63**, 1248 (1950) and private communication of George to Cocconi.
[3] E. Amaldi and G. Fidecaro, Phys. Rev. **81**, 339 (1950).
[4] G. Cocconi and V. Cocconi Tongiorgi, Phys. Rev. **84**, 29 (1951).
[5] L. M. Bollinger, Phys. Rev. **79**, 207 (1950); Cornell Thesis (1951).
[6] Greisen, Cocconi, and Bollinger, Phys. Rev. **82**, 294 (1951).

the dependence upon the energies of μ-mesons is supposed to be small at the depths where the experiments with photographic plates and neutron counters were performed, we may assume α_π and α_N (for which we do not have reliable knowledge) independent of the energies of μ-mesons, while we assume an empirical energy dependence, $\sim E^{\frac{1}{2}}$, for α_e, as will be seen later.

Each of these components can give rise to nuclear interactions, hence the total intensity of the particles responsible for nuclear disintegrations is given by

$$I=I_\mu+I_e+I_\pi+I_N=(\alpha_\mu+\alpha_e+\alpha_\pi+\alpha_N)I_\mu \equiv\sum\alpha_i I_\mu, \quad \alpha_\mu=1. \quad (2)$$

The frequency of the nuclear disintegrations occurring in an absorber of mass M is expressed by

$$f=NMI_\mu(\sum\alpha_i\sigma_i), \quad (3)$$

where σ_i is the cross section per nucleon for the process considered and N the Avogadro number.

If the thickness of the absorber in which nuclear disintegrations occur is greater than the interaction mean free path of the particle under consideration, the relation (3) fails and coherence effects must be taken into consideration. This is the case for the electronic component in a thick lead absorber and for the nucleon component, which undergoes the cascade development inside a nucleus.

The electronic cascade can be treated using the method of electron tracks, owing to the fact that the transition effect from the surrounding matter to the lead absorber is almost complete. If the absorber is thin enough, as in the case of photographic plates, it will not destroy the equilibrium of the electronic component with the μ-mesons existing in the surrounding matter.

For the nucleon component the interaction cross section is not large enough to create equilibrium even in the lead absorber. Let the energy of a nucleon initiating a cascade be ϵ, disregarding whether the nucleon comes from outside the apparatus or is produced inside a nucleus in the absorber by a μ-meson. Suppose the nucleon produces N_i particles of a certain kind after traversing a thickness of nuclear matter t. The number of particles, N_i, is a function of ϵ and t:

$$N_i=N_i(\epsilon, t). \quad (4)$$

If this functional relation and the thickness traversed, t, are known, we can obtain the relation between N_i and ϵ. For the case of photographic plates, t is limited to the size of a nucleus and the particles are the charged particles producing heavy tracks.[7] For the case of lead absorbers, t can be larger than the nuclear size and the particles are neutrons. Introducing the energy spectrum, $F(\epsilon)$, of the nucleons which cause the nuclear disintegrations, the multiplicity spectra of the heavy tracks in the photographic plates and of the neutrons produced in the lead absorbers are expressed by $F(\epsilon(N_h, t))$ and $F(\epsilon(N_n, t))$, respectively. Therefore, the two experiments are equivalent in principle. Unfortunately, however, we have only poor knowledge about the relations (4) and $F(\epsilon)$.

The nucleon cascade process can be formulated under the following assumptions considering that most of the nucleons are of nonrelativistic energies in our case.[8]

(1) Completely elastic scattering, since the inelastic scattering is less than one percent of the total scattering at 350-Mev incident energy, and is inferred to be less than $\frac{1}{3}$ between 1 and 2 Bev.[9]

(2) Constant cross section and uniform energy distribution of the secondary nucleons,[10] since the proton-proton scattering cross section is approximately constant and fairly isotropic in the center of mass system, and the variation of the proton-neutron scattering cross section and its angular anisotropy may be smeared out due both to the increase of the cross section at high energies and to the effect of nuclear binding at low energies. Thus we may adopt the simplified cross section:

$$\sigma(\epsilon, \epsilon')d\epsilon'=\sigma_0 d\epsilon'/\epsilon, \quad \sigma_0=40 \text{ mb},$$

where ϵ and ϵ' are the energies of the incident and scattered nucleons, respectively. This gives a collision mean free path

$$\lambda_0=2.9\times10^{-13} \text{ cm},$$

which will be used as a unit of length.

(3) One dimensional treatment and homogeneous nuclear matter, since the large angular divergence of secondary nucleons makes it almost impossible to take into account the geometrical effect of spherical nuclei. The zig-zagging of the nucleons is instead taken into account by increasing the path length by a factor of about $\sqrt{2}$. Hence the average path length inside a nucleus is taken as equal to the nuclear diameter.

(4) Introduction of a critical energy $\epsilon_V\sim50$ Mev under which nucleons do not further multiply, but consume their energies to heat up the nuclei, with subsequent production of nuclear evaporations.

(5) Linear relation between the excitation energy and the number of evaporated particles, which is approximately expected from the evaporation theory.[11] For the numbers of black prongs and neutrons, we shall use the expressions:

$$N_b=0.026U, \quad N_n=0.030U,$$

where U is the energy supplied by the nucleons of energies below ϵ_V. The number of grey prongs is evaluated from the number of protons among the nucleons of energies above ϵ_V.

The calculation was done by making use of the current methods of cascade theories. The result is compared with the data[12] on the ratio of grey to black prongs and on the relation between total incident energy and number of heavy prongs. The rough agreement justifies our choice of the values for λ_0 and ϵ_V.

III. ANALYSIS OF THE PHOTOGRAPHIC PLATE EXPERIMENT

The essential features of the nuclear disintegrations underground have been analyzed by George and Evans[2] (quoted hereafter as GE). Here we shall give a little more quantitative analysis taking into account the

[7] We use the terminologies adopted by R. H. Brown *et al*, Phil. Mag. **40**, 862 (1949).

[8] Nucleon cascade theories at high energies are reviewed by H. Messel, Phys. Rev. **83**, 21 (1951).

[9] Y. Fujimoto and S. Hayakawa, Prog. Theor. Phys. **6**, 96 (1951).

[10] This assumption was adopted by S. Lindenbaum (private communication).

[11] K. J. LeCouteur, Proc. Phys. Soc. (London) **A63**, 259 (1950).

[12] H. L. Bradt and M. F. Kaplon, Phys. Rev. **78**, 680 (1950).

nucleon cascade process. In (a) the contribution of photons, i.e., the product $\alpha_e\sigma_e$, is estimated. In (b) and (c), the cross sections for (μ, π) and (μ, N) processes will be given, using the experimental results of GE for the frequencies of stars produced by π^--mesons captured and by nucleons.

(a) Recent experiments have indicated the occurrence of nuclear disintegrations produced by photons of synchrotron energies.[13] This can be interpreted either with the reabsorption of photomesons in the nucleus or with some other mesonic interaction.[14] The cross section for this process has been estimated to be of the order of 100 μb per nucleon.[13] Assuming a cross section constant above 250 Mev, which is indicated by the flat excitation curve for the production of photomesons, we can estimate the contribution of photons to the nuclear disintegrations.

The intensity of photons in equilibrium with μ-mesons can be evaluated with the method of reference (1) and is approximately given by

$$\alpha_e = 8.0\times10^{-4}(ax)^{0.4}, \tag{5}$$

where $a = 2.2\times10^{-3}$ Bev per g cm^{-2} is the energy loss of μ-mesons in earth and x is the depth under consideration (ax is measured in Bev). At the depth of 60 m water equivalent, we obtain

$$\alpha_e\sigma_e = 2.2\ \mu\text{b}. \tag{5}$$

The photons coming from the round-about processes are estimated as negligibly small.

(b) The cross section for the production of charged π-mesons can be derived from the number of π^--mesons stopping in the photographic emulsion, provided that the π-mesons coming from the round-about processes, i.e. from photons and nucleons, are subtracted. In other words, one has to evaluate: $\sigma_{\mu\pi} = (\alpha\sigma_\pi)_{\text{tot}} - \alpha_e\sigma_{e\pi} - \alpha_N\sigma_{N\pi}$. The contribution from photons can be estimated in the same way as above. Taking the (γ, π) cross section as 40 μb per nucleon, the product $\alpha_e\sigma_{e\pi}$ is found to be about 1 μb. The contribution to π-mesons from nucleons, $\alpha_N\sigma_{N\pi}$, has been estimated and found smaller than that from photons. Thus the main contribution must be due to μ-mesons, for which the cross section was found by GE to be $\sim$5 μb.

The number of π-mesons stopping in unit mass of emulsion, N_π, should be equal to the number of those produced in the equivalent amount of matter. Some of the mesons produced, however, multiply and some are absorbed by nuclear collisions. Hence, the number of π-mesons produced in a nuclear collision of a μ-meson corresponds to an effective multiplicity m_π, which is the total number of π-mesons produced on the average as a consequence of the initial collision. It follows that

$$\sigma_{\mu\pi} = N_\pi / N m_\pi I_\mu.$$

Using the figure of N_π given by GE and the known value of I_μ, we obtain

$$m_\pi\sigma_{\mu\pi} = 10\pm2\ \mu\text{b}. \tag{6}$$

Direct evidence for the production of π-mesons by μ-mesons was obtained by GE and the cross section was found to be

$$\sigma_{\mu\pi} = 5\pm1\ \mu\text{b}. \tag{7}$$

This gives $m_\pi = 2.0\pm0.6$, which is not inconsistent with the multiplicity observed directly by GE.

(c) Most of the 0_s-stars observed by GE are considered to be due to the nucleons which are produced by μ-mesons with a cross section of about 10 μb. The contribution to the 0_s-stars from photons and π-mesons has been evaluated and found to be less than 10 percent of that from nucleons. Hence we assume that the 0_n-stars are produced by neutrons and the 0_p-stars by protons.

Notwithstanding the poor statistics, one can see the tendency of the frequency-size distribution of emitted heavy prongs to be flatter, and of the number of 0_p-stars to be relatively larger underground than in the stars at mountain altitude. The integral energy spectrum of the neutrons producing 0_n-stars can be approximated by the inverse energy law, as shown in Fig. 1, if the energy of an incident neutron is estimated from the energy prong number relation deduced from the photographic plate data.[12] The relatively large number of protons ($\frac{1}{3}$ of the number of neutrons, in contrast to $\frac{1}{7}$ in the

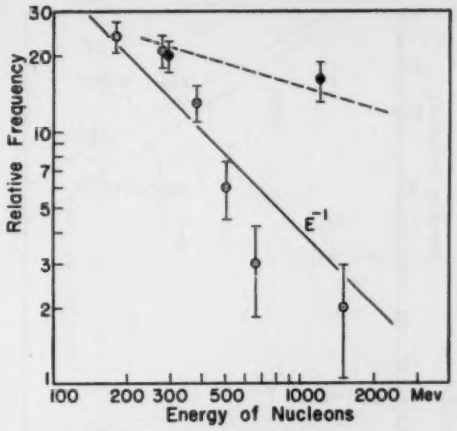

FIG. 1. Integral energy spectra of nucleons produced by μ-mesons. The open circles represent neutrons produced above the absorber and producing 0_n-stars. The solid line represents the energy spectrum of the neutrons. The solid circles represent nucleons produced inside the nuclei, 1_p-stars. The assumption is made that the scattering of a μ-meson causes a nucleon to recoil.

[13] S. Kikuchi, Phys. Rev. **81**, 1060 (1951); R. D. Miller, Phys. Rev. **82**, 260 (1951).

[14] J. Levinger, Phys. Rev. **84**, 43 (1951), tried to explain the photonuclear reaction at high energies by the photodisintegration of quasi-deuterons, but the result seems to give too small a cross section compared with the experimental results of reference 13. The high energy photonuclear reaction caused by the virtual photons of μ-mesons is found to be smaller than 0.5 μb, making use of Levinger's result.

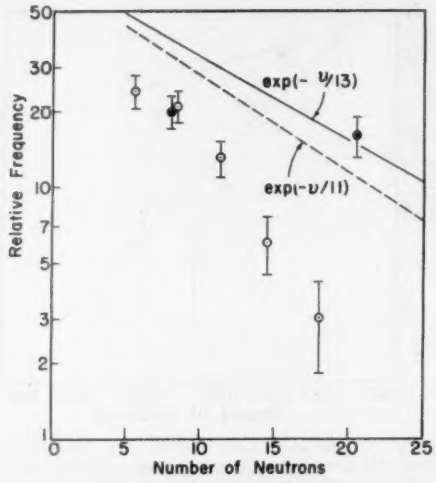

FIG. 2. Integral multiplicity spectrum of the neutrons produced in 4″ lead. The open circles represent neutrons produced by 0_p-stars. The solid circles represent neutrons produced by 1_p-stars. The solid line represents the sum of the two processes. The broken line represents the spectrum corrected for the ionization loss of fast protons. The experimental value of the average multiplicity is 17.

mountain experiments) also indicates a flat energy spectrum of nucleons. The inverse energy spectrum can be predicted from the nucleon cascade theory with a method similar to that of the electron tracks, since the nucleons are in equilibrium with the ancestor μ-mesons.

The total cross section for the production of nucleons is estimated in the same way as that for the production of π-mesons. For the neutrons with an energy of at least 100 Mev, which is required to produce stars of three or more prongs, the average energy is estimated as about 400 Mev and the average range is about 1.4 times the collision mean free path. The number of 0_n-stars per gram of emulsion, N_n, is expressed in terms of the cross section $\sigma_{\mu n}$ and of the multiplicity m_n, by

$$N_n = m_n \sigma_{\mu n} N (1.4\lambda_e/\lambda_p) I_\mu,$$

where λ_e and λ_p are the collision mean free paths in earth and in emulsion, respectively, which are likely of the same order of magnitude. From the data of GE for N_n, one gets

$$m_n \sigma_{\mu n} = 8.5 \pm 1.1 \ \mu\text{b}.$$

Including both neutrons and protons produced by μ-mesons, and considering only the nucleons of energy greater than about 100 Mev, we have

$$m_N \sigma_{\mu N} = 17 \pm 2 \ \mu\text{b}, \qquad (8)$$

where m_N and $\sigma_{\mu N}$ mean the multiplicity and cross section for both types of nucleons.

This value of $m_N \sigma_{\mu N}$ may be compared with the cross section deduced from the events observed to be produced directly by μ-mesons in photographic plates,

$$\sigma_{\mu N} = 15 \pm 2 \ \mu\text{b}, \qquad (9)$$

which leads us to a multiplicity of about one.

The figure given in Eq. (9) is deduced from the frequency of stars with one or more thin secondary tracks. Among these stars, the 1_p-stars are interpreted by GE to be the scattering of a σ-meson by a nucleon with the recoil nucleon subsequently producing a nucleon cascade inside the nucleus. The average path length of this nucleon cascade is twice smaller than that for a nucleon initiated cascade, and is equal to $2.2\lambda_0$ in AgBr nuclei. In such a short path only a small fraction of nucleons can fall into the slow region and, therefore, a small number of heavy tracks is predicted, namely about 4 for a recoil nucleon of 1 Bev. The energy distribution of the recoil nucleons is found to be very flat, as shown in Fig. 1. However, there is some ambiguity in this interpretation, as will be discussed in the later sections.

Stars with two or more thin secondary tracks are hard to interpret, though it is sure that they are associated with the production of π-mesons. The mesons could be produced directly by a μ-meson or indirectly by a recoil nucleon and its descendant nuclear interacting particles. The production of a number of thin tracks in a star may be either the genuine multiple production of π-mesons by a μ-meson or the plural production by successively produced nuclear interacting particles. Because of such an ambiguity in the interpretation, we shall not discuss further these multi-thin track stars.

IV. ANALYSIS OF NEUTRON SHOWER EXPERIMENT

A similar analysis can be applied to the neutron shower experiment performed by Cocconi and Tongiorgi. For the production of neutrons one must take into account a number of phenomena which are not important in photographic plate experiments, namely, (a) the (γ,n) reactions and (b) the neutron production by μ^--meson capture. Other phenomena like (c) the capture of π^--mesons and (d) the nuclear disintegrations caused by nucleons and μ-mesons in flight, are essentially the same as in the case of the photographic plate experiment.

(a) The intensity of photons considered here is different by a large factor from that calculated in the previous section owing to the transition effect. The number of photons with energy W in the interval dW produced by a μ-meson of energy E-Bev in lead is empirically given by

$$\alpha_1 E^{0.5} dW/W^2,$$

with α_1 defined by

$$\alpha_1/W_a = 3.0 \times 10^{-2}, \quad W_a = 0.02 \text{ Bev}.$$

The neutron yield due to the photons can be calculated following the method of Levinger:[15]

$$Y(E)=(N/A)(\alpha_1/W_a)\bar{Q}E^{0.5}\simeq 2.5\times 10^{-5}E^{0.5}, \quad (10)$$

where A is the atomic weight of lead and $\bar{Q}$ is the average cross section for the absorption of γ-rays. Equation (10) gives the absorption cross section of photons, and the number of neutrons produced is obtained by multiplying it by the multiplicity of neutrons.[16] The double absorption process produced by the photons accompanying a μ-meson in the lead absorber is negligible for the μ-mesons of energies around 10 Bev. The contribution from (γ, n) reaction is then obtained in terms of α and σ at 60 m water

$$\alpha\sigma(\gamma, n)=150\ \mu\text{b}. \quad (11)$$

This gives a quite large contribution to small neutron multiplicities.

(b) The neutrons produced by the capture of μ^--mesons are discussed in the preceding paper and here we give the value in terms of $\alpha\sigma$ at 60 m water for the convenience of comparison:

$$\alpha\sigma(\mu^-\text{-capture})=130\ \mu\text{b}. \quad (12)$$

(c) The same quantity for the capture of π^--mesons is estimated referring to the experiment of GE:

$$\alpha\sigma(\pi^-\text{-capture})=4\ \mu\text{b}. \quad (13)$$

The capture of a π^--meson will give rise to about four neutrons.

(d) For the nuclear disintegrations induced by nucleons and μ-mesons in flight, one has to take into account the change of the path lengths of nucleon cascades due to the selection bias set by the experiment under consideration. At least one neutron, i.e., at least one nuclear disintegration was required to occur inside the absorber. If λ is the nuclear interaction mean free path of nucleons in the absorber, whose effective thickness is D, taking into account the angular distribution of incident particles, the average interaction path length for an incident nucleon is given by

$$(\lambda+D)\exp(-D/\lambda)+D^2/\lambda.$$

If we express the path lengths in λ_0, as discussed in the previous sections, we obtain for the path lengths, t, for the nucleon cascade processes induced by nucleons and μ-mesons for 4″ and 1″ of absorbers:

$$\begin{aligned} t_N&=10.1\lambda_0, \quad t_\mu=7.3\lambda_0, \quad \text{for 4″ lead,}\\ t_N&=\ 5.9\lambda_0, \quad t_\mu=3.1\lambda_0, \quad \text{for 1″ lead.}\end{aligned} \quad (14)$$

Using these path lengths and applying our nucleon cascade theory, we can derive the multiplicity spectra of the neutrons produced in the absorbers considered, as shown in Figs. 2 and 3. Considering the ambiguity

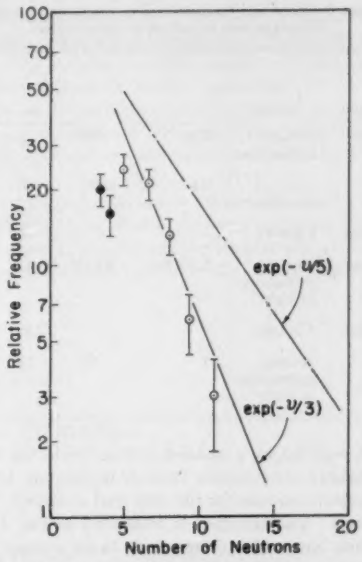

FIG. 3. Integral multiplicity spectrum of the neutrons produced in 1″ lead. The open circles represent neutrons produced by 0_γ-stars. The solid circles represent neutrons produced by 1_p-stars. The solid line represents the sum of the two processes. The dot-dash line represents the spectrum deduced by assuming that in 1_p-stars two nucleons start the nucleon cascade receiving the recoil energy from μ-mesons.

in the mechanism of the nuclear interaction of μ-mesons and the simplified assumptions in the nucleon cascade theory, however, it should not be taken as more than an illustration. Nevertheless, our results can show the general trend of the multiplicity spectra, especially their dependence upon the thickness of the absorber; adding the contributions from nucleons and direct μ-mesons, the resultant spectra are well approximated by exponential curves and their average multiplicities are 13 and 3 for 4″ and 1″ lead absorbers, respectively, while the experimental average multiplicity is 17 for 4″ lead.

In order to see how our average multiplicities are affected by possible corrections and modification in the models assumed, the following calculations have been made. In the first place, the ionization loss of the protons which link two successive nuclear disintegrations was taken into account, by cutting off all these protons and leaving only neutrons as links between successive disintegrations. This effect is appreciable only for 4″ lead and the corrected multiplicity spectrum is shown by the broken line in Fig. 2, which corresponds to an average multiplicity 11. In the second place, for the 1_p-stars the following model was assumed: two nucleons start nucleon cascades, each of them having a half of the energy transferred by a μ-meson. This mechanism corresponds to the reabsorption of a pro-

[15] J. Levinger, Nucleonics **6**, No. 5, 64 (1950).

[16] The most probable multiplicity of neutrons for heavy nuclei is estimated as about 2, by J. Heidmann, Phys. Rev. **83**, 237 (1951) and Cornell Thesis (1951), unpublished.

TABLE I. Contributions from various processes to nuclear disintegrations in lead 60 m under water.

Component	Process	α	σ	$\alpha\sigma$	Average neutron multiplicity
Photons	Mesonic interaction	0.01	100	1	several
	(γ,n) reaction	0.1	1500	150	1 to 2
π-Mesons	Capture	...	...	4	4 to 5
Nucleons (~0.1 Bev)	Nuclear interaction in flight	1.5×10^{-3}	1×10^{4}	15	Figs. 2 and 3
μ-Mesons	Capture	...	...	130	2
	Nuclear interaction in flight	1	15	15	Figs. 2 and 3

duced π-meson by a quasi-deuteron inside the nucleus and makes a considerable increase in the path length of the nucleon cascades for the thin lead absorber. The result for 1″ lead absorber is illustrated in Fig. 3 by the dot-dash line, which corresponds to an average multiplicity 5.

In the foregoing analysis the contribution from the multi-thin track stars is ignored, though their frequency is about one half of that of 1_p-stars. If this contribution were added to the two processes already considered, the multiplicity spectra would be flatter, giving higher average multiplicities than before. With our present knowledge, however, the quantitative treatment of the effect of these stars seems to us impossible.

As a summary of the foregoing results, the contribution from each process in terms of $\alpha\sigma$ is shown in Table I. This allows a comparison of the relative importance of each process for producing neutrons in lead under 60 m water. Needless to say, $\alpha\sigma$'s for the capture of π^-- and μ^--mesons have no meaning of cross sections, but are only useful for comparison.

V. RESULTS OBTAINED FROM THE EXPERIMENTS AT GREAT DEPTH

There is only scanty experimental information about the nature of cosmic rays at great depths, but the following results can be obtained on the basis of the recent experiments of a Cornell group,[5,6] under about 1600 m water equivalent (about 700 m of rock).

The energy loss of μ-mesons was shown by Bollinger[5] to be almost exclusively due to electromagnetic processes, and there may be only a small room for the energy loss due to nuclear interactions, although there are ambiguities in the theoretical value of the energy loss due to pair creation and in the experimental values of μ-meson intensities.[17] With such reservation, and with the assumption that the energy loss due to nuclear interactions is proportional to the energy of the incident particles, one can establish that the upper limit for the product $K\sigma_{\mu N}$ is 3 μb per nucleon, where K is the fraction of energy lost.

The cross section for producing nuclear interacting particles was estimated from the anomalous absorption as a few tens of a microbarn.[6] This means, together with the energy loss discussed, that the nuclear interaction cross section may not rapidly increase with increasing energies of μ-mesons.

The fairly large number of parallel μ-mesons observed, which are likely produced by a nuclear collision in the upper atmosphere, indicate that the scattering angles of these μ-mesons are quite small. As a μ-meson penetrating down to 700 m is expected to suffer a few scatterings, the average scattering angle per collision must be not greater than 10^{-3} rad.

The small scattering angle means a small momentum transfer, which is consistent with the small energy loss discussed above. Furthermore, the fact that the features of the nuclear interaction of μ-mesons do scarcely change with energy indicates, together with the smallness of the scattering angles, that the electric current and the magnetic moment of the struck system interacting with the electromagnetic field of a μ-meson do not increase with increasing energies so much as to counterbalance the gentle interaction due to the coulomb field of the μ-meson, which gives rise to the characteristic properties of the Rutherford scattering. This will give information about the interaction of photons with nucleons at high energies.

Furthermore, the Rutherford-like scattering of μ-mesons should give a small cross section for a large momentum transfer. If the momentum were transferred to a nucleon, the energy of the nucleon should not be high enough to produce stars with three or more prongs, as far as the cross section is required to be as large as 10 μb. Therefore, there should be a more efficient energy transfer, namely, a large energy transfer compared with a small momentum transfer. This is the case for the production of π-mesons, because their rest energy is consumed in nuclear disintegrations. This is also the case, if the π-meson is not produced immediately, but the struck nucleon is excited receiving a small momentum and subsequently emits π-mesons or loses its excitation energy colliding with another nucleon in the same nucleus. In either case, if the π-mesons are not emitted from the nucleus, the phenomenon is observed as the scattering of a μ-meson. Without such mesonic processes, the "scattering" of μ-mesons seems hard to understand.

We have so far considered only well known interactions of μ-mesons; one could instead introduce an *ad hoc* nuclear interaction of μ-mesons. Wenzel[18] invented a μ-pair theory, in which the "μ-mesons" are

[17] However, see C. M. Galleri and G. Wataghin, Phys. Rev. **79**, 718 (1950). The energy loss due to the nuclear interactions of μ-mesons adopted by these authors seems to be an overestimate: H. Fukuda, private communication.

[18] G. Wenzel, Phys. Rev. **79**, 710 (1950).

not necessarily the same as the μ-mesons commonly observed in cosmic rays. If there were the "μ-mesons" which constitute π-mesons, as suggested by Wenzel, the production of the "μ-mesons" in a high energy nucleon-nucleon collision ($\sim 10^{12}$ ev) is estimated by the statistical theory of Fermi[19] to be as large as that of π-mesons. Such "μ-mesons" should give a large contribution to the total intensity of cosmic rays at great depths and their intensity-depth relation would be considerably different from that of ordinary μ-mesons, since the effect of the decay process is quite important. The allowable fraction of undelayed particles at the depth under consideration is so small[5] that the existence of the hypothetical "μ-mesons" may be ruled out. As far as the experimental evidences underground thus far obtained are concerned, the introduction of new particles and new interactions seems to be unnecessary.

It is my great pleasure to express my hearty thanks to Professors Cocconi and Greisen, and Drs. Bollinger and Cocconi Tongiorgi for the communication of their experimental results and their stimulating discussions.

[19] E. Fermi, Prog. Theor. Phys. 5, 570 (1950).

PHYSICAL REVIEW VOLUME 84, NUMBER 1 OCTOBER 1, 1951

The High Energy Nuclear Photoeffect

J. S. LEVINGER*
Cornell University, Ithaca, New York
(Received March 29, 1951)

The nuclear photoeffect for photons of energy greater than 150 Mev is calculated assuming the two-nucleon model used by Heidmann. The main features of the nuclear photoeffect are then quite similar to those of the deuteron photoeffect. The cross section for nuclear absorption of a high energy photon is about 1.6A times the cross section for the deuteron photoeffect. The deuteron photoeffect gives a very strongly forward angular distribution for protons of a given energy, observed in the laboratory system. The angular distribution for protons from the nuclear photoeffect is almost as strongly forward: for 90-Mev protons in the laboratory system the ratio of the differential cross section at 60° to that at 90° is about 3. The proton energy spectrum decreases rapidly with proton energy, and becomes steeper for observations at large angles. The calculated angular distributions and proton energy spectra are in fair agreement with measurements by Walker. The absolute value of the differential cross section for 90-Mev protons from carbon at 30° (laboratory system) is about 0.2 μbarn/Mev steradian per Q, or about 20 μbarn/steradian per photon. This absolute value is about one-third the absolute value measured by Walker, and is somewhat larger than the absolute value measured by Levinthal and Silverman.

I. INTRODUCTION

RECENT experiments by Levinthal and Silverman,[1] Keck,[2] Walker,[3] and Kikuchi[4] have shown the production of high energy protons from nuclei irradiated by high energy photons. Protons up to energies of at least 150 Mev were produced by the bremsstrahlung photon spectra of the 300-Mev Berkeley and Cornell synchrotrons. Nuclear cross sections are of the order of 0.1 millibarn. The angular distribution of the emitted protons showed a marked forward asymmetry in the laboratory system, particularly for the higher energy protons.

At low excitation energies the compound nucleus picture has been successful. The compound nucleus picture fails to explain these observations at high excitation energies in two respects: (1) it predicts that very few high energy nucleons will be emitted; (2) it predicts an isotropic angular distribution. In fact, the compound nucleus model fails to explain the ratio of cross sections for (γ,ϕ) and (γ,n) processes,[5] and angular distributions for emitted protons,[6] at intermediate excitation energies (17.5 Mev). Courant[7] interprets the (γ,ϕ) processes at these intermediate energies as a direct photoelectric emission of protons. He uses two different models: (1) independent proton wave functions in a square well potential; (2) an approximate alpha-particle model. Somewhat better agreement with experimental results is found with the second model.

At extremely high excitation energies we might regard each nucleon in the nucleus as independent. High energy protons might be produced by independent Compton scattering by each proton in the nucleus. The cross section for this process is much smaller than that observed experimentally for the production of high energy protons.

Another possible mechanism for the photoproduction of high energy protons is via the production of photo-

* Now at Louisiana State University, Baton Rouge, Louisiana.
[1] C. Levinthal and A. Silverman, Phys. Rev. 82, 822 (1951).
[2] J. Keck (private communication).
[3] D. Walker, Phys. Rev. 81, 634 (1951).
[4] S. Kikuchi, Phys. Rev. 80, 492 (1950).
[5] O. Hirzel and H. Wäffler, Helv. Phys. Acta 20, 373 (1947).
[6] B. C. Diven and G. M. Almy, Phys. Rev. 80, 407 (1950).
[7] E. D. Courant, Phys. Rev. 82, 703 (1951).

mesons (either neutral or charged). The π-meson might subsequently be absorbed by another nucleon in the same nucleus, giving a star that might contain a high energy proton. This process would show a smaller foward asymmetry for proton production than was observed; so it cannot be the major process for production of high energy protons. It might be significant at large angles, where the process discussed below gives a very small cross section.

For the nuclear photoeffect by photons of energy greater than about 150 Mev we shall use a nuclear model intermediate between the compound nucleus model and the independent nucleon model: i.e., we assume the nuclear wave function to be the product of the wave function for two nucleons very close together with a wave function for the remaining nucleons. This two-nucleon model has been used by Tamor[8] in calculating the production of high energy protons following capture of π^- mesons. Tamor also used an alpha-particle model. Experimental results[9] are in better agreement with Tamor's calculations for the alpha-particle model. The two-nucleon model has been applied by Heidmann[10] to the pick-up reaction for high energy (90-Mev) neutrons. He finds reasonable agreement with York's measurements[11] on the production of fast deuterons by 90-Mev neutrons.

One might expect to use a similar model for the production of fast protons by π^- capture, for the pick-up reaction, and for the high energy nuclear photoeffect. In all three reactions the proton has a high momentum in the final state and, since it cannot gain much momentum in the reactions considered, it must have had a high momentum in the ground state. A proton will have a high momentum (far above that for the most energetic proton in a Fermi gas of nuclear density) if it is acted on by strong forces due to being very near other nucleons. If the distance from the proton to its nearest neighbor is much smaller than the average spacing of nucleons in the nucleus (1.4×10^{-13} cm), then it is likely that no other nucleons will be similarly near to the two nucleons which are very close together. Since small nucleon distances correspond to high nucleon momenta, the two-nucleon model should become more valid for very high momentum components of the ground-state nuclear wave function: i.e., for high energies of the emitted proton.[12]

Levinthal and Silverman[1] also reach the conclusion that high momentum components of the ground state wave function are responsible for the high energy photoeffect. (They use a mathematical argument to reach this conclusion, rather than the physical argument made above.) Chew and Goldberger[13] found an empirical momentum distribution to fit York's measurements[11] on the neutron pick-up reaction. Levinthal and Silverman use this empirical momentum distribution to find the cross section for the high energy photoeffect, and find approximate agreement with their experimental data. In principle there is no essential difference between their approach and ours; the difference is only one of method. Because of the absence of a model, their calculation gives no information on the angular distribution of the high energy protons.

Since we are using a two-nucleon, or deuteron model, many of the features of the high energy photoeffect are determined by those for the high energy photodisintegration of the deuteron. Schiff,[14] and Marshall and Guth,[15] (called SMG below) have calculated the deuteron photoeffect for photon energies from 20 to 140 Mev. They find that the electric dipole term provides almost all of the total photoelectric cross section; while interference between the electric dipole and the electric quadrupole interactions produces forward asymmetry for the proton angular distribution in the center-of-mass system.

The remaining $A-2$ nucleons in the nucleus will affect our results in two ways: they constitute a potential well in which the deuteron moves; and they may scatter the high energy nucleons. In this paper we shall be concerned with small nuclei (carbon) and as a first approximation neglect the effects of scattering by the other nucleons.

In Sec. II we calculate the ratio of the cross section for the high energy nuclear photoeffect to that for the deuteron photoeffect. In Sec. III we compare the high energy photoeffect with the calculated nuclear cross section for photon absorption integrated over all photon energies.[16] In Sec. IV we calculate the energy spectrum and the angular distribution (laboratory system) for protons and neutrons from photodisintegration of the deuteron. In Sec. V we find the energy spectrum and angular distribution for protons from the photodisintegration of carbon. In the last section we compare our calculations with recent experimental results.

II. THE DEUTERON MODEL

Since a proton-proton system has no dipole moment, and the dipole term in the photoelectric effect is predominant at the photon energies considered, we need consider only proton-neutron systems. The two-nucleon model becomes a deuteron model, for the high energy

[8] S. Tamor, Phys. Rev. **77**, 412 (1950).
[9] W. B. Cheston and L. J. B. Goldfarb, Phys. Rev. **78**, 683 (1950).
[10] J. Heidmann, Phys. Rev. **80**, 171 (1950).
[11] H. F. York, Phys. Rev. **75**, 1467 (1949).
[12] We are making an additional assumption that the potential between two nucleons increases rapidly with decreasing distances, for distances somewhat smaller than 1.4×10^{-13} cm. This assumption is valid for an exponential or a Yukawa potential, but not for a gaussian or square-well potential. Neutron-proton scattering experiments are in agreement with the first two potentials, but not with the last two. For the last two, the high momentum components of the potential, and hence of the wave function, would be too small to explain the high energy photoeffect.
[13] G. F. Chew and M. L. Goldberger, Phys. Rev. **77**, 470 (1950).
[14] L. I. Schiff, Phys. Rev. **78**, 733 (1950).
[15] J. F. Marshall and E. Guth, Phys. Rev. **78**, 738 (1950).
[16] J. S. Levinger and H. A. Bethe, Phys. Rev. **78**, 115 (1950).

photoeffect. The nuclear deuterons can be in either a triplet S state (probability $\frac{3}{4}$) or a singlet S state (probability $\frac{1}{4}$).[17] SMG's results apply exactly only for the triplet S state, but since our calculation is rather approximate, we shall use their results for both cases. Also the quasi-deuterons in the nucleus do not have a binding energy of 2.2 Mev; on the contrary, the proton and neutron have a positive energy, due to motions of nucleons in the nucleus. However, as shown below, the wave function of the quasi-deuteron, for the neutron and proton very close together, is a multiple of the wave function of the deuteron; so that the photodisintegration cross section for sufficiently high energies is that given by SMG for the deuteron, multiplied by a suitable factor.

Following Heidmann[10] we write the wave function for the ground state of the nucleus, with proton 1 very close to neutron 2, as

$$\Psi(1, 2, 3\cdots A)=\exp(i\mathbf{k}'\cdot\mathbf{r}')\psi_k(r)\varphi(3\cdots A). \quad (1)$$

The term $\exp(i\mathbf{k}'\cdot\mathbf{r}')$ represents the motion of the center of mass of the quasi-deuteron. We shall assume that the wave function φ for the remaining $A-2$ nucleons is the same for both initial and final states.[18] The cross section for the production of high energy protons will then depend only on the quasi-deuteron wave function $\psi_k(r)$, where r is the distance between the proton and neutron. This function can be written

$$\psi_k(r)=(4\pi)^{\frac{1}{2}}[\sin(kr+\delta)/\sin\delta-\chi]/(\alpha^2+k^2)^{\frac{1}{2}}v^{\frac{1}{2}}r. \quad (2)$$

χ is a function which is appreciable only inside the range of the nuclear forces and depends on the shape of the potential. Further, v is the volume of the nucleus, and k is the wave number for the relative motion of proton and neutron given by

$$k=\tfrac{1}{2}|\mathbf{k}_1-\mathbf{k}_2|. \quad (3)$$

$\mathbf{k}_1$ and $\mathbf{k}_2$ are wave numbers for proton and neutron when they are far from each other. From the theory of the effective range of nuclear forces[19,20] the phase shift δ is given approximately by

$$\cot\delta\cong-\alpha/k. \quad (4)$$

α^{-1} is the scattering length. The wave function of Eq. (2) becomes the S term of a plane wave for r larger than the range of nuclear forces. The plane wave is normalized so that integration over r gives one proton per volume v surrounding the neutron. (We are assuming that the nuclear density is constant.)

For the high energy photoeffect we are interested primarily in the behavior of ψ_k at small r where $kr\ll 1$. Expanding Eq. (2), and using Eq. (4) we have

$$\psi_k(r)=(4\pi/v)^{\frac{1}{2}}(\alpha^2+k^2)^{-\frac{1}{2}}r^{-1}[-(\alpha/k)\sin kr+\cos kr-\chi]$$
$$\cong(4\pi/v)^{\frac{1}{2}}(\alpha^2+k^2)^{-\frac{1}{2}}r^{-1}(1-\alpha r-\chi). \quad (5)$$

The wave function of the deuteron ground state is

$$\psi_d(r)=[2\alpha/(1-\alpha r_0)]^{\frac{1}{2}}r^{-1}(e^{-\alpha r}-\chi)$$
$$\cong[2\alpha/(1-\alpha r_0)]^{\frac{1}{2}}r^{-1}(1-\alpha r-\chi), \quad (6)$$

which follows from the theory of the effective range. (r_0 is the effective range.) In that theory it is shown that both the comparison function (asymptotic behavior for large r, there[19,20] denoted by ψ, in our case $\exp(-\alpha r)$) and the actual wave function in the potential (there called u, in our case $e^{-\alpha r}-\chi$) are very insensitive to the energy of the deuteron, as long as r is inside the range of nuclear forces. This is the reason why the wave functions given in Eq. (2) and Eq. (6) are proportional to each other in the relevant region of small r. For the photoelectric cross section of the quasi-deuteron we can then simply use the SMG result for the deuteron which must be multiplied by the ratio of the squares of the constant, or normalization factors in Eq. (5) and Eq. (6) giving

$$\sigma_{qd}/\sigma_d=(\psi_k/\psi_d)^2=2\pi(1-\alpha r_0)/\alpha(\alpha^2+k^2)v. \quad (7)$$

Here σ_{qd} is the photodisintegration cross section for a quasi-deuteron in which the neutron and proton have wave number k for their relative motion; and σ_d is the SMG result for the deuteron. Since have Z choices for proton 1, and N choices for neutron 2 ($N=A-Z$), the nuclear cross section is $NZ\sigma_{qd}$.

We must also average $(\alpha^2+k^2)^{-1}$ over all possible values of the wave number k. We assume Fermi distributions for proton wave number k_1, and neutron wave number k_2, up to the same maximum wave number k_m.

$$P(k_1)dk_1=(3/k_m^3)k_1^2dk_1, \quad k_1\leq k_m. \quad (8)$$

We also assume an isotropic distribution for the angle between $\mathbf{k}_1$ and $\mathbf{k}_2$. Using Eq. (3) for the value of k, we find

$$[(\alpha^2+k^2)^{-1}]_{\text{Av}}=9k_m^{-3}-24\alpha k_m^{-3}\tan^{-1}(k_m/\alpha)$$
$$-6\alpha^2k_m^{-4}+(18\alpha^2k_m^{-4}+6\alpha^4k_m^{-6})$$
$$\times\ln(1+k_m^2\alpha^{-2})=4.1k_m^{-3}. \quad (9)$$

The numerical result is found using $\alpha=0.23\times10^{13}$ cm^{-1}, and $k_m=1.0\times10^{13}$ cm^{-1}.

Equation (9) is substituted in Eq. (7). We shall take the volume of the nucleus as $v=(4/3)\pi A(1.4\times10^{-13})^3$, and multiply by NZ as discussed above. The cross section for photodisintegration of the nucleus becomes

$$\sigma=6.4(NZ/A)\sigma_d\cong1.6A\sigma_d. \quad (10)$$

The second expression holds for $N=Z=A/2$. Our result should be valid for high photon energies, say, greater than 150 Mev, and is expected to overestimate the nuclear cross section for lower photon energies.

[17] We are interested only in S states, because only for these states are the neutron and proton likely to be very close together.
[18] This assumption will in general overestimate the cross section, since the overlap integral for φ will be unity or less.
[19] H. A. Bethe, Phys. Rev. 76, 38 (1949).
[20] H. A. Bethe and C. Longmire, Phys. Rev. 77, 647 (1950).

III. COMPARISON WITH INTEGRATED CROSS SECTIONS

It is of interest to note that the proportionality to the quantity NZ/A (or approximately to A) which we have already found for the nuclear cross section for high energy photons, using the deuteron model, is just the same as the dependence of the dipole term in the nuclear absorption cross section integrated over photons of all energy.[16] (W is photon energy.)

$$\int_0^\infty \sigma dW = (2\pi^2 e^2 \hbar/Mc)(NZ/A)(1+0.8x) \cong 0.015A(1+0.8x) \text{ Mev barns.} \quad (11)$$

Here x is the fraction of attractive exchange force. The coefficient 0.8 depended somewhat on the nuclear model used; but except for this the result was completely independent of the nuclear model.[21]

We shall use the calculations by SMG for a Yukawa potential between neutron and proton. They assume exactly half ordinary and half exchange force ($x=\frac{1}{2}$), so that there is no force in the P state which is reached by dipole transitions. (A larger fraction of ordinary force would lower the high energy photodisintegration cross section; a larger fraction of exchange force would increase it.)

The dipole term σ_1 for deuteron photodisintegration calculated by SMG can be written[22]

$$\sigma_1 = [1-y^2(44+y)^{-2}]^2 \sigma_B/(1-\alpha r_0). \quad (12)$$

Here $\sigma_B/(1-\alpha r_0)$ is the Bethe-Peierls cross section, corrected using effective range theory,[20] and y=photon energy/binding energy of deuteron. To compare the cross section for the high energy nuclear photoeffect, with that integrated over all energies, we integrate Eq. (12) over photon energies from 220 Mev (chosen arbitrarily) to infinity, and use Eq. (10). We find that the integrated nuclear cross section is

$$\int_{220}^\infty \sigma_1 dW = 0.0029A \text{ Mev barn.} \quad (13)$$

This is 14 percent of the cross section integrated over all photon energies found from Eq. (11), using the value $x=\frac{1}{2}$, to correspond to SMG's calculations. Thus the high energy photoeffect is a small but not negligible part of the integrated photon absorption cross section.

The "tail" caused by the high energy photoeffect has a much larger effect on the mean energy $\bar{W}$ for photon absorption. By integrating Eq. (12) we find that

$$\int_{220}^\infty \sigma_1 W dW = 0.68A \text{ Mev}^2 \text{ barn.} \quad (14)$$

Defining $\Delta\bar{W}$ as the increase in the mean absorption energy due to the high energy tail, we have

$$\Delta\bar{W} = \int_{220}^\infty \sigma_1 W dW \Big/ \int_0^\infty \sigma_1 dW = 32 \text{ Mev.} \quad (15)$$

Since the high energy tail has such a large effect on the mean energy for photon absorption (assuming that the deuteron model calculation is correct) one cannot find reliable values of $\bar{W}$ from measurements at only moderate photon energies. Johns *et al*,[23] for example, have determined values of the integrated cross section and the mean energy $\bar{W}$ for certain photonuclear reactions. Since their measurements extend only up to photon energies of 26 Mev, the cross section integrated up to infinite photon energy is appreciable higher than their measured value, and the mean energy is very much higher than their measured value.

IV. THE DEUTERON PHOTOEFFECT

In this section we shall give the energy spectrum and angular distribution for protons, and neutrons, produced by photodisintegration of the deuteron. In the following section we shall calculate how these distributions are modified for protons and neutrons produced from heavier nuclei. The work of this section consists principally of transformation of the SMG results for the center of mass system to distributions in the laboratory system.

SMG calculate the deuteron photoeffect for a Yukawa potential between neutron and proton, half exchange and half ordinary in character, of effective range 1.74×10^{-13} cm. They have calculated the photoelectric dipole and quadrupole cross sections. SMG give their results only up to photon energies of 150 Mev, since they believe that mesonic effects, such as increased photomagnetic cross sections due to exchange currents, will have a marked effect at high photon energies.[24] Also, higher electric multipoles start becoming appreciable at higher energies. Since our whole calculation is rather approximate, we shall use the formulas of SMG up to photon energies of 300 Mev.

The high energy photodisintegration of the deuteron gives a strongly forward angular distribution for the emitted protons for three reasons, about equal in their effects. First, as discussed by SMG, interference between electric dipole and electric quadrupole matrix elements is constructive in the forward hemisphere (CM system) and destructive in the backwards hemisphere, for emitted protons. (For emitted neutrons the distribution will be backwards in the CM system.) Second, the forward motion of the CM system relative to the laboratory system, due to the photon momentum, shifts the angular distribution forward. Third, measure-

[21] However the theoretical result for the mean energy $\bar{W}$ is increased appreciably by the correlation involved in the use of the deuteron model for the high energy photoeffect. This can be seen from Eq. (27) of reference 16.

[22] See also J. S. Levinger, Phys. Rev. **76**, 699 (1949), with $\beta/\alpha=6.7$.

[23] Johns, Katz, Douglas, and Haslam, Phys. Rev. **80**, 1062 (1950).

[24] Photomagnetic transitions will be especially important for observations at angles near 0° and near 180°, where the photoelectric cross sections vanish.

ments made for fixed proton energy (laboratory system) favor protons emitted forward, since these protons were produced by lower energy photons than were protons of the same energy that were emitted backward. Here we make use of the fact that the cross section for the photoeffect and the photon intensity (for the bremsstrahlung spectrum) both decrease with increasing photon energy.

Given a proton (mass M) of energy T and momentum P, at an angle of θ with the photon direction (all in the laboratory system) the photon energy W is given by

$$W=2T/[1-T/M+P\cos\theta/M] \tag{16}$$

(here we are neglecting the binding energy of the deuteron).

For the transformation from the CM system to the laboratory system we shall also need the angle θ_c in the CM system in terms of the laboratory angle θ; and we shall need the ratio $\gamma=v'/v''=$ ratio of velocity of the CM system relative to the laboratory to proton velocity in the CM system. We can derive the relations

$$\sin\theta_c=(1-T/M+P\cos\theta/M)^{\frac{1}{2}}\sin\theta, \tag{17}$$

$$\gamma=v'/v''=[(W/4Mc^2)(1+3W/4Mc^2)]^{\frac{1}{2}}. \tag{18}$$

The differential cross section for proton production in the CM system is given by SMG as

$$d\sigma/d\Omega=(3/8\pi)\sigma_1(W)\sin^2\theta_c[1+(20\sigma_2/\sigma_1)^{\frac{1}{2}}\cos\theta_c+5(\sigma_2/\sigma_1)\cos^2\theta_c]. \tag{19}$$

For neutron production the interference term changes sign.

$$d\sigma'/d\Omega=(3/8\pi)\sigma_1(W)\sin^2\theta_c[1-(20\sigma_2/\sigma_1)^{\frac{1}{2}}\cos\theta_c+5(\sigma_2/\sigma_1)\cos^2\theta_c]. \tag{20}$$

In Eqs. (19) and (20), σ_1 is the total cross section for the electric dipole term [see Eq. (12)] and σ_2 for the electric quadrupole term. SMG's results can be represented within 10 percent accuracy, by the convenient relation

$$\sigma_2/\sigma_1=1.16\gamma^2. \tag{21}$$

The transformation from CM system (θ_c) to laboratory system (θ) is made using Eq. (17) to rewrite all functions of θ_c in terms of θ. We also use the factor for transformation of the solid angle[25]

$$(d\sigma/d\Omega)_{\text{Lab}}=(d\sigma/d\Omega)_{\text{CM}}(1+2\gamma\cos\theta_c+\gamma^2)^{\frac{1}{2}}/(1+\gamma\cos\theta_c). \tag{22}$$

Since measurements are made for constant proton energy T we have the third factor discussed above giving a forward angular distribution. This factor is the product of the photon absorption cross section, $\sigma_1(W)$, and the photon distribution in the incident beam. We take dW/W (an approximation to the bremsstrahlung spectrum) as the photon distribution, which corresponds

[25] See, for example, L. I. Schiff, *Quantum Mechanics* (McGraw-Hill Book Company, Inc., New York, 1949), Sec. 18.

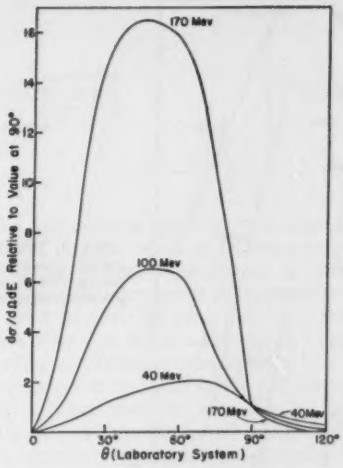

FIG. 1. Angular distribution of protons from deuteron photodisintegration.

to a beam intensity of one "Q." (The beam intensity in units of "Q" is defined as the ratio of the total energy in the beam to the energy of the most energetic photon.) Using Eq. (12) for σ_1, the third factor can be written

$$\sigma_1 dW/W=18.3[1-y^2(44+y)^{-2}]^2(y-1)^{\frac{1}{2}}y^{-3}dW/W \tag{23}$$

where $y=W/\epsilon$.

This gives us the cross section per differential photon energy dW. To convert to the cross section per differential proton energy dT, we use

$$d\sigma/d\Omega dT=(d\sigma/d\Omega dW)(dW/dT). \tag{24}$$

The results for the deuteron photodisintegration, using Eqs. (16) through (24), are shown in Figs. 1, 2, and 3. Figure 1 shows the angular distributions in the laboratory system for protons of 40 Mev, 100 Mev, and 170 Mev, expressed as ratios of the differential cross section to that at 90°. The angular distribution is markedly forward, even for proton energies as low as 40 Mev; and is very strongly peaked forward for higher proton energies. Since we are including only photoelectric transitions, the cross section falls to zero for 0°, and also for 180°.

The differential energy spectrum for emitted protons is drawn with a log-log scale in Fig. 2 for laboratory angles of 30°, 90°, and 120°.[26] The calculated results can be represented by a power law in the relevant energy range: $d\sigma$ is proportional to T^{-n}. For $\theta=30°$, $n=2.5$; for $\theta=90°$, $n=4.4$; for $\theta=120°$, $n=6.5$. The energy spectrum becomes very steep for larger angles, since at

[26] Note that a differential cross section for 100-Mev protons at 30° of 0.015 microbarn/steradian Mev per Q corresponds to a much larger cross section per photon. A Q value of unity means that there are only 2/200=1/100 photon in the range 200 to 202 Mev, which corresponds to protons in the range 100 to 101 Mev.

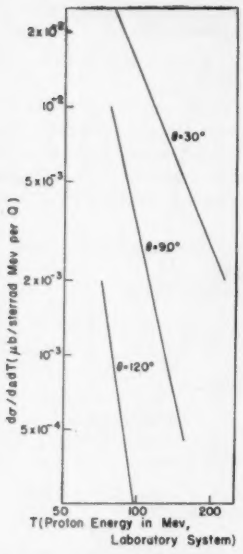

FIG. 2. Differential energy spectrum of protons from deuteron photodisintegration.

higher energies the angular distribution becomes extremely strongly forward.

Both Fig. 1 and Fig. 2 are drawn for a photon spectrum dW/W with no upper limit on the photon energy. Calculations in this paper apply to upper limits of 200 Mev, and 300 Mev, respectively. For the upper limit of 200 Mev, and for $T=100$ Mev the angular distribution of Fig. 1 should go to zero for a laboratory angle of 80°, and there will be no protons at all of energy 170 Mev. The cutoffs for the angular and energy distributions are shown in Table I, which is based on Eq. (16).

Figure 3 compares the differential cross sections for proton production and for neutron production, at energies of 100 Mev. (The cutoff shown in the second line of Table I applies to the angular distribution.) The neutron distribution is only moderately forward since the dipole-quadrupole interference term provide a backward asymmetry canceling much of the forward asymmetry due to motion of the CM system. The angular distributions of protons and neutrons are more alike for lower energies, and differ more widely than those of Fig. 3 for higher energies.

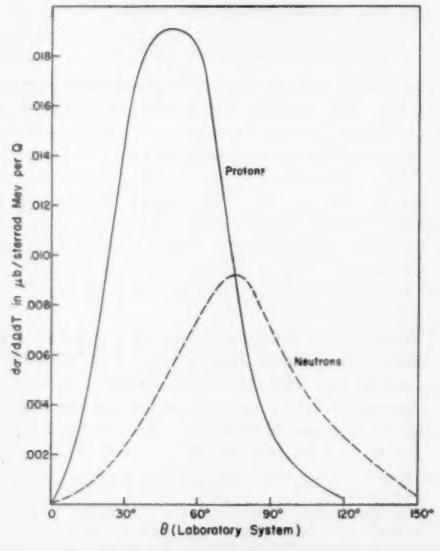

FIG. 3. Angular distribution for protons and neutrons from deuteron photodisintegration.

V. THE NUCLEAR PHOTOEFFECT

The general features of the angular distributions and energy spectrum of the deuteron photoeffect persist in the calculation of the nuclear photoeffect; but they are shifted in energy, and somewhat smeared out, due to the influence of the remainder of the nucleus.

First, the quasi-deuterons in the nucleus have a positive energy, corresponding to the wave number k, of Eq. (3). While there is a spread from 0 to 40 Mev in the positive energy, the effects of this spread are much smaller than the smearing effects of motion of the quasi-deuteron discussed below, and shall be neglected. We take the average positive energy as 12 Mev.

TABLE I. Cutoff due to upper limit on photon spectrum.

Proton energy:	for $W_{max}=200$ Mev	for $W_{max}=300$ Mev
$T=40$ Mev	all angles possible	all angles possible
$T=100$ Mev	$\theta_{max}=80°$	$\theta_{max}=120°$
$T=170$ Mev	no angles possible	$\theta_{max}=60°$
Angle of observation:		
$\theta=30°$	$T_{max}=135$ Mev	$T_{max}=210$ Mev
$\theta=90°$	$T_{max}=90$ Mev	$T_{max}=130$ Mev
$\theta=120°$	$T_{max}=72$ Mev	$T_{max}=98$ Mev

Correcting for this effect gives us the differential cross section for proton production, against proton angle and proton energy, for protons still in the nucleus. The proton energy in the laboratory is less than that inside the nucleus by the depth of the nuclear potential well, which is about 30 Mev for a typical nucleus.[27] The positive energy of the quasi-deuteron, and the nuclear potential shift the energy scale used in Fig. 2 for the deuteron photoeffect by 18 Mev.

[27] The nuclear potential well is a somewhat uncertain concept at high nuclear energies, as is indicated by recent work on scattering of high energy neutrons. [Fox, Leith, Wonters, and MacKenzie, Phys. Rev. **80**, 23 (1950); and J. DeJuren, Phys. Rev. **80**, 27 (1950)]. For example, it is not clear whether the potential well for a tighly bound nucleus, such as C^{12}, is deeper than that for a more typical nucleus. We shall use the value of 30 Mev. Our results are rather sensitive to the assumed depth of the potential well, since the proton energy spectrum is so steep. Thus a 10-Mev change in the assumed well depth, for proton energies of 100 Mev, causes about a 30 percent change in calculated differential cross section for 100-Mev protons.

The effects of the motion of the quasi-deuteron in the nucleus can be considered in terms of the components of its velocity: v_x along the direction of observation, and v_y perpendicular to the direction of observation, but in the plane formed by the photon direction and the direction of observation. $v_x=\frac{1}{2}(v_{1x}+v_{2x})$ where v_{1x} and v_{2x} are velocity components for the two nucleons when far apart from each other. (The third component v_z is not important for our present work.) The component v_x changes the observed energy, while v_y changes the observed angle. We shall make the approximation of considering that v_x and v_y have uncorrelated probability distributions. We shall make the further approximation that both v_x and v_y have the "triangular" probability distribution given in Eq. (25) and shown as the solid line in Fig. 4. (It would be more accurate to use the probability distribution for v_x given by the Fermi distribution for a nuclear temperature of about 8 Mev. This is sketched as the dotted curve in Fig. 4.) We use

$$P(v_x)=\begin{cases}(1-|v_x/v_m|)/v_m, & |v_x|\leq v_m\\ 0 & |v_x|\geq v_m.\end{cases} \tag{25}$$

Here v_m is the maximum velocity for a nucleon in a nucleus, which corresponds to a maximum kinetic energy of 20 Mev.

Consider a proton which outside the nucleus has energy T, and velocity v_1. It could have been produced with velocity $v''=v_1-v_x$, (and energy T'') from a quasi-deuteron which had velocity component v_x towards the observer. The differential cross section for production of a proton of energy T, is the differential cross section for production of protons of energy T'', convoluted with the probability distribution for v_x.

$$d\sigma(T)=\int d\sigma(T'')(dT''/dT)P(v_x)dv_x. \tag{26}$$

The component of motion v_y affects the direction in which the proton is observed. A proton produced at angle $\theta'=\theta-\varphi$ is observed at angle θ, where

$$\varphi=\tan^{-1}(v_y/v_1)=v_y/v_1. \tag{27}$$

The differential cross section, as a function of θ, is multiplied by the probability distribution for v_y, and integrated over all angles.

$$d\sigma(\theta)=\int d\sigma(\theta')(\sin\theta'/\sin\theta)P(v_y)dv_y. \tag{28}$$

The correction factors for the cutoff of the photon spectrum, at energy $W_{\max}$, combined with the integrals of Eq. (26) and Eq. (28) for the motion of the quasi-deuteron, are expressed as a correction factor M, multiplying the differential cross section for a deuteron at rest, with no cutoff on the photon spectrum. The motion of the quasi-deuteron tends to smooth out the angular distribution shown in Fig. 1 for a deuteron at rest since factor M is small for the peak of the angular distribution and becomes larger for both large and small angles. The principal effect on the energy spectrum is that appreciable numbers of protons are observed at energies above the sharp cutoff which would be observed for a quasi-deuteron at rest. However, the energy spectrum decreases much more rapidly for energies above the cutoff than for energies below the cutoff.

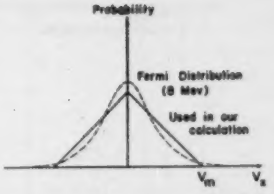

FIG. 4. Probability distribution for motion of center of mass of quasi-deuteron.

Using the factor 6.4 NZ/A of Eq. (10) for the carbon nucleus, together with the correction factor M discussed above, and the differential energy spectrum for protons produced by deuteron photodisintegration (Fig. 2), we find the differential energy spectrum shown in Fig. 5 for laboratory angles of 30° and 90°. The solid curves are for a photon cutoff at 200 Mev photon energy; the dotted curves for 300 Mev maximum photon energy. While Fig. 2 shows a power law energy spectrum, Fig. 5 shows a spectrum similar to a power law for energies below the cutoff, but decreasing much more rapidly at higher photon energies. The arrows indicate the proton cutoff energies that would be observed if there were no motion of the quasi-deuteron. Expressed as cross sections per Q, the cross sections for 200 and 300 Mev maximum photon energy are nearly the same for proton energies below the lower proton cutoff.

VI. COMPARISON WITH EXPERIMENT

Levinthal and Silverman[1] measured protons produced by photons from the 300-Mev Berkeley synchrotron.

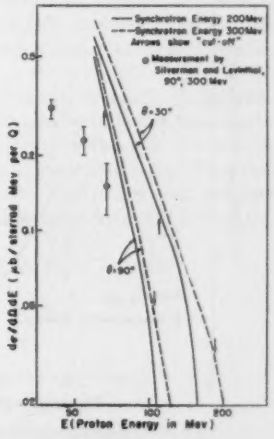

FIG. 5. Differential energy spectrum protons from carbon.

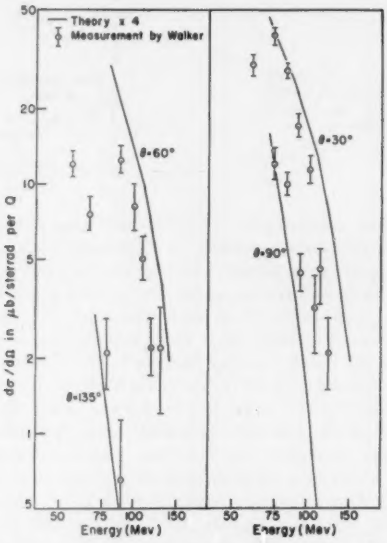

FIG. 6. Integral energy spectrum protons from carbon.

They used proportional counters to measure protons at the end of their range, thus obtaining a differential energy spectrum. Their experimental results for protons from carbon at 90°, in the laboratory system, are compared with our calculations in Fig. 5. The experimental points should be compared with the lower dotted curve.

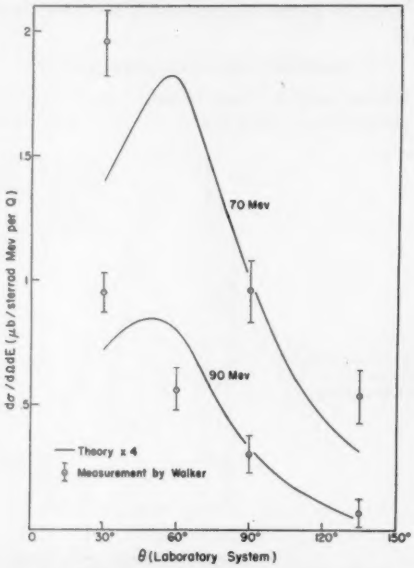

FIG. 7. Angular distribution protons from carbon.

We observe that the absolute cross section calculated at 67 Mev is about twice that measured by Levinthal and Silverman. The calculated energy spectrum is a much more rapidly varying function of proton energy than is the experimental energy spectrum. These discrepancies are not unexpected, since our method of calculation (setting the overlap integral for $\phi(3\cdots A)=1$ will overestimate the cross section and the error would be worse at low photon energies, where the quasi-deuteron model becomes poor.

Levinthal and Silverman[1] also measured the angular distribution for 40-Mev protons. They found that the differential cross sections at laboratory angles of 45°, 90°, and 135° had the ratios 1.6, 1, and 0.6. Our calculations do not extend to this low a proton energy. However their result is in qualitative agreement with the angular distribution of Fig. 2.

They also measured proton production from elements from beryllium to lead, and found that the cross section was proportional to Z.

Walker[3] has measured high energy protons from carbon by the Cornell synchrotron operating at 200 Mev. He used a photographic emulsion technique, which gives him an integral energy spectrum. That is, he measured $d\sigma/d\Omega$ for protons of energy greater than E_0. To compare with his results, we have integrated the differential energy spectrum shown in Fig. 5, and other similar curves at other angles. Figure 6 compares Walker's integral energy spectrum[2a] with our calculated result for laboratory angles of 135°, 90°, 60°, and 30° To facilitate the comparison we have multiplied our theoretical cross sections by a factor of four. We find fair agreement in the shapes of the curves between theory and experiment over a wide range of energies and angles. The probable errors are only those for relative measurements.

In Fig. 7 we compare the angular distribution for the differential energy spectrum, at proton energies of 70 Mev and 90 Mev, with values found by Walker. Again we have multiplied the calculated cross sections by the factor of four to facilitate comparison. We find fair agreement between theory and experiment in the shape of the angular distribution. Apparently the cross section measured experimentally rises from 60° to 30°, while the calculated cross section falls slightly. Also the measured cross section does not fall quite so low as the calculated cross section at 135°. The probable errors of the measurements are not small enough to establish these discrepancies. We shall suggest below possible causes for these discrepancies.

Keck[2] measured protons produced by the Cornell synchrotron operating at 300 Mev. He measured protons at the end of their range using scintillation counters. As his results are still preliminary, we shall

[2a] Note that, because of the recalibration of the photon intensity at the Cornell synchrotron, by J. DeWire and J. Keck, Walker's published results [Phys. Rev. 81, 634 (1951)] have been divided by the factor 1.44.

quote only their general features, to compare with the calculations of this paper. Keck measured the differential energy spectrum of protons from carbon, at 67½° in the laboratory system, for proton energies from 70 Mev to 240 Mev. The absolute cross section was about twice that calculated in this paper. Keck measured the angular distribution for angles from 15° to 120°, at proton energies of 95, 125, and 175 Mev. His measurements show the same discrepancies between calculations and experiment indicated by Walker's angular distribution, i.e., the calculations give too low a cross section both at very small angles, and at very large angles.

Like Levinthal and Silverman, Keck found that the photoproton yield was proportional to Z. Our calculations give a photoproton yield proportional to NZ/A, which is very close to proportional to A, and therefore increases somewhat more rapidly than Z. This more rapid increase with Z is counteracted by the probability of escape of the photoproton from the nucleus, which is a decreasing function of Z.

The measurements on photoprotons from carbon by Levinthal and Silverman, Walker, and Keck overlap at a proton energy of 70 Mev and angle of 90°, Their absolute values for this differential cross section are compared with each other, and with our calculation, in Table II. (Keck's measurement at 67½° are divided by a factor 1.5, based on Walker's angular distribution, to convert to a cross section at 90°.) The agreement among the experimental measurements of the absolute cross section is fair: i.e., not very far outside the maximum likely errors of measurement. The agreement between our calculations and the experiments is within the estimated errors.

Keck also used an organic scintillation counter to measure high energy photoneutrons from carbon. He found that their number agreed in order of magnitude with the number of high energy photoprotons.

Keck has measured some coincidences between high energy neutrons and protons, and finds some correlation between their directions of emission. The coincidence rate was much smaller than the single counting rate for high energy nucleons. Presumably this is the result of "smearing effects" such as motion of the quasi-deuteron, and scattering of the emitted neutron and proton. A detailed comparison between experiment and calculations from the deuteron model has not yet been made. Keck's observation of neutron-proton coincidences appears to be the crucial experiment in establishing the deuteron model for nuclear processes at very high excitation energy.

TABLE II. Comparison of absolute cross sections.

Worker	Method	Synchrotron energy	$d\sigma/d\Omega dE$ in μb/sterad Mev per Q	Maximum likely error
Levinthal and Silverman	Proportional counter	300 Mev	0.15	factor of 2
D. Walker	Photographic emulsion	200 Mev	0.95	55%
J. Keck	Scintillation	300 Mev	0.74	30%
J. Levinger	Calculation	200 Mev	0.25	factor of 3
J. Levinger	Calculation	300 Mev	0.29	factor of 3

There is also some evidence for neutron proton coincidences from the cloud chamber pictures by Gaerttner and Yeater.[29] They believe that the (γ,pn) process is the predominant mode of disintegration for nitrogen by the photon beam from the 100-Mev G.E. betatron.

The calculations of this paper have omitted various effects that might advantageously be considered in a more detailed treatment. We have taken no account of scattering of the high energy photoproton by other nucleons in the nucleus. This will tend to change the directions of some high energy protons, making for a more isotropic distribution in the laboratory system, and, particularly for large nuclei, will prevent the emission of some high energy protons. In correcting for the motion of the quasi-deuterons, one might use the Fermi distribution for 8 Mev sketched in Fig. 4, instead of the probability distribution used in this paper.

The process of meson emission and reabsorption to produce high energy protons is negligible for measurements with 200-Mev maximum photon energy since the cross section for meson production is so small at these energies, but it might be appreciable for higher photon energies. This is another process tending to give an angular distribution more isotropic in the laboratory system.

Finally, we have used an incomplete calculation of the deuteron photoeffect. If there are appreciable photomagnetic cross sections, this would give a significant increase in the cross section for small angles, in the laboratory system.

The author is grateul to H. A. Bethe, E. Salpeter, and J. Heidmann for discussions of theoretical aspects of this problem; and to A. Silverman, S. Kikuchi, J. Keck, and D. Walker for communication and discussion of their experimental results. Part of this work was done while the author was employed under an ONR contract.

[29] Gaerttner and Yeater, Phys. Rev. **77**, 714 (1950).

Radiochemical Studies on the Fission of Th^{232} with Pile Neutrons*

A. TURKEVICH AND J. B. NIDAY
Argonne National Laboratory and Institute for Nuclear Studies, University of Chicago, Chicago, Illinois

(Received June 11, 1951)

The relative yields of more than twenty products in thorium fission have been determined radiochemically. Pile neutrons with an estimated effective average energy of 2.6 Mev were used. The data have been used to construct a complete fission yield curve for Th^{232}. This is compared with the yield curves of other fissionable nuclei. Thorium fission is similar to the neutron fission of U^{235}, U^{233}, Pu^{239}, and U^{233} in being highly asymmetric. With the neutrons used in this work the peak yields occur 110 times as frequently as symmetrical products.

I. INTRODUCTION

THE nuclear fission processes that have been observed to date can be classified roughly into two categories: those which follow directly from the original excited compound nucleus, and those which involve the prior emission of one or more light particles (usually neutrons). In the former case the fragments, after division, may give off neutrons. For heavy nuclei (Z equal to or greater than 90), spontaneous fission and fission induced by photons or neutrons of energy less than roughly 8 Mev fall into the first category; fission produced by photons or particles of higher energy as well as by charged particles falls into the second category. This paper reports on the study of the nuclear fission of Th^{232} with moderate energy neutrons[1] as an example of fission of the first variety.

One of the characteristics of a fission reaction is the large number of products formed. Those found in detectable yields cover a mass range of up to 90 units. The relative yields of these products are characteristic of the fissioning nuclide and the excitation energy. The most sensitive and detailed method of investigating the yield-mass curve resulting from fission is the radiochemical technique. By this method the relative yields of β-radioactive nuclear species with moderate or long lives can be determined; the yields of such species usually represent all of the yield for the particular mass number from fission of the first category. In the mass region of interest, almost every second mass number is represented by a suitable nuclide for radiochemical analysis so that the method can be much more detailed than most other methods. Although the errors can be quite large (up to $\sim$30 percent) because of the uncertainties of β-counting, these errors are independent of the absolute yield over the entire range of about 10^6.

Previous radiochemical studies on the products of the low energy fission of heavy nuclei have established rather completely the fission yield curves[2-6] of U^{235}, Pu^{239}, and U^{233}. In all these cases it has been demonstrated that the most probable mode of fission is not into equal fragments, symmetrical fission being one of the least probable modes. The main difference in the yield-mass curves of these nuclides appears to be a shift in the light group to take care of the varying mass of the fissioning nuclide while the heavy group remains relatively fixed in position.

The much less sensitive and detailed ionization chamber technique has been used to study the fission of many nuclides.[7] In particular, the fission of Th^{232} by fast neutrons has been investigated by this method by Jentschke[8] and by Fowler and Rosen.[9] Although these studies could not establish the detailed course of the yield curve, they indicated that the fission of Th^{232} with neutrons of energy not too much above the threshold is similar to the slow-neutron examples in that symmetric and very asymmetric fission are quite improbable, and that the widths of the peaks of the yield-mass curves are comparable.

The first radiochemical work on the fission of Th^{232} dates, of course, to pre-1939 days. Thorium, as well as uranium, when irradiated with neutrons, had been found to produce the complex set of radioactivities that were eventually clarified as arising from nuclear fission.[10] Even in this early work it was recognized that the phenomenon in thorium required the use of more energetic neutrons than in uranium.

Subsequent to the elucidation of the phenomenon of

* A preliminary report on this work was made at the American Physical Society Meeting, June, 1950, Mexico City [J. Niday and A. Turkevich, Phys. Rev. **80**, 136(A) (1950)].

[1] A radiochemical study of the fission of Th^{232} with 37.5-Mev alpha-particles has been made by A. S. Newton, Phys. Rev. **75**, 17 (1949). The original compound nucleus in this case is U^{236}, excited by such a large amount, however, that its break-up probably represents fission of the second variety.

[2] The Plutonium Project, Revs. Modern Phys. **18**, 513 (1946).

[3] *Radiochemical Studies: The Fission Products* (McGraw-Hill Book Company, Inc., New York, 1951), National Nuclear Energy Series, Div. IV, Vol. 9, Appendix B.

[4] W. E. Grummit and G. Wilkinson, Nature **161**, 520 (1948).

[5] L. Yaffe and C. E. MacKintosh, Can. J. Research **B25**, 371 (1947).

[6] Steinberg, Seiler, Goldstein, and Dudley, talk before Am. Assoc. Advancement Sci., December, 1947; U. S. AEC declassified document, MDDC 1632 (January 6, 1948), unpublished.

[7] For example, D. C. Brunton and G. C. Hanna, Phys. Rev. **75**, 990 (1949). This note gives references to much of the other work of this type.

[8] W. Jentschke, Z. Physik **120**, 165 (1943).

[9] J. L. Fowler and L. Rosen, Phys. Rev. **72**, 926 (1947).

[10] See L. A. Turner, Revs. Modern Phys. **12**, 1 (1940), for a review of the radiochemical work on uranium and thorium leading to the discovery of nuclear fission. This article summarizes also the prewar work.

nuclear fission, many individual fission products were isolated from neutron-irradiated thorium.[10] In general, these appeared to be the same ones that were present in uranium fission. During the war, Sugarman and coworkers[11] on the Manhattan Project began a study of the fission products of thorium, but the work was interrupted after demonstrating that all of the radioactive nuclides formed in U^{235} fission that were looked for were also found in Th^{232} fission. In fact, several fission products were found first in such isolated studies of thorium fission and later identified in U^{235} fission.

The fundamental nuclear data pertaining to the neutron fission of Th^{232} are rather meager. Thermal neutrons apparently cause no observable fission. The cross section reaches detectable values[12] at a neutron energy of 1.10 ± 0.05 Mev. At 2.5 Mev it is reported[13] to be 10^{-25} cm² compared with 5×10^{-25} cm² for U^{238}.

In this paper we report the relative yields of twenty-three masses produced in the fission of thorium by neutrons in a uranium pile. The radiochemical technique has been used. The results are sufficient to characterize the yield-mass curve rather completely and make possible a comparison of Th^{232} fission with other known examples of fission.

II. GENERAL EXPERIMENTAL PROCEDURE

A. Irradiation Conditions

The source of neutrons for this work was the Argonne heavy-water pile (CP-3, before reconstruction). The irradiations were performed in the "thimble" of this pile, i.e., close to the geometrical center of the lattice. Although the position in the thimble varied from one irradiation to another, the gross number of fissions per gram of thorium per kilowatt-hour of operation of the pile was constant within the errors of comparing bombardments (±10 percent), indicating that neither the variation in position nor the variation in size of the samples, nor the frequent presence of neighboring samples was affecting the irradiation conditions appreciably.

The thorium was irradiated in the chemical form of $Th(NO_3)_4\cdot4H_2O$ ("Baker's Analyzed"). The samples varied in weight from 30 to 60 grams and were enclosed in corked quartz containers. These quartz containers were wrapped in cadmium foil to reduce the activation of thorium or impurities by the intense thermal-neutron flux of the pile, and the entire assemblage was then placed in standard aluminum containers (~1 in. diameter).

In the average position of irradiation, the samples were a few inches away from four uranium rods; the space between was occupied by heavy water, aluminum, and other small samples being irradiated simultaneously. In such a position, besides the intense flux of thermal neutrons, there are present large numbers of fast neutrons from the fissions occurring in the neighboring uranium rods. The distribution in energies of the neutrons which actually effected fission in the thorium is not readily estimated. If it is assumed that these are the primary fission neutrons with energy above the thorium fission threshold (1.1 Mev), we calculate that half of the fissions are caused by neutrons of energy greater than 2.7 Mev.

The time of irradiation was adjusted to be convenient for the particular nuclides being studied. It varied from 10 minutes to several days. In cases where the pile operation was not steady, it was assumed that during a given irradiation the fission rate varied directly with the power level. Most of the irradiations were performed with the power level varying by not more than 25 percent.

The fission yields to be reported were determined from seventeen different irradiations carried out over a period of several years. In about half of these, a sample of normal uranium was irradiated with thermal neutrons at the same time as the thorium samples. These experiments (called "comparison experiments") gave the relative yields of several fission products in Th^{232} and U^{235} rather independently of counting efficiencies or of uncertainties in decay constants or irradiation conditions.

B. General Radiochemical Procedure

After irradiation, the samples were dissolved in hot water containing nitric acid, and aliquots of this solution were taken for separation of the various fission products. The determinations were usually made in duplicate in each experiment, and only infrequently was the same aliquot portion used for more than one fission product.

The fission products were isolated by the standard radiochemical procedure of adding a known amount of inactive isotopic carrier, encouraging "exchange" between the carrier and the tracer quantities of the fission products, and then purifying the element in question from the matrix (uranium or thorium salts) and from other fission-product radioactivities. The carrier element was finally precipitated in a form suitable for weighing and counting, and the fraction recovered was determined from the weight.

In general, the chemical procedures followed were patterned on those developed in the Manhattan Project.[14] The main modifications were those necessitated by starting with a thorium salt rather than a uranium salt and by having this material in rather large amounts. Particular changes in the analytical procedures will be noted in the discussion of the different nuclides.

The radioactivity of the purified fission products was

[11] Ballou, Burgus, Dial, Glendenin, Finston, Ravely, Schloss, and Sugarman, see reference 3, paper 225.

[12] W. E. Shoupp and J. E. Hill, Westinghouse Research Laboratory, Scientific Paper 1390. Haxby, Shoupp, Stephens, and Wells, Phys. Rev. **57**, 1088 (1940).

[13] Ladenburg, Kanner, Barschall, and Van Voorhis, Phys. Rev. **56**, 168 (1939).

[14] See reference 3, Part VI.

measured usually with a glass-walled (~45 mg/cm²) Eck-and-Krebs-type Geiger tube. In a few cases the end-mica-window-type Geiger tube was used. The radiochemically pure precipitate, usually 5 to 25 mg, was filtered on a 1.5-cm² filter paper disk which was mounted on standard cardboard cards and covered with Cellophane. The behavior of the measuring tube was monitored by use of a beta-standard.

The purity of the radioactivity isolated was checked by following its decay and by comparing the absorption properties in aluminum of the radiations with the known characteristics of the nuclide in question. In some cases the presence of other isotopic radioactive nuclides had to be taken into account.

The low fission rate of thorium in the pile, corresponding to an "effective thermal fission cross section" of about 1 millibarn, and the low fission yields of some of the nuclides studied, made the thermal-neutron activation of impurities particularly serious. In general, an attempt was made to look for those fission products that would not be interfered with by products of (n,γ) processes on stable isotopes. Also, neutron irradiations of the thorium salt were performed in the thermal column of the pile, where fast neutrons are few, to prove that the uranium level was not high enough to affect the results. However, samarium and arsenic activities formed by neutron activation of impurities proved large compared with those formed in the fission process. It seemed impractical to remove the small amounts of samarium responsible, and analysis for this fission product was abandoned. In the case of arsenic, however, the product of the (n,γ) reaction, As^{76}, has sufficiently different radiation characteristics to be distinguished from the fission product As^{77}, and corrections could therefore be made in the fission-product analysis for arsenic.

In the case of several other impurities it was demonstrated by more conventional analytical techniques that they were not present in interfering amounts.

C. Treatment of Data

Two types of experiments were performed in getting relative fission yields. In one type, samples of normal uranium were irradiated with slow neutrons in the pile simultaneously with the thorium samples. If two fission products (B and X) are isolated from both the uranium and thorium samples and counted at the same time and under comparable conditions, then their fission yield ratio in thorium relative to their yield ratio in uranium is independent of the duration of the irradiation, the decay time, the half-lives of the nuclides, and the detection efficiencies for the radiations. The two yield ratios are related to each other and to the observed activity of the two fission products by the equation:

$$\frac{Y_X^{\mathrm{Th}}}{Y_B^{\mathrm{Th}}}=\frac{Y_X^{\mathrm{U}}}{Y_B^{\mathrm{U}}}\cdot\frac{A_X^{\mathrm{Th}}}{A_X^{\mathrm{U}}}\cdot\frac{A_B^{\mathrm{U}}}{A_B^{\mathrm{Th}}}.$$

In this equation the letters Y and A designate fission yields and measured activities (corrected to the total sample); subscript letters differentiate the fission products in question; superscript symbols denote the fissioning nuclide, e.g., A_B^{Th} = the activity of fission product B in the thorium sample measured at a standard time.

The values assumed for the fission yields in uranium fission (Y_B^{U}, Y_X^{U}) were taken from the literature data or from a smooth curve interpolation of experimental data,[8] and are indicated in the table of results (Table I).

In general one fission product, Sr^{89}, was isolated from each bombardment, and all thorium yields were expressed relative to an arbitrary value for the yield of mass 89. The relative fission yields for Th^{232} from these comparison experiments are, of course, no more accurate than the values for U^{235} on which they are based.

About half of the fission products studied were not isolated from simultaneously irradiated uranium. In these cases the measured radioactivity had to be corrected for growth during and decay subsequent to the irradiation, and for the genetic characteristics of the beta-decay chain. Besides this, the radioactivity also had to be corrected for differences in detection efficiencies for the radiations because of absorption in the sample covering, air, and counter walls, and scattering and self-absorption in the sample itself.

The first corrections are straightforward. The half-lives and genetic relationships used in the calculations were usually those of the *Table of Fission Products* issued by the Plutonium Project.[2,15] The corrections for absorption in the counter tube walls were made on the assumption that the beta-rays were being absorbed exponentially. The absorption coefficients used were obtained from aluminum absorption curves taken on end-window Geiger tubes, but were corrected empirically to apply to the cylindrical geometry of the "Eck and Krebs" tubes. The wall thicknesses of the tubes were estimated from the counting rate of a uranium standard. The relation of this counting rate to wall thickness was established from tubes where the wall thickness was available. The estimated wall thicknesses ranged from 40 to 52 mg/cm², and it was felt that they were known to ±5 mg/cm². The weight of Cellophane covering (~2.6 mg/cm²) and air (~1 mg/cm²) was also included in the absorption correction.

In estimating the effects of self-absorption and self-scattering and back-scattering from the samples,[16] no correction at all was applied if the sample weight, expressed as mg/cm², was less than half the half-thickness of the radiations involved. If the sample weight was greater than this, a self-absorption correction was

[15] The Plutonium Project, J. Am. Chem. Soc. **68**, 2411 (1946); see also reference 3, Appendices A and C.

[16] Engelkemeir, Seiler, Steinberg, and Winsberg, see reference 3, Paper 4.

applied according to the formula,[17]

$$K=(1-e^{-\mu d})/\mu d.$$

K is the fraction of the radiations with absorption coefficient μ emerging from a sample of weight d mg/cm^2.

D. Evaluation of Errors

The easily evaluated errors of timing, level of irradiation, uncertainties in half-lives of the fission products, etc., are unfortunately small compared with others that are not easily estimated. It is well known that the radiochemical method may not yield quantitative results if the element in question can exist in different forms in solution. For example, the different valence states of iodine in solution do not exchange readily.[18] In this work an effort was made to minimize trouble from this source. Even so, the iodine and rhodium results scatter much more than the others. In the case of molybdenum, where exchange troubles were at first encountered, conditions of analysis were found which gave consistent results.

Errors have been assigned to the reported fission yields which take into account the number of experiments performed, the agreement between duplicate determinations, the sensitivity of the relative yields to errors in beta-absorption corrections, and suspected chemical exchange troubles. These errors thus give the range within which we believe the true values lie.

III. COMMENTS ON INDIVIDUAL DETERMINATIONS

In general, the chemical procedures and analysis of the data were straightforward. There are given here the barest details except where warranted by specific circumstances.

Zinc (49-hr $Zn^{72}\rightarrow$14.3-hr Ga^{72})

The procedure used was almost identical with that of Siegel and Glendenin,[19] which makes use of the precipitation of $ZnHg(SCN)_4$, and scavenging operations. The original separation of zinc from the thorium, however, was made by precipitation of ZnS from an ammonium carbonate solution of the thorium nitrate.

Because of the low fission yield of this nuclide, quite low counting rates were obtained. The characteristic growth and decay of the chain, could not, however, be mistaken.

Gallium (5-hr Ga^{72})

The procedure used was practically identical with that of Siegel and Glendenin,[20] which depends primarily on the ether extraction of gallium from 6M HCl. Besides scavenging operations, two precipitations of gallium ferrocyanide were made. Unfortunately, the product was contaminated, apparently with 67-hr Mo^{99}.

Germanium and Arsenic (Mass 77 Chain)

The known characteristics[15] of the β-decay chain with mass 77 are:

$$\begin{array}{l} \text{59-sec } Ge^{77}\searrow \\ \qquad\qquad\quad \text{40-hr } As^{77}\rightarrow \text{stable } Se^{77}. \\ \text{12-hr } Ge^{77}\nearrow \end{array}$$

The yield of 12-hr Ge^{77} in Th^{232} fission was measured in two experiments. The germanium was isolated from the solution of irradiated thorium nitrate by first precipitating GeS_2 from 6N H_2SO_4 and then following the radiochemical procedure of Winsberg.[21] This depends primarily on two distillations of $GeCl_4$ from an HCl solution in a stream of chlorine. The latter keeps arsenic as the relatively nonvolatile $AsCl_5$. The arsenic is distilled later as $AsCl_3$.

As is well known[22,23] a part of the chain of mass 77 decays through the 59-sec isomer of Ge^{77}. The fraction of the total As^{77} that is formed by decay of the 59-sec isomer of Ge^{77} is reported as 0.59 for U^{235} and 0.55 for U^{233} fission. This fraction is determined by the yield of 12-hr Ge^{77} and the additional measurement of total 40-hr As^{77} formed in fission. In our work,[24] the 38-hr As^{77} isolated from the irradiated thorium nitrate showed radiochemical contamination from 26.8-hr As^{76} formed by (n,γ) processes on minute arsenic impurities in the thorium nitrate. About half of the measured arsenic radioactivity was this unwanted As^{76}. Although the amount present could be estimated from the absorption characteristics of the radiations (38-hr As^{77} has a 0.7-Mev β^-; the 26.8-hr. As^{76} has much more energetic beta-rays—up to 3 Mev), the resulting yield of As^{77} is appreciably more uncertain than that of Ge^{77}. Two experiments in this work gave values of 0.53 and 0.65 for the fraction of the As^{77} that does not come from 12-hr Ge^{77}. Thus, it appears as if the branching in the chain of mass 77 is the same in Th^{232} fission as it is in the slow neutron fission of U^{235} and U^{233}. The total yield of mass 77 is calculated from the yield of 12-hr Ge^{77} and a branching ratio of 0.57.

Bromine (2.4-hr Br^{83})

The procedure used was the same as that of Glendenin, Edwards, and Gest[25] which involved the addition of BrO_3^- carrier, reduction with H_2S, and then repeated oxidation-reduction cycles with extractions of the Br_2 into CCl_4. Several of these cycles were made under con-

[17] Henriques, Kistiakowsky, Margnetti, and Schneider, Ind. Eng. Chem., Anal. Ed. 18, 349 (1946).
[18] See, for example, W. H. Burgus and T. H. Davies, reference 3, Paper 19.
[19] J. M. Siegel and L. E. Glendenin, see reference 3, Paper 226.
[20] J. M. Siegel and L. E. Glendenin, see reference 3, Paper 227.
[21] L. Winsberg, see reference 3, Paper 228.
[22] E. P. Steinberg and D. W. Engelkemeir, see reference 3, Paper 54.
[23] J. Arnold and N. Sugarman, J. Chem. Phys. 15, 703 (1947).
[24] Although As^{77} is assigned a half-life of 40 hours in all standard compilations, the present study indicates that the proper half-life is closer to 38 hours, in accord with the work of N. Sugarman (reference 23, and private communication).
[25] Glendenin, Edwards, and Gest, see reference 3, Paper 232.

ditions that decontaminated the bromine from fission iodine. The calculations were made assuming[25] that 27/48 of the bromine came from 67-sec Se^{83} and the rest from 25-min Se^{83} as in U^{235} fission.

Strontium (53-day Sr^{89} and 9.7-hr Sr^{91}) (Comparison Experiments)

The procedure used for isolating strontium was essentially that of Glendenin,[26] although minor modifications were made from time to time. This procedure utilizes the fairly specific separation of strontium and barium nitrates from cold fuming nitric acid, the removal of barium as the chromate from a buffered acetate solution (pH$\sim$5), and hydroxide scavengings. In the first four experiments the final precipitate was strontium oxalate; in later experiments and in all the comparison experiments, $SrCO_3$ was used.[27]

Strontium (25-yr Sr^{90}→65-hr Y^{90})

This chain was determined by isolating strontium radiochemically (see above) and then milking the 65-hr Y^{90} daughter after it had grown in. Since rather large amounts of thorium had to be used to get enough of this activity, the thorium was first precipitated as the hydroxide, and the radiostrontium and its carrier were isolated from the supernate and washings.

The removal of the yttrium from the $SrCO_3$ precipitates consisted simply of solution in acid, several precipitations of the hydroxide (with strontium hold-back carrier), and final yttrium oxalate precipitation.

The half-life of the long-lived member of this chain, Sr^{90}, is reported as 25 years in standard compilations, but is apparently based partly on expected yields in U^{235} and Pu^{239} fission.[28] The recent observation[29] of actual decay of Sr^{90} indicates a half-life of 19.9±0.3 years. If this is the correct half-life, the value reported here for the fission yield of this chain in Th^{232} fission should be lowered by 20 percent, and definite irregularities in the yield-mass curves of U^{235}, Pu^{239}, and Th^{232} are indicated.

Zirconium (17-hr Zr^{97}) (Comparison Experiments)

The procedure for separating zirconium was essentially that of Hume,[30] which consists of complexing the zirconium with F^-, scavenging with LaF_3, precipitating $BaZrF_6$ several times, and dissolving in H_3BO_3. The zirconium is finally mounted and counted as the oxide.

In spite of the cadmium shielding around the thorium samples, very large amounts of Pa^{233} were formed from the Th^{232} by neutron capture. Since the attempts to separate protactinium and zirconium were not too successful at the time, the counting was done through 136 mg/cm² aluminum, which greatly emphasizes the Zr^{97} radiations.

[25] L. E. Glendenin, see reference 3, Paper 236.
[27] E. Hoagland, see reference 3, Page 237.
[28] See reference 3, R. W. Nottorf, Paper 77; and L. E. Glendenin and C. D. Coryell, Paper 78.
[29] R. I. Powers and A. F. Voigt, Phys. Rev. **79**, 175 (1950).
[30] D. N. Hume, see reference 3, Paper 245.

Molybdenum (67-hr Mo^{99}) (Comparison Experiments)

The chemical procedure was modified from that of Ballou[31] which consisted of specific precipitations of molybdenum with α-benzoinoxime and hydroxide scavengings after decomposition of the α-benzoinoxime precipitate in HNO_3-HClO_4. It was found necessary to dissolve the irradiated $Th(NO_3)_4\cdot 4H_2O$ in 6N HNO_3 to avoid loss of tracer molybdenum and also desirable to have a large excess of NH_4OH present during the hydroxide scavengings.

A final precipitation of $PbMoO_4$ from a buffered solution was used,[32] rather than Ag_2MoO_4.

Ruthenium[33] (42-day Ru^{103} and 1-yr Ru^{106}→30-sec Rh^{106}) (Comparison Experiments)

After ruthenium carrier was added to the matrix solutions, ruthenium metal was precipitated with zinc and magnesium. The metal was dissolved after KOH fusion, and the regular procedure of Glendenin based on RuO_4 distillations from perchloric acid was used.[34]

Since both Ru^{103} and Ru^{106} and its daughter Rh^{106} are present in the isolated ruthenium, the relative contributions of the two chains to the radioactivity had to be estimated either from the absorption characteristics or from the decay curve. Both methods were used. Since in both methods Ru^{103} is obtained by subtracting the contribution of chain 106, its yield carries a slightly higher estimate of error.

Rhodium (36.5-hr Rh^{105}) (Comparison Experiments)

In the case of rhodium, the use of procedures based on that of Ballou,[35] depending primarily on pyridine extractions of the rhodium, did not give satisfactory results. The presence of 36.5-hr Rh^{105} in thorium fission was definitely established although the yields varied among experiments and sometimes in duplicate samples within an experiment. These fluctuations are attributed to incomplete exchange between the added rhodium carrier and radiorhodium.

Palladium (13.4-hr Pd^{109} and 21-hr Pd^{112}→3.2-hr Ag^{112}) (Comparison Experiments[36])

The chemical procedure was essentially that of Seiler.[37] The first step in isolating the palladium from the thorium solution was to add carrier and then pour the entire solution into strong NH_4OH. This precipitated the thorium while keeping the palladium in solution. The main part of the procedure involved four dimethylglyoxime precipitations, interspersed with scavengings with $ZrO(OH)_2$ and AgCl.

[31] N. E. Ballou, see reference 3, Paper 257.
[32] Editor's note, Paper 209 of reference 3.
[33] We are indebted to Mr. Salter for the help in the chemical analyses and calculations on this fission product.
[34] L. E. Glendenin, Paper 260 of reference 3.
[35] N. E. Ballou, Paper 263 of reference 3.
[36] We are indebted to Mr. M. Kalkstein for help in these analyses.
[37] J. A. Seiler, Paper 264 of reference 3.

The yield of chain 112 was calculated from counting data taken through 355 mg/cm² of aluminum to absorb the radiation of Pd^{109}. The yield of chain 109 was obtained by least-squares analysis of the complex curve obtained with no added absorber, assuming the half-lives to be 13.4 hours for Pd^{109}, 21 hours for Pd^{112}, and 3.2 hours for Ag^{112}.

The literature values[3,15] of the yields in U^{235} fission are somewhat conflicting. The values chosen and listed in Table I were the result of consultation with E. P. Steinberg.[38]

Silver (7.5-day Ag^{111})

The procedure used was modified from that of Glendenin[39] in which silver is precipitated as the chloride, scavenged in ammoniacal solutions and collected as Ag_2S. Use was made of the solubility of AgCl in strong HCl and of precipitation by dilution in the presence of palladium and cadmium holdback carriers. Small amounts of bromide and iodide carriers were also used during the ammoniacal scavengings.

Cadmium (2.33-day $Cd^{115} \rightarrow$ 4.53-hr In^{115m} and 43-day Cd^{115m})

The procedure used was essentially that of Metcalf,[40] which is based on precipitations of CdS from dilute HCl solution and scavenging with basic ferric acetate and with PdS. The first step consisted of precipitation of CdS from a solution of thorium complexed with $(NH_4)_2CO_3$.

Iodine (8.0-day I^{131} and 2.4-hr I^{132})

The chemical procedure used was similar to that of Glendenin and Metcalf.[41] The thorium was complexed with $(NH_4)_2CO_3$, the iodide carrier oxidized to periodate with NaClO, and after acidification reduced to I_2 with $NH_2OH \cdot HCl$. The iodine was extracted into CCl_4 (BrO_3^- goes to Br^- and does not extract). The iodine was then extracted into water with $NaHSO_3$, oxidized with $NaNO_2$ (which does not oxidize Br^-), and re-extracted with CCl_4. The final precipitate was AgCl.

Caesium (33-yr Cs^{137} and 13.7-day Cs^{136}) (Comparison Experiment)

One experiment was performed to get the yield of 33-yr Cs^{137} in thorium fission and to get information on the yield of the shielded nuclide Cs^{136} (13.7-day). The radiochemical purification, following the suggestions of Glendenin and Nelson,[42] was based on repeated silicotungstate and perchlorate precipitations of the cesium interspersed with scavenging operations. In this experiment the samples were demonstrated to be radiochemically pure by chemical recycling.

The yield of the 33-yr Cs^{137} was determined from the activity after the 13.7-day Cs^{136} had decayed away. There was markedly less of this 13.7-day component in the samples isolated from thorium than in those isolated from uranium. Unfortunately, there was not enough activity to emphasize this component by counting through absorber, so the gross decay curves were analyzed by least squares into 13.7-day and 33-yr components.

The average of three samples gave, for the yield of the shielded isotope (Cs^{136}) relative to the yield of 33-yr Cs^{137} in thorium fission, only one quarter of the corresponding quantity in uranium fission. The sensitivity of the experiment to possible short-lived impurities makes us place somewhat larger negative than positive limits of error on this quantity.

Barium (12.8-day $Ba^{140} \rightarrow$ 40.0-hr La^{140})

The barium separations were essentially a combination of two methods by Glendenin utilizing the separation of $BaCl_2$ by HCl-ether solution[43] and of barium and strontium nitrates by fuming HNO_3, $Fe(OH)_3$ scavengings and $BaCrO_4$ precipitation.[26] In the first experiment the nitrate separation was not used; in all the others both purifications were used and the $BaCrO_4$ fractional precipitation technique initiated by Hahn and Strassman[44] was used in the final separation to reduce the contamination of barium by the radium isotopes from the natural decay of the thorium. The yield of the chain 140 was calculated from the counting rate of the barium extrapolated to the time of last $La(OH)_3$ precipitation.

Cerium (28-day Ce^{141} and 275-day Ce^{144})

The procedure used was essentially that of Boldridge and Hume,[45] which is based on separation of cerium and lanthanum fluorides in the presence of zirconium holdback carrier, several precipitations of $Ce(IO_3)_4$ after oxidation with BrO_3^-, solution of the precipitate by reduction to cerous ion with H_2O_2, scavengings with $Zr(IO_3)_4$, and finally precipitation as cerium oxalate. In two experiments, the first step consisted of the separation of cerium carbonate from the thorium complex in saturated $(NH_4)_2CO_3$ solution; in the third experiment, $Th(IO_3)_4$ was precipitated away from cerium reduced to the cerous state by H_2O_2.

IV. RESULTS

As discussed above, this work determined only relative fission yields. Sr^{89} was isolated in each experiment, and the yield of each nuclide investigated was calculated, assuming a fission yield of 6.7 percent[46] for Sr^{89}.

[38] E. P. Steinberg, Argonne National Laboratory, private communication.
[39] L. E. Glendenin, Paper 267 of reference 3.
[40] R. P. Metcalf, Paper 268 of reference 3.
[41] L. E. Glendenin and R. P. Metcalf, Paper 278 of reference 3.
[42] L. E. Glendenin and C. M. Nelson, Paper 283 of reference 3.
[43] L. E. Glendenin, Paper 288 of reference 3.
[44] O. Hahn and F. Strassman, Naturwiss. 27, 89 (1939); also N. Sugarman and co-workers, reference 11.
[45] W. F. Boldridge and D. N. Hume, Paper 294 of reference 3.
[46] The value of 6.7 percent for the yield of Sr^{89} was chosen in order to give an integral under the total smooth yield-mass curve of 200 percent.

TABLE I. Fission yields from Th^{232} and pile neutrons.

1 Mass number	2 Nuclides isolated and measured	3 Yields from U^{235} (slow) neutron fission)[a] percent	4 Yields from Th^{232} (pile neutron fission)[b] percent	5 Estimated reliability percent
72	49-hr Zn→14.3-hr Ga	0.000015	0.00033	±0.00008
73	5-hr Ga	0.00010	0.00045	±0.00022
77	12-hr Ge→38-hr As	0.0037	0.009	±0.002
	Total 38-hr As	0.0091	0.020	±0.007
83	2.4-hr Br	0.48	1.9	±0.45
89	53-day Sr	4.6	6.7	±0.7
90	25-yr Sr→65-hr Y		6.1	±1.2
91	9.7-hr Sr	5.0	6.4*	±0.7
97	17-hr Zr	6.1	5.4*	±0.8
99	67-hr Mo	6.2	2.9*	±0.3
103	42-day Ru	3.7	0.20*	±0.07
105	36.5-hr Rh	0.9	0.07*	±0.02
106	1-yr Ru→30-sec Rh	0.5	0.058*	±0.006
109	13.4-hr Pd	0.028	0.053*	±0.010
111	7.5-day Ag	0.018	0.052	±0.010
112	21-hr Pd→3.2-hr Ag	0.011	0.065*	±0.010
115	2.33-day Cd→4.53-hr In^{m}	0.011	0.072	±0.014
	43-day Cd^{m}	0.0008	0.003	±0.0015
	Total chain	0.012	0.075	±0.015
131	8.0-day I	2.8	1.2	±0.6
132	77-hr Te→2.4-hr I	4.4	2.4	±0.7
136	13.7-day Cs	0.0062	0.0017*	$^{+0.0009}_{-0.0017}$
137	33-yr Cs	(6.2)[c]	6.6*	±1.0
140	12.8-day Ba→40-hr La	6.17	6.2	±2.0
141	28-day Ce	5.7	9.0	±3.0
144	275-day Ce→17-min Pr	5.3	7.1	±1.0

[a] The yields for U^{235} with slow neutrons are taken from the compilation in Vol. 9 of reference 3.
[b] The yields with an asterisk were obtained in comparison-type experiments. The yields listed depend directly on the assumption that the corresponding yields in the slow-neutron fission of U^{235} are correct.
[c] Fission yield of Cs^{137} estimated from smooth fission yield curve (reference 3) for U^{235}.

The fission yields thus calculated are presented in Table I. Opposite each mass number are listed the radioactive species isolated or measured. Column 3 lists the yields[3] in U^{235} fission with slow neutrons. Column 4 presents our observed yields from the fission of Th^{232} with pile neutrons. Values accompanied by an asterisk were obtained in comparison experiments. These yields depend directly on the corresponding yields in U^{235}. The last column gives our estimate of the limits of error in the thorium fission yields. In the case of the comparison experiments these errors do not contain the uncertainty arising from possible errors in the U^{235} yield of this chain.

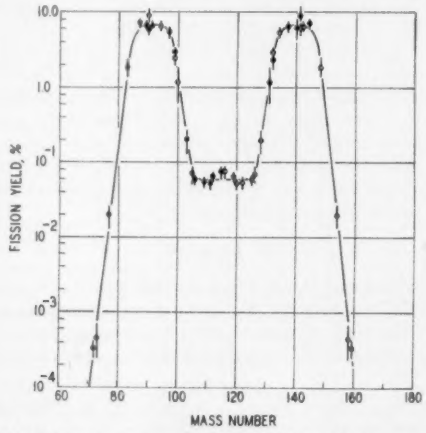

FIG. 1. Yield-mass curve for fission of Th^{232} with pile neutrons, normalized to 200 percent yield (assuming 2 neutrons given off). Solid circles represent experimental data, open circles represent the mirror points (231-A).

Since more than half of the fission yields have been determined for nuclides with mass numbers lighter than 116, a complete fission yield curve is best constructed by assuming that all fissions involve the formation of only two heavy particles,[47] and that a constant number of neutrons (we have arbitrarily assumed 2.0) are emitted. On these assumptions the yields of masses A and 231-A are equal. The data treated in this way are presented in Fig. 1, with a solid point indicating an experimental determination and an open circle representing the same yield for the mirror mass. Matching of the data is sensitive to the choice of the number of neutrons emitted only in the mass regions 97–105 and 126–134. Although the estimated errors here are rather large, it appears that fission into fragments with masses in these regions cannot be associated on the average with the emission of more than 2.5 or less than 1.5 neutrons.

Within estimated errors, the points lie on a smooth curve of the familiar "double-humped" shape. The maxima are at masses 91 and 140, giving $140/91=1.54$ for the most probable mass ratio. The widths of the peaks at half-height are 14 mass units. Products of symmetrical or nearly symmetrical fission occur 110 times less frequently than the most probable products.

The yield curve in the mass region near symmetrical fission is very flat compared with the corresponding curves for U^{233}, U^{235}, or Pu^{239}. Unfortunately, the experimental error in the yield of Cd^{115} is large, and so it is impossible to say whether there is a real subsidiary maximum in the region of symmetrical fission. The rather sharp transition from the steep side of the peak to the rather flat trough appears real, however.

The experimental data, of course, give only relative yields. The absolute values in Table I were obtained by requiring that the smooth curve through the points account for all of the fissions, i.e., that the integral under the yield-mass curve give 200 percent. The most probable yield (from the smooth curve) comes out to be 6.8 percent.

V. DISCUSSION

The mass ratio, 1.54, for the most probable mode of fission of Th^{232} with pile neutrons, agrees with the

[47] There have been numerous attempts to detect nuclear fission into three or more heavy fragments by radiochemical and ionization chamber studies and by examination of fission tracks in photographic plates. It appears as if the frequency of such events in less than a few percent of all fissions. See K. W. Allen and J. T. Dewan, Phys. Rev. **82**, 527 (1951); L. Marshall, Phys. Rev. **75**, 1339 (1939).

ionization chamber studies of thorium fission,[8,9] which gave 1.51 and 1.59 for the ratio of most probable energies. It has been shown[7] that the widths of the peaks in the yield-mass curves are not directly comparable to the widths of the energy peaks in ionization chamber studies because of the distribution in the energy of fission even for a fixed mass ratio.

The characteristics of the yield curve for Th^{232} are compared with those of the yield curves[48] for other neutron fissionable nuclides in Table II. The comparison between the lightest and heaviest members of this set (Th^{232} and Pu^{239}) is presented also in Fig. 2, which shows the smooth yield curves for these two nuclides. The effect of varying the mass of the fissioning nucleus upon the yield-mass curve is illustrated in Table II and Fig. 2. Most of the change is a shift of the light group, the heavy group remaining fixed in position within a few mass units. The widths at half-height of the peaks of the yield-mass curves are all close to 15 mass units. There may be a trend to slightly wider peaks for the heavier nuclei.

The observed ratios of most probable yields to yields for symmetrical division are also listed in Table II. Except for Pu^{239} (where the depth of the trough is determined by only one experimental point,[3] not necessarily at the minimum), the trough appears to be appreciably higher for U^{233} and Th^{232} fission than for nuclides fissionable with thermal neutrons. This may be accounted for by the following argument:

TABLE II. Characteristics of yield-mass curves of different heavy nuclides fissionable with neutrons.[a]

1 Nuclide	2 Most probable light mass	3 Most probable heavy mass	4 Ratio of most probable masses	5 Mass width at half-height	6 Ratio of peak to trough yields
Th^{232}	91	140	1.54	14	110[b]
U^{233}	93	137	1.48	14	400
U^{235}	97	138	1.42	15	600
U^{238}	98	140	1.43	17	100[b]
Pu^{239}	99	138	1.39	~16	140

[a] See reference 48. [b] Fast neutron fission.

In the fission of U^{235} with slow neutrons, the decomposition of the excited compound nucleus U^{236} is relatively slow, as evidenced by appreciable competition from gamma-emission leading to the formation of U^{236} in its ground state.[49] At the effective threshold for Th^{232} fission with neutrons (~1.1 Mev) the fission break-up of the excited Th^{232} nucleus must compete primarily with neutron emission and is therefore much faster than the break-up of the excited nucleus in the slow neutron fission of U^{235}. In addition, the average energy of the neutrons causing fission in our experiments on Th^{232} has been estimated as about 2.6 Mev; thus it is appreciably higher than the "threshold" energy. The U^{233} fission yields[50] were obtained under similar conditions. An increase in the neutron energy causing fission is known to raise the yield of symmetrical products.[51] Therefore,

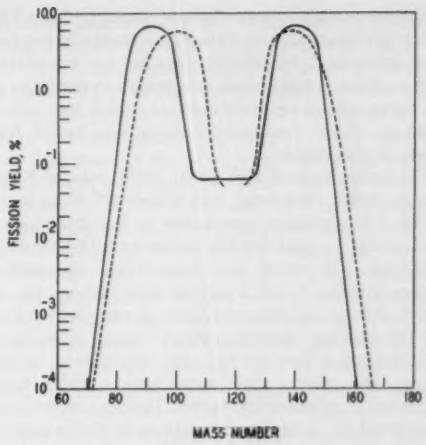

FIG. 2. Smooth yield-mass curve for fission of Th^{232} (solid line) compared with the curve for Pu^{239} (dashed line). The plutonium curve is from reference 3.

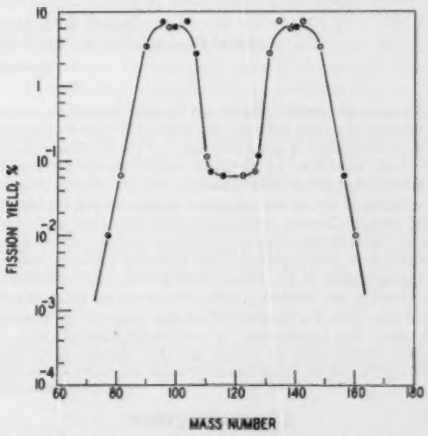

FIG. 3. Yield-mass curve for fission of U^{235} with pile neutrons constructed assuming binary fissions with two neutrons emitted (not normalized). Solid circles represent experimental data; open circles represent the mirror points (237-A). The experimental data are from reference 50.

[48] The data for U^{235} and Pu^{239} are from reference 3; for U^{238}, see subsequently in text; the data for U^{233} are from reference 6.

[49] Can. J. Research **29**, 203 (1951); Ghiorso, Brittain, Manning, and Seaborg, Phys. Rev. **82**, 558 (1951).

[50] Engelkemeir, Seiler, Steinberg, and Winsberg, Paper 218, of reference 3.

[51] This effect of neutron energy on the ratio of peak to trough yields has been established for U^{235} (R. W. Spence, Brookhaven Conference Report BNL-C-9, June 14, 15, 1949), for Pu^{239} (Engelkemeir, Freedman, Seiler, Steinberg, and Winsberg, Paper 204, see reference 3), and for Th^{232} (A. Turkevich, talk before Am. Assoc. Advancement Sci. meeting, Chicago, December 1, 1947, U. S. AEC declassified document, MDDC 1568).

the higher troughs observed in the case of U^{235} and Th^{232} fission are reasonable in view of the energy of the neutrons being used. Specifically, they are not inconsistent with a constant ratio of peak to trough in the fission of all heavy nuclei at excitations at which the rate of break-up of the compound nucleus into fission fragments is comparable.

The radiochemical U^{235} fission yield data of Engelkemeir, Seiler, Steinberg, and Winsberg[50] is presented in Fig. 3 in a manner comparable to that used for our data in Fig. 1 (assuming binary fission with loss of two neutrons). The rather flat regions near symmetrical fissions in Figs. 1 and 3 suggest that perhaps the observed curves are superpositions of two yield curves, one the familiar "double-humped "curve, whose shape and absolute values are not very sensitive to neutron energy, the other a yield curve with a rather broad maximum at symmetrical fission. The peak in the latter curve would be much lower than those in the asymmetric type, but the absolute values here would increase with increasing neutron energy.

The results reported in Table I also give a little information on the charge distribution in Th^{232} fission as compared with U^{235} or Pu^{239} fission. Because the neutron-to-proton ratio in Th^{232} is higher than that in U^{235} and Pu^{239}, slightly longer fission chains are expected in Th^{232} fission. For this reason there should be no change in the relative yields of isomers close to the end of a beta-chain, since these would be formed primarily by beta-decay of a fission product with lower charge rather than directly in the fission process. Within experimental error, this is borne out in the cases of isomers in the chains of mass 77 and 115.

On the other hand, because of the higher neutron to proton ratio in Th^{232} relative to U^{235} and Pu^{239}, a lower yield of shielded isotopes is to be expected.[52] In the one case investigated (Cs^{136}) this expectation was also realized: in Th^{232} fission, the yield of Cs^{136} is apparently no greater than one quarter of that in U^{235} fission with slow neutrons. The theory of Glendenin[52] predicts for Cs^{136} a yield in Th^{232} fission about 20 times lower than in U^{235} fission.

[52] L. E. Glendenin, Ph.D. thesis, Massachusetts Institute of Technology (July 29, 1949), unpublished.

PHYSICAL REVIEW VOLUME 84, NUMBER 1 OCTOBER 1, 1951

Neutron-Capture Theory of Element Formation in an Expanding Universe*†‡

RALPH A. ALPHER AND ROBERT C. HERMAN
Applied Physics Laboratory, The Johns Hopkins University, Silver Spring, Maryland

(Received June 11, 1951)

The neutron-capture theory of element formation by non-equilibrium processes has been extended to include explicitly the effect of the expansion of the universe, and the resulting equations have been solved on an electronic digital computing machine. Inclusion of the universal expansion is found to require an increase by a factor of five of the density of matter chosen for the start of the element-forming process over that previously found necessary to represent the observed relative abundance distribution of elements in a static universe. The following physical conditions lead to agreement in the over-all trend of theoretical with observed abundances: the element-forming process is taken to start at ~140 sec after the "beginning" of the universal expansion; at this time the temperature is $\sim 1.3\times 10^{9}$°K$\cong$0.11 Mev, the neutron-proton ratio is 7.33:1, and the density of matter is $\sim 0.9\times 10^{-6}$ g/cm³. This density value includes a correction made to account for the effect of groupiing together nuclear species in order to reduce the number of defferential equations required to describe the neutron-capture procss.

The effect of the choice of an initial neutron-proton ratio on the other physical conditions involved in representing the observed relative abundance data is considered. A neutron-proton starting ratio of 1:4, recently found by Hayashi to result from the interactions between matter and radiation in the pre-element-forming phase of the expanding universe, is shown to lead to some difficulties.

In an Appendix, Dr. T. H. Berlin, of The Johns Hopkins University, shows that the differential equations describing the element-forming process can be solved in closed form for the static case by the use of laplace transforms. However, the inclus on of the universal expansion precludes solution in closed form.

I. INTRODUCTION

THE work described in this paper serves to complete one aspect of the description of the origin and observed relative abundance distribution of the chemical elements according to a non-equilibrium neutron-capture theory. Calculations have been made of the dependence on atomic weight of the relative abundance distribution of nuclear species which results if the effect of the expansion of the universe is explicitly taken into account in the formation process. In previously reported work[1,2] the process of element formation by successive neutron captures was examined for a static universe; and it was shown that the general

* This work was supported by the U. S. Navy Bureau of Ordnance.

† Preliminary accounts of this work were presented at the New York meeting of the American Physical Society, February, 1951, Phys. Rev. 82, 296(A) (1951), and at the Washington meeting, April, 1951, Phys. Rev. 83, 236(T) (1951).

‡ This paper includes an Appendix by Dr. T. H. Berlin, Department of Physics, The Johns Hopkins University, on the exact solution of equations describing element formation in a static universe according to the neutron-capture theory.

[1] R. A. Alpher and R. C. Herman, Phys. Rev. 74, 1737 (1948).
[2] R. A. Alpher and R. C. Herman, Revs. Modern Phys. 22, 153 (1950).

trend of the observed relative abundance distribution in atomic weight, as given by Brown,[3] was theoretically reproduced over the entire atomic weight range. As will be seen in this paper, a satisfactory representation of the relative abundance data can also be obtained with a neutron-capture theory in an expanding universe. In this, as in previously reported work, the detailed features of the abundance data are not reproduced, since the theory does not contain the specific nuclear properties and processes involved. The theory of the formation process is based on the radiative capture of fast neutrons by all nuclear species, and a smoothed-out representation is taken for the well-defined dependence of fast neutron capture cross sections on atomic weight. The capture cross section data involved are those determined principally by Hughes, Spatz, and Goldstein,[4] and by Hughes and Sherman.[5]

The expansion of the universe was not explicitly included in previously reported work by the authors on the origin of the elements because of the computational labor involved. Recently, the Computation Laboratory of the National Bureau of Standards was kind enough to afford the authors the opportunity of using its new electronic computing machine, the SEAC (Bureau of Standards Eastern Automatic Computer), for the solution of this problem. The detailed coding of the problem for SEAC solution, together with the actual SEAC operation, was performed by Dr. Joseph H. Levin of the Computation Laboratory, National Bureau of Standards.

II. FORMULATION OF THE PROBLEM

While a detailed statement of the neutron-capture process of element formation in an expanding universe has already been given,[2] it seems worthwhile to describe briefly the proposed situation again here. The presently observed relative abundance distribution of nuclear species is believed to be universal, and to have been established in all essential details quite early in the history of the expanding universe, prior to the formation of galaxies and stars. In the present form of the theory, it is supposed that very shortly after the "start" of the universal expansion, the material content of the universe was neutrons. At the low densities of matter involved, neutrons were able to undergo free radioactive decay. At first the temperature was too high to allow the existence of nuclei in appreciable amounts. However, as the universe expanded and cooled, nuclear reactions yielding the various nuclear species became predominant as compared with photo and thermal dissociation processes. The first of these building-up reactions involved the neutrons and the appreciable number of protons already present from neutron decay, and yielded deuterons by radiative capture of neutrons. Heavier nuclei were built up by successive radiative capture of neutrons with intervening β-decay, the latter adjusting nuclear charge so that the resultant nuclei could continue to grow by neutron addition. Many simplifications are involved in the physical picture considered here. In particular, for species of atomic weight less than 15 or 20, reactions other than those of the (n,γ) type undoubtedly played an important role. Certainly other reactions must be introduced to carry the chain of element-building reactions past the non-existent nuclei at atomic weights 5 and 8. Moreover, the detailed abundances of heavier nuclei must have been influenced to some extent by the competition between (n,γ) reactions and β-decay, by (γ,n), $(n,2n)$ and other reactions insofar as the "shielded elements" and the abundance peak in the vicinity of iron are concerned, and by nuclear fission acting to terminate the element-forming process at high atomic weights. However, it appears that under the assumed physical conditions, (n,γ) reactions would generally be the most probable, and in predominating would determine the basic character of the relative abundance data. These and other detailed questions involved in the neutron-capture theory have been discussed elsewhere recently.[2]

The cosmological model chosen for the early stages of the expanding universe is the general nonstatic model, composed of an ideal fluid, exhibiting homogeneity and isotropy, and with no interconversion of matter and radiation. It can be shown that for the early times of interest in connection with the element-forming process, the physical state of the model can be described without recourse to any statement as to the nature of the radius of curvature of the universe at that time. Thus, it is not necessary to characterize the universe as being open, closed, or flat, questions which must be decided on the basis of information other than that gleaned from the theory of element formation.

It was shown in earlier work on the neutron-capture theory in a static medium that the density of matter must have been considerably less than the density of radiation during the formation process. In this situation, the radiation controls the expansion, and the field equations pertinent to the cosmological model described give the following time dependence for the density of matter,[2]

$$\rho_m = \rho_0 t^{-\frac{3}{2}} \text{ g/cm}^3, \tag{1}$$

and for the density of radiation,

$$\rho_r = (32\pi G/3)^{-1} t^{-2} = 4.48\times 10^{5} t^{-2} \text{ g/cm}^3, \tag{2}$$

where G is the gravitational constant, and time t is in seconds after the start of the expansion. The trace of matter is taken to be in thermal equilibrium with the radiation. If the universal expansion is supposed to involve the adiabatic expansion of black body radiation, then it follows from Eq. (2) that the temperature is given by

$$T = (c^3/a)^{\frac{1}{4}} \rho_r^{\frac{1}{4}} = 1.52\times 10^{10} t^{-\frac{1}{2}} \text{°K}, \tag{3}$$

[3] H. Brown, Revs. Modern Phys. 21, 625 (1949).
[4] Hughes, Spatz, and Goldstein, Phys. Rev. 75, 1781 (1949).
[5] D. J. Hughes and D. Sherman, Phys. Rev. 78, 632 (1950).

where a is the Stefan-Boltzmann constant and c the velocity of light.

The equations describing the successive neutron-capture processes are derived in terms of finite volume elements, so that again the question of the radius or the total mass of the universe need not be considered. Let C_n, C_1, and C_j be the concentrations of neutrons, protons, and nuclei of atomic weight j. Let C_0 be the concentration of nucleons at the time t_0 defining the start of the element-forming process according to the simplified theoretical picture. Then one defines normalized concentrations as

$$\xi_n=C_n/C_0, \quad \xi_1=C_1/C_0, \quad \xi_j=C_j/C_0. \tag{4}$$

Although physically it does not appear correct to select a starting time, since formation of nuclei will build up over a finite time as competing processes die out, actually it appears to be a reasonable as well as a sufficient approximation to select a time when the temperature has fallen below the deuteron binding energy. Assuming that element building starts at this time, the following equations then describe the neutron-capture process:

$$\begin{aligned} d\xi_n/d\tau &= -\xi_n-\sum_{j=1}^{J}P_j\xi_n\xi_j-3\xi_n/(2\tau), \\ d\xi_1/d\tau &= \xi_n-P_1\xi_n\xi_1-3\xi_1/(2\tau), \end{aligned} \tag{5}$$

and for the general case of species of atomic weight j,

$$d\xi_j/d\tau=P_{j-1}\xi_n\xi_{j-1}-P_j\xi_n\xi_j-3\xi_j/(2\tau).$$

In Eqs. (5), one has

$$\tau=\lambda t, \tag{5a}$$

where λ is the decay constant of the free neutron,

$$P_j=p_jC_0/\lambda, \tag{5b}$$

and the integration is started at a $\tau_0=\lambda t_0$. The quantities p_j are probabilities, per second, that a nucleus of atomic weight (j) will capture a neutron and become the species of atomic weight $(j+1)$. Equations (5) state that the neutron concentration decreases because of neutron decay, and because of radiative capture by all other nuclear species; the proton concentration is increased by free neutron decay and decreased by the formation of deuterons; the concentration of nuclei of atomic weight (j) is increased through radiative capture of neutrons by nuclei of atomic weight $(j-1)$ and is decreased through its own capture of neutrons, and, for all species the concentrations decrease as $3\xi/(2\tau)$, a term describing the dilution due to the expansion of the universe.

Qualitatively, the quantities p_j are the product of a capture cross section and a velocity. The cross sections actually used in calculations were, as already mentioned, values from a smoothed-out representation of the general dependence of fast neutron capture cross sections on atomic weight. The velocity factor was so determined as to account for the fact that at the temperature and density associated with the element-forming process the collisions among nuclei and nucleons must have obeyed the maxwell distribution law in energy. With the several factors in p_j so taken, the calculation of P_j is quite straightforward.[2]

An initial value of $\tau=\tau_0=0.128$ was chosen for integrating Eqs. (5). Because $\tau=\lambda t$, the corresponding initial time in seconds, measured from the "beginning" of the expansion, as well as the corresponding temperature, depend on the value used for the neutron decay constant. For a neutron half-life of 12.8 min,[6] the initial temperature and time are found to be $\sim 1.28 \times 10^{9}$°K (0.11 Mev) and ~ 142 seconds, respectively.[7] One must further select the initial concentration of nucleons, as well as the composition in terms of neutrons and protons. Clearly, the introduction of an initial time implies that there are no nuclear species present other than neutrons and protons to begin with. Electrical neutrality of the mixture is assumed. If the normalized concentration of neutrons, ξ_n, is taken to be unity at $\tau=0$, and if the only process that went on until $\tau=\tau_0=0.128$ was the free decay of neutrons, then the initial concentrations of neutrons and protons for the formation process would have been $\xi_n(\tau_0)=0.88$ and $\xi_1(\tau_0)=0.12$, respectively. These values, together with $\xi_j(\tau_0)=0$, were taken as initial conditions for the solutions of Eqs. (5). The effect of the particular choice of initial conditions is considered further in Sec. IV of this paper.

To reduce the number of Eqs. (5) to be solved simultaneously to a practical quantity,[2] the coefficients P_j were averaged for small groups of adjacent nuclear species, giving equivalent coefficients for each group as Π_j. Specifically, groups of five were taken for $5 \leqq j \leqq 94$, while for higher j twenty-element groups were used. The first five equations, applying to neutrons and species with j ranging from one to four, were included without change as part of the resulting twenty-seven equations, except that the summation in the neutron equation was taken up to $J=4$, since it seems reasonable from the observed relative abundance data to suppose that only a small fraction of the available neutrons were used by the process in producing the quite small amounts of heavier elements. The scheme of grouping to reduce the number of equations does not seriously affect the value of the initial nucleon concentration, C_0, which yields a satisfactory representation of the relative abundance data, nor does it alter the basic appearance

[6] The value 12.8±2.5 min for the half-life of the neutron was reported in an invited paper by Dr. J. M. Robson at the New York Meeting of the American Physical Society, February, 1951, Phys. Rev. 82, 306(T) (1951).

[7] These differ from previously reported values (see reference 2) of temperature and time corresponding to $\tau_0=0.128$ because of the use of a different decay constant in earlier work. When $\tau_0=0.128$ was first chosen, the value of the neutron decay constant was taken to be such as to yield 1 g/cm³ for the radiation density at the start of the process.

of the theoretical abundance curve. The averaged or grouped values of neutron capture cross sections did not differ in essential features from the smoothed-out data on capture cross section *versus* atomic weight previously described[2]; and, therefore, it was expected that the former would again determine, without serious difference, the general relative abundance curve arising from the neutron-capture theory.

III. RESULTS

The grouping of nuclear species described earlier reduced Eqs. (5) to twenty-seven in number. These equations were set up for "single-precision" calculation on the SEAC. With this precision it was possible just to cover the spread in the observed relative abundance data with theoretical solutions.[8] The nature of the solutions obtained of Eqs. (5), plotted as the logarithm of relative abundance *versus* $\log\tau$, is illustrated in Fig. 1. In this case the initial conditions are $\xi_n(\tau_0)=0.88$, $\xi_1(\tau_0)=0.12$, and $\tau_0=0.128$, while the initial nucleon concentration was taken to be $C_0'=1.07\times10^{17}$ cm^{-3}. As is clear from Fig. 1, after a sufficiently long τ the relative abundances of all species other than neutrons decrease as τ^{-1}. This means that the only further changes in abundance are those due to dilution in the continuing universal expansion. The relative abundances for large τ are therefore to be compared with the observed universal abundance data. Since the capture reactions become unimportant by large τ, the few percent of residual neutrons which will eventually decay into protons are then added to the proton concentration.

The nature of the growth curves depends quite strongly on the initial value chosen for C_0. For a C_0 larger than that used with Fig. 1, i.e., larger than $C_0'=1.07\times10^{17}$ cm^{-3}, the relative abundances rise more rapidly and go through a sharper maximum, whereas for a smaller C_0 the growth curve peaks are broadened. If C_0' is the value yielding a good representation of the general trend of the observed abundance data, then for $C_0>C_0'$ one finds too high a relative abundance of the heavier elements, while for $C_0<C_0'$ the only elements present in appreciable relative abundance are the lightest elements. These qualitative remarks, of course, imply the normalization of computed relative abundance values to the observed relative abundance of protons in all cases.

The final relative abundance values for the various solutions examined, i.e., corresponding to different values of C_0, are shown in Fig. 2, where all the solutions are joined to the data at $j=1$. Of the solutions shown, the best representation of the observed data is given by the curve marked C_0', which, as already mentioned,

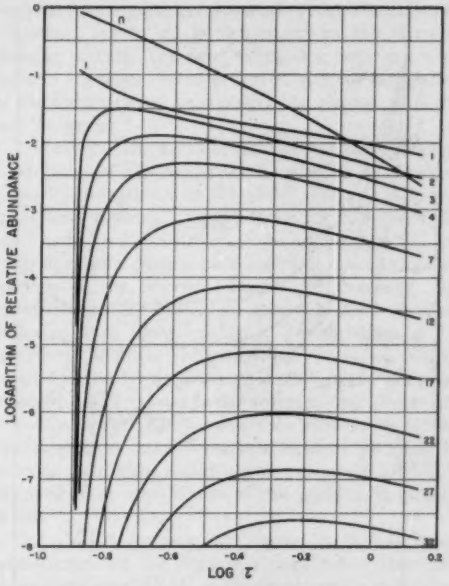

FIG. 1. Relative abundance as a function of time ($\tau=\lambda t$) according to the neutron-capture theory for an expanding universe. This is the case among those examined which best represents the observed data, namely, $C_0'=1.07\times10^{17}$ cm^{-3} at τ_0 (see Fig. 2). The curves are labeled to indicate atomic weight.

corresponds to a nucleon concentration at τ_0 of 1.07×10^{17} cm^{-3}. The solutions[9] shown cover a range 2.13×10^{16} cm$^{-3}\leqq C_0\leqq 2.13\times10^{18}$ cm^{-3}. The case $0.2C_0'$ runs out before reaching higher j values because the single-precision calculation did not permit greater accuracy. The dashed portion of the C_0' curve reflects the fact that for j greater than about 80 or 90, the accuracy of solution became as low as one significant figure. All curves are dashed past $j\cong185$, because by this j the general nature of the solutions permitted linear extrapolation to higher j. The data shown in Fig. 2 are those tabulated by Brown[2] as universal relative abundances, with circles and crosses distinguishing odd and even atomic weights, respectively. For $j<16$, Brown's values of elemental abundance were reduced to isobaric abundances with the aid of the tables of relative isotopic abundances given by Seaborg and Perlman.[10] For $j\geqq16$, isobaric abundances were computed directly from Brown's tables.[11]

The initial nucleon concentration C_0' associated with the solution giving an adequate representation of the observed data in Fig. 2 is five times the C_0 which was

[8] A "double-precision" calculation would have yielded more accuracy for the higher atomic weights when the C_0 chosen was too small (i.e., when the theoretical solution yielded too low abundances of the heavier elements), but it was not deemed desirable because of the very considerable additional labor and machine running time required to accomplish this.

[9] The solution marked $20C_0'$ was a hand-computed solution.

[10] G. T. Seaborg and I. Perlman, Revs. Modern Phys. **20**, 585 (1948).

[11] There are two misprints in Brown's abundance tabulation, Table IV, in reference 3. Sb^{123} should read Sb^{122} and the abundance of Sn^{118} should be 0.149.

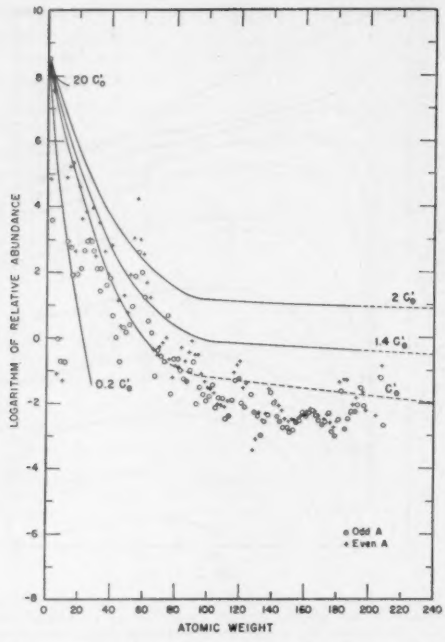

FIG. 2. Comparison of theoretical with observed relative abundances. The data are those of Brown (reference 3), while the curves are calculated according to Eqs. (5) with various values of C_0 to exhibit the effect of varying the initial nucleon concentration.

previously reported as being required in the case of element formation in a static medium.[2] The neutron-capture theory is thus seen to adequately describe the observed relative abundance data when the universal expansion is explicitly taken into account.

The effect of grouping nuclear species in order to reduce the number of Eqs. (5) was found to be small, as already mentioned. This was determined by integrating Eqs. (5) on the SEAC as in the grouped case, but with coefficients P_j corresponding to the first twenty-seven nuclear species individually, rather than with the grouped Π_j covering the entire atomic weight range by means of twenty-seven equations. The cases studied, which had initial nucleon concentrations of 1.4, 6, and 20 times the value C_0' already described as yielding an adequate solution with the grouped equations, indicated that an adequate solution would result with the ungrouped equations, provided the C_0 in the latter case was roughly five times the value in the case of grouping. Hence, a better estimate of the nucleon concentration to be assumed at $\tau=\tau_0$ in order to represent the general trend of the observed relative abundance data is $\sim 5.4\times 10^{17}$ cm^{-3}. This corresponds to a matter density of 8.9×10^{-7} g/cm^3 at $\tau_0=0.128$, or $\rho_0=1.5\times 10^{-3}$ g cm^{-3} sec$^{\frac{1}{2}}$ in Eq. (1).

It may be noted that,[2] in the nonstatic homogeneous isotropic cosmological model used in these calculations, there exists a relationship throughout the expansion between the densities of matter, ρ_m, and of radiation, ρ_r, namely, $\rho_r\rho_m^{-4/3}=$constant. Since $T=1.28\times 10^{9}$°K at τ_0, one obtains $\rho_r(\tau_0)=22.2$ g/cm^3. If one takes the smeared-out density of matter in the universe at the present time to be 10^{-29} g/cm^3 as suggested by Behr,[12] then according to the foregoing relationship, the present residual radiation density (not including that due to stellar radiation) is $\sim 5.5\times 10^{-30}$ g/cm^3 or $T\cong 28$°K.

IV. DISCUSSION

A. The Initial Neutron-Proton Ratio

As already mentioned, the neutron-capture theory in the approximation described does not include the variety of detailed processes and reactions which must have led in turn to the development of detailed features of the observed relative abundance data. In particular, a problem which merits more complete discussion here is the effect on the initial neutron-proton ratio of the physical conditions preceding the element-forming phase in the expansion. The choice of neutron and proton concentrations at $\tau=\tau_0$ influences the value of the initial nucleon concentration, C_0, and, therefore, of the density of matter which is required for the neutron-capture theory to represent the observed relative abundance data.

It will be recalled that the calculations described in this paper were based on initial values $\xi_n(\tau_0)=0.88$, $\xi_1(\tau_0)=0.12$. These are the neutron and proton concentrations which would result from the spontaneous decay of neutrons during the interval $0\leqq\tau\leqq 0.128$ with $\xi_n(0)=1$, and $\xi_1(0)=0$, where $\tau=0.128$ is the process starting time selected for reasons described in Sec. II. Such a formulation is a simplification of the more complex phenomena which may have occurred during the period of high temperature and density preceding the starting time selected for the element-forming process.

Hayashi[13] has recently examined in detail the many physical processes, including spontaneous neutron decay, which might have occurred during this period, the main purpose being to determine the effect of such processes on the neutron-proton ratio to be chosen as an initial condition for forming elements. Since the ratio obtained by Hayashi is quite different from that resulting from spontaneous neutron decay alone, it is desirable to discuss briefly his analysis and its effect on the neutron-capture theory.

Hayashi employed the cosmological model described in Sec. II, namely, an expanding universe of radiation with a trace of matter, in which the temperature and density of matter vary with time according to Eqs. (1) and (2). His analysis was restricted to the period of

[12] A. Behr, Astron. Nachr. **279**, 97 (1951).
[13] C. Hayashi, Prog. Theor. Phys. **5**, 224 (1950).

time after the temperature of the universe had decreased to a value less than that equivalent to the rest mass of the meson, viz., $\sim 10^{12}$°K. This temperature corresponds to a time of $\sim 2\times 10^{-4}$ sec after the "beginning" of the universal expansion.

The following reactions among protons, p, neutrons, n, electrons, e^-, positrons, e^+, neutrinos, ν, antineutrinos, ν^*, and radiation, $h\nu$, were considered:

$$\begin{aligned} n+e^+ &\rightleftharpoons p+\nu^*, \\ n+\nu &\rightleftharpoons p+e^-, \\ n &\rightleftharpoons p+e^-+\nu^*, \end{aligned} \tag{6}$$

and

$$e^+ + e^- \rightleftharpoons h\nu.$$

The reaction rates for the processes described by Eqs. (6) were examined and, with the exception of β-processes, found to be sufficiently high to maintain certain of the concentrations at equilibrium values, even though the universal temperature decreases rather rapidly during this period.

The electron, positron, and photon concentrations were determined purely on classical statistical considerations, since the number of electrons and positrons involved in the lagging β-possesses is small compared with the number involved in the pair production—annihilation processes. Nonlinear rate equations were written to describe the β-processes, with the rate coefficients being evaluated from the Fermi theory of β-decay. There are no problems of degeneracy at the temperatures and densities considered. The rate equations were integrated numerically by Hayashi subject to the initial condition that, at $T \cong 10^{12}$°K, all particles and photons were present in equilibrium concentrations. Consequently, the initial neutron-proton ratio for the period considered by Hayashi was taken as unity. The solutions show that during the first five seconds the induced β-decay of the neutron is more important than spontaneous β-decay. Starting at unity, the neutron-proton ratio decreases to $\sim\frac{1}{3}$ by one second, to $\sim\frac{1}{4}$ by ten seconds, and is controlled by the relatively slow process of spontaneous neutron decay thereafter.[14]

Hayashi suggests that if nuclei beyond He^4 are ignored and if β-processes for the light nuclei may be neglected, then He^4 is effectively formed as $2n+2p \rightarrow He^4$, regardless of the formation route. If one neglects neutron decay and takes a starting neutron-proton ratio of 1/4 for the element-forming period, the final helium-hydrogen abundance ratio according to these ideas would be 1/6. This result is compatible with observed values. However, such an approach would appear to be an oversimplification because at low matter densities β-processes cannot be ignored in considering the details of the light element reactions and because the competition of neutron decay and universal expansion appear to be important in the element-forming process. The exact effect of a neutron-proton ratio of 1/4 should be investigated by a re-examination of the light element reactions in the manner of Fermi and Turkevich.[2]

The effect of Hayashi's neutron-proton ratio of 1/4 on the solution of Eqs. (5) has been examined by means of numerical integration on the SEAC. For this ratio two cases were studied, namely, those for $C_0 = 2.13\times 10^{16}$ cm^{-3} and $C_0 = 2.13\times 10^{18}$ cm^{-3}. In neither case did the neutron-capture process yield sufficient relative concentrations of the heavier elements. Furthermore, the growth curves for individual species in the two cases indicated that lower or higher initial values of C_0 would not improve the situation.[15] It is, of course, possible that intermediate values of C_0 might bring the theoretical curve closer to the observed data. However, it would appear to be necessary to increase the initial neutron-proton ratio to perhaps as much as unity in order to yield a fit. Unfortunately, it was not feasible to continue an examination of this problem in greater detail.

Since the neutron-capture theory is in fact quite approximate for the lightest elements and since the above mentioned SEAC calculations are not definitive, the question as to whether or not a low initial neutron-proton ratio is compatible with a satisfactory fit to the observed abundances still requires study of the light element reactions in detail.

[14] The neutron half-life used in Hayashi's calculations was 30 minutes, which is quite different from Robson's latest value of 12.8 minutes (see footnote 6). Since the neutron half-life is involved in almost all of the rate constants for Eqs. (6), a determination of the effect of changing the neutron half-life on the neutron proton ratio would appear to require a new integration.

[15] In the low density case, the neutron-capture reaction rates are so low that effectively all of the neutrons decay into protons before they can be captured, and the heavier nuclei are formed in extremely low relative abundances. In the high density case neutron-capture reaction rates are so high that spontaneous neutron decay and the effect of the universal expansion can be neglected. The result of this situation is that the few neutrons present to start with are quickly used up in forming the very lightest species, and again the heavier elements are formed in very small relative amounts. It may be of interest to note that in this case where the neutron-proton ratio is low and C_0 is very high, one may obtain an approximate analytical solution of Eqs. (5). Under these conditions the expansion terms $-3\xi_j/(2\tau)$ and the decay terms ξ_n may be ignored. In addition, one takes $P_{j-1}\xi_n\xi_{j-1} \gg P_j\xi_n\xi_j$ in the jth equation. Then the approximate solutions describing the growth curves may be written as follows:

$$\xi_n = q_0\{r_0 \exp[q_0P_1(\tau-\tau_0)]-1\}^{-1},$$
$$\xi_1 = r_0\xi_n \exp[q_0P_1(\tau-\tau_0)],$$

and

$$\xi_j = \frac{q_0(r_0P_1)^{1-j}j^{-1}}{(j-1)!}\prod_{m=1}^{j-1}P_m\sum_{s=0}^{j-1}(-1)^s\binom{j-1}{s}\exp[-sq_0P_1(\tau-\tau_0)], \quad j>1,$$

where

$$q_0 = \xi_1(\tau_0)-\xi_n(\tau_0)$$

and

$$r_0 = \xi_1(\tau_0)/\xi_n(\tau_0).$$

In the limit of long τ, the foregoing equations reduce to the final relative abundances in this approximation, viz.,

$$(\xi_1)_{max} = q_0,\ (\xi_n)_{max} = 0, \text{ and } (\xi_j)_{max} = [q_0(r_0P_1)^{1-j}/(j-1)!]\prod_{m=1}^{j-1}P_m.$$

Calculations for the case $C_0 = 2.13\times 10^{18}$ cm^{-3}, with the Hayashi initial neutron-proton ratio of 1/4, check very well with solutions of the full Eqs. (5) as determined on the SEAC. The expression given for $(\xi_j)_{max}$ is also derived in the Appendix by a different procedure.

B. Gaps at Atomic Weights 5 and 8

Hayashi has pointed out that a high proton concentration might be expected to aid materially in carrying the chain of element-forming processes across the missing nuclei at atomic weights 5 and 8.[2] In this connection, Turkevich[16] has recently suggested a re-examination of the light element reactions taking into account the high energy nonthermalized reaction products. In their previous calculations Fermi and Turkevich[2] considered all particles to have energies corresponding to the universal temperature. Because of the rapid increase with increasing energy in reaction probabilities for charged particles, the higher energy particles may be expected to provide a means of increasing the flux of nuclei crossing the gaps[17] at $A=5$ and 8.

C. Remarks Concerning Equilibrium Theories

The work described in this paper demonstrates that the general trend with atomic weight of the observed relative abundances of the elements can be represented satisfactorily by the neutron-capture theory in an expanding universe. In view of the low matter density required and the rapidity of the decrease of temperature and density with the expansion of the universe, the implication of this result in connection with equilibrium theories of element formation should again be pointed out. In these theories[18] nuclear species formed in statistical equilibrium in stellar interiors and are supposed to be distributed in space by subsequent stellar explosions. All of these stellar models contain high neutron concentrations and have high densities, $\rho \cong 10^8$ g/cm^3, and high temperatures, $T \cong 1$ Mev. Under these conditions (densities $\sim 10^{15}$ times greater than those required in the non-equilibrium theory) one would expect during an explosion a very considerable modification of the original equilibrium distribution of the elements by neutron capture and other reactions. In order to obtain the presently observed relative abundances as the end result of such a stellar explosion, it would appear necessary to carry out a non-equilibrium calculation of the type described in this paper but with the following differences. The dynamics of the explosion, and the density and temperature variation with time, as well as an initial distribution of relative abundances, would have to be known. This difficult problem amounts to finding what initial abundance distribution must be taken in order that it be modified to the observed universal distribution during the explosion.

D. Analytic Solution of the Equations of the Neutron-Capture Theory

The question has frequently been raised as to whether or not Eqs. (5) could be solved analytically. It had been suggested[2] that this could not be the case because the equations are nonlinear and because the neutron and proton rate equations contain terms of different orders. Recently, Dr. T. H. Berlin, of The Johns Hopkins University, has examined this problem and found that solutions could be obtained in closed form only if the expansion of the universe is ignored. A discussion of this solution is given in the Appendix.

We should like to express our appreciation to the National Bureau of Standards for its kindness in extending to us the use of the SEAC, and to Dr. Joseph H. Levin for his complete cooperation in coding and running the SEAC solutions. The computational assistance of Miss K. E. Pace is acknowledged with thanks. Finally, we should like to thank Dr. T. H. Berlin for his continued interest in this work.

APPENDIX

The Neutron-Capture Equations of Element Formation in a Static Universe: An Exact Solution

T. H. BERLIN
Department of Physics, The Johns Hopkins University, Baltimore, Maryland

THE equations describing element formation by successive neutron captures in a static universe are the set:[2]

$$\begin{aligned} d\xi_n/d\tau &= -\xi_n - \sum_{j=1}^{J} P_j \xi_n \xi_j, \\ d\xi_1/d\tau &= \xi_n - P_1 \xi_n \xi_1, \\ d\xi_j/d\tau &= P_{j-1}\xi_n\xi_{j-1} - P_j \xi_n \xi_j, \quad 2 \leqq j \leqq J. \end{aligned} \tag{A1}$$

These equations are to be solved under the initial conditions:

$$\xi_j(\tau_0)=0, \quad 2 \leqq j \leqq J; \quad \xi_1(\tau_0)=\alpha; \quad \xi_n(\tau_0)=\beta,$$

where $\tau_0=0$ is obviously suitable for the static case.

Equations (A1) are linearized by changing the independent variable from τ to z so that

$$dz/d\tau = \xi_n. \tag{A2}$$

The equations become

$$\begin{aligned} dz/d\xi_n &= -1 - \sum_{j=1}^{J} P_j \xi_j \equiv -F(z), \\ d\xi_1/dz &= 1 - P_1 \xi_1, \\ d\xi_j/dz &= P_{j-1}\xi_{j-1} - P_j \xi_j, \quad 2 \leqq j \leqq J. \end{aligned} \tag{A3}$$

[16] Private communication.

[17] Turkevich (private communication) has also suggested using the higher energy neutrons formed as reaction products among the light nuclei in $(n,2n)$ reactions with heavier nuclei to form shielded isobars.

[18] See Sec. III of reference 2 for a discussion and bibliography.

Equations (A3) are conveniently solved by the use of the laplace transform.[19] Setting

$$f_j(\kappa)=\int_0^\infty e^{-\kappa z}\xi_j(z)dz, \tag{A4}$$

and using the initial conditions, we have from Eq. (A3)

$$\begin{aligned} f_1(\kappa)&=(\kappa^{-1}+\alpha)/(\kappa+P_1),\\ f_j(\kappa)&=[P_{j-1}/(\kappa+P_j)]f_{j-1}(\kappa), \quad 2\leqq j\leqq J. \end{aligned} \tag{A5}$$

Then,

$$f_j(\kappa)=P_j^{-1}(\kappa^{-1}+\alpha)\prod_{k=1}^{j}P_k(\kappa+P_k)^{-1}, \quad 1\leqq j\leqq J. \tag{A6}$$

Inverting Eq. (A4), we have

$$\xi_j(z)=(1/2\pi i)\int_{\kappa_0-i\infty}^{\kappa_0+i\infty}e^{\kappa z}f_j(\kappa)d\kappa, \tag{A7}$$

where the line $\kappa=\kappa_0$ is to the right of the singularities of $f_j(\kappa)$.

If it is assumed that the P_k are all different and not equal to α^{-1}, $f_j(\kappa)$ has simple poles at $\kappa=0, -P_1, -P_2, \cdots, -P_j$. Therefore, we have

$$\xi_j(z)=P_j^{-1}+\sum_{r=1}^{j}A_{jr}e^{-P_r z}, \tag{A8}$$

where

$$A_{jr}=\lim_{\kappa\to -P_r}(\kappa+P_r)f_j(\kappa).$$

On taking the limit, we obtain

$$A_{jr}=-P_r^{-1}(1-\alpha P_r)R_{jr}, \tag{A9}$$

where

$$R_{jr}=\prod_{\substack{k=1\\k\neq r}}^{j}P_k(-P_r+P_k)^{-1}; \quad R_{11}=1.$$

We now see that $F(z)$ is a known function of z. Hence, we have

$$\xi_n(z_0)-\xi_n(0)=-\int_0^{z_0}F(z)dz. \tag{A10}$$

This implies that $\tau(z)$ may be found from

$$\tau=\int_0^z ds/\xi_n(s). \tag{A11}$$

One is usually not interested in the ξ_j at a particular time but in the limiting value of ξ_j, that is, at $\tau=\infty$. This means that there is no necessity to use Eq. (A11).

From Eq. (A2), we see that $(dz/d\tau)_{\tau\to\infty}=0$, since all the neutrons are eventually captured or decay into protons, so that ξ_n approaches 0. Since $\xi_n\geqq 0$, z is a monotonically increasing function of τ and approaches a limiting value $z(\tau=\infty)=z_0$. Then $\xi_n(z_0)=0$, and from Eq. (A10) we have, because $\xi_n(0)=\beta$,

$$\beta=\int_0^{z_0}F(z)dz \tag{A12}$$

as the determining equation for z_0, which will have a unique solution for given α, β. The limiting values of the ξ_j are $\xi_j(z_0)$ obtained from Eq. (A8).

We may remark briefly on some aspects of the above solution of the problem. Let P_m, say, be zero. We then see from Eq. (A5) that $f_j(\kappa)=0$ for $j\geqq m+1$, so that $\xi_j=0$ for $j\geqq m+1$. In other words, if a species has zero (i.e., very small) capture cross section, then all heavier species will have effectively zero abundance. However, the formation chain would be expected to continue through isobars of more normal cross section.[2]

To facilitate numerical work with the approximations to the Eq. (A1), Alpher and Herman assumed that P was constant for those elements with $j\geqq 100$. This is an inconvenient assumption for the solution given. If some P's are alike, we see from Eq. (A6) that $f_j(\kappa)$ will have multiple poles. The exact inversion can easily be performed to give ξ_j but high order derivatives of $f_{100}(\kappa)$ will be involved. The resulting expression for ξ_j would be quite inconvenient for numerical work; and it would be very much simpler to assume that, instead of being constant, P_0 is a slowly increasing function of j for $j>100$ in order to maintain all P_j different. It appears from the cross-section data that this is as reasonable an assumption as taking the P_j the same.

The exact solution would be of increased interest if the dependence of the ξ_j on the initial conditions α, β and on density could be put into simple form. Since the P_j are all proportional to density, we note that R_{jr} [Eq. (A9)] is independent of density and may be computed, given the effective neutron capture cross section only.

If we set $z=y/n_0$, then from Eq. (A8), we have

$$P_j\xi_j=1-\sum_{r=1}^{j}R_{jr}\exp\left(\frac{-P_r y}{n_0}\right)+n_0\alpha\sum_{r=1}^{j}\left(\frac{P_r}{n_0}\right)R_{jr}\exp\left(\frac{-P_r y}{n_0}\right). \tag{A13}$$

The two sums over r are now density independent functions of y.

From the definition of $F(z)$, Eq. (A3), we find that Eq. (A12) may be written in the form

$$n_n(0)-n_1(0)G(y_0)=(J+1)y_0-H(y_0), \tag{A14}$$

where

$$\xi_j=n_j/n_0; \quad z_0=y_0/n_0;$$

$$G(y)=\sum_{j=1}^{J}\sum_{r=1}^{j}R_{jr}\left[1-\exp\left(\frac{-P_r y}{n_0}\right)\right];$$

$$H(y)=\sum_{j=1}^{J}\sum_{r=1}^{j}\left(\frac{n_0}{P_r}\right)R_{jr}\left[1-\exp\left(\frac{-P_r y}{n_0}\right)\right];$$

[19] H. Bateman, Proc. Camb. Phil. Soc. 15, 423 (1910). Bateman has solved an almost identical set of equations. The principal differences are in the equations for ξ_n and ξ_1.

and $G(y)$, $H(y)$ are density independent functions that can be computed given the capture cross sections.

In Eq. (A14) we see that the initial neutron and proton densities are very simply exhibited.

We can readily evaluate ξ_j in the two limiting cases $n_n(0)$ very much greater and very much less than $n_1(0)$.

Case: $n_n(0) \ll n_1(0)$*:*

From the definitions of G and H,

$$G(\infty)=\sum_{j=1}^{J}\sum_{r=1}^{j}R_{jr} \quad \text{and} \quad H(\infty)=\sum_{j=1}^{J}\sum_{r=1}^{j}\left(\frac{n_0}{P_r}\right)R_{jr}.$$

Therefore, as $n_n(0)$ becomes very large, we must have

$$y_0 \cong n_n(0)/(J+1).$$

From Eq. (A13), we have $P_j\xi_j \cong 1$, so that $n_j \cong n_0/P_j$, which is finite. Thus, with increasing initial neutron density, the abundance distribution approaches the stationary distribution for which $d\xi_j/d\tau=0$.

Case: $n_n(0) \ll n_1(0)$*:*

In this case we can expect that the solution, y_0/n_0, of Eq. (A14) is small. Dealing with the leading terms only, then, we have

$$\begin{aligned} G(y) &\cong \sum_{j=1}^{J}\sum_{r=1}^{j}R_{jr}\left(\frac{P_r y}{n_0}\right)=\left(\frac{P_1}{n_0}\right)y, \\ H(y) &\cong \sum_{j=1}^{J}\sum_{r=1}^{j}R_{jr}\left(y-\frac{P_r y^2}{2n_0}\right)=Jy. \end{aligned} \tag{A15}$$

These results are obtained by noting that

$$\sum_{j=1}^{J}P_j\xi_j(0)=P_1\alpha,$$

since only $\xi_1(0)\neq 0$, and by using Eq. (A13). Thus, Eq. (A14) becomes

$$n_n(0)-n_1(0)(P_1/n_0)y_0 \cong y_0,$$

so that

$$\begin{aligned} y_0/n_0 &\cong [n_n(0)/n_0]/[n_1(0)(P_1/n_0)+1] \\ &\cong [n_n(0)/n_1(0)]P_1^{-1}, \end{aligned} \tag{A16}$$

which is a small number for high density.

Now we must consider $\xi_j(z_0)$ for z_0 small, since $z_0=y_0/n_0$. This is conveniently done through Eqs. (A6) and (A7). We shall use

$$\xi_j(z_0)=\sum_{p=0}^{\infty}\left[\frac{d^p\xi_j(z)}{dz^p}\right]_{z=0}\left(\frac{z_0^p}{p!}\right). \tag{A17}$$

However, we have

$$[d^p\xi_j/dz^p]_{z=0}=(1/2\pi i)\int_{\kappa_0-i\infty}^{\kappa_0+i\infty}\kappa^p f_j(\kappa)d\kappa. \tag{A18}$$

From Eq. (A6) we see that as $\kappa\to\infty$, $f_j(\kappa)\to 1/\kappa^j$. Thus, for $p<j-1$, the integrand vanishes at infinity in the right half-plane faster than $1/\kappa$. Consequently, we have

$$[d^p\xi_j/dz^p]_{z=0}=0 \quad \text{for} \quad p<j-1. \tag{A19}$$

The first nonvanishing derivative of ξ_j at $z=0$ occurs for $p=j-1$. Transforming to the complex variable $\kappa=1/s$, we have

$$\begin{aligned} [d^{j-1}\xi_j/dz^{j-1}]_{z=0} &= (1/2\pi i)\int_{\kappa_0-i\infty}^{\kappa_0+i\infty}\kappa^{j-1}f_j(\kappa)d\kappa \\ &= (1/2\pi i)\int^{(0+)}s^{-j-1}f_j(1/s)ds, \end{aligned} \tag{A20}$$

and

$$\left[\frac{d^{j-1}\xi_j}{dz^{j-1}}\right]_{z=0}=\alpha\prod_{k=1}^{j-1}P_k.$$

Finally, the leading term, $p=j-1$, for $\xi_j=n_j/n_0$ is

$$n_j=\left[\frac{n_1(0)}{(j-1)!}\right]\left[\prod_{k=1}^{j-1}\left(\frac{P_k}{n_0}\right)\right]\left\{\left[\frac{n_n(0)}{n_1(0)}\right]\left(\frac{n_0}{P_1}\right)\right\}^{j-1}. \tag{A21}$$

The author wishes to thank Dr. Herman and Dr. Alpher for their many pertinent suggestions and clarifying discussions.

Total Cross Sections of Light Nuclei for p,T-Neutrons*

C. K. Bockelman,† D. W. Miller,† R. K. Adair, and H. H. Barschall
University of Wisconsin, Madison, Wisconsin

(Received June 11, 1951)

The total cross sections of Li, Be, B^{10}, B, C, and O were measured for neutrons of energies between 1 and 3.3 Mev. Neutrons of about 20-kev energy spread were produced by bombarding a thin layer of Zr in which tritium had been absorbed with protons from the electrostatic generator. Resonances were observed in all nuclei except Li. In addition to well-defined levels, evidence was found for slow variations of the cross sections with energy which might be explained by the presence of very wide levels in all these elements.

I. INTRODUCTION

An examination of the recent compilation of the energy levels of nuclei[1] shows that even for the lightest nuclei there are still large gaps in the knowledge of the position and character of their energy levels. In previous experiments carried out at this laboratory, the total cross sections of light nuclei had been measured for neutrons from the Li(p,n) reaction up to energies of 1.4 Mev. The availability of tritium has made it possible to extend these measurements to higher energies because the threshold of the T(p,n) reaction is about 1 Mev lower than that of the Li(p,n) reaction. An additional advantage of the T(p,n)He^3 reaction is the absence of excited states of He^3, while the excited state of Be^7 at 430 kev results in the presence of a second group of neutrons from the $Li^7(p,n)Be^7$ reaction at neutron energies above 650 kev.

II. EXPERIMENTAL PROCEDURE

According to the procedure described by Lillie and Connor,[2] thin tritium targets were prepared by evaporating a thin layer of zirconium metal onto a disk of wolfram 10 mils thick. The disk was then transferred to a tritium handling system, where it was heated inductively to a temperature of about 900°C in tritium gas at a pressure of 2 cm Hg. Targets prepared in this manner contained about one atom of tritium per atom of Zr.

The wolfram disk formed the end of the vacuum system of the electrostatic generator and was sealed to the system by means of an O-ring. As previously described,[3] heated air was blown against the target to reduce oil deposition, and the proton beam from the electrostatic generator was swept in a small circle on the target to prevent local heating. With these precautions thin Zr-T targets showed no measurable loss of tritium after bombardment by 1 μa of protons for several hundred hours.

The effective target thickness was measured by the rise method.[4] The target used for most of the present measurements caused an energy loss of 35 kev for 1-Mev protons. Because of the decrease of stopping power with increasing proton energy, the neutron energy spread resulting from the thickness of this target was only about 20 kev for most of the experiments.

Neutrons were detected by observing proton recoils in a cylindrical ionization chamber. This chamber had an active volume 9.5 cm long and 2.5 cm in diameter and was filled with hydrogen to a pressure of 30 atmos. After the hydrogen had been purified by being circulated over magnesium turnings at a temperature of 200°C, the counter gave a good signal-to-noise ratio with a collecting voltage of 2500.

The center of the counter was placed at a distance of 36 cm from the tritium target, and the axis of the counter was aligned with the proton beam from the electrostatic generator. Total cross sections were measured by observing the transmission through cylindrical samples, 4.45 cm in diameter, placed halfway between the target and the center of the detector. Since in this geometry the cross section for scattering through angles larger than 14° is observed, 1.5 percent of the neutrons would be scattered into the detector if the scattering were isotropic. A correction of 1.5 percent for scattering into the detector was applied to all the measured scattering cross sections, although this correction may be in error if there is an appreciable deviation from isotropic scattering. Samples of solid metal were used for the measurements on Li and Be, and graphite for the investigation of C. Samples of B and B^{10} consisted of metal powder. The cross section of O was obtained from a comparison of the transmission through a sample of BeO powder with that of Be metal.

The background of neutrons which did not come directly from the target was determined by interposing a paraffin shadow cone, 10 in. long, between the target and the detector. Measured backgrounds amounted to about two percent of the intensity observed in the absence of the shadow cone. In view of the fact that at least some of the background counts were due to neutrons transmitted through the shadow cone, no background correction was applied to the data.

In the geometry used in the present experiment, the

* Work supported by the AEC and the Wisconsin Alumni Research Foundation.

† AEC Predoctoral Fellow.

[1] Hornyak, Lauritsen, Morrison, and Fowler, Revs. Modern Phys. **22**, 291 (1950).

[2] A. Lillie and J. Connor, Rev. Sci. Instr. **22**, 210 (1951).

[3] Peterson, Barschall, and Bockelman, Phys. Rev. **79**, 593 (1950).

[4] R. F. Taschek and A. Hemmendinger, Phys. Rev. **74**, 373 (1948).

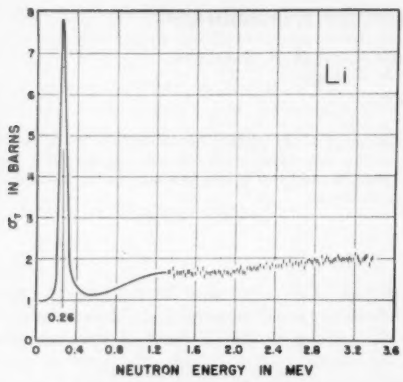

FIG. 1. Total cross section of Li. The solid curve reproduces the results published in reference 5. The lengths of the vertical lines represent the standard statistical errors of the present measurements.

spread in energy of the neutrons which is caused by the variation of neutron energy with the direction of emission of the neutrons with respect to the incident protons amounts to only about 1 kev. This energy spread may, therefore, be neglected, compared with that resulting from the target thickness.

III. RESULTS

(A) Lithium

Figure 1 shows the total cross section of lithium as a function of neutron energy. The solid curve reproduces data previously published,[5] while the points above 1.3 Mev represent the present measurements. The lengths of the vertical lines show the standard statistical errors.

In the earlier report[5] the peak at 0.26 Mev was attributed to the interaction of p-neutrons with Li^7 to form a compound state of spin 2, while the rise of the cross section above 0.8 Mev was explained as resulting from the interaction of s-neutrons with Li^7 to form a state of spin 2 at a neutron energy of about 1.15 Mev. Some doubt is thrown upon this latter interpretation by the fact that the cross section continues to rise at higher neutron energies. The observed value of 2 barns for the cross section at 3 Mev is much higher than the theoretical maximum for an s-resonance at this energy. In view of the rather large negative coherent scattering length[6] of Li^7, it seems possible that resonances occur for both spin states which can be formed by s-neutrons. On the other hand, even if both resonances occurred at the same energy, the observed cross section is still larger than the theoretical maximum. It is, therefore, necessary to assume that neutrons of higher angular momentum contribute to the rise. It does not appear possible that a single level of the compound nucleus formed by such neutrons could be several Mev wide. One is led to the conclusion, therefore, that the slow rise of the cross section of lithium at high energy must be due to the superposition of several broad resonances.

(B) Beryllium

In Fig. 2 the total cross section of beryllium is plotted as a function of neutron energy. The data at energies below 1.4 Mev are taken from a previous publication,[7] except that a small correction has been applied for the presence of the second group of neutrons from the Li(p,n) reaction. A peak in the cross section of beryllium at 2.7 Mev has been observed by Allen *et al.*[8] and by Stafford,[9] but the absolute value of the cross section found by these authors is less than the results shown in Fig. 2. The shape of the peak at 2.73 Mev indicates that it is due to the effect of more than one energy level. It may result from the superposition of a peak about 0.1 Mev wide at 2.73 Mev and a much broader peak with a maximum at about 2.85 Mev. Other very broad levels may be responsible for the rise of the cross section towards low energies extending from 2 Mev, where the cross section is 1.6 barns, to the epithermal region, where the cross section of beryllium is 6 barns.[10] Such broad levels might help to explain the large coherent scattering length at thermal energies.[6]

It appears very difficult to account for the magnitude of the peak at 2.8 Mev in terms of resonance theory by assuming that it is produced by a sharp level superimposed on a single broad level. The broad peak would have to have a maximum of about 3.4 barns, which is 1.8 barns higher than the cross section at 2 Mev. A resonance cross section of 1.8 barns at 2.8 Mev must be produced by neutrons of more than 3 units of orbital angular momentum. On the other hand, g-neutrons could not produce as wide a level as the experimental results indicate.

(C) Boron 10

For the interpretation of recent determinations[11] of the disintegration cross section of B^{10}, it appeared desirable to know also the total neutron cross section of this nucleus. Therefore, a sample enriched in B^{10} was procured from the Atomic Energy Commission. Data below 0.9 Mev were taken with a BF_3 counter, and a Li target of such thickness that the neutron energy spread was about 20 kev. For measurements at higher energies the tritium target and recoil counter were employed. The cross sections, shown in Fig. 3, are about 15 percent greater than those found at Los

[5] R. K. Adair, Phys. Rev. **79**, 1018 (1950).
[6] C. Shull and E. Wollan, Phys. Rev. **81**, 527 (1951).
[7] C. K. Bockelman, Phys. Rev. **80**, 1011 (1950).
[8] Allen, Burcham, and Wilkinson, Proc. Roy. Soc. (London) **A192**, 114 (1947).
[9] G. H. Stafford, Proc. Phys. Soc. (London) **A64**, 388 (1951).
[10] C. T. Hibdon and C. O. Muehlhause, Phys. Rev. **76**, 100 (1949).
[11] Petree, Johnson, and Miller, Phys. Rev., to be published.

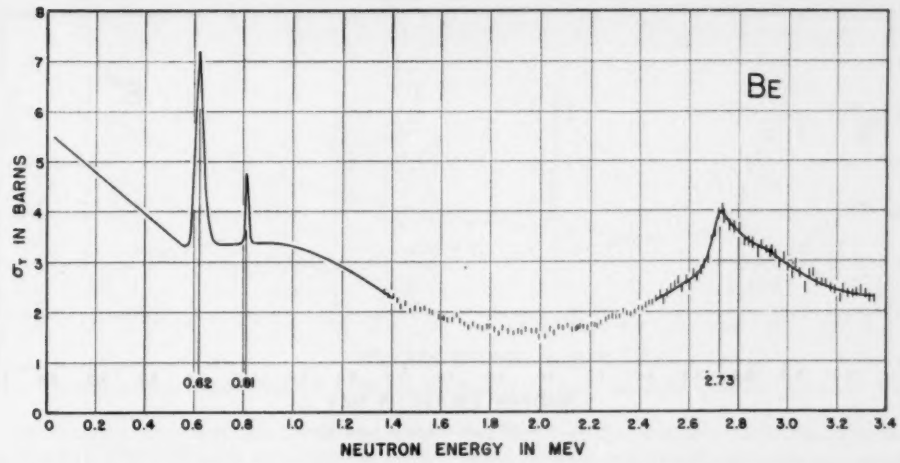

FIG. 2. Total cross sections of beryllium. The solid curve below 1.4 Mev represents data published in reference 7, corrected for the effects of the low energy Li(p,n) group. The lengths of the vertical lines represent the standard statistical errors of the present measurements.

Alamos.[12] This difference may be caused in part by an error in the determination of the isotopic composition of the samples.

Two broad maxima are shown in the present measurements, reaching their peak values at 1.8 and 2.8 Mev. There is possibly a third maximum at 0.2 Mev, but this is uncertain because the observed variation in cross section is comparable to the statistical errors.

There are known to be at least four levels in B^{11} with excitation energies between 8.5 and 9.5 Mev.[13] Since the binding energy of a neutron to B^{11} is about 11 Mev, it seems surprising that so few resonances are found in the present experiment. However, since B^{10} has a large spin, only compound states with rather large total angular momentum would be detected in the present work. Competition from the n,α reaction also tends to reduce the variations expected. Because of these circumstances, some resonances may have been missed.

The interpretation of the variation observed near 1.8 Mev is discussed in reference 11. Since the absorption measurements do not extend through the range of the 2.8-Mev maximum, no analysis of this resonance is attempted.

(D) Boron

Previous measurements on boron[7] are shown below 0.9 Mev by the solid curve in Fig. 4. The data are corrected for the presence of the second energy group from the Li(p,n) reaction. Since this correction is rather large and uncertain around 1 Mev because of the second appearance of the 0.43-Mev peak, this region was remeasured using T(p,n) neutrons. Measurements at higher neutron energies show four additional maxima at 1.28, 1.78, 2.45, and 2.58 Mev. A comparison of these results with the observations on B^{10} (Fig. 3) shows that these resonances are caused by levels in B^{12}. Their heights can be fitted best by assuming for the spins of the compound states the following values: 3 for the 1.28-Mev peak, 1 for the 1.78-Mev maximum, 2 for the 2.45-Mev peak, and 3 for the maximum at 2.58 Mev. The observed shapes exclude the possibility that any of these peaks are formed by s-neutrons, and their widths make their formation by neutrons of more than two units of orbital angular momentum unlikely. It is concluded, therefore, that all the observed resonances are caused by p- or d-neutrons. The rise of the cross section at low energies, similar to that found in Be, might be explained in terms of a broad level which can be reached by s-neutrons.

The values of the cross section of boron agree well with those reported from the Los Alamos Laboratory,[12] but not with recent measurements carried out at Massachusetts Institute of Technology,[14] although the Massachusetts Institute of Technology group found maxima in the cross section of boron at 1.245 Mev and 1.771 Mev in agreement with the present results.

(E) Carbon

Figure 5 shows the total cross section of carbon as a function of neutron energy. Below 1.2 Mev the solid line gives the best fit for the data previously obtained at this laboratory[15] and for those of the Minnesota

[13] Barschall, Battat, and Bright, Phys. Rev. **70**, 458 (1946).
[12] Van Patter, Buechner, and Sperduto, Phys. Rev. **82**, 248 (1951).
[14] Willard, Preston, and Goodman, M. I. T. Tech. Report 45 (1950), unpublished.
[15] D. W. Miller, Phys. Rev. **78**, 806 (1950).

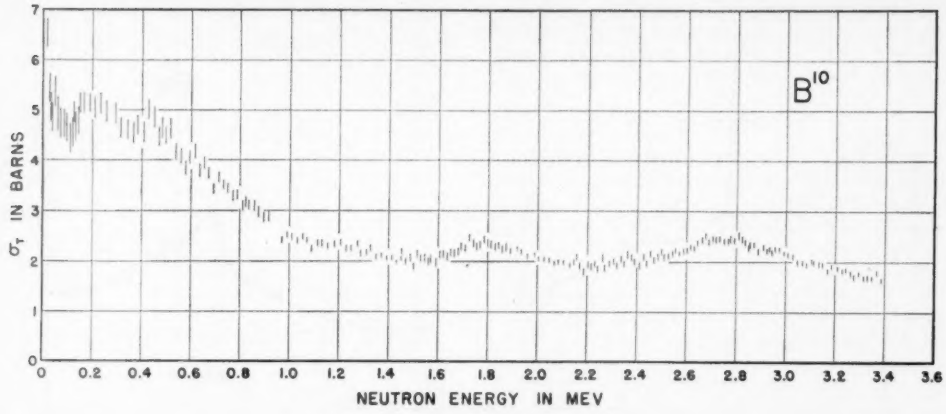

FIG. 3. Total cross section of boron 10.

group.[16] The latter results extend to a neutron energy of 1.8 Mev and are in excellent agreement with the present measurements.

Thomas[17] has pointed out that the variation of the cross section observed below 2 Mev may be interpreted in terms of the interaction of *s*-neutrons to form a broad level in C^{12}. Since preliminary runs with the tritium target indicated the presence of a sharp peak at 2.08 Mev, an attempt to determine the shape of this resonance was made by using neutrons from a Li target of such thickness that the effective energy spread was about 10 kev. The measured width of the resonance was approximately equal to this energy spread, a fact which indicates that the peak was not fully resolved. Its measured height above the background of potential scattering is 2.7 barns. This variation in cross section is about twice the theoretical maximum for a compound state of spin $\frac{1}{2}$. Consequently, the level of the compound nucleus which produces this peak must have a spin of at least $\frac{3}{2}$ and must be produced by neutrons of orbital angular momentum of 1 or higher.

The structure around 3 Mev has a shape which shows the effect of strong interference of the scattering produced by a resonance near 3-Mev neutron energy with potential scattering or with the scattering caused by another resonance. Only the phase shift associated with the potential scattering of *s*-neutrons is sufficiently large to produce the observed shape. On the other hand, the variation in the cross section near the peak is twice the theoretical maximum for *s*-neutrons of this energy,

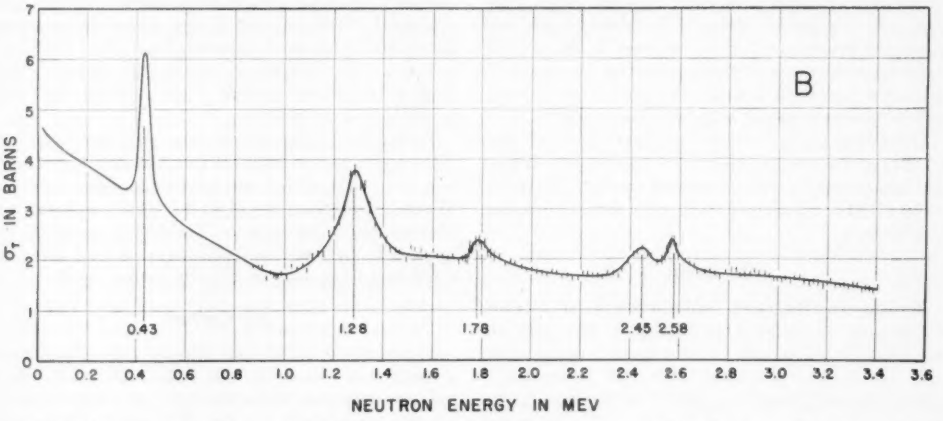

FIG. 4. Total cross section of normal boron. The solid line below 0.9 Mev is obtained from the data reported in reference 7.

[16] Freier, Fulk, Lampi, and Williams, Phys. Rev. **78**, 508 (1950).
[17] R. G. Thomas, Phys. Rev. **81**, 148 (1951).

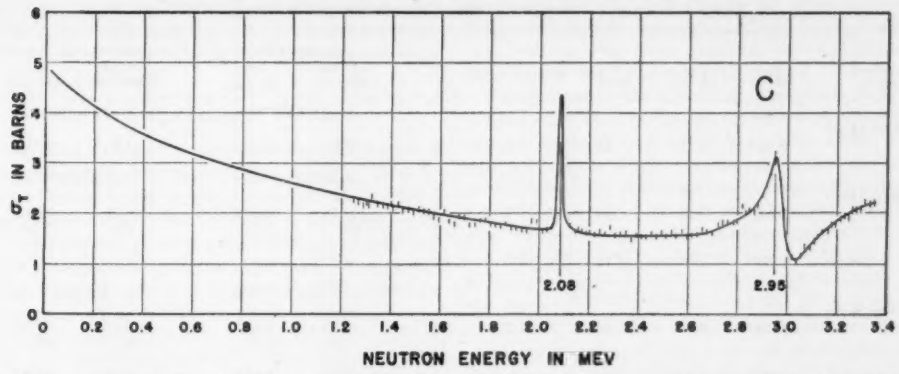

FIG. 5. Total cross section of carbon. The results published in references 15 and 16 are represented by the solid line below 1.2 Mev.

and approximately what is expected for a compound state of spin $\frac{3}{2}$. The most likely explanation is, therefore, that the structure is caused by the interference of two adjacent levels of spin $\frac{3}{2}$, formed by neutrons of the same orbital angular momentum. The second level should lie above the energy range explored in this experiment and may be responsible for the maximum observed by the Minnesota group at 3.5 Mev and by Ricamo *et al.* at 3.7 Mev.[17a]

(F) Oxygen

The neutron cross section of oxygen has been measured previously at this laboratory up to an energy of 1.4 Mev[7] and at Minnesota above 0.5 Mev.[16] Both measurements agree in the common energy interval and are shown by the solid line below 1.2 Mev in Fig. 6. The Minnesota results do not show the peak at 1.66 Mev found in the present measurements. This peak may have been missed because it is considerably narrower than the energy spread used in the Minnesota measurements. In an attempt to determine its shape, Li neutrons with a 7-kev energy spread were employed. The observed width was about equal to the energy spread, again indicating that the peak is not completely resolved. It must be due to the interaction of neutrons of one or more units of angular momentum to form a compound state of spin $\frac{3}{2}$ or more. The same statements about width and character which apply to the peak at 1.66 Mev can be made about the peak at 1.84 Mev. The maximum at 1.91 Mev, however, is considerably wider than the experimental energy spread and small enough to be caused by a compound state of spin $\frac{1}{2}$. Its shape excludes its formation by *s*-neutrons. It is, therefore, believed to be due to *p*-neutrons. At 2.37 Mev a minimum in the cross section appears which has the shape expected from interference between resonance scattering caused by a compound state of spin $\frac{1}{2}$ and *s*-wave potential scattering of phase shift $\pi/2$. How-

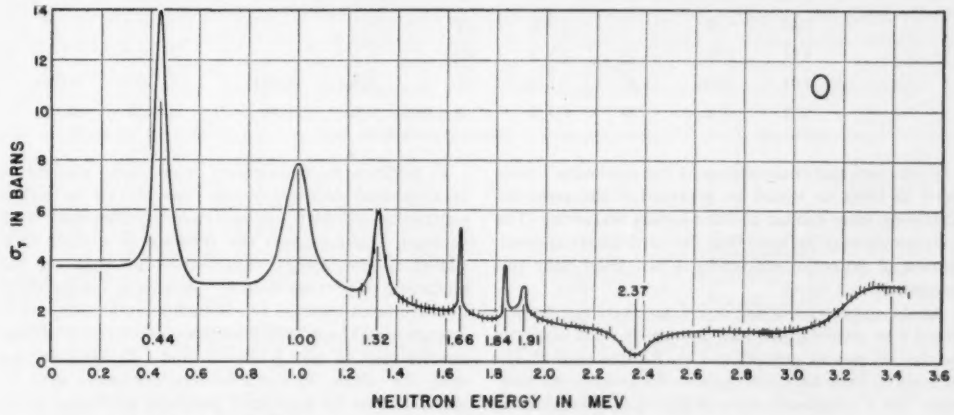

FIG. 6. Total cross section of oxygen. The solid line below 1.2 Mev shows the data of reference 7.

[17a] Ricamo, Zuenti, Baldinger, and Huber, Helv. Phys. Acta **23**, 508 (1950).

TABLE I. Summary of the characteristics of the observed narrow energy levels.

Compound nucleus	E_r (Mev)	E_{ex} (Mev)	Γ (kev)	J	l	$a\times10^{13}=1.5A^{\frac{1}{3}}$ $\gamma^2\times10^{13}$ (Mev cm)	$\frac{\gamma^2}{3\hbar^2/2Ma}$	$a\times10^{13}=1.5\{A^{\frac{1}{3}}+(0.5)^{\frac{1}{3}}\}$ $\gamma^2\times10^{13}$ (Mev cm)	$\frac{\gamma^2}{3\hbar^2/2Ma}$
Li^8						$a=2.9\times10^{-13}$ cm		$a=4.1\times10^{-13}$ cm	
($E_b=1.98$ Mev)	0.26	2.21	45	2	1	3.9	0.16	1.8	0.11
Be^{10}						$a=3.1\times10^{-13}$ cm		$a=4.3\times10^{-13}$ cm	
($E_b=6.69$ Mev)	0.62	7.25	30	3	1	0.45	0.020	0.28	0.017
					2	69	3.1	6.9	0.43
	0.81	7.42	≤11	≥1	>0	...	...	...	...
B^{12}						$a=3.3\times10^{-13}$ cm		$a=4.5\times10^{-13}$ cm	
($E_b=3.29$ Mev)	0.43	3.68	40	2	1	0.90	0.043	0.55	0.036
					(2)	∞	∞	94	6.2
	1.28	4.46	130	3	1	0.72	0.035	0.50	0.033
					2	18	0.87	4.2	0.28
	1.78	4.92	65	1	1	0.25	0.012	0.19	0.012
					2	2.7	0.13	0.85	0.056
					(3)	∞	∞	25	1.6
	2.45	5.53	120	2	1	0.34	0.016	0.26	0.017
					2	2.3	0.11	0.81	0.053
					3	∞	∞	12	0.82
	2.58	5.63	60	3	1	0.16	0.0077	0.12	0.0082
					2	0.90	0.044	0.38	0.025
					3	40	2.0	3.9	0.26
C^{13}						$a=3.4\times10^{-13}$ cm		$a=4.6\times10^{-13}$ cm	
($E_b=4.88$ Mev)	2.08	6.80	≤11	$\geq3/2$	>0	...	...	...	...
	2.95	7.60	120	3/2	1	0.28	0.014	0.23	0.015
					2	1.3	0.064	0.61	0.041
O^{17}						$a=3.8\times10^{-13}$ cm		$a=5.0\times10^{-13}$ cm	
($E_b=4.13$ Mev)	0.44	4.54	40	3/2	1	0.70	0.040	0.45	0.034
					(2)	∞	∞	18	1.3
	1.00	5.07	100	3/2	1	0.60	0.036	0.44	0.033
					2	13	0.75	3.5	0.26
	1.32	5.37	35	3/2	1	0.16	0.0090	0.12	0.0090
					2	1.43	0.081	0.57	0.043
	1.66	5.69	≤7	$\geq3/2$	>0	...	...	...	...
	1.84	5.86	≤10	$\geq3/2$	>0	...	...	...	...
	1.91	5.93	30	1/2	1	0.091	0.0053	0.074	0.0056
	2.37	6.36	120	1/2	0	0.18	0.010	0.18	0.013

ever, the residual cross section at the minimum is one-third as large as would be expected if the potential scattering were similar to hard-sphere scattering. The discrepancy may indicate that the hard sphere approximation of potential scattering is not valid near this resonance.

At the upper end of the investigated energy range a broad rise occurs which had previously been observed by the Minnesota group[16] and by Ricamo *et al.*[17a] The increase in cross section is equal to the theoretical maximum for a compound state of spin $\frac{3}{2}$. This maximum should, therefore, be attributed to neutrons of an orbital angular momentum of one or two units.

In addition to well-defined levels there appears to be a gradual decrease of the cross section to higher energies upon which the levels are superimposed. This decrease might suggest the presence of a very wide *s*-level at low energy. Laubenstein's[18] data on the scattering of protons from O^{16} indicate a similar effect for the mirror nucleus, F^{17}. If such a level exists, interference would be expected between it and the relatively narrow state of spin $\frac{1}{2}$ formed near 2.37 Mev. In this case, the shape of the 2.37-Mev minimum may be accounted for by an *s*-wave potential scattering phase

[18] R. A. Laubenstein and M. J. W. Laubenstein, Phys. Rev., to be published.

shift considerably less than $\pi/2$, and the residual cross section at the minimum may not be in disagreement with that expected from the hard-sphere approximation of potential scattering.

IV. SUMMARY

A summary of the information concerning the narrow energy levels discussed in Sec. III is given in Table I. For the sake of completeness, the resonances described in references 5 and 7 are included in this table. The first column lists the compound nuclei studied, together with the binding energy of the neutron, E_b. In the next four columns the resonance energies, E_r, the excitation energies E_{ex}, the observed widths Γ, corrected for experimental resolution, and the total angular momenta J are given. In the assignment of values of J it has been assumed that the resonances are entirely due to elastic scattering. Available experimental data indicate that for the nuclei listed in Table I, processes other than elastic scattering are probably negligible in the energy range under investigation. The unresolved resonances are also tabulated together with the lower bounds of their total angular momenta and the upper limits of their widths. For these maxima, no correction for experimental resolution has been applied.

The reduced widths,[19] γ^2, of the levels listed in Table I have been computed for values of the orbital angular momentum, l, which have been shown to be reasonable in the previous section. Since the calculation of reduced widths is sensitive to the interaction radius, a, the computation has been performed for two values of a. The observed widths have been corrected for the variation of the level shift with energy.[17] Also included in Table I is the ratio of the reduced widths to the sum-rule limit,[19] $3\hbar^2/2Ma$, where M is the reduced mass of the system. Values of l which result in reduced widths exceeding the sum rule limit for the interaction radii used are shown in parentheses and can probably be excluded. In addition, those values of l yielding reduced widths which are large fractions of $3\hbar^2/2Ma$ are not likely to be applicable.

[19] E. P. Wigner, Am. J. Phys. **17**, 99 (1949).

PHYSICAL REVIEW VOLUME 84, NUMBER 1 OCTOBER 1, 1951

Energy Distribution of Fission Fragments of U^{235} Produced by 2.5-Mev and 14-Mev Neutrons*

STEPHEN S. FRIEDLAND†
University of California, Los Alamos Scientific Laboratory, Los Alamos, New Mexico
(Received February 19, 1951)

The kinetic energy released in the fission of U^{235} by 2.5-Mev and 14-Mev neutrons has been measured. The results show the familiar two-peak curve when intensity of a fragment with a given energy is plotted against energy. However, the dip between the peaks apparently disappears with increasing energy of the neutrons and the distribution approaches a single symmetrical peak.

INTRODUCTION

SEVERAL investigators have studied the kinetic energy released by the fission of U^{235} when induced by thermal neutrons.[1–4] Their results showed the now familiar double peak curve when the intensity of fission fragments with a given energy is plotted against the kinetic energy of the fragments. Recently Jungerman and Wright[5] studied the energy released in the fission process when neutrons at 90 Mev and 45 Mev are used. Their 45-Mev data showed a large decrease in the size of the dip between the two peaks, whereas their 90-Mev data showed no dip whatsoever but a single peak curve. This paper reports on the results of measurements taken when fission is induced in U^{235} by 2.5-Mev and 14-Mev neutrons.

EXPERIMENTAL METHOD

The method used in this experiment was essentially the same as that used by other investigators, that is, the ionization produced in an ionization chamber by the fission fragments was compared to the ionization produced by alpha-particles of a known energy. An

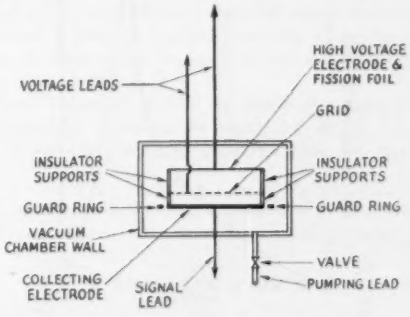

FIG. 1. Schematic diagram of ionization chamber.

* Work done under the auspices of the AEC.
† Now at the University of Connecticut, Department of Physics, Storrs, Connecticut.
[1] W. Jentschke, Z. Physik, **120**, 165 (1943).
[2] A. Flammersfeld, Z. Physik **120**, 450 (1943).
[3] M. Deutsch, MDDC-945 (unpublished).
[4] J. L. Fowler and L. Rosen, Phys. Rev. **72**, 926 (1947).
[5] J. Jungerman and S. C. Wright, Phys. Rev. **76**, 1112 (1949).

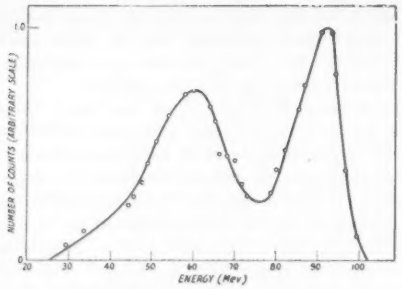

FIG. 2. Energy spectrum of U^{235} fission fragments induced by thermal neutrons.

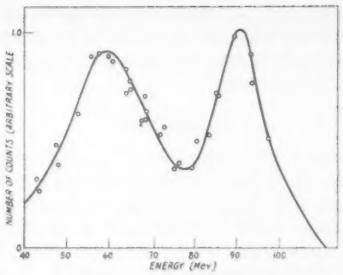

FIG. 4. Energy spectrum of U^{235} fission fragments induced by 2.5-Mev neutrons.

ionization chamber designed by Fowler and Rosen, and similar to the one described in their paper,[4] was used. The details of the construction may be found in their paper. The chamber, Fig. 1, was of the electron-collection type. The screen, which shields the collecting electrode from the positive ions, was one cm from the collecting electrode and 2.2 cm from the high voltage electrode. The high voltage electrode, upon which was deposited the fissionable material, was maintained at 4000 volts while the grid was maintained at 1850 volts. The high field region between the grid and the collecting electrode was established to insure the "funnel effect"[5] for the electrons through the grid wires. The chamber was filled to a total pressure of 162 cm of mercury of which 95 percent was argon and 5 percent was CO_2. This pressure was more than sufficient to stop the longest range fission fragments, as well as the calibrating alpha particles before they reached the grid. The CO_2 was present to hasten the collection time of the ions. The gas was continuously purified by passing it over calcium metal which was heated to 180°C.

TABLE I. Data on high and low energy fission products.

	Position of high energy peak	Position of low energy peak	Ratio of minimum to high energy peak (per-cent)	Ratio of peak energies	Ratio of high energy peak to low energy peak	Foil thickness (mg/cm²)
U^{235} thermal neutrons						
Fowler and Rosen	93	61.8	21	1.50	1.43	0.105
Friedland	93	60.1	23	1.54	1.37	0.140
U^{235} 2.5-Mev neutrons	91	59	36	1.5	1.1	0.140
U^{235} 14-Mev neutrons	91	59	57	1.5	1.1	0.140

The pulse obtained from the chamber was amplified with a Model 100 preamplifier before passing on to the amplifier.[6]

A clipping circuit, consisting of a 3-μsec delay line was used to place on the grid of the amplifier the original signal which had been inverted by reflection. The amplified signal was fed into a 10-channel pulse amplitude analyzer,[6] which had been adjusted to have each channel accept pulses over equal ranges. For the amplification used the channel widths were set either at 0.8 Mev or 2.0 Mev. By shifting the bias on the analyzer, it was possible to cover the entire range of the fission pulses, taking nine points at a time. Because of the tendency of the 10-channel analyzer to drift, it was calibrated before and after each run.

The neutron source used was the Los Alamos Cockroft-Walton set. For the 14-Mev neutrons the $H^3(H^2, n)He^4$ reaction was used, while for the 2.5-Mev neutrons the $H^2(H^2, n)He^3$ reaction was used.

The fission foil was made by John Povelites and

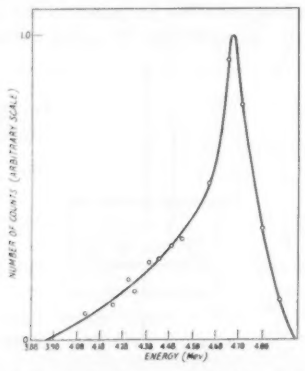

FIG. 3. Energy distribution of U^{234} alpha-particles.

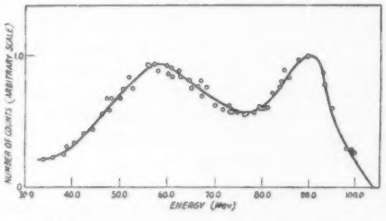

FIG. 5. Energy spectrum of U^{235} fission fragments induced by 14-Mev neutrons.

[6] W. C. Elmore and M. Sands, *Electronics: Experimental Techniques* (McGraw-Hill Book Company, Inc., New York, 1949).

had a foil thickness of 0.14 mg/cm² and a total weight of 5.42 mg.

To check the apparatus and the techniques required for the experiment, a thermal source of neutrons was obtained by placing a Po-Be source in a graphite pile and the distribution of the energy of the fission fragments was obtained. The results are shown in Fig. 2 and are compared to the results of Fowler and Rosen[4] in Table I.

The distribution of the energy of ionization produced by the alpha-particles of U^{234} is shown in Fig. 3. The width at half maximum serves as a measure of the resolution of the ionization chamber and is approximately 0.2 Mev.

RESULTS

Figures 4 and 5 show the energy distribution of the fission fragments for U^{235} when induced by neutrons of 2.5 Mev and 14 Mev, respectively. Table I compares these with results obtained with thermal neutrons.

The data obtained is in agreement with those of Jungerman and Wright. The dip between the peaks apparently disappears with increasing energy and the distribution approaches a single symmetrical peak.

Acknowledgments are due Mr. R. W. Davis for operating the Cockroft-Walton set and Drs. J. H. Coon, J. L. Fowler, E. R. Graves and L. Rosen for many discussions.

PHYSICAL REVIEW VOLUME 84, NUMBER 1 OCTOBER 1, 1951

Absorption Length and Collision Length of Hard-Shower-Producing Radiation

DAVID POMEROY*
University of New Mexico, Albuquerque, New Mexico
(Received February 23, 1951)

By combining techniques of coincidence counter circuits and nuclear photographic emulsions, values are obtained for the absorption length in air of 104±6 (p.e.) g/cm², and for the collision length in paraffin of 61±6 (p.e.) g/cm² for hard-shower-producing radiation. The method also provides evidence of a cascade mechanism by which the hard showers are produced.

TWO experiments have been conducted in order to obtain the values of the absorption length in air, and of the collision length in paraffin, for the hard-shower-producing component of cosmic radiation. The results provide evidence on how the hard showers are produced. Both experiments were performed at two elevations, namely, at 5200 feet (University of New Mexico) and at 10,700 feet (Sandia Crest, New Mexico), referred to as "roof" and "crest" in the sequence, respectively. The first experiment made use of photographic emulsions, while the second experiment utilized the techniques of counter tube circuits.

FIRST EXPERIMENT

Two dozen Ilford G5 plates (200μ emulsion thickness) were exposed to cosmic radiation at each of the two elevations. In each case one dozen plates were placed vertically under a hemisphere of paraffin of radius 38 cm, with the other dozen near by without shielding. After 10 to 14 days exposure, the plates were processed by the method reported by Dilworth, Occhialini, and Payne.[1] The plates were then subjected to microscopic examination for the detection of hard showers.

Since the showers always formed part of stars, counts were also made of stars with 5 or more prongs whether they were accompanied by hard showers or not. Radioactive contamination stars were eliminated by the criterion that at least one of the prongs of the 5 prong stars had to exceed 55μ in length.

Preliminary examination was made under low magnification (10× objective). In order to check on the accuracy of this procedure, tests were made on the number of stars found at different scanning rates, using an old Ilford C2 plate which had been in a drawer for several months, so that the star density was relatively high. The results are shown in Table I.

The final results are based on a 9 hour scanning time per plate under low power. Every star accepted was later examined under oil immersion (95× objective) for hard showers.

A listing of the number of stars and hard showers found at the two different altitudes with and without absorber is given in Tables II and III. From the data given in those tables we calculate the standard deviations listed in Table IV.

From Tables II and IV we obtain the altitude dependence and calculate the absorption length L_{star} in air of the star-producing radiation from the relative

TABLE I. Effect of scanning rate on accuracy.

Scanning hours	Objective	No. of 5 prong stars
5	10×	33
7	10×	42
9	10×	46
24	44×	51

* Now at the University of Florida, Gainesville, Florida.
[1] Dilworth, Occhialini, and Payne, Nature **162**, 102 (1948).

TABLE II. Analysis of data for stars of five or more prongs obtained on Sandia Crest (el. 10,700 ft) and on the roof of Administration Building, University of New Mexico (el. 5200 ft).

Crest	Days exposed	Days before processing	Cm² plate	Cm² plate	Total stars	With corr. (a)	Stars ≥5 prongs With corr. (a) and (b)	Stars ≥5 prongs Stars per cm² per day with corr. (a) and (b)
With absorber	14	1	107	2.14	142	139.4	101.5	3.39
Without absorber	14	3	120	2.40	149	140.3	97.8	2.95
Roof								
With absorber	10	—	75	1.50	40	40	19.7	1.31
Without absorber	11	—	80	1.60	43	43	21.3	1.21

Corrections:
(a) Delay before processing at the rate of 1.21/cm² day.
(b) Delay from date of manufacture: Plates used on crest: 17 days. Plates used on roof: 13 days.
This correction is computed from the observation of 7 stars ≥5 prongs in 24 cm² (=0.48 cm²) control plates in 14 days = (25/24)/cm² day.

intensities found at the two different altitudes without absorber, using the relationship $I = I_0 e^{-X/L}$. The atmospheric depth of the crest (el. 10,700 ft) is 700 g/cm², and on the University roof (el. 5200 ft) it is 860 g/cm². (See Rossi's table.[2]) This gives the equivalent layer X to be 160 g/cm². Since I_0 (crest) = 2.95/cm³ day, and I (roof) = 1.21/cm³ day, we have $L_{\text{star}} = X/\ln(I_0/I) = 180$ g/cm² in air. From the standard deviations in Table IV we calculate the standard error in L to be ±80 g/cm², or the probable error to be ±53 g/cm². Therefore our result is: absorption length in air for star-producing radiation = (180±53) g/cm².

Following the same procedure for the hard shower data, we obtain: Absorption length in air for hard-shower-producing radiation = (100±33) g/cm². If we assume an absorption length equal to twice the geometric nuclear length,[3–5] we get the following values: $L_{\text{coll}} = 45.5$ g/cm² in paraffin; $L_{\text{abs}} = 2L_{\text{coll}} = 91$ g/cm² in paraffin. The density of the paraffin wax used was 0.82 g/cm³; therefore 38 cm paraffin are equivalent to 31 g/cm². The expected absorption factor is thus $e^{-31/91} = 0.71$.

The data given in Tables II and III are summarized in Tables V and VI. The probable errors have been computed from Table IV. The number of stars and hard showers per cm³ day expected from the data with no paraffin and the expected absorption, are compared with the number actually obtained under 31 g/cm² of paraffin. We see from the tables that at 10,700 feet, for which we have better statistics than at the 5200-foot level, the transition effect exceeds the statistical error. We have, in fact, in the case of stars, the ratio 3.39/2.09 = 1.62, with a probable error of ±0.21.

When the results of the experiment are compared with those of Perkins[6] and Cortini,[7] it will be noted that the transition effects for stars at sea level and at 5200 feet, although positive, are within the probable errors. The relatively large positive result obtained by Cortini under Pb at 3500 m for stars of less than 5 prongs, as compared with disappearance of this effect at sea level as obtained by Perkins, suggests the possibility that if Perkins' experiment had been conducted above 10,000 feet altitude the transition effect under paraffin would have been larger. Indeed, this is borne out by our own experiment, for at 10,700 feet the effect is three times as large as the probable error, when the effect due to absorption is included. It would be interesting in a future experiment to obtain data above 10,000 feet for smaller amounts of paraffin absorber.

TABLE III. Analysis of data for hard showers containing two or more particles obtained on Sandia Crest and on the roof, University of New Mexico.

Crest	Days exposed	Days before processing	Cm² plate	Cm² plate	Total hard showers	With corr. (a)	With corr. (b)	Hard showers per cm² day with corr. (a) and (b)
With absorber	14	1	107	2.14	44	43.5	38.1	1.27
Without absorber	14	3	120	2.40	44	42.4	36.3	1.08
Roof								
With absorber	10	—	75	1.50	7	7	4.1	0.27
Without absorber	11	—	80	1.60	7	7	3.9	0.22

Corrections:
(a) Delay before processing at the rate of 0.22/cm² day.
(b) Delay from date of manufacture: Plates used on crest: 17 days. Plates used on roof: 13 days.
This correction is computed from the observation of 1 shower ≥2 particles in 24 cm² control plate in 14 days = (25/268)/cm² day.

[2] B. Rossi, Revs. Modern Phys. **20**, 537 (1948).
[3] G. Cocconi and V. C. Tongiorgi, Phys. Rev. **75**, 1058 (1949).
[4] E. P. George and A. C. Jason, *Cosmic Radiation* (Interscience Publishers, Inc., New York, 1948).
[5] G. Bernardini, *Cosmic Radiation* (Interscience Publishers, Inc., New York, 1949).
[6] D. H. Perkins, Nature **160**, 707 (1947).
[7] G. Cortini, Nature **163**, 991 (1949).

In the case of hard showers we have a transition effect at 10,700 feet equal to 1.65±0.30 under paraffin.

The indication of a transition effect under paraffin both for stars and hard showers suggests that the mechanisms for their formation is of a cascade rather than a multiple type, although a combination of the two processes is not excluded from consideration. Thus a transition effect can occur if some of the hard shower particles produce, in turn, hard showers. Such an effect is impossible if the energy of the primary is non-catastrophically absorbed in direct, successive, hard-shower-producing collisions. In the latter event we should clearly get a reduction in the number of stars and hard showers observed under absorber.

After the data had been examined the possibility occurred to us that some 5 prong stars resulting from π^- meson capture might have contributed to the transition effect in the case of stars. Of the 142 stars obtained on the crest under the absorber and the 149 stars without absorber, the numbers of 5 prong stars were 33 and 23, respectively. Similarly, of the 40 stars on the roof under absorber and the 43 without absorber, the numbers of 5 prong stars were 15 and 9. To verify that

TABLE IV. Standard deviations for star and hard shower values listed in Tables II and III.

	Stars	Stars per cm² per day	Showers	Showers per cm² per day
Crest				
With absorber	13.5	0.45	7.0	0.23
Without absorber	14.1	0.42	7.2	0.21
Roof				
With absorber	7.8	0.52	3.1	0.20
Without absorber	8.0	0.45	3.1	0.17

the relative increase under the absorber was really attributable to π^- stars would have entailed re-scanning all the plates. This task was rendered impossible in any case by the peeling of the emulsions in the dry New Mexico climate. However, if we subtract the 5 prong stars we get the results given in Table VII. From this table we see that the transition effect for stars under 38-cm paraffin is no longer present at 5200 feet when we do not include the 5 prong stars, and is considerably reduced at 10,700 feet. This strengthens the assumption that the transition effect, as far as stars are concerned, can possibly be attributed to the local production of π^- mesons which would preferably lead to the formation of additional small stars.

If, as we have suggested, the transition effect under paraffin in the case of hard showers has its origin in a cascade process, the question arises as to how this is brought about. Do some of the hard shower particles give rise to further showers of π-mesons, protons or neutrons? At relativistic energies it would be difficult to distinguish between charged π-mesons and protons while neutrons could not, of course, be observed. Recent experiments indicate, however, that about 80

TABLE V. Assumed absorption and actual transition effect under paraffin for stars $\geqslant 5$ prongs per cm² day.

Altitude	Without absorber	Number expected as a result of absorption alone without transition effect	Actual observation under 31 g/cm² paraffin
10,700 ft	2.95±0.28	2.09±0.20	3.39±0.30
5200 ft	1.21±0.30	0.86±0.21	1.31±0.35

percent of the shower particles are π-mesons.[8] We must not exclude the possibility, however, that the composition of the shower particles may be materially affected when the plates are under paraffin and the percentage of π-mesons increased as in the case of stars, although for hard showers the π-mesons would be fast. We occasionally saw in the plates a double star accompanied by penetrating particles connected by an ionizing link which may have been a π-meson. Although an analysis was not undertaken, close pairs and close triplets also occurred with a frequency well above what might have been expected from a random distribution and some of these were conceivably connected by a non-ionizing link. It would be fair to say in general that a transition effect for hard showers under paraffin at 10,700 feet can possibly be attributed to fast π-mesons, neutrons, and protons produced in the absorber.

SECOND EXPERIMENT

The counter tube experiment was designed to measure the collision length in paraffin of the neutral radiation which produces hard showers. The counter tubes used were of the cosmic-ray type designed by Regener[9]; they were 2″ in diameter and up to 36″ long.

The arrangement is illustrated in Fig. 1. Hard showers produced in the paraffin layer (b) were detected by an arrangement of crossed counter tubes in threefold coincidence (B_1C_1) and twofold coincidence (B_2C_2) respectively, as explained in Table VIII. The electronic circuits were designed to record only those events in which a threefold coincidence (B_1C_1) occurs simultaneously with a twofold coincidence (B_2C_2). Such an event we call a fivefold coincidence ($B_1C_1B_2C_2$) and it is recorded in one or both of the two mechanical recorders in a manner shortly to be explained. By crossing the (B_1C_1) and (B_2C_2) arrangements, the solid angle subtended by the counter tubes is controlled on

TABLE VI. Assumed absorption and actual transition effect under paraffin for hard showers $\geqslant 2$ particles per cm² day.

Altitude	Without absorber	Number expected as a result of absorption alone without transition effect	Actual observation under 31 g/cm² paraffin
10,700 ft	1.08±0.14	0.77±0.10	1.27±0.15
5200 ft	0.22±0.11	0.16±0.08	0.27±0.13

[8] P. H. Fowler, Phil. Mag. **41**, 169 (1950).
[9] V. H. Regener, Rev. Sci. Instr. **18**, 267 (1947).

TABLE VII. Data for stars ≥ 6 prongs including assumed absorption and actual transition effect.

Crest	Days exposed	Days before processing	Cm² plate	Cm² plate	Total stars	With corr. (a) and (b)	Per cm² per day	Number expected from absorption effect alone
With 38-cm paraffin absorber	14	1	107	2.14	109	69.7	2.32	1.86
Without absorber	14	3	120	2.40	126	87.9	2.62	2.62
Roof								
With 38-cm paraffin absorber	10	—	75	1.50	25	10.3	0.69	0.74
Without absorber	11	—	80	1.60	34	18.5	1.05	1.05

Corrections:
(a) Delay before processing at rate of 1.05/cm² day.
(b) Delay from date of manufacture: see footnote to Table II.
This correction is computed from the observation of 5 stars ≥ 6 prongs in 24 cm² control plates in 14 days = 125/168 per cm² per day.

all sides in such a way as to give complete coverage by layers of paraffin placed above A as shown in Fig. 1.

As explained in Table VIII most of the coincidence counter tubes in trays B_1 and C_1 participate in more than one threefold arrangement. Two twofold arrangements in the trays B_2 and C_2 serve to limit the solid angle subtended by the counter tubes in trays B_1 and C_1 in their axial direction. The fivefold coincidence method adopted here has the additional advantage of minimizing the possibility of chance coincidences. The radiation which gives rise to all coincidence counts must penetrate layer C of 10 cm of lead. This removes the possibility of a count produced by a cascade-type event of the soft component.

The counter tubes in the battery A, which is sufficiently long and wide to cover the solid angle subtended at A by the fivefold arrangements $(B_1C_1B_2C_2)$, are used for the purpose of detecting ionizing radiation which may have entered the block of paraffin (b) simultaneously with a "hard shower" fivefold coincidence $(B_1C_1B_2C_2)$ and for preventing such an event from being recorded in recorder (A) (see Fig. 2). Recorder (A) is thus driven by a fivefold coincidence but is not activated when such a coincidence is accompanied by the arrival of a pulse from the counter tubes in the anticoincidence battery A. Such an event will be called an anticoincidence $(B_1C_1B_2C_2-A)$ and may be ascribed to a hard shower produced in the paraffin (b) by a neutral primary.

It would have been desirable, of course, to record hard showers produced by both ionizing and non-ionizing primaries but we would then have had to cope with the problem of a high background due to extensive air showers from the soft cosmic-ray component which are incident from all directions and which would thus nearly always have hit counter tubes A. This is inherent in the procedure adopted in this experiment, which follows the experiment of Rossi and Regener on the production of mesons by penetrating non-ionizing rays.[10]

We wish to measure the collision length of the non-ionizing radiation which produces hard showers in the block of paraffin (b); as explained above, the presence of these showers is revealed by the registration of anticoincidence counts $(B_1C_1B_2C_2-A)$. If we place an additional layer of paraffin (a) above the anticoincidence trays A, a neutral primary which might otherwise have produced a hard shower in (b) now has the possibility of producing "prematurely" a hard shower in (a). As a consequence, the anticoincidence count $(B_1C_1B_2C_2-A)$ should decrease exponentially with the thickness of (a). This assumes that none of the showers produced in (a) suffers complete absorption in (a), which seems a reasonable assumption.

A preliminary check on the correct design of the experimental details was made by placing the bank of counter tubes (B_2) above A. If everything was in

TABLE VIII. Selected arrangements for twofold and threefold coincidence circuits.

View	Selected coincidence (by counter tube number)
Front	1 is in threefold coincidence with 1′ and 2′
	2 is in threefold coincidence 1′ and 2′ and with 2′ and 3′
	3 is in threefold coincidence with 3′ and 4′ and with 4′ and 5′
	4 is in threefold coincidence with 4′ and 5′
Side	5 and 6 (in parallel) are in twofold coincidence with 6′, 7′ and 8′ (in parallel)
	7 and 8 (in parallel) are in twofold coincidence with 9′, 10′ and 11′ (in parallel)

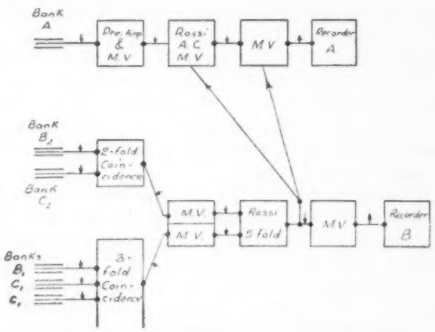

FIG. 1. Block diagram for counter tube circuit.

[10] B. Rossi and V. H. Regener, Phys. Rev. **58**, 837 (1940).

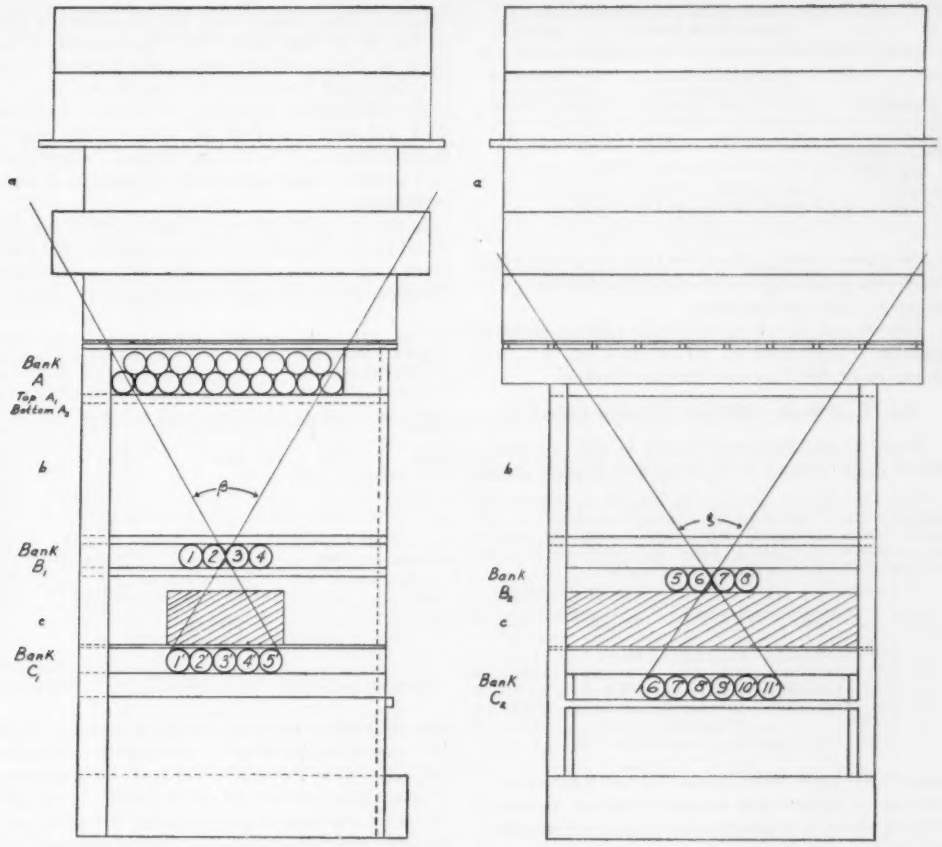

FIG. 2. Counter tube arrangement.

working order we should then have expected to obtain fivefold counts ($B_1B_2C_1C_2$) but not anticoincidence counts ($B_1B_2C_1C_2-A$) since, in the latter case, a charged particle would have to pass from (B_2) to (B_1) without discharging the intercepting anticoincidence counter bank A. The only way in which counter tubes in (B_1) and (B_2) would be fired without affecting A would be in the event of a side shower, but even in that case it would still be very unlikely for an anticoincidence counts ($B_1B_2C_1C_2\,A$) to be registered. From the results of this preliminary experiment (see Table IX) it is apparent that few if any such side showers occurred. The counts recorded for different arrangements in the experiment proper are summarized in Table X.

As a basis for our calculations we first assume a background obtained by removing the paraffin layer (b) from below the anticoincidence trays A and placing the paraffin layer (a) of 42-cm paraffin above A. This gives us arrangement C of Table X. We then have the counting rates

$$I_0=A-C=24.5\pm1.2 \text{ (crest)}, \quad 5.26\pm0.58 \text{ (roof)}.$$

$$I_{42}=D-C=13.8\pm1.1 \text{ (crest)}, \quad 3.31\pm0.69 \text{ (roof)}.$$

From these values we obtain $L_{\text{coll}}=(61\pm6)$ g/cm² in paraffin. In an analogous manner, we calculate L_{coll} in paraffin for the counts on the roof to be (75 ± 19) g/cm². From the ratio A minus C counts for the roof and crest data we get the absorption length in air of the neutral component which produces hard showers. The results are summarized in Table XI where, for comparison, we have also included the results from the nuclear plate experiment.

It might be argued that in order to obtain the absorption length we should compare the ratios of A minus B or D minus C counts at two altitudes, in order that the amount of absorber above the counter tubes A be the same. We have done this and get $L_{\text{abs}}(A-B)$

TABLE IX. Data for preliminary experiment to test for absence of side showers.

Arranged for	30-cm paraffin in (b) Fivefold coincidences Hours	Counts	Counts/hr	No paraffin in (a) Anticoincidences Counts	Counts/hr
Showers	17	138	8.1	2	0.1
Predominantly single particles.	3	1743	581	0	0

Connect 1′ with 2′ and 3′ with 4′ (see Table VIII).

$=(91\pm18)$ g/cm²; $L_{abs}(D-C)=(112\pm12)$ g/cm². These results are sufficiently close to the value (104 ± 6) g/cm² as not to affect our discussion.

The value of (61 ± 6) g/cm² for the collision length in paraffin is equivalent to $(61\pm6)(14.4/7.2)^{\frac{1}{2}}=(77\pm8)$ g/cm² in air. We thus have for hard showers

$$(L_{abs}/L_{coll}) \text{ in air}=(104\pm6)/(77\pm8)=1.35\pm0.16.$$

There is one important feature in our experiment which is also present in the Rossi and Regener experiment.[10] In their investigation of the production of mesons by penetrating neutral radiation, increasing thicknesses of lead placed above their anticoincidence layers A, corresponding to our arrangements D and E of Table X, resulted in an asymptotic background which was roughly $1\frac{1}{2}$ times the background counts obtained in the absence of the detecting layer corresponding to our arrangement C. In a review article by Rossi,[2] a collision length value in lead based on the asymptotic background gave a result which is much smaller than a collision length value based on the geometric cross section of the lead nuclei. Had the calculation been based on the lower background value the result would have been more reasonable. We cite this as an argument in favor of adopting arrangement C for our background. This still leaves unexplained, however, the differing backgrounds as well as the size of these backgrounds—such problems were incidental to the purpose of Rossi's experiment.

TABLE X. Summary of counts for different arrangements of absorber. The ± values are the standard deviations. The subscripts and superscripts in the first column of the table refer to the number of cm of paraffin below (in layer b) and above the anticoincidence trays (in layer a), respectively.

Arrangement	Anticoincidence counts/hr Roof	Crest	Fivefold counts/hr Roof	Crest
$A=P_{30}^{0}$	16.80±0.37	46.3±1.0	111.3±1.0	215.6±2.2
$B=P_{0}^{0}$	13.6±1.6	27.7±1.1	94.8±4.3	190.3±2.9
$C=p_{0}^{42}$	11.54±0.57	21.79±0.68	105.0±1.7	211.5±2.0
$D=p_{30}^{42}$	14.85±0.39	35.56±0.89	119.3±1.1	224.8±3.0
$E=P_{30}^{72}$	——	34.72±0.86	——	213.6±3.0

TABLE XI. Summary of results.

Subject of measurement	Result and probable error
1. Collision length in paraffin in g/cm² of neutral hard-shower-producing component as obtained from the counter tube experiment (a) at 5200 ft (b) at 10,700 ft on basis of $(A)-(C)$ counts	(a) 75±19 (b) 61±6
2. Absorption length in air in g/cm² of neutral hard-shower-producing component as obtained from the counter tube experiment on basis of $(A)-(C)$ counts	104±6
3. Absorption length in air in g/cm² of total component producing (a) hard showers (b) stars as obtained from the altitude dependence of the nuclear experiment.	(a) 100±33 (b) 180±53

In the first place, we would have expected the additional layer of paraffin (a) in arrangement E to have given lower anticoincidence counts than those actually obtained. Even allowing for poor geometry to give us effectively about 60 cm of paraffin in layer (a) instead of 72 cm (compare Fig. 1), the counts obtained are still too close to the number registered in arrangement D where there are only 42 cm of paraffin in (a). As in the Rossi experiment it seems that the piling up of absorber above (a) does not succeed in eliminating the hard-shower-producing effects of the penetrating neutral radiation. This raises the question as to whether we have disregarded a mechanism which would artificially increase the collision length of the neutral hard-shower-producing radiation as the paraffin thickness (a) is increased. A possible explanation is that a fast proton may produce a star in (a) which is accompanied by one two hard neutral particles. One of these neutral particles could then proceed without being detected in A and produce a hard shower in (b). The likelihood of such an event would be expected to increase with (a) for the thicknesses used.

TABLE XII. Values reported by different observers for collision length and absorption length of hard-shower-producing radiation, for various absorbers.

Absorber	L_{abs} g/cm²	El. in m	L_{coll} g/cm²	El. in m
Lead	500	3250	*300	3250
			*310	4250
			160±15	3250
			160±10	4250
Iron			*200	4250
			135±15	3250
Carbon	500	3250	*140±20	250
			*120	3250
			100±5	3250
			81±5	4250
Air	120	250–3250		
	118±2	0–9000		

* These are probably absorption lengths rather than collision lengths.

The difference between the counts in the B and C arrangements as well as the size of the background remain somewhat of a mystery in view of the known absence of side showers (see Table IX). The systematic errors thereby introduced are possibly much greater than the statistical errors as far as the collision length results are concerned.

It is necessary to proceed with great care in comparing our results with those previously reported. A

lack of correspondence can often be attributed to the loose manner in which the term "mean free path" is employed, and the disposition of the apparatus is often such that a distinction between collision length and absorption length is hard to make. Results obtained by other workers are recorded in Table XII.[11–17] In general it may be stated that the ratio L_{abs}/L_{coll} varies from 1.4 to 2.0 and increases with the atomic number of the absorber.

The existence of a cascade type of hard shower is shown by the transition effect in our nuclear plate experiment which also eliminated the possibility of a pure multiple process. The question as to whether this is a pure cascade process or whether it is mixed with a multiple process cannot be decided at present.

The experiments were the subject of a Ph.D. thesis under the expert guidance of V. H. Regener. I wish also to express my appreciation to Dr. Darol Froman, Assistant Director of Los Alamos Laboratories, for the kindness and encouragement he bestowed on me.

[11] J. H. Tinlot, Phys. Rev. **73**, 1476 (1947).
[12] Walker, Walker, and Greisen, Phys. Rev. **80**, 546 (1950).
[13] J. H. Tinlot, Phys. Rev. **74**, 1197 (1948).
[14] J. H. Tinlot and B. P. Gregory, Phys. Rev. **75**, 519 (1949).
[15] G. Cocconi, Phys. Rev. **75**, 1074 (1949).
[16] G. Cocconi, Phys. Rev. **76**, 984 (1949).
[17] R. H. Rediker and H. S. Bridge, Phys. Rev. **79**, 206 (1950).

PHYSICAL REVIEW VOLUME 84, NUMBER 1 OCTOBER 1, 1951

The Penetration of Particles Associated with Cosmic-Ray Stars. II*†

J. A. NORTHROP‡
Sloane Physics Laboratory, Yale University, New Haven, Connecticut
(Received June 22, 1951)

A second series of measurements has been made at Climax, Colorado (elevation 3510 meters), of the particles associated with nuclear explosions, or stars, in a thin-walled ionization chamber. The associated particles were detected by observing coincidences between the ion chamber and appropriately placed trays of Geiger counters. The experiment was planned in such a way as to distinguish between those particles which are products of nuclear disintegrations which emerge from the ion chamber and those particles which are incident in the atmosphere in association with the particles producing the stars. Absorption measurements were made of both the low energy and penetrating product particles. There was no conclusive evidence indicating the presence of electrons or photons among the disintegration products. The absorption mean free path in lead was not exponential but increased to 190 ± 40 g/cm² at the maximum of eight inches of lead. Absorption measurements of the associated particles which are not disintegration products of the stars indicate that they are parts of local penetrating showers having mean free paths greater than 500 g/cm². Absorber placed over the ion chamber produced bursts of electrons in the chamber whose number greatly exceeded that of extensive air showers. These bursts have been tentatively identified with narrow air showers.

I. INTRODUCTION

PRELIMINARY measurements of the particles associated with cosmic-ray stars, or nuclear disintegrations, taking place in a thin-walled ionization chamber at 3510 meters altitude have been reported previously.[1] Although cloud-chamber photographs[2] show stars being produced along with many penetrating particles and electron showers, the counter arrays used to trigger the chamber select high energy events. It is to be assumed that low energy nuclear events would be much more common. The initial measurements, in which trays of Geiger counters were operated in coincidence with an ionization chamber, indicated that this was, indeed, the case. It was found that in only 2 percent of the cases of bursts in the chamber produced by stars were there at least two associated particles striking the counter tray directly beneath the chamber, and in only 0.02 percent of the cases were the particles capable of penetrating 8 inches of lead.

Because the rate of occurrence of star bursts in the chamber having associated particles was so low, the absorption curves obtained were not very accurate. However, absorption measurements showed the pres-

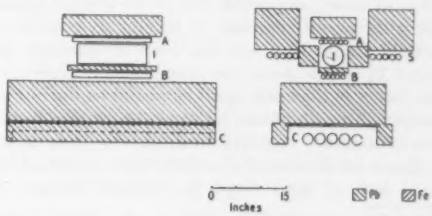

FIG. 1. Scale diagram of apparatus. The ionization chamber is I and A, B, C, and S represent the active areas of trays of counters. The S counters and the lead above and between them and the chamber are not shown in the side view.

* Part of a dissertation presented to the faculty of the Graduate School of Yale University in candidacy for the degree of Doctor of Philosophy.
† Assisted by the joint program of the ONR and the AEC.
‡ Supported (September, 1950, to June, 1951) by a Sterling Predoctoral Fellowship from Yale University.
[1] Montgomery, Montgomery, and Northrop, Phys. Rev. **79**, 293 (1950).
[2] W. B. Fretter, Phys. Rev. **76**, 511 (1949); M. B. Gottlieb, Phys. Rev. **82**, 349 (1951).

ence of both a penetrating component and, possibly, a soft electron component of these associated particles. There was also evidence that some of these particles were disintegration products of the stars with enough energy to escape through the walls of the ion chamber, while others were incident in the atmosphere with the star-producing radiation. The present paper reports an extension of these measurements, using a similar geometrical arrangement of ion chamber, counters, and absorber, but modified in several ways to improve the rates of occurrence of coincidences between the chamber and the counter trays.

II. ARRANGEMENT OF APPARATUS

Figure 1 is a scale diagram of the apparatus. Stars were produced and detected in the brass ionization chamber, designated by I in the following sections. It was a 14-inch cylinder with a 4-inch diameter and a 30-mil wall, and was filled with commercial tank argon[3] to 140 lb/in.^{2} gauge pressure, or 10.2 atmospheres absolute at Climax altitude. The $\frac{1}{4}$-inch diameter brass center electrode was supported at the ends by Kovar-glass seals (Stupakoff Ceramic and Manufacturing Company parts 95.2013 and 95.2042) using the guard ring system described by Tongiorgi.[4] Satisfactory operation using electron collection was obtained with 1800 volts collection potential on the center electrode, which was adequate to produce saturation of the pulses from an artificial polonium-alpha source near the grounded outer cylinder. Potential changes induced on the center electrode by bursts of ionization in the gas of the chamber were amplified first by a preamplifier (similar to the Los Alamos Model 500) attached directly to the chamber and then by a linear amplifier similar to the Atomic Instrument Company Model 204-B. With the amplifier set on 0.8 microsecond rise time, the rise time of the pulses was observed to be seven microseconds, which is a characteristic of the electron collection time in the chamber. The amplifier was followed by a four-channel amplitude discriminator of the conventional Schmitt trigger circuit type, each channel accepting all bursts in the chamber greater than a given size. The one selected the smallest bursts provided a master pulse used in coincidence with the various counters.

The arrangement of the counter trays was intended to follow as closely as possible that of the original apparatus, with several additions. A tray of six counters A, each 16 inches long and one inch in diameter, was placed $2\frac{3}{4}$ inches above the chamber axis. Lead up to four inches in thickness could be placed on top of these counters. Tray B, placed 3.3 inches below the chamber axis, contained 5 counters identical with those in tray A. Small thicknesses of absorber (up to 1 inch of lead or $1\frac{1}{2}$ inch of iron) could be inserted between the chamber and the B counters. Another tray of 5 counters C, each 40 inches long, two inches in diameter, and separated from each other by $\frac{3}{8}$ inch, was placed 14.8 inches below the chamber axis. Lead blocks up to a thickness of 8 inches and supported on a $\frac{1}{2}$-inch iron plate could be placed between the B and C trays. Side shielding for the C counters was provided as shown in the diagram. The designation "zero inches C lead" in the data means that only the iron plate above and the lead blocks to the side were present. During some of the measurements an additional set of counters, S, were present, level with the axis of I and always shielded from it by 4 inches of lead. Each of these 10 counters was 3.2 cm in diameter and had an active area of 60 cm^2. Lead up to 8 inches in thickness could be placed above each of the two S trays. Finally, there were 4 shower counters D, each 2 inches in diameter and 40 inches long, arranged at the corners of a rectangle 46 inches by 67 inches and centered approximately 30 inches to the side of the ionization chamber.

Direct calibration of the sizes of bursts produced in the chamber was obtained by a Po$-\alpha$ source on the end of an iron rod which could be slid into or out of the active area of the chamber by a magnet. Calibration was checked every 12 hours. The discriminators were set at various levels between $\frac{1}{2}$ and 8 Po$-\alpha$ burst size during the different runs. However, the data obtained were so nearly the same for all energy ranges that they have been consolidated into three groups in the data tables. On the assumption that a shower ray produces 80 ion pairs per cm in argon at atmospheric pressure,[5] one finds that a 5.3-Mev burst, equivalent to a Po$-\alpha$ particle, is produced by 32.6 electrons passing through the chamber. Bursts of $\frac{1}{2}$Po$-\alpha$ size or larger produced in the chamber under large thicknesses of absorber at sea level are almost entirely due to radioactive contamination of the chamber walls. The burst rates at mountain altitude have been corrected for this contamination.

Coincidences between the master pulse from the ion-chamber discriminator and the individual counters of the A, B, C and S trays were recorded on an Esterline-Angus 20-pen Operations Recorder. To reduce the accidental coincidence rate each counter was followed by an amplifier, an RC differentiation circuit, and a univibrator adjusted to give 15-microsecond gates. This short resolving time made the accidental coincidence rate negligible compared to the observed true rate. The univibrators were followed by diode coincidence circuits recording twofold coincidences between the chamber and individual counters, and finally by the driver circuit for the pen recorder. Pulses from the four shower counters, D, were added in a circuit which gave an output signal only when there were at least three simultaneous counter discharges. This signal was put in coincidence with the master pulse from the chamber.

[3] Supplied by the Matheson Company. A purified type from the Cleveland Wire Works of the General Electric Company was also tested. The slightly smaller saturation voltage of this highly purified gas did not seem to warrant its added cost.

[4] Vanna Tongiorgi, Phys. Rev. **75**, 1532 (1949).

[5] C. G. Montgomery and D. D. Montgomery, Phys. Rev. **76**, 1482 (1949).

Of the 20 pens available on the chart recorder, 16 recorded coincidences between the individual counters in A, B, and C trays and the master. Another pen recorded coincidences between the shower pulse and the master. The remaining three were for the three highest settings of the four-channel discriminator on the ion chamber. The rates of all four discriminators were obtained independently of the chart on mechanical recorders. The bursts of smallest size in the chamber unaccompanied by a counter discharge were not recorded on the chart. Counters S symmetrically placed on each side of the chamber were connected in parallel to make five pairs. When these counters were in operation, they utilized the circuits and recorder pens of either the A or C trays. Thus only three of the four trays A, B, C and S could be operated at the same time.

III. OBSERVATIONS WITH THE B COUNTERS

The bursts in ion chambers at mountain altitude have been analyzed by several observers.[5,6] Bursts of size greater than that corresponding to about $\frac{1}{2}\mathrm{Po}-\alpha$ in the present chamber are found to be produced by three things: (1) radioactive contamination in the walls and the gas of the chamber, (2) nuclear disintegrations in the walls or the gas, and (3) extensive air showers. Corrections were made for the contamination as described previously. Extensive air showers were identified by a coincidence between the D counters and the chamber. It was thus possible to identify star bursts. The 20-pen recorder allowed observation of coincidences IB between the ion chamber I and individual B counters, as well as threefold coincidences IBD in which there was a simultaneous discharge of the shower counters D. Events $IB-IBD$ were separated first into four groups according to the energy range of the burst in I and second by the number (between one and five) of B counters which were simultaneously discharged. Shower-accompanied events ID were separated only by energy ranges. IB was defined as the number of events in I having one or more B counters discharged. Preliminary analysis of the data was made using other criteria for an IB coincidence, such as requiring at least two counters to be discharged or by considering the total number of counters discharged in coincidence with I rather than the number of events. However, the absorption curves obtained by these various methods did not differ significantly, so the original definition was finally used. The fraction of the stars accompanied by the discharge of one or more B counters, $(IB-IBD)/(I-ID-\alpha)$, is the quantity calculated. This corresponds closely to the quantity $AB-ABD/A$ observed in the preliminary experiment.[1] The numerator is the number of coincidences between the chamber and the B counters corrected for extensive air showers. The denominator is the number of bursts caused by stars, which is the total number of bursts corrected for extensive showers and alpha-particle contamination.

[6] Bridge, Hazen, Rossi, and Williams, Phys. Rev. 74, 1083 (1948).

TABLE I. Rates of occurrence of coincidences of the ion chamber I with the counter tray B.

Absorber thickness over B / Burst size	0″	¼″	½″	¾″	1″	1¼″
(a) $(IB-IBD)/(I-ID-\alpha)$ Lead absorber						
$\frac{1}{2}$–$1\frac{1}{2}\alpha$	0.110 ±0.003	0.098 ±0.004	0.094 ±0.003	0.081 ±0.002	0.071 ±0.002	—
$>1\frac{1}{2}\alpha$	0.220 ±0.010	0.185 ±0.016	0.178 ±0.008	0.158 ±0.008	0.137 ±0.008	—
$>3\alpha$	0.137 ±0.016	0.134 ±0.016	0.095 ±0.018	0.099 ±0.014	0.083 ±0.012	—
(b) $(IB-IBD)/(I-ID-\alpha)$ Iron absorber						
$\frac{1}{2}$–$1\frac{1}{2}\alpha$	0.058 ±0.004	—	0.047 ±0.003	0.054 ±0.004	0.041 ±0.003	0.036 ±0.003
$>1\frac{1}{2}\alpha$	0.223 ±0.019	—	0.161 ±0.015	0.171 ±0.017	0.121 ±0.012	0.090 ±0.010
(c) $\frac{(IB-IBD)-(IBS-IBDS)}{I-IS-ID+IDS-\alpha}$ Lead absorber						
$\frac{1}{2}$–$1\frac{1}{2}\alpha$	0.197 ±0.006	0.219 ±0.007	0.181 ±0.006	0.174 ±0.006	0.151 ±0.005	—
$>1\frac{1}{2}\alpha$	0.254 ±0.014	0.230 ±0.017	0.215 ±0.015	0.193 ±0.015	0.184 ±0.015	—
$>3\alpha$	0.253 ±0.030	0.239 ±0.030	—	0.198 ±0.027	0.159 ±0.023	—

Absorption runs were made using lead up to one inch and iron up to $1\frac{1}{2}$ inches between the chamber and the B counters. The S counters and the shielding lead between them and the ion chamber were not present. The data for all the thicknesses of lead over the C counters have been combined. No systematic variation of IB rate with C lead was observed, indicating that there was a negligible number of particles produced in this lead traveling upward into the B tray. Tables I(a) and I(b) are the summary of these data in one differential and two integral energy ranges. The statistical errors shown are the standard deviations of the total number of coincidences at each point. Figure 2 shows a plot of the

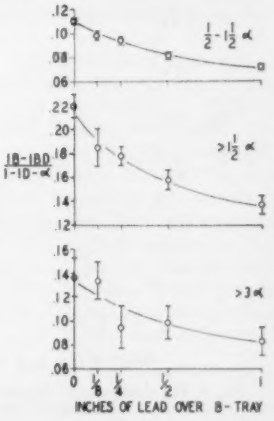

FIG. 2. Fraction of the stars in the chamber having at least one particle capable of penetrating the absorber over the B tray.

TABLE II. Rates of occurrence of coincidences of the ion chamber I with the C counters.

Absorber thickness / Burst size	0″	2″	4″	8″
(a) $(IBC-IBCD)/(IB-IBD)$ Lead absorber				
$\frac{1}{2}$–1$\frac{1}{2}\alpha$	0.59 ±0.03	0.31 ±0.01	0.20 ±0.01	0.125 ±0.010
>1$\frac{1}{2}\alpha$	0.54 ±0.04	0.36 ±0.03	0.23 ±0.02	0.120 ±0.019
>3α	0.56 ±0.07	0.40 ±0.07	0.39 ±0.08	0.31 ±0.08
(b) $\frac{(IBC-IBCD)-(IBCS-IBCDS)}{(IB-IBD)-(IBS-IBDS)}$ Lead absorber				
$\frac{1}{2}$–1$\frac{1}{2}\alpha$	0.562 ±0.022	0.300 ±0.012	0.181 ±0.010	0.097 ±0.008
>1$\frac{1}{2}\alpha$	0.49 ±0.05	0.36 ±0.04	0.23 ±0.03	0.15 ±0.02
>3α	0.50 ±0.09	0.36 ±0.07	0.22 ±0.05	0.15 ±0.05

data of Table I(a). The ordinate is the fraction of stars in the chamber having at least one particle capable of penetrating the corresponding thickness of lead over the B counters. There seems to be little evidence for the presence of electrons, either accompanying the star-producing radiation or which are themselves products of such nuclear disintegrations. There is a range of densities over which there is a reasonable probability of such electrons' striking the B counters and missing the D counters, although an accompanying nuclear disintegration would be required to produce the large burst in the chamber. These results are at variance

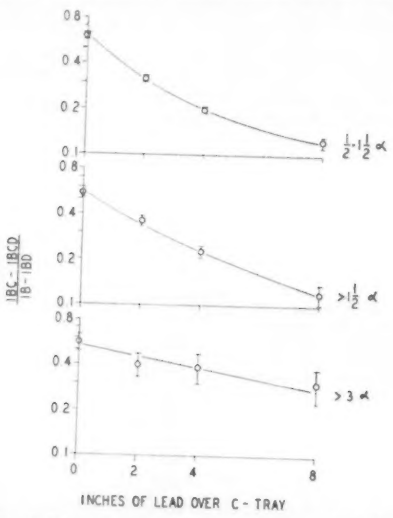

FIG. 3. The absorption of the penetrating rays in the lead over the C counters.

with many cloud-chamber pictures, a recent example being that of Hartzler,[7] in which electrons are frequently observed with penetrating showers and nuclear disintegrations. Counter experiments on penetrating showers[8] have also indicated the presence of electrons.

It was not possible from these measurements to know whether the particles observed by the B tray are products of nuclear disintegrations in the ion chamber or whether they arrived accompanying the star-producing radiation. The S counters were added in an attempt to clarify this problem. Nuclear emulsion data indicate that the penetrating component of nuclear disintegrations is usually collimated about the direction of the incident particle, while the low energy evaporation particles are nearly isotropically distributed. Thus, since the star-producing radiation is predominantly in the vertical direction, any penetrating products should also continue nearly vertically, with only low energy particles being projected at right angles. The 116 g/cm^2 in the four inches of shielding lead between the ion chamber and the S counters is sufficient to stop 320-Mev protons. Thus there should be no product particles of the star capable of reaching the S counters. The data for these absorption measurements with lead over the B tray are listed in Table I(c). Any burst in the chamber in which there was a coincident discharge of any of the S counters was rejected. The quantity $(IB-IBD-IBS+IBDS)/(I-IS-ID+IDS-\alpha)$ is the fraction of the stars not accompanied by a particle through the S tray which have at least one particle capable of penetrating the lead over the B tray. About ten percent of the $(IB-IBD)$ events were rejected because of a coincident discharge of the S tray. This number was much smaller than expected. Although only short runs were made with this arrangement, the rejection of such a small number of events would not be expected to change the shape of the absorption curve noticeably. Note that the rates in Table I(c) are slightly higher, even after correcting for S events, than those in Table I(a). This is probably due to disintegrations taking place in the lead between S and I which produce heavily ionizing particles passing through the chamber and others striking the B counters.

IV. OBSERVATIONS WITH THE C COUNTERS

The penetrating particles of stars produced in the ion chamber were detected by the counters of the C tray, over which lead bricks up to a total thickness of eight inches could be placed. The data are analyzed in much the same way as those of the B tray. The coincidence IBC is defined as the simultaneous discharge of the ion chamber and at least one counter each in the B and C trays, while $IBCD$ includes the discharge of at least three of the four shower counters. Because of the low rates obtained, it was necessary to average each point on the C absorption curve over all the small

[7] A. J. Hartzler, Phys. Rev. **82**, 359 (1951).
[8] Greisen, Walker, and Walker, Phys. Rev. **80**, 535 (1950).

TABLE III(a). Rates of occurrence of coincidences between the ion chamber and the S counters.

	$(IS-ISD)/(I-ID-\alpha)$ Lead absorber						
Absorber thickness	0″	¼″	½″	1″	2″	4″	8″
Bursts $\frac{1}{2}-1\frac{1}{2}\alpha$	0.024 ±0.001	0.027 ±0.004	0.019 ±0.003	0.021 ±0.002	0.025 ±0.003	0.020 ±0.002	0.021 ±0.002
Bursts $>1\frac{1}{2}\alpha$	0.029 ±0.003	0.021 ±0.007	0.026 ±0.008	0.029 ±0.006	0.031 ±0.007	0.029 ±0.006	0.016 ±0.005

thicknesses of B lead. The effect of the B lead is minimized by calculating the quantity $(IBC-IBCD)/(IB-IBD)$, the fraction of the stars in the chamber having at least one particle striking the B tray and at least one able to penetrate the lead over the C tray. This corresponds to the quantity $(ABC-ABCD)/AB$ observed in the preliminary experiment. Table II(a) gives the data obtained by adding lead over the C counters and Fig. 3 is the semilogarithmic plot of the data in the three energy ranges. At least four runs were made at each point and were self-consistent. The statistical errors are the standard deviations of the total data for each point.

Table II(b) lists the data obtained from runs made after the addition of the S counters and the shielding lead between them and the chamber. The rejection of all coincidences in which an S counter was discharged should eliminate any contribution from particles not actually disintegration products of the star. The data listed represent the quantity $(IBC-IBCD-IBCS+IBCDS)/(IB-IBD-IBS+IBDS)$. Elimination of the S-accompanied events changes the data only slightly.

If one assumes that the particles of this penetrating component undergo catastrophic collisions in the lead over the C counters, the absorption mean free path may be obtained from the above data. The data of Table II(a) in the $\frac{1}{2}$–$1\frac{1}{2}\alpha$ energy range correspond to a mean free path of 91 ± 10 g/cm² at small thicknesses of lead and 250 ± 80 g/cm² at the maximum thickness. The corresponding values for Table II(b) are 92 ± 11 g/cm² and 190 ± 40 g/cm², respectively. The curves on a semilogarithmic plot for the intermediate energy range, $>1\frac{1}{2}\alpha$, are linear within the statistical errors and correspond to mean free paths of 154 ± 20 g/cm² and 191 ± 40 g/cm² for II(a) and II(b), respectively. The data are so few for the highest energy range that any such calculations would be meaningless. It should be noted that the average number of penetrating particles per star is approximately the same in all three energy ranges. It must be concluded that large bursts in the chamber do not necessarily correspond to high energy nuclear events since these latter would be expected to have larger numbers of penetrating particles.

V. ABSORPTION OF THE ASSOCIATED PARTICLES

It was mentioned previously that approximately ten percent of the stars in the chamber having B counters discharged also had at least one S counter discharged. Absorption measurements were made of these "accompanying" particles using lead on top of the two S trays. Table III(a) is a summary of the results. The errors are, again, standard deviations. The quantity calculated is $(IS-ISD)/(I-ID-\alpha)$, which is the fraction of the stars in the chamber having at least one associated particle which strikes the S counters as a function of the thickness of lead directly above the two S trays. The shielding lead between the chamber and the S counters was present at all times in these runs.

TABLE III(b). Number of S counter discharges in coincidence with the ion chamber as a function of distance between the counter and chamber axis.

Lateral distance between S counter and chamber	7½″	8½″	9½″	10½″	11½″
Counts	411	382	281	225	235

Although the small number of events makes the accuracy of the points very poor, especially in the higher energy range, we still have some idea of the absorption characteristics. There is no significant indication of absorption or production at small thicknesses, eliminating the possibility that any appreciable fraction of these particles are electrons or low energy protons or mesons. There is hardly a statistically significant decrease in rate even up to the maximum of eight inches of lead. The lower limit for the mean free path for absorption in both energy ranges is 500 g/cm². This result might well be misleading for either of two reasons. In the first place, the above conclusion that the particles are very little absorbed would suggest that perhaps these bursts in the chamber are produced by particles arriving in nearly the horizontal direction, striking the S tray, and producing a burst in the chamber. Particles moving in such a direction would have to discharge several counters in the S tray. The number of events in which $1,\cdots5$ pairs of counters in the S tray were discharged were 909, 331, 144, 90, 80, respectively. There is thus no indication of a predominant number of particles arriving in a horizontal plane and thus missing the S lead.

There is a second, more probable, interpretation of such a very long mean free path. Showers of penetrating particles, produced by the "N-component" of cosmic rays, have been measured by many observers.[8,9] They are thought to be mostly nucleons and mesons formed in some sort of a nuclear cascade process. Care must be taken in designing an experiment to measure the absorption of these particles since there is simultaneous production of particles along with the absorption. Such processes can give data indicating very long mean free paths.[10] The very high penetration of the particles triggering the S counters in the present experiment indicates that some such nuclear cascade process is

[9] J. Ise, Jr., and W. B. Fretter, Phys. Rev. **76**, 933 (1949); K. Sitte, Phys. Rev. **78**, 714 (1950).
[10] O. Piccioni, Phys. Rev. **77**, 6 (1950).

TABLE IV. Transition effect obtained with lead over the A-tray.

Absorber thickness / Burst size	0″	¼″	½″	1″	2″	4″
	(a) $(IA-IAD)/(I-ID-\alpha)$					
½–1½α	0.167 ±0.008	0.226 ±0.009	0.336 ±0.010	0.363 ±0.010	0.299 ±0.009	0.209 ±0.011
>1½α	0.256 ±0.026	0.307 ±0.028	0.363 ±0.028	0.524 ±0.030	0.432 ±0.026	0.321 ±0.033
	(b) $(IB-IBD)/(I-ID-\alpha)$					
½–1½α	0.053 ±0.004	0.119 ±0.006	0.230 ±0.008	0.253 ±0.008	0.193 ±0.007	0.120 ±0.008
>1½α	0.199 ±0.022	0.231 ±0.024	0.393 ±0.032	0.498 ±0.029	0.375 ±0.024	0.294 ±0.032
	(c) Average number of counters per event in A-tray					
½–1½α	1.24 ±0.02	1.96 ±0.05	2.61 ±0.05	2.83 ±0.04	2.64 ±0.05	2.30 ±0.08
>1½α	1.43 ±0.10	1.92 ±0.08	3.28 ±0.14	4.02 ±0.11	3.26 ±0.14	3.23 ±0.21
	(d) Chamber bursts per hour corrected for contamination					
>½α	219 ±11	298 ±12	418 ±14	382 ±13	300 ±12	236 ±11
>1α	78 ±6	81 ±6	116 ±7	123 ±7	101 ±7	80 ±6
>1½α	34 ±3	41 ±4	56 ±4	62 ±4	45 ±4	41 ±4
>2α	20 ±3	23 ±3	30 ±3	35 ±3	23 ±3	23 ±3

taking place. One of the particles of such a shower could cause a burst in the ion chamber. The grouping of the ten S counters into five pairs makes it possible to obtain decoherence data for the accompanying particles that give an idea of their lateral spread. The number of times given pairs of S counters were discharged is listed in Table III(b).

VI. OBSERVATIONS WITH LEAD OVER THE A TRAY

Earlier work by the Montgomerys[5] indicated that a ¼-inch lead shield placed on top of an ion chamber produced multiplication of the electrons in extensive air showers by the factor 1.7. The star rate, after correction for extensive showers, was hardly increased beyond the error of measurement. It was thought feasible to make absorption measurement using, above the chamber, a tray of counters covered with small thicknesses of lead. Discharges of these A counters in coincidence with the chamber would be caused either by the incident primary particle which produces the star or some other particle accompanying it, or by a disintegration product of the star being projected in the backwards direction. Neither high energy ionizing particles nor neutral particles would be absorbed in a measurable amount in the small thicknesses of lead originally intended to be used above the A counters. In the preliminary experiment,[1] the B-tray data indicated the possible presence of electrons accompanying the incident particle producing the star. If such electrons exist, the lead should produce a transition effect in the A and B counter trays. A very large transition effect of this kind was observed. The measured quantity for the A tray is $(IA-IAD)/(I-ID-\alpha)$, the fraction of the bursts in the chamber accompanied by the discharge of at least one counter in the A tray, after correction for extensive air showers. The same effect is found in the B tray, where the quantity $(IB-IBD)/(I-ID-\alpha)$ as a function of lead over the A tray is measured. The data for these runs are listed in Tables IV(a) and IV(b). The data charts were also analyzed in such a way as to know the number of counters discharged in each tray in each chamber event, so that the average number of counters per coincidence event could be calculated. The transition effect in this quantity for the A tray is shown by the data in Table IV(c). Much the same data are obtained from the B tray and are not listed.

The very large transition with a maximum at about one inch of lead indicates that the particles discharging the counters are electrons. Observations were also made when the S counters were present. The curves are quite similar to those obtained without the S counters and shielding lead, both before and after correcting the data for those events in which at least one S counter was triggered. These electrons cannot be coming from the star since the A lead is on the opposite side of the A tray from the chamber. A second alternative, that the electrons accompany a particle producing the burst in the chamber, is not possible since an equivalent transition effect in the B tray would be observed with the addition of B lead. If the particles had a lateral distribution of at least a foot, the same transition should have been observed for lead placed over the S trays. It was concluded that this large number of coincidences came from additional bursts in the chamber caused by electron cascades produced in the lead above.

To test this hypothesis careful measurements were made during short runs to obtain the variation in chamber burst rate alone as a function of lead thickness above. The results are listed in Table IV(d) giving the rate per hour of occurrence of bursts greater than a given size. Integral corrections for radioactive contamination of 125 bursts per hour at one-half alpha size and 30 per hour at one alpha size have been applied. There is a marked transition effect in all burst ranges. Approximately 16 electrons, traveling an average path length of $\frac{1}{4}\pi D$ through the chamber in the vertical direction, would be necessary to produce a burst one-half the size of an alpha-particle. It is instructive to make some approximate calculations on the rates of occurrence of low density extensive air showers. The maximum of the chamber transition curve for the smallest energy range is estimated to be at ⅝ inch of lead, equivalent to 3.1 radiation lengths. Curves given by Montgomery[11] may be used to estimate the multi-

[11] D. J. X. Montgomery, *Cosmic Ray Physics* (Princeton University Press, Princeton, 1949), p. 71.

plication factor. Assuming that the average energy of an electron incident on top of the lead is 100 Mev, the critical energy for air, and that all electrons under the lead having energies greater than 1 Mev will pass through the chamber wall and be detected, then the curves show that the peak multiplication factor at that point is seven. Thus, on the average, 2.3 air-shower electrons incident on top of the A lead in an area equal to that of the ion chamber will produce a burst of 16 electrons in the chamber. Since the area of the chamber is 356 cm^2, showers of density greater than 65 electrons per square meter will be detected. Cocconi[12] has found the number of showers per second with densities greater than D electrons per square meter at Echo Lake to be $1.68D^{-1.46}$. This rate will be increased by the factor 1.25 at Climax because of the difference in altitude. This gives 17 showers per hour that should be detected at the maximum of the transition. The ID rate, the extensive showers detected by the chamber and the shower counters, is about two per hour with no A lead and twelve per hour at the maximum, which is in fair agreement with the rough calculations above. The shower counters are 96 percent efficient for the density of 65 particles per square meter.

It is thus evident that the observed chamber transition of an additional 200 bursts per hour cannot be due to low density extensive air showers. Wei[13] has obtained rates of occurrence of narrow air showers and their absorption properties, concluding that they are mixtures of electrons and a hard component, very likely mesons. He finds[14] 160 narrow showers per hour of two particles and 87 per hour of three particles. These rates are comparable to the observed increase in ion chamber rate of about 200 per hour. Thus it is possible we were detecting the electron component of narrow air showers. The average energy of such electrons, and thus the transition effect to be expected, is not known.

The author wishes to express his indebtedness to Professor C. G. Montgomery who suggested this work and directed it through most of its stages. D. D. Montgomery has been very helpful in directing the final parts of the data analysis. The experiments at Climax, Colorado, were made possible through the hospitality of Professor Marcel Schein and Mr. Thomas Stinchcomb of the University of Chicago, Professor J. C. Street of Harvard University, the members of the High Altitude Observatory of Harvard University and the University of Colorado, and Mr. C. J. Abrams of the Climax Molybdenum Company.

[12] G. Cocconi and V. Tongiorgi, Phys. Rev. **75**, 1058 (1949).

[13] J. P. N. Wei, Phys. Rev. **79**, 670 (1950).

[14] J. P. N. Wei, thesis, Yale University, 1950.

PHYSICAL REVIEW VOLUME 84, NUMBER 1 OCTOBER 1, 1951

A Note on Isotropy in Nuclear Gamma-Radiation*

G. B. Arfken, L. C. Biedenharn, and M. E. Rose
Oak Ridge National Laboratory, Oak Ridge, Tennessee

(Received June 22, 1951)

The question of the possibility of competing radiations exhibiting different angular distributions (in the sense that one radiation is isotropic and another anisotropic) is investigated. Except for the singular cases $\frac{1}{2}\to\frac{1}{2}$ and $5\to4$ by quadrupole emission, our conclusion is as follows: if one radiation of multipole order 2^L is observed to be isotropic, all competing gamma-radiation will be isotropic if $L\geq j-\frac{1}{2}$, where j is the angular momentum of the emitting state. The possibility of occurrence of singular cases, for which the conclusion would not apply, has been investigated for all radiations for which $L\leq3$. In the case $\frac{1}{2}\to\frac{1}{2}$, $L=2$ the radiation is isotropic and the applicability of this to the problem of the excited state of Li^7 is briefly discussed.

I. INTRODUCTION

We consider a compound nuclear state formed by capture of some particle by a target nucleus and the subsequent decay of the state by two (or more) competing processes. In what follows we restrict our attention to the case in which the competing radiations are γ-rays. It will be clear that our conclusions apply equally well for the emission of α-particles (or, in general, spinless particles). The problem to be considered may be stated as follows: if one of the gamma-radiations is observed to be isotropic, under what conditions must the competing radiations also exhibit isotropic angular distributions? Conversely, under what circumstances may the competing radiations exhibit an anisotropic distribution with respect to the incident beam or some other physically defined direction? It is understood, of course, that the transmutation leading to the γ-emitting state involves p (or higher angular momentum) waves for the relative motion of incident particles and target nucleus. This problem arises, for example, in the proton bombardment of B^{11} with the subsequent emission of an isotropic (within experimental error) 16-Mev γ-ray to the C^{12} ground state presumably competing with a double cascade of 12- and 4-Mev radiations.[1]

* This paper is based on work performed for the AEC at the Oak Ridge National Laboratory.

[1] Kern, Moak, Good, and Robinson, Phys. Rev. **83**, 211(A) (1951); G. B. Arfken and L. C. Biedenharn, *ibid.*, 238(A).

It is obvious that from a compound state of angular momentum j with all $2j+1$ degenerate substates equally populated and randomly phased (e.g., capture of unpolarized s-particles), all radiation must be isotropic. If the converse were valid, i.e., if isotropy of one radiation implied equal populations and random phases for the emitting state, it would follow that all other radiation would have to be isotropic. However, while this would be a sufficient condition for isotropy, it is not a necessary one, since isotropy follows even with unequal populations. Thus, gamma-radiation, observed with polarization insensitive detectors, would have the same angular distribution for emission from the substates $\pm m$. Then, if the population of the substate m is a_m, a sufficient condition for isotropy is

$$2a_0=a_1+a_{-1}=\cdots=a_j+a_{-j} \quad (j \text{ integer}), \tag{1}$$

or, generally, a_m+a_{-m} independent of m. Of course, uniform population is a special case. As is shown below, Eq. (1) is a necessary condition for isotropy except in a very few special cases which are explicitly exhibited in the following. Therefore, the question in hand is to determine whether the observation of a single isotropic 2^L pole radiation implies Eq. (1).

II. ISOTROPY THEOREM

Following Falkoff and Uhlenbeck[2] we write the angular distribution of pure 2^L pole gamma-radiation from the state j, m with population a_m to a state j', m' in the form,

$$I(\vartheta)\sim\sum_{mM} a_m(C_{mM}{}^{jLj'})^2F_L{}^M(\vartheta). \tag{2}$$

Here $C_{mM}{}^{jLj'}$ is the vector addition coefficient, and M is the magnetic quantum number of the radiation. The $F_L{}^M(\vartheta)$ are the classical angular distribution functions for 2^L pole electromagnetic radiation and for our purposes it is most convenient to represent them in the form[3]

$$F_L{}^M(\vartheta)=\sum_{P=\pm1}[D_{MP}{}^{(L)}(0\vartheta 0)]^2, \tag{3}$$

where the $D_{MP}{}^{(L)}$ are the elements of the irreducible rotation matrix of order L. It will be noted that, by the assumption of random phases, we have eliminated cross terms in Eq. (2). If the state j is excited by a process that defines only a single direction in space, this assumption is always justified.

Using the properties of the rotation matrices $D^{(L)}$, we can transform $F_L{}^M$ as follows:[3]

$$\begin{aligned}F_L{}^M(\vartheta)&=(-)^{M+1}\sum_P D_{MP}{}^{(L)}(0\vartheta 0)D_{-M-P}{}^{(L)}(0\vartheta 0)\\&=(-)^{M+1}\sum_P\sum_{\tau=0}^{2L}C_{P-P}{}^{LL\tau}C_{M-M}{}^{LL\tau}D_{00}{}^{(\tau)}(0\vartheta 0)\\&=(-)^{L+1}\left(\frac{16\pi}{2L+1}\right)^{\frac{1}{2}}\\&\quad\times\sum_{\nu=0}^{L}C_{1-1}{}^{LL2\nu}C_{M0}{}^{L2\nu L}Y_{2\nu}{}^0(\cos\vartheta),\end{aligned} \tag{4}$$

since $C_{1-1}{}^{LL\tau}+C_{-11}{}^{LL\tau}$ vanishes when $2L-\tau$ is odd. We now introduce a notation for the sum over M in Eq. (2),

$$f_{Ljj'}{}^m\equiv\sum_M(C_{mM}{}^{jLj'})^2F_L{}^M(\vartheta), \tag{5}$$

which is the quantum-mechanical angular distribution function for radiation emitted from the substate m. From the definition it is clear that the functions f are even in m, since $F_L{}^M$ is even in M. We utilize this symmetry by summing in Eq. (2) over non-negative m only and, after introducing the new populations b_m defined by

$$\begin{aligned}b_m&=a_m+a_{-m}, \quad m\neq0,\\b_0&=a_0,\end{aligned} \tag{6}$$

where the second of Eq. (6) applies only for j integer, Eq. (2) takes the form,

$$I(\vartheta)\sim\sum_{m\geq0}^{j}b_mf_{Ljj'}{}^m(\vartheta). \tag{7}$$

By hypothesis $I(\vartheta)$ is independent of ϑ for one pair of values of L, j'. If the $f_{Ljj'}{}^m$ are a linearly independent set of functions in m for each L, j, j', it would follow that all radiation from j is isotropic. This is because a known solution of Eq. (7) is b_m a constant independent of $m(b_m=2b_0)$. If the $f_{Ljj'}{}^m$ are linearly independent, the solution for the b_m is unique. Therefore, we investigate the conditions under which the f^m-functions form a linearly independent set. Substituting Eq. (4) into Eq. (5), we obtain

$$\begin{aligned}f_{Ljj'}{}^m(\vartheta)&=(-)^{L+1}\left(\frac{16\pi}{2L+1}\right)^{\frac{1}{2}}\\&\quad\times\sum_{\nu=0}^{L}\sum_M(C_{mM}{}^{jLj'})^2C_{1-1}{}^{LL2\nu}C_{M0}{}^{L2\nu L}Y_{2\nu}{}^0.\end{aligned} \tag{8}$$

Using the Racah coefficients,[4] the summation over M can be performed. The relation required is

$$\begin{aligned}C_{M0}{}^{L2\nu L}C_{Mm}{}^{Lj j'}&=\sum_{j_1}(2L+1)^{\frac{1}{2}}(2j_1+1)^{\frac{1}{2}}\\&\quad\times C_{0m}{}^{2\nu jj_1}C_{Mm}{}^{Lj_1j'}W(L2\nu j'j;Lj_1).\end{aligned} \tag{9}$$

From the properties of the vector addition coefficients we have

$$\begin{aligned}\sum_M(C_{mM}{}^{jLj'})^2C_{M0}{}^{L2\nu L}&=(2j'+1)(2L+1)^{\frac{1}{2}}(2j+1)^{-\frac{1}{2}}\\&\quad\times C_{0m}{}^{2\nu jj}W(L2\nu j'j;Lj).\end{aligned} \tag{10}$$

Then the final form for $f_{Ljj'}{}^m(\vartheta)$ is[4]

$$\begin{aligned}f_{Ljj'}{}^m(\vartheta)&=(-)^{L+1+j-m}(16\pi)^{\frac{1}{2}}(2j'+1)\\&\quad\times\sum_{\nu=0}^{L}C_{m-m}{}^{jj2\nu}C_{1-1}{}^{LL2\nu}(4\nu+1)^{-\frac{1}{2}}\\&\quad\times W(L2\nu j'j;Lj)Y_{2\nu}{}^0(\cos\vartheta).\end{aligned} \tag{11}$$

We now establish a necessary condition for the linear independence of the f^m set. The Racah coefficients in

[2] D. L. Falkoff and G. E. Uhlenbeck, Phys. Rev. **79**, 323 (1950).
[3] For example, G. Goertzel, Phys. Rev. **70**, 897 (1946).
[4] G. Racah, Phys. Rev. **62**, 438 (1942); Phys. Rev. **63**, 367 (1943).

Eq. (11) vanish unless the "triangular conditions" are simultaneously satisfied for all three sets $(LL2\nu)$, $(Lj'j)$, and $(jj2\nu)$. That is, it must be possible to form a triangle from each of these sets of three numbers. This condition is just the angular momentum conservation for $(Lj'j)$. For the other pair we deduce that the maximum value of ν is the lesser of the two numbers j and L, if j is an integer, or the lesser of $j-\frac{1}{2}$ and L if j is a half-integer. Since the $Y_{2\nu}{}^0$ are linearly independent, it is necessary that

$$L \geqslant j-\tfrac{1}{2} \tag{12}$$

for the $f_{Lj'j}{}^m$ to be linearly independent. This covers both cases: j integer or half-integer.

If the condition expressed by Eq. (12) is fulfilled, the linear independence of the f^m is assured, provided that the determinant

$$|d_m{}^\nu| \equiv |C_{m-m}{}^{ij2\nu} C_{1-1}{}^{LL2\nu} W(L2\nu j'j; Lj)| \neq 0. \tag{13}$$

Since the factors depending only on ν factor out of the determinant, we must investigate (a) the possibility of $\det C_{m-m}{}^{ij2\nu}$ vanishing, (b) the possibility of roots of $C_{1-1}{}^{LL2\nu}$, and (c) the possible roots of $W(L2\nu j'j; Lj)$.

(a) We cannot immediately conclude that $\det C_{m-m}{}^{ij2\nu} \neq 0$ from the unitary property of the vector addition coefficients, since we have restricted m to non-negative values and also because 2ν is always an even integer. This reduces the determinant in question to dimension $j+1$ (j integer) or $j+\frac{1}{2}$ (j half-integer). Nevertheless, we can show that $\det C_{m-m}{}^{ij2\nu} \neq 0$ by defining a matrix $B_m{}^\nu$ whose rows are $C_{m-m}{}^{ij2\nu}$ except for $m=0$, and for $m=0$ we set $B_0{}^\nu = 2^{-\frac{1}{2}} C_{00}{}^{ij2\nu}$. Then, we have

$$(\bar{B}B)_{\lambda\nu} = \sum_\mu \bar{B}_{\lambda\mu} B_{\mu\nu} = \sum_{\mu \neq 0} C_{\mu-\mu}{}^{ij2\nu} C_{\mu-\mu}{}^{ij2\lambda} + \tfrac{1}{2} C_{00}{}^{ij2\nu} C_{00}{}^{ij2\lambda}$$

$$= \tfrac{1}{2} \sum_{\mu=-j}^{j} C_{\mu-\mu}{}^{ij2\nu} C_{\mu-\mu}{}^{ij2\lambda} = \tfrac{1}{2} \delta_{\lambda\nu}. \tag{14}$$

Therefore $\det B_m{}^\nu \neq 0$ and $\det C_{m-m}{}^{ij2\nu} \neq 0$.

(b) The vector addition coefficient $C_{1-1}{}^{LL2\nu}$ can be expressed in terms of $C_{00}{}^{LL2\nu}$ by using

$$Y_L{}^M Y_L{}^{-M} = \tfrac{1}{2}(2L+1)\pi^{-\frac{1}{2}} \times \sum_{\nu=0}^{L} (4\nu+1)^{-\frac{1}{2}} C_{00}{}^{LL2\nu} C_{M-M}{}^{LL2\nu} Y_{2\nu}{}^0.$$

Using the properties of the spherical harmonics, we obtain

$$C_{1-1}{}^{LL2\nu} = C_{00}{}^{LL2\nu} [\nu(2\nu+1) - L(L+1)] / L(L+1). \tag{15}$$

Since $C_{00}{}^{LL2\nu} \neq 0$ for any L, ν, the roots in question are those of the square bracket in Eq. (15). With $L \geqslant 1$ the lowest root is $L=14$, $\nu=10$; and, although our isotropy theorem does not hold in this case, 2^{14} pole radiation is hardly of physical interest. (For spinless particles the only change in Eq. (11) is the replacement of $C_{1-1}{}^{LL2\nu}$ by $C_{00}{}^{LL2\nu}$.)

(c) Investigation of the Racah coefficient $W(L2\nu j'j; Lj)$ shows that (with the triangular conditions satisfied) this coefficient vanishes for

$$j = j' = \tfrac{3}{2}, \quad L=2, \quad \nu=1, \tag{16a}$$

and for

$$j=5, \quad j'=4, \quad L=2, \quad \nu=1. \tag{16b}$$

We have investigated all cases for $L=1$, 2, and 3. Thus, while there may be similar anomalous cases for radiation higher than octupole (the investigation of which would be exceedingly laborious), it is felt that from a practical point of view these cases would not be of great interest.

We therefore conclude that for the emission of octupole or lower multipole radiation a necessary and sufficient condition for the impossibility of isotropic and anisotropic radiations originating from the same level is $L \geqslant j-\frac{1}{2}$, where L refers to the isotropic radiation, and that neither Eq. (16a) nor Eq. (16b) applies.

In the $B^{11}(p,\gamma)C^{12}$ reaction preliminary results[4] show isotropy for the cross-over and definite anisotropy for the 12-Mev radiation which is known to precede the 4-Mev γ-ray. The condition (12) is fulfilled. Therefore, accepting the experimental evidence at face value, we must conclude that the 16- and 12-Mev radiations originate from different levels.

For the quadrupole emission from $j=\frac{3}{2}$ to $j'=\frac{3}{2}$ the angular distribution of the radiation will be isotropic.[5] This result has a possible application to the interpretation of the $Li^7(p,p')Li^{7*}(\gamma)Li^7$ and $B^{10}(n,\alpha)Li^{7*}(\gamma)Li^7$ reactions. The observation of isotropic γ's in these cases does not compel one to conclude that $j=\frac{1}{2}$ for the relevant state of Li^{7*}. As a logical possibility $j=\frac{3}{2}$ should be considered. However, other evidence may be cited which makes the interpretation $j=\frac{3}{2}$ somewhat difficult.[6] Nevertheless, it may be of interest in connection with other reactions that isotropic radiation emitted from odd mass nuclei does not necessarily imply $j=\frac{1}{2}$ for the emitting state.

[5] This conclusion is implicitly contained in the results of S. Devons, Proc. Phys. Soc. (London) **62A**, 580 (1949) and also in the results of reference 2. For Eq. (16b) only the coefficient of $Y_2{}^0$ is absent and the angular distribution is not isotropic.

[6] D. R. Inglis, Phys. Rev. **82**, 181 (1951); L. G. Elliott and R. E. Bell, Phys. Rev. **76**, 178 (1949).

Point-to-Plane Corona in Dry Air*

HERMAN W. BANDEL
Department of Physics, University of California, Berkeley, California
(Received April 30, 1951)

A survey study has been made of point-to-plane corona in dried air for a range of pressures and point sizes. It has been found that negative points can be satisfactorily triggered by ultraviolet illumination and that the difficulties encountered in past attempts have probably been due to too intense illumination and possibly the presence of dust on the points. Under some conditions transitions from Trichel pulses to a pulseless Townsend-type discharge have been observed for negative points at high voltage. With positive points the occurrence of pre-onset streamers has been found to depend on higher pressures and the presence of water vapor to give sufficiently high photon absorbtion. Breakdown streamers are not observed with standard geometry for the usual points sizes, because the first one always closes the gap resulting in breakdown. For points of around 2-mm diameter the gap must be about twice standard length with room air, and about two and one-half times standard length with dried air, for breakdown streamers to be observed.

INTRODUCTION

DESPITE all the corona studies with point-to-plane geometry, no set of consistent data has been obtained for any one gas over an extended pressure range. Miller and Loeb have recently shown the value of such a study with coaxial cylindrical geometry.[1] The recent indication of suitable gap conditions for point-to-plane study permit of such an investigation at this time.[2] The gas chosen was air, since it yields the various manifestations more completely than most gases. In the course of the study numerous apparent contradictions with earlier observations necessitated further study, the results of which are presented in this paper.

APPARATUS

In Fig. 1 the chamber and its parts are drawn approximately to scale. The chamber was a brass cylinder ~30 cm high and 30 cm in diameter. The plane electrode was a 26-cm diameter brass plate.

The points, with one exception mentioned later, were made from platinum wire of 1.0, 0.5, and 0.25 mm diameter. They were worked to the shape of hemispherically capped cylinders accurate to within 2 percent of the diameter and polished with tin oxide. They ranged from 2 to 4 cm in length and were soldered into small mounts that screwed into the end of an 8-mm diameter polished brass rod. The Wilson seal holder was $1\frac{1}{2}$ in. in diameter and was 19.7 cm above the plane, except that when ultraviolet triggering was used for the 0.5- and 0.25-mm points, the plane was raised to about 15.7 and 14.7 cm, respectively, below the seal holder.

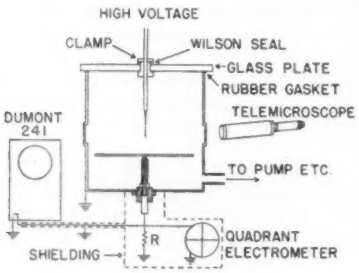

FIG. 1. Diagram of the apparatus.

A standard gap length to point radius ratio of 160 was used throughout.[2] Gap length was set by measuring the distance from the plane to the top of the Wilson seal and then adjusting a clamp on the point holder to the correct distance from the tip of the point, allowing for compression of the rubber gasket. Errors in gap length were probably not greater than 0.25 mm, certainly less than 0.5 mm.

The gas used was room air filtered through glass wool, $CaCl_2$, glass wool, and then a trap cooled by CO_2 snow in alcohol. Pressure was measured with a simple manometer and could be read to within 0.5 mm Hg.

The high voltage was a rectified 500-cycle stabilized and controlled through a saturable core reactor in the transformer primary circuit. The voltage was stable to much better than 1 percent and could be measured to within 10 volts up to 16 kv and within 100 volts above 16 kv.

Low currents were measured with a quadrant electrometer using Victoreen resistors up to 10^{12} ohms for R.

A thorianite ore source of gamma-rays was placed outside the chamber to "trigger" the discharge. This source was strong enough to make burst pulse onset determinations easier and quicker without causing any measurable change in the onset voltages. The low voltage portion of the negative point data was repeated using ultraviolet light triggering as discussed later.

LOW VOLTAGE UP THROUGH ONSET

For the lower voltage part of this work the general procedure was to start at low voltage taking data up to well above onset and then back down again. With positive points using gamma-ray triggering, the data (currents

* This work was done under contract to the ONR.
[1] C. G. Miller and L. B. Loeb, J. Appl. Phys. **22**, 494, 614, 740 (1951).
[2] Loeb, Parker, Dodd, and English, Rev. Sci. Instr. **21**, 42 (1950).

and onsets) for decreasing voltage were always identical with that for increasing voltage, so this repetition was discontinued except for checking onsets (or offsets) after each run. The only data for decreasing positive voltage in the work reported here is shown for the two higher pressure curves in Fig. 3.

The current measurements of 10^{-13} amp and less are only approximate because with a dropping resistor $R=10^{12}$ ohms the plane is nearly insulated from ground and the high voltage is capacity coupled to the electrometer through the point-to-plane capacitance. Then a variation of a few volts in the high voltage results in a strong deflection of the electrometer, while the very low currents to be measured require many minutes to charge the plane and electrometer up to an equilibrium reading. However, the decrease of the ion-collection current with time as seen on the foot of many of these curves (Fig. 3, and tracings of gamma-ray triggered negative curves Figs. 5–7) was a real effect.

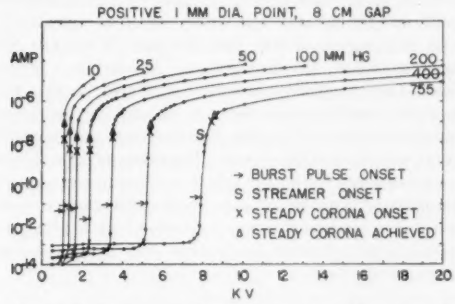

FIG. 2. Positive corona thresholds for 1-mm diameter point, 8-cm gap in air at various pressures indicated on the curves. Note the various thresholds listed in the legend on the figure.

Positive Points (Figs. 2–4)

In general, starting at low voltage with a positive point the current is at first merely the collection of ions formed by external agents. As the voltage is raised, the first change is a gradual increase in current as the electrons moving in the field begin to acquire energies high enough to ionize the gas. The next change is the burst pulse threshold which in this work was taken as the lowest voltage at which pulses could be seen on the Dumont 241 oscilloscope using $R=1$ megohm. This voltage appears quite precise for small points and low pressures where the whole transition from ion collection to steady corona occurs in a range of only tens or hundreds of volts. For a 1-mm point and atmospheric pressure, on the other hand, a number of successive determinations may easily show a spread of 30 to 40 volts. This is because burst pulses are not all the same amplitude and occur randomly, and in the cases of higher pressures and larger points, threshold occurs at higher voltages, so that the same fractional variation in voltage in a larger number of volts.

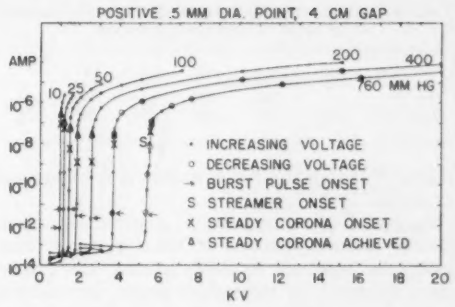

FIG. 3. Positive point corona, 0.5-mm diameter point, 4-cm gap in air at various pressures. Pressures and thresholds indicated on the figure. Note that the curves were retraced with increasing and decreasing voltage to indicate reproducibility.

When the burst pulse duration becomes long enough, or the frequency high enough, the discharge becomes continuous. Although the distinction is somewhat vague, the change to steady corona on the CRO favors an increase in duration with lower pressures and smaller points, and an increase in frequency with higher pressures and larger points. Since burst pulse duration is random, steady corona onset is not sharply defined. In Figs. 2, 3, and 4 the steady corona onset indicated was taken as that point on the curve at which the discharge began to be steady corona for appreciable periods of time, e.g., of the order of $\frac{1}{10}$ of a second. Plots of $\Delta I/\Delta V$ for several cases in which experimental points in this region were especially taken at very close voltage intervals show that the slope of the I-V curves has a strong maximum at this point, but with the CRO this onset can neither be defined nor determined with much precision. Above this voltage, individual burst pulses may still be seen sometimes, and the discharge will still go out for an instant at time intervals up to several seconds. The point at which the discharge is truly continuous and shows no more breaks in the CRO pattern is indicated by the words "steady corona

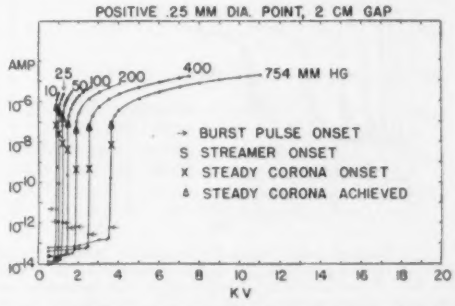

FIG. 4. Positive point corona, 0.25-mm diameter point, 2-cm gap in air at various pressures. Pressures and thresholds indicated on the figure.

TABLE I. Pressure, in mm Hg, below which pre-onset streamers do not occur with standard geometries.

Point diam.	0.08	0.25	0.5	1	1.47	2
Dry air		(760)	670	630	640	690
Room air	720	610	500	360	290	220

achieved," though this too is statistical in nature and not precise.

Because of the uncertainty in determining onsets, and the extreme steepness of the *I-V* curves from burst pulse onset up to steady corona, the current values measured for the various onsets, and marked on the plots, are only order-of-magnitude indications. With reasonable dark adaptation, a long train of burst pulses gives a visible flash of light, so that steady corona onset is also approximately the onset of visible corona.

Above steady corona onset the CRO shows only a wiggly line that gradually smooths out into a clear trace as the voltage is raised. The glow becomes blue and spreads over the point and back along the sides. The visible glow on a positive point appears the same for all geometries and pressures and for dried or moist air.

With either positive or negative points, the current values plotted from onset (burst or Trichel pulse) up to steady corona at about 10^{-7} amp are, of course, only mean values because, owing to the pulsed and intermittent nature of the discharge, the current is continually fluctuating.

With dried air, pre-onset streamers were observed only with the two larger points at atmospheric pressure as indicated on the plotted curves. A brief investigation of this point was necessitated by the general impression form earlier work that such streamers were usual. It appeared that such streamers are not universal with all geometries and with clean, dry air at all pressures. The data are summarized in Table I. The values listed are the pressures below which pre-onset streamers did not occur. These determinations are not very precise or reproducible, since in a given case, as the pressure is lowered, the streamers become only gradually less frequent. Relative humidity of the room air ranged from about 35 to 45 percent. The figure (760) for the 0.25-mm point was inferred partly from extrapolation of a plotted curve and partly from the fact that streamers did appear at atmospheric pressure when the air was not dried carefully enough. Data for the 2-mm point are perhaps questionable because the chamber was not large enough to obtain a reasonable approximation of point-to-plane geometry with a 16-cm gap.

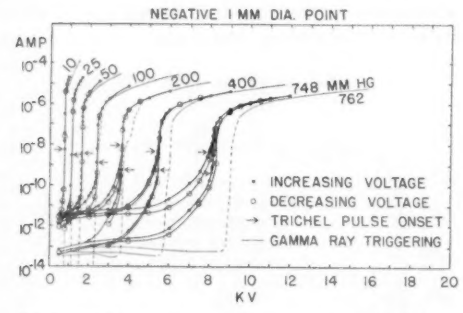

FIG. 5. Negative point corona, 1-mm diameter point, 8-cm gap in air at various pressures. Thresholds indicated in the legend. Note lack of reproducibility of points taken with increasing and decreasing voltage during a single run. Note the difference in the thresholds and the curves with ultraviolet triggering and with gamma-ray triggering. Dashes represent data which are not reproducible because of current fluctuations.

Clearly, the occurence of pre-onset streamers depends on the relative humidity, pressure, and geometry. The dependence on humidity is to be expected in view of the known high absorbtion and photoionization of ultraviolet by water vapor.[3] When the photon absorption is high enough, the emitted photons are absorbed near the tip of an advancing streamer, so that the resulting electron avalanches feeding into the tip can effectively build out the positive ion space charge to extend the high field region farther into the gap. When the absorption is low, the electrons are liberated in a larger volume and their avalanches are scattered, so that the resulting positive ions are too diffuse effectively to extend the high field region. The discharge then spreads over the point as a burst pulse. The pressure dependence is also due merely to the effect of pressure on photon absorption. Why larger point radius favors streamers is not clear, unless the more extensive high field region favors larger electron avalanches and thus streamer propagation.

Negative Points (Figs. 5–7)

With positive points the triggering by gamma-rays is quite satisfactory, because an electron liberated anywhere in the gap passes through the high field region as it goes to the point. With negative points, on the other hand, in order to determine the lowest voltage at which an electron can initiate a Trichel pulse, i.e., a significant onset, there must be electrons starting out from the point surface so as to pass through all of the high field region. With gamma-ray triggering of reasonable intensities the number of electrons liberated near enough to the point to approximate this is very small. Therefore, onset voltage determinations are quite uncertain and usually too high, and above onset the discharge consists of sporadic groups of regular Trichel pulses. It often goes out for seconds or minutes at a time, because whenever the photons and positive ions from one pulse fail to start a following one, the discharge must wait for triggering by the external source. As the voltage is raised, the sensitive volume about the point, from which a liberated electron will pass through enough of the high region to initiate a pulse, increases, so that the times that the discharge is out become shorter.

[3] L. P. Granath, Phys. Rev. **34**, 1045 (1929).

They also become less frequent because more ions are produced per pulse. At high enough voltage, of course, the discharge becomes independent of external triggering.

Previous workers[4,5] have tried various techniques to obtain suitable triggering of negative points, including photo- and thermal emission, and triggering by dusts on the point. MgO and Al_2O_3 powers were tried in this work but were deemed unsatisfactory because, in addition to the difficulty of keeping the dust on the point, it was found that the discharge characteristics (onset voltage, current, and visual and oscilloscopic appearance) depended markedly on the size of the dust particles or aggregates, and at least somewhat on their density on the point. Always, these changes in the character of the discharge become objectionably large before the dusting was sufficient to give continuous triggering.

Satisfactory triggering was ultimately achieved by illuminating the point with ultraviolet light to liberate photoelectrons. A quartz lens was used to focus the light from a quartz mercury arc lamp onto the point. With this triggering, random Trichel pulses appeared as soon as the threshold voltage was reached; and as the voltage was raised, they occurred more frequently and quickly became regular in frequency and amplitude. The reason why this method had failed to give suitable triggering in earlier attempts could not at first be found. The work was, however, continued with this triggering to obtain the data of Figs. 5–7. For the 1-mm point comparison curves were run at 1 atmos, 400 mm, and 200 mm Hg with the intensity of the light very much reduced by stopping down the beam. The atmospheric pressure curves cannot be directly compared because of the difference in pressure, but at 200 and 400 mm Hg the Trichel pulse thresholds were the same in both cases. After this check the more intense illumination was used because of greater speed and ease of measuring prethreshold currents. The effectiveness of the photoelectric currents of two amplitudes is clearly reflected in the prethreshold currents. Compare these with corresponding portions of the positive curves of Fig. 2. That the electrons came from the point on ultraviolet illumination was confirmed by illuminating the gas near the point. No triggering was experienced.

The failure of earlier workers to achieve satisfactory ultraviolet triggering merited further study. It had been noted by English[6] that sometimes ultraviolet illumination had the effect of inhibiting Trichel pulses, i.e., an increase in light intensity just above onset would sometimes stop the pulses rather than increase the number of them. In this work it was found that this effect could usually be observed by using a dusted point, though not always. It also occurred to some extent with a clean point. Current measurements with a 1-mm diameter

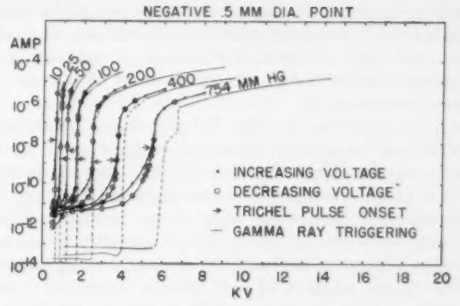

FIG. 6. Negative point corona, 0.5-mm diameter, 4-cm gap in air at various pressures with gamma-ray and ultraviolet triggering and increasing and decreasing voltages indicated on the figure.

point showed that when this inverse effect occurred strongly enough to raise Trichel pulse onset by 100 volts or more, the current before onset was already greater than 10^{-8} amp, while above onset it was appreciably less than the current measured when this inverse effect did not occur. The interpretation is simply that the dust serves as a triggering agent in addition to the ultraviolet light. When this excessive triggering gives pre-onset currents of 10^{-8} amp and greater, the negative ion space charge is sufficient to limit the current continuously and thus prevent Trichel pulses at the normal threshold voltage. After the voltage has been raised enough so that pulses begin to occur anyway, because the space charge resulting from the excessive triggering is not localized in a narrow region out from the one spot on the tip of the point as it is from a Trichel pulse, and because it is formed continuously, the field clears more slowly than it would with less triggering. This results in less frequent Trichel pulses and less average current. The dust then is not necessary to get this inhibiting effect; it is only the total amount of triggering, however achieved, that causes it. To get good triggering for onset determinations, the point should be clean and the illumination not too strong. A lens to focus the light on the point is

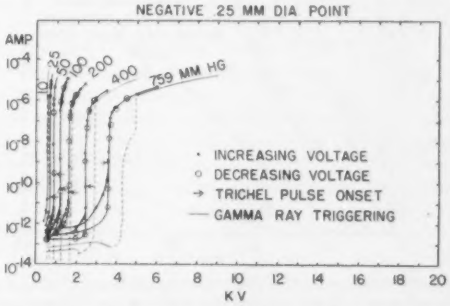

FIG. 7. Negative point corona, 0.25-mm diameter point, 2-cm gap in air at various pressures. Increasing and decreasing voltage. Gamma-ray and photoelectric triggering.

[4] Loeb, Kip, Hudson, and Bennett, Phys. Rev. **60**, 714 (1941).
[5] W. N. English, Phys. Rev. **74**, 170 (1948).
[6] W. N. English and L. B. Loeb, J. Appl. Phys. **20**, 707 (1949).

not necessary. With this in mind, a glance at the data shows the illumination used in this work to have been stronger than is desirable; however, a recheck with weaker illumination gave the same onset voltages so it was not too strong.

The light lines in Figs. 5–7 are traces from data taken with the same gamma-ray triggering as used with positive points. The dashed portion shows approximate mean values in the region where the discharge is intermittent; and there really is no current voltage curve, since the current fluctuates randomly by many orders of magnitude. One of the reasons for studying this was to see whether or not, after a point had been cleaned up by running a discharge, it would remain cleaned up as the voltage was decreased below the original onset of steady corona. That is, if the higher γ (coefficient for emission of secondary electrons by positive ion bombardment) resulting from clean-up persisted as the voltage decreased, the discharge could continue to be steady corona down into the voltage range where it had been intermittent on the way up. This did occur to some extent with the 0.25-mm points where the high field region, and therefore the discharge, is confined to a small region on the tip, but not appreciably with the larger points where the discharge tends to move about from one active cathode spot to another anyway. This data is not included because it does not warrant additional figures or further confusion of the ones shown.

The *I-V* curves for decreasing voltage begin to drop below those for increasing voltage shortly above Trichel pulse threshold and for low voltages are considerably below. This may be partially due to changes in the gas as the discharge is run, but is probably mainly due to photoelectric fatigue of the point, since the effect is the same as would be caused by a decrease in intensity of the triggering source; i.e., at higher voltage where the discharge is independent of the triggering source, the currents are not measurably lower, and although the current at onset is lower, the onset voltage is not measurably different.

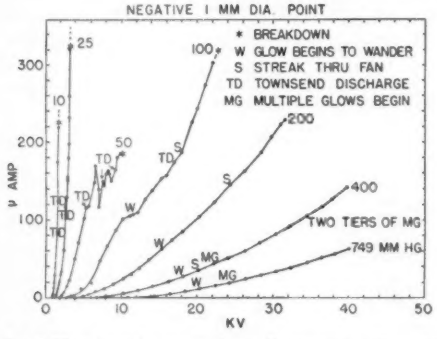

FIG. 8. Negative point corona, 1-mm diameter point, 8-cm gap in air, extended to higher voltages and breakdown at different pressures. Various thresholds indicated on figure. Note the irregularities in the lower pressure curves caused by fluctuations between the pulsed and the continuous Townsend discharge.

Concerning reproducibility of the data, several of the runs were repeated once or more. That part of the *I-V* curves below onset of course depends on the illumination of the point, and varies; but the curves above onset could not be resolved on the scale of plotting used here. With this triggering, the reproducibility of Trichel pulse onset voltages is as good as the well-known reproducibility of burst pulse onsets.

With the ultraviolet light triggering, at pressures of 200 mm Hg and less, a second type of negative pulses appeared on the oscilloscope coincident with Trichel pulse threshold. Their amplitude was random but small, being never more than perhaps $\frac{1}{3}$ the amplitude of Trichel pulses, and usually much less. Just at threshold they often occurred more frequently than Trichel pulses; but as the voltage was raised and Trichel pulses began to occur regularly, they disappeared. Their amplitude, like that of Trichel pulses, was greater at lower pressures. They were seen infrequently and with very small amplitude at 400 mm Hg and once at atmospheric pressure with the 0.5-mm point. It is suspected that these may have been statistically determined accumulations of avalanches which were recently studied in more detail by Lauer in H_2, and which would appear integrated on the oscilloscope used here.

ONSET UP TO BREAKDOWN

Negative Points (Figs. 8–10)

In these figures a continuation of the data above corona onset is shown plotted on a linear scale. For this part of the work the negative points were triggered by gamma-rays. The mercury arc lamp has the disadvantage of masking the visual discharge manifestations. Above 10 μa the discharges are independent of external triggering, but an initiation is in any case desirable.

If the size of the button of negative glow is small compared with the end of the point, the discharge will tend to wander around on the point from one active cathode spot to another. Apparently, the intense ion bombardment degasses and deactivates the spot, and the marginal discharge cleans up a new area to which the discharge wanders. Because the size of the negative glow varies approximately inversely as the pressure at lower pressures, this depends on pressure as well as point size. The wandering occurred mainly with a 1-mm point at 200 mm Hg and up, with a 0.5-mm point at 400 mm Hg and up, and with a 0.25-mm point at atmospheric pressures, being negligible at the lower pressures, owing to the restricted area of the high field region. As the current increases further, the discharge moves farther and faster around on the point, and sometimes the fan appears to oscillate to and from the point as well. If the glow to point size ratio is small enough, this random dancing about becomes more

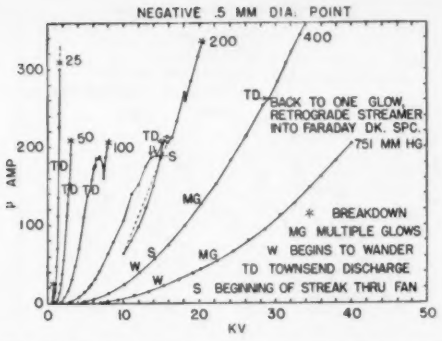

FIG. 9. Negative point corona, 0.5-mm diameter point and 4-cm gap, in air extended to higher voltages and breakdown at different pressures. Various thresholds indicated on figure.

and more rapid until the glow is sometimes in two or more places at once. When many spots are active at once, they often fall into orderly patterns, being spaced at equal intervals in one or two circles around the tip and moving slowly around the point. This shows nicely the limited current capacity of a single active spot and the mutual repulsion between discharges.[7]

The points on the curves marked *TD* indicate a transition from the characteristic Trichel pulse negative corona to a pulseless Townsend-type discharge. There appears to be no specific voltage at which this occurs, but rather it seems to be associated with some conditioning of the point such that it occurs at lower voltages if the discharge has first been run for a longer time at lower currents. This may explain its nonappearance on some of the lower pressure runs which were completed in comparatively shorter times.

On the oscilloscope the transition is marked by the disappearance of Trichel pulses. When it occurred at higher voltages, it could not be studied very closely because the oscilloscope pattern was confused by secondary discharges from the sides of the point, or because the pulse amplitude of the main discharge was already too low. In those cases it could be seen only that the amplitude of Trichel pulses decreased to zero in a range of a few volts' increase. However, in a number of lower pressure cases the transition could be seen clearly. In those cases the Trichel pulses began to have a reduced frequency and show a duration in time of the pulse peak. As the voltage was raised a few volts, this duration in time quickly became infinite, leaving the pulseless discharge. This lengthening of the pulses was, of course, accompanied by a reduction in amplitude, since the current increases observed with the transitions were only 5 to 10 μa out of one or two hundred. The usual trend with a negative point as the voltage is raised is for the Trichel pulses to increase in frequency and decrease somewhat in amplitude, but sometimes a gradual decrease in pulse frequency was observed to begin as much as 100 volts below where any change could be seen in pulse shape with the Dumont 241.

Visually, in the cases that could be studied in detail, the negative glow was observed to lift somewhat from the point, lengthen in the direction away from the point, and decrease in diameter. The entire visible discharge shared in this lateral constriction. At low pressures the fan disappeared at once, leaving only a fainter diffuse positive column which could sometimes be seen all the way to the plane. At higher pressures, instead of the fan disappearing suddenly when the pulses disappeared from the CRO, it suddenly contracted to one-half or less in diameter, and at times was even more intense and left the Faraday dark space somewhat lengthened and more sharply delineated than before. After this it grew fainter gradually and disappeared as the voltage was raised.

The transition to a pulseless discharge was actually accompanied by a jump in current of from 5 to 10 μa,

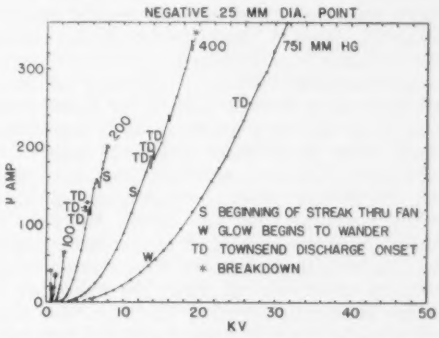

FIG. 10. Negative point corona, 0.25-mm diameter point, 2-cm gap, in air extended to higher voltages and breakdown at different pressures. Various thresholds indicated on figure.

but this doesn't show on the plotted data because the lower pressures curves are too steep and at higher pressures, if the voltage was held constant after the transition, the current decreased and Trichel pulses reappeared. The latter accounts for all the breaks in the negative point curves in Figs. 8–10. In Fig. 9, for 200-mm Hg the portion of the curve run back down in voltage after the transition had been observed several times indicates clearly that the point had been altered by the discharge. Points examined under the microscope after this transition had been observed showed a circular area on the tip that was highly polished, apparently due to surface melting, surrounded by a sputtered area that had lost its original polish.

The cessation of pulses means that the negative ion space charge is no longer sufficient to choke off the discharge. This is indicated by the pulse shape during transition when the pulse drops only slowly from peak value for some time before the space charge builds up

[7] L. B. Loeb, J. Appl. Phys. **19**, 882 (1948).

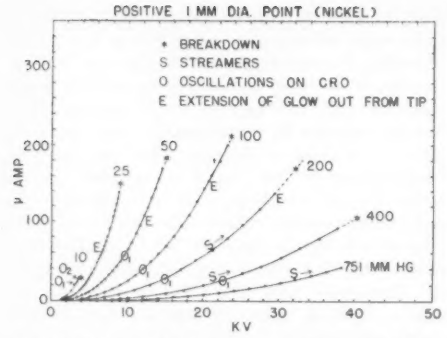

FIG. 11. Positive point corona, 1-mm diameter nickel point, 8-cm gap, in air, indicating various transitions up to spark breakdown. The various phenomena are indicated by letters and the legend on the figure.

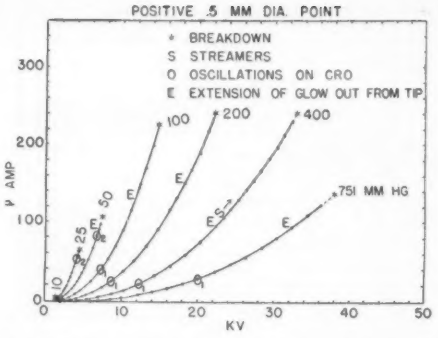

FIG. 12. Positive point corona, 5-mm diameter platinum point, 4-cm gap, in air at various pressures extended up to breakdown. Various phenomena are indicated on legend in the figure.

enough to choke it off. Also, the lateral constriction of the discharge after transition would be expected if the negative space charge were markedly reduced allowing the existing distorted potential curve to fall farther below the curve for an undistorted gap.[7] This constriction of the pulseless discharge is similar to the differences observed by Weissler[8] between the Trichel pulse corona in air and the pulseless corona in oxygen-free nitrogen where the discharge showed the usual structure, Crooke's dark space, negative glow, Faraday dark space, and positive column, but was much contracted laterally compared with that in air. However, in Weissler's work the choking off of the discharge into Trichel pulses by the introduction of oxygen reduced the current by about one-half. Since the transitions to pulseless discharge observed in this work show only small increases in current, it would seem that the formation of space charge is being limited by the supply of electrons rather than the lack of oxygen molecules for them to attach to. The change in the point that is responsible for this decreasing supply of secondary electrons can also account for the subsequent decrease in current at constant voltage. The cause of this decreasing secondary emission of the point is not known. If the area of the point that afterward appears to have been melted were all melted at one time, it would furnish more than enough electrons by thermionic emission alone, but there may be only microscopic areas melted at any one time. Nothing is known about this melting process or at what state of development it occurs. Further work should be done to examine points microscopically after successive stages of development of the transition, and also with points of other materials.

Why the discharge should revert back to Trichel pulses at constant voltage after the current has dropped appreciably is not clear, but certainly by then the point is much altered. Possibly, the melting of the tip flattens it enough so that the region of highest field shifts out to portions of the point that have not yet suffered the change to a decreased secondary emission.

At higher voltages, for the higher pressures, the retrograde streamers reported by Loeb *et al.*[4] were also seen in this work. As observed here, their development always started with the appearance of a streak of increased intensity through the center of the fan. In some cases this streak clearly extended well out into the gap beyond the fan. However, only with the two larger points at higher pressures did this streak develop into the very intense and sharp projection back into the Faraday dark space.

Positive Points (Figs. 11–13)

In these figures is shown a corresponding plot of data above onset for positive points. The 1-mm points for that part of the work shown on Fig. 11 were made of nickel merely because platinum wire of the required size was not readily available at the time and the positive point discharge is independent of point material. As the voltage is increased above steady corona onset, the CRO trace quickly smooths out and the visible electric blue glow becomes more intense and covers all of the point and even the point holder.

For a considerable range in voltage beyond steady corona onset nothing is seen on the CRO. However, some kind of oscillations usually do occur before breakdown is reached. One type of oscillation observed appears as an irregular bobbing up and down motion of the whole CRO trace. This is random in time and amplitude with times of the order of large fractions of a second. It looks like sudden large increases or decreases of the current. Such fluctuations are small to begin with and, as the voltage is raised, gradually increase in both frequency and amplitude up to times of the order of hundredths of a second, but remain random. This occurs more with larger points and higher pressures. The portions of the curves where this becomes noticeable are indicated on

[8] G. L. Weissler, Phys. Rev. **63**, 96 (1943).

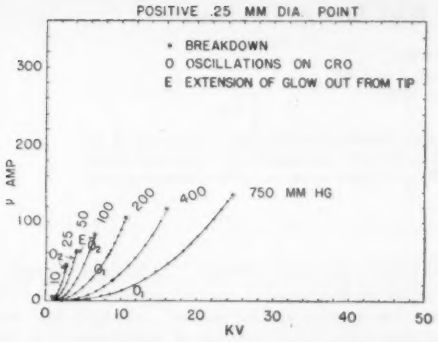

FIG. 13. Positive point corona, 0.25-mm diameter platinum point, 2-cm gap, in air at various pressures extended up to breakdown. Various phenomena are indicated on legend in the figure.

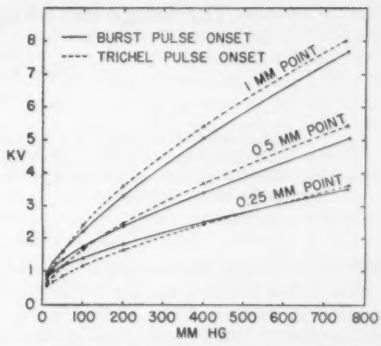

FIG. 14. Threshold potentials of positive burst pulse corona and of negative threshold pulse corona in air as a function of pressure for points of various diameters. Note that in all of the curves negative threshold is below the positive at low pressures and crosses over at higher pressures, the transition pressure being the lower, the larger the point.

the plots by O_1. It is not impossible that these are caused by secondary discharges from clouds of ionized gas swept around the chamber by the electric wind. They could also be discharges from the sides and mountings of the point. Another type of oscillation may be caused by plasma oscillations. This appeared as a sinusoidal wave of low amplitude with frequencies of the order of 10^5 cycles/second, and was seen only at lower pressures. Its appearance is indicated on the plots by O_2. No visible change in the discharge could be associated with either of these oscillations.

At the points on the curves indicated by E the glow began to be noticeably brighter on the tip and to extend out into the gap. As the voltage is raised, this grows to an intense blue streak extending up to several point diameters out from the point. It has the appearance of a superposition of many streamers, but although occasional streamers were sometimes seen, there was nothing on the CRO that could be associated with this.

With the larger points and higher pressures, occasional streamers that looked just like pre-onset streamers did sometimes appear on the CRO from seconds to many minutes apart. These could not be mistaken for breakdown streamers, which have amplitudes many times greater. Breakdown streamers were not seen with any of the standard geometries used in this work, because the first one always closed the gap to give breakdown. With a 0.25-mm diameter point and a 4-cm gap (twice standard) at atmospheric pressure and ~40 percent relative humidity, a few breakdown streamers were observed just before breakdown at ~37 kv; but with dried air no streamers were observed before breakdown at ~43 kv. Available voltages would not break down long enough gaps with the larger points so that 0.15-mm diameter points were used. With these points and ~40 percent humidity, the gap length had to be about twice the standard length or greater for breakdown streamers to be observed just as with the 0.25-mm point. With dried air it had to be about two and one-half times the standard length or greater for them to be observed. However, with small points of ~0.08-mm tip diameter, breakdown streamers were observed with standard gap lengths. Thus, the breakdown streamers are not observed for larger points and gaps of standard geometry, as the fields are too high across the gap. When such streamers start, they cross the gap and give a spark. With finer points and larger gaps the streamers are less vigorous and do not cause breakdown when they first appear.

Figure 14 is a plot of onset voltage against pressure for the three geometries used. It is noted as pointed out by English and Loeb[6] that while at low pressures the negative thresholds are lower than the positive, there is a transition at higher pressures where photoionization is more effective and back diffusion reduces secondary emission as well as requiring higher current densities for conditioning. It should further be noted that the cross-over occurs at lower pressures for the large points where current densities are less and fields are higher.

The writer wishes to express his gratitude to Professor L. B. Loeb, under whose direction this work was done, for his guidance and unfailing interest and to Dr. W. N. English for his kind assistance in the beginning of the work.

The Range and Straggling of High Energy Electrons

ROBERT R. WILSON
Cornell University, Ithaca, New York
(Received May 4, 1951)

Simple expressions are derived for the range and straggling of individual electrons. Large energy losses due to bremsstrahlung make the average range smaller than would be calculated from the average energy loss. Effects of multiple scattering are included. The results are in good agreement with numerical calculations by the Monte Carlo method.

THE electron range is a somewhat indefinite concept: at low energies, because of the large multiple scattering, electrons diffuse through matter, and at high energies the initial electron is soon obscured by an accompanying shower of electrons. The propagation of electrons at low energies, less than 10 Mev, has been treated by Bothe[1] and by Fowler.[2] The emphasis in this paper is on high energy; and the problem is considered because of its bearing on calculations concerning shower production.

Let us first neglect the effects of multiple scattering which, at high energy, are important only near the end of the electrons' range and which can be corrected for later. The simple methods of calculating range and straggling which are useful for protons are vitiated by the occurrence of large energy fluctuations corresponding to the emission of high energy photons. Bethe and Heitler[3,4] give the solution to the problem of the fluctuations of energy of electrons which have traversed a given thickness of matter. They approximate the radiation spectrum by

$$\sigma(k)dk=\frac{dk dt}{E\ln[E/(E-k)]}, \tag{1}$$

where $\sigma(k)$ is the probability of an electron of energy E radiating a photon of energy k in passing through a distance dt measured in shower units of length,[5] i.e., radiation lengths divided by ln2; and they find that the probability of an electron of initial energy E_0 still having energy greater than E after traversing a distance t is

$$W(y, t)=(t-1, y)!/(t-1)! \tag{2}$$

in terms of the incomplete gamma-function, $(t-1, y)!$, where $y=\ln(E_0/E)$.

The following approximation for (2) was guessed by the author:

$$W(y, t)=1-\int_0^t e^{-y}y^x/x!dx; \tag{3}$$

it is accurate for y and t large compared to unity. The probability, wdt, that an electron's energy falls below E between t and $t+dt$ is found from (3) by differentiation;[6] i.e.,

$$w(y, t)dt=e^{-y}y_t dt/t! \tag{4}$$

For large values of y and t this can be further approximated by the gaussian form,

$$w(y, t)dt=(2\pi y)^{-\frac{1}{2}}\exp[-(t-y)^2/2y]dt. \tag{5}$$

From this the mean range r will be

$$r=y_{\max} \tag{6}$$

if we can define a value of $y_{\max}$ corresponding to the loss of all the energy by radiation only, when the particle has stopped. To do this the loss of energy by ionization must be included. Expressing (6) in terms of energy, and differentiating the mean range with respect to the initial energy, gives[7] for the average radia-

TABLE I. Monte Carlo calculations of electron range.*

E (Mev)	n	r	s/r	ϵ
10	466	0.85	0.38	0.02
20	461	1.12	0.43	0.02
50	346	1.75	0.42	0.04
100	292	2.45	0.36	0.05
200	95	2.56	0.43	0.11
500	100	3.04	0.46	0.14
1000	100	3.72	0.40	0.15

* E = initial electron energy, n = number of Monte Carlo trials, r = mean range in radiation lengths, s/r = fractional rms straggling, ϵ = statistical error of Monte Carlo mean range determination.

[1] W. Bothe, *Handbuch der Physik* **2212**, 1 (1933).
[2] Fowler, Lauritsen, and Lauritsen, Revs. Modern Phys. **20**, 236 (1948); see also J. Steinberger, Phys. Rev. **75**, 1136 (1949).
[3] H. A. Bethe and W. Heitler, Proc. Roy. Soc. (London) **146**, 84 (1934). W. Heitler, *The Quantum Theory of Radiation* (Oxford University Press, London, 1944), second edition, p. 224. Heitler also calculates the range of electrons, p. 223, but with considerably different results because of his neglect of fluctuations which shorten the range considerably.
[4] L. Eyges, Phys. Rev. **76**, 264 (1949). Eyges has extended the calculation to more refined approximations of the radiation spectrum.
[5] Shower units of length and energy are used in all equations in this paper, but results and numbers mentioned are given in radiation lengths and Mev.
[6] Equation (4) may be derived directly from Eq. (2) in the following way. Using

$$\int_0^y x^t e^{-x}dx=t!-e^{-y}\sum_0^t t!/\mu!y^\mu,$$

which can be derived by successive partial integrations (for integral t), one obtains equation (4) by taking the difference between t and $(t-1)$.
[7] If we integrate (1) over k to find the average loss of energy, we would get the usual expression $-dE/dt=E\ln 2$, remembering that t is in shower units. The difference comes about because fluctuations have been included in arriving at (7).

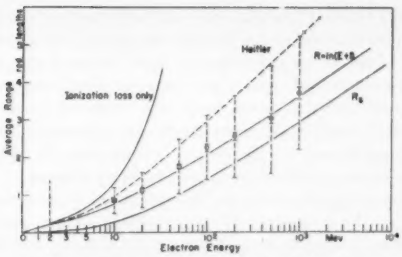

FIG. 1. The average range of electrons in lead is plotted against the energy in Mev. The dashed line curve is taken from W. Heitler, *The Quantum Theory of Radiation*. The full line marked $R=\ln(E+1)$ is given by that expression if the range is measured in shower units of length, i.e., (r.l./ln2) and the initial energy in units of critical energy times ln2, i.e., $(E_{\text{Mev}}/\beta \ln 2)$. The circles indicate the Monte Carlo results: the short bars represent the statistical accuracy of the mean, and the long dashed vertical bars represent the mean square deviation of a single electron track from the mean range. The curve marked R_s shows the mean range as corrected for multiple scattering.

tion loss on traveling a distance dt

$$-dE/dt=E. \tag{7}$$

Let the energy be measured in units equal to ln2 times the ionization loss in radiation lengths, i.e., $E=E_{\text{Mev}}/\beta \ln 2$. Then ionization loss can be added to (7), i.e.,

$$-dE/dt=E+1, \tag{8}$$

and integrating this over the energy gives for the mean range corresponding to the stopping of electrons,

$$r=\log(E_0+1). \tag{9}$$

If s is defined as the root-mean-square deviation of a track length from the mean range, it is evident from (5) that for high energies where ionization can be neglected,

$$s^2=y_{\max}=r. \tag{10}$$

Thus, surprisingly, enough the percentage straggling decreases with increasing energy. At lower energies ionization loss becomes important. Now the average energy loss by ionization for the electrons traveling a distance r is just r in the above energy units; hence a fraction of the range r/E_0 can be ascribed to ionization loss and the straggling of this part will be negligible compared to the straggling due to the part of the range corresponding to radiation loss. The simplest procedure for correcting the straggling as calculated from (5), then, will be to reduce the straggling by the fraction, r/E_0, i.e.,

$$s/r=(1-r/E_0)r^{-\frac{1}{2}}. \tag{11}$$

The above expressions for the range and straggling were checked for Pb in the energy interval from 10 to 1000 Mev using the Monte Carlo device already described.[8] Exactly the same procedure was used as for showers except that only the initial electron was followed. The results are summarized in Table I which shows the number of electrons followed in each case, the mean range, the rms straggling, and the standard error of the mean. In Figs. 1 and 4 these values are compared with the theoretical expressions (9) and (11). It can be seen that the agreement is well within the accuracy of the Monte Carlo method, about five percent. In Fig. 2 the empirical range distributions found for a few low energies are compared to the gaussian expression (5): the agreement is satisfactory.

That the rough theory outlined above compares so well with the Monte Carlo calculations is probably fortuitous: it is better to regard the expressions derived as semi-empirical formulas summarizing the Monte Carlo calculations.

Multiple scattering can now be included. Inasmuch as the scattering is appreciable only near the end of the track, we will make the approximation that the electrons proceed in the original direction until they reach an energy at which the calculated rms angle of multiple scattering has attained such a large value that the electrons thereafter diffuse in a random manner. The average straight distance will then be the mean range, and the random motion will contribute only to the straggling.

The mean square angle of multiple scattering $\langle\theta^2\rangle_{Av}$ of an electron of initial energy E_0 is readily calculated

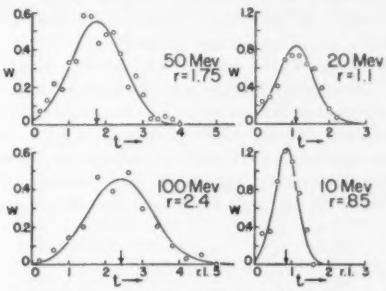

FIG. 2. Monte Carlo results for the probability w of an electron stopping between t and $t+dt$. The curves drawn through the points are theoretical and are given by expression (5) of the text. The arrow indicates the mean range.

using $\langle d\theta^2\rangle_{Av}=(K^2/E^2)dt$,[9] where the constant K^2 has the value $21^2/\beta^2 \ln 2$ for shower units (β is the ionization energy lost by an electron in passing through a radiation length, i.e., the critical energy), and (8) to give[10]

$$\langle\theta^2\rangle_{Av}=\int_E^{E_0}\frac{K^2dE}{E^2(E+1)}=K^2\left[\frac{1}{E}-\frac{1}{E_0}-\ln\frac{E_0(E+1)}{E(E_0+1)}\right]. \tag{12}$$

[8] R. R. Wilson, Phys. Rev. **79**, 204 (1950).

[9] E. J. Williams, Proc. Roy. Soc. (London) **169**, 531 (1939); B. Rossi and K. Greisen, Revs. Modern Phys. **13**, 263 (1941).

[10] For the case of large E_0, (12) reduces to

$$\langle\theta^2\rangle_{Av}=21^2\left(\frac{1}{E}-\ln\frac{E+1}{E}\right)\Big/\beta^2 \ln 2,$$

which can be compared to the careful numerical computations of J. Roberg and L. W. Nordheim, Phys. Rev. **75**, 444 (1949), for the mean square angle of electrons in showers. The agreement is surprisingly good, especially at low energies.

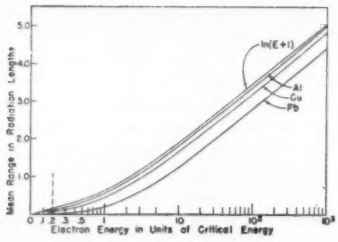

FIG. 3. Mean range in radiation lengths is plotted as a function of energy in units of the critical energy. The upper curve neglects multiple scattering and is given by Eq. (9) of the text (note the units). Multiple scattering has been included in the curves marked Al, Cu, and Pb.

We want to set this characteristic angle equal to $\langle\theta_r^2\rangle_{Av}$, a value which if reached corresponds to random motion, and then to solve for E_r, the energy at which the motion of the electron becomes random. In the Appendix it is shown that $\langle\theta_r^2\rangle_{Av}$ is 2. Hence E_r is given by,

$$E_r^{-1} \doteq 2\beta^2 21^{-2} \ln 2 + E_0^{-1} + \ln[E_0(E_r+1)/E_r(E_0+1)]. \quad (14)$$

Values of E_r were found from this expression[11] and the range r_r corresponding to E_r given by (9) is subtracted from the total range corresponding to E_0 to give the mean range, R, including multiple scattering. This is plotted in Fig. 3 for various elements.

The Monte Carlo method was used to check this result empirically. Electrons of 50-Mev initial energy were followed in lead as before but the angle of scattering was also determined at each interval by a chance method similar to that used for finding the radiation. A three-dimensional protractor was constructed[12] to keep track of the angle of the electron direction with respect to its initial direction. At each interval the forward component of the distance moved by the electron was added to give finally the total forward range of each electron followed. One thousand electrons[13] were followed and the mean range was observed to be reduced by 0.65 radiation length in exact agreement with that predicted by the above calculation. A similar calculation at 1000 Mev gave similar agreement.

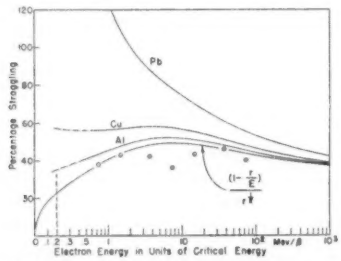

FIG. 4. The percentage root mean square straggling from the mean range. The lower curve is given by the indicated formula and neglects multiple scattering. The circles indicate Monte Carlo calculations which also neglect multiple scattering. Multiple scattering has been included in the curves marked Al, Cu, and Pb.

The straggling can also be considered in two parts: firstly, the variation in range produced by photon emission as the electron is slowed down to E_r, and then secondly the random motion due to scattering which takes place until the electron comes to rest.

The straggling produced while the path is straight, S_s^2, can be calculated from our previous result by considering the straggling of the total path length as being compounded also of two parts, i.e.,

$$s^2 = S_s^2 + s_r^2, \quad (13)$$

where s_r^2 is the straggling of the electrons of initial energy E_r as given by (12), i.e., without considering the multiple scattering. The quantities s_r^2 and s^2 can be calculated from (11), and then S_s^2 can be obtained from (13).

The straggling, S_r, due to random motion over a total path length r_r will be given by the usual expression for random walk:

$$S_r^2 = \frac{1}{3}\int_0^{r_r} \lambda_{tr}\,dt, \quad (14)$$

if we can define an equivalent mean free path, λ_{tr}, that would characterize the diffusion of electrons by multiple scattering—evidently the equivalent of a transport mean free path. In the appendix, it is shown that

$$\lambda_{tr} = 2E^2/K^2. \quad (15)$$

Then from (13) we get

$$S_r^2 = \frac{2}{3K^2}\int_0^{r_r} E^2 dt = \frac{2\beta^2 \ln 2}{3\times 21^2}\int_0^{E_r} E^2 dE/(E+1),$$

and integrating,

$$S_r^2 = 1.0\times 10^{-3}\beta^2[\log(E_r+1) - E_r + E_r^2/2]. \quad (16)$$

The total straggling including multiple scattering effects is $S^2 = S_s^2 + S_r^2$, and the fractional total straggling S/R calculated from (13) and (15) is plotted as a function of E in Fig. 4 for various elements.

[11] E_r is given approximately by the formula: $E_r = E_r'[1 - \exp(-E_0/E_r')]$, where $E_r' = (10/\beta)^{\frac{4}{3}}$, if the critical energy β is in Mev.

[12] Miss Leonilda Altman, who operated the Monte Carlo machine, also constructed an electronic device which was equivalent to the protractor but more accurate and convenient. The details will be published elsewhere by her.

[13] The graphs of electron energy against distance already obtained in preparing Fig. 1 were used again for this calculation. Each electron was followed and the angle at each interval was determined from a family of curves drawn on the chance cylinder used previously. Each electron graph was used successively five times to give five different angle histories for each energy history.

The straggling produced while the electron has energy below E_r is small, i.e., both S_r^2 and s_r^2 are small compared to S_s^2; hence to about ten percent $S^2=s^2$, so Eq. (11) can be used to obtain the total straggling directly.

A useful concept in calculating shower phenomena is the "pair range," i.e., the average distance traveled by the electrons resulting from pair production. Because all energies up to the photon energy are possible in pair production, the number-distance curve looks more like a simple exponential than the integrated gaussians which characterize monoenergetic electrons. This is true only at not too high energies.

If we assume an exponential distribution, then the number of electrons (apart from secondaries) at a distance t from the place of pair production is

$$n=2\exp(-t/R_\pi) \tag{17}$$

which defines R_π, the pair range. Now if we consider the energy lost by ionization, we can write

$$\int_0^\infty n\beta dt=2\int_0^W P(E)R(E)\beta dE, \tag{18}$$

where $P(E)$ is the probability of one member of the pair receiving an energy between E and $E+dE$. This was assumed to be a constant, and using expression (9) to determine $R(E)$ and (17) for n, we get upon integrating both sides of (18)

$$R_\pi=(1+1/W)\ln(W+1)-1, \tag{19}$$

where W is the initiating photon energy. This relation neglects multiple scattering, which can be best included by subtracting the random part of the range corresponding to E_r given by (14).[11] At high energy, E_r is independent of the initial electron energy and the problem is simple. At low energies, an appropriate average must be taken. The normalizing factor in (17) must now be increased so that the total energy loss will still come out right. How this should be done depends exactly on the problem being considered, so no details will be given here. At high energy, $E>100$, an integrated gaussian form must be used, but (19) is still correct for the average.

APPENDIX

Let us calculate the mean square multiple scattering angle of an electron after going through dt in terms of a fictitious cross section $\sigma(\theta)$, i.e.,

$$\langle d\theta^2\rangle_{Av}=\int\theta^2\sigma(\theta)d\Omega dt$$

$$=2\int\sigma(\theta)(1-\cos\theta)d\Omega dt$$

$$=2dt/\lambda_{tr},$$

by definition of the transport mean free path.[14] We can equate the $\langle d\theta^2\rangle_{Av}$ so obtained to the usual expression,[9] i.e., $\langle d\theta^2\rangle_{Av}=K^2dt/E^2$. Solving for λ_{tr} we get

$$\lambda_{tr}=2E^2/K^2. \tag{15}$$

For the moment let us assume that the energy remains constant, then the characteristic random angle is given by

$$\langle\theta_r^2\rangle_{Av}=\int_0^{\lambda_{tr}}K^2dt/E^2=K^2\lambda_{tr}/E^2$$

and using (15) for λ_{tr}

$$\langle\theta_r^2\rangle_{Av}=2.$$

[14] I am indebted to Dr. R. P. Feynman for a discussion on this point.

Eddy Currents and Supercurrents in Rotating Metal Spheres at Liquid Helium Temperatures*

P. B. Alers,† J. W. McWhirter, and C. F. Squire
Rice Institute, Houston, Texas

(Received June 4, 1951)

These experiments show that large eddy currents are set up in a tin sphere rotating at 4.6 or more revolutions per second in the earth's magnetic field and at 3.8°K. Within experimental determination, the eddy currents have the same magnitude and distribution on the sphere as the supercurrents which cause the Meissner effect at 3.7°K. These results are in accord with classical electromagnetic theory for a normal conductor and with the London theory for a superconductor. The Meissner effect has been produced in bulk tantalum metal by rotating the specimen while cooling through the superconducting transition temperature.

I. INTRODUCTION

FOR some time we have known[1] that a solid sphere of superconducting metal would show a perfect Meissner effect if the following experimental steps were taken: (a) rotate rapidly in the normal conducting state; (b) cool the sphere slowly through the superconducting transition temperature while still rotating; (c) stop the rotation and experimental investigation shows that the sphere has undergone a perfect Meissner effect. The present investigation has put some quantitative understanding behind the effects both from the experimental and theoretical side.

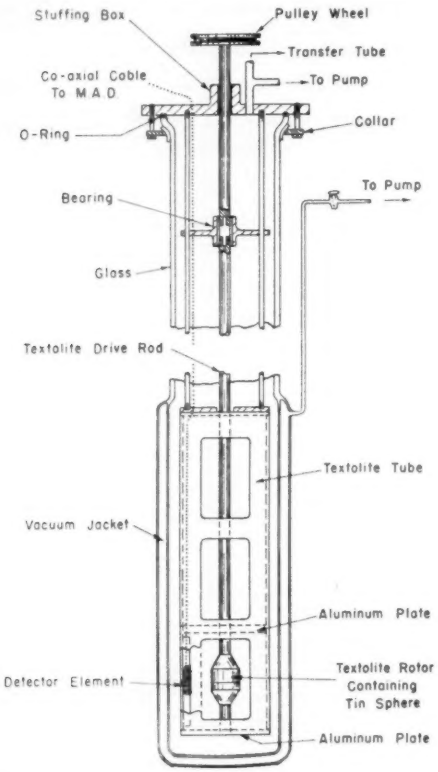

FIG. 1. Cryostat.

II. APPARATUS

Figure 1 shows the cryostat schematically. The sphere of tin housed in Textolite may be rotated at speeds, ω, through a driving torque on the shaft extending upward and out of the liquid helium bath. A magnetic detector (saturable core reactor) is shown in Fig. 1, and this is located close to the rotor in such a way that any changes in the vertical magnetic field component results in a steady signal on a meter. Most of the vertical field component of the earth was removed by use of compensating Helmholtz coils placed external to the Dewar flasks. Figure 2 shows the rotor and the detector element with the horizontal flux distorted by the eddy currents induced because of the rotation of the sphere.

The changes in the magnetic field were measured by a device known as the magnetic airborne detector (AN ASQ-3), which was provided by the Office of Naval Research. Although certain alterations have been made on the magnetic airborne detector, the operation of the detector is approximately the same as the original design. Figure 3 is a block diagram of the detector. The output of a 1000-cycle oscillator is carefully filtered so that there does not exist any other frequency components, especially the 2000-cycle component. After passing through the filter, the 1000-cycle output then is sent through a resonent series circuit consisting of a capacitor and the detector element. This resonant series circuit is shunted by a 200-ohm resistor. The detector element is the only part of the above circuit that is cooled to 4.2°K.

If the detector element is in a small magnetic field, a 2000-cycle component is generated. The output goes through a band-pass filter which transmits only the 2000-cycle component. The 2000-cycle component is

* This work was supported by the ONR.
† Now with Naval Research Laboratory, Washington, D. C.
[1] Love, Blunt, and Alers, Phys. Rev. **76**, 305 (1949).

then fed into a resistance-coupled amplifier with four stages. At the third stage, two leads are taken off and the signal presented on the oscilloscope. The output current from the fourth stage passes through a 5000-ohm resistor to an Ayrton shunt and galvanometer. In parallel with the fourth stages is a 1.5-volt dry cell battery and a resistance box. The dry cell battery is used to buck out the small detector current that exists as background signal. The magnetic field from the Helmholtz coils was set so as to produce a minimum deflection on the oscilloscope. A change in the magnetic field appears on the galvanometer as an unbalance. Field changes of 10^{-4} gauss gave deflection of three centimeters on the galvanometer scale with Ayrton shunt on one-tenth sensitivity. The sensitivity reported[2] for the equipment is better than ten microvolts per ten microgauss at the output of the 2000-cycle filter.

This experiment can be divided into two parts. The first part of the experiment consisted of finding the dependency of eddy currents induced on the tin sphere with respect to the rotational speed of the rotor. Above the transition temperature the sphere was rotated at varying speeds, and the deflections on the galvanometer and the speeds of rotation were recorded. After each determination of speed *versus* amplitude, the rotor was then stopped, and a check was made of the zero position of the galvanometer. At slow speeds the rotational speed was determined by the use of a stop watch. At faster rotational speeds where the revolutions could not be counted accurately, a stroboscope was used to measure the speed of rotation. The rotational speed was varied between 0.3 and 5.0 revolutions per second.

During the second part of the experiment, the specimen was rotated at a certain speed and cooled through the transition temperature. The deflection on the galvanometer was observed during the transition. If on passing through the transition temperature, a magnetic flux was frozen in, the deflection on the galvanometer would oscillate about a steady deflection with a frequency determined by the rotational speed of the rotor. But, on the other hand, if no flux were frozen in, the galvanometer would retain a steady deflection even if the rotation of the rotor was stopped. This would indicate a perfect Meissner effect.

These experiments were performed with a tin sphere one and one-half inches in diameter, and with a tantalum cylinder one inch in diameter and one and one-half inches long. The transition temperature for tin is 3.69°K, so in order to cool through the transition temperature of tin, it was necessary to pump on the liquid helium until the absolute pressure of the helium vapor was 441 mm of mercury. Since the transition temperature of tantalum is 4.38°K, tantalum when immersed in liquid helium at a pressure of 760 mm of mercury is in the superconducting state. With an overpressure on the helium greater than 980 mm of mercury, the tantalum was rotated as a normal conductor; and by reducing the pressure to the atmospheric pressure, the tantalum passed through its transition temperature while rotating.

[2] Trans. Am. Inst. Elec. Engrs. **66**, 641 (1947).

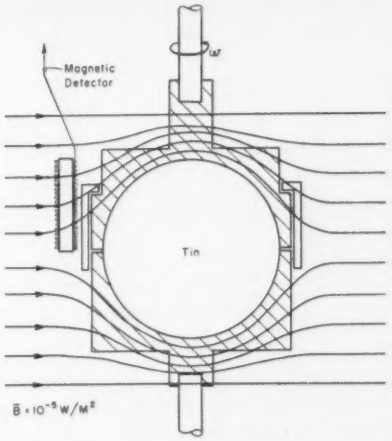

FIG. 2. Rotor and lines of $\bar{B}$ about a rotating sphere.

III. EXPERIMENTAL RESULTS

Tantalum on going superconducting has the property of freezing in most of the magnetic flux that exists in the material. In other words, it shows no Meissner effect. Figure 4 illustrates the large frozen-in moment produced in tantalum when allowed to go superconducting while at rest. Figure 4 shows the detector signal as a function of the angle of the rotor with respect to the position of the detector element. Such a large frozen-in moment existed that the less sensitive oscilloscope was used to give an indication of the magnitude of this frozen-in moment. The magnetic moment locked into the superconductor is independent of the angular orientation of the rotor. The direction of the magnetic moment is determined only by the direction of the magnetic field existing when the transition temperature was passed. The zero position of the rotor was therefore

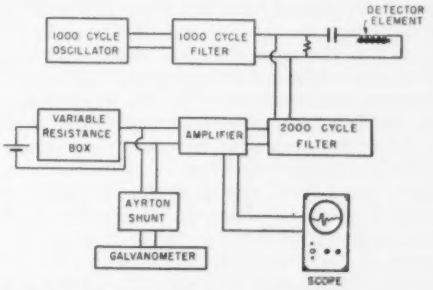

FIG. 3. Block diagram of magnetic detection equipment.

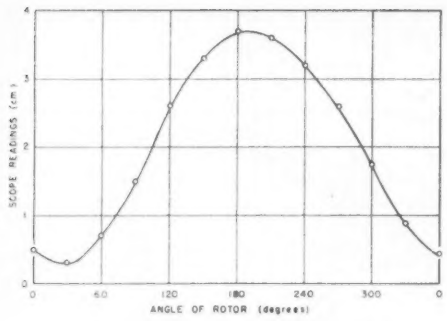

FIG. 4. Frozen-in moment of tantalum.

arbitrarily chosen. A rotation of the tantalum then gave a new position of the axis of the frozen-in moment with respect to the detector element.

The next part of the study on tantalum consisted of rotating the tantalum while cooling through the transition temperature. The speed of rotation was 0.35 revolution per second during the transition. The plot of the detector signal as a function of the angle of the rotor is shown in Fig. 5. There was a steady deflection with a small variation superimposed. This means a large Meissner effect had occurred.

Tin is a better behaved superconductor than tantalum in that tin freezes in a smaller amount of flux. Figure 6 is a typical plot of the galvanometer reading *versus* the rotational speed of the normal conducting tin rotor. Before going into the discussion of this graph, it would be best to explain further what the magnetic detector element measures. The detector element will measure only a vertical component of the magnetic induction, $\bar{B}$. By looking at Fig. 2 the lines of $\bar{B}$ are seen to be bent around the rotating specimen. If only a small amount of eddy currents is induced on the surface of the sphere, most of the lines of $\bar{B}$ continue straight on through the detector element and pass through the sphere. As the eddy currents increase, the lines of $\bar{B}$ are forced over the sphere. This gives a vertical component of $\bar{B}$ in the detector element which appears as an unbalance on the galvanometer scale. The graph, Fig. 6, shows an exponential rise at first with a gradual leveling off. However, the curve is still slightly rising with increases of the rotational speed. Table I gives the galvanometer deflection at various rotational speeds at a constant temperature of 4.2°K. At a higher temperature, say 20°K, the electrical conductivity is smaller, so that at the same rotational speeds one obtains a smaller galvanometer deflection.

With the sphere rotating at 4.6 revolutions per second, it was observed that the amplitude of the flux being kicked out by the eddy currents increased by 10 percent as the sphere was cooled from 4.2°K to the transition temperature. The deflection on the galvanometer remained at this maximum value while passing through the transition temperature. Further, the deflection on the galvanometer remained at this maximum value when the superconducting rotor was brought to rest.

IV. DISCUSSION

It is well known that for tantalum the Meissner effect is practically nonexistent because the metal freezes in all of the existing flux when it goes superconducting. Pure tantalum in bulk quantity is made by sintering together the small flakes or grains. Sound pulses were found to scatter very badly on passing through tantalum metal.[3] Thus from a physical point of view the metal is not homogeneous and one can understand that the Meissner effect might not be realized by a metal of this physical make-up. We have found that our specimen of pure tantalum was of this sort but that we could force it to have a complete Meissner effect through the technique of rotating in the normal state and cooling while rotating into the superconducting state. The cooling must be done very slowly and adequate rotational speeds must be used, else some frozen-in flux will result.

The results on tin show that the magnitude of the eddy currents produced are dependent on the speed of rotation and on the temperature. The dependence on temperature is connected with the electrical conductivity. These effects may be understood from the following classical electromagnetic theory:[4] A simple change of coordinate system will allow the sphere of metal to stay fixed and the magnetic field to rotate around. The equation to be satisfied is then (mks units):

$$\nabla^2\bar{B}-j\omega\mu\sigma\bar{B}=0,$$

where ω equals angular velocity, μ magnetic permeability, j equals $(-1)^{\frac{1}{2}}$, and σ is the electrical conductivity. The eddy currents induced by the rotating magnetic field produce a magnetic field which outside the sphere is equivalent to a magnetic dipole of strength $(4\pi/\mu)(BD/2)$ at the center of the sphere, where B is the magnetic field in which the sphere is rotated, and D

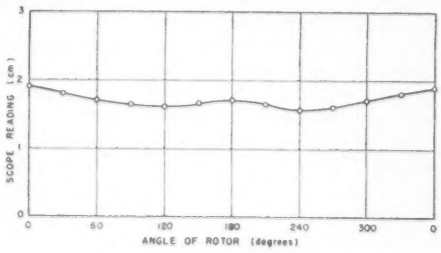

FIG. 5. Meissner effect of tantalum.

[3] W. C. Overton, Jr., Ph.D. thesis, Rice Institute, Houston, Texas (1950), unpublished.

[4] W. R. Smythe, *Static and Dynamic Electricity* (McGraw-Hill Book Company, Inc., New York, 1950), p. 395.

is given by

$$D=-a^3\left\{1-\frac{3}{(2\rho)^{\frac{1}{2}}a}\frac{\sinh(2\rho)^{\frac{1}{2}}a-\sin(2\rho)^{\frac{1}{2}}a}{\cosh(2\rho)^{\frac{1}{2}}a-\cos(2\rho)^{\frac{1}{2}}a}\right\}$$
$$-ja^3\left\{-\frac{3}{\rho a^2}+\frac{3}{(2\rho)^{\frac{1}{2}}a}\frac{\sinh(2\rho)^{\frac{1}{2}}a+\sin(2\rho)^{\frac{1}{2}}a}{\cosh(2\rho)^{\frac{1}{2}}a-\cos(2\rho)^{\frac{1}{2}}a}\right\},$$

with $\rho=\omega\mu\sigma$, and a is the radius of the sphere. When the conductivity, σ, and the angular velocity, ω, are low, the imaginary component is the predominant term. The axis of the dipole will then be nearly perpendicular to the applied magnetic field. If either the conductivity or angular velocity become very large, the imaginary component approaches zero, and the dipole axis then coincides with the direction of the magnetic field. At 4.2°K, for five revolutions per second and $\sigma=4\times10^{10}$ mhos/meter, the imaginary component is one one-tenth of the real component. The magnetic dipole axis is then almost parallel with the applied field.

In his recent book, Fritz London[5] has shown that the magnetic field of a superconducting sphere at a large distance is equivalent to a magnetic dipole of strength, M, at the center of the sphere where M is given by

$$M=-(4\pi/\mu)(a^3B/2)$$
$$\times\{1-[3/(\mu/\lambda)^{\frac{1}{2}}a]\coth(\mu/\lambda)^{\frac{1}{2}}a+3/(\mu/\lambda)a^2\}.$$

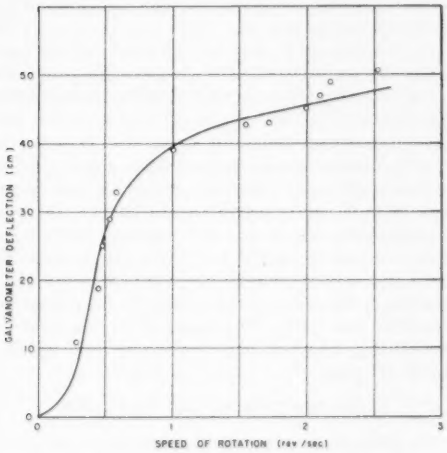

FIG. 6. Eddy currents in tin at 4.2°K.

[5] F. London, *Superfluids* (John Wiley and Sons, Inc., New York, 1950), Vol. I, pp. 34–35.

TABLE I. Galvanometer deflection at various rotational speeds, at 4.2°K.

Galvanometer deflection (cm)	Rotational speed (rev/sec)
11	0.30
19	0.40
25	0.45
29	0.55
33	0.70
39	1.0
43	1.6
43.5	1.7
45	2.0
47	2.2
49.5	2.35
50.5	2.55

Comparing this with the dipole set up by the eddy currents, one sees that they are equal in the limit of very fast speeds of rotation with high conductivity. At about 3.8°K with the sphere rotating at 4.6 revolutions per second, the detector element could not observe any change in the magnetic field when the sphere became superconducting. That is, the field change at the detector element was less than 10^{-4} gauss. The skin depth, $1/\sqrt{\rho}$, for the eddy currents was 0.6 mm at 4.6 revolutions per second, while the skin depth $(\mu/\lambda)^{-\frac{1}{2}}$ of supercurrents was 1.6×10^{-5} mm.

We may conclude that:

(1) The eddy currents in the tin sphere have the same space distribution as the superconducting Meissner currents, within the sensitivity of the magnetic detection equipment.

(2) The tantalum metal which has been sintered together to make the bulk specimen will perform like a normal superconductor if the magnetic field within the interior of the metal is largely removed by the rotation of the specimen while cooling through the transition temperature.

An Operator Calculus Having Applications in Quantum Electrodynamics

RICHARD P. FEYNMAN*
California Institute of Technology, Pasadena, California
(Received May 23, 1951)

An alteration in the notation used to indicate the order of operation of noncommuting quantities is suggested. Instead of the order being defined by the position on the paper, an ordering subscript is introduced so that $A_sB_{s'}$ means AB or BA depending on whether s exceeds s' or *vice versa*. Then A_s can be handled as though it were an ordinary numerical function of s. An increase in ease of manipulating some operator expressions results. Connection to the theory of functionals is discussed in an appendix. Illustrative applications to quantum mechanics are made. In quantum electrodynamics it permits a simple formal understanding of the interrelation of the various present day theoretical formulations.

The operator expression of the Dirac equation is related to the author's previous description of positrons. An attempt is made to interpret the operator ordering parameter in this case as a fifth coordinate variable in an extended Dirac equation. Fock's parametrization, discussed in an appendix, seems to be easier to interpret.

In the last section a summary of the numerical constants appearing in formulas for transition probabilities is given.

IN this paper we suggest an alteration in the mathematical notation for handling operators. This new notation permits a considerable increase in the ease of manipulation of complicated expressions involving operators. No results which are new are obtained in this way, but it does permit one to relate various formulas of operator algebra in quantum mechanics in a simpler manner than is often available. In particular, it is applied to quantum electrodynamics to permit an easier way of seeing the relationships among the conventional formulations, that of Schwinger and Tomanaga,[1] and that of the author.[2] These relationships have already been discussed by many people, particularly Dyson.[3] The connection was shown by means of a re-ordering of operators in each term of a perturbation power series. Here, the same end is achieved in much the same way without having to resort to such an expansion.

It is felt, in the face of daily experimental surprises for meson theory, that it might be worth while to spend one's time expressing electrodynamics in every physical and mathematical way possible. There may be some hope that a thorough understanding of electrodynamics might give a clue as to the possible structure of the more complete theory to which it is an approximation. This is one reason that this paper is published, even though it is little more than a mathematical re-expression of old material. A second reason is the desire to describe a mathematical method which may be useful in other fields.

The mathematics is not completely satisfactory. No attempt has been made to maintain mathematical rigor. The excuse is not that it is expected that rigorous demonstrations can be easily supplied. Quite the contrary, it is believed that to put the present methods on a rigorous basis may be quite a difficult task, beyond the abilities of the author.

The mathematical ideas are described and are illustrated with simple applications to quantum mechanics, in the first four sections. Some possible mathematical relations between the operator calculus described here and the theory of functionals is described in Appendix A, with further specific mathematical applications in Appendixes B and C. Section 5, and more particularly Secs. 6 to 9, apply specifically to quantum electrodynamics and may be omitted without loss by those whose interest is limited to mathematical questions. The use of a fifth variable to parametrize the Dirac equation is discussed in Secs. 8 and 9. An alternative procedure due to V. Fock[4] appears in Appendix D. Section 10 gives a summary of the rules for computing matrix elements.

1. DESCRIPTION OF THE NOTATION

The order of operation of operators is conventionally represented by the position in which the operators are written on the paper. Thus, the product AB of two operators A and B is to be distinguished from the product in reverse order BA. The algebra of operators is noncommutative, so that all of the ordinary algebra, calculus, and analysis with ordinary numbers becomes of small utility for operators. Thus, for a single operator, α, ordinary functions of this operator, such as $A=\exp\alpha$, can be defined, for example, by power series. These functions obey the rules of ordinary analysis even though α is an operator. But if another operator β is introduced with which α does not commute, the question of functions of the two variables α, β is beset with commutation difficulties and the simplest theorems of analysis are lost. For example, if $B=\exp\beta$, it is not true

* Absent on leave at the University of Brazil, Rio de Janeiro, Brazil.

[1] See J. Schwinger, Phys. Rev. **76**, 790 (1949), and S. Tomonaga, Phys. Rev. **74**, 224 (1948), where additional references to previous work may be found.

[2] The author's previous papers will hereafter be designated as follows: R. P. Feynman, Revs. Modern Phys. **20**, 367 (1948)—C; Phys. Rev. **76**, 749 (1949)—I; Phys. Rev. **76**, 769 (1949)—II; and Phys. Rev. **80**, 440 (1950)—III.

[3] F. Dyson, Phys. Rev. **75**, 486, 1736 (1949).

[4] V. Fock, Physik. Z. Sowjetunion **12**, 404 (1937).

that BA, that is, $\exp\beta\exp\alpha$, is equal to $\exp(\beta+\alpha)$. Thus, the law of addition of exponents fails. Consequently, the principles of elementary calculus are no longer operative in a simple way. For example, expand $\exp(\alpha+\beta)$ to first order in β, assuming β small. The zero-order term is $\exp\alpha$, but the first-order term is neither $\beta\exp\alpha$ nor $(\exp\alpha)\beta$ nor the average of the two. From the theory of time-dependent perturbations in quantum mechanics we learn that it is

$$\exp(\alpha+\beta) = \exp\alpha + \int_0^1 \exp[(1-s)\alpha]\beta\exp(s\alpha)ds + \cdots. \quad (1)$$

The appearance of the integral in this analytic result appears surprising and its derivation does not indicate clearly how to differentiate or expand other functions of $\alpha+\beta$. Further, the simple integral on s is not easy to perform, although the results can be given in several ways as power series. That the integral cannot be done in a general fashion is clearly due to a weakness of notation, for in a representation in which α is diagonal with eigenvalues α_n we can of course verify directly the usual result,

$$\langle\exp(\alpha+\beta)\rangle_{mn} = (\exp\alpha_n)\delta_{mn} + (\exp\alpha_m - \exp\alpha_n)\beta_{mn}(\alpha_m-\alpha_n)^{-1} + \cdots \quad (2)$$

of the perturbation theory of stationary states.

We shall change the usual notation of the theory of operators and indicate the order in which operators are to operate by a different device. We attach an index to the operator with the rule that the operator with higher index operates later. Thus, BA may be written B_1A_0 or A_0B_1. The order no longer depends on the position on the paper, so that all of the ordinary processes of analysis may be applied as though A_0 and B_1 were commuting numbers. It is only at the end of a calculation, when the quantities are to be interpreted as operators, that the indices 0 and 1 are of importance if one wishes to reconvert an expression to the usual notation. Thus, if $A=\exp\alpha$ and $B=\exp\beta$, we can now safely write $BA=\exp(\alpha_0+\beta_1)$, as there is only one way to interpret the latter expression. Other analytic processes then become valid. For example,

$$\exp(\alpha_0+\beta_1) = 1+(\alpha_0+\beta_1)+\frac{1}{2!}(\alpha_0+\beta_1)^2+\cdots = 1+\alpha+\beta+\tfrac{1}{2}(\alpha^2+2\beta\alpha+\beta^2)+\cdots$$

in the conventional notation. For on squaring

$$(\alpha_0+\beta_1)^2 = \alpha_0^2+2\alpha_0\beta_1+\beta_1^2,$$

we must interpret the quantity $\alpha_0\beta_1$ as $\beta\alpha$ in accordance with our convention. The quantity β_1^2 alone (that is, not multiplied by any other expression with an index, such as α_0) is simply β^2, since the index is no longer necessary to define the order of operations, there being only one operator in the term.

The notation is to be extended so that the index need not be integral, for example, $A_{-\frac{1}{2}}B_{3.2}=BA$, since $3.1>-\frac{1}{2}$, and in general $A_sB_{s'}=BA$ if $s'>s$ and AB if $s>s'$ and is undefined if $s=s'$.

How can we work with an expression such as $\exp(\alpha+\beta)$ so as to free the α and β of their noncommutative aspects and thus utilize the theory of functions for rearranging the expressions? Take a quantity N very large and write

$$\exp(\alpha+\beta) \approx \left[\exp\frac{1}{N}(\alpha+\beta)\right]^N \approx \left[1+\frac{1}{N}(\alpha+\beta)\right]^N = \left[1+\frac{1}{N}(\alpha+\beta)\right]\left[1+\frac{1}{N}(\alpha+\beta)\right]\cdots \times\left[1+\frac{1}{N}(\alpha+\beta)\right] \text{ for } N \text{ factors.}$$

In each factor we replace $\alpha+\beta$ by $\alpha_i+\beta_i$, where i is an index running to N, and write

$$\exp(\alpha+\beta) = \lim_{N\to\infty}\prod_{i=1}^{N}\left[1+\frac{1}{N}(\alpha_i+\beta_i)\right] = \lim_{N\to\infty}\exp\left[\frac{1}{N}\sum_{i=1}^{N}(\alpha_i+\beta_i)\right],$$

where the last expression is written in accordance with the new convention that the index i controls the order of operation. (The ambiguity arising from α_i and β_i with the same index can only cause trouble in a product $\alpha_i\beta_i$, and such products are of vanishing importance as $N\to\infty$.) More simply, calling $s=i/N$, we can take the limit and write

$$\exp(\alpha+\beta) = \exp\left[\int_0^1(\alpha_s+\beta_s)ds\right]. \quad (3)$$

That this is valid is, of course, evident, since we could call $\alpha_s+\beta_s=\gamma_s$ with γ a definite operator operating at order s, so that

$$\exp\left(\int_0^1\gamma_s ds\right) = \exp\left(\int_0^1\gamma ds\right),$$

for in this expression the order index is unnecessary, only one operator γ being involved. The integral is just γ,

$$\int_0^1\gamma ds = \gamma\int_0^1 ds = \gamma,$$

since γ does not now depend on s. Therefore, Eq. (3) is trivial as it stands; but what is not trivial is the fact

that the right-hand side of Eq. (3) may be manipulated just as though α_s and β_s were numerical functions of s, with the assurance that now the order of operations will always be automatically specified by the index. For example, from Eq. (3) we have the legitimate relation

$$\exp(\alpha+\beta)=\exp\left(\int_0^1 \alpha_s ds\right)\exp\left(\int_0^1 \beta_s ds\right). \quad (4)$$

As an example, showing that such manipulations do not destroy the validity of equations, consider the term of first order in both α and β on both sides of Eq. (4). Expanding the left side as $1+(\alpha+\beta)+\frac{1}{2}(\alpha+\beta)^2+\cdots$, we see that the term in question is $\frac{1}{2}(\alpha\beta+\beta\alpha)$, while expansion of the right side gives for the corresponding term $(\int_0^1 \alpha_s ds)(\int_0^1 \beta_s ds)$. This can be simplified by being written as

$$\int_0^1\int_0^1 \alpha_s ds\beta_{s'}ds'=\int_0^1\int_0^s \alpha_s\beta_{s'}dsds'+\int_0^1\int_s^1 \alpha_s\beta_{s'}dsds'.$$

In the first integral we have $s>s'$, so that $\alpha_s\beta_{s'}$ is equal to $\alpha\beta$, while in the second $s<s'$, so it is $\beta\alpha$. Hence, there results $\alpha\beta\int_0^1\int_0^s dsds'+\beta\alpha\int_0^1\int_s^1 dsds'$; thus on performing the integrations we find finally

$$\left(\int_0^1 \alpha_s ds\right)\left(\int_0^1 \beta_s ds\right)=\tfrac{1}{2}(\alpha\beta+\beta\alpha).$$

This process of rearranging the form of expressions involving operators ordered by indices so that they may be written in conventional form we shall call disentangling the operators. The process is not always easy to perform and, in fact, is the central problem of this operator calculus. As a second example of disentangling, consider the problem of expanding Eq. (4) to the first order in β. It is evidently

$$\exp(\alpha+\beta)=\exp\left(\int_0^1 \alpha_s ds\right)+\exp\left(\int_0^1 \alpha_{s'}ds'\right)\cdot\int_0^1 \beta_s ds+\cdots. \quad (5)$$

The first term is simply $\exp\alpha$, for α_s is independent of s, as there is no other operator with which α_s does not commute in this term. The next is the integral over s of $\exp(\int_0^1 \alpha_{s'}ds')\beta_s$. In the integral on s' we can split the range, according to whether $s'<s$ or $s'>s$: $\exp(\int_s^1 \alpha_{s'}ds')\exp(\int_0^s \alpha_{s'}ds')\beta_s$. The $\alpha_{s'}$ in the first factor acts after the β_s and is otherwise independent of s', while the $\alpha_{s'}$ in the second factor is to act before the β_s. Hence, if we write these factors respectively after and before the β_s and imply the usual convention, the $\alpha_{s'}$ will be independent of s' in the range 0 to s and we may perform the integral. Hence, the result is the integral on s of $\exp[(1-s)\alpha]\beta\exp(s\alpha)$ in agreement with Eq. (1).

Incidentally, by applying new subscripts in another way the term may be also written as $\int_0^1 \exp[(1-s)\alpha_2]\beta_1\times\exp(s\alpha_0)ds$, in which case the integral may be immediately performed to give

$$[(d/d\epsilon)\exp(\alpha+\epsilon\beta)]_{\epsilon=0}$$
$$=\exp\left(\int_0^1 \alpha_{s'}ds'\right)\int_0^1 \beta_s ds$$
$$=\int_0^1 \exp[(1-s)\alpha]\beta\exp(s\alpha)ds$$
$$=(\exp\alpha_2-\exp\alpha_0)(\alpha_2-\alpha_0)^{-1}\beta_1. \quad (6)$$

All the four expressions are equivalent as has been shown, but only the first and third are in a form in which the operators are disentangled so that the conventional expressions may be used. In the representation in which α is diagonal, it should be evident that the matrix element of the last expression is that given in Eq. (2)

Any operator function of $\alpha+\beta$ can, by replacing $\alpha+\beta$ by $\int_0^1 \alpha_s ds+\int_0^1 \beta_s ds$, be manipulated in a manifold of ways, many of which lead to useful formulas. In a like manner, more complicated operator expressions can be rewritten using ordering indices. They may then be manipulated using all of the results of ordinary analysis.

A word about notation: Inasmuch as in mathematics and physics there are already many uses of the subscript notation, very often we shall write $\alpha(s)$ for α_s. In a sense, $\alpha(s)$ is a function of s, namely, in the sense that although the operator α may be definite, its order of operation is not—so that the operator plus a prescription of where it is to operate, $\alpha(s)$, is a function of s. Furthermore, there will be many cases in which the operator actually depends explicitly on the parameter of order. In this case we should have strictly to write $\alpha_s(s)$ but will omit the subscript when no ambiguity will result from the change.

We may remark in a general sense about the mathematical character of our expressions. Given an expression such as $\int_0^1 \beta(s)ds$, we are not concerned with evaluating the integral, for the quantity when separated from other factors with which it might be multiplied is incompletely defined. Thus, although $\int_0^1 \beta_s ds$ standing alone is equivalent simply to β, this is far from true when $\int_0^1 \beta_s ds$ is multiplied by other expressions such as $\exp\int_0^1 \alpha_s ds$. Thus, we must consider the complete expression as a complete functional of the argument functions $\alpha(s)$, $\beta(s)$, etc. With each such functional we are endeavoring to associate an operator. The operator depends on the functional in a complex way (the operator is a functional of a functional) so that, for example, the operator corresponding to the product of two functionals is not (in general) the simple product of the operators corresponding to the separate factors. (The corresponding statement equating the sum of two

functionals and the sum of the corresponding operators is true, however.) Hence, we can consider the most complex expressions involving a number of operators M, N, as described by functionals $F[M(s), N(s)\cdots]$ of the argument functions $M(s)$, $N(s)\cdots(\equiv M_s, N_s\cdots)$. For each functional we are to find the corresponding operator in some simple form;[6] that is, we wish to disentangle the functional. One fact we know is that any analytic rearrangement may be performed which leaves the value of the functional unchanged for arbitrary $M(s)$, $N(s)\cdots$ considered as ordinary numerical functions. Besides, there are a few special operations which we may perform on $F[M(s), N(s)\cdots]$, to disentangle the expressions, which are valid only because the functional does represent an operator according to our rules. These special operations (such as extracting an exponential factor discussed in Sec. 3) are, of course, proper to the new calculus; and our powers of analysis in this field will increase as we develop more of them.

2. APPLICATIONS IN QUANTUM MECHANICS

The wave equation $i\partial\psi/\partial t = H\psi$ determines the wave function $\psi(t_2)$ at time t_2 in terms of that at time t_1, $\psi(t_1)$. In fact, they are related by a unitary transformation $\psi(t_2)=\Omega(t_2, t_1)\psi(t_1)$. The unitary operator $\Omega(t_2, t_1)$ can be expressed as $\Omega(t_2, t_1)=\exp(-i(t_2-t_1)H)$ in the case that H is independent of the time. In spite of the simple appearance of the analytic form of Ω in terms of H, little has been done except formally with this expression for the reasons outlined in the previous section. We may readily re-express it as

$$\Omega(t_2, t_1)=\exp\left(-i\int_{t_1}^{t_2} H_t dt\right)$$

and may then find the expression easy to utilize. Further, if H is an explicit function of the time $H(t)$, we can consider the Ω to be developed as a large number of small unitary transformations in succession, so that we have directly

$$\Omega(t_2, t_1)=\exp\left[-i\int_{t_1}^{t_2} H_t(t)dt\right]. \tag{7}$$

Hereafter in this section we shall make the convention that time is the ordering parameter and simply write $H(t)$ for $H_t(t)$.

We can use this expression to derive many results in quantum theory. Thus, if $H(t)$ can be written as the sum of two parts $H^{(0)}(t)$ and $U(t)$, we have

$$\Omega^{(U)}(t_2, t_1)=\exp\left(-i\int_{t_1}^{t_2} H^{(0)}(t)dt\right)\times\exp\left(-i\int_{t_1}^{t_2} U(t)dt\right). \tag{8}$$

[6] This point of view is discussed in further detail in Appendix A.

If $H^{(0)}$ is simple and U is small, an expansion in powers of U is simple. We call $\Omega^{(U)}$ the operator corresponding to the hamiltonian $H^{(0)}+U$ and $\Omega^{(0)}$ that corresponding to $H^{(0)}$. The first-order difference of $\Omega^{(U)}$and $\Omega^{(0)}$ is

$$-i\int_{t_1}^{t_2} U(t)dt\exp\left[-i\int_{t_1}^{t_2} H(t')dt'\right],$$

which may be disentangled as

$$-i\int_{t_1}^{t_2}\exp\left[-i\int_{t}^{t_2} H(t')dt'\right]U(t)\exp\left[-i\int_{t_1}^{t} H(t')dt'\right]dt = -i\int_{t_1}^{t_2}\Omega^{(0)}(t_2, t)U(t)\Omega^{(0)}(t, t_1)dt, \tag{9}$$

as explained in connection with Eq. (6). This is a standard result of time-dependent perturbation theory.

As a second example consider the perturbation term of first order in U and in V arising from the hamiltonian $H^{(0)}(t)+U(t)+V(t)$. It is

$$-\int_{t_1}^{t_2} U(t')dt'\int_{t_1}^{t_2} V(t'')dt''\exp\left[-i\int_{t_1}^{t_2} H(t)dt\right].$$

In order to disentangle this, we can break the t'' integral into two regions, $t''<t'$ and $t''>t'$. The term arising from the first region has V operating before U, while the reverse is true for the other region. (The integral on t for each region is then divided into three parts determined by the relation of t to t', t''.) Thus, the term becomes, when disentangled, the sum of two terms:

$$\begin{aligned}&-\int_{t_1}^{t_2}\int_{t_1}^{t'}\Omega^{(0)}(t_2, t')U(t')\Omega^{(0)}(t', t'')V(t'')\\&\qquad\times\Omega^{(0)}(t'', t_1)dt''dt',\\&-\int_{t_1}^{t_2}\int_{t'}^{t_2}\Omega^{(0)}(t_2, t'')V(t'')\Omega^{(0)}(t'', t')U(t')\\&\qquad\times\Omega^{(0)}(t', t_1)dt''dt'.\end{aligned} \tag{10}$$

This is the way that the various terms corresponding to the different diagrams arise in quantum electrodynamics when an attempt is made to calculate explicitly a single operator expression arising in perturbation theory.

The results here are very similar to those derived from the lagrangian form of quantum mechanics as in III. Here we have the advantage of being able to use the more familiar operator concepts and to work in greater generality from the start. For it is not necessary that H be restricted to coordinate and momentum operators only. Equations (7) and (8) are correct for any H; for example, one containing creation and annihilation operators of second quantization, or Dirac matrices, etc.

The connection of these formulas to those given in I is simple. $K(x_2, t_2; x_1, t_1)$ is just a coordinate integral

kernel representation of the operator $\Omega(t_2, t_1)$ so that, for example, Eq. (9) gives directly

$$-i\int_{t_1}^{t_2} K^{(0)}(x_2, t_2; x, t)U(x, t)K^{(0)}(x, t; x_1, t_1)dxdt,$$

the expression (9) of I, while Eq. (10) translates immediately into the expression (30) of III.

As another type of application, consider two interacting systems whose hamiltonian is $H^{(a)}+H^{(b)}+U[x^{(a)}, x^{(b)}]$, where $H^{(a)}$ involves operators of system (a) only, $H^{(b)}$ involves only those of system (b), and U involves both. Then we may ask for the amplitude, if at t_1 system (a) is in state ψ_1 and system (b) in ϕ_1, that at t_2 they are in ψ_2, ϕ_2. This is the matrix element

$$m=\left\langle \psi_2\phi_2 \middle| \exp\left(-i\int_{t_1}^{t_2} H^{(a)}(t)dt - i\int_{t_1}^{t_2} H^{(b)}(t)dt - i\int_{t_1}^{t_2} U[x^{(a)}(t), x^{(b)}(t)]dt\right) \middle| \psi_1\phi_1 \right\rangle. \quad (11)$$

But this may be split into two problems. We may first find the matrix element

$$T^{(a)}[x^{(b)}(t)]=\left\langle \psi_2 \middle| \exp\left(-i\int_{t_1}^{t_2} H^{(a)}(t)dt - i\int_{t_1}^{t_2} U[x^{(a)}(t), x^{(b)}(t)]dt\right) \middle| \psi_1 \right\rangle \quad (12)$$

for the system (a) alone, considering that in the interaction potential $U[x^{(a)}, x^{(b)}]$, all operators referring to (b) are arbitrary numerical functions of t. (We have been writing as though U depends on (b) only through the coordinate, $x^{(b)}$; but the same method applies if it is also a function of momentum, or spin, or other operators on system (b).) Then the matrix element $T^{(a)}$ depends on the function $x^{(b)}(t)$. As we indicate, it is a functional of $x^{(b)}(t)$. The final answer, m, is then a matrix element $\langle\phi_2|M|\phi_1\rangle$ between the states ϕ_1 and ϕ_2;

$$m=\left\langle \phi_2 \middle| \exp\left(-i\int_{t_1}^{t_2} H^{(b)}(t)dt\right) T^{(a)}[x^{(b)}(t)] \middle| \phi_1 \right\rangle, \quad (13)$$

wherein now the quantities $x^{(b)}(t)$ are considered as ordered operators operating relative to each other and to $H^{(b)}(t)$ in accordance with the time parametrization.

In this way we can analyze one part of a pair of interacting systems without having yet analyzed the other. The influence of a on b is completely contained in the operator functional $T^{(a)}[x^{(b)}(t)]$. This separation may be useful in analysis of the theory of measurement and of quantum statistical mechanics. It is the possibility of such a separation which exists also in the case[2] of the lagrangian form of quantum mechanics, **C**, which makes that form useful in analyzing the quantum properties of the electromagnetic field. We may therefore expect that with the present operator notation it should be equally easy to make this analysis. That this is indeed true we show by example further on. Since this, the main advantage of the lagrangian form, can be so easily managed with the new notation for operators, this may well take the place of the lagrangian form in many applications. It is in some ways a more powerful and general form than the lagrangian. It is not restricted to the nonrelativistic mechanics in any way. A possible advantage of the other form at present might be a slight increase in *anschaulichkeit* offered for the interpretation of the nonrelativistic quantum mechanics.

3. DISENTANGLING AN EXPERIMENTAL FACTOR

There is one theorem which is very useful in disentangling operator expressions. We shall give it in this section. Suppose we have several operators M, N, etc. (which may also be functions of time, or more generally, the ordering parameter s), which are ordered in some way.

Let us say the functional $F[M(s), N(s)\cdots]$ defines the ordered operator. Now suppose we replace $M(s)$ by $M'(s)=U^{-1}M(s)U$, $N(s)$ by $N'=U^{-1}NU$, etc., where U is some constant operator. Then, as is well known, in $F[M(s), N(s)\cdots]$ in any product of successive operators, such as $M(s+ds)N(s)$, the UU^{-1} cancel out in between (that is, $MN=U^{-1}MUU^{-1}NU=U^{-1}MNU$, etc.), so that there results

$$F[M'(s), N'(s)\cdots]=U^{-1}F[M(s), N(s)\cdots]U, \quad (14)$$

where the U's are written to operate in the correct order. (If we wish to be more specific, we can imagine the range of the ordering parameter to be $s=0$ to 1 and write the right-hand side as $U_1^{-1}FU_0$.)

This is a simple rewriting of a well-known theorem of equivalence transformations. However, a much more interesting case is that in which $U(s)$ is actually a function of the ordering parameter. That is, we contemplate performing different transformations on the operators $M(s)$ depending on the value of s at which they are to operate. Then in a product of successive operators such as $M'(s+ds)N'(s)$, where

$$M'(s+ds)=U^{-1}(s+ds)M(s+ds)U(s+ds)$$

(operating in the order indicated by the position of U^{-1}, M and U) and $N'(s)=U^{-1}(s)N(s)U(s)$, the factors $U(s+ds)$ and $U^{-1}(s)$ will not cancel out, but we will find the operator $U(s+ds)U^{-1}(s)$ operating between times s and $s+ds$, say at $s+\frac{1}{2}ds$. If we assume U continuous, we can imagine $U(s)$ differs from $U(s+ds)$ to the first order in ds, and hence that $U(s+ds)U^{-1}(s)$ equals to first order in ds:

$$U(s+ds)U^{-1}(s)=1+P(s)ds,$$

where $P(s)$ is an operator defined by this relation in the

limit $ds \to 0$. We may write this relation

$$dU(s)/ds = P(s)U(s) \tag{15}$$

with positional ordering. Hence, between s and $s+ds$ there should operate an additional factor $1+P(s)ds$, which for convenience we may write, valid to first order, as $\exp[P(s+\frac{1}{2}ds)ds]$. The $s+\frac{1}{2}ds$ in $P(s+\frac{1}{2}ds)$ will automatically locate the factor in the correct order. But there is a factor of this kind appearing between the operators for each value of s, or multiplying the factors all together, we obtain the net factor $\exp\int_0^1 P(s)ds$, the product becoming a sum, or integral in the exponent. Hence, we have the general theorem:

$$F[M'(s), N'(s)\cdots] = U^{-1}(1)F[M(s), N(s)\cdots] \times \exp\left(\int_0^1 P(s)ds\right)U(0),$$

where

$$M'(s) = U^{-1}(s)M(s)U(s) \tag{16}$$

and

$$U(s) = \exp\left[\int_0^s P(s')ds'\right]U(0), \tag{17}$$

this last coming from integrating Eq. (15). We shall use the theorem by writing it in the form

$$\exp\int_0^1 P(s)ds F[M(s), N(s)\cdots] = U(1)F[M'(s), N'(s)\cdots]U^{-1}(0), \tag{18}$$

in which form it serves as a rule for disentangling an exponential factor from another expression. A word of caution is necessary in reading Eqs. (18), (16), and (17), for three different notations are used in the expressions. In Eq. (18) the new ordered notation is used in its complete form; for example, the s in $\exp\int_0^1 P(s)ds$ gives the order in which the P is to operate relative to the M, N of the functional F which it multiplies. In Eq. (16), however, all the operators are to operate at s, but the relative order in M' of U, M, and U^{-1} is as given by the usual position convention. Finally, Eq. (17) would be less ambiguous if it were replaced by the differential equation (15). For in the solution (17), the s' are to bear no relation to the s in Eq. (16) or Eq. (18). The operator $U(s)$ is to be computed from P by Eq. (17) first, then the whole operator $U(s)$ is to operate in Eq. (16), and then in Eq. (18) at the position s.

We shall use this theorem in several applications related to quantum electrodynamics. Most particularly, we shall find a certain special case useful enough to warrant special mention. It is the case that $P(s)$ is of the form $\alpha(s)P_s$, where $\alpha(s)$ is a simple numerical function, and P_s is an operator whose form does not depend on s but whose order of operation does. Then if we call $a(s) = \int_0^s \alpha(s')ds'$, so that $a(s)$ is also a numerical function, Eq. (17) gives $U(s) = \exp[a(s)P_s]U(0)$. We shall further choose to specialize $U(0) = 1$. (The more general case corresponds to a final simple constant equivalence transformation (14) with $U(0)$.) Then our theorem may be written

$$\exp\left[\int_0^1 \alpha(s)P_s ds\right]F[M(s), N(s)\cdots] = \exp\left[P_1\int_0^1 \alpha(s)ds\right]F[M'(s), N'(s)\cdots], \tag{19}$$

where

$$M'(s) = \exp\left[-P_s\int_0^s \alpha(s')ds'\right]M(s) \times \exp\left[+P_s\int_0^s \alpha(s')ds'\right]. \tag{20}$$

Further, since this theorem with Eq. (20) substituted into Eq. (19) is valid when $\alpha(s)$ is an *arbitrary* numerical function, it is also true if $\alpha(s)$ is any ordered operator $\alpha(s)$ commuting with P for all s, provided that in *all* expressions involving α, the parameter s or s' is consistently interpreted as giving the order in which the α operates.[6]

The mathematical proof of the theorems (18) and (19) offered here is admittedly very sketchy; but since the theorems are true, it should not be hard to supply them with more satisfactory demonstrations (see Appendix A for an alternative demonstration).

There are a number of other interesting relations which we may derive from Eq. (19), but which we shall not need in this paper. One is included here because it has been found useful in certain other applications. If $\alpha(s)$ is considered infinitesimal in Eqs. (19) and (20), expansion in first order in α gives the following result (or differentiate each side with respect to $\alpha(t)$ and set $\alpha(s) = 0$),

$$P_t F[M(s)] = P_1 F[M(s)] - \int_t^1 (PM - MP)_s \delta F/\delta M(s)ds$$

(if we assume F can be represented by a functional having a derivative $\delta F/\delta M(s)$). We have taken F to depend only on one operator $M(s)$, but the generalization is clear. Here, $(PM-MP)_s$ is conventional ordering is $PM(s) - M(s)P$ and is considered to act as an entity at s. The differential form

$$(dP_t/dt)F[M(s)] = (PM - MP)_t \delta F/\delta M(t) \tag{21}$$

is also useful.

[6] To simplify such descriptions, in a situation involving two sets of operators, any one of the first set commuting with any one of the second, it is often convenient to generalize to the use of two different ordering parameters—one for first set, and one for the second.

4. THE INTERACTION REPRESENTATION

As a first simple direct application of our theorem consider again the perturbation problem (8) of computing the operator

$$\Omega^{(U)}(t_2, t_1) = \exp\left[-i\int_{t_1}^{t_2} H^{(0)}(t)dt\right]\exp\left[-i\int_{t_1}^{t_2} U(t)dt\right]. \quad (8)$$

If we suppose the properties of $H^{(0)}$ to be known and simple, the right side of Eq. (8) may be disentangled by means of our theorem (18). We consider $-iH^{(0)}(t)$ as an operator $P(s)$ and

$$\exp\left[-i\int_{t_1}^{t_2} U(t)dt\right]$$

as the functional F from which the

$$\exp\left[-i\int H^{(0)}(t)dt\right]$$

is to be disentangled. Hence, a direct application of Eq. (18) gives

$$\exp\left[-i\int_{t_1}^{t_2} H^{(0)}(t)dt\right]\exp\left[-i\int_{t_1}^{t_2} U(t)dt\right] = S(t_2)\exp\left[-i\int_{t_1}^{t_2} U'(t)dt\right]S^{-1}(t_1), \quad (22)$$

where

$$S(t) = \exp\left[-i\int_a^t H^{(0)}(t')dt'\right]$$

(the lower limit a used in defining S is arbitrary; it may be taken as t_1 so $S(t_1)=1$ if that is convenient), and

$$U'(t) = S^{-1}(t)U(t)S(t) \quad (23)$$

(operating in positional order). If we take matrix elements not between states ψ_1 and ψ_2 but between $\psi_1' = S^{-1}(t_1)\psi_1$ and $\psi_2' = S^{-1}(t_2)\psi_2$, we may call the Ω-matrix Ω' and omit the $S(t_2)$ and $S^{-1}(t_1)$ factors in Eq. (22). These new time-dependent states ψ' are evidently states that would give rise to ψ_1 at t_1 and ψ_2 at t_2 (from some fixed reference time a) if the perturbation were not acting. Then the time-dependent perturbation theory simply comes to evaluating

$$\Omega'(t_2, t_1) = \exp\left(-i\int_{t_1}^{t_2} U'(t)dt\right). \quad (24)$$

Expansion in power series, substitution of U' from Eq. (23), and use of the relation $\Omega^{(0)}(t', t'') = S(t')S^{-1}(t'')$ leads immediately to the formulas (9) and (10), so that Eqs. (23) and (24) give the simplest form to the time-dependent perturbation theory. Of course, the same results may be obtained by a unitary transformation in the conventional way. Ordinarily, result (24) is not written in this way, for it involves the time convention on the ordering of the operators. (It is usually expressed as a differential equation for Ω'.) If the perturbation U represents an interaction between some systems described by $H^{(0)}$, the reduction of Eq. (8) to Eq. (24) is called passing to the interaction representation.

5. SYSTEM COUPLED TO AN HARMONIC OSCILLATOR

As a further example of the use of the notation we solve completely the problem of a particle or system of particles coupled linearly to an harmonic oscillator. This problem in greater generality is the main problem of quantum electrodynamics. It has been thoroughly studied in III, but we solve it again as an illustration of the new notation. Let the hamiltonian of the combined system be

$$H = H_p(t) + H_{\text{osc}} - \Gamma(t)q,$$

where H_{osc} is the hamiltonian of the oscillator alone,

$$H_{\text{osc}} = (1/2m)(p^2 + \omega^2 q^2),$$

where p is the momentum conjugate to q, the coordinate of the oscillator. Further, H_p, which may depend explicitly on time, is the hamiltonian of the particles, and Γ may contain any operators pertaining to the particles as well as possibly being an explicit function of the time. We ask for the matrix element for finding the particles in state $\chi_{t''}$ and the oscillator in some eigenstate m at time t'', if at a previous time t' the particles are in state $\chi_{t'}$, and the oscillator in its nth eigenstate. It is the matrix element

$$\left\langle \chi_{t''}\phi_m \middle| \exp -i\int_{t'}^{t''} [H_p(t) + H_{\text{osc}}(t) - \Gamma(t)q(t)]dt \middle| \phi_n\chi_{t'} \right\rangle$$

using the time ordering convention. As already discussed in Sec. 2, this can be considered as the matrix element between states $\chi_{t'}$ and $\chi_{t''}$ of the matrix

$$M = \exp\left(-i\int_{t'}^{t''} H_p(t)dt\right)G_{mn}, \quad (25)$$

where G_{mn} (the analog of T of Sec. 2), a functional of $\Gamma(t)$, serves to define the net effect on the particles of their interaction with the oscillator. Calculation of G_{mn} means evaluating

$$G_{mn} = \left\langle \phi_m \middle| \exp -i\int_{t'}^{t''} H_{\text{osc}}(t)dt \cdot \exp i\int_{t'}^{t''} \Gamma(t)q(t)dt \middle| \phi_n \right\rangle \quad (26)$$

in a general way as a functional of $\Gamma(t)$. We are to consider $\Gamma(t)$ here as a simple numerical function, and

only later utilize the fact that it is an operator involving the particles when we go to evaluate the matrix M, Eq. (25), between the particle states $\chi_{t'}$ and $\chi_{t''}$. The evaluation of G_{mn} for an arbitrary numerical function $\Gamma(t)$ may be performed in a variety of ways. One is by the lagrangian form of quantum mechanics given explicitly in III, Sec. 3, with the sole difference (which is unessential for this part of the problem) that there $\Gamma(t)$ was called $\gamma(t)$ and was a functional of the coordinates $x(t)$ of the particles, while here we see we are in a more general position as $\Gamma(t)$ may be a functional of any ordered operators referring to the particles. We find, for example [III, Eq. (14)],

$$G_{00}=\exp\left[-(1/4\omega)\int_{t'}^{t''}\int_{t'}^{t''}\exp(-i\omega|t-s|)\times\Gamma(t)\Gamma(s)dtds\right]. \quad (27)$$

The same result may also be obtained by a direct solution of the Schrödinger equation for the forced oscillator. The great advantage of the operator notation is to allow this formal solution for an oscillator forced by an *arbitrary potential function* $\Gamma(t)$ to be equally useful when the oscillator is actually in interaction with a quantum-mechanical system!

Thus, we have the answer for G_{mn} in III, Eq. (57), using Γ for γ. It is, however, interesting to see how this expression for G_{mn} could be worked out directly using the methods of the ordered operator calculus. We want to disentangle the operator

$$G=\exp\left(-i\int_{t'}^{t''}H_{\text{osc},t}dt\right)\exp\left(i\int_{t'}^{t''}\Gamma(t)q_t dt\right). \quad (26')$$

Let us call, in the usual way, $Q^*=(\frac{1}{2}\omega)^{\frac{1}{2}}(q-i\omega^{-1}p)$ and $Q=(\frac{1}{2}\omega)^{\frac{1}{2}}(q+i\omega^{-1}p)$ the creation and annihilation operators. They satisfy the commutation relation

$$QQ^*-Q^*Q=1. \quad (28)$$

In terms of them $H_{\text{osc}}=\frac{1}{2}\omega(Q^*Q+QQ^*)$ and

$$q=(2\omega)^{-\frac{1}{2}}(Q+Q^*). \quad (29)$$

Now as a first step we pass to the interaction representation (Sec. 4). We use the theorem (20) with $P_s=-iH_{\text{osc}}$, $\alpha(s)=1$, to disentangle the $\exp[-i\int H_{\text{osc}}(t)dt]$ factor, obtaining

$$G=S(t'')\exp\left\{i(2\omega)^{-\frac{1}{2}}\int_{t'}^{t''}\Gamma(t)[Q'(t)+Q'^*(t)]dt\right\}S^{-1}(t'),$$

where $Q'(t)=S^{-1}(t)QS(t)$, $Q'^*(t)=S^{-1}(t)Q^*S(t)$, and $S(t)=\exp(-itH_{\text{osc}})$. By redefining the wave functions so they contain $S(t)$, or, for eigenstates, the energy factors $\exp(-iE_n t)$ for the free oscillator, we can eliminate the $S(t'')$ and $S^{-1}(t')$ and need merely calculate the matrix element of

$$G'=\exp i(2\omega)^{-\frac{1}{2}}\int_{t'}^{t''}\Gamma(t)[Q'(t)+Q'^*(t)]dt.$$

From Eq. (28) we readily calculate that[7]

$$Q'(t)=Qe^{-i\omega t} \quad \text{and} \quad Q'^*(t)=Q^*e^{+i\omega t}, \quad (30)$$

so that the problem becomes the disentanglement of

$$G'=\exp\left[i(2\omega)^{-\frac{1}{2}}\int_{t'}^{t''}\Gamma(t)e^{+i\omega t}Q_t^*dt\right]\times\exp\left[i(2\omega)^{-\frac{1}{2}}\int_{t'}^{t''}\Gamma(s)e^{-i\omega s}Q_s ds\right].$$

We shall find it most convenient to disentangle this into a form in which all the annihilation operators operate first, and then come the creation operators (since the nth state cannot suffer more than n annihilation operators, $Q^{n+1}\phi_n$ vanishing, the expression will be easy to evaluate in this form). To this end let us use theorem (19) again, this time with $P=Q^*$,

$$\alpha(s)=i(2\omega)^{-\frac{1}{2}}\Gamma(t)e^{+i\omega t}.$$

Calling, temporarily,

$$A(t)=i(2\omega)^{-\frac{1}{2}}\int_{t'}^{t}\Gamma(t)e^{+i\omega t}dt,$$

we find

$$G'=\exp[A(t'')Q_{t''}^*]\exp\left[i(2\omega)^{-\frac{1}{2}}\int_{t'}^{t''}\Gamma(t)e^{-i\omega t}Q''(t)dt\right],$$

where

$$Q''(t)=\exp[-A(t)Q^*]Q\exp[+A(t)Q^*]. \quad (31)$$

The commutation relation (28) here gives[8]

$$Q''(t)=Q_t+A(t), \quad (32)$$

so that

$$G'=\exp[A(t'')Q_{t''}^*]\times\exp\left[i(2\omega)^{-\frac{1}{2}}\int_{t'}^{t''}\Gamma(t)e^{-i\omega t}\{Q_t+A(t)\}dt\right].$$

In the last factor Q_t can be replaced by $Q_{t'}$ since t is in any case less than t'', so that all the Q_t's come before the $Q_{t''}^*$, and Q_t need not be ordered relative to itself as it is a constant operator. Hence, we may, with a slight rewriting (for example, $i\beta^*$ for $A(t'')$), write

$$G'=\exp(i\beta^*Q_{t''}^*)\exp(i\beta Q_{t'})G_{00} \quad (33)$$

[7] For, $Q'(t)=\exp(itH_{\text{osc}})Q\exp(-itH_{\text{osc}})$ implies $dQ'/dt=iS^{-1}(t)\times(H_{\text{osc}}Q-QH_{\text{osc}})S(t)=-i\omega Q'(t)$, since $H_{\text{osc}}Q-QH_{\text{osc}}=-\omega Q$ by Eq. (28). Thus, since $Q'(0)=Q$, one obtains $Q'(t)=e^{-i\omega t}Q$.

[8] For, differentiation of the expression for $Q''(t)$ gives $dQ''(t)/dt=-A'(t)\exp(-A(t)Q^*)(Q^*Q-QQ^*)\exp(+A(t)Q^*)=A'(t)$ by Eq. (28), so integration gives $Q''(t)=A(t)+Q$, since $Q''(t')=Q$, inasmuch as $A(t')=0$.

with G_{00} equal to $\exp i(2\omega)^{-\frac{1}{2}}\int_{t'}^{t''}\Gamma(t)e^{-i\omega t}A(t)dt$ and therefore identical to Eq. (27), and with

$$\beta=(2\omega)^{-\frac{1}{2}}\int_{t'}^{t''}\Gamma(t)e^{-i\omega t}dt,$$
$$\beta^*=(2\omega)^{-\frac{1}{2}}\int_{t'}^{t''}\Gamma(t)e^{+i\omega t}dt, \tag{34}$$

just as in III, Eq. (58). The operator G' is now completely disentangled. Its matrix element between n and m we call G_{mn}. The matrix element may be evaluated by ordinary methods, since the t' and t'' in Q and Q^*, respectively, in Eq. (33) are unnecessary if the positional notation is used. That the element for $n=0$, $m=0$ is just what we call G_{00} is evident, for if $\exp(i\beta Q)$ be expanded as $1+\beta Q+\beta^2Q^2\cdots$ and the result applied to ϕ_0, all the terms beyond the first give zero for $Q\phi_0=0$. Thus, this exponential may effectively be replaced by unity. Likewise, the second can be replaced by unity for $\phi_0{}^*Q^*=0$.

The case of more general values of m, n, may be worked out by writing

$$\phi_n=(n!)^{-\frac{1}{2}}Q^{*n}\phi_0, \tag{35}$$

so that

$$G_{mn}=\langle\phi_0|(m!)^{-\frac{1}{2}}(n!)^{-\frac{1}{2}}Q^me^{i\beta^*Q^*}e^{i\beta Q}Q^{*n}|\phi_0\rangle G_{00}. \tag{36}$$

Then, since $e^{i\beta Q}Q^*=(Q^*+i\beta)e^{i\beta Q}$ (as in Eqs. (31), (32)), repetition n times gives $e^{i\beta Q}Q^{*n}=(Q^*+i\beta)^ne^{i\beta Q}$, and likewise $Q^me^{i\beta^*Q^*}=e^{i\beta^*Q^*}(Q+i\beta^*)^m$. We find

$$G_{mn}=\langle\phi_0|(m!)^{-\frac{1}{2}}(n!)^{-\frac{1}{2}}e^{i\beta^*Q^*}(Q+i\beta^*)^m \times(Q^*+i\beta)^ne^{i\beta Q}|\phi_0\rangle G_{00}. \tag{37}$$

The exponentials may now be replaced by unity as previously discussed. The other factors expanded by the binomial theorem give

$$G_{mn}=(m!)^{-\frac{1}{2}}(n!)^{-\frac{1}{2}}\sum_r\binom{m}{r}\sum_s\binom{n}{s}(i\beta^*)^{m-r} \times(i\beta)^{n-s}\langle\phi_0|Q^rQ^{*s}|\phi_0\rangle G_{00}.$$

The next to last factor by Eq. (35) is

$$(s!)^{\frac{1}{2}}(r!)^{\frac{1}{2}}\langle\phi_r|\phi_s\rangle=(s!)^{\frac{1}{2}}(r!)^{\frac{1}{2}}\delta_{rs},$$

so that finally

$$G_{mn}=(m!n!)^{-\frac{1}{2}}\sum_r\binom{m}{r}\binom{n}{r}r!(i\beta^*)^{m-r}(i\beta)^{n-r}G_{00} \tag{38}$$

as in III, Eq. (57).

Having this form for the behavior of a system of particles interacting with a single oscillator, we could go on and discuss the quantum electromagnetic field as a set of such oscillators. It is evident that to do so would be simply to repeat the steps described in III, Sec. 4, using Γ for γ and reinterpreting the symbols as ordered operators rather than as amplitudes associated with a path. The result in general is Eq. (43) below [in agreement with III, Eq. (48)], and there is no need to go into the details again of summing the effects of all the oscillators to obtain this result. We will pass directly to a discussion of the complete electromagnetic field.

6. QUANTUM ELECTRODYNAMICS

There are available several equivalent formulations of quantum electrodynamics.[1,2,9] We shall give a very brief outline of their interrelationships using the ordered operator notation. We can start with the usual formalism of Heisenberg, Pauli, and Dirac.[9] The wave function of the system, consisting of the electron-positron field and of the electromagnetic field in interaction, satisfies a wave equation $i\partial\psi/\partial t=H\psi$, where the hamiltonian for the system may be written $H=H_m+H_f+H_i$, where H_m is that of the electron-positron field free of potentials, H_f is that of the electromagnetic field in empty space, and H_i represents the interaction of the two fields. The problem is to obtain the wave function at time t_2 in terms of its value at a previous time t_1. It is therefore a study of the operator

$$\exp\left\{-i\int_{t_1}^{t_2}[H_m(t)+H_f(t)+H_i(t)]dt\right\}.$$

We can simplify this by first disentangling the exponential factor

$$\exp\left\{-i\int_{t_1}^{t_2}[H_m(t)+H_f(t)]dt\right\}.$$

That is, we go directly to the interaction representation, and find that we must analyze

$$\exp\left\{-i\int_{t_1}^{t_2}H_i'(t)dt\right\}.$$

We shall always use the interaction representation and shall omit the prime here for simplicity of notation. Furthermore, it will be sufficient for our purpose to consider only the case $t_1\rightarrow-\infty$ and $t_2\rightarrow+\infty$, so that quantum electrodynamics is a study of the operator[10]

$$S=\exp\left[-i\int_{-\infty}^{\infty}j_\mu(\mathbf{x},t)A_\mu(\mathbf{x},t)d^3\mathbf{x}dt\right], \tag{39}$$

where the $A_\mu(1)$ is the operator potential of the electromagnetic field and $j_\mu(1)$ is the operator current of the

[9] See, for example, P. A. M. Dirac, *The Principles of Quantum Mechanics*, (The Clarendon Press, Oxford, 1947), third edition, Chapter 12.

[10] For systems with particles of spin zero or one, S may be written in this same form by use of the Kemmer-Duffin matrices β_μ, as is shown by C. N. Yang and D. Feldman, Phys. Rev. **79**, 972 (1950), for example, Eq. (33). Thus, all of these results given here for the Dirac field are equally correct for spin zero or one if γ_μ is replaced by β_μ. See also M. Neumann and W. H. Furry, Phys. Rev. **76**, 1677 (1949), and R. Moorhouse, Phys. Rev. **76**, 1691 (1949).

Dirac electron-positron field. They, of course, commute with each other, since they refer to different systems. Further,[11] $A_\mu(1)$, $A_\mu(2)$ commute if 1 and 2 are separated by a spacelike interval, as do $j_\mu(1)$, $j_\mu(2)$. In the expression for S the operators are ordered in accordance with the time t.

We may thus define the problem of quantum electrodynamics as a study of the operator S. Let us imagine for purposes of discussion that we disregard the derivation of S given in the preceding paragraph. We imagine the problem is given directly as the analysis of the operator S defined in Eq. (39) (assuming the commutation rules, reference 11). Let us see how the various formalisms are simply different ways of expressing or analyzing S.

First, we might try to define S in some way which would not require the use of the ordering notation. Suppose we split the range of integration of t into two regions $-\infty$ to τ and τ to ∞. Then the integral may be split into two parts. We can write the factors, as

$$S=\exp\left[-i\int_\tau^\infty j_\mu(\mathbf{x},t)A_\mu(\mathbf{x},t)d^3\mathbf{x}dt\right]$$
$$\times\exp\left[-i\int_{-\infty}^{\tau} j_\mu(\mathbf{x}',t')A_\mu(\mathbf{x}',t')d^3\mathbf{x}'dt'\right].$$

Now, since $t'<t$, all the operators on the last factor act before those of the first factor, so they are disentangled relative to the first factor. Hence, we are led to define an operator function of τ,

$$\Omega(\tau)=\exp\left[-i\int_{-\infty}^{\tau} j_\mu(\mathbf{x},t)A_\mu(\mathbf{x},t)d^3\mathbf{x}dt\right].$$

If τ is changed to $\tau+d\tau$, an additional factor appears operating in front of all other $t\leqslant\tau$, namely, $\exp[-i\Delta\tau\int j_\mu(\mathbf{x},\tau)A_\mu(\mathbf{x},\tau)d^3\mathbf{x}]$. Hence, $\Omega(\tau)$ satisfies the differential equation

$$id\Omega/d\tau=\left[\int j_\mu(\mathbf{x},\tau)A_\mu(\mathbf{x},\tau)d^3\mathbf{x}\right]\Omega(\tau), \qquad (40)$$

the operators operating in positional order.

Thus, we are lead to a differential equation, the solution of which can be used to define S (for S is $\Omega(\tau)$ as $\tau\to+\infty$ when $\Omega(\tau)$ is that solution of Eq. (40) which $\to I$ as $\tau\to-\infty$). If we define $\psi(-\infty)$ as an initial state wave function, clearly, $\psi(\tau)=\Omega(\tau)\psi(-\infty)$ satisfies the same equation as Ω. This is the Schrödinger equation in the usual formulation if written in interaction representation. (We probably would not be led to go back to the ordinary representation as this is an unnecessary increase in complexity.)

The apparent lack of covariance implied by using time to define the differential equation can be remedied by analyzing S in a slightly different manner, suggested by Tomanaga and by Schwinger.[1]

The variables $\mathbf{x}$, t over which one integrates in Eq. (39) may be divided into two groups in another way; those previous to and those following an arbitrary spacelike surface σ:

$$S=\exp\left[-i\int_b j_\mu(\mathbf{x},t)A_\mu(\mathbf{x},t)d^3\mathbf{x}dt\right]$$
$$\times\exp\left[-i\int_a j_\nu(\mathbf{x}',t')A_\nu(\mathbf{x}',t')d^3\mathbf{x}'dt'\right],$$

where the region a of integration of the second factor are those points of space-time previous to σ, while b are those following σ. Now again the factors are disentangled. It might at first be argued that since there are some values of t' greater than t, the corresponding operators in $\int_a$ should follow, not precede, those in $\int_b$. But for those t' which exceed t, the points $\mathbf{x}$, $\mathbf{x}'$ are separated by a spacelike interval (as σ is a spacelike surface); hence the order of the $A_\mu(\mathbf{x},t)$ and $A_\nu(\mathbf{x}',t')$ as well as of $j_\mu(\mathbf{x},t)$ and $j_\nu(\mathbf{x}',t')$ is irrelevant, as these commute. Hence, the operators are, in fact, disentangled; and we can define

$$\Omega(\sigma)=\exp\left[-i\int_a j_\mu(\mathbf{x},t)A_\mu(\mathbf{x},t)d^3\mathbf{x}dt\right]$$

as an operator defined as a functional of the surface σ. A small change in surface at $\mathbf{x}$, t changes the operator by

$$\delta\Omega(\sigma)/\delta\sigma(\mathbf{x},t)=-ij_\mu(\mathbf{x},t)A_\mu(\mathbf{x},t)\Omega(\sigma), \qquad (41)$$

the equation of Schwinger[12] for $\Omega(\sigma)$ (and also for $\psi(\sigma)$ defined by $\Omega(\sigma)\psi(-\infty)$). Again, S is $\Omega(\sigma)$ as the surface σ is removed to $+\infty$.

These differential equations (40) or (41) are therefore needed to define the operator S if one is limited to conventional notation. The form (41) has the advantage of putting the relativistic invariance more into evidence. However, the solution (39) is common to both and is more easily used. It is likewise evidently invariant if we write it

$$S=\exp\left[-i\int j_\mu(1)A_\mu(1)d\tau_1\right] \qquad (42)$$

(with the point 1 representing $\mathbf{x}_1$, t_1 and $d\tau_1=d^3\mathbf{x}_1dt_1$) and assume the convention here that *if two operators in Eq. (42) correspond to points separated by either a timelike or a zero interval, that operates first which corresponds*

[11] See, for example, J. Schwinger, Phys. Rev. **74**, 1439 (1948). In his notation (except that we put a factor e in A_μ rather than j_μ), the commutation relations are [his Eqs. (2.28) and (2.29)]

$$[A_\mu(x),A_\nu(x')]=4\pi e^2i\delta_{\mu\nu}D(x-x')$$

and $j_\mu(x)=\bar\psi(x)\gamma_\mu\psi(x)$ with $\{\psi_\alpha(x),\bar\psi_\beta(x')\}=-iS_{\alpha\beta}(x-x')$ if no external potential is acting. Other combinations commute.

[12] I. Schwinger. Phys. Rev. **74**, 1439 (1948).

to the earlier time. If they are separated by a spacelike interval, no definition is necessary, for they commute.

The other developments consist in methods of actually evaluating Eq. (42), given the commutation relations[11] of the $A_\mu(1)$. The method explained by Dyson[3] consists of making a power series expansion of S and disentangling it term by term. For example, the second-order term is

$$-\tfrac{1}{2}\int j_\mu(1)A_\mu(1)d\tau_1\int j_\nu(2)A_\nu(2)d\tau_2.$$

This term may then be analyzed into the conventional notation by reordering the operators. In this example it is necessary merely to break the region of integration in t_2 up into two, $t_2<t_1$ and $t_2>t_1$. Actually, because of the symmetry they give equal contributions, so that the result is

$$-\int\int j_\mu(1)A_\mu(1)d^3\mathbf{x}_1dt_1\int^{t_1}\int j_\nu(2)A_\nu(2)d^3\mathbf{x}_2dt_2,$$

the ordering now being conventional. From here the matrix elements are computed between given states by use of the commutation relations (46) below. For further details we refer to Dyson's papers.[3] The result is that given by the rules of II.

Another method is to notice that the entire dependence of S on A_μ can be directly evaluated. As far as the states of the field are concerned, the evaluation of matrix elements of S is exactly the same as though $j_\mu(1)$ were a numerical function (since it commutes with all $A_\mu(1)$). Hence, these may be worked out by first obtaining the result for a field interacting with a given unquantized current distribution $j_\mu(1)$. This can be done, for example, by using the lagrangian methods described in III. For example, the matrix taken between states in which the field is empty of photons initially and finally is

$$S_{00}=\exp\left[-\tfrac{1}{2}ie^2\int\int j_\mu(1)j_\mu(2)\delta_+(s_{12}^2)d\tau_1d\tau_2\right] \quad (43)$$

as is shown in III (for j_μ a numerical function). This may now be interpreted as follows: The matrix element of S for a transition in which at $t=-\infty$ there are no real photons and the matter is in state χ_-, to the state at $+\infty$ also empty of photons with the matter in state χ_+, is the matrix element of S_{00} between χ_- and χ_+, where S_{00}, given in Eq. (43), operates now only on matter variables, the order of operators $j_\mu(1)$, $j_\mu(2)$ being determined just as in Eq. (42). This expression forms the basis for the author's treatment of virtual photon processes (II).

If an additional unquantized potential $B_\mu(1)$ is present, the expression (42) for S is altered just by the replacement of $A_\mu(1)$ by $A_\mu(1)+B_\mu(1)$.

The matrix corresponding to Eq. (43) would be a functional of $B_\mu(1)$ and a function of e^2:

$$S_e[B]=\exp\left[-\tfrac{1}{2}ie^2\int\int j_\mu(1)j_\mu(2)\delta_+(s_{12}^2)d\tau_1d\tau_2\right]$$
$$\times\exp\left[-i\int j_\nu(1)B_\nu(1)d\tau_1\right]. \quad (44)$$

It is evident by direct substitution, that $S_e[B]$ satisfies

$$dS_e/d(e^2)=\tfrac{1}{2}i\int\int\delta^2S_e/\delta B_\mu(1)\delta B_\mu(2)\delta_+(s_{12}^2)d\tau_1d\tau_2. \quad (45)$$

Since the equation is linear, any matrix element of S_e, say $T_e[B]$, between two states of the matter satisfies same equation. This is Eq. (45) of III, which is shown in III to be a general statement of the rules given in II for solving electrodynamic problems. Evidently, the case of real photons in initial or final state can be carried through in parallel to the discussion in III, with $j_\mu(1)$ now as an operator.

This completes our discussion in a general way of the relations between the various representations of electrodynamics. However, we wish to add a word concerning the derivation of Eq. (43). We have indicated how this may be done using the lagrangian method. However, we have seen from our example with the single forced oscillator that the same results may be obtained directly with the operator method, in just as simple a manner. Of course, by considering the field as a set of such oscillators we will arrive at Eq. (43), thus completely avoiding the lagrangian formulation. However, since the relation between Eqs. (42) and (43) is so fundamental, we should like to show how the operator method permits a simple direct passage from Eq. (42) to Eq. (43).[12] (We are simply following the steps leading from Eq. (26′) to Eq. (33) for the single harmonic oscillator, but are using $A_\mu(1)$ to replace q.)

The field operator $A_\mu(1)$ can be split into two parts $A_\mu(1)=A_\mu^+(1)+A_\mu^-(1)$, where the first $A_\mu^+(1)$ annihilates photons, and the second $A_\mu^-(1)$ creates them.[14] They satisfy the commutation relations (positional

[12] We omit the usual extra complications in all such demonstrations concerned with showing that disregard of the supplementary conditions on $\partial A_\mu/\partial x_\mu$ is legitimate.

[14] Ordinarily, the field operator $A_\mu(1)$ is expanded into modes $A_\mu(1)=\sum_i A_{\mu i}(x)(Q_i^*e^{i\omega_i t}+Q_ie^{-i\omega_i t})$, where $A_{\mu i}$ is the numerical function [for example, cosines or sines, III Eq. (1)] describing the classical mode i of frequency ω_i and Q_i^*, Q_i are the creation and annihilation operators into which q_i, the coordinate of the oscillator of this mode, has been split (29). The factors $e^{\pm i\omega t}$ result from use of interaction representation (30). Then, we have $A_\mu^-(1)=\sum_i A_{\mu i}(x)Q_i^*e^{i\omega_i t}$ and $A_\mu^+(1)=\sum_i A_{\mu i}(x)Q_ie^{-i\omega_i t}$. The commutation rule (46) then results from that of the Q and Q^* (28). Using the representation of III Eq. (1), the right-hand side of Eq. (46) comes from Eq. (28) directly in the form

$$(2\pi)^{-3}e^2\delta_{\mu\nu}\int\exp[-ik(t_2-t_1)]\cos(\mathbf{K}\cdot\mathbf{x}_1-\mathbf{K}\cdot\mathbf{x}_2)d^3\mathbf{K}/k,$$

which on integration for $t_2>t_1$ [see III Eq. (22)] is Eq. (46). The separation has been accomplished directly in coordinate space by J. Schwinger, Phys. Rev. **75**, 651 (1949).

ordering)

$$A_\mu^-(1)A_\nu^+(2)-A_\nu^+(2)A_\mu^-(1)=-ie^2\delta_{\mu\nu}\delta_+(s_{12}^2) \quad (46)$$

for[15] $t_1<t_2$. We have set $s_{12}^2=(x_{1\mu}-x_{2\mu})(x_{1\mu}-x_{2\mu})$.

On the basis of this commutation rule, we are to disentangle the operator

$$S=\exp\left[-i\int j_\mu(1)A_{\mu t_1}^-(1)d\tau_1\right]\times\exp\left[-i\int j_\nu(2)A_{\nu t_2}^+(2)d\tau_2\right], \quad (42')$$

where for definiteness we indicate the time of operation by the subscript. This is already of the exponential form of theorem (18), using $-i\int j_\mu(1)A_{\mu t_2}^-(1)d^3\mathbf{x}_1$ as $P(s)$, $s=t_2$. Hence, the result is

$$S=\exp\left[-i\int j_\mu(1)A_{\mu\infty}^-(1)d\tau_1\right]\times\exp\left[-i\int j_\nu(2)A_{\nu t_2}{}''^+(2)d\tau_2\right],$$

where

$$A_{\nu t_2}{}''^+(2)=\exp\left[+i\int_{-\infty}^{t_2} j_\mu(1)A_\mu^-(1)d\tau_1\right]A_{\nu t_2}^+(2)\times\exp\left[-i\int_{-\infty}^{t_2} j_\mu(1')A_\mu^-(1')d\tau_{1'}\right], \quad (47)$$

where in Eq. (47) we suppress the ordering rules for A^+, A^- and use instead positional notation (but maintain the rules for j_μ).

The commutation rule (46) permits Eq. (47) to be written[16]

$$A_{\nu t_2}{}''^+(2)=A_{\nu t_2}^+(2)+\int_{-\infty}^{t_2} e^2\delta_+(s_{12}^2)j_\mu(1)d\tau_1. \quad (48)$$

Hence, we have

$$S=\exp\left[-i\int j_\mu(1)A_{\mu\infty}^-(1)d\tau_1\right]\times\exp\left[-\tfrac{1}{2}ie^2\int\int j_\mu(1)j_\mu(2)\delta_+(s_{12}^2)d\tau_1d\tau_2\right]\times\exp\left[-i\int j_\mu(2)A_{\mu-\infty}^+(2)d\tau_2\right], \quad (49)$$

the A operators being entirely disentangled (the j's are still entangled). The ordering index t_2 on $A_{\mu t_2}^+$ has been changed to $-\infty$ in Eq. (49), since all the A^+ commute and act before $A_{\mu\infty}^-$, so that no ordering is necessary.

Taken between states empty of photons the result is just S_{00} of Eq. (43), for the annihilation operation A^+ on the state of zero photons is zero, and creation operation of A^- has zero amplitude of leaving a state without photons. If there is one photon present initially and we ask that no photons remain, we shall have to annihilate it and create none, so that if the A^- and A^+ exponentials are expanded in power series, we must take only the term linear in A^+ and independent of A^-. This is equivalent to a first-order action of the potential B_μ in Eq. (44) in perturbation. The corresponding rules for higher numbers of real photons are readily derived from Eq. (49). In this way we have completed an independent deduction of all the main formal results in quantum electrodynamics, by use of the operator notation.

7. THE DIRAC EQUATION

Up to now we have discussed the matter system using the description of second quantization. It was pointed out in I in the case of the electron-positron field where a small number of charges is involved, another simple interpretation is available. In this section we should like to discuss this from an operator point of view and to give in the following sections the formulas in this picture for electrons interacting through the agency of the electromagnetic field.

We begin by discussing the behavior of a single charge (plus the virtual pairs produced from it) in an unquantized potential $\boldsymbol{B}=\gamma_\mu B_\mu$, omitting the contributions from closed loop diagrams. This section will therefore constitute a brief summary of I using operator notation.

The behavior of a single charge is obtained by solving the Dirac equation

$$(i\nabla-\boldsymbol{B}-m)\psi=0 \quad (50)$$

with suitable boundary conditions and interpreting the solution as described in I. For convenience we shall always solve, instead,

$$(i\nabla-\boldsymbol{B}-m)\psi=iF, \quad (51)$$

where F is a source function, by writing

$$\psi=(i\nabla-\boldsymbol{B}-m)^{-1}iF \quad (52)$$

and interpreting the reciprocal operator in the definite sense implied by the limit of the operator when m has a vanishingly small negative imaginary part. If, for example, we wish the ordinary solution for $t>t_0$ which at $t=t_0$ has the form $f(\mathbf{x})$ representing an electron (i.e., $f(\mathbf{x})$ has only positive energy components), that solution

---

[15] This restriction at first sight looks unrelativistic. For $t_1>t_2$ we would have the complex conjugate of $-ie^2\delta_{\mu\nu}\delta_+(s_{12}^2)$, but $-i\delta_+(s_{12}^2)$ is real in spacelike regions (as $\delta_+(x)=\delta(x)-i\pi x^{-2}$).

[16] For, if $A_{\nu t_2}{}''^+(2)$ of (47) is considered as a functional of j_μ its first variation with respect to $j_\mu(3)$ is $(t_3<t_2)$.

$$i\exp\left(+i\int_{-\infty}^{t_2} j_\mu A_\mu^- d\tau\right)[A_\mu^-(3)A_\nu^+(2)-A_\nu^+(2)A_\mu^-(3)]\times\exp\left(-i\int_{-\infty}^{t_2} j_\mu A_\mu^- d\tau\right)=e^2\delta_{\mu\nu}\delta_+(s_{12})$$

by Eq. (46). The first variation of expression (48) gives the same result, so that Eq. (48) is correct for all j_μ, since it obviously is correct for $j_\mu=0$.

is the ψ obtained from Eq. (52) by setting[17] $F(1)=\gamma_t\delta(t_1-t_0)f(\mathbf{x}_1)$. If f contains negative energy components, Eq. (52) gives the desired solution for these components for $t<t_0$.

From the definition of $K_+^{(B)}(2,1)$ in I, Eq. (15), we can write

$$K_+^{(B)}(2,1)=(i\nabla-\boldsymbol{B}-m)^{-1}i\delta(2,1), \quad (53)$$

so that $-iK_+^{(B)}(2,1)$ is the space-time representation of the operator $(i\nabla-\boldsymbol{B}-m)^{-1}$ needed for Eq. (52). Thus, the solution (52) is

$$\psi(2)=\int K_+^{(B)}(2,1)F(1)d\tau_1. \quad (54)$$

The perturbation theory, considering $\boldsymbol{B}$ as a perturbation on the free particle, arises from Eq. (53) from a power series expansion in $\boldsymbol{B}$. For any pair of operators A, B we have

$$(A+B)^{-1}=A^{-1}-A^{-1}BA^{-1}+A^{-1}BA^{-1}BA^{-1}\cdots, \quad (55)$$

so that with $A=(i\nabla-m)$, $B=-\boldsymbol{B}$ we have

$$(i\nabla-\boldsymbol{B}-m)^{-1}=(i\nabla-m)^{-1}+(i\nabla-m)^{-1}\boldsymbol{B}(i\nabla-m)^{-1}$$
$$+(i\nabla-m)^{-1}\boldsymbol{B}(i\nabla-m)^{-1}\boldsymbol{B}(i\nabla-m)^{-1}+\cdots \quad (56)$$

or in space representation (putting

$$K_+(2,1)=i(i\nabla-m)^{-1}\delta(2,1))$$

$$K_+^{(B)}(2,1)=K_+(2,1)-i\int K_+(2,3)\boldsymbol{B}(3)K_+(3,1)d\tau_3$$

$$-\int\int K_+(2,4)\boldsymbol{B}(4)K_+(4,3)\boldsymbol{B}(3)K_+(3,1)d\tau_4 d\tau_3, \quad (57)$$

as in I, Eqs. (13) and (14). The corresponding momentum representation is evident directly from Eq. (56), for $(i\nabla-m)^{-1}$ is $(\not{p}-m)^{-1}$.

If F is to represent an initial state, it is also convenient to use the free particle solution $f(1)=(i\nabla-m)^{-1}iF(1)$ to represent the state. We are often interested in the amplitude that the system is in a final state $g(\mathbf{x})$. In this case, we can define a sink function G and a corresponding free particle solution $\bar{g}=i\bar{G}(i\nabla-m)^{-1}$ (where we write the adjoint so that it will correspond to the solution $g(1)=-i(i\nabla-m')^{-1}G(1)$ corresponding to m' having the opposite sign of the imaginary part to m). The matrix element to go from f to g is then the space-time integral of

$$i\bar{G}(i\nabla-\boldsymbol{B}-m)^{-1}F. \quad (58)$$

The expansion (56) gives for this element

$$-i\bar{g}\boldsymbol{B}f-i\bar{g}\boldsymbol{B}(i\nabla-m)^{-1}\boldsymbol{B}f$$
$$-i\bar{g}\boldsymbol{B}(i\nabla-m)^{-1}\boldsymbol{B}(i\nabla-m)^{-1}\boldsymbol{B}f-\cdots \quad (59)$$

(assuming $\bar{g}$, f are orthogonal states, $\int\bar{g}(1)F(1)d\tau_1=0$ so the leading term vanishes). In space representation the first two terms of this are I, Eq. (22), and I, Eq. (23); in momentum representation the second term is I, Eq. (35).

If more than one real charge is present without interaction, there is an operator $(i\nabla-\boldsymbol{B}-m)^{-1}$ for each charge, operating exclusively on the space and spinor coordinates of that charge. Operators corresponding to distinct charges commute. Matrix elements are taken in the antisymmetric way described in I, Sec. 4, for accord with the exclusion principle.

The contribution from closed loops is a factor $C_v=\exp(-L)$, where L is not very easily defined directly in operators. But the first-order change on changing the potential from $\boldsymbol{B}$ to $\boldsymbol{B}+\Delta\boldsymbol{B}$ is

$$\Delta L=\text{trace}[\{(i\nabla-\boldsymbol{B}-m)^{-1}-(i\nabla-m)^{-1}\}\Delta\boldsymbol{B}], \quad (60)$$

where the "trace" means the diagonal integral in coordinates and the "Sp" on the spinor indices, in space-time representation just I, Eq. (29).

This completes our summary in terms of operators of the results given in paper I on the theory of positrons. The main point is that aside from the problems of closed loops, one is merely analyzing by various techniques the consequences of Eq. (52) and, therefore, in general, the properties of the operator

$$(i\nabla-\boldsymbol{B}-m)^{-1}. \quad (61)$$

We may now turn to the quantum electrodynamics of such a particle, or system of particles. For simplicity we may restrict ourselves to the case of all virtual photons. The real photon case can, of course, as always be obtained by considering also the effects of external potentials. For simplicity further assume, at first, zero external potential. Our central problem, then, is the calculation of the matrix element

$$R={}_0\langle(i\nabla-\boldsymbol{A}-m)^{-1}\rangle_0 \quad (62)$$

of $(i\nabla-\boldsymbol{A}-m)^{-1}$ between states of the field empty of photons initially and finally. Here $\boldsymbol{A}=\gamma_\mu A_\mu$ and $A_\mu(1)$ is the operator $A_\mu^+(1)+A_\mu^-(1)$ acting on the field coordinates and satisfying commutation rules (46). This problem is relatively hard to solve directly. We do have the matrix element of any exponential form in A_μ in (43); but with A_μ involved in a reciprocal, it is another matter. We shall represent the reciprocal as a superposition of exponentials in the next section.

From Eq. (62) we can derive in a simple direct manner the perturbation series results of II. For we know[18] that

$${}_0\langle A_\mu(1)\rangle_0=0, \quad {}_0\langle A_\mu(1)A_\nu(2)\rangle_0=ie^2\delta_{\mu\nu}\delta_+(s_{12}^2), \quad \text{etc.} \quad (63)$$

[17] For $t<t_0$, the ψ from Eq. (52) would be zero and would not be the solution desired; it can be obtained only from F with a different definition of the poles of the reciprocal operator. We assume we are only interested in the solutions in regions of space-time later than the time the "initial" electron wave functions are specified and earlier than the "initial" positron function is given. Since we will take matrix elements between two states, this represents no real limitation (see I).

[18] The order of the A_μ operators in Eq. (63) is according to the time convention. If we put $A=A^++A^-$ and use Eq. (46) to rearrange factors, they are evident, since A_μ^+ on the initial (and A_μ^- into the final) photon-free state vanishes. They are identical to the lagrangian relations III, Eq. (52), and form the basis of Dyson's description.

Hence, if we expand the reciprocal in power series as Eq. (56), in coordinate representation (57), with $\boldsymbol{B}$ replaced by $\boldsymbol{A}$ (or by $\boldsymbol{A}+\boldsymbol{B}$ if an unquantized potential $\boldsymbol{B}$ is present along with $\boldsymbol{A}$), we may readily write down the zero-zero matrix element of each term. For example, third term of Eq. (57) gives the self-energy contribution in accord with II, Eq. (6). The other results of II are just further consequences of this series expansion as we have emphasized in III.

8. USE OF A FIFTH PARAMETER IN DIRAC'S EQUATION

In this section we discuss the representation of the reciprocal operator in exponential form. Since $\int_0^\infty \exp(iWx)dW = i/x$ (or rather $\lim_{\epsilon\to 0} i/(x+i\epsilon)$), we we may write

$$i(i\nabla - \boldsymbol{B} - m)^{-1} = \int_0^\infty \exp[i(i\nabla - \boldsymbol{B} - m)W]dW, \quad (64)$$

the definition of the singularity (as the limit with m having an infinitesimal negative imaginary part) being automatically represented. (See, however, the remarks at the end of this section.) We can also write this in the ordered operator form,

$$\int_0^\infty \exp\left[i\int_0^W \{i\nabla(w) - \boldsymbol{B}(w)\}dw\right]\exp(-imW)dW, \quad (65)$$

where we have written $\boldsymbol{B}(w)$ for $\gamma_\mu(w)B_\mu(x_\nu(w))$, where $x_\nu(w)$ are the four ($\nu = 1$ to 4) coordinate operators, of which B_μ is a function, ordered by the ordering parameter w and $\gamma_\mu(w)$ are the four Dirac matrices similarly ordered. Likewise, we have $i\nabla(w) = \gamma_\mu(w)i\partial_\mu(w)$, where $i\partial_\mu(w)$ are the four ordered momentum operators conjugate to x_μ.

In this form $\boldsymbol{B}$ can be replaced by $\boldsymbol{A}$ and the expectation value for virtual transitions can be taken. This is done in the next section. We continue here with a more complete discussion of Eq. (65).

The perturbation expansion in $\boldsymbol{B}$ of Eq. (65) should lead, of course, to Eq. (56). For example, the term first order in $\boldsymbol{B}$ in Eq. (65) is evidently

$$-i\int_0^\infty \exp(imW) \times \exp\left[i\int_0^W i\nabla(w')dw'\right]\int_0^W \boldsymbol{B}(w)dwdW. \quad (66)$$

Now the range of the w' may be divided into two regions and the quantities reordered (just as in Eqs. (5) and (6)) to

$$-i\int_0^\infty\int_0^W dWdw\exp[i(W-w)(i\nabla - m)]\boldsymbol{B} \times \exp[iw(i\nabla - m)],$$

so that changing the order of integration, one finds immediately from

$$\int_0^\infty \exp[iv(i\nabla - m)]dv = i(i\nabla - m)^{-1}$$

the result $-i(i\nabla - m)^{-1}\boldsymbol{B}(i\nabla - m)^{-1}$ as required.

The contribution L of a closed loop can be written directly in exponential form. It is easily shown from Eqs. (60) and (65) that

$$L = \int_0^\infty \operatorname{trace}\left[\exp\left\{i\int_0^W (i\nabla(w) - \boldsymbol{B}(w))\right\}dw\right]\frac{dW}{W} \times \exp(-imW). \quad (67)$$

(The second term in Eq. (60) actually has zero trace and was added only to make convergence problems appear less difficult. It has been omitted in writing Eq. (67). Also, the value of Eq. (67) when $\boldsymbol{B}=0$ may be subtracted away, if desired, for a constant addition on L changes only the normalization of all probabilties.)

Incidentally, the method of rendering this expression convergent (see II, Sec. 7) for further calculations, is to call its value for mass m, $L(m^2)$ and then to calculate

$$L^P = \int_0^\infty [L(m^2) - L(m^2+\lambda^2)]G(\lambda)d\lambda,$$

where

$$\int_0^\infty G(\lambda)d\lambda = 1 \quad \text{and} \quad \int_0^\infty \lambda^2 G(\lambda)d\lambda = 0$$

and to assume that L^P is to be used as the correct value of L in place of $L(m^2)$. This is equivalent to replacing the factor $\exp(-imW)$ in the integrand of Eq. (67) by another function $F(W)$, where

$$F(W) = \int_0^\infty [\exp(-imW) - \exp\{-i(m^2+\lambda^2)^{\frac{1}{2}}W\}] \times G(\lambda)d\lambda.$$

For large W this approaches $\exp(-imW)$, but for small W it falls off, the real part of it, at least, varying as W^4. This renders Eq. (67) convergent. (The imaginary part of $F(W)$ does not seem to lead to momentum space integrals whose convergence would be in question.) This suggests a general method of maintaining convergence; by keeping processes corresponding to small intervals of w from occurring with large amplitude. This is briefly discussed in III in reference 22. What is said there applies qualitatively as well to the Dirac case analyzed here, with u replaced by w.

If there are several charges in the system, we must associate a separate w, for each, say w_n for the nth. Each must have its own set of matrices $\gamma_\mu^{(n)}$ and coordinates $x^{(n)}$ (γ's for different charges commute). If we call

$$\boldsymbol{B}^{(n)} = \gamma_\mu^{(n)}(w_n)B_\mu(x^{(n)}),$$

the total matrix for all N particles is

$$\prod_{n=1}^{N}\int_0^\infty \exp\left\{i\int_0^{W_n}[i\nabla^{(n)}(w_n)-\boldsymbol{B}^{(n)}(w_n)]dw_n\right\}$$
$$\times\exp(-imW_n)dW_n. \quad (68)$$

If in addition there are present a number of closed loops, the corresponding number of factors L must be multiplied in.

One might try to give a kind of physical or, rather, mathematical view by which the form of Eq. (65) can be appreciated, in the following manner:

We may deal with the Dirac equation somewhat in analogy to the method used in the discussion of the Klein-Gordon equation in the Appendix A of III. Consider a fifth variable w in addition to the four x, and that we have a wave function $\phi(x, w)$, which is to satisfy

$$-i\partial\phi/\partial w=(i\nabla-\boldsymbol{B})\phi. \quad (69)$$

Then since the potentials $B_\mu(x)$ are independent of w, the equation is separable in w, so that $\phi(x, w)=\exp(imw)\psi(x)$ is a solution of Eq. (69), if $\psi(x)$ is a solution of the Dirac Eq. (50). Also, if we have any special solution of Eq. (69), $\phi(x, w)$, we may obtain a solution of Eq. (50) by finding

$$\psi(x)=\int_{-\infty}^{\infty}\phi(x, w)\exp(-imw)dw. \quad (70)$$

Hence, by studying Eq. (69), we are at the same time studying the Dirac equation.

Given the wave function $\phi(x, 0)$ for $w=0$, the wave function at $w=W$ is given by

$$\phi(x, W)=\theta(W)\phi(x, 0), \quad (71)$$

where the operator $\theta(W)$ is

$$\theta(W)=\exp i\int_0^W[i\nabla(w)-\boldsymbol{B}(w)]dw \quad (72)$$

for $W>0$ and, for convenience,[17] we take $\theta=0$ for $W<0$. The important operator for the Dirac equation, in view of Eqs. (70) and (71), is

$$\int_{-\infty}^{\infty}\theta(W)\exp(-imW)dW,$$

which is just Eq. (65)

This interpretation suffers from a difficulty, however. For a free particle the operator $\theta(W)$ in momentum space is $\theta(W)=\exp(iW\not{p})=\cos(Wp)+i(\not{p}/p)\sin(pW)$, where $p=(p^2)^{\frac{1}{2}}$. The integral of this times $\exp(-imW)$ is really not always defined, even if m has a small negative imaginary part, for in intermediate states p^2 may be negative and p imaginary, so that θ contains positive exponentials in W and the integrand is oscillating with ever increasing amplitude. We therefore look at Eq. (64) as a *formal* definition of the value of the integral in all cases. Although this is satisfactory in a formal way for operators, it means that our interpretation cannot be taken literally. For example, we cannot obtain an unambiguous integral representation of $\theta(W)$ in coordinate space, for the requisite integral $\int\exp(-i\not{p}W)\exp(-ip\cdot x)d^4p$ is undefined. This is because it is probably not possible to obtain the wave function (71) at any value of W from that at $W=0$ from Eq. (69) without further definitions. At least, the corresponding second-order equation $(\partial^2\phi/\partial t^2)-\nabla^2\phi-\partial^2\phi/\partial W^2=0$ is apparently not of the kind for which this type of Huygens principle applies.

An alternative method of parametrizing the equation which does not seem to suffer from this interpretational difficulty is given in Appendix D. It leads, however, to more complicated (although algebraically equivalent) expressions for matrix elements than does Eq. (64).

9. DIRAC ELECTRONS IN QUANTUM ELECTRODYNAMICS

Returning now to quantum electrodynamics, for a single charge we want the expectation between photon free states of R in Eq. (62). This by Eq. (65) is the integral over all positive W of $\exp(-imW)$ times

$$\left\langle\exp i\int_0^W[i\nabla(w)-\boldsymbol{A}(w)]dw\right\rangle_0.$$

This is just $\exp[i\int_0^W i\nabla(w)dw]$ times (the $\langle\ \rangle_0$ refers to the photon states, that is, affects A_μ only)

$$\left\langle\exp-i\int_0^W\gamma_\mu(w)A_\mu(x(w))dw\right\rangle_0,$$

which is of the form

$$\left\langle\exp-i\int A_\mu(1)j_\mu(1)d\tau_1\right\rangle_0$$

of Eq. (42) with

$$j_\mu(1)=\int_0^W\gamma_\mu(w)\delta^4(x_\nu(w)-x_{\nu 1})dw, \quad (73)$$

where $x_{\nu 1}$ is the field point at which j_μ is calculated and $\delta^4(x_{\nu 2}-x_{\nu 1})$ means $\delta(2, 1)$. Thus, we may find the expectation value with the relation (43). With this value of j_μ substituted on the right side of Eq. (43), the δ^4 functions are immediately integrable, and we find finally

$$R=\int_0^\infty\exp\left[-\int_0^W\nabla(w)dw\right]$$
$$\times\exp\left[-\tfrac{1}{2}ie^2\int_0^W\int_0^W\gamma_\mu(w')\gamma_\mu(w'')\right.$$
$$\left.\times\delta_+(s^2_{w'w''})dw'dw''\right]\exp(-imW)dW, \quad (74)$$

in which we have written $s^{2}_{w'w''}$ for $[x_\mu(w')-x_\mu(w'')]\times[x_\mu(w')-x_\mu(w'')]$.

This expression then contains a description of a Dirac electron interacting with itself. If an extra factor $\exp(-i\int_0^W \boldsymbol{B}(w)dw)$ is included, it describes such an electron also in an external potential. The terms may be expanded in powers of $\boldsymbol{B}$ and e^2, and each term may then be simplified in the way we have described many times before, for example, in connection with Eq. (66).

When several charges are present, the result from Eq. (68) is the integral[19]

$$\int_0^\infty\int_0^\infty\cdots\int_0^\infty \exp\left\{i\sum_n\int_0^{W_n}[i\nabla^{(n)}(w_n)-m]dw_n\right\}$$

$$\times\exp\left[-\tfrac{1}{2}i\sum_n\sum_m e^2\int_0^{W_n}\int_0^{W_m}\gamma_\mu^{(n)}(w_n)\gamma_\mu^{(m)}(w_m)\right.$$

$$\left.\times\delta_+(s^2{}_{w_nw_m})dw_ndw_m\right]dW_1dW_2\cdots dW_m. \quad (75)$$

The contributions from closed loops may be obtained from this by choosing some value of n, say, $n=i$, to represent matrices applying to a loop, dividing under the integral sign by W_i, and taking the trace with respect to the variables i.

The various present-day meson theories of nuclear interaction may be set up in quite analogous ways. For example, a nucleon interacting with itself through the agency of neutral pseudoscalar mesons with pseudoscalar coupling is evidently described by Eq. (74); but with m replaced by the proton mass, and the interaction term altered by the replacement of e^2 by g^2, γ_μ by γ_5, and $\delta_+(s^2)$ by $4\pi I_+(s^2)$, the appropriate propagation function for mesons of mass μ (I_+ is defined in I, Eq. (32), but $m=\mu$). Charged mesons may be represented by the use of isotopic spin operators also ordered by w.

10. SUMMARY OF NUMERICAL FACTORS FOR TRANSITION PROBABILITIES

The exact values of the numerical factors appearing in the rules of II for computing transition probabilities are not clearly stated there, so we give a brief summary here.[20]

The probability of transition per second from an initial state of energy E to a final state of the same total energy (assumed to be in a continuum) is given by ($\hbar=c=1$),

$$\text{Prob. trans/sec}=2\pi N^{-1}|\mathfrak{M}|^2\rho(E),$$

where $\rho(E)$ is the density of final states per unit energy range at energy E and $|\mathfrak{M}|^2$ is the square of the matrix element taken between the initial and final state of the transition matrix $\mathfrak{M}$ appropriate to the problem. N is a normalizing constant. For bound states conventionally normalized it is 1. For free particle states it is a product of a factor N_i for each particle in the initial and for each in the final energy state. N_i depends on the normalization of the wave functions of the particles (photons are considered as particles) which is used in computing the matrix element of $\mathfrak{M}$. The simplest rule (which does not destroy the apparent covariance of $\mathfrak{M}$), is[21] $N_i=2\epsilon_i$, where ϵ_i is the energy of the particle. This corresponds to choosing in momentum space, plane waves for photons of unit vector potential, $\boldsymbol{e}^2=-1$. For electrons it corresponds to using $(\bar{u}u)=2m$ (so that, for example, if an electron is deviated from initial $\boldsymbol{p}_1$ to final $\boldsymbol{p}_2$, the sum over all initial and final spin states of $|\mathfrak{M}|^2$ is $\mathrm{Sp}[(\boldsymbol{p}_2+m)\mathfrak{M}(\boldsymbol{p}_1+m)\overline{\mathfrak{M}}]$). Choice of normalization $(\bar{u}\gamma_t u)=1$ results in $N_i=1$ for electrons. The matrix $\mathfrak{M}$ is evaluated by making the diagrams and following the rules of II, but with the following definition of numerical factors. (We give them here for the special case that the initial, final, and intermediate states consist of free particles. The momentum space representation is then most convenient.)

First, write down the matrix directly without numerical factors. Thus, electron propagation factor is $(\boldsymbol{p}-m)^{-1}$, virtual photon factor is $\boldsymbol{k}^{-2}$ with couplings $\gamma_\mu\cdots\gamma_\mu$. A real photon of polarization vector e_μ contributes factor $\boldsymbol{e}$. A potential (times the electron charge, e) $A_\mu(x)$ contributes momentum $\boldsymbol{q}$ with amplitude $\boldsymbol{a}(q)$, where $a_\mu(q)=\int A_\mu(1)\exp(iq\cdot x_1)d^4x_1$. (Note: On this point we deviate from the definition of $\boldsymbol{a}$ in I which is there $(2\pi)^{-2}$ times as large.) A spur is taken on the matrices of a closed loop. Because of the Pauli principle the sign is altered on contributions corresponding to an exchange of electron identity, and for each closed loop. One multiplies by $(2\pi)^{-4}d^4p=(2\pi)^{-4}dp_tdp_xdp_ydp_z$ and integrates over all values of any undetermined momentum variable $\boldsymbol{p}$. (Note: On this point we again differ.[20])

The correct numerical value of $\mathfrak{M}$ is then obtained by multiplication by the following factors. (1) A factor $(4\pi)^{\frac{1}{2}}e$ for each coupling of an electron to a photon. Thus, a virtual photon, having two such couplings, contributes $4\pi e^2$. (In the units here, $e^2=1/137$ approximately and $(4\pi)^{\frac{1}{2}}e$ is just the charge on an electron in heaviside units.) (2) A further factor $-i$ for each virtual photon.

For meson theories the changes discussed in II, Sec. 10 are made in writing $\mathfrak{M}$, then further factors are

[19] This equation with its interpretation was proposed as a formulation of the laws of quantum electrodynamics (for virtual photons) by the author at the Pocono Conference of Theoretical Physics (1948). The notation for ordering operators was explained there. However, at this time, the author had no complete formal derivation of Eq. (75) from the conventional electrodynamics, nor did he know of a satisfactory method of dealing with the closed loop divergences.

[20] In I and II the unfortunate convention was made that d^4k means $dk_tdk_1dk_2dk_3(2\pi)^{-2}$ for momentum space integrals. The confusing factor $(2\pi)^{-2}$ here serves no useful purpose, so the convention will be abandoned. In this section d^4k has its usual meaning, $dk_tdk_1dk_2dk_3$.

[21] In general, N_i is the particle density. It is $N_i=(\bar{u}\gamma_t u)$ for spin one-half fields and $i[(\phi^*\partial\phi/\partial t)-\phi\partial\phi^*/\partial t]$ for scalar fields. The latter is $2\epsilon_i$ if the field amplitude ϕ is taken as unity.

(1) $(4\pi)^{\frac{1}{2}}g$ for each meson-nucleon coupling and (2) a factor $-i$ for each virtual spin one meson, but $+i$ for each virtual spin zero meson.

This suffices for transition probabilities, in which only the absolute square of $\mathfrak{M}$ is required. To get $\mathfrak{M}$ to be the actual phase shift per unit volume and time, additional factors of i for each virtual electron propagation, and $-i$ for each potential or photon interaction, are necessary. Then, for energy perturbation problems the energy shift is the expected value of $i\mathfrak{M}$ for the unperturbed state in question divided by the normalization constant N_i belonging to each particle comprising the unperturbed state.

The author has profited from discussions with M. Peshkin and L. Brown.

APPENDIX

In this Appendix (A, B, C) an attempt will be made to discuss some of the properties of ordered operators and of functionals in a somewhat more general way.

Almost certainly many of the equations will be incorrect in their general form. This is especially true of those involving fourier transforms in function space. However, it is expected that they are correct in the special cases in which the formulas have been applied in the main part of the paper. Therefore, at least at first, when new results using these methods are derived, care should be taken to check the final result in some independent way. It is analogous to using power series expansions, or fourier transforms, in a calculation in a situation in which the conditions for the validity of the power expansions or of the transform have not been checked, or are not known to be satisfied. The physicist is very familiar with such a situation and usually satisfied with it, especially since he is confident that he can tell if the answer is physically reasonable. But mathematicians may be completely repelled by the liberties taken here. The liberties are taken not because the mathematical problems are considered unimportant. On the contrary, this appendix is written to encourage the study of these forms from a mathematical standpoint. In the meantime, just as a poet often has license from the rules of grammar and pronunciation, we should like to ask for "physicists' license" from the rules of mathematics in order to express what we wish to say in as simple a manner as possible. (These remarks do not apply to Appendix D.)

A. Relation to Theory of Functionals

In this section we would like to suggest how a general theory of ordered operators might be built up, and in particular, to point out certain relations to the theory of functionals. For clarity of exposition in this Sec. A, only, we represent all operators by bold-faced letters $\mathbf{M}$ and ordinary functions in regular type M. We have mentioned that with every functional $F[M(s), N(s)\cdots]$ of the argument functions $M(s)$, $N(s)$ we wish to associate an operator (by identifying $M(s)$ with an operator $\mathbf{M}(s)$ interpreting s as an ordering parameter with the operators $\mathbf{M}(s)$, $\mathbf{N}(s)$ supposedly known and with known commutation relations). The general theory of these associations might instead have begun by defining the meaning for the special case of the exponential functional $\exp\int_0^1 M(s)ds$ (we assume throughout this section, for convenience, that the range of s is 0 to 1). The corresponding operator

$$\mathbf{R}=\exp\int_0^1 \mathbf{M}(s)ds \tag{1-a}$$

is defined as the value $\mathbf{G}(1)$ at $s=1$ of that solution of the operator differential equation

$$d\mathbf{G}(s)/ds=\mathbf{M}(s)\mathbf{G}(s), \tag{2-a}$$

which is the identity operator at $s=0$, i.e., $\mathbf{G}(0)=\mathbf{I}$. We have thereby defined the operators corresponding to more complex functionals such as $F=\exp\int_0^1[\mu(s)\mathbf{M}(s)+\nu(s)\mathbf{N}(s)+\cdots]ds$, where $\mu(s)$, $\nu(s)\cdots$ are numerical functions and $\mathbf{M}$, $\mathbf{N}$ arbitrary operators (which need not commute) as the $\mathbf{G}(1)$ from

$$d\mathbf{G}(s)/ds=[\mu(s)\mathbf{M}(s)+\nu(s)\mathbf{N}(s)+\cdots]\mathbf{G}(s) \tag{3-a}$$

with $\mathbf{G}(0)=\mathbf{I}$. For clearly $\mu(s)\mathbf{M}(s)+\nu(s)\mathbf{N}(s)+\cdots$ can be considered as a single operator function of s, the $\mathbf{M}(s)$ in Eqs. (1-a) and (2-a).

Next we make the general definition that the operator to be associated with the sum of two or more functions $F_1[M(s), N(s)\cdots]+F_2[M(s), N(s)\cdots]$ is the sum of the operators $F_1[\mathbf{M}(s), \mathbf{N}(s)\cdots]+F_2[\mathbf{M}(s), \mathbf{N}(s)\cdots]$ corresponding to each separately.

Considering a derivative as the limit of a difference, we can use this idea of superposition to further extend the range of functionals for which operators are defined. As an example, in virtue of the fact that $\int_0^1 M(s)ds\int_0^1 N(s)ds$ is the first derivative with respect to both μ, ν of $\exp\int_0^1[\mu M(s)+\nu N(s)]ds$ evaluated at $\mu, \nu=0$ we may define the operator corresponding to $\int_0^1 \mathbf{M}(s)ds\int_0^1 \mathbf{N}(s)ds$ as the corresponding derivative of the operator $\exp\int_0^1[\mu\mathbf{M}(s)+\nu\mathbf{N}(s)]ds$. Then from a study of the properties of the solution of Eq. (3-a) expanded in powers of μ, ν we may readily verify that $\int_0^1 \mathbf{M}(s)ds\int_0^1 \mathbf{N}(s)ds$ could also be evaluated directly by considering s as an ordering index on the operators.

Thus, the superposition rule permits a wide increase in the class of functionals for which we have defined operators. In fact, with some mathematical license, we have defined the operator for any functional. We wish to imagine that any functional can be represented as a superposition of exponential ones in a manner analogous to the representation of an arbitrary function as a superposition of exponential functions. Thus, we expect to be able to write for any functional $F[M(s)]$ (the true mathematical restrictions are completely unknown to me)

$$F[M(s)]=\int \exp\left[i\int_0^1 \mu(s)M(s)ds\right]\mathfrak{F}[\mu(s)]\mathfrak{D}\mu(s), \tag{4-a}$$

where $\mathfrak{F}[\mu(s)]$ is a new (complex) functional, the functional transform of $F[M(s)]$, and $\int\cdots\mathfrak{D}\mu(s)$ represents (some kind of an) integration over the space of functions $\mu(s)$. For simplicity we take the case of just one argument function $M(s)$. If $F[M(s)]$ is given, $\mathfrak{F}$ can be determined perhaps from

$$\mathfrak{F}[\mu(s)]=\int \exp\left[-i\int_0^1 \mu(s)M(s)ds\right]F[M(s)]\mathfrak{D}M(s) \tag{5-a}$$

with suitable normalization. Then, if $\mathfrak{F}$ is known, we define the operator $F[\mathbf{M}(s)]$ as

$$F[\mathbf{M}(s)]=\int \exp\left[i\int_0^1 \mu(s)\mathbf{M}(s)ds\right]\mathfrak{F}[\mu(s)]\mathfrak{D}\mu(s), \tag{6-a}$$

where $\mu(s)$ is a numerical function. Since we have already defined the operator $\exp[i\int_0^1 \mu(s)\mathbf{M}(s)ds]$ (by Eq. (3-a) with μ replaced by $i\mu$), we now simply require superposition of such operators for various $\mu(s)$. The extension to functionals of several variables is evident.

With these definitions of operators in terms of exponential functionals, the various theorems are easily proved. For example, the theorem (18) of Sec. 3 is first readily demonstrated for the special case that F is an exponential (1-a). Thus, to calculate

$$\mathbf{R}=\exp\int_0^1 \mathbf{P}(s)ds\exp\int_0^1 \mathbf{M}(s)ds$$

we must solve $d\mathbf{G}(s)/ds=[\mathbf{P}(s)+\mathbf{M}(s)]\mathbf{G}(s)$. We try a solution $\mathbf{G}(s)=\mathbf{U}(s)\mathbf{X}(s)$, so that $d\mathbf{G}/ds=(d\mathbf{U}/ds)\mathbf{X}+\mathbf{U}d\mathbf{X}/ds=\mathbf{PG}+\mathbf{U}d\mathbf{X}/ds$ in virtue of Eq. (15). Thus, we have a solution if $d\mathbf{X}/ds=\mathbf{U}^{-1}\mathbf{MG}=\mathbf{U}^{-1}\mathbf{MUX}=\mathbf{M}'\mathbf{X}$ with $\mathbf{M}'$ as in Eq. (16). Since $\mathbf{G}(0)=1$, if $\mathbf{U}(0)=1$, we must have $\mathbf{X}(0)=1$ so the solution of the $\mathbf{X}$ equation is $\exp\int_0^1 \mathbf{M}'(s)ds$ in accordance with the definition (1-a), (2-a). (If $\mathbf{U}(0)\neq 1$, replace $\mathbf{X}$ by $\mathbf{XU}^{-1}(0)$ throughout.) Hence, Eq. (18) is established for exponential functionals. And since the theorem involves F linearly, it is therefore true for any

superposition of exponentials and hence for any functional which can be defined by means of such superposition.

B. Momentum and Coordinate Operators

In nonrelativistic quantum mechanics, without spin, all operators can be made up of coordinate operators and their conjugate momentum operators. We show in this section how, at least in principle, all such operator functions can be disentangled.

We can consider the case of one degree of freedom Q, and its momentum P. (When more variables are present, they present no new problem as variables corresponding to different independent coordinates commute.) Thus, we are to disentangle the general operator $F[P(s), Q(s)]$ subject to the condition

$$PQ-QP=-i. \tag{7-a}$$

This is the problem solved in this section. We can satisfy the commutation relation by putting $P=-id/dQ$ (so that our solution may have applications outside quantum mechanics for the combination of operators X, d/dX are of frequent occurrence). Then the operator F can be defined by giving the function g of Q resulting from

$$g(Q)=F[P(s), Q(s)]f(Q) \tag{8-a}$$

for arbitrary functions $f(Q)$, where $Q(s)$ and $P(s)$ are interpreted as multiplication by Q, and $-i$ times differentiation with respect to Q in the order defined by F.

To obtain the relation of g, f suppose the P-dependence of F can be expanded as a functional transform, ($p(s)$, $q(s)$, $v(s)$ are numerical functions)

$$F[p(s), q(s)]=\int \exp\left[-i\int_0^1 p(s)v(s)ds\right]\mathfrak{F}[q(s), v(s)]\mathfrak{D}v(s), \tag{9-a}$$

where $\mathfrak{F}$ is a functional of $v(s)$ and of $q(s)$. Now to evaluate the operator

$$\exp\left[-i\int_0^1 P(s)v(s)ds\right]\mathfrak{F}[Q(s), v(s)] \tag{10-a}$$

we use our theorem (20) to disentangle the $P(s)$ operator. We use $\alpha(s)=-iv(s)$ in Eq. (20), calling $y(s)=\int_0^s v(s')ds'$, so that Eq. (10-a) is

$$e^{-iy(1)P(1)}\mathfrak{F}[Q'(s), v(s)], \tag{11-a}$$

where $Q'(s)=e^{+iy(s)P}Qe^{-iy(s)P}$. As is well known from Taylor's theorem, the operator $e^{hd/ds}$ displaces x by h so that[22]

$$Q'(s)=Q_s+y(s). \tag{12-a}$$

Substitution into Eq. (11-a) finds all the Q_s preceding the $P(1)$ so the operators are disentangled and Q_s may be written simply Q_0, whence we have

$$F[P(s), Q(s)]=\int \exp\left[-iP_1\int_0^1 v(s)ds\right] \times\mathfrak{F}\left[Q_0+\int_0^s v(s')ds', v(s)\right]\mathfrak{D}v(s), \tag{13-a}$$

which in principle, at least, solves the problem.

We can go a bit further and assume Eq. (9-a) can be inverted as

$$\mathfrak{F}[q(s), v(s)]=\int \exp\left[i\int_0^1 p(s)v(s)ds\right]F[p(s), q(s)]\mathfrak{D}p(s), \tag{14-a}$$

where $p(s)$ is a numerical function for transforming F. Also, $y(s)=\int_0^s v(s)ds$ is as good a function as $v(s)$ for purposes of integration,[23] and we may write, substituting Eq. (14-a) into Eq. (13-a),

$$F[P(s), Q(s)]=\int\int \exp\left[-iP_1y(1)+i\int_0^1 p(s)\dot{y}(s)ds\right] \times F[p(s), Q_0+y(s)]\mathfrak{D}p(s)\mathfrak{D}y(s), \tag{15-a}$$

the integral extending over all $p(s)$, and all $y(s)$ subject to $y(0)=0$.

Considering P as $-id/dQ$, the operator $F[P(s), Q(s)]$ may be considered to operate on a function $f(Q)$ to produce another function of Q. In particular, we are often interested in quantum mechanics in the projection of this final function into a given "final state" function g; that is, F is often defined through its matrix element

$$(g^*Ff)=\int g^*(Q)F[P(s), Q(s)]f(Q)dQ.$$

If we substitute into this expression (15-a), the P_1 can be considered to act entirely on $g^*(Q)$ and since $\exp(+iyP)g(Q)=g(Q+y)$, we find

$$(g^*Ff)=\int g^*(Q_0+y(1))\exp\left[i\int p(s)\dot{y}(s)ds\right]F[p(s), Q_0+y(s)] \times\mathfrak{D}p(s)\mathfrak{D}y(s)\cdot f(Q_0)dQ_0.$$

Define $q(s)$ as the numerical function $q(s)=Q_0+y(s)$ and write finally ($q_0=Q_0$)

$$(g^*Ff)=\int\int g^*(q_1)\exp\left[i\int p(s)\dot{q}(s)ds\right]F[p(s), q(s)] \times\mathfrak{D}p(s)\mathfrak{D}q(s)f(q_0)dq_0dq_1, \tag{16-a}$$

where the integral $\mathfrak{D}p(s)$ is over all $p(s)$ and the integral $\mathfrak{D}q(s)$ is over all trajectories $q(s)$ which go between the initial position q_0 and the final one q_1, the final integration on dq_1 being represented explicitly. This represents a complete reduction of an ordered operator $F[P(s), Q(s)]$ involving conjugate operators P, Q (7-a)to a property of the corresponding numerical functional $F[p(s), q(s)]$, for in Eq. (16-a) $p(s)$, $q(s)$ are numerical functions so that all the operators have been eliminated.

This is obviously related to the lagrangian form of quantum mechanics of C. In fact, for transitions, we are interested in the operator $S=\exp[-i\int_0^T H(t)dt]$, where, for example, $H=(1/2m)P^2+V(Q, t)$. The matrix elements of this, according to Eq. (16-a) are (use t for s in range 0 to T)

$$(g^*Sf)=\int\int g^*(q_T)\exp\left[i\int_0^T p(t)\dot{q}(t)dt-i\int_0^T (1/2m)p(t)^2dt -i\int_0^T V(q(t), t)dt\right]f(q_0)\mathfrak{D}p(t)\mathfrak{D}q(t)dq_0dq_T.$$

The integral on $p(t)$ is easily done. (See Appendix C for a more general discussion of gaussian integrals.) Substitute $p(t)=m\dot{q}+p'(t)$, so that

$$\int_0^T [(1/2m)p(t)^2-p(t)\dot{q}(t)]dt=(1/2m)\int_0^T p'(t)^2dt-\tfrac{1}{2}m\int_0^T \dot{q}(t)^2dt.$$

Also, $\mathfrak{D}p(t)=\mathfrak{D}p'(t)$, since p and p' differ by a constant at each t (keeping $q(t)$ integration until later). The $\mathfrak{D}p'$ (t) integral then separates out and integrates to some constant. Hence, within such a normalizing constant, the matrix element is

$$(g^*Sf)=\int g^*(q_T)\exp\left\{+i\int_0^T [\tfrac{1}{2}m\dot{q}(t)^2-V(q(t), t)]dt\right\} \times f(q_0)\mathfrak{D}q(t)dq_0dq_T. \tag{17-a}$$

That is, the transition amplitude from point q_0 at $t=0$ to q_T at $t=T$ is the integral over all trajectories connecting these points of $\exp i\int_0^T L[q(t), \dot{q}(t)]dt$, L being the lagrangian for this problem. This is the fundamental theorem on which the interpretation of C is based.

The fact that the nonrelativistic quantum mechanical operators (other than spin) can be expressed in terms of an integral over

---

[22] Or, differentiating $Q'(s)$ with respect to s, find $dQ'(s)/ds=ie^{iy(s)P}(PQ-QP)e^{-iy(s)P}dy/ds$. If we use the commutation relation, this is dy/ds, whence $Q'(s)$ differs from $y(s)$ by the constant operator Q, the evident value of Q' for $y(s)=0$, establishing Eq. (12-a).

[23] For, if $\mathfrak{D}v(s)$ be considered as the limit as $\Delta\to 0$ of an integration over all the variables $v_i=v(s_i)$ with $s_{i+1}-s_i=\Delta$, then the change is from the variables $v_i=(y_{i+1}-y_i)\Delta^{-1}$. Integration over y_i for all $i>0$ is equivalent to integration on all v_i. (Since $dv_i=\Delta^{-1}dy_{i+1}$, the jacobian of the transformation is $\Delta^{-(1/\Delta)}$, which is only a change of normalization, and we are disregarding normalization factors.)

trajectories is based on the fact that the operators involved satisfy Eq. (7-a). If other operators are involved, such as Pauli's spin operators σ, or Dirac matrices γ_μ, which satisfy different commutation rules, a complete reduction eliminating all the operators is not nearly so easily affected. It is possible to eliminate the $\not p$ operators in the Dirac or Pauli equation and get forms like Eq. (17-a), but the amplitude for a single trajectory is then a hypercomplex quantity in the algebra of the γ_μ or σ. We give an example of this.

Without disentangling the γ_μ operators we shall disentangle the momentum operators $p_\mu = i\partial/\partial x_\mu$ from the operator $\theta(W)$ of Eq. (72), which is a key operator in the analyses of the Dirac equation.

If we write

$$\theta(W) = \exp\left[i\int_0^W \gamma_\mu(w)p_\mu(w)dw\right]\exp\left[-i\int_0^W B[x(w), w]dw\right],$$

the $\not p_\mu$ operators are already in exponential form and no fourier transforms are necessary. We may disentangle the p_μ in the first integral by a direct use of the theorem (20) with $P(s) = p_\mu(w)$ (p_μ for each value μ is disentangled separately) and $\alpha(s) = i\gamma_\mu(w)$. The resulting $x_\mu'(w)$ operator is $x_\mu(w) + \int_w^\infty \gamma_\mu(w')dw'$ just as in Eq. (12-a) so that we obtain

$$\theta(W) = \exp\left[ip_\mu(W)\int_0^W \gamma_\mu(w)dw\right]$$
$$\times\exp\left[-i\int_0^W B\left\{x_\mu(0) + \int_0^W \gamma_\mu(w')dw', w\right\}dw\right]. \quad (18\text{-a})$$

Here the x_μ and p_μ are completely separated, but the γ_μ are thoroughly entangled. The w in B keeps track of the fact that the γ_μ in its definition acts at the order w; thus, it is $\gamma_\mu(w)B_\mu[x_\mu(0) + \int_w^\infty \gamma_\mu(w')dw']$. A similar separation may be made in the operator for self-action (74) which now is

$$R = \int_0^\infty \exp[ip_{\mu,\infty}C_\mu(W)]\exp\left\{-\tfrac{1}{2}ie^2\int_0^W\int_0^W \dot C_\mu(w')\dot C_\mu(w'')\right.$$
$$\left.\times\delta_+[\{C_\mu(w') - C_\mu(w'')\}^2]dw'dw''\right\}\exp(-imW)dW, \quad (19\text{-a})$$

where one must substitute $C_\mu(w) = \int_0^w \gamma_\mu(w')dw'$, $\dot C_\mu(w) = \gamma_\mu(w)$ ($p_{\mu,\infty}$ refers to the momentum operator operating on the final state). All reference to space coordinates have disappeared. The problem of self-energy of an electron is reduced to the algebraic one of disentangling a combination of γ_μ in an expression in which, however, they are almost hopelessly tangled up. Not much has been done with this expression. (It is suggestive that perhaps coordinates and the space-time they represent may in some future theory be replaced completely by an analysis of ordered quantities in some hypercomplex algebra).

Since the spin operators are so simple and fundamental to quantum mechanics, they present some interesting unsolved problems. For example, if $F[x(s), y(s), z(s)]$ is a known functional of a three-space trajectory $x(s)$, $y(s)$, $z(s)$, evaluate in terms of this functional, the operator $F[\sigma_x(s), \sigma_y(s), \sigma_z(s)]$, where the σ_x, σ_y, σ_z are the anticommuting Pauli operators of unit square satisfying $\sigma_x\sigma_y\sigma_z = i$. The corresponding problem with Dirac operators is a kind of four-dimensional generalization of this. Alternatively, since the Dirac operators can be represented as the outer product of two commuting sets of Pauli operators, the solution of the problem with Pauli operators could be directly extended to the Dirac case. The Pauli matrices (times i) are the basis for the algebra of quaternions so that the solution of such problems might open up the possibility of a true infinitesimal calculus of quantities in the field of hypercomplex numbers.

C. Gaussian Functionals

In a large number of problems the operators appear in exponentials only up to the second degree. For this reason it is handy to have available a formula for the integration of gaussian functionals. We can define a gaussian functional $G[y(s)]$, of one function $y(s)$, as one of the form, $G[y(s)] = \exp iE[y(s)]$ with $E[y(s)]$ quadratic. Thus, we have

$$E[y(s)] = \tfrac{1}{2}\int_0^1\int_0^1 A(t, s)y(t)y(s)dtds + \int_0^1 B(s)y(s)ds, \quad (20\text{-a})$$

where $A(t, s)$, $B(s)$ are functions independent of y (that is, G is gaussian if the second functional derivative of $\ln G$ is independent of y). Gaussian functionals of several variables are of frequent occurrence. All the quantum field theory hamiltonians and lagrangians are of this form in the field variables. A formula for the integral of $G[y(s)]$ over all paths $y(s)$ has been found useful. It will be developed here. Consider the integral (we suppose $A(t, s)$ real, or at least has a positive definite imaginary part)

$$I[A, B] = \int \exp\{iE[y(s)]\}\mathfrak{D}y(s). \quad (21\text{-a})$$

It is a functional of $A(t, s)$ and $B(s)$. First, the dependence on B may be determined, as follows.

Let $\bar y(s)$ be that trajectory which makes the exponent $E[y(s)]$ an extremum. That is, $\bar y$ is a solution of (assuming A symmetric)

$$\int_0^1 A(t, s)\bar y(s)ds = -B(t). \quad (22\text{-a})$$

Or, if N be the reciprocal kernel to A (which can often most easily be found merely by solving Eq. (22-a)),

$$\bar y(s) = -\int_0^1 N(t, s)B(t)dt. \quad (23\text{-a})$$

Then put $y(s) = \bar y(s) + x(s)$. (Note, $\mathfrak{D}y(s) = \mathfrak{D}x(s)$.) In virtue of Eq. (22-a), one finds $E[y] = E[\bar y] + \frac{1}{2}\int_0^1\int_0^1 A(t, s)x(t)x(s)dtds$. Here, $E[\bar y(s)]$ can also be written explicitly as $-\frac{1}{2}\int_0^1\int_0^1 B(s)N(t, s)B(t)dtds$, using Eq. (23-a). Substituting this into Eq. (21-a), we see a factor $\exp\{iE[\bar y(s)]\} = G[\bar y(s)]$ may be taken outside the integral, as it is independent of $x(s)$. Hence, we have

$$I[A, B] = G[\bar y(s)]J[A], \quad (24\text{-a})$$

where

$$J[A] = \exp\left[\tfrac{1}{2}i\int_0^1\int_0^1 A(t, s)x(t)x(s)dtds\right]\mathfrak{D}x(s) = I[A, 0] \quad (25\text{-a})$$

does not depend on B, and

$$G[\bar y(s)] = \exp\{iE[\bar y(s)]\}$$
$$= \exp\left[-\tfrac{1}{2}i\int_0^1\int_0^1 B(s)N(t, s)B(t)dtds\right]. \quad (26\text{-a})$$

Often this is as far as it is necessary to go, as the dependence of I on B may have been all that is necessary to know, $J[A]$ being a kind of normalizing factor that is not of importance or that can be obtained in some other manner.

Having this form for I, we may obtain other integrals. For example, since

$$\delta I[A, B]/\delta B(t) = i\int G[y(s)]y(t)\mathfrak{D}y(t),$$

this integral can be immediately evaluated by differentiation of the expression (24-a) for I with respect to $B(t)$. Since

$$\delta G[\bar y(s)]/\delta B(t) = iG[\bar y(s)]\delta E(\bar y(s))/\delta B(t)$$
$$= -i\int_0^1 B(s)N(t, s)ds\cdot G[\bar y(s)],$$

we find

$$\int G[y(s)]y(t)\mathfrak{D}y(s) = \bar y(t)I[A, B]. \quad (27\text{-a})$$

Differentiating a second time, since $\delta\bar y(t)/\delta B(t') = -N(t, t')$, one finds

$$\int G[y(s)]y(t)y(t')\mathfrak{D}y(s) = [\bar y(t)\bar y(t') + iN(t, t')]I[A, B], \quad (28\text{-a})$$

etc., for higher powers of y.

Incidentally, this permits us to obtain the properties of J. For the left-hand side of (28-a) is also $-2i\delta I[A, B]/\delta A(t, t')$. In the special case $B = 0$, we have $\bar y = 0$ from (23-a), and since $J(A) = I[A, 0]$, we find

$$\delta J/\delta A(t, t') = -\tfrac{1}{2}N(t, t')J. \quad (29\text{-a})$$

This property of J determines it to within a numerical factor independent of A.

We have used these theorems, or something like them, on various occasions. One example was the passage from Eq. (16-a) to Eq. (17-a). In more generality, put

$$F=\exp\Big[-i\int H(p(s),q(s))ds\Big],$$

where H is quadratic in p. The integrations on $p(s)$ in Eq. (16-a) now represent an example of our theorem with $y=p$ and $E[p(s)]=\int[pq-H(p,q)]ds$. The extremum requires $\partial H/\partial p=\dot{q}$. If the solution of this is $\bar{p}$, considered as a function of $\dot{q}$, q, then the integral on p produces within unimportant factors an exponential of $\int[pq-H(p,q)]ds$, that is, $i\int Lds$, where L is the lagrangian. This example shows that in our discussion, we have not been sufficiently rigorous mathematically, for the important problem of the order of noncommuting operators p, q, in the original definition of H does not seem to have arisen.

A second example is the integration of $\exp(i\int Ldt)$ when L is quadratic in $\dot{q}$, q. For the forced harmonic oscillator where $L=\frac{1}{2}(\dot{q}^2-\omega^2q^2)+\gamma(t)q(t)$, the integral was carried out in III, footnote 7. The operator $A(t,s)$ is $-[(d^2/dt^2)+\omega^2]\delta(t-s)$, the inverse N of which involves sines and cosines but is not unique. However, in this case boundary conditions exist at the end points $q(0)$, $q(T)$, and these boundary conditions determine N and also restrict the range of y integration. The footnote serves a model of what to do under circumstances and will not be discussed further here.

The problem of integrating

$$\exp\Big[-i\int j_\mu(1)A_\mu(1)d\tau_1\Big]\cdot\exp\Big[i\int(\partial A_\mu/\partial x_\nu)^2d\tau\Big](8\pi e^2)^{-1}$$

over all distributions of field $A_\mu(1)$ required in III, Sec. VIII, serves as a further example. Here $y(s)$ is replaced by $A_\mu(1)$, and $B(s)$ by $j_\mu(1)$. The operator $A(t,s)$ becomes $\Box_1^2\delta(2,1)$, the inverse of which is again not unique. The inverse $N(t,s)$ required in III is $\delta_+(s_{12}^2)$. (The boundary conditions required to define this particular inverse are probably related to the condition that no photons are supplied in the past and none are wanted in the future, so that the inverse must have no positive frequencies for $t\to-\infty$ and no negative ones to $t\to+\infty$.) Thus, $E[g(s)]$ becomes the important quantity $-\frac{1}{2}\int\int j_\mu(1)j_\mu(2)\delta_+(s_{12}^2)d\tau_1d\tau_2$, so that Eq. (24-a) gives Eq. (43) or III, Eq. (48), which we had taken such pains in III to derive in a more rigorous manner. In none of these examples do we require J.

A more complicated example is that of the analysis of the operators corresponding to the electron-positron field given in I, Appendix. If electrons obeyed Bose statistics, the commutation rules would have been altered, the net effect being just to change a few signs in the final expressions. Analyzed as an Einstein-Bose field, however, the operators Ψ^* can be considered as ordinary functions, and the lagrangian technique may be used. The problem then requires gaussian integrals (actually, integrals of exponentials of bilinear expressions, but these are as easy to work out). The y corresponds to Ψ^* (or $\Psi^{*\dagger}$), the $A(t,s)$ is related to the Dirac hamiltonian, and its inverse $K_+^{(4)}(2,1)$ replaces N. The problem of determining C_s corresponds to that of finding $J[A]$. The problem is complicated somewhat by the necessity of keeping the order of the γ_μ-operators correctly.

The relation of problems with operators obeying Fermi-Dirac statistics and those with the same operators obeying Einstein-Bose commutation rules is very close. The results of the former in practical cases,[24] at least, may be obtained from the latter by simply altering some signs. The Einstein-Bose case is very easily analyzed by ordered operator algebra (as in Sec. 7) or by the lagrangian integral methods. The anticommuting operators seem at first sight more complicated; but this they cannot be, as the results are just as simple. It would seem worth while to develop the analysis of anticommuting operators in much more detail than has been given here. Presumably, good use can be made of the similarity to the Einstein-Bose case. The theorems developed in analysis of this problem may conceivably have application in the problem of disentangling Pauli spin operators.

[24] The only known practical case, of course, is the electron-positron field. Here the problem has been completely worked out. I seem to be affected by the disease so prevalent today in theoretical physics, to delight in seeing a very general method of solving a problem, when actually in physics only one example of the type of problem exists and this has already been worked out.

D. Fock's Parameterization of the Dirac Equation

We wish to call attention to an interesting alternative method of parameterizing the Dirac equation, suggested by Fock.[4] It, like that of Sec. 8, would also have permitted us to pass directly to the formulation of electrodynamic problems. It is more readily interpreted than that of Sec. 8.[25]

As a consequence of the Dirac equation $(i\nabla-B)\psi=m\psi$, ψ also satisfies $(i\nabla-B)(i\nabla-B)\psi=m^2\psi$. Expanding the operator, this is equivalent to

$$[(i\partial/\partial x_\mu)-B_\mu]^2\psi-\tfrac{1}{2}\sigma_{\mu\nu}F_{\mu\nu}\psi=m^2\psi, \tag{30-a}$$

with $\sigma_{\mu\nu}=\frac{1}{2}i(\gamma_\mu\gamma_\nu-\gamma_\nu\gamma_\mu)$. This differs from the Klein-Gordon equation only through the addition of the term $-\frac{1}{2}\sigma_{\mu\nu}F_{\mu\nu}$, where $F_{\mu\nu}=(\partial B_\nu/\partial x_\mu)-\partial B_\mu/\partial x_\nu$ is the field tensor.

Just as in the Klein-Gordon case, III, Appendix A, this can be converted by the aid of a fifth parameter to Fock's equation,

$$i\partial\phi/\partial u=\tfrac{1}{2}[(i\partial/\partial x_\mu)-B_\mu]^2\phi-\tfrac{1}{4}\sigma_{\mu\nu}F_{\mu\nu}\phi, \tag{31-a}$$

for which the special solution $\phi=\exp(-\frac{1}{2}im^2u)\psi$ leads back to Eq. (30-a). It can then be analyzed by the lagrangian method. The final result is that the amplitude to go from one point to another [see III Eq. (5-a)] is the sum over all trajectories $x_\mu(u)$ of the hypercomplex amplitude

$$\exp\Big\{-i\int_0^\infty[\tfrac{1}{2}(dx_\mu/du)^2+(dx_\mu/du)B_\mu(x)-\tfrac{1}{4}\sigma_{\mu\nu}F_{\mu\nu}(x(u))]du\Big\}, \tag{32-a}$$

the order of operation of the $\sigma_{\mu\nu}$ being determined by the parameter u. This, in fact, is the lagrangian formulation of the Dirac equation suggested in C, Sec. XIV.

A rotation (and Lorentz transformation) by angle $\omega_{\mu\nu}$ in the $\mu\nu$-plane, is represented in Dirac theory by the operator $\exp(\frac{1}{4}i\omega_{\mu\nu}\sigma_{\mu\nu})$. (The summation on both μ and ν accounts for a factor 2.) Hence, we can say that Eq. (32-a) means that the amplitude for arrival is $\exp(iS)$, where S is the classical action $-\int[\frac{1}{2}(dx_\mu/du)^2+B_\mu dx_\mu/du]du$, but the orientation represented by the hypercomplex amplitude has rotated at each point in its path at an angular velocity (per du) equal to the field strength at that point. (Angular velocity in four dimensions is an antisymmetric tensor of second rank, as is the field strength.)

Since the potentials appear in exponential form, this may be directly connected to the form representing the action of virtual photons. The result is a set of rules like that for the Klein-Gordon case, Sec. IX, but with an additional coupling $F_{\mu\nu}\gamma_\mu\gamma_\nu$. They may be shown to be algebraically equivalent to the rules usually given for the Dirac equation, but are somewhat more complicated and not very interesting. There are some properties of the Dirac electron, however, which are more obvious in this formulation than in the usual one, and these we will discuss.

It is apparent from Eq. (32-a) that in the classical limit the trajectory is that of minimum S and therefore satisfies

$$d^2x_\mu/ds^2=(dx_\nu/du)F_{\nu\mu}. \tag{33-a}$$

(Hence, $(dx_\mu/du)^2=(ds/du)^2$ is a constant of the motion where s is the proper time, and the minimum action S is $-\frac{1}{2}(ds/du)^2u$ plus a term independent of u. Since this is to vary as $-\frac{1}{2}m^2u$, we find $ds=mdu$.) As $\hbar\to0$, the magnetic moment approaches zero and does not affect the trajectory. But since the intrinsic spin angular momentum also goes to zero, the rate of precession of spin has a classical limit. For completeness we should also give the equation

[25] Y. Nambu, Prog. Theor. Phys. (Japan) 5, 82, 1950.

of motion of the spin axis (just as the spot on a billiard cue ball has a motion, although it does not affect the trajectory of the ball). From Eq. (32-a) we see the spin axis precesses at angular velocity $F_{\mu\nu}$ (per du). (These are well-known results of the WKB approximation method when applied to the Dirac equation.) Since Eq. (33-a) says only that dx_μ/du precesses at the same angular velocity, we can summarize the classical equations of motion, and of spin precession for a Dirac electron as: *The velocity vector and spin plane are fixed in a four-dimensional coordinate system turning at each instant at an angular velocity per unit proper time equal to e/m times the field strength acting on the electron at that instant.* (For example, for a slowly moving electron in a magnetic field $\mathbf{B}$ the velocity vector revolves about the magnetic field as an axis at angular velocity $\boldsymbol{\omega}=(e/m)\mathbf{B}$, the cyclotron frequency. The spin does likewise precessing therefore at the same frequency, which is twice the Larmor frequency.)

I have expended considerable effort to obtain an equally simple word description of the quantum mechanics of the Dirac equation. Very many modes of description have been found, but none are thoroughly satisfactory. For example, that of Eq. (32-a) is incomplete, even aside from the geometrical mysteries involved in the superposition of hypercomplex numbers. For in (32-a) the field enters in two *apparently unrelated* ways, once into defining S and again in the rotation rate. In the classical limit both effects of the field can be neatly stated in one principle. What makes things particularly simple in quantum mechanics if, for a diffusing wave, a rotation at rate $F_{\mu\nu}$ is accompanied by a phase shift equal to the line integral of A_μ?[26]

In the case that the fields $F_{\mu\nu}$ are constant in space and time, the operator factor $\exp(\frac{1}{4}iu\sigma_{\mu\nu}F_{\mu\nu})$ is independent of the trajectory and factors out of Eq. (32-a). The remaining path integral is gaussian and can be carried out exactly (Appendix C), giving the results of Fock[4] and Nambu.[25]

If the operator on the right-hand side of Eq. (31-a) is considered as a type of hamiltonian, the rate of change with u of all the relevant physical quantities (given by the commutator with this operator) are very easily interpreted by classical analogy.

There are, of course, twice as many solutions of Eq. (30-a) as solutions of the Dirac equation (50). (The others correspond to Eq. (50) with negative m.) If χ is a solution of Eq. (30-a), the projected part $\psi=(2m)^{-1}(i\nabla-B+m)\chi$ solves the Dirac equation (50). Projection operators must still be used, therefore, in calculating matrix elements if Eq. (30-a) in perturbation is used instead of the Dirac equation.[27]

[26] If the $\frac{1}{4}\sigma_{\mu\nu}F_{\mu\nu}$ term is considered to have a coefficient α analogous to a kind of anomalous magnetic moment, difficulties arise in the resulting theory unless $\alpha=1$ or $\alpha=0$. Thus, the real part of L, in the amplitude for a vacuum to remain a vacuum, $C_v=\exp(-L)$, should always be positive if the theory is to be easily interpreted (see I, Sec. V). For general α, it seems that the real part of L is positive for some processes (or potentials), negative for others. It is always positive only if $\alpha=1$. But for $\alpha=0$ it is always negative, so we can reinterpret the theory in this case as referring to Bose particles, in which case C_v should be $\exp(+L)$ (I, Sec. V). For $\alpha=0$, Eq. (30-a) becomes the Klein-Gordon equation, of course.

[27] A convenient way to make the correspondence of solutions χ of Eq. (30-a) and ψ of the Dirac equation unique is to assume χ is also an eigenfunction of γ_5, that is, $\gamma_5\chi=i\chi$. This is possible, as γ_5 commutes with the operators of Eq. (30-a). Then, for each ψ, the corresponding χ is $\chi=(1-i\gamma_5)\psi$.

The Effects of Pressure and Temperature on the Resistance of $p-n$ Junctions in Germanium*

HARRY H. HALL
University of New Hampshire, Durham, New Hampshire

AND

J. BARDEEN AND G. L. PEARSON
Bell Telephone Laboratories, Murray Hill, New Jersey

(Received June 12, 1951)

According to Shockley's theory, the low voltage resistance, R_0, of a $p-n$ junction is proportional to $\exp(E_G/kT)$, where E_G is the energy gap. Measurements of the change with pressure of the characteristics of a junction in a single crystal of germanium indicate a change $\Delta R_0/R_0$ of 12.5 percent, corresponding to a change ΔE_G of about 3.1×10^{-3} ev, for a pressure change of 10,000 lbs/in^2. Analysis of measurements made at temperatures between 16.5°C and 20.5°C give values of E_G averaging about 0.72 ev. These values are in agreement with those obtained from the change in intrinsic resistivity with temperature and pressure.

I. INTRODUCTION

IN the energy level structure of the diamond-type lattice, such as that of silicon or germanium, the energy gap, E_G, between the valence-bond and conduction bands increases with decreasing atomic spacing and therefore with pressure.[1] Direct evidence for this effect comes from the increase in intrinsic resistivity with pressure as observed by Miller and Taylor.[2] Shifts of the energy bands with dilation have been related[3] to the mobilities of the conduction electrons and holes.

It is generally necessary to make measurements of intrinsic conductivity at elevated temperatures. On the other hand, Shockley's theory[4] of the $p-n$ junction indicates that the junction resistance should depend critically on E_G and thus on pressure even at room temperature. Some preliminary measurements, made both at the Bell Telephone Laboratories and at the University of New Hampshire, confirmed this effect.[5] Measurements have now been repeated under more carefully controlled conditions on a junction whose current-voltage characteristic is close to theoretical.[6]

The junction was formed by bombarding high-purity n-type germanium with α-particles. The effect of the bombardment is to produce acceptor centers and thus convert the n-type material to p-type in a depth corresponding to the range of the α-particles in the germanium. Probe electrodes were introduced so as to measure only that part of the voltage drop which occurs across the junction itself.

According to Shockley's theory,[4] current flowing at not too large reverse voltages consists mainly of holes which diffuse to the junction from the n-type side and electrons which diffuse to the junction from the p-type side. These currents depend on the concentration of holes, p_n, in the n-type and of electrons, n_p, in the p-type sides, both of which vary as $\exp(-E_G/kT)$. In the forward direction, holes flow from the p-side to the n-side and electrons from the n-side to the p-side. For not too large voltages in either direction, the expression for the total current flow is

$$I=I_p+I_n=I_0(\exp(eV/kT)-1), \tag{1.1}$$

where

$$I_0=e[(D_p p_n/L_p)+D_n n_p/L_n], \tag{1.2}$$

and e=electronic charge (1.6×10^{-19} coulomb), D_p =diffusion constant of holes in n-type material. D_n =diffusion constant of electrons in p-type material, L_p=diffusion length of holes in n-type material, L_n =diffusion length of electrons in p-type material, p_n=concentration of holes in n-type material, n_p=concentration of electrons in p-type material, V=difference of potential applied to junction, k=Boltzmann's constant (8.69×10^{-5} ev/deg), and T=absolute temperature.

Statistical theory shows that the product of the concentrations of holes and electrons without regard to impurities depends on E_G,[7] thus

$$n_p p_p=p_n n_n=A\exp(-E_G/kT), \tag{1.3}$$

where n_n=concentration of electrons in n-type material. p_p=concentration of holes in p-type material.

Since n_n and p_p are substantially constant near room temperature in germanium, p_n and n_p must each vary with $\exp(-E_G/kT)$. Thus assuming that the other

* The measurements of resistance under pressure were made with equipment built under contract between the University of New Hampshire and the Bureau of Ordnance of the Navy.

[1] G. E. Kimball, J. Chem. Phys. 3, 560 (1935) (diamond); J. F. Mullaney, Phys. Rev. 66, 326 (1944) (silicon).

[2] P. H. Miller and J. Taylor, Phys. Rev. 76, 179 (1949); and Julius H. Taylor, Phys. Rev. 80, 919 (1950).

[3] W. Shockley and J. Bardeen, Phys. Rev. 77, 407 (1950); 80, 72 (1950). The data reported here were discussed in the second of these.

[4] W. Shockley, Bell System Tech. J. 28, 435 (1949).

[5] W. Shockley, *Electrons and Holes in Semiconductors* (Van Nostrand Company, Inc., New York, 1950), p. 309 and following.

[6] For a comparison between theory and experiment of the current-voltage characteristic of a junction formed in a different way see Teal, Sparks, and Buehler, Phys. Rev. 81, 637 (1951); Croucher, Pearson, Teal, Sparks, and Shockley, *ibid.*

[7] See, for example, reference 5, p. 245. Actually, the factor A varies as T^3, but this variation is slow compared with the exponential.

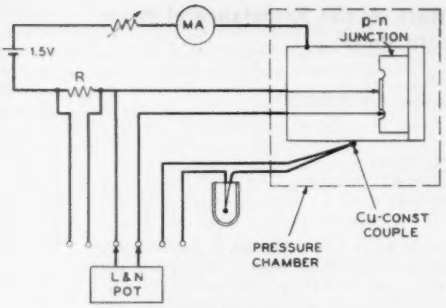

FIG. 1. Circuit diagram of measuring equipment.

factors do not vary rapidly with temperature, $I_0 \propto \exp(-E_G/kT)$. The expected increase of E_G with pressure will be evidenced by a decrease in I_0 and an increase in junction resistance. The current I_0 is closely related to the resistance, R_0, and in the low voltage limit,

$$R_0=(kT/eI_0). \tag{1.4}$$

In subsequent analysis we use R_0, which can be obtained rather directly from the experimental data, rather than I_0, to estimate the variation of E_G with pressure. Thus we take

$$R_0=A\exp(E_G/kT) \tag{1.5}$$

and assume that the effect of changes in A with pressure is negligible compared with changes in E_G. Because of the large value of the exponent[8] ($E_G\sim 0.72$ ev, $kT\sim 0.025$ ev), a very small percentage change in E_G will have a large effect on R_0.

II. PREPARATION OF THE $p-n$ JUNCTIONS

The $p-n$ junctions were prepared by bombarding high purity n-type germanium with α-particles.[9] A disk 0.3 cm in diameter and 0.05 cm thick was cut from an ingot of single crystal germanium having a resistivity of 8 ohm-cm. One side was bombarded for 72 hours with a collimated beam of 5.3-Mev polonium α-particles amounting to 6×10^9 particles per square cm per hour. This converted a surface layer 1.9×10^{-3} cm deep to p-type, thus forming a $p-n$ junction at this depth below the surface.

After electroplating rhodium electrodes on either side of the disk, the electrode on the n-type surface was soldered to a brass disk suitable for mounting in a type A transistor shell. A small circular cut about 0.01 cm in depth was then made through the remaining rhodium electrode, the p-type layer of germanium, the $p-n$ junction, and into the n-type germanium thus forming a circular $p-n$ junction 0.16 cm in diameter with ohmic electrodes attached. The germanium surface formed by the circular groove was etched with a mixture of hydrofluoric and nitric acids to clean off the debris and give the $p-n$ junction a high reverse voltage characteristic.

The completed sample was mounted in a standard type A transistor shell as shown schematically in Fig. 1. Phosphor bronze spring contacts bear on the p-type rhodium electrode, and on the n-type germanium at the bottom of the circular groove. A third electrical connection is made through the metal shell to the rhodium electrode on the n-type germanium. This permits potential probe measurements directly across the $p-n$ junction without introducing errors due to potential drop in the body resistance of the n-type germanium.

III. EXPERIMENTAL PROCEDURE AND RESULTS

The fundamental experimental data obtained in this study are the potential differences across the $p-n$ junction during passage of a fixed dc current of about 30 microamperes in both the forward and the reverse directions under varying conditions of temperature and pressure. As shown in Fig. 1, a Leeds and Northrup type K potentiometer in conjunction with a selector switch was used to measure the $p-n$ junction potential difference, as well as the voltage drop in the standard resistance R, and the thermoelectric voltage of a copper-constantan thermocouple soldered to the junction case.

Pressure was applied in a steel cylinder containing an axial chamber 0.875 inch in diameter and 3.0 inches long. The outer surface of the cylinder was jacketed with copper around which passed copper cooling and heating coils. The heating current was controlled by a thermostatic element in good thermal contact with the copper jacket as tap water circulated through the cooling coils. The temperature inside the test chamber, as measured by the copper-constantan thermocouple, could be regulated to a few hundredths of a degree by this means. The test chamber was filled with SAE No. 10 oil which transmitted the pressure applied by a hand-operated pump of 0.125 inch piston diameter. Pressure was measured by a bourdon gauge which was calibrated against a "dead weight" piston at frequent intervals. The readings were accurate to ± 25 lb/in.^{2} over a range from 0 to 10,000 lb/in.^{2}

The three leads from the $p-n$ junction and the two from the thermocouple were brought out of the pressure chamber through a 0.125-inch diameter copper tube, the inner end of which had been flared to about twice its diameter. The leads were sealed into the copper tube with De Khotinsky cement, the flare serving to support a conical wedge of cement against the outward thrust of the oil. The tube passed through two pairs of split steel disks, separated by a Neoprene washer, which were compressed by a plug threaded into the pressure chamber. Outward movement through the pressure seal was prevented by a metal collar soldered to the copper tube.

[8] Reference 5, p. 22.

[9] W. H. Brattain and G. L. Pearson, Phys. Rev. **78**, 646 (1950); and W. E. Johnson and K. Lark-Horovitz, Phys. Rev. **76**, 442 (1949).

Two series of measurements were made. In the first series, the resistance of the $p-n$ junction ($R=V/I$) was measured as a function of temperature for a constant current of 30.91 microamperes in both forward and reverse directions while pressure was varied in steps of 2000 lb/in.^{2} from atmospheric to 10,000 lb/in.^{2}. (The analysis in terms of the rectification theory is given in Sec. IV.) As shown in Fig. 2, R increased with pressure and decreased with temperature for both the forward and reverse directions of current flow. At 17 degrees centigrade the increase in resistance between one atmosphere and 10,000 lb/in.^{2} is 26.7 percent in the reverse direction, and 13.6 percent in the forward direction, while at 21 degrees centigrade the increases are 23.8 and 11.0 percent, respectively. At one atmosphere the decrease in resistance between 17 degrees centigrade and 21 degrees centigrade is 43.4 percent in the reverse direction, and 26.1 percent in the forward direction, while at 10,000 lb/in.^{2} the decreases are 44.7 and 27.8 percent, respectively.

In the second series of measurements, the resistance of the $p-n$ junction was measured as a function of pressure at a fixed current of 30 microamperes and a constant temperature of 18.55 degrees centigrade. The data, which are shown in Fig. 3, indicate an increase in resistance of 18.5 percent in the reverse direction and an increase of 11.5 percent in the forward direction between one atmosphere and 10,000 lb/in.^{2}, the change being approximately linear. The data of this series are considered the more reliable for determining the effects of pressure, since the current was determined with greater accuracy and the temperature stabilization appeared to have been more successful.

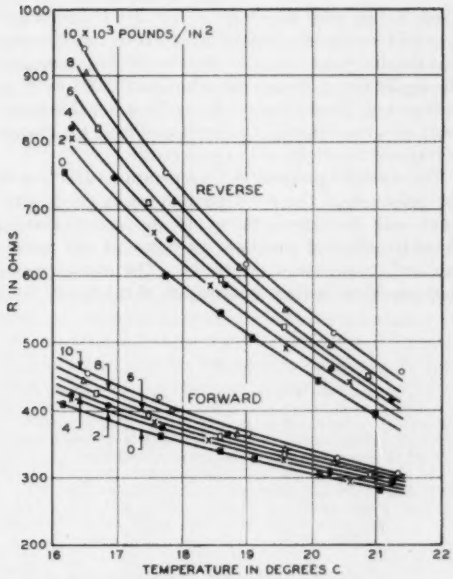

FIG. 2. Resistance (V/I) *versus* temperature characteristic of $p-n$ junction for a constant current of 30.91 microamperes in either direction. The pressures are as indicated.

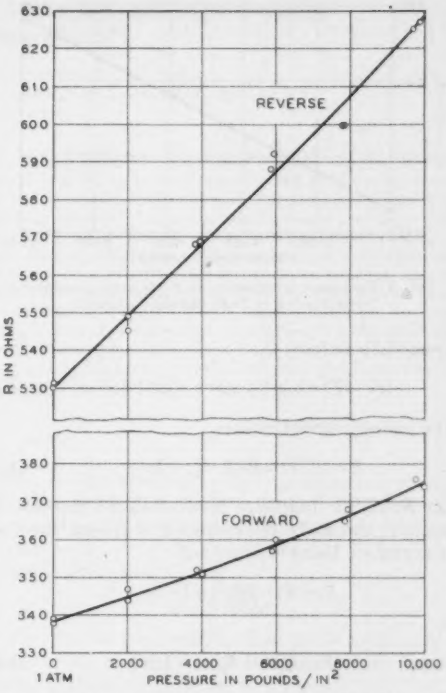

FIG. 3. Resistance (V/I) *versus* pressure characteristic of $p-n$ junction for a constant current of 30.00 microamperes in either direction and a fixed temperature of 18.85 degrees centigrade.

The resistances, which are plotted in Fig. 2 and Fig. 3, are the ratios V/I rather than the differential values dV/dI. From these we have estimated the differential resistances, R_0, for the limit $I\to 0$, as described in the following section.

IV. ANALYSIS OF DATA

Resistance measurements were made for fixed values of the current in both the forward and reverse directions. For purposes of analysis we have extrapolated between these values to get the resistance, R_0, in the limit $I\to 0$. This was done by the following method. By differentiating (1.1) with respect to I and then setting $V=0$ we find

$$R_0=(dV/dI)_0=(kT/eI_0). \tag{4.1}$$

In the following we shall use a reduced current $x=(I/I_0)$. We want to determine the resistance in the limit $x\to 0$ from measurements made at small fixed values of x in both the forward and reverse directions.

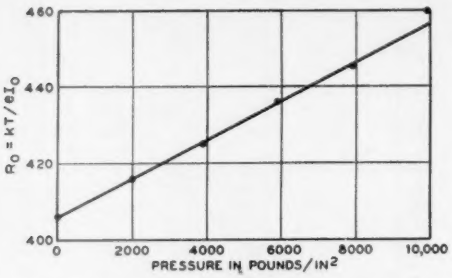

FIG. 4. Resistance extrapolated to $V=0$ *versus* pressure for $p-n$ junction at 18.85 degrees centigrade.

From (1.1) we have

$$(eV/kT)=\log(1+x)=x-\tfrac{1}{2}x^2+\tfrac{1}{3}x^3-\cdots. \quad (4.2)$$

The voltage/current ratio is

$$R=(V/I)=R_0(1-\tfrac{1}{2}x+\tfrac{1}{3}x^2-\cdots). \quad (4.3)$$

Let R_f be the resistance in the forward direction (x positive) and R_b be the resistance in reverse direction (x negative). Using (4.3) we find

$$R_b+R_f=2R_0(1+\tfrac{1}{3}x^2+\cdots),$$

or

$$R_0\simeq\tfrac{1}{2}(R_b+R_f)(1-\tfrac{1}{3}x^2\cdots). \quad (4.4)$$

The value of x to use in the correction factor can be obtained from

$$R_b-R_f=R_0(x+\cdots),$$

or

$$x\simeq 2(R_b-R_f)/(R_b+R_f). \quad (4.5)$$

Values of R_0 estimated from the values of R_b and R_f in Fig. 3 are shown in Fig. 4. The change in R_0 with pressure is approximately linear, and is approximately 1.25 percent for 1000 lb/in.^{2}

If it is assumed, as seems reasonable, that the change in I_0, and thus of R_0, results almost entirely from the change in E_G with pressure, we have

$$\frac{R_0(P)}{R_0(0)}=\frac{\exp[E_G(P)/kT]}{\exp[E_G(0)/kT]}, \quad (4.6)$$

and for small changes

$$\Delta R_0/R_0\simeq\Delta E_G/kT. \quad (4.7)$$

A change $\Delta R_0/R_0$ of 1.25 percent corresponds to a change ΔE_G of about 3.1×10^{-4} ev at room temperature. The dilation for 1000 lb/in.^{2} is about 7×10^{-5}, so that the rate of change of energy gap with dilation is about

$$dE_G/d\log v=-3.1\times10^{-4}/7\times10^{-5}=-4.5 \text{ ev}.$$

This value is in good agreement with those based on earlier measurements on $p-n$ junctions quoted in reference (3) and also with those of Miller and Taylor based on changes in intrinsic conductivity with pressure.

The value of E_G can be estimated from the temperature variation of R_0. If $R_0(T)$ corresponds to the value of R_0 at temperature T at a fixed pressure, we have

$$\log[R_0(T+\Delta T)/R_0(T)]=-(E_G/kT)(\Delta T/T).$$

From the data of Fig. 2 we have estimated the values of R_0 given below:

$T=16.5$°C	$P=1$ atmos	$R_0=497$
$T=20.5$°C	$P=1$ atmos	$R_0=343$
$T=16.5$°C	$P=10{,}000$ lb/in.^{2}	$R_0=590$
$T=20.5$°C	$P=10{,}000$ lb/in.^{2}	$R_0=390$.

These values give $E_G=0.69$ ev for $P=1$ atmos and $E_G=0.75$ ev for $P=10{,}000$ lb/in.^{2} It is not believed that the differences in E_G at the two different pressures are significant; a change of only about 0.003 ev is to be expected. These values of E_G are in reasonable agreement with the value 0.72 ev estimated from the change in intrinsic resistivity with temperature.

The observed pressure and temperature variations of the resistance of the $p-n$ junction are in good agreement with Shockley's theory of the current-voltage characteristic and previous estimates of the energy gap and its change with pressure. The measurements thus provide a further confirmation of the theory.

Investigation of Nuclear Effects in Paramagnetic Single Crystals at Very Low Temperatures*†

STEPHEN F. MALAKER‡§
Oak Ridge National Laboratory, Oak Ridge, Tennessee, and Catholic University, Washington, D. C.
(Received May 21, 1951)

The hyperfine structure coupling of the magnetic moment of the nucleus with the magnetic moment of the electronic cloud of a paramagnetic ion gives rise to a Schottky specific heat anomaly at an appropriate temperature. For the cobaltous ion in a single crystal of cobalt ammonium sulfate this temperature is about 0.1°K. In the region where the specific heat goes as A/T^2 and where the Curie law $\chi=C/T$ holds, one can make measurements of A by means of an ac mutual inductance bridge which measures the susceptibility of the paramagnetic salt. The method of measurement consists in superposing a dc magnetic field on the salt already in the ac field of the bridge. This dc field depresses the susceptibility an amount depending on the parameter C/A which is therefore a constant of the material being investigated. If one knows the Curie constant, then one has A immediately. This measured A, however, is made up of two contributions: (a) that arising from the nuclear-electronic coupling and (b) that arising from the dipole interaction of neighboring paramagnetic ions. The (b) contribution is a function of concentration of the ions, so that by making measurements of A at various dilutions and plotting A as a function of dilution, one obtains an intercept by extrapolation to infinite dilution which is the part of A due to nuclear specific heat. The thermodynamic measurements made thus give a nuclear specific heat of $C_vT^2=16.1\times10^{-4}R$, where R is the gas constant, which is in excellent agreement with $C_vT^2=16\times10^{-4}R$ calculated from microwave data. It is observed that pure cobalt ammonium sulfate has a Curie point at ~0.125°K, while the diluted salts do not possess one in the same temperature region.

I. INTRODUCTION

THE existence of hyperfine structure coupling for paramagnetic ions in the solid state was suggested independently by Rose[1] and Gorter.[2] That this coupling should cause a splitting of the energy levels of the system and consequently give rise to a Schottky[3] specific heat anomaly was pointed out by Garrett,[4] who corroborated his interpretation with experimental work on powdered copper potassium sulfate and powdered cobalt ammonium sulfate.

Because of the paucity of information on paramagnetic single crystals and because of its importance in quantitative treatments of the solid state, our investigations on the specific heat anomaly due to the hyperfine structure coupling in cobalt ammonium sulfate were carried out on single crystals.

II. THEORY

In paramagnetic salts there are several types of interaction, any and all of which may remove degeneracies. The main interactions are (1) interaction of the paramagnetic ion with the strong crystalline electric field (Stark effect) caused by the water dipole environment, (2) exchange interactions between electrons of the paramagnetic ion and other electrons in the crystal, (3) interaction between neighboring paramagnetic ions, often called the dipole-dipole interaction, (4) hyperfine structure coupling and quadrupole coupling between the electronic "clouds" of the paramagnetic ions and their own nuclei, (5) interaction between nuclei of adjacent paramagnetic ions. The interaction (4) is the chief concern of the present paper.

Stark Effect

The effect of the crystalline field can be treated as a perturbation on the free ion. If one writes the hamiltonian of the spin system as

$$\mathcal{H}=\sum_i \mathcal{H}_i, \tag{1}$$

where $\mathcal{H}_i$ is the hamiltonian of the ith paramagnetic ion and the sum is taken over all ions, then $\mathcal{H}_i$ will have the form,

$$\mathcal{H}_i=\mathcal{H}_0+\lambda(\mathbf{L}\cdot\mathbf{S})+V+\beta(\mathbf{L}+2\mathbf{S})\cdot\mathbf{H}, \tag{2}$$

where $\mathcal{H}_0$ is the hamiltonian of the free ion without spin orbit coupling, $\lambda(\mathbf{L}\cdot\mathbf{S})$ is the spin-orbit interaction, V is the potential of the crystalline field, and the last term describes the influence of an external magnetic field $\mathbf{H}$; β is the Bohr magneton and $\mathbf{L}$ and $\mathbf{S}$ are the angular momenta operators for the orbital motion and spin. Higher terms proportional to $\mathbf{H}^2$ and to $(\mathbf{L}\cdot\mathbf{S})^2$ for ions which, when free, have Russell-Saunders coupling are neglected. Pryce[5] and Jauch[6] have recently given alternative approaches utilizing the eigenvalues of an observable involving only spin variables, with the energy levels correct to the second order.

In the case of ions of the iron group, the incomplete d-shell is not screened; and because of the lack of screening, the spin-orbit coupling is strongly affected by the crystalline electric field.

In cobalt ammonium sulfate $Co(NH_4)_2(SO_4)_2\cdot6H_2O$, the waters of hydration form an octahedron around the Co^{++} ion, and one can treat the $Co^{++}\cdot6H_2O$ unit as a

* Presented in partial fulfillment of the requirements for the degree of Doctor of Philosophy at Catholic University, Washington, D. C. Presented at New York Meeting of American Physical Society, February 3, 1951 [Phys. Rev. **82**, 343 (1951)].

† This work was performed under the auspices of the U. S. AEC.

‡ This work was performed while the author was a Graduate Fellow of the Oak Ridge Institute of Nuclear Studies.

§ Now at Ohio State University, Columbus, Ohio.

[1] M. E. Rose, Phys. Rev. **75**, 213 (1949).

[2] C. J. Gorter, Physica **14**, 504 (1948).

[3] W. Schottky, Z. Physik **23**, 448 (1922).

[4] C. G. B. Garrett, Nature **163** (1949); thesis, Trinity College (1949, unpublished).

[5] M. H. L. Pryce, Proc. Phys. Soc. (London) **A63**, 25 (1950).

[6] J. M. Jauch, ORNL 813 (1950), unpublished.

nonlinear "molecule." Since the "molecule" does have cubic symmetry, one must consider the Jahn-Teller effect.[7] Jahn and Teller considered a molecule in a state with a degenerate energy level as being a result of some symmetry property. Their group-theoretical arguments showed that such a state cannot be stable, and therefore a distortion will occur which will lead to a state with lower symmetry removing the original degeneracy. Van Vleck[8] applied this theorem to $Co^{++}\cdot 6H_2O$ and showed that such a deformation removes all degeneracy except the Kramers[9] degeneracy.

The configuration of Co^{++} is $1s^2\,2s^2\,2p^6\,3s^2\,3p^6\,3d^7$ and the state according to Hund's rule is $^4F_{9/2}$. It has been calculated by Laporte[10] that the parameter λ for the spin orbit coupling in the hamiltonian given by Eq. (2) is $\lambda = 180\ cm^{-1}$.

In a cubic field the orbital F level ($L=3$) is split according to $D_3 = \Gamma_2+\Gamma_4+\Gamma_5$ with the Γ_4-level lowest. In salts of the Tutton group where the symmetry of the field is predominantly tetragonal the lowest cubic level splits into a doublet and a singlet $\Gamma_4 = \Gamma_3+\Gamma_5$ with the singlet lying lower. Introduction of the spins makes the degeneracy of the tetragonal levels four times as much, but the strong spin-orbit coupling splits these levels into Kramers' doublets according to $A_2D_1 = \Gamma_6+\Gamma_7$ and $ED_1 = 2\Gamma_6+2\Gamma_7$ giving again six doublets. Pryce[5] has shown that the tetragonal splitting is smaller than the LS coupling splitting. This is the result of the almost complete cancellation of the contributions of the second- and fourth-order terms in the series expansion of the crystalline potential. The splitting between the two lowest doublets is estimated to be about $300\ cm^{-1}$ in cobalt ammonium sulfate so that the contribution of the Stark splitting to the specific heat below 1°K is negligible. This is one reason for choosing this particular salt. The higher levels influence the properties of these paramagnetic salts only indirectly through their influence on the lower levels.

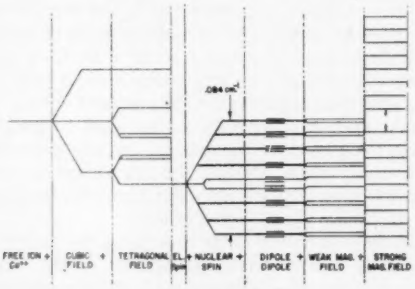

FIG. 1. Energy level scheme for Co^{++} in cobalt ammonium sulfate.

[7] H. A. Jahn and E. Teller, Proc. Roy. Soc. (London) **A161**, 220 (1937).
[8] J. Van Vleck, J. Chem. Phys. **7**, 72 (1939).
[9] H. A. Kramers, Proc. Acad. Amsterdam **32**, 1176 (1929); **33**; 959 (1930).
[10] O. Laporte, Z. Physik **47**, 76 (1928).

Exchange and Dipole Interactions

It is convenient to treat these two interactions simultaneously as was done by Van Vleck.[11] The results of his calculation show that the specific heat arising from these interactions is given by

$$C_v = (Nk)(Q/6)[g^2\beta^2NJ(J+1)/k]^2/T^2, \qquad (3)$$

where N is Avogadro's number, g is the splitting factor, β is the Bohr magneton, J is the total angular momentum quantum number, k is the Boltzmann constant, T is the absolute temperature, and Q is a lattice geometry factor.

As is always the case when $kT \gg$ splitting, the specific heat goes as $1/T^2$ and one can write the dipole-dipole specific heat as

$$C_v = A_{DD}/T^2, \qquad (4)$$

where A_{DD} is a constant. The exchange terms are neglected here because, as will be seen later, there is experimental evidence that exchange effects in cobalt ammonium sulfate appear to be negligible.

It is interesting to consider the effect of magnetically diluting the already dilute paramagnetic salt. This dilution can be accomplished by replacing some of the paramagnetic ions by diamagnetic ions. Experimentally this can be accomplished by co-crystallizing isomorphous salts.

It can be shown that the dipole-dipole specific heat and the exchange specific heat vary linearly with random dilution. This suggests the important experimental procedure of measuring the specific heat in crystals of varying dilution and extrapolating the measured results to infinite dilution, thereby eliminating any contribution to the specific heat from phenomena which are functions of concentration.[12] The effect of the dipole-dipole coupling is not to give sharply defined lines in the energy level scheme but rather to broaden the lines because of the production of large numbers of levels of the order 2^N which form a band of width approximated by β^2/N, where β is the Bohr magneton. This is indicated in the energy level scheme shown in Fig. 1, by placing dashes above and below the sharp lines in the spectrum.

Interaction between the Nucleus and Electron Cloud

The interaction between the nucleus and electrons can be broken down into at least three parts: (*a*) magnetic interaction of the nuclear magnetic moment with the moment due to electron spin and unquenched residual orbital angular momentum of the electron, (*b*) nuclear quadrupole interaction with the gradient of the electric field in the electron cloud, and (*c*) coulombic interaction.

We consider here only the interaction given by (*a*). Assuming that both the nuclear spin and electron spin

[11] J. H. Van Vleck, J. Chem. Phys. **5**, 320 (1937).
[12] R. Benzie and J. Cooke, Nature **164**, 837 (1949).

magnetic moments can be treated as dipoles, one can write down immediately the interaction energy as

$$W_{I,J}=-(\beta\mu_I/r^3)[\mathbf{I}\cdot\mathbf{S}-(3(\mathbf{I}\cdot\mathbf{r})(\mathbf{S}\cdot\mathbf{r})/r^2)-\mathbf{I}\cdot\mathbf{L}], \quad (5)$$

where μ_I is the nuclear magnetic moment, **I**, **S**, and **L** are the usual angular momentum operators, and **r** is the radius vector with modulus r. A simple calculation shows that the $\mathbf{I}\cdot\mathbf{L}$ term in cobalt ammonium sulfate is negligible, the splitting being of the order 10^{-8} cm^{-1}.

If one now assumes that the electric field surrounding the ion is cylindrical in symmetry about the z axis (it is actually tetragonal in cobalt ammonium sulfate), one can integrate (5) over space in cylindrical coordinates, getting[12]

$$\mathcal{H}_{\text{hfs}}=A^*I_zS_z+B(S_zI_x+S_yI_y), \quad (6)$$

where A^* and B are determinable from microwave measurements.

If quadrupole terms are included, the hyperfine structure hamiltonian given by (6) must include another term given by

$$\mathcal{H}_{\text{quad}}=Q\{I_z^2-\tfrac{1}{3}I(I+1)\}. \quad (7)$$

Indications are that Q is very small in cobalt ammonium sulfate.

Setting up the energy matrix by means of Eq. (6) shows, from symmetry considerations of the diagonal elements, that the hyperfine structure in cobalt ammonium sulfate is composed of 7 doublets and 2 singlets. (See Fig. 1.) The off-diagonal elements given by the second member of the hamiltonian of (6) produce such a small perturbation for cobalt ammonium sulfate that the energy level system may be considered at eight equally spaced doublets with an over-all splitting of 0.084 cm^{-1}. The values of A^* and B are 0.024 cm^{-1} and 0.0028 cm^{-1}, respectively.[12]

On the high temperature side of the Schottky anomaly the hyperfine structure contribution to the specific heat is given by[13]

$$C_N=R(hc/kT)^2[\tfrac{1}{3}(A^{*2}+2B^2)S(S+1)I(I+1)], \quad (8)$$

where h=Planck's constant and c=velocity of light. The specific heat calculated from Eq. (8) is given by[13]

$$C_NT^2/R=16\times10^{-4}=A_N. \quad (9)$$

One could, in principle, measure this specific heat by making measurements on crystals possessing an ion having a nuclear spin, repeating the measurements using an isotope of the ion without nuclear spin, and taking the difference as the nuclear specific heat. The present measurements have been made using the random dilution technique. Cobalt is monoisotopic and is an excellent ion for the present purposes.

III. ENTROPY CONSIDERATIONS

There are several advantages to using a single crystal in measurements at low temperatures, among which one of the most important is the fact that the entropy is known very accurately. In addition, in the case of a magnetically anisotropic crystal like cobalt ammonium sulfate, the crystal can be so oriented that a larger portion of the entropy can be removed along one axis than another. In cobalt ammonium sulfate[13] with its g-factors‖ of 6.2, 3.0, and 3.0 along the K_1, K_2, and K_3 magnetic axes, respectively, the entropy removal is considerably greater along the K_1 axis.

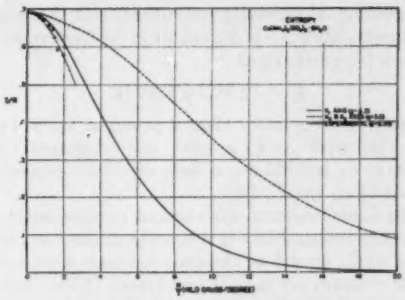

FIG. 2. Entropy removal upon magnetization along various magnetic axes.

From microwave measurements it is known that the ground state of the Co^{++} ion in cobalt ammonium sulfate is a Kramers' degeneracy doublet which is tractable as an $S=\frac{1}{2}$ system and which can be split by means of a small magnetic field.

Since the crystal is magnetically anisotropic, the energy is given by

$$W=\pm\tfrac{1}{2}\beta\theta, \quad (10)$$

where

$$\theta=[\textstyle\sum(g_{ik}H_k)^2]^{\frac{1}{2}}, \quad (11)$$

in which g_{ik} is the tensorial g-factor, H_k the applied field in the kth direction, and β the Bohr magneton.

From this it follows that the entropy is given by

$$S/R=[\ln\{2\cosh(\beta\theta/2kT)\}-(\beta\theta/2kT)\tanh(\beta\theta/2kT)]. \quad (12)$$

The calculated electronic entropy removal upon magnetization at ~1°K along the principal magnetic axes is shown in Fig. 2, from which it is evident that a much greater entropy removal for a given H/T can be effected along the K_1 axis. The present experiment was performed by suspending the crystal with the K_2 axis vertical and the K_1 axis in the horizontal plane free to rotate so that it would be parallel to the applied magnetizing field. It is interesting to note that a directional magnetic specific heat may exist in an anisotropic crystal, and it is hoped to pursue this point experimentally at a later date.

As usual in measurements below 1°K, the temperature $T+$ was obtained by extrapolation of the Curie law.

[12] B. Bleaney, Phys. Rev. **78**, 214 (1950).

‖ *Note added in proof:*—The g-values of 6.2 and 3.0 are ionic values; the crystalline g-values are $g_1=5.71$, $g_2=3.00$, and $g_3=4.34$.

Assuming, as previously mentioned, that the ground electronic state is $S=\frac{1}{2}$, one can write the Curie constant along a principal axis as

$$C_i=Ng_i^2S(S+1)\beta^2/3k, \tag{13}$$

where g_i is the g-factor along a principal axis i. From Eq. (13) with $S=\frac{1}{2}$, $g_i=3.0$, the calculated Curie constant C_2 is 0.852 for a mole of cobalt ammonium sulfate along the K_2 axis.

The Curie constant was checked experimentally by obtaining susceptibility-temperature calibration curves for a single crystal of chrome potassium alum whose Curie constant per mole is well known (1.760) and for the pure cobalt ammonium sulfate crystals along their K_2 axis. Knowing the ratio of the slopes of these curves and making appropriate mass corrections, we have determined the Curie constant C_2 of the cobalt ammonium sulfate to be 0.858. This figure has been used in the calculations throughout this paper. The single crystals of cobalt ammonium sulfate were ground to spherical form (~13.5-mm diameter). They were the best of the crystals left after continuous culling from several hundred seed crystals.

IV. METHOD OF MEASUREMENT

Consider now a paramagnetic salt at liquid helium temperatures. In the salt there are three separate statistical systems, with separate temperatures, namely, the lattice and the electronic and nuclear spins. Since an alternating current mutual inductance bridge is the actual measuring device, the observed susceptibility is frequency dependent. At low frequencies, the observable is the isothermal susceptibility χ_0 because heat transfer between the lattice and spin can take place. At high frequencies the adiabatic susceptibility χ_s is the observable, considering the spin system along and assuming the nuclear electronic spin relaxation time to be small compared with the period of the measuring field. The dispersion at intermediate frequencies can be explained in terms of a relaxation time of the spin-lattice system.[14]

The present experiment, however, below 1°K is such that both the lattice and spin can oscillate at the same frequency. As the temperature is decreased below 1°K, the ratio of C_L/C_S, where C_L is the lattice and C_S the spin specific heat, respectively, becomes very small; i.e., the lattice thermal capacity is negligible. Thus the observable susceptibility will be the adiabatic susceptibility χ_s, and dispersion phenomena completely irrelevant to the measurements.

If one assumes that the Curie law is valid ($\chi=C/T$) and that the specific heat is given by A/T^2, it can be shown that[4]

$$\chi_{SH}=\chi_{00}(1-\tfrac{3}{2}\Xi H^2), \tag{14}$$

where χ_{SH} is the adiabatic susceptibility in a field H, χ_{00} is the isothermal susceptibility in zero magnetic field, H is a superposed constant magnetic field and Ξ is defined by

$$\Xi=-\frac{1}{\chi}\frac{d\chi}{dT}\frac{d\chi}{dS}=\frac{C}{A}, \tag{15}$$

in which S is the entropy, T is the temperature, and χ is the susceptibility.

The application of the steady field has two effects, namely, (1) decreasing the isothermal susceptibility by production of reversible warming effects, and (2) depressing χ_S below χ_0. The two susceptibilities would be equal only in zero field but at the temperature T_H.

In terms of the measured quantities Eq. (14) can be rewritten as

$$\Xi=\frac{2}{3H^2}\left(\frac{\mathfrak{M}_S-\mathfrak{M}_0}{\mathfrak{M}_0}\right)=\frac{C}{A}, \tag{16}$$

where $\mathfrak{M}$ is the mutual inductance due to the salt, so that if one knows the Curie constant, a measurement of Ξ gives A immediately. Thus, the superposition of a steady magnetic field of proper magnitude on the ac magnetic field of the bridge enables one to measure the tail of the Schottky specific heat anomaly without recourse to calorimetry.

V. CRYSTALLOGRAPHY OF HEXAHYDRATED COBALT AMMONIUM SULFATE

The crystal structure of cobalt ammonium sulfate hexahydrate has been studied by Halla,[15] and in greater detail several isomorphic salts have been studied by Hofmann.[16] Detailed analysis of x-ray data has enabled one to draw a fair picture of the unit cell. In Fig. 3 is shown a view of the unit crystal structure, the b axis being normal to the plane of the paper. It might be pointed out here that the legend of Fig. 63 in Strukturbericht[17] is incorrect in that the **a** and **c** vectors have been interchanged. This projection demonstrates what Hofmann calls the pseudocubic structure of the salt.

These isomorphic salts are monoclinic, contain two molecules in the unit cell, and have arrangements developed from the space group C_{2h}^5. All atoms, except Co^{++}, are located in the general position $[\pm(x, y, z); \pm(x+\frac{1}{2}, \frac{1}{2}-y, z)]$. The Co^{++} atoms are located at $(000; \frac{1}{2}\,\frac{1}{2}\,0)$. As pointed out by Wyckoff,[18] however, this arrangement cannot be correct because although the NH_4-O and $Co^{++}-H_2O$ separations are satisfactory, the sulfate oxygens belonging to the different SO_4 groups are much too close together. The given values of the O−O distance are about 2.1A, while the minimum permissible distance should be ~2.7A, indicating a variation of the order 0.5A, a quantity which is not negligible.

[14] C. J. Gorter, *Paramagnetic Relaxation* (Elsevier Publishing Company, Inc., New York, 1947).

[15] F. Halla and E. Z. Mehl, Z. anorg. u. allgem. Chem. **199**, 379–383 (1931).

[16] W. Hofmann, Z. Krist. **78**, 279–333 (1931).

[17] Strukturbericht, *Band II* (1928–1932), p. 94.

[18] R. Wyckoff, *Structure of Crystals* (Reinhold Publishing Corporation, 1931), second edition, p. 93.

For an adequate quantum-mechanical treatment of the properties of the salt, the wave function of the paramagnetic ions must be known accurately. This calls for a much better picture of the crystal structure than is available at present, and to this end the problem is being investigated by Dr. Max Bredig and Mr. B. S. Borie of the Metallurgy Division of ORNL, who have begun preliminary fourier analysis of the x-ray pictures taken of single crystals grown in this laboratory.

The three crystallographic axes (a, b, c) are very nearly in the ratio (3, 4, 2). The a axis makes an angle of 106° 56′ with the c axis in cobalt ammonium sulfate. The Co^{++} ions lie in the points mentioned previously and are surrounded by an octahedron of water molecules, four of which lie nearly at the corners of a square at a distance of about 1.9A from the Co^{++} and the other two slightly farther away at about 2.15A. The electric crystalline field per ion then should have approximately tetragonal symmetry about the line joining the more distant waters. As already indicated, however, there are two Co^{++} ions per unit cell and in a spatial average over the crystal one has two tetragonal axes equally inclined to the ac plane. The angle between the tetragonal axes and the ac plane, in cobalt ammonium sulfate, is about 33°.

It is known from microwave measurements that magnetic anisotropy exists, and it is necessary to correlate the readily identifiable crystallographic axes with the magnetic axes. In Fig. 4 are shown views of a crystal drawn from an actual specimen grown in the laboratory. It is not a perfect crystal, in that all faces are not equally developed; but it is a typical crystal. In (a) is seen a view taken along the crystallographic b axis. Note the well-defined ac axes. In (b) is shown a side elevation and also in (c) in the directions indicated. In (d) is shown a perspective view of the entire crystal. The circles in Fig. 4 (a) and (b) show from what portion the spherical samples actually used in the experiment were cut. The view given by (b) determines what size crystal must be grown to obtain a sphere of given diameter. The dotted line in (a) shows the direction of the principal magnetic axis K_1 with respect to the crystallographic axis. This was determined by placing the crystal in a strong magnetic field (~5 kilogauss) at room temperature and observing the orientation of the crystal suspended along various axes. Observe also that the K_1 axis is very nearly, within a few degrees, the short diagonal of the parallelogram representing the ac plane of the crystal. Furthermore, it was found that the K_1 axis is in the ac plane, in good agreement with Bleaney *et al.*[19]

The relationship between the various axes—crystalline electric field, magnetic, and crystallographic—is shown in Fig. 5. Note that the K_1 axis lies in the ac plane and that the major projections of the tetragonal axes lie along it.

[19] Bleaney, Penrose, and Plumpton, Proc. Roy. Soc. (London) A198, 406 (1949).

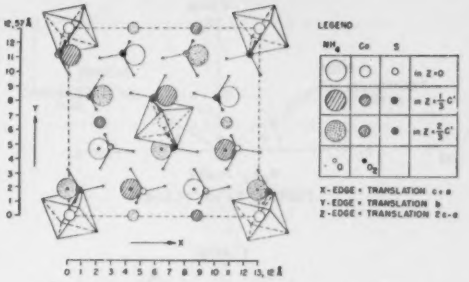

FIG. 3. Crystal structure of cobalt ammonium sulfate.

Paramagnetic absorption measurements[20] indicate that g-values have tetragonal symmetry the values of which are 6.2, 3.0, and 3.0, respectively, and these values have been used in the calculations in this paper.

The crystals used in the present experiments were grown from saturated solutions in a constant temperature bath. Growth rate was controlled by keeping moistened paper covers on the beakers. The diluted crystals were grown by mixing together saturated solutions of the isomorphous salts. The resultant crystals were checked by means of x-rays, and the dilution was found to be random indeed. No evidence of order could be found in the Mg diluted salt, and the tacit assumption is made that Zn behaves in a similar fashion. The magnetic dilution was performed using Zn and Mg as the dilution ions. The manufacturer's specifications for the cobalt ammonium sulfate lists, as impurities: Fe=0.001 percent, Ni=0.06 percent and Zn=0.005 percent (J. T. Baker Chemical Company, lot No. 41548). Analyses of impurities in the isomorphous salts are not available.

VI. APPARATUS AND EXPERIMENTAL PROCEDURES

The measurements were carried out below 1°K, and this necessitated the use of the adiabatic demagnetiza-

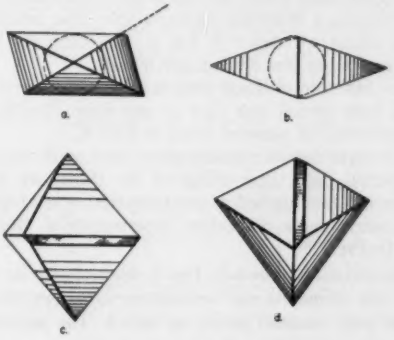

FIG. 4. Actual crystal grown in the laboratory.

[20] B. Bleaney and D. J. E. Ingram, Nature 164, 116 (1949).

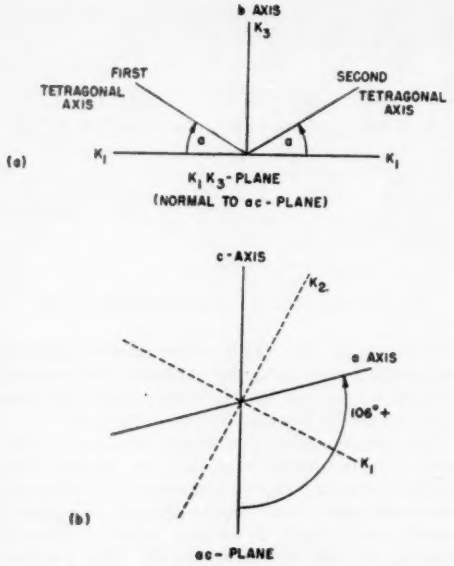

FIG. 5. Relationship of axes in cobalt ammonium sulfate.

tion technique. The magnet used in the adiabatic demagnetizations was a large Weiss-type electromagnet. The field was very uniform over a cylindrical volume, and variation was negligible over the diameter of the spherical single crystal of ~13.5 millimeter diameter.

The current through the coils was controlled to 0.1 percent by means of an amplidyne-controlled saturable reactor. The maximum magnetic field over the 2-inch gap was about 13 kilogauss at slightly less than 6-kw input. The magnet was mounted on a carriage and track and could be rolled away when necessary.

The present cryostat was constructed so that the sample could be changed quite easily, even during a run, if one could afford the loss of the helium boiled off by inserting a relatively warm sample. The details of the cryostat are shown in Fig. 6. The measured heat leak to the salt was 3.6 ergs per minute.

The loss rate of liquid helium as measured over an eight hour period was 22.6 cc per hour. The liquid helium could be pumped down to 0.95°K.

The experimental measurements were made with an ac mutual inductance bridge of the Hartshorn type, which was first applied to low temperature methods in the paramagnetic relaxation experiments of DeHaas and DuPré.[21–23]

The circuit is shown in Fig. 7, where it can be seen that the primaries and secondaries are connected in series with common points as shown. The secondary consists of, in addition to the mutual inductance, secondary coils, an amplifier, tuned circuit, cathode follower, and the detector, a vibration galvanometer tuned to 35 cps. The amplifier contained a specially designed filter having a resonant frequency of 35 cps and a bandwidth ~4 cps. A cathode follower, essentially an impedance transformer, was required to match the output of the amplifier to the galvanometer. The ac bridge method is chosen because it enables one to measure both components of a complex susceptibility

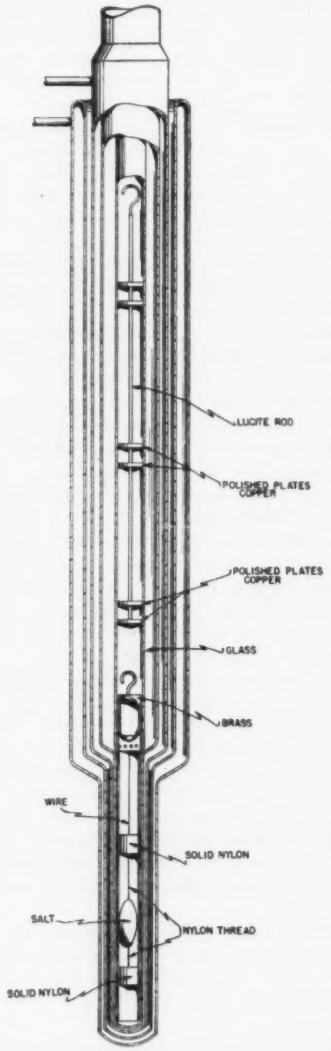

FIG. 6. Details of cryostat design.

[21] W. J. DeHaas and F. K. DuPré, Physica **6**, 705 (1939).
[22] D. DeKlerk, thesis, Leiden (1948), unpublished.
[23] D. Bijl, thesis, Leiden (1950), unpublished.

simultaneously and rapidly. A low frequency was required because one does not desire complications arising from spin-lattice relaxation in the salt.

It can be shown that the real and imaginary parts of the susceptibility denoted by χ' and χ'', respectively, can be measured in arbitrary units without calibrating for absolute susceptibilities. Thus one gets

$$\chi' = (C/K)\Delta\mathfrak{M} \tag{17}$$

and

$$\chi'' = (C/K\omega)(\Delta R_{eff}), \tag{18}$$

where C is the Curie constant, ω is 2π times the frequency, K is the slope of the temperature calibration curve in the liquid helium temperature region, $\mathfrak{M}$ is the mutual inductance in arbitrary units, and R_{eff} is defined by $R_{eff}=r_1r_2/(R_0+r_1+r_2)$, where r_1, r_2, and R_0 are shown in Fig. 7.

The results presented here were obtained in 16 helium runs and well over 100 demagnetizations, the results being quite reproducible.

Demagnetizations were made from various H/T values, and during the ensuing warm-up time many Ξ values could be obtained. The measurements were taken over a period of about 45 minutes, after which it was assumed temperature inhomogeneities might exist. Because of the very small heat input ($\sim$0.06 erg/sec), the warm-ups were very slow and good values of the Ξ parameter could be obtained.

Since at the very low temperatures, the effects of the earth's magnetic field could be quite large, two measurements were always made, one with the superposed constant magnetic field directed upward and one with the field downward. The Ξ-parameter was calculated from the equation,

$$\Xi = \frac{1}{3H^2}\left[\frac{\mathfrak{M}\uparrow - \mathfrak{M}\uparrow_0}{\mathfrak{M}\uparrow_0} + \frac{\mathfrak{M}\downarrow - \mathfrak{M}\downarrow_0}{\mathfrak{M}\downarrow_0}\right], \tag{19}$$

where $\mathfrak{M}\uparrow$ is the susceptibility in arbitrary units with the applied field up and $\mathfrak{M}\uparrow_0$ is the susceptibility the salt would have if the field were not applied, and similarly for $\mathfrak{M}\downarrow$. The $\mathfrak{M}\uparrow_0$ were obtained by plotting from the normal warm-up curve with no applied field.

In our case the constant magnetic field was supplied by a double-layered solenoid, operating on storage batteries, the magnitude of the fields being 1 to 75 gauss.

VII. EXPERIMENTAL RESULTS

The measured values of Ξ for pure cobalt ammonium sulfate plotted against T^* (see Fig. 8) show that it is indeed a constant in the region of about 0.125 to 0.6°. Its value, as calculated from the average of several dozen points, is 2.43×10^{-6} gauss^{-2}. Above 0.6°K it decreases slightly because of the effect of the lattice. Using the value of 2.43×10^{-6} gauss^{-2} for Ξ and the Curie constant of 0.858, one obtains for CT^2 a value of $42.5\times10^{-4}R$. Assuming exchange and quadrupole effects are negligible, this value of CT^2 is made up of

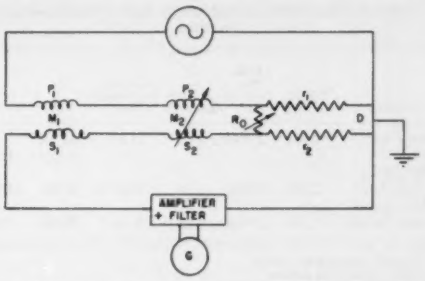

FIG. 7. Bridge circuit for measurement of complex susceptibility.

two contributions, namely, dipole-dipole coupling and hyperfine structure coupling specific heats.

Because of the extreme anisotropy of the crystal, the calculation of the dipole-dipole specific heat with Eq. (3) is not feasible. By the aforementioned dilution procedure, however, one can reduce the dipole-dipole contribution and obtain two equations with two unknowns, A_N and A_{DD}. The values measured on the Zn diluted salt were not so accurate as those for the pure salt, because of the faster warm-up rate, but averaging several dozen points gives a good result. The warm-up rate of the Mg diluted salt was relatively more rapid and consequently the measured Ξ-values had a larger spread, although the constancy of the parameter was evident. The results of the Ξ-measurements are tabulated in Table I, and the resultant curves are shown in Fig. 8. If one defines the Curie point as that temperature at which hysteresis absorption commences, this temperature is $T^*=0.120°$. Note the sudden increase in Ξ due to saturation effects as one reaches the Curie point. From this it would appear that the TT^* relationship is linear ($T=T^*$) in cobalt ammonium sulfate down to about 0.125°K.

In Table I and Fig. 8 are also shown the final T^* temperatures reached on demagnetizing from H/T equal to 13.5 kilogauss/degree. The pure crystal went through a maximum in susceptibility and its decrease below the Curie point indicates that cobalt ammonium sulfate becomes antiferromagnetic. No susceptibility

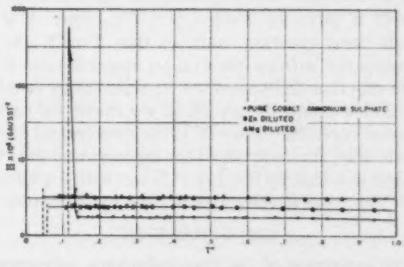

FIG. 8. Ξ as a function of T^*. The vertical dashed lines show T^* final after demagnetizing from same H/T (13.5 kilogauss degree).

TABLE I. Chemical data and specific heat values for single crystals.

Crystal	Weight (grams)	Relative conc. of Co^{++}	$\Xi\times10^8$ (gauss^{-2})	Weight percentage of Co^{++}	A[e]	T_f[e]
Pure CAS[a]	2.461	1.000[d]	2.43	14.91	42.55×10^{-4}	0.117
CAS diluted with ZAS[b]	2.729	0.436	3.76	6.5±0.2	27.45	0.059
CAS diluted with MAS[c]	2.351	0.174	5.01	2.6±0.1	20.61	0.048

[a] Cobalt ammonium sulfate.
[b] Zinc ammonium sulfate.
[c] Magnesium ammonium sulfate.
[d] The theoretical percentage of Co^{++} in CAS is 14.91 percent; the gravimetric sample analysis was 14.9 percent.
[e] $A=CT^2/R$.

maximum was found for the diluted salts but much lower T^* final temperatures were reached because of the decreased dipole-dipole interaction. An indication of the behavior of cobalt ammonium sulfate at very low temperatures is given in Fig. 9, which shows χ' and χ'' plotted against time as a parameter. The heating in this region is due entirely to absorption, because the natural heat leak was negligible in magnitude as compared to that supplied by the ac field. While only a few points are shown on the curves, there are actually many hundred points measured all along the curve. This curve (χ'') is of use in the calculation of absolute T below the Curie point. The curve is actually a composite of about a dozen warm-up curves all of which were readily reproducible.

In Fig. 10 are shown the final results in plotting the values of the specific heat constant in terms of concentration of the Co^{++} ion. The intercept gives the nuclear contribution to the specific heat CT^2/R, and the value of 16.1×10^{-4} is in excellent agreement with the value 16×10^{-4} derived from microwave measurements.[18] The value of A from Ξ is in good agreement with that derivable from the slope of S/R against $1/2T^{*2}$ in the region above $T^*=0.5°$K. A representative selection of demagnetization data are shown in Table II, where H_i is the initial field in kilogauss, T_i is the initial temperature, and T_f^* is the temperature reached upon demagnetization. Remembering that the demagnetization is adiabatic and assuming (a) that the entropy ($H=0$) is given by $S=S_0+\frac{1}{2}(A/T^2)$, where A is the specific heat constant, and (b) that $T=T^*$, one can calculate the entropy removal on magnetization at T_i; some experimental values are represented by points in Fig. 2. The points do not fall on the calculated entropy removal curve, but below it. If the assumptions (a) and (b) are true, then one can fit the experimental data with an equation exactly like Eq. (12) but with a g-factor of 6.55. The curve so calculated is given by the dotted line.

VIII. DISCUSSION

The agreement of the thermodynamic measurement of the nuclear specific heat with that calculable from microwave data is good. The concentration coordinates used in Fig. 10 are the most probable values of the concentration. The chemical analyses of the dilute salts were made polarimetrically and colorimetrically with an accuracy of ±3 percent. This uncertainty of absolute concentration would shift the intercept up or down somewhat, so that the best one can say is that the nuclear specific heat is $(16.1\pm0.3)\times10^{-4}R$.

The absence of a Curie-Weiss constant Δ seems to indicate that exchange is very small, and this is substantiated by microwave data.[20] It can be shown that if the susceptibility follows a Curie-Weiss law instead of a Curie law that the Garrett parameter has the form,

$$\Xi=C/A(1+\chi\Delta/C)^3, \tag{20}$$

where C and A are as previously, χ is the susceptibility, and Δ is the Curie-Weiss constant. From Fig. 8 and Eq. (20) it can be seen that the constancy of Ξ indicates that $\Delta\leq0.005°$K down to about $0.125°T^*$.

The change in slope of both χ' and χ'' in Fig. 9 seems to indicate that one is over a specific heat hump, and it would be of interest to investigate this point. Unfortunately, the magnetic fields available for the experiment at present are not sufficient to pursue the point further.

The crystals were spherical in shape, and no correction for shape in the T^* values have been included. The usual shape demagnetization factors are calculated on the assumption of an isotropic substance with the ions placed at the points of a cubic lattice and are certainly not applicable in the present case of an anisotropic monoclinic lattice.

An interesting point, determinable from Fig. 8, is that the slow decrease of the value of the Ξ-parameter with temperature indicates that the factor B in the lattice specific heat $C_L=BT^3$ is very small or that the spin-lattice relaxation time is no longer short compared with the period of the ac measuring field. Susceptibility measurements at various frequencies would distinguish between the effects.

The diluted salts showed no hysteresis absorption, no maximum in susceptibility, and no saturation effects in the temperature region available with the present magnet. Measurements of the Curie points in the diluted salts may shed some light on the mechanism that produces antiferromagnetism in cobalt ammonium sulfate. It is very astonishing that antiferromagnetisms should occur, since the exchange effects seem to be very small. The Curie-Weiss $\Delta\leq0.005°$ seems to be much too small to be felt at the Curie point temperature of about 0.12°K. One might infer dipole-dipole coupling as a possible mechanism, a process which has achieved considerable success in the theory of ferroelectricity. An alternative is that the Curie point is due to nuclear interaction; but, since this is an internal interaction, it does not seem probable that it can cause large scale cooperative phenomena. Neutron diffraction experiments by Wollan, Strauser and Shull,[24] of the Oak Ridge

[24] Shull, Strauser, and Wollan, Phys. Rev. **83**, 333 (1951).

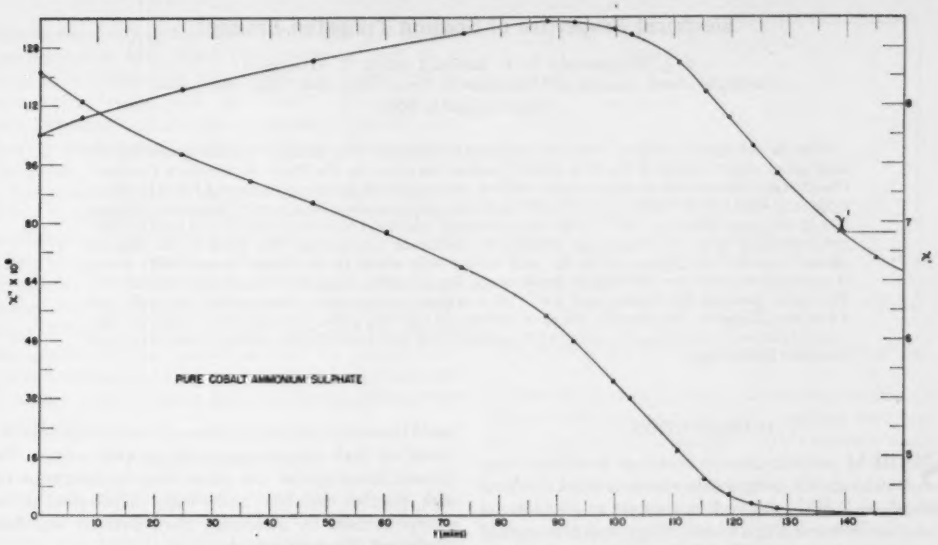

FIG. 9. Real and imaginary components of susceptibility using time as a parameter.

National Laboratory, on even-even isotopes show antiferromagnetism for substances in which there are no nuclear moments, but this does not exclude the possibility of hyperfine structure coupling or quadrupole coupling as a mechanism in cobalt ammonium sulfate.

Assuming the measured nuclear specific heat of $16.1\times10^{-4}R$ to be the true value, this leaves for the pure cobalt ammonium sulfate a dipole-dipole specific heat of $26.4\times10^{-4}R$, which is some 40 percent higher than that calculable from Van Vleck's formula given by Eq. (3) using $\bar{g}^2=18.8$. As pointed out previously, the Stark specific heat is zero.

The experimentally determined g-value along the K_1 axis is 6.55, which is some 5 percent higher than the published values from microwave measurements. This would increase the susceptibility along K_1 by about 10 percent.

It would be very desirable to continue the investigation of cobalt ammonium sulfate single crystals, pure and diluted, since the disparity of the g-factors along the various magnetic axes make the crystals almost ferromagnetic and because information may be obtained on antiferromagnetism-producing phenomena.

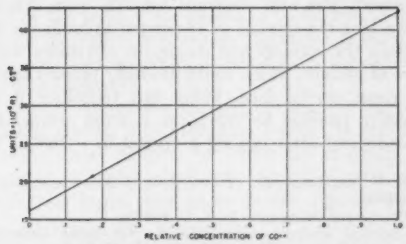

FIG. 10. CT^2 as a function of Co^{++} concentration.

The author is happy to acknowledge the grant of a fellowship from the Oak Ridge Institute of Nuclear Studies to pursue this research. To name those persons who have been of assistance in this problem would be equivalent to giving a roster of personnel at the Oak Ridge National Laboratory, but the author is especially indebted to Dr. L. D. Roberts, Dr. S. Bernstein, and Dr. M. E. Rose for numerous helpful discussions, to Dr. E. O. Wollan and Dr. A. H. Snell for kind use of the facilities of the Physics Division, to Dr. Max Bredig and Mr. B. S. Borie for aid in crystallography, to Mr. P. Thomason for chemical analyses, and to Mr. R. A. Erickson and Mr. J. H. Kahn for assistance with the measurements. It is a deep pleasure to express gratitude to Dr. J. G. Daunt of Ohio State University, consultant to the Laboratory, who suggested the problem and was a constant aid throughout the problem, theoretically and experimentally, and to Dr. K. F. Herzfeld and Dr. F. L. Talbott of Catholic University for numerous discussions and comments.

TABLE II. Entropy calculated from demagnetization data.

H_i (kilogauss)	T_i (°K)	H_i/T_i	T_f*	$\frac{A}{2}\left[\frac{1}{T_f^2}-\frac{1}{T_i^2}\right]$
0.625	1.125	0.55	0.803	0.003
1.25	1.125	1.11	0.345	0.019
1.50	1.125	1.33	0.272	0.027
1.52	0.989	1.53	0.174	0.047
1.68	0.989	1.70	0.148	0.077
12.1	1.005	11.94	0.114	——

Electrical Properties of Sodium Tungsten Bronze*

E. J. HUIBREGTSE,† D. B. BARKER,‡ AND G. C. DANIELSON
Institute for Atomic Research and Department of Physics, Iowa State College, Ames, Iowa
(Received June 4, 1951)

With the addition of sodium atoms the ferroelectric insulator WO_3 acquires metallic properties. We have grown single crystals of Na_xWO_3 using a method developed at the Linde Air Products Company. Chemical analyses for sodium concentration showed $x=0.66$. The electrical resistivity was found to have a value of $(1.9\pm0.2)\times10^{-4}$ ohm-cm at 0°C and to decrease approximately linearly with decreasing temperature in the range 20°C to −160°C. The Hall coefficient was found to have a value of $(-5.1\pm0.2)\times10^{-4}$ cm³/coulomb at 20°C and to decrease slightly with decreasing temperature. This value for the Hall coefficient indicates one electron carrier for each sodium atom added to the crystal. Using Pauli's theory of paramagnetism for free electrons in simple metals the calculated magnetic susceptibility is 0.53×10^{-6}. The value observed by Stubbin and Mellor for a sodium concentration corresponding to $x=0.9$ was 0.45×10^{-6}. Using the free electron theory of metals, the following properties have been calculated: electron mobility and mean free path, energy at the surface of the Fermi distribution, thermal conductivity, and electronic specific heat.

1. INTRODUCTION

SODIUM tungsten bronze is one of a series of nonstoichiometric compounds whose general chemical formula is R_xWO_3, where R represents an alkali metal and x lies between zero and one. Hägg[1] and Straumanis[2] have shown by x-ray diffraction studies that the structure of these compounds is cubic and that the lattice constant increases as x increases. When x is zero, Matthias[3] has shown the crystals to be ferroelectric like $BaTiO_3$, which has a similar crystal structure. Both Hägg and Straumanis have described the remarkable color changes from blue to red to yellow as x increases. However, there has been some uncertainty regarding the nature of the high electrical conductivity. Hägg reported the bronze to be a semiconductor of high conductivity between 20°C and 350°C. Straumanis and Dravnieks[4] reported a different conduction behavior based on their experiments with sintered masses. The present investigation was undertaken to determine the sign, number, mobility, and energy distribution of the charge carriers by measuring the resistivity and Hall coefficient of single crystals.

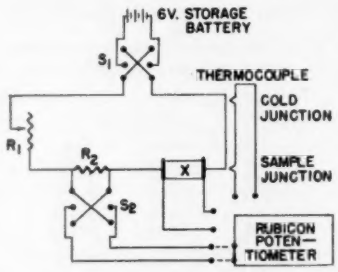

FIG. 1. Experimental arrangement for resistivity measurement.

2. CRYSTAL GROWTH

Crystals of sodium tungsten bronze were prepared according to the chemical reaction:

$$3Na_2WO_4+2WO_3+W\rightarrow6Na_xWO_3.$$

The method was developed at the Linde Air Products Company.[5] Measurements were made on cubes about 2 mm to an edge. Chemical analyses[6] of random samples indicated the percentage of sodium by weight to be 6.18 ± 0.14, from which x was calculated to be 0.664 ± 0.015. Consequently, approximately two-thirds of the sodium sites were occupied.

3. ELECTRICAL CONDUCTIVITY

The resistance of a 2-mm crystal of the bronze is about one milliohm, which makes the comparable resistance of the crystal holder and connecting wires a disturbing factor. After experiencing some trouble in measuring the resistances directly with a Kelvin double bridge, a null direct current potential measurement with a known current flowing through the crystal was employed. The best electrical contacts were obtained by washing the crystals in 48 percent hydrofluoric acid to clean the surfaces and facing the electrodes with a layer of indium, which could be easily pressed against the clean crystal face. Using this technique it was generally possible to reproduce a room temperature measurement after cooling a crystal to −160°C. The

* Contribution No. 147 from the Institute for Atomic Research and Department of Physics, Iowa State College, Ames, Iowa. Work was performed in the Ames Laboratory of the AEC.

† Now at International Business Machines Corporation, Poughkeepsie, New York.

‡ Now at Research Laboratory of Electronics, Massachusetts Institute of Technology, Cambridge, Massachusetts.

[1] G. Z. Hägg, Nature **135**, 874 (1935). The perovskite structure (when $x=1$) was first suggested by W. F. de Jong, Z. Krist. **81**, 314 (1932).

[2] M. E. Straumanis, J. Am. Chem. Soc. **71**, 679 (1949).

[3] B. T. Matthias, Phys. Rev. **76**, 430 (1949).

[4] M. E. Straumanis and A. Dravnieks, J. Am. Chem. Soc. **71**, 683 (1949).

[5] Private communication by E. O. Brimm.

[6] Chemical analyses were made by the Ames Laboratory Analytical Chemistry Group directed by C. V. Banks.

experimental arrangement is shown in Fig. 1. Potential measurements were taken on the crystal and on a standard resistance in series with the crystal in the temperature range 20°C to −160°C. Temperatures were measured with a copper-constantan thermocouple making good thermal contact with one of the crystal electrodes.

The resistivity as a function of temperature is shown in Fig. 2. All crystals exhibited the positive temperature coefficient of resistivity characteristic of thermal scattering in metals. The mean resistivity of these three crystals at 0°C is $(1.9\pm0.2)\times10^{-4}$ ohm-cm. The mean temperature coefficient of resistivity in the temperature range 20°C to −160°C is $(2.1\pm0.4)\times10^{-3}$ per degree centigrade. Principal sources of error are probably (a) contact resistance at the crystal faces and (b) inaccurate dimension measurements owing to irregularities in the crystal shape.

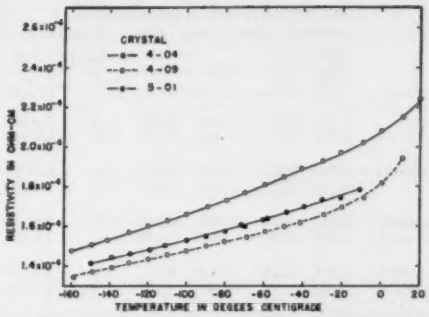

FIG. 2. Resistivity of sodium tungsten bronze ($Na_{0.68}WO_3$).

4. HALL COEFFICIENT

A direct current method, which was initially employed in attempting to determine the Hall coefficient, proved unsuccessful owing to spurious thermal voltages larger than the Hall voltage. In order to eliminate these spurious effects (including the Ettinghausen effect) an alternating current method was used. Similar methods have been described by Smith,[7] by Wood,[8] and most recently by Leverton and Dekker.[9]

A block diagram of the Hall equipment is shown in Fig. 3. A ten-cycle-per-second current of approximately ten amperes was passed through the crystal. The Hall voltage was amplified through a narrow-band amplifier and measured on a Hewlett-Packard type A vacuum-tube volt meter. The sign of the Hall coefficient was determined by use of the electronic switch and oscilloscope. The voltage divider paralleling the standard 0.1-ohm resistor was used to determine the primary current. In practical units the Hall coefficient is given by the equation

$$R_H=10^8V_Hl/IH \text{ cm}^3/\text{coulomb}.$$

The Hall voltage V_H appears in the numerator and the crystal current I in the denominator. By measuring both V_H and I through the amplifier, the gain of the amplifier canceled, eliminating the necessity for an auxiliary determination of this unknown quantity. The value of the resistor was chosen as 0.002 ohm in order that the impedance and voltage conditions at the input of the amplifier would be approximately the same for both measurements.

The Hall voltage was obtained by means of the three probes as shown. Two probes were connected through a low resistance helipot, the center tap of which was connected through the primary winding of a ten-cycle transformer to the third probe on the opposite side of the crystal. After adjusting the center tap for minimum voltage with zero magnetic field, readings were taken with a field of approximately 10,000 oersteds applied successively in opposite directions. The probes were made of 0.010-inch tungsten wire which was sharpened by inserting a heated end into potassium nitrite. The spring tension in the wire held the probes securely against the crystal. For Hall measurements at reduced temperatures a stream of chilled helium gas was passed over the crystal holder assembly.

A Consolidated Model 23–104A electromagnet furnished a stable field for the Hall measurements. The current lead-in wires were brought to the holder through a one-half-inch iron pipe which served as a rigid support for the holder and as a magnetic shield for the wires. The three probe leads were enclosed in a flexible steel conduit to minimize pick-up from stray magnetic fields.

The algebraic sign of the Hall voltage was obtained through the use of the electronic switch and oscilloscope. By comparing the phase relationship between the current and the Hall voltage for metals of known sign

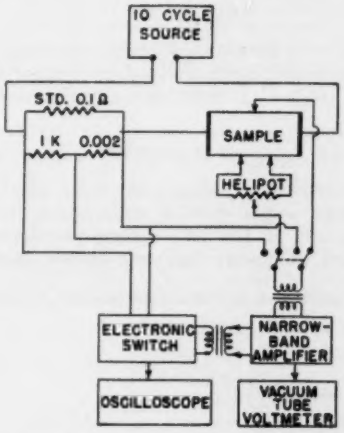

FIG. 3. Block diagram of Hall equipment.

[7] A. Smith, Phys. Rev. **35**, 81 (1912).
[8] L. A. Wood, Phys. Rev. **41**, 231 (1932).
[9] W. F. Leverton and A. J. Dekker, Phys. Rev. **80**, 732 (1950).

TABLE I. Hall coefficient measurements.

Material	Mean Hall voltage (V_HG)*	Current (IGr)*	Field (H) oersteds	Thickness (l) cm	Isenberg correction factor	Hall coefficient (R_H) cm³/coulomb
Copper	0.085	0.13	+9190	0.043	0.90	$-5.9(10^{-5})$
	0.070	0.13	−9190	0.043	0.90	$-4.9(10^{-5})$
Magnesium	0.097	0.12	+9190	0.035	0.89	$-6.0(10^{-5})$
	0.140	0.12	−9190	0.035	0.89	$-8.7(10^{-5})$
$Na_{0.66}WO_3$ (Crystal A)	0.253	0.18	+9800	0.168	0.92	$-4.6(10^{-4})$
	0.273	0.18	−9800	0.168	0.92	$-4.9(10^{-4})$
$Na_{0.66}WO_3$ (Crystal C)	0.357	0.15	+9800	0.12	0.93	$-5.5(10^{-4})$
	0.347	0.15	−9800	0.12	0.93	$-5.3(10^{-4})$

* G is the gain of the amplifier and $r=1.74(10^{-7})$ is the voltage divider ratio.

with the phase relationship for the bronze, the sign was definitely established to be negative. Hence, the charge carriers are predominantly electrons rather than holes.

The Hall coefficients listed in Table I have been corrected for the length to width ratio of the samples as described by Isenberg, Russell, and Greene.[10] The Hall coefficient for copper and magnesium polycrystalline sheet metal were measured to test the sensitivity and reliability of the equipment. Reasonably good agreement was obtained with values taken from the *International Critical Tables*. The average value for the Hall coefficient of these bronze crystals is $(-5.1\pm0.2)\times10^{-4}$ cm³/coulomb. The decrease in the Hall coefficient with decrease in temperature was approximately 0.2 percent per degree Centigrade in the temperature range 25°C to −80°C.

5. ELECTRON AND SODIUM CONCENTRATIONS

In the free-electron theory of metals the Hall coefficient R_H is related to the concentration of charge carriers n by the expression,

$$R_H=\pm1/n|e|,$$

in which $|e|$ is the electronic charge. The positive sign is chosen for hole conduction and the negative sign for electron conduction. Inserting our experimental value for R_H,

$$n=-1/R_H|e|=(1.23\pm0.05)10^{22} \text{ electrons/cm}^3.$$

The concentration of sodium atoms in $Na_{0.66}WO_3$, using a molecular weight of 247.2 grams and a density of 7.169 g/cm³, is $1.16(10^{22})$ sodium atoms per cm³. Therefore, it appears that each sodium atom contributes its one valence electron to the conduction band, which is empty in the insulator WO_3. It seems probable that these compounds exhibit a continuous transition from insulator to normal metal with increasing sodium content. However, we have not been able to verify this continuity of transition for want of single crystals with substantially different sodium content.

6. ELECTRONIC PROPERTIES

Other electronic properties can be calculated from the free-electron theory. The mobility of the electrons at 0°C from the product of the Hall coefficient and electrical conductivity is $\mu=R_H\sigma_E=2.7$ cm²/volt sec. The mean free path at 0°C is $l=h/2e(3n/\pi)^{\frac{1}{3}}\mu=13\times10^{-8}$ cm. The mobility and mean free path are both considerably smaller than these values for most pure metals.

The energy of the electrons at the surface of the Fermi distribution is $E_F=(h^2/2m)(3n/8\pi)^{\frac{2}{3}}=3.1\times10^{-12}$ ergs$=1.9$ ev, where the effective mass m is taken as the electronic mass.

The paramagnetic susceptibility from Pauli's theory for free electrons in simple metals is

$$\chi=(3/2)n\beta^2/E_F=0.53\times10^{-6},$$

in which β is the Bohr magneton. Stubbin and Mellor[11] report an experimental room temperature value for the magnetic susceptibility of $Na_{0.9}WO_3$ as $(0.45\pm0.03)\times10^{-6}$. This agreement lends some reliability to the application of free electron theory to these compounds.[12]

Using the Wiedemann-Franz ratio, the thermal conductivity at 0°C is $2.0(10^{-3})$ watts/cm degree. The electronic contribution to the specific heat is

$$\gamma=N\pi^2k^2T/2E_F=2.2\times10^{-4}RT,$$

where N is Avogadro's number.

The authors appreciate the assistance of W. C. Caldwell, who was largely responsible for the design of the Hall equipment, and R. G. Morris, who helped obtain some of the measurements. For many crystal specimens and for the method of growing these crystals we are indebted to E. O. Brimm and his associates of the Linde Air Products Company.

[10] Isenberg, Russell, and Greene, Rev. Sci. Instr. **19**, 685 (1948).

[11] P. M. Stubben and D. P. Mellor, J. Proc. Roy. Soc. N. S. Wales **82**, 225 (1948).

[12] *Note added in proof:*—The agreement must be considered somewhat fortuitous even for perfectly free electrons, since the orbital diamagnetism of the electrons as well as the exchange and correlation contributions have not been included. See F. Seitz, *Modern Theory of Solids* (McGraw-Hill Book Company, Inc., New York, 1940), p. 599.

Letters to the Editor

PUBLICATION of brief reports of important discoveries in physics may be secured by addressing them to this department. The closing date for this department is five weeks prior to the date of issue. No proof will be sent to the authors. The Board of Editors does not hold itself responsible for the opinions expressed by the correspondents. Communications should not exceed 600 words in length.

Boundary Effects in the Striated Positive Column

RICHARD G. FOWLER
Department of Physics, University of Oklahoma, Norman, Oklahoma
(Received July 26, 1951)

DURING experiments on the luminosity which has been observed in side tubes connected to tubes in which low pressure spark discharges[1] are being studied, a phenomenon relative to glow discharges was noticed to which the author has seen no reference in the literature. Occasionally, owing to switch leakage, weak glow discharges occurred in the main discharge tube prior to the closing of the switch which set off the spark discharge. This glow discharge exhibited striations in hydrogen gas, which changed position gradually as the current of the discharge increased because of increasing potential of the condenser.

At the junction of the main and side tubes, a remarkable property of the striations was observed. Although stable striations could exist on both sides of this junction, no striation ever existed at A, the dotted position in Fig. 1, where the bounding wall is incomplete on one side. Striations were stable on either side of the opening, clinging to the complete walls of the main tube, and even bowing out into the region of instability. But when the vicissitudes of increasing current compelled striation S_1 to move, it moved abruptly and very quickly to position S_2. In all other positions the striations moved slowly and smoothly along the tube.

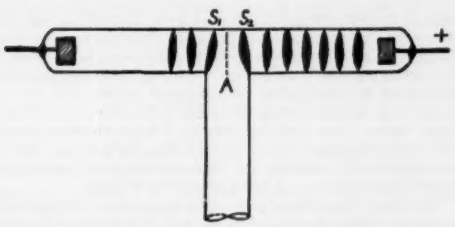

FIG. 1. Branched discharge tube exhibiting a striated glow discharge.

It is suggested that the striations can only exist when completely bounded on their periphery by matter, so that any theory of striations must make use of the concept of boundary conditions.

[1] Fowler, Goldstein, and Clotfelter, Phys. Rev. **82**, 879 (1951).

Beta-Inner Bremsstrahlung Angular Correlation

T. B. NOVEY
Argonne National Laboratory, Chicago, Illinois
(Received August 10, 1951)

DURING an extension of previous measurements[1] of the angular correlation between the 885-kev beta-branch and the 85-kev gamma in Tm^{170}, a strongly interfering effect was observed which has been established as being due to the angular correlation between beta-particles and gamma-radiation emitted during the beta-emission process.

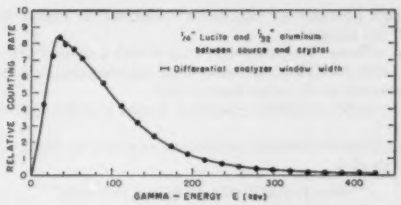
RELATIVE COUNTING RATE
GAMMA – ENERGY E (kev)
1/16" Lucite and 1/32" aluminum between source and crystal
Differential analyzer window width

FIG. 1. P^{32} bremsstrahlung NaI(Tl) scintillation spectrometer differential pulse-height analysis.

The theory of this inner bremsstrahlung has been developed by Knipp and Uhlenbeck[2] for allowed spectra and extended to first- and second-forbidden transitions by Wang Chang and Falkoff.[3] The theories predict gamma-emission predominantly in the direction of electron emission. The theoretical angular distribution is not sensitive to the nature of the interaction process in beta-decay.

In order to eliminate true beta-gamma coincidences, the effect was studied in P^{32}, which emits no monoenergetic gamma-radiation. The source was mounted in a thin film in a 7-inch diameter plastic vacuum chamber to avoid air scattering of the beta-particles. The beta-particles were detected by a stilbene crystal, $\frac{1}{4}$ inch thick$\times 1\frac{1}{4}$-inch diameter, mounted on a 5819 photomultiplier tube. The crystal was in the vacuum, an O-ring seal to the face of the photomultiplier being used as a vacuum seal. A 0.2-mg/cm^2 aluminum foil was placed over the stilbene crystal to increase the collection efficiency of the light pulse and to prevent rapid sublimation of the stilbene.

The beta-detector, source, and vacuum chamber rotated as a unit with respect to the gamma-detector, which consisted of a thallium-activated sodium iodide crystal, $\frac{1}{4}$ inch thick$\times 1\frac{1}{4}$-inch diameter, mounted on a 5819 photomultiplier tube. A gamma pulse-height analysis of the continuous gamma-radiation from a P^{32} source is shown in Fig. 1. The cutoff in the neighborhood of 40 kev is due to absorption of the gamma-radiation in the plastic chamber wall, which is sufficiently thick to absorb all of the beta-particles.

The intensity of the gamma-radiation is low (one gamma of energy greater than 40 kev for several hundred beta-particles). It is thus necessary to use a fairly fast coincidence resolving time in order to obtain a true coincidence rate comparable to the chance coincidence rate and still maintain good angular resolution, i.e., a solid geometry factor of 0.5 percent of 0.06 steradian. By double delay line shaping of the relatively slow rising NaI pulse (*ca* 0.25 μsec) a pulse of 0.08-μsec width was obtained. In spite of a loss of a factor of six in pulse height due to the shaping, a considerable advantage in average pulse height was realized compared with anthracene for gamma-energies below 250 kev, mainly owing to

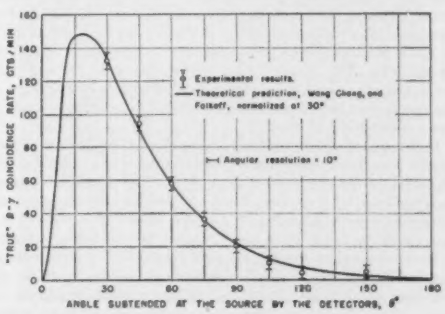
"TRUE" β-γ COINCIDENCE RATE, CTS/MIN
ANGLE SUBTENDED AT THE SOURCE BY THE DETECTORS, θ°
Experimental results.
Theoretical prediction, Wang Chang, and Falkoff, normalized at 30°
Angular resolution = 10°

FIG. 2. P^{32} Beta-inner bremsstrahlung angular correlation.

the high photoelectric absorption coefficient in sodium iodide below this energy.[4]

The stilbene beta-pulses were shaped with a shorted delay line to a width of 0.03 μsec, and an over-all resolving time of 0.11 μsec was obtained in the coincidence circuit.

The angular correlation measured is shown by the open circles in Fig. 2.

The theoretical angular correlation as given by Wang Chang and Falkoff is

$$d\Phi(v,\theta,\omega)/d\Omega = 2\beta^2\sin^2\theta/2\pi\omega(1-\beta\cos\theta)^2,$$

the probability per unit solid angle for an electron with velocity v to emit a quantum of a frequency ω at an angle θ.

This was averaged over an experimental beta-distribution and over the range of detection of the gamma-ray:

$$\frac{d\Phi}{d\Omega} = c\int_0^{E_{\beta\max}}\int_{40\text{ kev}}^{E_\beta}\frac{N(E_\beta)}{E_\gamma}\frac{\beta^2\sin^2\theta}{(1-\beta\cos\theta)^2}E_\gamma dE_\beta$$
$$= c\int_0^{E_{\beta\max}}\ln(E_\beta/40\text{ kev})N(E_\beta)\frac{\beta^2\sin^2\theta}{(1-\beta\cos\theta)^2}dE_\beta,$$

the probability per unit solid angle for a quantum of energy greater than 40 kev to be detected at an angle θ.

The result of numerical integration of the above expression was normalized to the experimental result at 30°. It can be seen that the data are in excellent agreement with the theory.

A recent article[5] on the intensity and energy distribution of inner-bremsstrahlung mentioned a preliminary experimental affirmation of the angular correlation as found in this work.

[1] T. B. Novey, Phys. Rev. **78**, 66 (1950).
[2] J. K. Knipp and G. E. Uhlenbeck, Physica **3**, 425 (1936). See also F. Bloch, Phys. Rev. **50**, 272 (1936).
[3] C. S. Wang Chang and D. L. Falkoff, Phys. Rev. **76**, 365 (1949).
[4] Details of this pulse shaping have been submitted for publication to the *Review of Scientific Instruments*.
[5] L. Madansky and F. Rasetti, Phys. Rev. **83**, 187 (1951).

On the Interaction in Pb of the Secondaries Produced in Penetrating Showers*

G. M. Branch and G. Cocconi
Cornell University, Ithaca, New York
(Received July 23, 1951)

DURING the months from August, 1949, to January, 1950, the cloud-chamber assembly sketched in Fig. 1 was operated at Echo Lake, Colorado (altitude 3260 m, average pressure 706 g cm^{-2}), in order to measure the collision mean free path (m.f.p.) in Pb of the secondary particles produced in penetrating showers and to investigate the nature of the penetrating particles in extensive air showers.

Here we give the results of the first experiment. The two chambers, 24 in.×12 in.×12 in., were filled with argon at about atmospheric pressure, and each contained five ½-inch Pb plates; they were located one above the other and separated by a slab of Pb 6 in. thick. Stereoscopic pictures were taken with a single camera on 70-mm film. The master pulse triggering the expansions was generated whenever a coincidence $2A+3B$ among two or more of the counters of tray A and three or more of the counters of tray B was registered.

In the analysis of the pictures obtained, only the cases were considered in which a penetrating shower was generated either in the plates inside the upper chamber or in the 6-in. absorber between the chambers, showed in the lower chamber penetrating particles recognizable as coming from a common center, and was not accompanied by dense air showers. Among the particles belonging to the showers thus selected, the ones considered for the measurement of the collision mean free path were required to fulfill the following conditions: (a) to be minimum ionizing and to be scattered less than 1° in crossing any plate (except for cases judged to be nuclear scatterings, when the particles were deflected less

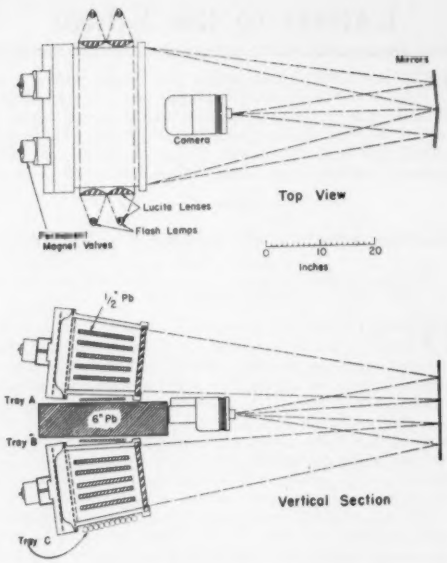

FIG. 1. Diagram of dual cloud-chamber assembly.

than 1° in every plate but one, and more than 10° in that one plate) and (b) to cross at least the middle three plates of the lower chamber in the case of non-interacting particles. In the case of interacting particles the direction of the particle in the space was determined by reprojection on translucent screens, and was required to be such as to cross the middle three plates in the illuminated region. Since particles ionizing 2 times minimum would have been recognized, and since scattering angles larger than 1° were measurable, condition (a) ruled out particles of momentum smaller than $\sim Mc$ or ~ 2 Bev/c, whichever is larger.

The observed number of plate traversals without interaction by particles fulfilling the conditions (a) and (b) was $N=1977$, while the number of interactions observed was $\Delta N_0=91$. If the condition (b) is modified so as to consider the traversals and interactions in one plate only if the particle is observed to traverse at least the preceding plate,[1] the total number of such traversals without interaction is $N=2568$, and the number of observed interactions $\Delta N_0=111$. The observed collision m.f.p. Λ is then

$$\Lambda = h/\ln(1+\Delta N_0/N) = \begin{cases}354\pm39\text{ g cm}^{-2}\text{ of Pb},\\ 376\pm40\text{ g cm}^{-2}\text{ of Pb},\end{cases}$$

where $h=15.9$ g cm^{-2} is the thickness of the Pb plates averaged over the zenith distribution of the particles. The errors given are the statistical ones. The two values practically coincide.

Λ is certainly larger than the real collision m.f.p., λ, because an appreciable number of interactions occurring inside the plates do not give rise to secondaries of energy sufficient to escape from the plates and be seen.

The correction can be evaluated with the aid of Fig. 2, where is plotted the number of interactions observed to start at various depths inside the plates.[2] The point where the interaction occurred inside the plates was identified with the common point of origin of the secondary tracks. From Fig. 2 it clearly appears that many of the interactions occurring inside the plates were lost. An examination of the particles emitted shows that the ratio of the number of heavy prongs to that of light prongs sharply decreases when the interaction occurs more deeply inside the plate; this indicates that the less energetic interactions are more likely

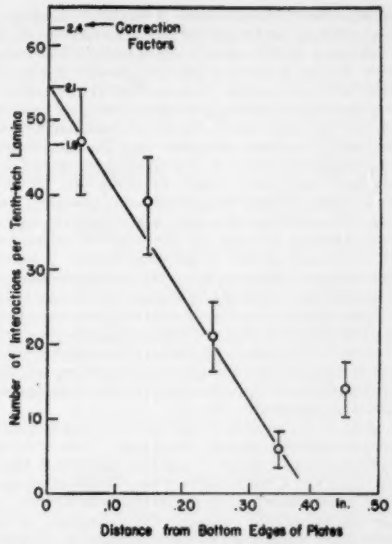

FIG. 2. Distribution of observed nuclear interactions in the lead plates.

to be lost. The factor K by which it is necessary to multiply ΔN_0 in order to obtain the real number of interactions, ΔN, in our case turns out to be $K=2.1\pm0.3$. The uncertainty in K arises from both the statistical errors and the extrapolation. With this correction we deduce λ to be

$$\lambda=172\pm29 \text{ g cm}^{-2} \text{ of Pb},$$

a value quite close to the geometric m.f.p.

The value of K is expected to decrease strongly when the thickness of the absorber is decreased. With plates of ¼-in. Pb one can anticipate a value $K=\sim1.1$. In fact, Gregory and Tinlot[3] with plates of ¼-in. Pb found $\Lambda=172\pm20$ g cm^{-2}.

In the past years several authors (see bibliography in the paper of Gregory and Tinlot) obtained much higher values for λ in Pb; probably the reason for the discrepancy with the present determination is due to the fact that generally they used thick absorbers inside the chambers and did not select energetic secondaries, hence making the number of missed interactions too high to permit accurate correction. The same conclusion was reached by Lovati *et al.*,[4] who found a value $\Lambda=200\pm50$ g cm^{-2} Pb using plates 0.5 mm thick.

* This work was supported in part by a grant from the Research Corporation.

[1] This prevents consideration of interactions and traversals in the top plate of the lower chamber, but makes the discrimination against electrons and low energy particles more effective than if all single traversals and interactions were counted.

[2] W. W. Brown and A. S. McKay, Phys. Rev. **77**, 342 (1950).

[3] B. P. Gregory and J. H. Tinlot, Phys. Rev. **81**, 675 (1951).

[4] Lovati, Mura, Succi, and Tagliaferri, Nuovo cimento **8**, 271 (1951).

A Dual Cloud-Chamber Study of Extensive Air Showers*

G. M. BRANCH
Cornell University, Ithaca, New York
(Received July 23, 1951)

DURING the fall of 1949 the dual cloud-chamber assembly described in the preceding letter was operated at Echo Lake, Colorado, to obtain photographs of penetrating particles in extensive air showers. The counter tray A, indicated in Fig. 1 of the previous letter,[1] was removed; and two unshielded trays, X and Y, each of about 500-cm² area, were placed at distances of about two meters from the cloud-chamber assembly. About 400

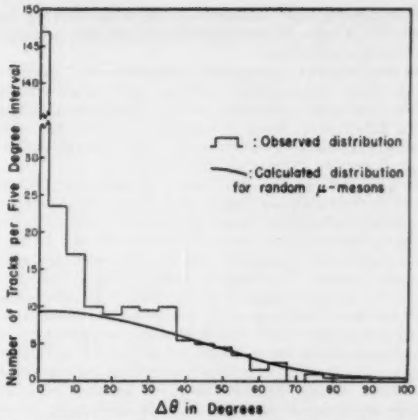
: Observed distribution
: Calculated distribution for random μ-mesons
Number of Tracks per Five Degree Interval
Δθ in Degrees

FIG. 1. Distribution of deviations, $\Delta\Theta$, between the projected zenith angles of penetrating particles and their respective extensive air shower axes. Note that the ordinate scale has been broken to show the relatively high peak at small deviations.

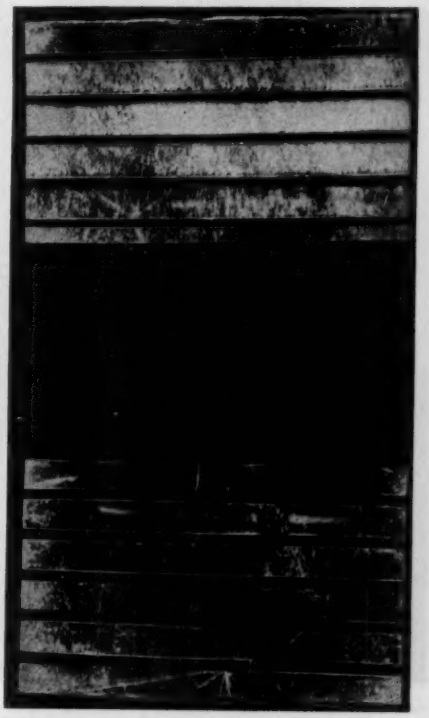

FIG. 2. An extensive air shower containing a coherent particle generating the nuclear cascade beginning in the fifth plate of the upper chamber.

good photographs were obtained with the simple fourfold coincidence $(X+Y+B+C)$, for which only one counter was required to be struck in each tray.

The cloud-chamber photographs demonstrate the occurrence of strongly interacting nucleonic particles in air showers and thus provide qualitative verification of the interpretation of recent counter experiments. These photographs also show that nuclear cascades contributing to the electronic cascade development exist within air showers at mountain altitudes.

The projected angular distribution of penetrating particles relative to their corresponding air shower axes was measured in 173 selected photographs showing air showers of sufficient electron density to indicate the inclination of the shower axis within one degree and showing one or more counter-age penetrating tracks in the lower chamber. The result is shown in Fig. 1. The smooth curve is the calculated shape of the distribution of random mesons which has been fitted to the data at large angles where few penetrating particles associated with air showers are expected to occur. This analysis shows that at angles of less than 10° in projection 92 percent of the observed penetrating particles are coherent with air showers. About three-fourths of the coherent penetrating particles are deviated less than 3° from the shower axis; i.e., they are scattered less than 3° in the air and lead above the lower chamber and hence have momenta greater than 2 Bev/c.

An approximate analysis of the observed flux of charged penetrating particles into a strongly interacting component (protons and pi-mesons) and a weakly interacting component (mu-mesons) can be made from the relative numbers of traversals and nuclear interactions observed in the plates of the lower chamber. (The numerous electron tracks prevent similar consideration of the upper chamber.) In 134 selected photographs, 155±5 coherent externally incident penetrating particles (parallel to the shower axis within 10°) were observed to make 606±20 traversals of lead plates in the lower chamber, producing three local penetrating showers and two local mixed showers. A background of 15±5 random mesons has been subtracted from the total number of penetrating particles observed; the expected number of chance interactions is negligible (<0.01). Assuming that the N-component of energy sufficient to produce local penetrating showers has a geometric collision mean free path in lead, the number of traversals expected to yield the five observed interactions is 53±24, or 8.6±3.8 percent of the total number of traversals. Taking into account the absorption of the N-component in traversing the apparatus to reach the lower chamber by using the interactions mean free path for single energetic N-component particles measured by Walker, Walker, and Greisen,[3] one estimates the fraction of energetic N-component in the flux of air shower penetrating particles incident on the apparatus to be 26±10 percent. Similar results were deduced in shielded counter studies of the penetrating particles in air showers.[3-5]

Examples of photographs of air showers containing strongly interacting particles are given in Figs. 2 and 3. Many of the photographs showed large numbers of energetic electrons in the lower chamber, as in Fig. 3, which could not have developed through the 29 radiation lengths of lead in the intermediate layer by means of pure electromagnetic cascades. The observation of locally generated mixed showers in air showers incident on the apparatus suggests that similar processes occur in the air also.

FIG. 3. Large numbers of electrons and slow heavy particles emerge from each of the lead plates in the lower chamber along the axis of this mixed shower. The primary of this local mixed shower traveled parallel to the energetic electrons in the air shower and passed through the upper chamber.

* This work was supported in part by a grant from the Research Corporation.

[1] G. M. Branch and G. Cocconi, Phys. Rev. **84**, 146 (1951).
[3] Walker, Walker, and Greisen, Phys. Rev. **80**, 546 (1950). This measurement gives the appropriate mean free path for the present application, since here as well as in their experiment the detected particles were required to emerge from the absorber singly. Coherent groups of penetrating particles diverging from some point of generation in the absorber were not considered.
[3] K. Sitte, Phys. Rev. **78**, 721 (1950).
[4] Greisen, Walker, and Walker, Phys. Rev. **80**, 535 (1950).
[5] C. B. A. McCusker, Proc. Roy. Soc. (London) **A63**, 1240 (1950).

Diffuse X-Ray Scattering by Disordered Binary Alloys. II

WILLIAM J. TAYLOR
Department of Chemistry, Ohio State University, Columbus, Ohio
(Received August 6, 1951)

THE analysis of diffuse x-ray scattering in disordered binary alloys presented recently[1] may be extended as follows. Let k, L denote the kth site in the Lth unit cell, and denote by $[kk', M]$ the set of site-pairs, k, L and k', $L-M$, where M remains fixed, while L assumes all possible values (L and M represent number triples). The sets $[kk', M]$ and $[k'k, -M]$ are identical, since the ordering of the pairs is immaterial. The two types of atoms will be denoted by A and B, while X will be used to represent either an A or a B atom. The atom symbol will be primed if the atom is at the k'th site, unprimed if at the kth site. Let $w_{XX'}{}^{M}$ be the fraction of site-pairs in the set $[kk', M]$ for which the kth site is occupied by X and the k'th site by X'. There are four such parameters, $w_{AA'}{}^{M}$, $w_{AB'}{}^{M}$, etc., and their sum is, of course, unity. It is evident that these parameters satisfy the additional identities,

$$w_{XA'}{}^{M}+w_{XB'}{}^{M}=x_X{}^{k}, \quad w_{AX'}{}^{M}+w_{BX'}{}^{M}=x_{X'}{}^{k'}, \tag{1}$$

where $x_X{}^{k}$ is the fraction of all sites of the kth type (kth sublattice) which are occupied by atoms of type X ($X=A$ or B), and similarly for $x_{X'}{}^{k'}$. In the present discussion, we regard the $x_X{}^{k}$ as known, either from measurements of long-range order, or from the stoichiometry of the crystal, in the absence of long-range order. Of the four relations, Eqs. (1), three are independent, so that one additional independent relation is required to determine the four

parameters, $w_{XX'}{}^{M}$. If $k=k'$, then, as can be shown from Eqs. (1), $w_{AB}{}^{M}=w_{BA}{}^{M}$, so that there are only three distinct parameters. However, Eqs. (1) then reduce to two independent relations, so that an additional relation is still required.

It follows from Eqs. (6) and (8) of reference 1 that the fourier coefficients of the diffuse scattering (in reciprocal space) may be put in the form

$$\alpha_{kk'}{}^{M}=2(z_{kk'}{}^{M}-z_{kk'}{}^{\infty}), \tag{2}$$

where $z_{kk'}{}^{M}$ was defined as

$$z_{kk'}{}^{M}=w_{AA'}{}^{M}+w_{BB'}{}^{M}. \tag{3}$$

Also (see the following paragraph), we have

$$z_{kk'}{}^{\infty}=x_A{}^{k}x_{A'}{}^{k'}+x_B{}^{k}x_{B'}{}^{k'}, \tag{4}$$

where $z_{kk'}{}^{\infty}$ is the limiting value of $z_{kk'}{}^{M}$ as the "magnitude" of M increases indefinitely. Equations (2), (3), and (4), together with the value of $\alpha_{kk'}{}^{M}$ calculated from diffuse scattering data, provide the additional relation required for the individual determination of the four parameters, $w_{XX'}{}^{M}$ (three, for $k=k'$).

We now define the conditional probability $p_{XX'}{}^{M}$ as the probability that the k', $L-M$ site is occupied by X' if the k, L site is occupied by X. Since the probability of the latter event is $x_X{}^{k}$, it is obvious that

$$w_{XX'}{}^{M}=x_X{}^{k}p_{XX'}{}^{M}. \tag{5}$$

The four probabilities $p_{XX'}{}^{M}$ may therefore be calculated if the $w_{XX'}{}^{M}$ are known. It may be seen, either directly, or from Eqs. (1) and (5), that $p_{XA'}{}^{M}+p_{XB'}{}^{M}=1$. We also note that $p_{XX'}{}^{\infty}=x_{X'}{}^{k'}$, which, with Eqs. (3) and (5), justifies Eq. (4).

It has been remarked that the sets $[kk', M]$ and $[k'k, -M]$ are identical, and therefore, $w_{XX'}{}^{M}=w_{X'X}{}^{-M}$. However, if $k\neq k'$, the set of probabilities, $p_{X'X}{}^{-M}$, that the k, L site be occupied by X if the k', $L-M$ site is occupied by X', is, in general, distinct from the set of probabilities, $p_{XX'}{}^{M}$, defined in the predeeding paragraph. For a general set, $[kk', M]$, there are, therefore, four additional probabilities, which may be obtained from the relations,

$$w_{XX'}{}^{M}=x_{X'}{}^{k'}p_{X'X}{}^{-M}. \tag{6}$$

If $k=k'$, Eqs. (5) and (6), and the relation $w_{AB}{}^{M}=w_{BA}{}^{M}$, yield $p_{AA}{}^{M}=p_{AA}{}^{-M}$, $p_{AB}{}^{M}=p_{AB}{}^{-M}$, etc., so that there are only four distinct probabilities in this case. In the absence of long-range order, all sites will usually be equivalent, and the simplification $k=k'$ will be applicable. However, $p_{AB}{}^{M}=p_{BA}{}^{M}$, only if $x_A{}^{k}=x_B{}^{k}=\frac{1}{2}$.

The preceding analysis is sufficient to establish the equivalence of the treatment given in reference 1 and the formulation of Cowley,[2] for the special case which he considers (absence of long-range order). Cowley's parameter α_{lmn} is equivalent to $(\alpha_{11}{}^{M}/\alpha_{11}{}^{0})$, or $\alpha_{11}{}^{M}/4x_Ax_B$, in the present notation (here $k=k'=1$). The writer regrets that in his original article it was implied that Cowley's treatment was not entirely correct.

[1] W. J. Taylor, Phys. Rev. **82**, 279 (1951).
[2] J. M. Cowley, J. Appl. Phys. **21**, 24 (1950).

High Energy Nuclear Photoeffect in Carbon

D. WALKER*
Newman Laboratory of Nuclear Studies, Cornell University, Ithaca, New York
(Received March 15, 1951)

A PREVIOUS letter[1] (referred to as I) described an investigation of the high energy protons emitted by a carbon target under bombardment by bremsstrahlung from an electron synchrotron operated at (195±5) Mev. The method used for investigating the energy distribution of the protons has since been described in more detail.[2] In I an approximate method was used to measure the bremsstrahlung beam intensity. Subsequently, J. W. DeWire and J. C. Keck compared the bremsstrahlung intensities as measured by that method and by counting electron pairs ejected from a gold foil. These measurements showed that the values marked on the cross-section scale in I should be divided by 1.44. The scale values are then correct within the limits of ±40 percent instead of the factor of 3 given in I.

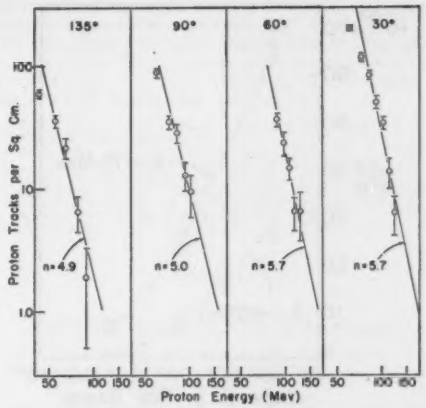

FIG. 1. Integral proton spectra. The normalized number (N) of protons with an energy exceeding E, plotted against E. Lines of the form $N=N_0E^{-n}$ are not fitted mathematically to the spectra but serve to illustrate the rate of fall-off of N with increasing E. Errors are statistical probable errors. Angles are laboratory angles.

It is of interest to compute the total nuclear cross section for the production of high energy protons. (For consistency in the figures we use the same scales as in I.) Figure 1 shows the relative integral proton spectra at 135°, 90°, 60°, and 30° to the bremsstrahlung beam, corrected for the loss of proton tracks in the earlier photographic plates of the stacks due to the fact that Ilford C2 plates record only protons with residual energies less than about 50 Mev. No statistically significant numbers of protons were observed at energies 10 Mev higher than the highest energy points plotted. The experiment does not yield information about the proton spectra at lower energies down to a few Mev, although there were indications that the integral spectra at lower energies could be represented by an n much less than 5. (The experimental conditions ruled out the confusion of protons with other high energy particles from the target, except for the possible presence of deuterons or tritons. There appears to be no reason, however, why deuterons or tritons could account for more than a small fraction of the observed tracks. Moreover, near the upper energy limit of the recorded proton spectrum, the range-energy relations discriminate against deuterons or tritons.) Figure 2 shows the differential cross section per steradian $(d\sigma/d\Omega)$ plotted as a function of the angle of emission (θ) for protons with energies (E) greater than 70 Mev and greater than 90 Mev. These cross sections are computed directly from the corresponding points in Fig. 1. Total nuclear cross sections (σ) are obtained by graphical evaluation of $\sigma=(1/1.44)\int_0^{\pi}2\pi\sin\theta(d\sigma/d\Omega)d\theta$. It is assumed that $d\sigma/d\Omega$ does not diverge strongly for $\theta<30°$ or $\theta>135°$. For $E>70$ Mev, we obtain $\sigma=(2.3\pm1.6)\times10^{-28}$ cm² per unit Q, and for $E>90$ Mev, $\sigma=(9\pm6)\times10^{-29}$ cm² per unit Q. The errors given for σ are estimated maximum possible errors.

As implied in I, the strong forward bias in the angular distribution of the high energy protons requires, because of momentum considerations, that only a small subgroup of nucleons be involved in the primary interaction with a high energy photon. Levinger[3] has pointed out that the results are in qualitative agreement with a two-nucleon ("quasi-deuteron") model for the interaction. From the point of view of momentum, the results could also be consistent with a sub-group as large as an α-particle. (Tamor[4] has used an α-particle model in discussing the emission of high energy protons by nuclei which have captured negative π-mesons.) The

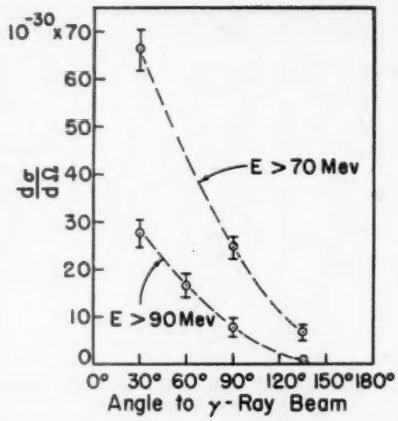

FIG. 2. Differential nuclear cross section of carbon for the production of high energy protons plotted against the angle of proton emission. The differential cross section is expressed as cm² per steradian per unit Q. Errors are probable errors.

cross section is too large to admit Compton recoil protons as a main effect, while, in addition, the high energy protons at large angles would not be produced by the Compton effect.

A synchrotron energy near 200 Mev is advantageous for studying the high energy photoeffect. It is about as high an energy as can be used while avoiding possible complications due to appreciable photomeson production.[5]

* Now at Birmingham University, England.
[1] D. Walker, Phys. Rev. **81**, 634 (1951). In this previous letter, on line 7 of paragraph 3, "less than" should be changed to "exceeding."
[2] D. Walker, Rev. Sci. Instr. **22**, 607 (1951).
[3] J. Levinger, Phys. Rev. **82**, 300 (1951).
[4] S. Tamor, Phys. Rev. **77**, 412 (1950).
[5] McMillan, Peterson, and White, Science **110**, 579 (1949).

Radiative Corrections to the Intensities for Hydrogenlike Atoms

T. TATI
Tokyo Bunrika Daigaku, Tokyo, Japan
(Received August 14, 1951)

THE radiative corrections to the transition probabilities for the transitions of excited hydrogenlike atoms with single photon emission are calculated, in nonrelativistic approximation.

The hamiltonian, which has been studied by Pauli and Fierz,[1] is used, and it is

$$H=(\mathbf{p}^2/2m)+V(\mathbf{q}-i\lambda\Sigma_K(k^3V)^{-\frac{1}{2}}\mathbf{e}_K(a_K-a_K^+))+\Sigma_K a_K^+ a_K\hbar ck, \quad (1)$$

where $\mathbf{p}$ and $\mathbf{q}$ are the momentum and coordinate of the electron, $V(\mathbf{q})$ is the electrostatic potential energy, a_K and a_K^+ are destruction and creation operators for a light quantum with wave number K, $\mathbf{e}_K$ is a unit vector in the direction of polarization, m is the observed mass of the electron, and

$$\lambda=[(2\pi\hbar/mc)(e^2/mc^2)]^{\frac{1}{2}}.$$

We expand the second term of Eq. (1) and obtain[2]

$$\begin{aligned}V(\mathbf{q})&-i\lambda\Sigma_K(k^3V)^{-\frac{1}{2}}(a_K-a_K^+)\ \mathrm{grad}_K V(\mathbf{q})\\&-\tfrac{1}{2}\lambda^2\{\Sigma_K(k^3V)^{-\frac{1}{2}}(a_K-a_K^+)\ \mathrm{grad}_K\}^2V(\mathbf{q})\\&+i\tfrac{1}{6}\lambda^3\{\Sigma_K(k^3V)^{-\frac{1}{2}}(a_K-a_K^+)\ \mathrm{grad}_K\}^3V(\mathbf{q})+\cdots, \quad (2)\end{aligned}$$

where $\mathrm{grad}_K=\mathbf{e}_K\cdot\mathrm{grad}$.

The fourth term of expansion (2) gives the main contribution to the transition which we now consider. Other terms contribute to cancel the infrared divergence. We rearrange the operators a_K and a_K^+ in the fourth terms of Eq. (2), using the commutation relations $[a_K, a_L^+]=\delta_{KL}$, and choose the following single-photon emission terms:

$$\begin{aligned}&\tfrac{1}{6}i\lambda^3\sum_{KLM}\frac{1}{V^{\frac{1}{2}}k^{\frac{3}{2}}p_M^3}(\mathrm{grad}_K\,\mathrm{grad}_L\,\mathrm{grad}_M)\\&\qquad\times V(\mathbf{q})(a_K^+\delta_{LM}+a_L^+\delta_{MK}+a_M^+\delta_{KL})\\&\qquad=\tfrac{1}{2}i\sum_L\frac{1}{Vp}(\mathrm{grad}_L)^2\sum_K\frac{1}{(k^3V)^{\frac{1}{2}}}\mathrm{grad}_K V(\mathbf{q})a_K^+\\&\qquad=i\frac{2}{3(2\pi)^2}\lambda^3B\Delta\sum_K\left(\frac{1}{k^3V}\right)^{\frac{1}{2}}\mathrm{grad}_K V(\mathbf{q})a_K^+, \quad (3)\end{aligned}$$

where B is the Bethe term, $\int_{k_0}^{K}dl/l=\log(mc^2/\hbar ck_0)$. We replace the $\Delta V(\mathbf{q})$ by the charge density of nucleus $\rho(\mathbf{q})$; then Eq. (3) becomes as follows:

$$i(2/3\pi)e\lambda^3B\Sigma_K(k^3V)^{-\frac{1}{2}}\mathrm{grad}_K\rho(\mathbf{q})a_K^+. \quad (4)$$

The transition probabilities per unit time for the transitions of hydrogenlike atoms from the excited state ψ_A to the lower state ψ_B, caused by the interaction term (4), are

$$\gamma=\frac{2}{9}\frac{1}{\pi^4}\lambda^6B^2\frac{e^2}{\hbar^2c}\frac{1}{k}\int|\{\mathrm{grad}_K\rho(\mathbf{q})\}_{AB}|^2d\Omega \quad (5)$$

where $\{\mathrm{grad}_K\rho(\mathbf{q})\}_{AB}=\int\bar{\psi}_A(\mathbf{q})(\mathrm{grad}_K\rho(\mathbf{q}))\psi_B(\mathbf{q})d\mathbf{q}$. The quantity γ is proportional to the inverse of k. The smaller the energy difference between two levels of the atom, the greater is the transition probability between the levels with one-photon emission due to the radiative correction.

The value of γ depends on the size and shape of the charge distribution $\rho(\mathbf{q})$. If the charge has uniform spherical distribution of radius R, then we have

$$\begin{aligned}&\rho=\rho(r)=\rho_0=3e/4\pi R^3\quad\text{for}\quad r<R,\quad \rho=0\quad\text{for}\quad r>R,\\&\qquad\mathrm{grad}_K\rho=\rho_0\delta(r-R)\cos\theta,\\&\{\mathrm{grad}_K\rho\}_{AB}=\int\rho_0\bar{\psi}_A(R,\theta,\varphi)\cos\theta\psi_B(R,\theta,\varphi)R^2d\Omega\\&\qquad=(3e/4\pi)\int R^{-1}\bar{\psi}_A(R,\theta,\varphi)\cos\theta\psi_B(R,\theta,\varphi)d\Omega,\end{aligned}$$

and γ is given by

$$\gamma=\frac{1}{2\pi^5}\frac{e^4}{\hbar^3c^2}\lambda^6B^2\frac{c}{k}\left|\int\frac{1}{R}\bar{\psi}_A(R,\theta,\varphi)\cos\theta\psi_B(R,\theta,\varphi)d\Omega\right|^2. \quad (6)$$

Breit and Teller[3] calculated the probability for the $2s\to1s$ transition of hydrogen with the emission of two photons and obtained 1/7 sec for the mean life of the $2s$ state. The $2s_{\frac{1}{2}}$ state of hydrogen is raised by the radiative reaction and is 0.03 cm^{-1} higher than the $2p_{\frac{1}{2}}$ state.[4] For the probability of the $2s_{\frac{1}{2}}\to2p_{\frac{1}{2}}$ transition caused by the radiative reaction, Eq. (6) gives the value 2×10^4 sec^{-1}. Here we assume $B=10$, and R is much smaller than the Bohr radius.

[1] W. Pauli and M. Fierz, Nuovo cimento **15**, 167 (1938).
[2] This method in the nonrelativistic radiation theory is discussed in detail by T. A. Welton, Phys. Rev. **74**, 1157 (1948). This method was also stated by the author at a seminar in theoretical physics of Tokyo Bunrika Daigaku, May, 1947.
[3] G. Breit and E. Teller, Astrophys. J. **91**, 215 (1940).
[4] W. E. Lamb and R. C. Retherford, Phys. Rev. **72**, 241 (1947).

Mixed Invariants in Beta-Decay and Symmetries Imposed on the Interaction Hamiltonian

H. A. TOLHOEK AND S. R. DE GROOT
Institute for Theoretical Physics, The University, Utrecht, Netherlands
(Received June 21, 1951)

THE interaction hamiltonian, which is used in the theory of beta-radioactivity, can be a linear combination of the scalar (1), vector (2), tensor (3), axial vector (4), and pseudoscalar (5) interactions. If we put

$$V_k=(\psi^*\,{}^k\Omega_L\varphi)Q\,{}^k\Omega_N\quad(k=1,\cdots,5), \quad (1)$$

then $V_k+V_k^+$ give the usual five operators for the β-interaction. We have previously taken as interaction hamiltonian a linear combination[1]

$$V=G\sum_{k=1}^{5} C_k(V_k+V_k^+), \tag{2}$$

in which the constants C_k must be real in order that V be hermitian.[2,3] Trigg and Feenberg[4] have given the generalization to the (hermitian) linear combinations using complex constants C_k

$$V=G\sum_{k=1}^{5} (C_kV_k+C_k^*V_k^+). \tag{3}$$

Using the conventional transformations of the wave functions in the Dirac equation,[5] it is easily verified that the interactions according to Eqs. (2) and (3) are invariant for (continuous) lorentz transformations, reflection of space, and reversal of time.

We now give two types of symmetries that can be imposed on the interaction.

I. First condition of symmetry.—The interaction energy must be invariant, if we transform all four particles to the anti-particles. (This is done by taking charge-conjugated solutions.[3]) In this way a transformed interaction

$$V'=G\sum_{k=1}^{5} (C_k^*V_k+C_kV_k^+), \tag{4}$$

is obtained from Eq. (3). Biedenharn and Rose have obtained this result by employing Wigner's time-reversal operator, a procedure equivalent to the use of charge conjugation here. In order that Eqs. (3) and (4) have the same meaning, the coefficients C_k must be real, so that Eq. (3) reduces to Eq. (2). This is especially clear if we consider the lower sign expressions (5) occurring in the formulas, taking the polarization into account (see below). These expressions would change their sign, when taking everywhere the "anti-particles."[6]

II. Second condition of symmetry.—We give two alternative formulations *a* and *b* of a second condition of symmetry, proposed earlier. (a) The processes of negatron and positron emission must be symmetrical in such a way that if coulomb interaction is neglected, the expressions for the interaction energy H_β^- and H_β^+ are equal (possibly with the exception of a phase factor $e^{i\delta}$) if the following conditions are satisfied: the wave functions of the emitted (positive and negative) electrons and neutrinos must be physically equivalent, and $\psi_f(p)$ and $\psi_i(n)$ for negatron emission must be respectively the same as $\psi_f(n)$ and $\psi_i(p)$ for positron emission (i initial; f final; n neutron; p proton). (b) The interaction energy must be invariant (or differ only by a phase factor $e^{i\delta}$), when we take positions as real particles, negatrons as holes, and perform a corresponding change for the neutrinos, but not for the nucleons (see formulas (65), (70), and (75) of reference 1).

The consequences of symmetry principle *II* are as follows:

1. Using (2), we have either combinations of S, A, and P only, or combinations of V and T only.
2. Using (3), one obtains,[4] with $\epsilon_1=\epsilon_4=\epsilon_5=-1$, and $\epsilon_2=\epsilon_3=1$,

$$C_kC_l^*\pm C_kC_l^*=0, \quad \text{if} \quad \epsilon_k\epsilon_l=\mp 1 \quad (k,l=1,\cdots,5). \tag{5}$$

We have also calculated the transition probabilities for β-emission taking into account the orientation of the nucleus, the polarization of the emitted electron, and the $e-\nu$ angular correlation (for allowed transitions).[7] We then get cross terms that differ in sign for β^+ and β^- emission, with coefficients (5), but for $k,l=1,2,3,4$ only. The pseudoscalar ($k=5$) gives no cross terms with the other invariants for allowed transitions, as the selection rule for the parity of its matrix element is different from that for the other invariants.

If we now compare these results with the consequences (5) of the symmetry principle, we come to the following conclusion: the condition, that the transition probability for allowed transitions (taking the polarization of the electron into account) has no terms that differ in sign for β^+ and β^- emission, is already equivalent to the symmetry principle *II* (except for a possible admixture of the pseudoscalar interaction).

(We may remark here that a common change in the phases of the C_k, *viz.*, $C_k'=e^{i\gamma}C_k$, is a purely formal change for which the expressions $|C_k|^2$, $\mathrm{Re}(C_kC_l^*)$, and $\mathrm{Im}(C_kC_l^*)$, which occur as coefficients in the final formulas, are invariant.)

[1] S. R. de Groot and H. A. Tolhoek, Physica **16**, 456 (1950).
[2] M. Fierz, Z. Physik **104**, 553 (1937).
[3] L. Michel, Proc. Phys. Soc. (London) **A63**, 514 (1950).
[4] G. L. Trigg and E. Feenberg, Phys. Rev. **82**, 982 (1951).
[5] W. Pauli, Revs. Modern Phys. **13**, 203 (1941), pp. 220–222.
[6] L. C. Biedenharn and M. E. Rose, Phys. Rev. **83**, 459 (1951). We prefer to use charge conjugation, and we mean Racah's time-reversal operator (see reference 5) in the preceding paragraph.
[7] H. A. Tolhoek and S. R. de Groot, Physica **17**, 81 (1951).

The Natural Radioactivity of Rubidium

S. C. Curran, D. Dixon, and H. W. Wilson
Department of Natural Philosophy, The University, Glasgow, Scotland

(Received August 15, 1951)

UNCERTAINTY regarding the decay process[1] of Rb^{87} and its rather unique position in regard to β-theory seemed good reasons for investigating the radiation with a large proportional tube spectrometer.[2] The internal diameter was 5.5 in. and the fully effective length[3] 10 in. The operating pressure was 5 atmospheres of argon +20 cm of methane. The tube was shielded with 2 in. of lead and an array of Geiger tubes could be put in anticoincidence for protection from cosmic radiation. The source, RbCl spread uniformly over the inner surface of a cylinder of aluminum acting as cathode, covered an area of between 800 and 900 cm^2. Two thicknesses were employed, 1.5 mg/cm^2 above 40 kev and 0.128 mg/cm^2 for lower energies.

The β-spectrum observed is shown by the full curve in Fig. 1, constructed from three sets of observations which overlapped each other, two with the thicker source and one with the inner (indicated by triangles). Extra detail near the end point is shown in the inset figure. A Kurie plot is given in Fig. 2 where, as in Fig. 1, the limiting energy E_0 is found to be 275 kev, considerably higher than the generally accepted value[1] of about 130 kev. However the very unusual shape of the spectrum no doubt contributed to the failure of the rather tentative earlier attempt to analyze it correctly. No maximum is observed on the curve, Fig. 1, and the intensity increases rapidly with decreasing energy down to at least

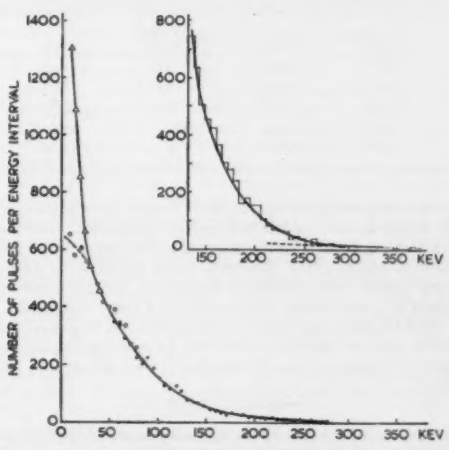

FIG. 1. Beta-spectrum of Rb^{87}.

10 kev, below which point we have not pursued our observations. The average energy is only 44 kev. The known spins of both ground states involve a spin change $\Delta I=3(3/2\rightarrow 9/2)$ and the ft value ($\log ft=17.6$ for $E_0=275$ kev, half-life $\tau=6.15\times10^{10}$ yr) indicates a definitely third-forbidden transition. The very remarkable departure of the Kurie plot from the straight line qualitatively agrees with expectations for the case $\Delta I=3$, yes. Calculation[4] of the required correction factor $C_3\tau$ has not been attempted, although the adjustment might well prove successful.

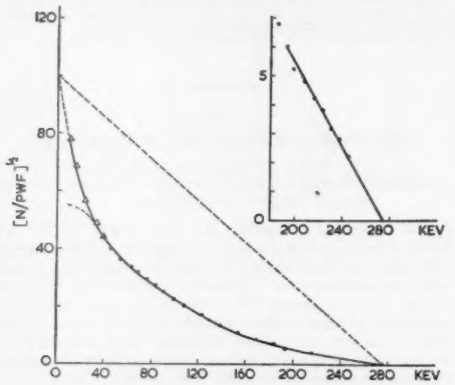

FIG. 2. Fermi plot of Rb^{87} beta-spectrum.

The absence of conversion electron peaks implies simple decay, but to verify this a search for K or L x-rays was carried out with the same equipment. Careful examination of counting rate as the discriminator level was varied through 1.8 kev failed to produce any evidence of L x-rays, while the spectrum observed with aluminum (58 mg/cm²) covering the source to absorb β-rays showed that the intensity of K x-radiation corresponded to about one quantum per 500 β-particles. Unambiguous allocation to Rb or Sr was not possible. A scintillation spectrometer gave an upper limit of the γ-quantum per 5×10^3 β-rays.[5] Both of these low intensity radiations could be due to bombardment of the source by β-particles, and we conclude that the process $Rb^{87}\rightarrow Sr^{87}+\beta^-$ is a simple ground to ground-state transition, contradicting some previous findings. The conversion peaks described by Ollano[6] would appear to be statistical fluctuations, and previously observed $\beta-e$ coincidences[7] perhaps had their origin in reflection.

TABLE I. Decay data for natural β-emitters.

Source	E_0(Mev)	Half-life $\tau(10^{10}$ yr)	$\log ft$
Rb^{87}	0.275	6.15	17.6
K^{40}	1.36	0.11	18.05
Lu^{176}	0.215 or 0.4	2.4	18.02 or 18.91
Re^{187}	0.043	400	17.73
Nd^{150}	0.011	5	13.73

With the thin source we found that 0.10075 g of RbCl gave 1477 counts per min. Applying corrections for reflection[8] at the support (+7.5 percent) and self-absorption (−4.5 percent), the half-life is

$$\tau=(6.15\pm0.3)\times10^{10}\text{ yr},$$

in good agreement with the latest value measured directly[7] and that deduced from the uranium-lead method.[9]

Our new value for E_0 increases $\log ft$ to 17.6 and shows, when tabulated with recent data[10] for the other natural sources ($Z<80$), a notable grouping of $\log ft$ values near 18 (see Table I). Nd^{150} seems exceptional, but preliminary work[11] shows Libby's data[12] are probably wrong and E_0 may greatly exceed 11 kev. Further examination is necessary but Nd^{150} may prove consistent in ft, and a considerable gap will exist between ft for these elements and that for the nearest neighbor, Be^{10} at $\log ft=13.65$.

We should like to thank Professor P. I. Dee for his interest and encouragement in this work. A fuller account will be published elsewhere.

[1] *Nuclear Data*, National Bureau of Standards circular 499 (1950).
[2] Curran, Angus, and Cockroft, Phil. Mag. **40**, 36 (1949).
[3] A. L. Cockroft and S. C. Curran, Rev. Sci. Instr. **22**, 37 (1951).
[4] E. Greuling, Phys. Rev. **61**, 568 (1942).
[5] We are indebted to Mr. R. C. Bannerman for this result.
[6] Z. Ollano, Nuovo cimento **18**, 11 (1941).
[7] Haxel, Houtermans, and Kemmerich, Z. Physik **124**, 705 (1948); Phys. Rev. **74**, 1886 (1948).
[8] *Conference on Absolute β Counting*, National Research Council, Nuc. Sci. Ser. Prelim. Rep. No. 8 (1950), papers by B. P. Burtt and L. Yaffe.
[9] F. Strassman and E. Walling, Ber. deut. chem. Ges. **71**, 1 (1938).
[10] A. M. Feingold, Revs. Modern Phys. **23**, 10 (1951).
[11] Private communication from Professor T. P. Kohman shows that independently he has adopted a rather similar method for the same type of investigation, and his work likewise suggests disagreement with existing data for Nd^{150}.
[12] W. F. Libby, Phys. Rev. **45**, 845 (1934).

Acoustic Streaming and the Conservation of Angular Momentum*

P. J. WESTERVELT
Research Analysis Group, Physics Department, Brown University, Providence, Rhode Island
(Received July 23, 1951)

IN this note we derive a quantity related to the rate at which angular momentum is transferred from an acoustic wave to a lossy medium; as Eckart[1] has recently pointed out, this transfer of angular momentum generates time-independent vorticity. In the interest of simplicity inviscid diabatic flow will be considered, although it is necessary to take into account viscous forces if the streaming velocity is to be calculated from the transfer of angular momentum. The artifice of attributing acoustic losses (including those due to shear viscosity) to the diabatic character of the flow simplifies the argument without altering its validity.

Euler's equation of motion may be written[1]

$$(\partial\rho\mathbf{u}/\partial t)+\rho(\mathbf{u}\cdot\nabla)\mathbf{u}+\mathbf{u}\nabla\cdot\rho\mathbf{u}=-\nabla p. \tag{1}$$

Equation (1) may also be written in terms of the flux of momentum density dyadic $\rho\mathbf{uu}$

$$(\partial\rho\mathbf{u}/\partial t)+\nabla\cdot\rho\mathbf{uu}=-\nabla p. \tag{2}$$

We now assume, with Eckart, that the solution to Eq. (2) is the sum of a first- and a second-order term, $\mathbf{u}_1$ and $\mathbf{u}_2$, respectively, where $\mathbf{u}_1$ is irrotational and has a simple harmonic time dependence. Upon taking the curl of Eq. (2), there results

$$\nabla\times\rho_0\partial\mathbf{u}_2/\partial t=-(\partial/\partial t)(\mathbf{u}_1\times\nabla\rho_1)-\nabla\times\nabla\cdot\rho_0\mathbf{u}_1\mathbf{u}_1, \tag{3}$$

where we denote the equilibrium density by ρ_0, and in which ρ_1 represents the density associated with the solution $\mathbf{u}_1$ to the first-order equations of motion. The time average of the right-hand side of Eq. (3) is equal to

$$-\nabla\times\nabla\cdot\langle\rho_0\mathbf{u}_1\mathbf{u}_1\rangle_{Av}, \tag{4}$$

which is related to the average rate at which angular momentum is communicated from the wave to the medium. In the steady state, conservation of angular momentum requires that (4) be balanced by stresses arising from the streaming of the fluid. It is pertinent to note that (4) is the curl of the divergence of the average value of Brillouin's[2] radiation stress tensor. Should the fluid be homogeneous, ρ_0 may be taken outside the differential operators. For a homogeneous medium with $\nabla\times\mathbf{u}_1=0$, we have

$$\nabla\times\nabla\cdot\langle\rho_0\mathbf{u}_1\mathbf{u}_1\rangle_{Av}=\rho_0[\nabla(\nabla\cdot\mathbf{u}_1)\times\mathbf{u}_1]_{Av}. \tag{5}$$

In the special case of a homogeneous viscous isobaric fluid where $\mathbf{u}_1$ is assumed to satisfy the first-order Navier-Stokes equations with μ_0 the viscosity coefficient, Eq. (5) reduces to

$$\nabla\times\nabla\cdot\langle\rho_0\mathbf{u}_1\mathbf{u}_1\rangle_{\text{Av}}=(-4\mu_0/3\rho_0)[\nabla\rho_1\times\nabla(\partial\rho_1/\partial t)]_{\text{Av}}, \quad (6)$$

an expression obtained by Eckart[1] for the forcing term responsible for the generation of vorticity.

Fox and Herzfeld[2] have implied that the linear wave momentum is responsible for streaming. It is clear that the wave momentum equals the average flux of momentum in general only for plane progressive waves, in agreement with the statement of Fox and Herzfeld that the concept of wave momentum is useful only in cases where the wave pattern can be approximated locally by plane waves.

Finally, in discussing second-order velocities, it is important to understand certain paradoxes that can arise in alternating flow. Letting $\mathbf{u}$ represent the velocity in fixed coordinates and $\partial\mathbf{d}/\partial t$ the velocity in moving[4] coordinates, the following transformations relate the two velocities (to second order in the variables):

$$\mathbf{u}=(\partial\mathbf{d}/\partial t)-(\textstyle\int\partial\mathbf{d}/\partial t)\cdot\nabla\partial\mathbf{d}/\partial t, \quad \partial\mathbf{d}/\partial t=\mathbf{u}+(\textstyle\int\mathbf{u}dt)\cdot\nabla\mathbf{u}. \quad (7)$$

Mass velocity is usually denoted as the product of the density and the particle velocity, $\rho\mathbf{u}$. It is important to realize that a non-zero mass velocity does not necessarily imply a streaming velocity. A simple example results when in two-dimensional cartesian coordinates, $\partial\mathbf{d}/\partial t$ is given by

$$\partial\mathbf{d}/\partial t=\mathbf{i}\sin kx\sin\omega t+\mathbf{j}\sin ky\cos\omega t. \quad (8)$$

For this solution, representing crossed standing waves, it is easily verified that the average mass velocity $(\rho u)_{\text{Av}}$ is non-zero. Yet the particles of the fluid oscillate about a fixed mean position; hence, there is no streaming associated with the solution [Eq. (8)].

In a plane progressive wave represented by

$$\partial\mathbf{d}/\partial t=\mathbf{i}\sin(\omega t-kx), \quad (9)$$

it can be verified[4] that both $\partial\mathbf{d}/\partial t$ and $\rho\mathbf{u}$ are zero on the average, while the average of $\mathbf{u}$ is non-zero, yet there is no streaming associated with this solution.

The author acknowledges with thanks the helpful discussions he has had with W. L. Nyborg concerning this note.

* Work supported in part by ONR contract.

[1] C. Eckart, Phys. Rev. **73**, 68 (1948).
[2] L. Brillouin, *Les tenseurs en mechanique et en élasticité* (Dover Publications, New York, 1946), p. 290.
[3] F. Fox and K. H. Herzfeld, Phys. Rev. **78**, 156 (1950).
[4] P. J. Westervelt, J. Acoust. Soc. Am. **22**, 319 (1950).

Thermoelectric Power of Carbons and Graphite

EGON E. LOEBNER*
Department of Physics, University of Buffalo, Buffalo, New York
(Received July 20, 1951)

THE thermoelectric power of carbon and of graphite has been investigated a number of times, and results giving scattered values varying in magnitude and sign based on a platinum standard have been reported. The kind of samples, their preparation, and heat treatment were seldom mentioned.

To clarify this, a study of the thermoelectric power, its origin, and its dependence upon heat treatment was undertaken. In the initial phase of this work it was decided to determine the emf's at room temperature using *CP* platinum leads as a standard. The 6-inch long carbon and graphite samples were placed between two graphite blocks. One block was electrically heated by a nichrome coil and the other was cooled in a water bath. A gradient of between 1 and 5°C/inch was maintained along the samples. The junctions were separated about 4½ inches and their temperatures were determined with two Alumel-Chromel thermocouples. All emf's were read on a type *K* potentiometer.

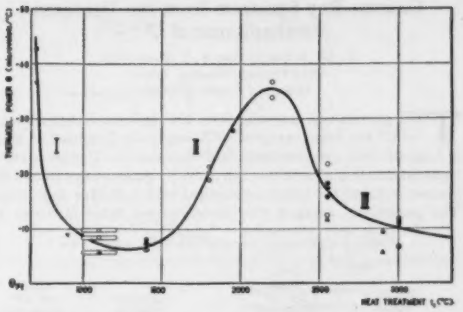

FIG. 1. Thermoelectric power of petroleum coke products. ■—Laboratory prepared petroleum coke 1; ▼—Laboratory prepared petroleum coke 2; ▲—Laboratory prepared petroleum coke rods; ○—National Carbon Company baked rods, batch 1; ●—National Carbon Company baked rods, batch 2; ⊗—National Carbon Company baked rods, batch 3.

The results of measurements on petroleum coke products are plotted in Fig. 1. Three kinds of laboratory prepared cokes and three batches of National Carbon Company baked rods were heat treated to temperatures ranging from 700°C to 3000°C. Rods from batch 2, after being heat treated to various values t_c, were reheated to higher temperatures. The thermoelectric powers of all the rods were determined before and after heat treatment. All the above emf's are negative and their absolute values show an interesting variation with heat treatment. Part I of the curve starts with high values for cokes heat treated to 700°C, for which the resistivity is low enough to make measurements possible, and drops to a minimum at about 1400°C. Part II increases to a maximum at about 2200°C and part III drops again to lower values.

A limiting value of minus 4.5 microvolts/°C was observed for a Ceylon graphite piece, which has been made by compressing highly purified Ceylon graphite powder. As platinum is negative on the absolute thermoelectric scale at room temperature, the negative thermoelectric effect for graphite shows a higher mobility for electrons than for holes. This is in disagreement with the widely quoted result of a positive Hall effect in graphite reported by Onnes and Hoff.[1] Since a positive thermoelectric power has been found by the author using an impure natural Ceylon graphite, it seems probable that Onnes and Hoff used an impure graphite. As is evident from Fig. 1, for samples treated to higher temperatures than 2200°C a larger scattering of results was observed. For a few graphitized samples much lower values were observed, but no excessive negative values were recorded.

A coke of the amorphous type has been investigated and showed a shallower minimum and a much less pronounced maximum.

The general trend of the observed curve agrees best with the proposed explanation on the electronic conductivity of graphite and carbons.[2] The treatment dependence in part I is characterized by an increasing number of excess electrons supplied into the conduction band by the free valencies after a gradual elimination of hydrogen from the complex hydrocarbons. This is followed in part II by a decrease of the relative number of excess electrons due either to crystallite growth causing a diminution in the number of peripheral free bonds or to impurities being driven out of the lattice or both. The last part of the curve gives evidence of the decrease in the energy gap ΔE with heat treatment. Above 2200°C, kT is $\sim\Delta E$ and additional electrons are activated from the lower into the upper band.

It is a pleasure to acknowledge the friendly advice and guidance of Professor S. Mrozowski and valuable assistance given by other members of the Physics laboratory.

* B'nai B'rith Hillel Foundation scholar.
[1] H. K. Onnes and K. Hoff, Proc. Royal Acad. Amsterdam **17**, 520 (1915).
[2] S. Mrozowski, Phys. Rev. **77**, 838 (1950).

Gamma-Ray Spectrum from the Deuteron Bombardment of C^{13}*

L. M. Baggett† and S. J. Bame, Jr.†
Rice Institute, Houston, Texas
(Received August 6, 1951)

THE gamma-ray spectrum from the deuteron bombardment of C^{13} has been measured by Thomas and Lauritsen.[1] Using a magnetic lens spectrometer, they observed the Compton electrons produced in a beryllium converter by gamma-rays from a 50 percent enriched C^{13} target bombarded with 1.58-Mev deuterons. The gamma-ray energies thus measured are listed in Table I.

TABLE I. Gamma-ray energies and yields from $C^{13}+d$.

Energy[a] (Mev)	Yield[a] per 10^6 deuterons	Energy[b] (Mev)	Yield[b] per 10^4 deuterons
0.729 ± 0.022	1.3		
1.643 ± 0.004	1.4		
2.318 ± 0.008	4.5		
		3.05 ± 0.09[c]	30
3.390 ± 0.010	1.6	3.40 ± 0.15	1.7
3.9(?)			
5.056 ± 0.025	1.2	5.04 ± 0.09	1.2
$5.69\ \pm0.050$	0.6		
6.115 ± 0.030	2.0	6.10 ± 0.10	1.5

[a] Results of Thomas and Lauritsen using a 50 percent enriched C^{13} target, $E_d=1.58$ Mev.
[b] Results from pair spectrometer using a 35 percent enriched C^{13} target, $E_d=1.65$ Mev, uncorrected for relative abundance of the isotopes.
[c] Line from $C^{13}(d,p)C^{14}$, uncorrected for relative abundance of the isotopes.

Since the cross section for production of Compton electrons is decreasing at higher energies, it was thought worthwhile to measure this spectrum with a pair spectrometer.

A 180° magnetic pair spectrometer designed and constructed by Terrell[2] was used. A thick target of carbon enriched to 35 percent C^{13} (kindly presented to us by Professor H. C. Urey) was bombarded with 1.65-Mev deuterons from the Rice Van de Graaff accelerator, and the gamma-rays were observed at 90° to the beam. A 31 mg/cm² tin radiator was used. Figure 1 shows the spectrum

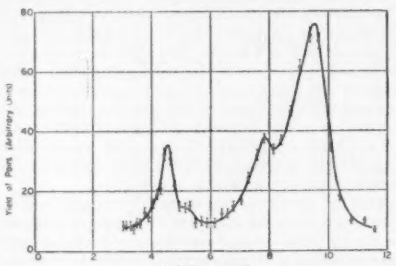

FIG. 1. Gamma-ray spectrum from $C^{13}+d$, obtained with a 180° magnetic pair spectrometer.

obtained with a no radiator background subtracted. Three strong lines appear at 4550, 7850, and 9570 gauss-cm, and a weak line appears at about 5150 gauss-cm. The line at 4550 is due to $C^{13}(d,p)C^{14}$. Applying peak shift corrections, the line energies were calculated and are listed in Table I. The lower energy lines found by Thomas and Lauritsen were not detected in the present experiment due to the low efficiency of a pair spectrometer below 3 Mev. The 5.69-Mev line was not resolved; however, the broadness of the upper energy lines suggests that this line may be present. The counting efficiency of the spectrometer was calibrated[2] at 2.62 Mev using a Th C″ source, and at 4.5 Mev using a Po—Be source. Using these efficiencies along with a calculated efficiency at 9.0 Mev, the yields for the different lines were calculated and are shown in Table I. These yields are for a 35 percent enriched C^{13} target and are uncorrected for relative abundance. The 6.10-Mev line has been assigned[1] to $C^{13}(d,p)C^{14}$ because it is also observed at $E_d\sim0.6$ Mev where only this assignment is energetically possible, while the 3.40- and 5.04-Mev lines have been assigned to $C^{13}(d,n)N^{14}$.

* Assisted by the joint program of the ONR and AEC.
† Now at the Los Alamos Scientific Laboratory, Los Alamos, New Mexico.
[1] R. G. Thomas and T. Lauritsen, Phys. Rev. **78**, 88 (1950); Hornyak, Lauritsen, Morrison, and Fowler, Revs. Modern Phys. **22**, 336 (1950).
[2] J. Terrell, Phys. Rev. **80**, 1076 (1950); J. Terrell and G. C. Phillips, Phys. Rev. **83**, 703 (1951).

Applicability of the Renormalization Theory and the Structure of Elementary Particles*

Shoichi Sakata, Hiroomi Umezawa, and Susumu Kamefuchi
Institute of Theoretical Physics, Nagoya University, Nagoya, Japan
(Received July 23, 1951)

SOME of the fundamental difficulties in the theory of elementary particles have been circumvented by the development of the renormalization theory. As we have pointed out in previous papers,[1] this theory should be regarded as an abstract formalism, behind which the concrete structures of the elementary particles lie hidden. So long as the renormalization procedure is successful, it is unnecessary to know the detailed features of the structures; but, as soon as defects of the renormalization theory become obvious, we must seriously consider the structures of the elementary particles.

As is well known, one of the most striking defects of the renormalization theory is found in the problem of the anomalous magnetic moment of the nucleon. In fact, none of the four types of the meson theory has yet been able to explain this anomaly. However, it seems to us that it is still too early to accept this as conclusive, since it is always possible to add a magnetic moment of Pauli type having finite or infinite value in accordance with the idea of renormalization. If such an addition were made, the great success of the renormalization theory in quantum electrodynamics would also be regarded as merely accidental. In the philosophy of renormalization, there is no reason why we should exclude the possible existence of a magnetic moment of Pauli type in the case of the electron.

If the structure of the elementary particles were known, the qualitative differences among the various types of interactions would surely be clarified. However, in the present stage, we must content ourselves with a more formal or phenomenological classification of the interactions. Although the renormalization theory treats all kinds of interactions in the same manner, it has become clear[2-4] recently that they may be classified into two groups, which give rise, respectively, to different situations: (a) those interactions which can be renormalized by assuming the coexistence of a finite number of interactions belonging to the same group and (b) those interactions which require the further introduction of infinitely many interaction terms having successively higher derivatives of the field quantities. The electromagnetic interaction of the electron and the scalar interaction of the scalar meson with a nucleon are examples of the former group, while the electromagnetic interaction of the vector meson[2] and the direct interaction between spinor particles[3] belong to the latter.

If there were only interactions belonging to the first group, the renormalization theory would form a closed system in the frame of the present quantum field theory. However, as the existence of the direct interaction between spinor particles is indispensable for interpreting beta-decay experiments, it seems premature to content ourselves with the success of the renormalization theory in quantum electrodynamics. The assembly of the infinite number of interactions having successively higher derivatives is equivalent to a nonlocal interaction, which is intimately connected with the structure of the elementary particles.

In order to classify all the interactions in this way, we have investigated the condition for the "closing" in the renormalization theory as applied to the most general type of interaction. Let the number of field quantities U^α of the field (α), and the maximum number of the derivation operators which operate on the $U^\alpha(\alpha=1, 2, \cdots)$ in the interaction hamiltonian $H_l(l=1, 2, \cdots)$ be k_l^α and a_l, respectively, and let the asymptotic form of the fourier amplitude $\Delta^\alpha(p)$ of the propagation function of the field (α) be $p^{b^\alpha+2}$ for large p. Then, the condition for the closing is given by

$$K_l \equiv -\Sigma_\alpha \tfrac{1}{2}(b^\alpha+2)k_l^\alpha+4-a_l \geqq 0 \quad (l=1, 2, \cdots). \qquad (1)$$

The results so far obtained for various cases by actual calculations[4] are found to be compatible with the conclusions from condition (1).

Now, in connection with the requirement (1) concerning the limit of applicability of the renormalization theory, it is of interest to recall Heisenberg's[5] classification of interaction types into first and second kinds. According to his considerations, when the coupling constant is of the dimension l^n with $n>0$, the present quantum field theory cannot give correct results for phenomena relating to a wavelength shorter than l (in this case the series expanded in powers of the coupling constant does not converge).[6] Such phenomena are regarded as being closely connected with the so-called "universal length r_0,"[7] and so with the structure of elementary particles.

Now, it can be verified that n is equal to $-K_l$, whose value is the criterion for the applicability of the renormalization procedure. This important fact gives the physical basis for condition (1) and also clarifies the reason that the renormalization theory has succeeded in the electrodynamics of the electron.

In view of condition (1), we may classify the interaction types as follows: (a) the case in which the renormalization procedure gives a consistent closed theory, i.e., interaction of the first kind of Heisenberg with $n=-K=0$, (b) the case in which the renormalization procedure gives a consistent closed theory, i.e., interaction with $n=-K<0$, (c) the case in which the renormalization fails, i.e., interaction of the second kind of Heisenberg with $n=-K>0$.

For the closing of the theory type (a) occasionally requires the further introduction of type (b). As an example of such cases, we may mention the interaction between a nucleon and a scalar meson via scalar coupling, where a $\lambda\phi^3$-term is required. Type (c) corresponds to the case in which the perturbation expansion does not converge.

* Read at the Nagoya meeting of REKS (the Kansai Branch of the Elementary Particle Theory Group), held on February 6, 1951.

[1] S. Sakata, Prog. Theor. Phys. **2**, 145 (1947); S. Sakata and H. Umezawa, *ibid.* **5**, 682 (1950).
[2] H. Umezawa and R. Kawabe, Prog. Theor. Phys. **4**, 423, 443 (1949); D. Feldman, Phys. Rev. **76**, 1369 (1949).
[3] S. Kamefuchi, Prog. Theor. Phys. **6**, 175 (1951).
[4] See references 2 and 3; and M. Neuman and W. H. Furry, Phys. Rev. **76**, 1677 (1949); F. J. Dyson, *ibid.* **75**, 1736 (1949); P. T. Matthews, Phil. Mag. **41**, 185 (1950); Phys. Rev. **81**, 936 (1951); F. Rohrlich, Phys. Rev. **80**, 666 (1950); T. Kinoshita and Y. Nambu, Prog. Theor. Phys. **5**, 473 (1950).
[5] W. Heisenberg, Solvay Ber. Kap. III, IV (1939).
[6] W. Heisenberg, Z. Physik **101**, 533 (1936); Oppenheimer, Snyder, and Serber, Phys. Rev. **57**, 75 (1940).
[7] W. Heisenberg, Ann. Physik **32**, 20 (1938); W. Heisenberg, Z. Physik **110**, 251 (1938).

The $\alpha-\gamma$ Angular Correlation in the Decay of Radiothorium*

J. K. Beling,† B. T. Feld, and I. Halpern
Laboratory for Nuclear Science and Engineering, and Department of Physics, Massachusetts Institute of Technology, Cambridge, Massachusetts
(Received August 7, 1951)

THE most reasonable energy level diagram for those levels in RdTh and ThX that are displayed in the α-decay of RdTh is given in Fig. 1. This arrangement of levels is based on a number of measurements of the various radiations involved in the α-decay. The α fine structure was measured by Rosenblum and co-workers.[1]

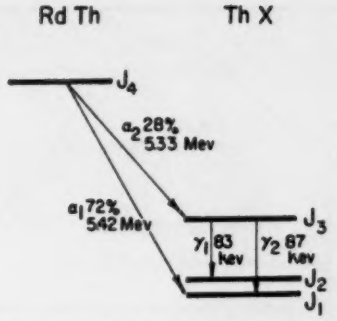

FIG. 1. Energy levels in the decay of RdTh.

They found only the two α-lines shown, except that the line α_1 showed a broadening that would be consistent with the existence of the close doublet at the ground state of ThX. This doublet is suggested by the observations of two gamma-rays (of energies 83.3 and 86.8 kev) by Surugue and Tsien[2] and by Riou.[3] The conversion coefficients for the γ's can be computed from their data and they both correspond to electric quadrupole transitions. It is likely that the spins J_1 and J_4 are equal to zero because the nuclei involved are even-even. All these data together imply that all the levels have the same parity.

The measurement of angular correlations between successive nuclear decay radiations is a means of checking a given set of assumptions concerning the spins and parities of the levels involved. In the case of the natural radioactivities, e.g., RdTh, many data have been accumulated. It was felt that an $\alpha-\gamma$ angular correlation in this case, would have the property of confirming or denying the validity of the accumulated picture (Fig. 1) in all of its details. The results of a previous attempt[4] to measure this correlation were not sufficiently reliable for this purpose.

In the present experiment scintillation counters were used for both the α- and γ-detectors. A large number of runs, each lasting several hours and including angles in all four quadrants, were made

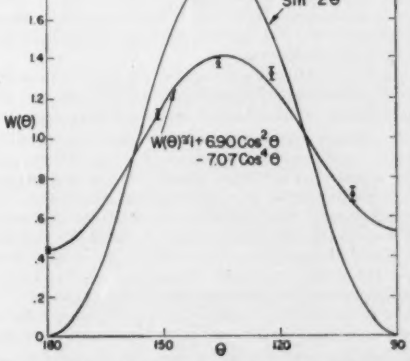

FIG. 2. The observed correlation with both γ-rays. $W(\theta)$ is the least squares fit to the data. $\sin^2 2\theta$ is the theoretical correlation corresponding to the spin sequence $0 \xrightarrow{a} 2 \xrightarrow{\gamma} 0$. The two curves are normalized to the same total coincidence rate.

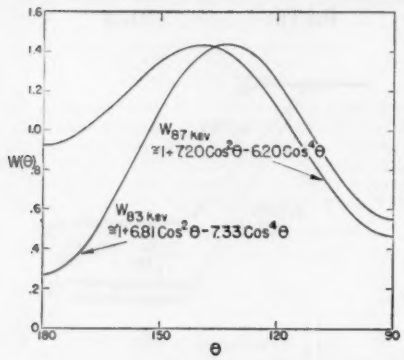

FIG. 3. The separate correlations of the 83- and 87-kev photons. The data for the five angles, from which W_{83} was constructed, were known only to about 10 percent. The errors on the individual points for W_{87} are closer to 50 percent, since they were obtained by a subtraction procedure.

on thin sources of RdTh freshly separated from the equilibrium mixture of RdTh and its decay products. Various checks showed that possible spurious effects of long-lived radioactive impurities and of the build-up of removed activities were negligible. The experimental chamber was lined with lead to reduce effects of photon scattering. As a further precaution, differential discrimination was used on both the α- and γ-pulses.

It was possible to confirm a number of features of the decay scheme in Fig. 1. Absorption measurements of the coincidences showed that the γ's have energies between the K edges of gold and lead (81 and 88.5 kev) and that their intensity relative to α's is roughly as expected. The fact that the coincidences are observable with a 0.3 μsec resolving time implies that the γ-multipolarity is probably no higher than electric quadrupole.[5] The large $\cos^4\theta$ term in the observed correlation indicates that the radiations are at least quadrupole. These results are thus in agreement with the implications of the conversion coefficients on the nature of the γ-radiation. It was also possible to confirm that the γ-rays do not occur in cascade.

The observed correlation between the α's and both γ's was very pronounced and is shown in Fig. 2. It was also possible to obtain a relatively rough idea of the separate correlations for the two γ-rays by the use of thallium absorbers (the K-edge of Tl falls between the two γ's). These results are given in Fig. 3. The observed correlations are fairly close to those expected for the spin assignment $J_2=0$, $J_3=2$, but the differences are significantly outside the experimental error.

A number of attempts were made to account for these differences. Partial reorientation of the excited ThX nucleus, before γ-ray emission, could account for the differences between the observed correlation and the one with the spin sequence $0\xrightarrow{\alpha}2\xrightarrow{\gamma}0$. However, these interactions which we have been able to consider do not appear to be sufficiently strong to induce reorientation in the required time. Other level schemes (some admittedly inconsistent with accepted data) including a large number of reasonable (and unreasonable) spin assignments were considered in computations of new correlation functions in order to find a better fit than the one above. Mixtures of different angular momenta for both the α- and γ-emissions were also considered. It has not, however, been possible to find a really convincing fit. In fact, most of the computed correlations are not nearly as sharp as the observed one. It is felt that the sequence $0\xrightarrow{\alpha}2\xrightarrow{\gamma}0$ must play a prominent role in the RdTh decay.

The authors are greatly indebted to Mrs. E. W. Backofen for the generous performance of the many chemical separations that were required, and to Miss M. Karakashian and Mrs. P. Halpern for their help with the computations.

* This work was supported in part by the joint program of the ONR and AEC.

† Now with the ONR, London, England.

[1] Rosenblum, Valadares and Perey, Compt. rend. **228**, 385 (1949).

[2] J. Surugue and Tsien-San-Tsiang, Compt. rend. **213**, 172 (1941).

[3] Michel Riou, J. phys. radium **11**, 185 (1950).

[4] Kulchitski, Latyshev, and Bulyginski, Bulletin Acad. Sci. URSS **13**, 331 (1949). (In this work the counting rates were low because the γ-rays were detected with Geiger tubes; moreover there was no chemical separation of the many troublesome decay products of RdTh.)

[5] Lifetime formulas for γ-emissions are given by P. Axel and S. M. Dancoff, Phys. Rev. **76**, 892 (1949); V. Weisskopf (unpublished); see R. D. Hill, Phys. Rev. **81**, 470 (1951).

The K-Capture/Positron Branching Ratio in Cu^{64}

E. PLASSMANN AND F. R. SCOTT
Physics Department, Indiana University, Bloomington, Indiana
(Received August 6, 1951)

THE K-capture/positron branching ratio in Cu^{64} has been measured in a 180° magnetic spectrometer by comparing the relative intensities of the K Auger electrons and the positrons. The branching ratio for this isotope has been reported by several investigators,[1–4] but previous to this letter only Cook and Langer have obtained a ratio by comparing relative Auger electron and positron intensities. Improved techniques in the detection of low energy electrons and in source preparation[5] have made it possible to obtain more reliable data.

The copper activity was obtained in the cyclotron by bombarding a copper probe with 8-Mev deuterons. Then approximately 0.1 mg of active copper, removed from the tip of the probe, was placed in a platinum boat which was the filament of a vacuum evaporator. The spectrometer source was prepared by thermal evaporation of the metallic radioactive copper from this filament in a vacuum. This source, estimated to be 5 micrograms/cm² thick, was deposited on a double layer of zapon 15 micrograms/cm² thick and was grounded by means of a previously evaporated and extremely thin copper film. By overlapping points throughout the experiment, a single half-life of 12.9 hours was observed, indicating the absence of any noticeable impurities.

The measurements were made in a 15-cm radius of curvature, shaped magnetic field spectrometer.[6] A zapon side window counter was used as a detector. The zapon film was supported by a Lectromesh grid, and the 2-cm total pressure in the counter was maintained constant by means of a cartesian monostat system.[7]

Figure 1 shows the K Auger electron lines at 6.56 kev and 7.48 kev which correspond to K-$2L$ and K-L-M energy differences in nickel.[8] Part of the line width is attributed to the unresolved energy difference between L_{II} and L_{III} electrons. The normal resolution from monogenergetic electrons from a thin source 0.3 cm wide is 1 percent in this spectrometer. The absence of any appreciable low energy tail indicates that there was negligible source absorption at this energy.

The positron intensity was obtained by taking measurements in the region below 250 kev with the zapon side window counter. This data was then analyzed into a Fermi plot with the appropriate corrections for screening.[9] The resulting straight line was extended to the known end-point energy of 657 kev. The complete momentum distribution for the positrons was obtained from this Fermi plot. From this a ratio of 1.18 ± 0.10 is found for the intensity of the K Auger electrons to the intensity of the positrons.

To obtain the K capture/positron ratio for Cu^{64}, this K Auger electron/positron ratio must be divided by one minus the fluorescent yield in nickel. If the value of 0.38 is used for this fluorescent yield,[8] the K-capture/positron branching ratio of Cu^{64} is 1.90 ± 0.20. Recently, West and Rothwell[10] measured the fluorescent yield in krypton and obtained a value 20 percent higher than previously reported. Using their value and extrapolating to $Z=28$, a fluorescent yield of 0.45 is obtained for nickel. This gives a

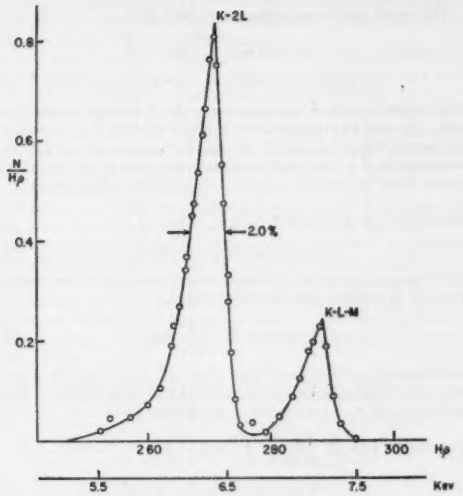

FIG. 1. K Auger electron distribution of Cu^{64}.

K-capture/positron ratio of 2.18 ± 0.20 for Cu^{64}. When this is corrected for the 5 percent branching to the 1.35-Mev excited state of nickel, the K-capture/positron ratio to the ground state is 2.07 ± 0.20, in excellent agreement with the theoretically predicted value of 2.08.[11]

The authors wish to thank Professor Lawrence M. Langer for suggesting the problem and for his encouragement and advice. This work has been assisted by a grant from the Frederick Gardner Cottrell Fund of the Research Corporation and by the joint program of the ONR and AEC.

[1] R. Bouchez and G. Kayas, J. phys. et radium (8) **10**, 110 (1949).
[2] Huber, Ruetschi, and Scherrer, Helv. Phys. Acta **22**, 375 (1949).
[3] C. S. Cook and L. M. Langer, Phys. Rev. **74**, 1241 (1948).
[4] J. H. Reynolds, Phys. Rev. **79**, 243(A) (1950).
[5] Langer, Moffat, and Price, Phys. Rev. **76**, 1725 (1949).
[6] J. A. Bruner and F. R. Scott, Rev. Sci. Instr. **21**, 545 (1950).
[7] L. M. Langer and R. D. Moffat, Phys. Rev. **80**, 651 (1950).
[8] A. H. Compton and S. K. Allison, *X-Rays in Theory and Experiment* (D. Van Nostrand Company, Inc., New York, 1935), p. 784.
[9] John R. Reitz, Phys. Rev. **77**, 10 (1950).
[10] D. West and P. Rothwell, Phil. Mag. **41**, 873 (1950).
[11] E. Feenberg and G. Trigg, Revs. Modern Phys. **22**, 399 (1950).

A Steady-State Transient Technique in Nuclear Induction*

R. BRADFORD, C. CLAY, AND E. STRICK
University of Wyoming, Laramie, Wyoming
(Received July 30, 1951)

A NEW nuclear resonance transient phenomenon was initially observed by Bradford[1] and theoretically justified by Uehling,[2] and is now under investigation in our laboratory. Previous investigators[3,4] have described "turn on" transients corresponding to a discontinuous variation of the amplitude of the radiofrequency field. These investigators worked with times between transients that were effectively infinite compared with the time constants, T_1 and T_2, of the nuclear system. The present transient phenomenon is observed during the time between radiofrequency pulses when this time is of the order of the nuclear relaxation time, T_2. The new transient consists of the expected "free" decay following removal of the rf field, plus an attenuated mirror image

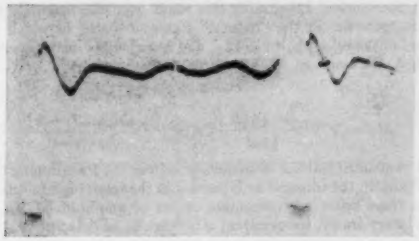

FIG. 1. $0.001M$ $MnSO_4$; prf 400 cps; 3500 μsec sweep.

of this decay, inverted in sign and running backward in time from the onset of the next pulse. This phenomenon occurs as a result of the establishment of a "steady-state" transient in the presence of magnetic field inhomogeneities. A typical photograph of the complete phenomenon is shown in Fig. 1.

Uehling has described a solution of the Bloch[5] equations with suitable boundary conditions, specialized for a "delta-function" periodically repeated rf field pulse, normalized so that $\sin\gamma\int H_1 dt$ over the pulse is unity, followed by an integration of this solution over the magnetic field inhomogeneities. His result for the transient between pulses in the rotating coordinate system before introduction of field inhomogeneities is

$$M_x' = C[e^{-\tau/T_2}\sin\Delta\tau\cos\Delta t + (1-e^{-\tau/T_2}\cos\Delta\tau)\sin\Delta t]e^{-t/T_2} \quad (1a)$$

$$M_y' = C[(1-e^{-\tau/T_2}\cos\Delta\tau)\cos\Delta t - e^{-\tau/T_2}\sin\Delta\tau\sin\Delta t]e^{-t/T_2} \quad (1b)$$

where

$$C \equiv M_0(1-e^{-\tau/T_1})/[1-e^{-\tau/T_2}(1-e^{-\tau/T_1})\cos\Delta\tau - e^{-2\tau/T_1-\tau/T_2}]$$

and $\Delta \equiv \gamma H_0 - \omega$. A reasonable form for the normalized weight factor, $g(\Delta)$, due to magnet inhomogeneities is the uniform distribution $g(\Delta) = 1/\Delta_m$, where Δ_m is the "width" of the rectangular

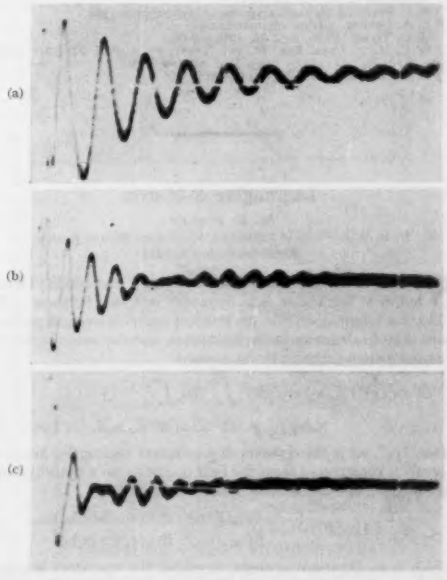

FIG. 2. $0.01M$ $MnSO_4$; prf 100 cps; 2500 μsec sweep. Curve (a): $(\Delta_m)_{\text{gauss}} \sim 0$. Curve (b): $(\Delta_m)_{\text{gauss}} \sim 0.23$. Curve (c): $(\Delta_m)_{\text{gauss}} \sim 0.37$.

field distribution. Integrating this result over the magnetic field inhomogeneities in the "natural" frame $\omega'=\gamma H_0$, in which the limits of Δ are $-\frac{1}{2}\Delta_m$ to $+\frac{1}{2}\Delta_m$, and ignoring the variation of C with Δ, the result is

$$M_x'=0 \tag{2a}$$

$$M_y'=Ce^{-t/T_2}\frac{\sin(\frac{1}{2}\Delta_m t)}{\frac{1}{2}\Delta_m t}-Ce^{-(t+\tau)/T_2}\frac{\sin[\frac{1}{2}\Delta_m(\tau-t)]}{\frac{1}{2}\Delta_m(\tau-t)}. \tag{2b}$$

A controlled leakage of frequency ω from the free running base oscillator in the transmitter is present in the receiving equipment; thus there exists a predominate carrier of amplitude A. In the laboratory frame, the resultant rf voltage to be detected is

$$M_y=M_y'\sin\omega' t+A\sin\omega t,$$

where $\omega'-\omega=\delta$, the nominal angular frequency off resonance. Since $A\gg M_y'$, and $\frac{1}{2}(\omega'+\omega)\sim\omega$, this reduces to

$$M_y=[A+2M_y'\cos(\tfrac{1}{2}\delta t)]\sin\omega t. \tag{3}$$

Thus M_y appears as an amplitude-modulated carrier. M_y' appears as the envelope of the $\cos(\frac{1}{2}\delta t)$ beat, and the first term in Eq. (2b) is just the normal free decay while the second term describes the mirror signal.

Equation (2b) indicates a convenient means for determining the homogeneity of the magnet, i.e., the mean gradient of the field over the sample region. This effect is shown in Fig. 2, in which the inhomogeneity was varied by placing a small screwdriver blade a few cm from the sample. Δ_m can be calculated by noting the time interval between the end of the pulse and the first zero of $\sin(\frac{1}{2}\Delta_m t)$.

These equations can be used for an experimentally simple determination of T_2. For proper experimental conditions, the ratio $M_y'(\tau)$ to $M_y'(0)$ reduces to

$$M_y'(\tau)/M_y'(0)=e^{-2\tau/T_2}. \tag{4}$$

This technique is particularly useful for $T_2>10^{-2}$ sec, a region common to many liquids and usually obscured by magnet inhomogeneities. We are in the process of using this method for the measurement of T_2 for a series of related liquid hydrocarbons.

* Supported in part by the AEC.
[1] R. S. Bradford, thesis, University of Washington, 1951.
[2] E. A. Uehling, private communication.
[3] H. C. Torrey, Phys. Rev. **76**, 1059 (1949).
[4] E. L. Hahn, Phys. Rev. **76**, 461 (1949); Phys. Rev. **77**, 297 (1950); Phys. Rev. **76**, 145 (1949); Phys. Rev. **80**, 580 (1950).
[5] F. Bloch, Phys. Rev. **70**, 460 (1946).

Lagrangian *S*-Matrix

W. K. Burton*
H. H. Wills Physical Laboratory, Royal Fort, Bristol, England
(Received August 8, 1951)

SCHWINGER[1] has constructed an elegant and concise formulation of lagrangian field dynamics in which he shows [Eq. (2.133) of reference 1] that the result of applying two independent variations in structure to the lagrangian operator is to change the transformation function by an amount

$$\delta^{(1)}\delta^{(2)}\langle\zeta_1',\sigma_1|\zeta_2'',\sigma_2\rangle=(i/\hbar c)^2\int_{\sigma_2}^{\sigma_1}dx_1\int_{\sigma_2}^{\sigma_1}dx_2\langle\zeta_1',\sigma_1|(\delta^{(1)}\mathfrak{L}[x_1]\delta^{(2)}\mathfrak{L}[x_2])_+|\zeta_2'',\sigma_2\rangle. \tag{1}$$

Here, $|\zeta_2'',\sigma_2\rangle$ is the eigenket of a complete commuting set ζ_2 of operators constructed from the field operators on a spacelike surface σ_2, etc., and the bracket symbol is defined by

$$(A(x_1)B(x_2))_+=\begin{cases}A(x_1)B(x_2) & \text{if } (x_1)_0>(x_2)_0,\\ B(x_2)A(x_1) & \text{if } (x_2)_0>(x_1)_0,\end{cases} \tag{2}$$

which is an invariant concept, provided the operators involved commute when x_1-x_2 is a spacelike interval, and the positive sense of time is preserved.

This result can be generalized at once to give

$$\delta^{(1)}\cdots\delta^{(n)}\langle\zeta_1',\sigma_1|\zeta_2'',\sigma_2\rangle=(i/\hbar c)^n\int_{\sigma_2}^{\sigma_1}dx_1\cdots\int_{\sigma_2}^{\sigma_1}dx_n\langle\zeta_1',\sigma_1|(\delta^{(1)}\mathfrak{L}[x_1]\cdots\delta^{(n)}\mathfrak{L}[x_n])_+|\zeta_2'',\sigma_2\rangle, \tag{3}$$

which leads to a simple construction of the S-matrix in lagrangian form. Suppose the lagrangian is $\mathfrak{L}+\lambda\mathfrak{L}^i$ where λ is a numerical parameter. Then, if $\mathfrak{L}$ and $\mathfrak{L}^i$ are regarded as fixed, $\langle\zeta_1',\sigma_1|\zeta_2'',\sigma_2\rangle$ is a function of λ; the variation in structure now to be considered comes about by varying λ, and for this case Eq. (3) becomes

$$(d^n/d\lambda^n)\langle\zeta_1',\sigma_1|\zeta_2'',\sigma_2\rangle=(i/\hbar c)^n\int_{\sigma_2}^{\sigma_1}dx_1\cdots\int_{\sigma_2}^{\sigma_1}dx_n\langle\zeta_1',\sigma_1|(\mathfrak{L}^i[x_1]\cdots\mathfrak{L}^i[x_n])_+|\zeta_2'',\sigma_2\rangle. \tag{4}$$

The bras and kets in Eq. (4) refer to a system with the lagrangian $\mathfrak{L}+\lambda\mathfrak{L}^i$. We now invoke Taylor's formula,

$$f(\lambda+1)=\sum_{n=0}^{\infty}\frac{1}{n!}\frac{d^n}{d\lambda^n}f(\lambda), \tag{5}$$

subsequently putting $\lambda=0$. This gives $\langle\zeta_1',\sigma_1|\zeta_2'',\sigma_2\rangle$ for a system with a lagrangian $\mathfrak{L}+\mathfrak{L}^i$ in terms of a series in which the bras and kets refer to a system with a lagrangian $\mathfrak{L}$:

$$\langle\zeta_1',\sigma_1|\zeta_2'',\sigma_2\rangle=\sum_{n=0}^{\infty}\frac{1}{n!}\left(\frac{i}{\hbar c}\right)^n\int_{\sigma_2}^{\sigma_1}dx_1\cdots\int_{\sigma_2}^{\sigma_1}dx_n\langle\zeta_1',\sigma_1|(\mathfrak{L}^i[x_1]\cdots\mathfrak{L}^i[x_n])_+|\zeta_2'',\sigma_2\rangle. \tag{6}$$

Hence, the S-matrix is given by

$$S=\sum_{n=0}^{\infty}\frac{1}{n!}\left(\frac{i}{\hbar c}\right)^n\int_{-\infty}^{\infty}dx_1\cdots\int_{-\infty}^{\infty}dx_n(\mathfrak{L}^i[x_1]\cdots\mathfrak{L}^i[x_n])_+. \tag{7}$$

[1] J. Schwinger, Phys. Rev. **82**, 914 (1951).
* Seconded from I.C.I., Ltd., Butterwick Research Laboratories, The Frythe, Welwyn, Herts, England. Now at Department of Natural Philosophy University of Glasgow, Scotland.

Erratum: Spectrometer and Coincidence Studies on Np^{238}

[Phys. Rev. **79**, 410 (1950)]
M. S. Freedman, A. H. Jaffey, and F. Wagner, Jr.
Argonne National Laboratory, Chicago, Illinois

IN Table I the conversion coefficients of the 0.1028-Mev gamma-ray relative to the 0.258-Mev beta-ray were incorrectly reported to be 4.7 percent (M) and 7.5 percent (L). The correct figures are 2.5 percent (M) and 3.9 percent (L).

Half-Lives of Cu^{66}, Cu^{64}, Fe^{59}, and Ce^{144}

Robert P. Schuman and Anita Camilli
Knolls Atomic Power Laboratory, Schenectady, New York
(Received August 7, 1951)

IN the course of our work, the half-lives of Cu^{66}, Cu^{64}, Fe^{59}, and Ce^{144} have been determined with considerable precision. The half-lives of the copper isotopes were determined on samples of electrolytic copper foil irradiated with water-moderated radium beryllium neutrons. The Fe^{59} sample was from a cyclotron irradiation unit, free of Fe^{55}, obtained from the Isotopes Division of the Atomic Energy Commission. The Ce^{144} sample was obtained by the radiochemical isolation of cerium from fission products after a decay of over one year so that the sample would be free of Ce^{141}. The counting has been done with a flow proportional counter (nucleometer) using an external sample counter. All counts were checked against a standard to insure a constant counting efficiency.

We have obtained a half-life of 5.12±0.05 min for Cu^{66}, in good agreement with the values of 5.18±0.10 min by Cameron and Katz,[1] and 5.05 min by L. Meitner,[2] but differing from the value of 4.34±0.03 min by Silver.[3] An irradiation was made of a Cd-shielded Cu foil which showed that most of the activation was due

to thermal neutrons; the Cd-shielded Cu foil also showed a 5-min half-life. Our value for the Cu^{64} half-life is 12.74±0.07 hr, in agreement with the present literature.[4]

Our value for the half-life of Fe^{59} is 45.1±0.2 days. The decay of the sample has been followed for over eight half-lives, and does not show any tendency to tail out into a longer half-life. The Ce^{141} sample has been followed for two half-lives, and shows a half-life of 282±3 days. Our half-life for Fe^{59} is slightly lower than the published values of 45.5 days[5] and 46.3 days.[4] The half-life of Ce^{144} is in general agreement with the literature values of 275 days, 290 days, and 310 days.[4]

We have also followed samples of Fe^{55} and Pm^{147} for a period of one year. The Fe^{55} sample was obtained from the Isotopes Division of the Atomic Energy Commission, and the Pm^{147} sample was radiochemically isolated from fission products. Both samples were shown to be radiochemically pure by absorption curves. The preliminary value of the Fe^{55} half-life is 3.0±0.15 years, in good agreement with the better value of 2.94 yr.[6] The Pm^{147} half-life is 2.6±0.2 years, compared with literature values of 2.26 years[7] and 3.7 years.[4]

[1] A. G. W. Cameron and L. Katz, Phys. Rev. **80**, 904 (1950).
[2] L. Meitner, Arkiv Mat. Astron. Fysik **33A**, No. 3 (1946).
[3] L. M. Silver, Phys. Rev. **76**, 589 (1949).
[4] *Nuclear Data*, National Bureau of Standards Circular 499 (1950).
[5] J. Govaerts, Bull. Soc. Roy. Sci. Liege **12**, 555 (1943).
[6] G. L. Brownell and C. J. Meletskos, Phys. Rev. **80**, 1102 (1950).
[7] Ingram, Hayden, and Hess, Phys. Rev. **79**, 271 (1950).

Microwave Paramagnetic Spectra of Iron Alum Salts*

C. A. Whitmer and R. T. Weidner
Department of Physics, Rutgers University, New Brunswick, New Jersey
(Received August 10, 1951)

THE paramagnetic resonance absorption at 9375 Mc/sec by diluted single crystals or iron ammonium alum and iron potassium alum has been observed for temperatures of 4°, 77°, and 293°K. The spectra show that the splitting of the ground state of the iron ion cannot be accounted for by assuming a crystalline electric field of purely cubic symmetry and that the iron and potassium salts have markedly different spectra.

Figure 1 shows the absorption spectra for iron ammonium alum. The single crystals, grown from a mixed solution of iron ammonium alum and aluminum ammonium alum, contained one iron atom for every 38 aluminum atoms. The measurements were made with the dc magnetic field perpendicular to the (100) crystalline face because the spectra are most highly dispersed for this orientation. Earlier measurements[1] showed that the room-temperature spectra were in accord with the theoretical patterns deduced on the basis of the splitting of the ^6S state of the iron ion into a double degenerate and a quadruply degenerate level by a crystalline electric field of cubic symmetry. The theoretical spectrum fitting the observed absorption at 293°K is shown by vertical lines in Fig. 1. The main central peak was observed, however, to be relatively more intense than the theory predicted. A zero-field splitting of 0.032 cm^{-1} was deduced for the diluted samples. The five distinct peaks in the spectrum at 77°K are incompatible with the theoretical cubic-field spectrum for the choice of any single value of the zero-field splitting; the increased breadth of the spectrum over that for room temperature suggests, however, that the splitting increases in going from 293°K to 77°K.

The spectrum observed for iron ammonium alum at 4°K is in agreement with the measurements of Ubbink, Poulis, and Gorter,[2] who attribute the very weak resonances occurring at fields one-half the values for the main side peaks to ordinarily "forbidden" transitions in which the magnetic quantum number changes by ±2. The main side peaks show an asymmetry with respect to the main resonance; and the latter is relatively more intense and narrow than the main resonance observed at 293°K. If the asymmetry in the side peaks is disregarded, the cubic-field assumption

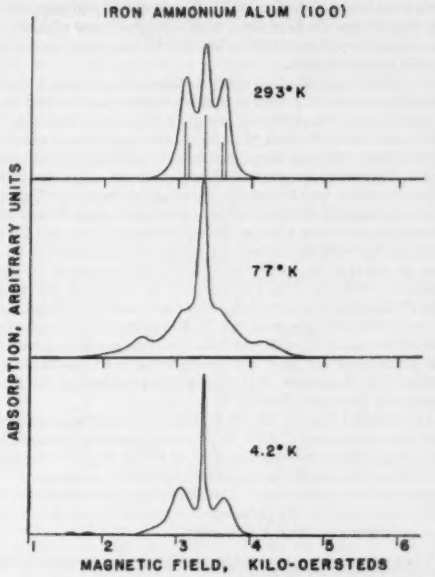

FIG. 1. Absorption spectra for diluted iron ammonium alum in the (100) orientation. The theoretical cubic-field spectrum is shown in the 293°K curve.

leads to the value 0.036 cm^{-1} for the zero-field splitting. This value is in clear disagreement with the value 0.14 cm^{-1}, which specific heat measurements[3] yield for the splitting for tempera-

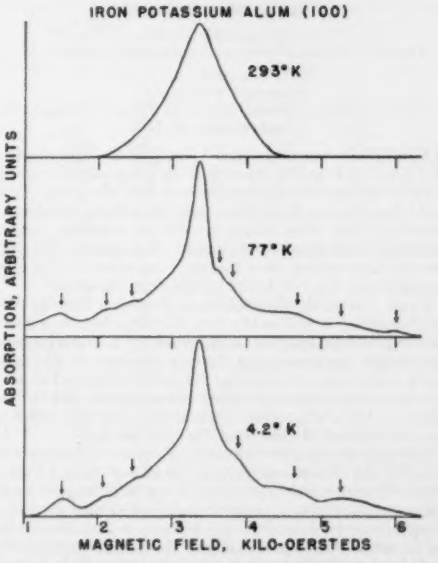

FIG. 2. Absorption spectra for diluted iron potassium alum in the (100) orientation. The arrows indicate the positions of absorption peaks.

tures from less than 1°K to 90°K. Benzie and Cooke[4] suggest, on the basis of specific-heat data, that a noncubic contribution to the crystalline electric field splits the ^6S iron state into three equally spaced doublets.

It might be expected that iron potassium alum, having a similar crystalline structure to that of iron ammonium alum, would show absorption spectra similar to those of the ammonium salt. In other salts the chief effect of replacing the ammonium radical by a potassium atom has been a relatively small change in the zero-field splitting but no marked difference in the character of the crystalline field, and hence, the paramagnetic spectra.[5] Figure 2 shows the spectra observed for iron potassium alum diluted with aluminum potassium alum at the same temperatures and for the same crystal orientation used for the ammonium salt. No structure is observed at room temperature. The positions of broad peaks at 77°K and 4°K are indicated by arrows in the figure. The 77°K and 4°K spectra differ essentially only in the appearance of two additional peaks in the 77°K spectrum. Although these spectra are markedly different from the corresponding spectra for the ammonium salt and are incompatible with the cubic-field assumption, it appears that the splitting undergoes no severe changes in the region from 77°K to 4°K.

Unpublished work by Mr. P. E. Baker of this laboratory shows that for a frequency of 9375 Mc/sec aluminum ammonium alum has a large dielectric absorption peak at 175°K, whereas aluminum potassium alum shows no appreciable dielectric absorption in the region of this temperature. This effect may be relevant to the differences found in the paramagnetic spectra for the ammonium and potassium varieties of iron alum.

* This work has been supported by the ONR, by the Rutgers University Research Council, and by RCA.

[1] Weidner, Weiss, Whitmer, and Blosser, Phys. Rev. **76**, 1727 (1949).
[2] Ubbink, Poulis, and Gorter, Physica **17**, 213 (1951).
[3] J. H. Van Vleck, Am. J. Phys. **18**, 495 (1950).
[4] R. J. Benzie and A. H. Cooke, Proc. Phys. Soc. (London) **A63**, 213 (1950).
[5] Whitmer, Weidner, Hsiang, and Weiss, Phys. Rev. **74**, 1478 (1948).

Behavior in Pb of the Nucleonic Component in the Stratosphere*

MAURICE M. SHAPIRO
Nucleonics Division, Naval Research Laboratory, Washington, D. C.
AND
ANDREW F. GABRYSH
Department of Physics, Catholic University of America, Washington, D. C.
(Received August 13, 1951)

PREVIOUS communications[1,2] described an experiment (denoted by I) on the behavior of the star-producing radiation in the stratosphere as it passes from air into Pb. It was pointed out[2,3] that the transition effects must be strongly influenced by geometry, since these effects are due to secondary processes generated inside the absorber. Results which support this conclusion and also confirm other findings in experiment I, have been obtained from two "Skyhook" balloon flight exposures.[4]

Figure 1 shows the Pb block inside of which 6 Eastman NTB3 (ultrasensitive) emulsions 15×5 cm and 200μ thick were inserted vertically in a central slot. As in experiment I, this arrangement permitted a measurement of the star frequency at any desired depth in the block. The absorber differed from that in I in having (a) no covering slab of Pb above the emulsions, and (b) more restricted lateral dimensions, particularly in the base which was narrower, instead of wider, than the upper portion.

The apparatus floated for 8 hours at a pressure altitude of 1 to 4 cm Hg, the time-average pressure "at ceiling" being 2.3 cm Hg. Data used in this study were collected only from the upper (wider) portion of the block, in order to avoid—or at least to reduce—complications introduced by rays incident at large zenith angles. As an index of star size we adopted the number of "black" and "gray" tracks (grain density>1.4 times minimum). σ-stars were excluded.

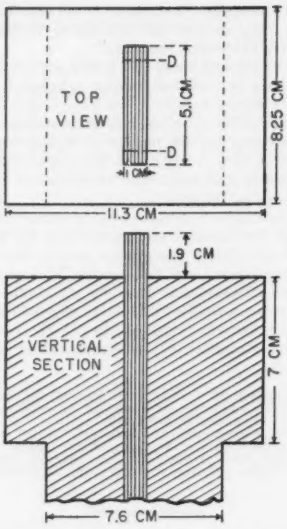

FIG. 1. Pb absorber, showing top view and vertical section cutting through the emulsions. In scanning the photoplates, star data were gathered only from the region *DD* in any horizontal plane, and from the upper portion of the Pb block. Zero-point data were collected from the region directly above the Pb. Total depth of the block was 12.5 cm.

Figure 2, based on 934 stars, gives the relative frequency as a function of depth in the Pb for stars with ≥ 3 prongs and also for small (3- to 6-prong) stars. A prominent feature is the peak at ≈ 27 g/cm^2, a depth which agrees closely with that observed in two other experiments.[1,5] This agreement is not unexpected, despite the diverse geometries employed, since the main differences between them occurred at depths >40 g/cm^2. At shallow depths, the several Pb absorbers were more nearly alike. Another interesting, though minor, feature is the indication of a slight initial decrease in frequency of the small stars, which corroborates a similar observation in I. A possible explanation of this effect was suggested in reference 2.

The major difference between the present results and those in I is the absence of the broad peak at $\approx$60–70 g/cm^2 which in the previous results suggested that a saturation of the star-producing

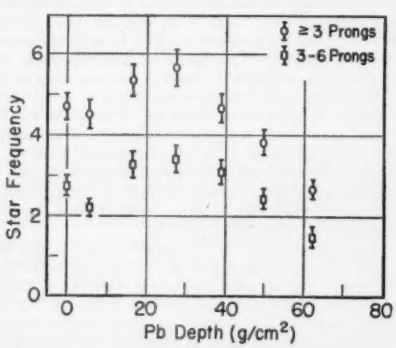

FIG. 2. Transition effect curves obtained using the absorber in Fig. 1, for (a) stars regardless of size (circles), and (b) small stars alone (squares). Star frequency is expressed in arbitrary units. Probable errors, based on counting-statistics alone, are given.

secondaries sets in at about this depth (see Fig. 3 of reference 1). This difference probably stems from the lack of a massive Pb base, such as that in I, in which a substantial development of the nucleonic cascade could take place. If this interpretation is correct, it supports the view that a considerable fraction of the secondary star-producing radiation generated in the Pb has an upward component.[5,6]

In the second stratosphere exposure, the mean pressure altitude above 70,000 ft for 7 hours was 2.5 cm Hg. A particularly simple geometry was involved: a massive horizontal Pb slab, 30×30 ×2.15 cm, was sent aloft for a counter experiment.[7] This provided an opportunity to measure the rates of star production in a central location above and below the Pb slab. We used NT4 emulsions, 200μ thick, made by the Kodak Company in England.

The following ratios of star frequencies below/above the 2.15 cm Pb were observed: for stars with $\geq$3 prongs, 1.74±0.16; for small ($\leq$6-fold) stars, 1.86±0.22; for large (>6-fold) stars, 1.55±0.22. Probable errors are given throughout. Our results showed no significant difference between vertical and horizontal plates above the lead. These values of the ratios are larger than those obtained in our absorbers having smaller lateral dimensions. They agree better with ratios observed by Blau *et al.*,[8] using Ilford *C.2* emulsions in a rather shallow absorber.

We are grateful to Mr. Bertram Stiller for his able help with the flights and the emulsion processing, and to Mr. Francis Booth for scanning some of the plates. It is a pleasure to acknowledge the support and advice of Dr. F. N. D. Kurie. One of us (A. F. G.) is indebted to Professor F. L. Talbott for guidance and encouragement.

[4] Phys. Rev. **83**, 874 (1951).
[5] Shapiro, Stiller, Birnbaum, and O'Dell, Phys. Rev. **83**, 455 (1951).
[6] Maurice M. Shapiro, Phys. Rev. **83**, 456 (1951).
[7] Dallaporta, Merlin, and Puppi, Nuovo cimento **7**, 99 (1950).
[8] Chronologically earlier than those in reference 1. These flights, arranged with the help of the ONR and the General Mills Laboratories, took place on June 21, 1949 and October 15, 1949 at geomagnetic latitude 56°N.
[9] In I (reference 1), the evidence for this peak, though fairly good, was not conclusive. The authors nevertheless felt justified in referring to it as a definite effect because (a) the confirmatory evidence presented here was known to them, and (b) a similar maximum had been observed at ≈23 g/cm² by Blau, Nafe, and Bramson, Phys. Rev. **78**, 320(A) (1950).
[10] J. J. Lord and M. Schein, Phys. Rev. **75**, 1956 (1949).
[11] By Dr. G. J. Perlow, whose kind cooperation is gratefully acknowledged.
[12] Marietta Blau (private communication).

Statistical Significance of Small Samples of Cosmic-Ray Counts

VICTOR H. REGENER
Department of Physics, University of New Mexico, Albuquerque, New Mexico
(Received August 13, 1951)

IT is occasionally desirable in cosmic-ray research that conclusions of a tentative nature be drawn from a small total number of counts obtained in a counter tube experiment. When the number n of measured counts is large, it is customary to indicate the statistical uncertainty by quoting precision limits located at $n\pm\sqrt{n}$. This procedure is usually described as giving a probability of 0.1587, or roughly 16 percent, that the unknown average number of counts a for the duration of the experiment lies below the lower precision limit $n-\sqrt{n}$, and also a probability of 16 percent that a lies above $n+\sqrt{n}$. When n is small, this use of the standard deviation of a gaussian distribution should, of course, be replaced by a similar prescription based on the less easily manipulated poisson distribution, but the quoted statement of probability also contains the illegitimate assumption of a constant *a priori* probability for the existence of the average count a on both sides of the value n. This difficulty is here briefly examined for the poisson distribution, and appropriate precision limits for low values of n are given.

If the poisson probability $W_n=a^n e^{-a}(n!)^{-1}$ for the occurrence of just n counts could be interpreted as being a normalized probability density distribution $W_n(a)$ for the average count a, an integration over $W_n(a)$ between appropriate limits of a would appear to give the probability that the average count lies between these limits. Inherent in such an interpretation is the illegitimate assumption that all average counts a contained between arbitrary limits are *a priori* equally probable or, in other words, that physical reality contains a population of counting rates which is known to be uniformly dense. Fisher[1] made it clear that ignorance of an *a priori* distribution does not justify the assumption that it is constant any more than that it is of any other form.[2]

A legitimate procedure for the assignment of precision limits has been suggested by Fisher.[3] Consider, for example, a total measured count $n=3$. It is possible to determine a value a_1 for a hypothetical average count which lies so far below 3 that the total probability for the actual count to fall anywhere below 3 assumes a specified value p. Above 3, another value a_2 can be determined so that the total probability for the count to fall anywhere above 3 assumes again the value p. If p is made 0.8413, the result is 1.37 for a_1, and 5.92 for a_2. The fiducial limits a_1 and a_2 should replace the customary precision limits for small values of n.

TABLE I. Poisson fiducial limits and normal limits for $p=0.8413$, $x_p=1.00$.

Lower limit $d_0=0$				Upper limit $d_0=1.00$		
Normal	d	Poisson fiducial	n	Poisson fiducial	d	Normal
...	...	0	0	1.84	1.84	0
0	0.17	0.17	1	3.30	1.30	2.00
0.59	0.12	0.71	2	4.64	1.23	3.41
1.27	0.10	1.37	3	5.92	1.19	4.73
2.00	0.09	2.09	4	7.16	1.16	6.00
3.55	0.07	3.62	6	9.58	1.13	8.45
6.84	0.05	6.89	10	14.26	1.10	13.16
15.53	0.04	15.57	20	25.54	1.07	24.47
42.93	0.02	42.95	50	58.11	1.04	57.07

TABLE II. Poisson fiducial limits and normal limits for $p=0.9500$, $x_p=1.645$.

Lower limit $d_0=0.57$				Upper limit $d_0=1.57$		
Normal	d	Poisson fiducial	n	Poisson fiducial	d	Normal
...	...	0	0	3.00	3.00	0
...	...	0.05	1	4.74	2.09	2.65
...	...	0.35	2	6.30	1.98	4.32
0.15	0.67	0.82	3	7.75	1.90	5.85
0.71	0.66	1.37	4	9.15	1.86	7.29
1.97	0.64	2.61	6	11.84	1.81	10.03
4.80	0.63	5.43	10	16.96	1.76	15.20
12.64	0.62	13.26	20	29.06	1.70	27.36
38.37	0.59	38.96	50	63.28	1.65	61.63

These fiducial limits are computed by evaluating A in the expression

$$P=e^{-A}\sum_{m=0}^{N}A^m(m!)^{-1},$$

with $P=p$, $N=n-1$, $A=a_1$ in case of the lower limit a_1, and with $P=1-p$, $N=n$, $A=a_2$ in case of the upper limit a_2. The identity

$$1-P=(N!)^{-1}\int_0^A A^N e^{-A}dA=F$$

allows[4] the use of published tables for the incomplete factorial function F. Tables I and II give poisson fiducial limits for certain values of n from zero to 50, as computed from interpolations of Pearson's table[5] with $p=0.8413$ (Table I) and $p=0.9500$ (Table II). For comparison, the tables also contain conventional precision limits based on the gaussian distribution, here called normal limits, where the probability defined by the statement at the beginning of this note now corresponds to $1-p$. The poisson fiducial limits differ from the normal limits by an additive amount d

which approaches a constant value d_0 for large values of n. For $p=0.8413=1-0.1587$ (Table I) they approach the normal limits computed from the standard deviation. The asymptotic values d_0 can be computed explicitly; for the lower limit one obtains $d_0=(x_p^2-1)/3$ and for the upper limit $d_0=(x_p^2+2)/3$, where x_p depends on the choice of p and is defined by the appropriate expression for the gaussian normal limits $n\pm x_p\sqrt{n}$.

The author is indebted to Roy Thomas for valuable discussions.

[1] R. A. Fisher, Proc. Cambridge Phil. Soc. **26**, 528 (1930).

[2] If a constant *a priori* distribution were accepted as legitimate, it would discredit the established custom of quoting, for the most likely average number of counts, the observed number n which is located where the probability density function $W_n(a)$ has its maximum. Instead, the median or the average value of $W_n(a)$ should be used (Fisher, reference 1); the most likely value for a would then have to be given as approximately $n+2/3$ if the median were chosen (2/3 is exact for large values of n), or as $n+1$ if the average were chosen. However, the argument should be confined to the statement that the probability for the occurrence of just n counts is highest for that average count which is numerically equal to n; this supports the customary method for choosing the most likely value of a.

[3] R. A. Fisher, Econometrica **3**, 353 (1935).

[4] It can be seen that this means, in the case of the upper limit, a return to the integration over $W_n(a)$ which was rejected above when it was to have served the original purpose of evaluating conventional precision limits. On the other hand, the evaluation of the lower limit now consists of an integration over $W_{n-1}(a)$.

[5] K. Pearson, *Tables of the Incomplete Gamma-Function* (Cambridge University Press, London, 1934).

Resonance in the Neutron Cross Section of Lithium*

P. H. Stelson and W. M. Preston
Laboratory for Nuclear Science and Engineering, Massachusetts Institute of Technology, Cambridge, Massachusetts
(Received August 6, 1951)

THE total neutron cross section of lithium from 20 to 1400 kev has been measured by Adair using a neutron energy spread of about 20 kev.[1] A large resonance was found at 270 kev, which was interpreted as an excited state in Li^8 with total angular momentum $J=2$, formed by $l=1$ neutrons. In connection with measurements of the total cross section of nitrogen, using the compound LiN_3, we have recently remeasured the total cross section of lithium. We find a higher value for the maximum cross section of this resonance, which agrees well with a $J=3$ assignment.

The total cross section of lithium was measured using neutrons produced by the Li(p, n) reaction, which are monoenergetic in this energy range. The first run was made with 10-kev resolution using a metallic lithium scatterer, one inch in diameter and 0.472×10^{24} nuclei/cm^2 thick, encased in a thin-walled (5 mil) steel cylinder. The scatterer was placed a mean distance of 12 cm from the target in the forward direction and the detector, a one-inch diameter, propane gas counter was placed a mean distance of 28 cm from the target. The data are shown in Fig. 1 as circles. The second run, indicated by the solid dots, was done with 5-kev resolution under the same geometrical conditions but with a scatterer of 0.118×10^{24} nuclei/cm^2 thickness. Corrections for target thickness were applied to the neutron energies. The incident proton energies are based on the $Li^6(p, n)$ threshold calibration point of 1.882 Mev. A scattering-in correction was applied which increased the cross-section values by 2 percent in the case of the long scatterer and was negligible for the short scatterer. The resulting data are shown in Fig. 1.

Since the first excited state of the Li^7 nucleus is 479 kev above the ground state, one can assume that elastic scattering is the only process contributing to the cross section. The neutron energies are low enough so that only $l=0$ neutrons will contribute to the potential scattering, and, in fact, the value given by theory using the nuclear radius $R=1.5A^{\frac{1}{3}}\times10^{-13}$ cm agrees well with the value indicated by experiment. Since a dip due to interference is not observed near the resonance, one deduces that the resonance is not excited by $l=0$ neutrons. Therefore the cross section in the neighborhood of the resonance is given by:

$$\sigma_{n,n}=\pi\lambda^2(2I+1)G_{Jl}\frac{\Gamma_n^2}{(E-E_r)^2+\Gamma_n^2/4}+\sigma_{\text{potential}}, \qquad (1)$$

using the conventional notation.[2] The maximum cross-section value of the resonance depends on the magnitude and orientation of the angular momentum vectors s, l, and $\mathbf{I}$. For a given configuration of the vectors s, $\mathbf{I}$, and l to form the compound state of angular momentum J, the statistical weight factor is

$$(2J+1)/[(2I+1)(2l+1)(2s+1)]. \qquad (2)$$

There are cases where two different configurations of the vectors s, I, and l can form the same resultant J vector. One then has to decide whether the correct value is given by expression (2) or by twice that value, i.e., whether the states are degenerate. The question of the proper statistical weight factor or the strength of the spin-orbit coupling makes the large resonance in lithium especially interesting.

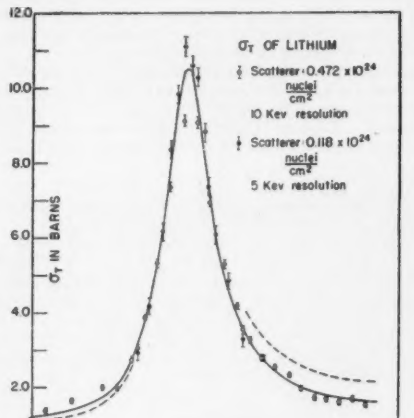

FIG. 1. The total cross section of lithium. The solid curve is calculated from theory for a $J=3$, $l=1$ assignment. The dashed curve is calculated for a $J=3$, $l=2$ assignment. Neutron energies are corrected for target thickness.

Adair pointed out that the resonance probably has too large a width to be attributed to $l=2$ neutrons. In addition we find that the shape (asymmetry) of the resonance does not fit an $l=2$ assignment (see below). Therefore, taking the resonance as excited by $l=1$ neutrons, the possible values of J are 0, 1, 2, or 3 since $s=\frac{1}{2}$ and $I=\frac{3}{2}$. Using the statistical weight factor (2) the $\sigma_{\max}-\sigma_{\text{potential}}$ values for these different J values are calculated as 1.3, 4.0, 6.7, and 9.4 barns, respectively, where $(E_r)_{\text{lab}}$ is taken as 256 kev and a correction is applied for the 92.5 percent Li^7 isotopic abundance. The states with $J=1$ or 2 can be formed by two different relative orientations of the vectors s, l, and I and if these are degenerate the $\sigma_{\max}-\sigma_{\text{potential}}$ values are 8.0 and 13.4 barns. From Adair's curve one obtains the value of 6.8 barns, which would indicate $J=2$ and no degeneracy. However, considering the resolution employed, one would expect the true value to be somewhat larger, thus perhaps supporting the assignment $J=1$ and degeneracy.

The best curve drawn through our experimental points taken with the 5-kev resolution gives a value for $\sigma_{\max}-\sigma_{\text{potential}}$ of 10.0 barns, which agrees reasonably well with the calculated value of 9.4 barns for $J=3$. Unfortunately, this compound state is formed

by only one configuration of the vectors s, l, and I and therefore cannot yield information on the strength of spin-orbit coupling. The solid curve drawn in Fig. 1 is calculated from formula (1) taking $\sigma_{\text{potential}}=1.1$ barns, $(E_r)_{\text{lab}}=256$ kev, $J=3$, $l=1$, and $(\Gamma_n)_{\text{lab}}=40$ kev. In computing the curve, the variation of λ and Γ_n with energy was taken into account. It is seen that the asymmetry of the resonance is nicely accounted for by the variation with energy of these two quantities. The dashed curve shows the behavior of the calculated curve away from resonance (fitted at resonance) for the assignment $J=3$ but $l=2$.

An almost coincident resonance ($E_n=270$ kev) has been reported for the $Li^6(n,\alpha)$ reaction.[5] If, by chance, there were a large coincident resonance in the σ_T of Li^6, calculations indicate that its maximum value could not exceed $\sim$10 barns. When multiplied by the relative abundance of Li^6 (7.5 percent) it would contribute, at most, 0.75 barn to the σ_T of lithium at the peak of the resonance. The presence of such a resonance would, therefore, tend to improve the agreement of the calculated and experimental curves.

* This work was jointly supported by the ONR and the Bureau of Ships.
[1] R. K. Adair, Phys. Rev. **79**, 1018 (1950).
[2] R. K. Adair, Revs. Modern Phys. **22**, 249 (1950).
[3] J. M. Blair *et al.*, quoted by Goldsmith *et al.*, Revs. Modern Phys. **19**, 259 (1947).

On the Nature of the Superconducting State*

LASZLO TISZA
Department of Physics and Research Laboratory of Electronics, Massachusetts Institute of Technology, Cambridge, Massachusetts
(Received August 6, 1951)

IN a recent paper[1] the author advanced the view that the discussion of superconductivity requires the use of many-electron wave functions. The superconducting transition was considered to be somewhat similar to an order-disorder transformation, with a characteristic difference. Instead of being frozen in a definite position in the crystal, the superlattice describing the ordered state is supposed to resonate, say, among ω-positions equivalent under the translation group of the crystal. An external electric or magnetic field would induce a supercurrent provided $\omega\geqq 3$. The case $\omega=2$ corresponds to an insulating state.

The superlattice itself was attributed to the electronic distribution alone; in other words the vibrations of the ions around the ideal lattice positions were ignored. However, recent experimental[2] and theoretical work[3] has provided convincing evidence that the interaction of the electrons with the lattice vibrations constitutes an essential aspect of superconductivity. Therefore, the study of the many-electron eigenfunctions has been reopened from a more systematic point of view. A detailed paper is now completed for publication, the results of which may be summed up as follows.

Fundamentally a crystal is a collection of electrons and nuclei. The usual separation of the electronic and vibrational wave functions is based on the adiabatic approximation.[4] One solves the electronic eigenvalue problem for fixed nuclear positions, and the electronic energy provides the potential for the nuclear vibrations. The validity of this method depends on the assumption that the electronic level is nondegenerate and its separation from the next one is large compared to the spacing of the nuclear states. This condition is not satisfied for the case of metals; hence a rigorous quantitative theory will have to overcome unusual difficulties.

We have applied symmetry considerations to obtain a qualitative insight into the possible coupling cases. The usual method of considering the metal as a mixture of an electron gas and a phonon gas appears only as one limiting case. This state may become unstable, resulting in a phase transition into a state exhibiting a resonating superstructure. This has the same symmetry properties as the superstructure postulated in reference 1 and could be used in a similar fashion to explain superconductivity and the well-known increase of the resistivity of certain metals at low temperatures. On the other hand, the dynamic properties of the superstructure are essentially different from those considered earlier. The superstructure is produced by the interlocking of the electronic and nuclear fluctuations; the coupling is so strong that it is no longer possible to consider the nuclear vibration as occurring in a fixed potential.

The present ideas are compatible with the Fröhlich-Bardeen conception[5] of the nature of the interaction responsible for superconductivity. However, the latter theories lead only to a short-range order, whereas we were able to define a parameter of long-range order marking the emergence of the above-mentioned superstructure.

The correspondence between the experimental facts and the theoretical possibilities provided by the symmetry consideration is suggestive. The conclusions obtained can be submitted also to a severe experimental test. Our postulated superlattice should give rise to x-ray superstructure lines. Existing x-ray investigations[6] are scanty and were carried out in view of finding variations in the lattice constant. Hence an x-ray study of the superconducting transition would be of considerable interest.

* This work was supported in part by the Signal Corps, the Air Materiel Command, and the ONR.
[1] L. Tisza, Phys. Rev. **80**, 717 (1950).
[2] E. Maxwell, Phys. Rev. **78**, 477 (1950); Reynolds, Serin, Wright, and Nesbitt, Phys. Rev. **78**, 487 (1950).
[3] H. Fröhlich, Phys. Rev. **79**, 845 (1950); Proc. Phys. Soc. (London) **A64**, 129 (1951); J. Bardeen, Phys. Rev. **80**, 567 (1950), **81**, 469, 829 (1951).
[4] M. Born and R. Oppenheimer, Ann. Physik **84**, 457 (1927).
[5] W. H. Keesom and H. Kamerlingh Onnes, Leiden Comm. **174b** (1924).

A Search for Charge-Exchange Scattering of π^+ Mesons*

RICHARD WILSON† AND JOHN P. PERRY
University of Rochester, Rochester, New York
(Received August 8, 1951)

EXPERIMENTS with photographic plates[1,2] showed meson tracks which stopped without any apparent nuclear interaction. These could be attributed to charge-exchange scattering events or to stars where only fast neutrons were emitted. Moreover, charge-exchange scattering need not always lead to events of this type, for some of the scatterings might be inelastic and give rise to proton recoils.

We have made a direct search for charge-exchange scattering of 44-Mev π^+ mesons on Be and D_2O. The experimental arrangement is shown in Fig. 1. The scintillation crystals 1, 2, and 3 count

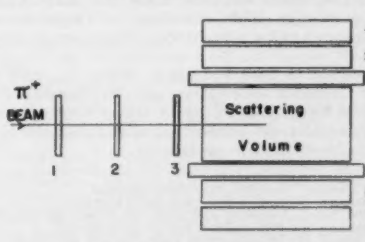

FIG. 1. Experimental arrangement.

the incident 50-Mev π^+ mesons defined as previously described.[3] After passing through the telescope, the mesons have a residual energy of 44 Mev and impinge upon targets of Be or D_2O. The Be target stops the mesons; that of D_2O slows them to 20 Mev. We look for pairs of γ-rays from π^0 decay by two scintillation counter telescopes 4, 5 and 6, 7, each with a Pb radiator of two radiation lengths thickness. The fraction of the total solid angle subtended is 0.06. We assume the scattering is isotropic.

Random counts are assessed by means of a channel which records the coincidence of a pulse from a coincidence in crystals 4, 5, 6, and 7 with a delayed meson pulse. This should indicate

TABLE I. Comparison of experimental result with that expected for one-millibarn cross sections for Be, D, and O.

Target	Number of mesons	Number of coincidences	Number of delayed coincidences	Estimated randoms	Residual effect	Expected for 1-mb cross section
Be	1.3×10^6	8	43	4.7	3.3 ± 3	3.7
D$_2$O	0.6×10^6	5	26	2.9	2.1 ± 3	1.5 from deuterium 0.75 from oxygen

the main contribution to random events, although it should be regarded as giving a lower limit. The resolving time in this channel is about 10 times greater than in the "instantaneous" channel.

The results are shown in Table I. They indicate that upper limits on the cross section for charge-exchange scattering may reasonably be set at 2 millibarns for Be, 3 mb for D, and 6 mb for O.

We have checked the operation of the apparatus before and after each run by counting cosmic-ray mesons in counters 4, 5, 6, and 7 in coincidence in the expected numbers. The counters are therefore sufficiently sensitive to detect minimum ionization particles. The various delays have been checked both by artificial pulses and by placing one of the crystals which normally was in the meson telescope so that cosmic-rays were counted by it in coincidence with counters 4, 5, 6, and 7.

Charge-exchange scattering has been calculated for $\pi^+ + n$ and for $\pi^- + p$ under various assumptions about meson theory.[4] We consider that at least one neutron in the Be^9 nucleus may be regarded as free because of the energy balance in the reaction $\pi^+ + Be^9 \rightarrow B^9 + \pi^0$. Evidence for this comes from the anomalously high production of π^- by γ-rays according to the reaction $\gamma + Be^9 \rightarrow B^9 + \pi^-$.[5] On the other hand, the Pauli exclusion principle may reduce the cross section in O^{16} appreciably because of the energy balance in the reaction $\pi^+ + O^{16} \rightarrow F^{16} + \pi^0$. The exclusion principle is also expected to reduce the cross section in D by a sizeable factor below the free neutron cross section.[6] Accordingly, the highest cross section would be expected in Be for π^+ mesons.

The low upper limit which we find for the charge exchange cross section in Be for 44-Mev π^+ mesons is to be compared with the total scattering cross section (direct plus charge exchange) of 13.3 mb which Chedester *et al.*[7] find for 85-Mev π^- mesons on protons. This would imply that the chief contribution to the 13.3 mb comes from direct scattering unless the charge-exchange cross section increases rapidly with energy. It is hoped to repeat our measurements with a more intense π^+ beam now in preparation.

We should like to thank Professor R. Wilson of Cornell University for the loan of the beryllium used, Mr. Donald L. Clark for the use of his electronic equipment, the cyclotron crew under Mr. F. Palmer for the bombardments, and Professor R. E. Marshak for his continual encouragement.

* This work was assisted by the AEC.
† Now at Stanford University, Palo Alto, California.
[1] H. Bradner and B. Rankin, Phys. Rev. **80**, 916 (1950).
[2] Bernardini, Booth, Lederman, and Tinlot, Phys. Rev. **80**, 924 (1950).
[3] Clark, Roberts, and Wilson, Phys. Rev. (to be published).
[4] Ashkin, Simon, and Marshak, Prog. Theor. Phys. **V**, 634 (1950).
[5] R. M. Littauer and D. Walker, Phys. Rev. **83**, 206 (1951).
[6] W. Cheston, private communication.
[7] Chedester, Isaacs, Sachs, and Steinberger, Phys. Rev. **82**, 958 (1951).

Theory of Internal Conversion

H. R. COISH
Mathematical Physics Department, University of Manitoba, Winnipeg, Canada
(Received August 13, 1951)

TRALLI and Goertzel,[1] under the above title, have recently set up for the first time the completely quantum-mechanical int rnal conversion problem, and have solved it in successive approximations. They verify the first-order correction to N_q, the rate of radiation of photons, which Taylor and Mott[2] obtained by semiclassical correspondence principle methods. In this communication we call attention to further corrections, of the same order in e^2, to the internal conversion coefficient N_e/N_q, which are obtained when the approximation for N_e is extended to the same relative order in e^2 as N_q.

Before the higher order expression for N_e can be written down correctly, it is necessary to modify the expressions (3q) and (3r) of TG for N_e and N_q—an evident necessity, since they do not satisfy the conservation equation,

$$N_e + N_q = 1. \tag{1}$$

To remove this inconsistency we re-examine the evaluation

$$U_{0f} = U_{f0}^* \tag{2}$$

given in TG.[3]

In terms of the matrix elements $(2f)$ of TG, Eq. (B3′) of TG may be written[4]

$$U_{f0} = i\pi H_{\omega k}^{(1)} H_{\omega 0}. \tag{3}$$

Direct comparison of the defining expressions for U_{f0} and U_{0f} (Appendix B, Secs. 1 and 4, of TG) shows U_{0f} to be the complex conjugate of $U_{f0}^{(-)}$, where $U_{f0}^{(-)}$ is obtained from U_{f0} by change of sign of η. This change of sign replaces the hankel function of the first kind by that of the second kind and reverses the sign of the whole expression:

$$U_{f0}^{(-)} = -i\pi H_{\omega k}^{(2)} H_{\omega 0} = U_{0f}^*. \tag{4}$$

We define

$$\gamma_2' = \pi U_{f0} U_{0f}, \tag{5}$$

which is complex. Redefining γ_2 as the real part of γ_2' validates Eqs. (3q), (3r) of TG for N_e, N_q and reinstates the conservation equation.

To extend the approximation for N_e we substitute Eqs. (3k), (3l) from TG into Eq. (3e) of TG.

In Eq. (3i) of TG this replaces H_{k0} by

$$H_{k0} + i\pi U_{f0} H_{k\omega} = H_{k0} - \pi^2 H_{\omega 0} \Sigma H_{k\omega} H_{\omega k}^{(1)}, \tag{6}$$

where Σ has been inserted as a reminder of the summation over the spin states of the continuum electron. For future convenience we display the form which Eq. (6) takes when $k = \omega$:

$$H_{\omega 0}[1 - \pi^2 \Sigma H_{k\omega} H_{\omega k}^{(1)}]. \tag{7}$$

The correction term in Eq. (7) is the TM correction term which is referred to in TG.

In addition to the integration over γ-ray energies, Eq. (3i) of TG involves a summation over multipoles. If we make the usual assumption that in H_{k0} nuclear selection rules annul all but one of these (called the principal multipole), then this term of Eq. (6) contributes but one term to (3i) of TG.

In $H_{k\omega}$ of Eq. (6) this assumption does not hold and there will be a (small) number of terms of the multipole summation to contend with. We will use Σ_L to distinguish this summation.

The consequence of all this is that, in the solution (3i′) of TG for C_E, the expression U_{f0} is replaced by

$$i\pi H_{\omega 0}[H_{Ek}^{(1)} - \pi^2 \Sigma H_{Ek} H_{k\omega} H_{\omega k}^{(1)}] \tag{8}$$

with $k = \omega$.

In Eq. (8) the order of writing factors has been chosen such that the summations refer to repeated subscripts which are adjacent.

Now, to the same relative order in e^2 the probabilities of observing electrons and photons are, respectively,

$$N_e = |\pi^2(\gamma_1+\gamma_2)^{-1}| H_{\omega 0}|^2 \Sigma\, |H_{\omega k}^{(1)} - \pi^2 \Sigma_L \Sigma H_{\omega k} H_{k\omega} H_{\omega k}^{(1)}|^2, \tag{9}$$

$$N_q = \pi(\gamma_1+\gamma_2)^{-1} |H_{\omega 0}|^2 |1 - \pi^2 \Sigma H_{k\omega} H_{\omega k}^{(1)}|^2, \tag{10}$$

and finally the internal conversion coefficient is

$$\frac{N_e}{N_q} = \pi^2 \Sigma \left| \frac{H_{\omega k}^{(1)} - \pi^2 \Sigma_L \Sigma H_{\omega k} H_{k\omega} H_{\omega k}^{(1)}}{1 - \pi^2 \Sigma H_{k\omega} H_{\omega k}^{(1)}} \right|^2. \tag{11}$$

It is not hard to show (though we refrain from doing so here) that to this order of approximation the effect of the TM correction term in the denominator of Eq. (11) is actually canceled by some of the terms in the numerator which correspond to the principal multipole.

[1] N. Tralli and G. Goertzel, Phys. Rev. **83**, 399 (1951), henceforth referred to as TG.
[2] H. M. Taylor and N. F. Mott, Proc. Roy. Soc. (London) **A142**, 215 (1933), henceforth referred to as TM.
[3] Appendix B, Sec. 4, of TG.
[4] The superscript (1) indicates that in the matrix element a hankel function of the first kind replaces the bessel function. Similarly, we signal the presence of a hankel function of the second kind by a superscript (2).

Gamma-Ray Spectrum and Yield from Tritium Bombarded by Protons*

R. S. Rochlin
Cornell University, Ithaca, New York
(Received August 10, 1951)

THE energy spectrum and yield of the gamma-radiation[1-5] from the reaction $T^3(p,\gamma)He^4$ has been measured with a gamma-ray pair spectrometer previously described.[4,6] Tritium absorbed in a zirconium target[4,7] was bombarded by 0.96±0.06-Mev protons from the Cornell cyclotron. The proton energy was kept below 1.02 Mev so as to avoid a large neutron background from the $T^3(p,n)He^3$ reaction.[8] The zirconium used was 5.5 mg/cm² thick, and contained 0.47±0.05 atom of T^3 per atom of Zr throughout the bombardment. The gamma-rays were observed at an angle of 54.5 degrees to the proton beam in the laboratory system.

The energy region from 3 to 22 Mev was surveyed, using a 0.003-inch Pb radiator in the spectrometer. A single line was observed at an energy of 20.4±0.2 Mev. To obtain better resolution, additional data were taken around this line with a 0.002-inch Cu radiator. The data for both radiators are plotted in Fig. 1.

Correcting for the effective mean energy of the protons in the "thick" Zr target,[9] the doppler effect, and the recoil of the compound nucleus, we obtain a Q-value for this reaction of 19.7±0.3 Mev. By calculating the weighted mean Q-values from several independent cycles of more precise measurements on other nuclear reactions, Li *et al.*[10] have obtained 19.802±0.008 Mev for this Q-value.

The counting efficiency of the spectrometer decreases rapidly for lower gamma-ray energies for the following reasons: (a) the cross section for pair production in the radiator decreases; (b) each counting channel counts a smaller energy interval; (c) more electrons are lost through vertical multiple scattering in the radiator; (d) the resolution of the spectrometer decreases, due mainly to horizontal multiple scattering in the radiator. (The last reason is of importance only when considering the height of observed peaks, rather than the area under them.)

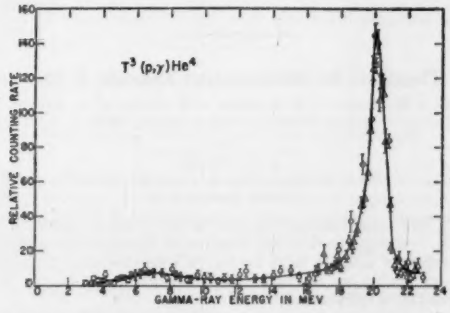

FIG. 1. Survey of the tritium gamma-ray spectrum. The circles represent data taken with a 0.003-in. Pb radiator and the triangles represent data taken with a 0.002-in. Cu radiator. Data for the two radiators are normalized to the same peak height. Standard deviations are indicated for each point.

Correcting[8] for these effects, it is estimated that any gamma-radiation from the tritium near 10 Mev and ¼ as intense as the 20.4-Mev line would have been observed if present. Near 6 Mev a line would have been observed if about 1.5 times as intense, and near 3 Mev only if roughly 40 times as intense.

The background at low energies shown in Fig. 1 is believed to come mainly from degraded radiation arising in the Pb collimator. The cosmic-ray shower background and accidental coincidences were found to be negligible.

The observed line width at half-maximum, which is about 5.4 percent in the case of the 0.002-inch Cu radiator, can be accounted for entirely by the resolution of the spectrometer. The resolution would not be significantly improved by the use of a thinner tritium target, since the target used caused a spread of only 1.1 percent of the total gamma-ray energy.

The yield from the $T^3(p,\gamma)He^4$ reaction was measured relative to the 17.6-Mev gamma-rays from the $Li^7(p,\gamma)Be^8$ reaction, using the pair spectrometer. The tritium-zirconium target was replaced by a thick lithium metal target. The proton energy and angle of observation were kept at the values given in the first paragraph. The proton beam was measured with a current integrator, and the two identical target holders were designed to eliminate error due to secondary electron emission. Correcting for the variation of spectrometer efficiency with energy, a (T+Zr)/Li yield ratio of 0.016±0.004 was found.

Argo *et al.*[1] made a similar yield comparison, except that they observed at 90 degrees and used a detector which counted the 14.8-Mev lithium line also. Adjusting[11,12] our value to their conditions would give a ratio of 0.012, while they[12] obtain 0.043. This discrepancy may be partly explained by a possible difference in the T^3/Zr atomic ratio in their target and ours.

From the lithium data of Fowler and Lauritsen,[11] the absolute yield of our tritium-zirconium target at 90 degrees was about 3×10^{-11} gamma-ray per steradian per proton. A $\sin^2\theta$ angular distribution[1] was assumed for the tritium gamma-rays.

In addition to its intrinsic interest for a study of the excited He^4 nucleus, the $T^3(p,\gamma)$ reaction should prove widely useful as a gamma-ray source. It provides the highest energy gamma-rays of any known nuclear reaction, is probably monoenergetic, and under suitable bombarding conditions can provide gamma-rays of an energy known to about 0.04 percent.

I want to thank Professor B. D. McDaniel for many valuable discussions.

* Work assisted by the ONR.
[1] Argo, Gittings, Hemmendinger, Jarvis, and Taschek, Phys. Rev. **78**, 691 (1950).
[2] R. S. Rochlin and B. D. McDaniel, Phys. Rev. **82**, 298(A) (1951).
[3] C. E. Falk and G. C. Phillips, Phys. Rev. **83**, 468 (1951).
[4] R. L. Walker and B. D. McDaniel, Phys. Rev. **74**, 315 (1948).
[5] R. L. Walker, Ph.D. thesis, Cornell University, June, 1948.
[6] Graves, Rodrigues, Goldblatt, and Meyer, Rev. Sci. Instr. **20**, 579 (1949).
[7] A. B. Lillie and J. P. Conner, Rev. Sci. Instr. **22**, 210 (1951).
[8] Jervis, Hemmendinger, Argo, and Taschek, Phys. Rev. **79**, 929 (1950).
[9] This correction of 0.6 percent is based on Fig. 4 of reference 1. A uniform distribution of T^3 in the Zr is assumed.
[10] Li, Whaling, Fowler, and Lauritsen, Phys. Rev. **83**, 298(A) (1951).
[11] W. A. Fowler and C. C. Lauritsen, Phys. Rev. **76**, 314 (1949).
[12] M. B. Stearns and B. D. McDaniel, Phys. Rev. **82**, 450 (1951).
[13] H. V. Argo, private communication. In reference 1 this ratio is incorrectly stated to be 0.117.

Properties of the Isotope Pu^{243}

S. G. Thompson, K. Street, Jr., A. Ghiorso, and F. L. Reynolds*
Radiation Laboratory and Department of Chemistry, University of California, Berkeley, California
(Received July 30, 1951)

INVESTIGATION in this laboratory of the higher isotopes of plutonium produced by neutron irradiation has provided confirmation of the existence and properties of the new isotope Pu^{243}

recently reported in this journal by Sullivan *et al.*[1] The work reported here was done using the extensively neutron irradiated plutonium samples previously described in this journal.[2] Following the irradiation, the plutonium, americium, and curium were separated from each other and from fission products and impurities. The relative amounts of plutonium, americium, and curium were measured and the isotopic compositions of the americium and plutonium were determined using a mass spectrograph. The ratio of the numbers of alpha-disintegrations from the isotopes Am^{242} and Am^{243} was determined by chemical separation with measured yield of the beta-particle emitting daughters Np^{238} and Np^{239} and the measurement of their relative amounts by differential absorption methods using conventional Geiger counters as a means of detection. It was found that the ratio of Am^{242}/Am^{243} was higher by a factor of more than ten than in samples of Am^{241} which had been subjected to comparable neutron irradiations. This result is interpreted to mean that essentially all of the Am^{243} was formed according to the reaction sequence (a) rather than (b).

$$\text{(a)}\quad Pu^{242}(n,\gamma)Pu^{243} \xrightarrow{\beta^-} Am^{243}$$

$$\text{(b)}\quad Am^{241}(n,\gamma)Am^{242}(n,\gamma)Am^{243}.$$

The total amounts of the isotopes Pu^{242} and Am^{243} found in the irradiated plutonium sample allow a calculation of the cross section for the reaction $Pu^{242}(n,\gamma)Pu^{243}$. This cross section was calculated as very roughly 10^2 barns, using an estimated value for the neutron flux. The cross section is subject to a large error due to uncertainty in the estimation of the flux.

Subsequently, samples of plutonium of relatively large Pu^{242} content were produced as indicated in part by the following reactions:

$$Am^{241}(n,\gamma)Am^{242} \xrightarrow{\text{electron capture}} Pu^{242}.$$

Samples of this plutonium were then irradiated with neutrons to produce the isotope Pu^{243}. Following radiochemical purification of the plutonium, O'Kelley and Orth[3] made a rough investigation of the radiations of Pu^{243} using a beta-ray spectrograph and conventional absorption methods. They found the maximum energy of the beta-particles to be 0.39 Mev and gamma-ray energies of 0.095 Mev and 0.12 Mev, thus confirming the beta-particle energy of ~0.5 Mev measured by Sullivan *et al.*[1] The observed half-life of the radioactivity was 5.0±0.2 hours, and the amount of it corresponded roughly with the 10^2-barn cross section estimated above.

We wish to acknowledge the advice and assistance of Professor Glenn T. Seaborg whose help contributed greatly to the success of this work.

The successful handling in a safe manner of the radioactivity involved was made possible through the use of remote control equipment and excellent protective devices provided by Nelson Garden and the members of his Health Chemistry group. In this connection we especially wish to thank C. M. Gordon, W. G. Ruehle, and J. M. Davis for assistance during the experiments.

* This work was performed under the auspices of the AEC.

[1] Sullivan, Pyle, Studier, Fields, and Manning, Phys. Rev. **83**, 1267 (1951).

[2] Thompson, Street, Jr., Ghiorso, and Reynolds, Phys. Rev. **80**, 1180 (1950).

[3] G. D. O'Kelley and D. A. Orth, private communication.

Volkoff's Massive Spheres

AMAL KUMAR RAYCHAUDHURI
Physics Laboratory, Asutosh College, Calcutta, India
(Received July 26, 1951)

If one writes the static spherically symmetric line element in the form

$$ds^2=-e^{\lambda}dr^2-r^2(d\theta^2+\sin^2\theta d\varphi^2)+e^{\nu}dt^2\ldots \qquad (1)$$

where λ and ν are functions of r alone, one gets for a sphere of constant density ρ,

$$e^{-\lambda}=1-x^2+(K/x)\ldots \qquad (2)$$

where $x=r/R$, $R^2=3/8\pi\rho$ and K is an integration constant.

While in the usual Schwarzschild interior solution, K is put equal to zero to avoid a singularity at the origin, Volkoff[1] and Wyman[2] have recently considered interesting solutions with $K>0$ and have found that as K increases the radius of a sphere of a given density increases, tending to infinity as K is indefinitely increased. However they have restricted their considerations to the coordinate radius which has no physical significance. If instead, one considers the proper radius r_0 given by $\int_0^r e^{\lambda/2}dr$, one gets the interesting and rather surprising result that as K increases, the proper radius r_0 decreases monotonically, tending to a finite lower limit as $K\to\infty$. From the point of view of radial length, therefore, these spheres for a given density have definite upper and lower limits to their dimension.

One may, however, also consider the proper volume given by $v_0=4\pi\int_0^r e^{\lambda/2}r^2dr$ and this quantity is found to tend to infinity as K tends to infinity.

Another point of some interest in the Volkoff-Wyman solution is the influence of the singularity on the field. For weak fields, $\frac{1}{2}\nu'(=\frac{1}{2}d\log g_{44}/dr)$ gives the newtonian gravitational force and, although this approximation breaks down for strong fields, ν' always gives qualitatively some idea about the nature of the "field of force." In the Volkoff-Wyman solution, the condition of fit gives [Eq. (3.13) of Wyman's paper]—

$$m=(4/3)\pi\rho r_b^3-\tfrac{1}{2}KR=M-\tfrac{1}{2}KR \qquad (3)$$

and in the outside space $r\geq r_b$, $e^{\nu}=1-2(m/r)$, so that

$$\tfrac{1}{2}\nu'=m/r^2=(1/r^2)(M-\tfrac{1}{2}KR).$$

Thus in this region the effect of the singularity is to decrease the attractive field. Near the origin, as $r\to 0$, with $K=0$, $\nu'\to 0$, and one gets a vanishing gravitational intensity at the center just as in newtonian theory; however, with $K>0$, ν' tends to $+\infty$ as $1/r$. Thus, in the neighborhood of the origin, the singularity introduces an attractive field of force. The presence of an infinite attractive field in this region is also apparent from the infinite negative pressure gradient.

Equation (3) suggests an identification of the singularity with a negative mass particle; in fact, if ρ and K together tend to zero keeping $K/\rho^{\frac{1}{2}}$ constant, the solution degenerates to the Schwarzschild solution for a particle of negative mass at the origin. The foregoing considerations therefore seem to indicate that a negative-mass particle (placed at the center of a sphere of positive density) acts as the source of an attractive field at short distances and a repulsive field at large distances.

[1] G. M. Volkoff, Phys. Rev. **55**, 413 (1939).

[2] M. Wyman, Phys. Rev. **75**, 1930 (1949).

Threshold for Photoneutron Reaction in Th^{232}

L. B. MAGNUSSON, J. R. HUIZENGA, P. R. FIELDS, M. H. STUDIER,
Argonne National Laboratory, Chicago, Illinois
AND
R. B. DUFFIELD
Physics Research Laboratory, Champaign, Illinois*
(Received August 6, 1951)

THE mass difference between the $4n+3$ and $4n$ series is accurately known at lead from various experimental measurements.[1] An accurate value for the Th^{232} photoneutron threshold would enable one to check alpha- and beta-decay energies by closed cycle calculations.

The method of detecting the (γ,n) product nucleus used for the U^{238} threshold[2] was applied in a similar manner for determination of the Th^{232} threshold. Samples of thorium nitrate were bombarded in the betatron x-ray beam at six energies in the range 6.7

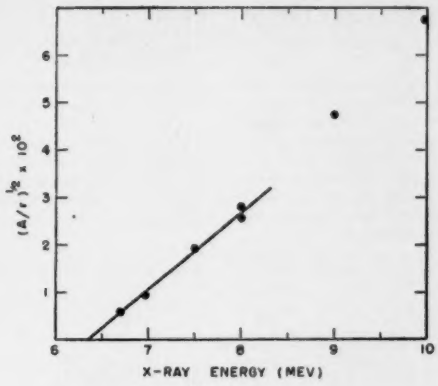

FIG. 1.

to 10 Mev. The bombarded thorium was chemically purified to remove fission products and thorium daughters. Uniform 25-mg samples of ThO_2 were prepared for counting by igniting painted layers of an organic thorium solution. The Th^{231} activity was measured with a thin window Amperex Geiger tube. The samples were covered with an aluminum absorber (7 mg/cm^2) to stop alpha-particles. Purified, unirradiated ThO_2 samples (25 mg) gave a counting rate of 3 count/min over background (16 count/min) with this arrangement. Growth of the Th^{231} daughters amounted to 1 count/min three hours after purification. Observed Th^{231} activities ranged from 2 to 60 count/min. The activities decayed with the correct half-life of about 26 hours. The x-ray beam intensity was monitored with a Victoreen integrating roentgen meter.

The square root of the total Th^{231} activity produced in each bombardment divided by the total roentgens registered by the Victoreen meter, i.e., $(A/r)^{\frac{1}{2}}$, appeared to be a linear function of bombardment energy within experimental error up to 8 Mev. The data are given in Fig. 1. Extrapolation by the method of least squares gives a threshold of 6.35±0.04 Mev for the $Th^{232}(\gamma, n)Th^{231}$ reaction. This value is in fair agreement with 6.1±0.2 Mev obtained indirectly by the method of neutron detection.[3]

* This work was supported in part by the joint program of the AEC and ONR.

[1] Huizenga, Magnusson, Simpson, and Winslow, Phys. Rev. **79**, 908 (1950); J. A. Harvey, Phys. Rev. **81**, 353 (1951); Kinsey, Bartholomew, and Walker, Phys. Rev. **82**, 380 (1951).

[2] Huizenga, Magnusson, Fields, Studier, and Duffield, Phys. Rev. **82**, 561 (1951).

[3] R. W. Parsons and C. H. Collie, Proc. Phys. Soc. (London) **A63**, 839 (1950).

Theory of Dibaric Particles

JANE S. PEASE*
Department of Physics and Laboratory for Nuclear Science and Engineering, Massachusetts Institute of Technology, Cambridge, Massachusetts
(Received August 3, 1951)

IN a series of seminars on the self-energy of the vector meson, J. Schwinger found it convenient to introduce as a mathematical artifice a system of spin 1 whose properties were intermediate between those of the vector meson and those of the electron. It is the purpose of this note to discuss the possible physical significance of this system.

A study was made of a quantum-mechanical system postulated to obey the equation of motion

$$(p_\mu\beta_\mu - ik)\psi = 0,$$

where β_μ was formed from the fusion of two Dirac-like matrices

$$\beta_\mu = \tfrac{1}{2}(\gamma_\mu^{(1)} + \gamma_\mu^{(2)})$$

obeying the commutation rules

$$\gamma_\mu^{(i)}\gamma_\nu^{(i)} + \gamma_\nu^{(i)}\gamma_\mu^{(i)} = 2\lambda^{(i)}\delta_{\mu\nu},$$
$$\gamma_\mu^{(1)}\gamma_\nu^{(2)} - \gamma_\nu^{(2)}\gamma_\mu^{(1)} = 0,$$

where $\lambda^{(1)} + \lambda^{(2)} = 2$. Such a system may be interpreted physically as a pair of strongly coupled spin ½ particles of different mass.

The β's are represented as 16×16 matrices using a fusion representation developed by de Broglie.[1] The present theory is intermediate between that of Kemmer[2] (in which $\lambda^{(1)} = \lambda^{(2)} = 1$) and that of Dirac (in which $\lambda^{(1)} = 2$, $\lambda^{(2)} = 0$), but because of the occurrence of discontinuities does not include either of these extreme cases.

The system was found to have the following properties:

(1) It could exist in either of two mass states, with masses

$$m = (k/c)[2/(1 \pm \lambda)]^{\frac{1}{2}}, \quad \lambda = (\lambda^{(1)}\lambda^{(2)})^{\frac{1}{2}},$$

from which it is evident that the phenomenon of dibarism is peculiar to this intermediate case and would occur in neither the Kemmer case ($\lambda = 1$) nor the Dirac case ($\lambda = 0$).

(2) The spin angular momentum operator had eigenvalues 0, $\pm\hbar$; we note that the particle is a boson.

(3) The magnetic moment was similar to that of the Kemmer particle, except for an additional term (which vanished for spin eigenstates) of value

$$\pm(e\hbar c/2k)(\lambda^{(1)} \pm \lambda^{(2)});$$

there thus appear nonzero spin magnetic moments for states of zero spin, as might be expected from the fact that one is adding magnetic moments of particles of different masses.

(4) Transitions from the heavier (mass $n+\Delta n$) electron masses) to the lighter (mass n electron masses) state accompanied by gamma-emission were investigated. The lifetime of the heavier state, approximately

$$(9\times10^{-17}/n)(n/\Delta n)^2 \text{ sec},$$

proved too short to measure except for very small mass difference.

(5) Coulomb scattering, with and without change of mass, was also investigated; the cross section for the latter case reduced to the Rutherford formula as would be expected.

In its relativistic form, the theory was found to be unrealistic, because of the existence of negative energy states which, since the particle is a boson, cannot be filled up arbitrarily. These negative energy solutions may be accounted for by the binding energy associated with the fusion of the two spin ½ particles. It would therefore seem that the theory discussed above is meaningful only in the nonrelativistic limit.

The author would like to express her thanks to Professor Herman Feshbach for suggesting the problem and for many stimulating discussions.

* Now at the Rand Corporation, Santa Monica, California.

[1] L. de Broglie, Actualités sci. et ind. **181** (1934); **411** (1936).

[2] N. Kemmer, Proc. Roy. Soc. (London) **A173**, 91 (1939).

Note on the Relativistic Formula for Photoelectric Absorption

HARVEY HALL
University of Southern California, Los Angeles, California
(Received August 14, 1951)

RECURRING references[1] in the literature to the relativistic photoeffect formula

$$\frac{\phi_K}{\phi_0} \cong \frac{3}{2}\frac{Z^5}{137^4}\frac{\mu}{k}\exp[-\pi\alpha + 2\alpha^2(1-\log\alpha)] \qquad (1)$$

contain comments which indicate that the degree of validity of this formula is not generally understood. The notation of Eq. (1) is Heitler's.[2]

The derivation of this formula, published in 1934,[3] was originally criticized by Hulme *et al.*[4] It appears to have escaped attention,

however, that Hulme's criticism was removed in a rigorous treatment of the problem for the high energy limit in 1936.[6] Heitler in particular requotes the same criticism in the second edition of reference 2 in 1945. Current practice, on the other hand, appears to follow the pattern of quoting the criticism stated by Heitler, and then of using the formula anyway because it fits the data so well.

It is hoped that the present letter will suffice to establish recognition of the rigorous treatment on which Eq. (1) is based.

[1] E.g., W. Heitler, *The Quantum Theory of Radiation* (Clarendon Press, Oxford, 1945), second edition; Bishop, Collie, Halban, Hedgran, Siegbahn, du Toit, and Wilson, Phys. Rev. **70**, 113 (1950).
[2] See W. Heitler, reference 1, p. 126.
[3] H. Hall, Phys. Rev. **45**, 620 (1934).
[4] Hulme, McDougall, Buckingham, and Fowler, Proc. Roy. Soc. (London) **139**, 131 (1935).
[5] H. Hall, Revs. Modern Phys. **8**, 395 (1936).

New Aspects of the Pseudoscalar Meson Theory*

L. L. Foldy
Case Institute of Technology, Cleveland, Ohio
(Received August 16, 1951)

We wish to demonstrate here a canonical transformation on the hamiltonian describing the interaction of a neutral pseudoscalar meson field with a single nucleon through pseudoscalar coupling, which has the property that it reveals the equivalence theorem between pseudoscalar and pseudovector coupling in a new light and at the same time reduces the hamiltonian to a form in which it may be amenable to strong-coupling treatment.

The hamiltonian with which we begin is

$$H=\beta M+\boldsymbol{\alpha}\cdot\mathbf{p}+ig\beta\gamma^5\varphi_0+H_\pi,\quad H_\pi=\tfrac{1}{2}\int\{\pi^2+(\nabla\varphi)^2+\mu^2\varphi^2\}d\mathbf{x},\tag{1}$$

where all symbols have their usual meaning, units are chosen so that $\hbar$ and c are unity, and the subscript 0 represents the evaluation of the corresponding meson field quantity at the nucleon position. Under the canonical transformation

$$H\rightarrow H'=e^{iS}He^{-iS}$$

with

$$S=\tfrac{1}{2}\gamma^5\tan^{-1}\{g\varphi_0/M\}\tag{2}$$

the hamiltonian takes the form

$$H'=\beta M[1+g^2\varphi_0^2/M]^{\frac{1}{2}}+\boldsymbol{\alpha}\cdot\mathbf{p}+H_\pi+\frac{g}{4M}\int\frac{1}{1+g^2\varphi_0^2/M^2}[\boldsymbol{\sigma}\cdot\nabla\varphi_0-\gamma^5\pi_0]+[\boldsymbol{\sigma}\cdot\nabla\varphi_0-\gamma^5\pi_0]\frac{1}{1+g^2\varphi_0^2/M^2}\Big\}+\frac{g^2}{8M^2}\int\left[\frac{\delta(\mathbf{x}-\mathbf{x}_0)}{1+g^2\varphi_0^2/M^2}\right]^2d\mathbf{x}.\tag{3}$$

Hence we see that pseudoscalar coupling is equivalent to a nonlinear pseudovector coupling together with some additional non-spin-dependent nonlinear coupling terms.[1] It should be noted that the above transformation is exact to all orders in the coupling constant in contradistinction to other derived forms of the equivalence theorem.[2] The strong nonlinearity of the hamiltonian in the meson field is reminiscent of recent heuristic proposals by Heisenberg,[3] Finkelstein and Ruderman,[4] and Schiff,[5] and suggests the possibility that pseudoscalar meson coupling may provide the elements required for the explanation of nuclear force saturation and of the relative independence of one-particle motions in nuclei required by the nuclear shell model on a basis other than exchange forces.

The hamiltonian (3) is in a form such that the method of Foldy and Wouthuysen[6] may be applied to obtain the equivalent nonrelativistic hamiltonian. The result, disregarding all terms which vanish as the nucleon becomes infinitely heavy (after writing $g=fM$ and assuming f remains finite as $M\rightarrow\infty$), is

$$\mathcal{H}=M[1+f^2\varphi_0^2]^{\frac{1}{2}}-[\tfrac{1}{2}f\boldsymbol{\sigma}\cdot\nabla\varphi_0/(1+f^2\varphi_0^2)]+H_\mu+\frac{f^2}{8}\int\left[\frac{\delta(\mathbf{x}-\mathbf{x}_0)}{1+f^2\varphi_0^2}\right]^2d\mathbf{x}.\tag{4}$$

By the introduction of suitable source functions, it would appear possible to treat the hamiltonian (4) by the methods previously developed for strong coupling.

Similar treatments are possible for the charged pseudoscalar meson field with pseudoscalar coupling and for the second-quantized form of the Dirac field in both the Schrödinger and interaction representations. These, together with further investigations of the strong-coupling theory, will be presented in future publications.

* This work was supported by the AEC. Part of this work was carried out during a week's visit of the author to the University of Rochester. The hospitality of the latter institution is gratefully acknowledged.
[1] The last term is of course strongly divergent. However, in the second-quantized form of the Dirac theory its analog is the more familiar "contact" term.
[2] See, for example, K. M. Case, Phys. Rev. **76**, 1 (1949).
[3] W. Heisenberg, Z. Naturforsch. **5a**, 151 (1950).
[4] R. Finkelstein and M. Ruderman, Phys. Rev. **81**, 655 (1951).
[5] L. I. Schiff, Phys. Rev. **80**, 137 (1950); Phys. Rev. **83**, 239 (1951).
[6] L. L. Foldy and S. A. Wouthuysen, Phys. Rev. **78**, 29 (1950).

Nuclear Spin of Actinium 227

Frank S. Tomkins and Mark Fred
Argonne National Laboratory, Chicago, Illinois
and
William F. Meggers
National Bureau of Standards, Washington, D. C.
(Received August 13, 1951)

As part of a joint investigation of the actinium spectrum, interferometer exposures were made which yielded about 15 lines showing well-resolved hyperfine structure. The structure was in the form of flag patterns with either three or four components, with large degradation of spacing and intensity indicating a low nuclear spin. Since no more than four components were observed in spite of J values of at least 3 as shown by a term analysis, the number of levels in the split term is spin-limited, with $I=\frac{3}{2}$ for Ac^{227}, the isotope used. Evaluation of the nuclear magnetic dipole and electric quadrupole moments must await a more complete analysis of the spectrum, and will be reported later.

Erratum: A Self-Consistent Treatment of the Oxygen Dissociation Region in the Upper Atmosphere

[Phys. Rev. **83**, 109 (1951)]
H. E. Moses*
Department of Physics, Columbia University, New York, New York
and
Ta-You Wu
National Research Council of Canada, Ottawa, Canada

In Eq. (25) replace G_2 by G_2'.

In Appendix 1, replace the last two lines by "where G_1' is the statistical weight of two atoms in the ^3P state, and G_2' is 1 and is hence different from G_2."

In Appendix 4, Eq. (50) should be replaced by

$$B=\int_0^\infty\beta_\tau vF(v)dv=4.20\times10^{-21}T^{\frac{1}{2}}.\tag{50}$$

The value of B for $T=300°\text{K}$ is 7.25×10^{-20}. The equation for B' should be replaced by

$$B'=\int_0^\infty\beta_\tau' vF(v)dv=(G_1/G_1')(G_2'/G_2)(\nu_1^0/\nu_0)^3B\cong(1/24)B.$$

The above corrections do not affect any of the other results in the paper, since the correct expressions were used in calculating the results.
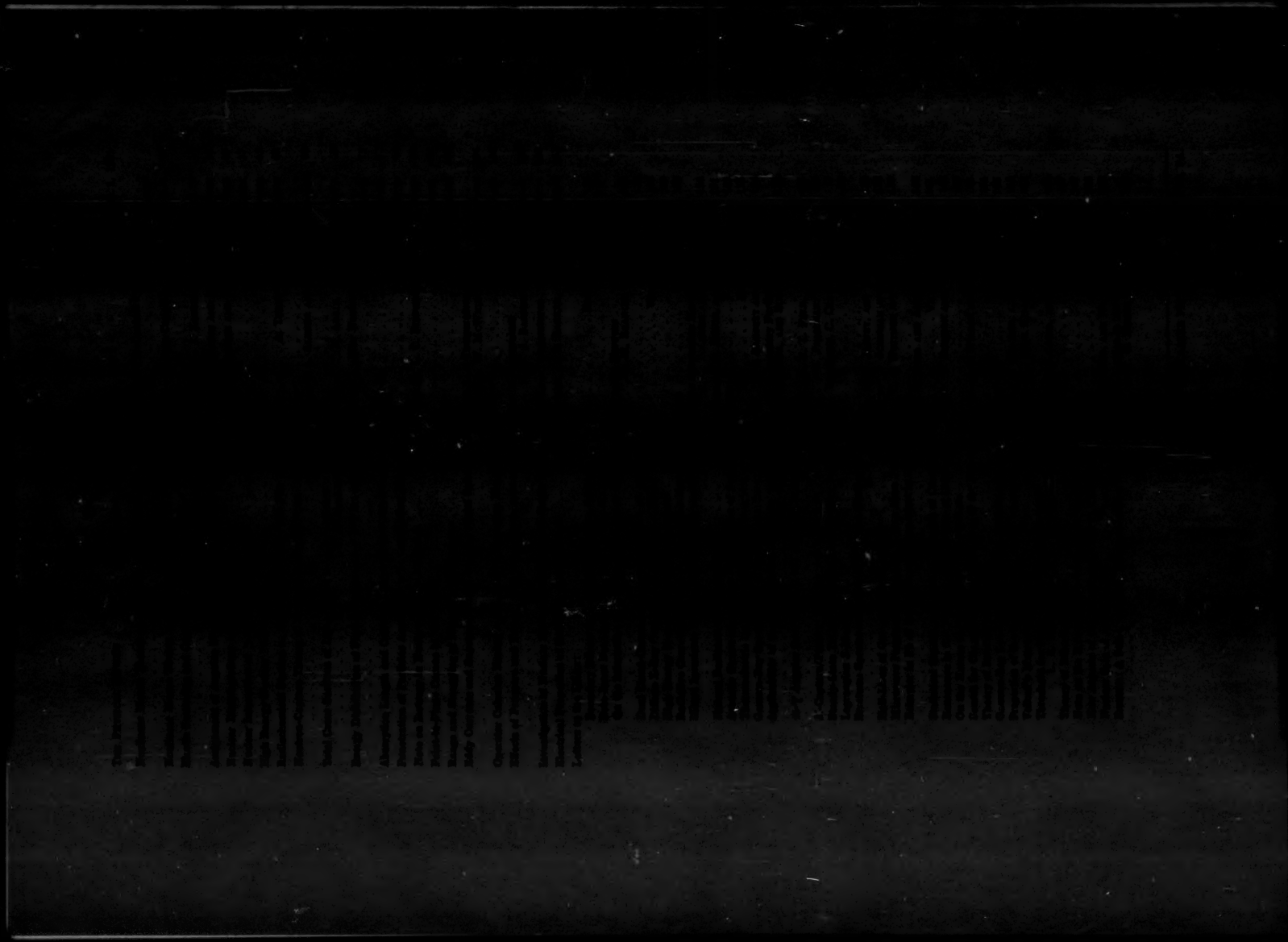
* Present address: Institute of Mathematics and Mechanics, New York University, New York, New York.